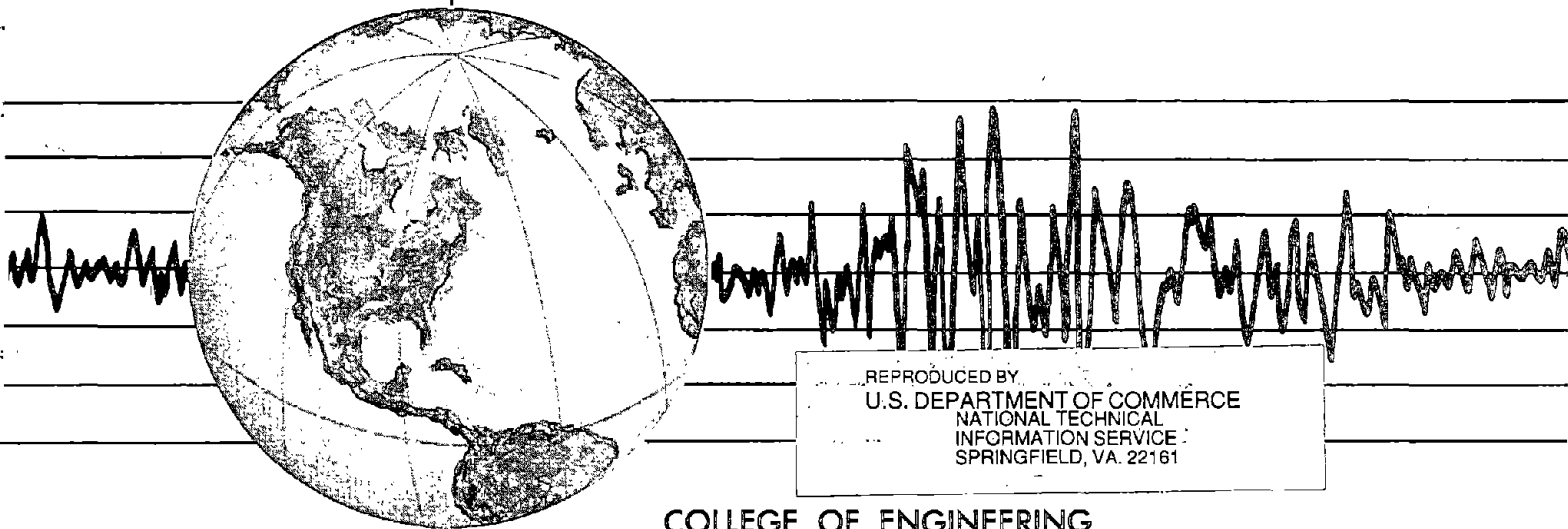REPORT NO.
UCB/EERC-87/07
JUNE 1987

EARTHQUAKE ENGINEERING RESEARCH CENTER

DYNAMIC ANALYSIS OF SEISMICALLY RESISTANT ECCENTRICALLY BRACED FRAMES

by

JAMES M. RICLES

EGOR P. POPOV

COLLEGE OF ENGINEERING

UNIVERSITY OF CALIFORNIA · Berkeley, California

50272-101

REPORT DOCUMENTATION PAGE	1. REPORT NO. NSF/ENG-87034	2.	3. Recipient's Accession No. PB88 173075/AS
4. Title and Subtitle Dynamic Analysis of Seismically Resistant Eccentrically Braced Frames			**5. Report Date** June 1987
			6.
7. Author(s) James M. Ricles and Egor P. Popov			**8. Performing Organization Rept. No.** UCB/EERC - 87/07
9. Performing Organization Name and Address Earthquake Engineering Research Center University of California 1301 South 46th Street Richmond, California 94804			**10. Project/Task/Work Unit No.**
			11. Contract(C) or Grant(G) No. (C) (G) ECE-8418487 CEE82-8402268
12. Sponsoring Organization Name and Address National Science Foundation American Iron & Steel Institute 1800 G. Street, N.W. 1000 16th Street, N.W. Washington, D.C. 20550 Washington, D.C. 20036			**13. Type of Report & Period Covered**
			14.

15. Supplementary Notes

16. Abstract (Limit: 200 words)

This report, which is a companion report to "Experiments on Eccentrically Braced Frames with Composite Floors", EERC Report No. 87-06, deals with the nonlinear analysis of eccentrically braced steel frames (EBFs) for cyclic static and dynamic loading conditions.

Two analytical models are developed using a finite element stress resultant formulation for the purpose of performing static and dynamic nonlinear analyses. The first of these elements is intended to model links in EBFs. The second element is used to model composite floor beams outside the link, accounting for moment-axial force interaction and the cyclic effects of composite action in a practical manner. Three numerical examples are presented concerning the nonlinear static analysis of links and EBFs. In the first two examples a bare steel and composite link specimen of the experimental study are analyzed. The third example involves an analysis of a previously tested EBF specimen. The results of the analyses are compared with the experimental behavior related to the three examples to illustrate the reliability and accuracy of the elements in predicting local link behavior as well as global frame response.

The report also deals with the seismic assessment of EBFs designed by plastic design principles.

17. Document Analysis   a. Descriptors

    earthquake engineering   dynamic analysis
    earthquake resistance
    eccentrically braced frames
    link

b. Identifiers/Open-Ended Terms

c. COSATI Field/Group

18. Availability Statement	19. Security Class (This Report) Unclassified	21. No. of Pages 359
Release unlimited	20. Security Class (This Page) Unclassified	22. Price

(See ANSI–Z39.18)   See Instructions on Reverse   OPTIONAL FORM 272 (4-77)
                                                            (Formerly NTIS–35)
                                                            Department of Commerce

DYNAMIC ANALYSIS OF
SEISMICALLY RESISTANT ECCENTRICALLY BRACED FRAMES

by

James M. Ricles

and

Egor P. Popov

DYNAMIC ANALYSIS OF

SEISMICALLY RESISTANT ECCENTRICALLY BRACED FRAMES

Abstract

This report deals with the nonlinear analysis of eccentrically braced steel frames for cyclic static and dynamic loading conditions. A companion report entitled *Experiments On Eccentrically Braced Frames With Composite Floors,* EERC Report No. 87/06, discusses experimental results obtained from a test program involving the seismic behavior of bare steel and composite links in eccentrically braced frames. Included in this companion report is a description of the eccentrically braced structural system, in addition to the need for analytical research which lead to the work presented in this report. Throughout this report reference will be made to Chapters 1 to 5 of the companion report.

In the first part of this report two analytical models are developed using a finite element stress resultant formulation for the purpose of performing static and dynamic nonlinear analyses. The first of these elements is intended to model links in eccentrically braced steel frames. The second element is used to model composite floor beams outside the link, accounting for moment-axial force interaction and the cyclic effects of composite action in a practical manner. Three numerical examples are then presented concerning the nonlinear static analysis of links and eccentrically braced steel frames. In the first two examples a bare steel and composite link specimen of the experimental study presented in the companion report are analyzed. The third example involves an analysis of a previously tested eccentrically braced steel frame specimen. The results of the analyses are compared with the experimental behavior related to the three examples to illustrate the reliability and accuracy of the elements in predicting local link behavior as well as global frame response.

The remaining portion of this report deals with the seismic assessment of eccentrically braced frames designed by plastic design principles. To achieve this task, a procedure for

nonlinear dynamic analysis is adopted to analyze eccentrically braced frames subjected to strong ground motions. In all, a total of three six-story designs were performed (Designs 1, 2, and 3) followed by analysis using several major earthquake records. Design 1 consists of an eccentrically braced frame with moment connections throughout the structural system. Design 2 is similar to Design 1 except that the links of the lower floors in Design 2 were strengthened in order to achieve better performance during an earthquake. Unlike Designs 1 and 2, pin connections were used in conjunction with moment connections in Design 3. Design 3 was analyzed several times where the pin connections were assumed to be flexible as well as rigid, respectively, enabling an evaluation of the use of flexible connections in eccentrically braced steel frames.

ACKNOWLEDGEMENTS

This report is largely based on the doctoral dissertation of James M. Ricles entitled "Experimental and Analytical Studies of Seismic Resistant Eccentrically Braced Steel Frames having Composite Floors," submitted in May 1987 to the Graduate Division of the University of California, Berkeley. The opinions expressed in the report are those of the authors and do not necessarily reflect the views of the sponsors.

TABLE OF CONTENTS

Preceding page blank

CHAPTER 6

CYCLICALLY LOADED LINK MODEL

6.1. General

The inelastic response of an EBF is dominated by the behavior of the active link regions. Therefore, the modeling of links must be accurate if reasonable results are to be obtained. Since high shear forces act in the active link regions, any appropriate formulation must include shear effects at the elastic and inelastic states. Recognizing this, previous researchers have developed models for active links taking into account both elastic and inelastic shear deformations.

One of these earlier models was that developed by Roeder [6]. Roeder modeled the shear link as a sandwich beam [69], where the web resisted shear force and the flanges resisted moment. The parallel component model [70,71] was utilized, with strain hardening due to shear and moment approximated by bilinear relationships for the action-deformation relationships. Combined isotropic and kinematic hardening were considered for shear. For moment, only kinematic hardening was considered. This model was intended to be primarily used in the case where the links yield in shear and the moment is small. However, as noted in this report and in previous findings [7], shear links are generally subjected to both high moments and shear forces. Primarily for this reason this element was not considered to be sufficiently accurate for proper EBF analysis.

Yang [72] attempted to model an active link using an inclined truss model. The approach, however, assumed equal end moments at both ends of the link. This is not the case for a general analysis of EBFs, for experimental results reported herein and by others [7] indicate that larger moments develop at the end of a link adjacent to a column.

A finite element model using a stress resultant formulation had been proposed by Hjelmstad [3]. The formulation utilized a yield surface similar to that suggested by Neal

[19,73]. However, the effects of strain hardening were not included. The use of this element by others [7] indicated that the link must be discretized into many elements in order to minimize the error in estimating the moment. This makes the element inefficient for global nonlinear analysis of EBFs. Furthermore, the fact that strain hardening is not included does not correlate with the cyclic link behavior of test specimens.

From the above discussion it appears that none of the previously developed link elements are suitable for an accurate prediction of link behavior under random cyclic loading. Consequently, a method was developed to more accurately and yet efficiently predict random cyclic link behavior in order to perform global static and dynamic nonlinear analyses of EBFs. The method involved a simplification of an enchanced general theory, which had been presented by Chen and Powell [79]. This general theory was enhanced by accounting for the effects of nonlinear shear deformations. Using the simplified formulation, a planar link element was developed.

The enhanced general theory and simplification of it are described below. In addition, a simple means of incorporating the effects of composite action is presented, based on the experimental behavior discussed in Chapters 3 and 4. This involved adjusting the parameters for the link element, in addition to developing a composite beam-column element to model the floor beam outside the link. Chapter 6 concludes with a presentation of the results of analyses of test specimens which had developed nonlinear cyclic behavior. The analyses were performed using the newly developed elements.

6.2. General Formulation

6.2.1. General Description

Consider a three-dimensional steel beam-column element which exhibits hysteretic behavior when subjected to cyclic loads. Such an element may be arbitrarily oriented in the global XYZ coordinate system, Fig. 6.1, where nodes I, J, and K define the element's length L and position. A local xyz coordinate system is also defined for the element, where node

K, together with nodes I and J, define the plane containing the local y-axis. Element properties are typically specified in the local xyz coordinate system.

The element consists of a linear elastic beam element with a nonlinear hinge at each end, as shown in Fig. 6.2. To facilitate the discussion this element will be referred to as the complete element, consisting of both hinges and the elastic beam. The hinges are considered to have a zero length. Inelastic behavior of the element is concentrated in the hinges, where each hinge is affected by axial force, two shear forces, two flexural moments, and a torsional moment. Both hinges are assumed to be initially rigid, therefore the initial stiffness of the complete element is that of only the elastic beam. As the forces at the element ends increase, the hinges can yield, resulting in a reduced stiffness of the complete element.

Each hinge consists of a series of subhinges, Fig. 6.3, where each subhinge possesses a rigid plastic action-deformation relationship. Each subhinge has a yield surface, where the yield surfaces of the subhinges are arranged in a consecutive manner as shown in Fig. 6.4(a) for a two-dimensional action space. The rigid plastic action-deformation relationships for a series of subhinges combine to produce a multi-linear function for each hinge as shown, and hence multi-linear relationships for the complete element. Under increasing deformation, the hinges strain harden, following the multi-linear action-deformation relationships. Strain hardening results in a translation of the yield surfaces, as shown in Fig. 6.4(b). The Mroz theory for yielding of metals [75,76] is used to establish tangent stiffness relationships between the actions and deformations of a yielded subhinge. The tangent stiffness of the subhinges are then combined with the elastic beam stiffness to produce the tangent stiffness of the complete element. If the actions at a hinge decrease, the hinge becomes rigid again as unloading occurs. Under such conditions the stiffness of the complete element is equal to that of the elastic beam element.

6.2.2. Degrees of Freedom

The complete element has two external nodes and two internal nodes, as shown in Fig. 6.2. The internal nodes exist at the end of the elastic beam element. The hinges connect the internal nodes with the external nodes. The external nodes connect to the global structure and have six degrees of freedom each, namely global translations and rotations about the XYZ axis, as shown in Fig. 6.5(a). In the local element coordinate system, six deformation degrees of freedom exist as shown in Fig. 6.5(b).

The transformation from the global displacements $\underline{r}$ to the element deformations $\underline{v}$ is accomplished by:

$$\underline{v} = \underline{a} \cdot \underline{r} \tag{6.1}$$

where

$$\underline{v}^T = \begin{bmatrix} v_1, & v_2, & v_3, & v_4, & v_5, & v_6 \end{bmatrix}$$

$$\underline{r}^T = \begin{bmatrix} r_1, & r_2, & \dots, & r_{11}, & r_{12} \end{bmatrix}$$

The displacement transformation matrix $\underline{a}$ is well known, and can be found in the literature [74].

The elastic element has degrees of freedom $\underline{q}$ which act at the internal nodes, as shown in Fig. 6.6, and are defined as:

$$\underline{q}^T = \begin{bmatrix} q_1, & q_2, & q_3, & q_4, & q_5, & q_6 \end{bmatrix} \tag{6.2}$$

The hinges at nodes I and J have deformations degrees of freedom $\underline{w}_p^I$ and $\underline{w}_p^J$, respectively, where:

$$\left[\underline{w}_p^I \right]^T = \begin{bmatrix} (v_1 - q_1), & (v_3 - q_3), & (v_5 - q_5)^*, & (v_6 - q_6)^* \end{bmatrix} \tag{6.3a}$$

and

$$\left[\underline{w}_p^J \right]^T = \begin{bmatrix} (v_2 - q_2), & (v_4 - q_4), & (v_5 - q_5)^{**}, & (v_6 - q_6)^{**} \end{bmatrix} \tag{6.3b}$$

The hinge deformations $\underline{w}_p^I$ and $\underline{w}_p^J$ represent the plastic deformations of the complete element. The torsional and axial hinge deformations are shared between the hinges at nodes I and J, hence:

$$(v_5 - q_5)^* + (v_5 - q_5)^{**} = (v_5 - q_5) \tag{6.4a}$$

$$(v_6 - q_6)^* + (v_6 - q_6)^{**} = (v_6 - q_6) \tag{6.4b}$$

The remaining terms in $\underline{w}_p^I$ and $\underline{w}_p^J$ represent total rotational deformations, that is, flexural and shear deformations are included in each term.

Each subhinge can in turn be expressed in terms of four deformation degrees of freedom $\underline{w}_{sp}$ which are associated with the hinge deformations $\underline{w}_p$. The sum of $\underline{w}_{sp}$ of each subhinge gives the deformation $\underline{w}_p$ of the hinge at a particular end of the complete element. The deformations $\underline{v}$ of the complete element are obtained by summing the elastic beam deformations and deformations of both hinges:

$$\underline{v} = \underline{q} + \underline{w}_p^* \tag{6.5}$$

where $\underline{w}_p^*$ are the deformations of both hinges, reading:

$$\left[\underline{w}_p^*\right]^T = \left[(v_1 - q_1), (v_2 - q_2), (v_3 - q_3), (v_4 - q_4), (v_5 - q_5), (v_6 - q_6)\right]$$

6.2.3. Complete Element Stiffness

A flexibility matrix is first formed for the elastic beam in terms of degrees of freedom $\underline{q}$. Thus, the beam element stiffness relationship in matrix form can be written as:

$$\underline{S} = \underline{K} \cdot \underline{q} \tag{6.6}$$

where $\underline{S}$ and $\underline{K}$, respectively, are the nodal force vector and stiffness matrix for the elastic beam element, in which

$$\underline{S}^T = \left[M_z^I, M_z^J, M_y^I, M_y^J, M_x, F\right]$$

6

and

$$
\underline{K} = \begin{bmatrix}
\dfrac{EI_z}{L}K_{ii} & \dfrac{EI_z}{L}K_{ij} & 0 & 0 & 0 & 0 \\
\dfrac{EI_z}{L}K_{ij} & \dfrac{EI_z}{L}K_{jj} & 0 & 0 & 0 & 0 \\
0 & 0 & \dfrac{EI_y}{L}K_{ii} & \dfrac{EI_y}{L}K_{ij} & 0 & 0 \\
0 & 0 & \dfrac{EI_y}{L}K_{ij} & \dfrac{EI_y}{L}K_{jj} & 0 & 0 \\
0 & 0 & 0 & 0 & \dfrac{GJ}{L} & 0 \\
0 & 0 & 0 & 0 & 0 & \dfrac{EA}{L}
\end{bmatrix}
$$

where

M_y, M_z = bending moments about the local y and z axes,

I, J = superscripts to identify end of element associated with nodes I and J,

M_x = torsional moment,

F = axial force,

K_{ii}, K_{ij}, K_{jj} = flexural stiffness factors,

EI_y, EI_z = bending rigidities about the local y and z axes,

GJ, EA = torsional and axial rigidities.

The relationship expressed by Eq. 6.6 is inverted to obtain a flexibility matrix for the elastic beam element. Elastic shear deformations are accounted for by appropriately adding shear flexibility matrices $\underline{f}_{sy}$ and $\underline{f}_{sz}$ to the flexibility matrix of the elastic beam, where:

$$
\underline{f}_{sy} = \frac{1}{GA_y^* L}\begin{bmatrix} 1 & 1 \\ 1 & 1 \end{bmatrix} \tag{6.7a}
$$

$$
\underline{f}_{sz} = \frac{1}{GA_z^* L}\begin{bmatrix} 1 & 1 \\ 1 & 1 \end{bmatrix} \tag{6.7b}
$$

in which GA_y^* and GA_z^*, respectively, are the effective shear rigidities associated with shear

deformations about the y and z axes.

Thus, the elastic beam element flexibility relationship is obtained which includes the effects of shear, reading:

$$\underline{q} = \underline{F} \cdot \underline{S}$$

(6.8)

where $\underline{F}$ is the flexibility matrix for the elastic beam element defined as:

$$\underline{F} = \begin{bmatrix} \frac{L}{EI_z}F_{ii_z} + \frac{1}{GA_z^*L} & -\frac{L}{EI_z}F_{ij_z} + \frac{1}{GA_z^*L} & 0 & 0 & 0 & 0 \\ -\frac{L}{EI_z}F_{ij_z} + \frac{1}{GA_z^*L} & \frac{L}{EI_z}F_{jj_z} + \frac{1}{GA_z^*L} & 0 & 0 & 0 & 0 \\ 0 & 0 & \frac{L}{EI_y}F_{ii_y} + \frac{1}{GA_y^*L} & -\frac{L}{EI_y}F_{ij_y} + \frac{1}{GA_y^*L} & 0 & 0 \\ 0 & 0 & -\frac{L}{EI_y}F_{ij_y} + \frac{1}{GA_y^*L} & \frac{L}{EI_y}F_{jj_y} + \frac{1}{GA_y^*L} & 0 & 0 \\ 0 & 0 & 0 & 0 & \frac{L}{GJ} & 0 \\ 0 & 0 & 0 & 0 & 0 & \frac{L}{EA} \end{bmatrix}$$

This elastic beam flexibility matrix $\underline{F}$ is modified by adding the flexibility of the hinges, resulting in the flexibility matrix for the complete element.

In multi-dimensional action space, each hinge has a 6x6 flexibility matrix $\tilde{f}_p$ in terms of its axial and torsional deformations associated with the x axis, and flexural and shear deformations about the y and z axes. As noted previously, the deformation of the hinge is the sum of the corresponding deformations of its yielding subhinges. Hence:

$$d\underline{\tilde{w}}_p = \sum_i d\underline{\tilde{w}}_{spi}$$

(6.9)

where

$d\underline{\tilde{w}}_p$ = deformation increment of a hinge,

$d\underline{\tilde{w}}_{spi}$ = deformation increment of associated subhinge i.

The hinge flexibility matrix $\tilde{f}_p$ in turn is the sum of the subhinge flexibility matrices. That is, a hinge flexibility relationship can be written as:

$$d\underline{\tilde{w}}_p = \underline{\tilde{f}}_p \cdot d\underline{\tilde{S}}$$

$$= \sum_i \underline{\tilde{f}}_{spi} \cdot d\underline{\tilde{S}} \tag{6.10}$$

where $\underline{\tilde{f}}_{spi}$ and $d\underline{\tilde{S}}$, respectively, are the flexibility matrix of a subhinge, and action increment acting on the hinge, defined as

$$d\underline{\tilde{S}}^T = \left[dM_z, \; dM_y, \; dM_x, \; dV_y, \; dV_z, \; dF \right]$$

The actions V_y and V_z represent the shear forces acting along the y and z axes.

Before yielding of a subhinge occurs, the flexibility matrix of the subhinge is null and therefore has no effect on the flexibility of the hinge and the complete element. After yielding, the subhinge develops flexibility and therefore contributes to the flexibility of the hinge and complete element. For the hinge at node I, the incremental action-deformation relationship can be expressed as:

$$d\underline{\tilde{w}}_p^I = \begin{Bmatrix} d\Theta_z^I \\ d\Theta_y^I \\ (dv_5 - dq_5)^* \\ d\gamma_z^I \\ d\gamma_y^I \\ (dv_6 - dq_6)^* \end{Bmatrix} = \underline{\tilde{f}}_P^I \begin{Bmatrix} dM_z^I \\ dM_y^I \\ dM_x \\ dV_y \\ dV_z \\ dF \end{Bmatrix} \tag{6.11a}$$

Likewise, for the complete hinge at node J:

$$d\underline{\tilde{w}}_P^J = \left\{ \begin{array}{c} d\Theta_z^J \\ d\Theta_y^J \\ (dv_5 - dq_5)^{**} \\ d\gamma_z^J \\ d\gamma_y^J \\ (dv_6 - dq_6)^{**} \end{array} \right\} = \tilde{f}_P^J \left\{ \begin{array}{c} dM_z^J \\ dM_y^J \\ dM_x \\ dV_y \\ dV_z \\ dF \end{array} \right\} \tag{6.11b}$$

where

$d\underline{\tilde{w}}_P^I, d\underline{\tilde{w}}_P^J$ = vectors of complete set of hinge deformations at nodes I and J,

$d\Theta_y, d\Theta_z$ = incremental rotation due to flexural deformations about the y and z axes,

$d\gamma_y, d\gamma_z$ = incremental rotation due to shear deformations about the the y and z axes,

I, J = superscripts to identify the nodes of the complete element,

$\tilde{f}_P^I, \tilde{f}_P^J$ = hinge flexibility matrices at nodes I and J.

The increment of total rotational deformation $d\phi$ is the sum of the flexural and shear deformations, where at node I:

$$d\phi_y^I = d\Theta_y^I + d\gamma_y^I$$

$$d\phi_z^I = d\Theta_z^I + d\gamma_z^I \tag{6.12a}$$

and at node J:

$$d\phi_y^J = d\Theta_y^J + d\gamma_y^J$$

$$d\phi_z^J = d\Theta_z^J + d\gamma_z^J \tag{6.12b}$$

According to Figs. 6.5(b) and 6.6, the above rotational deformation components have the following meaning:

$$d\phi_z^I = dv_1 - dq_1$$

$$d\phi_z^J = dv_2 - dq_2$$

$$d\phi_y^I = dv_3 - dq_3$$

$$d\phi_y^J = dv_4 - dq_4 \tag{6.13}$$

On neglecting second-order effects, the relationships between the shear forces and moments are:

$$dV_y = \frac{dM_z^I + dM_z^J}{L} \tag{6.14a}$$

$$dV_z = \frac{dM_y^I + dM_y^J}{L} \tag{6.14b}$$

Hence, the incremental action-deformation hinge relationships of Eqs. 6.11 (a) and 6.11 (b) can be expressed in terms of the deformation degrees of freedom $\underline{w}_P^I$ and $\underline{w}_P^J$. That is, at node I:

$$d\underline{w}_P^I = \begin{Bmatrix} (dv_1 - dq_1) \\ (dv_3 - dq_3) \\ (dv_5 - dq_5)^* \\ (dv_6 - dq_6)^* \end{Bmatrix} = \underline{f}_P^I \begin{Bmatrix} dM_z^I \\ dM_z^J \\ dM_y^I \\ dM_y^J \\ dM_x \\ dF \end{Bmatrix} \tag{6.15a}$$

and at node J:

$$dw_P^J = \begin{Bmatrix} (dv_2 - dq_2) \\ (dv_4 - dq_4) \\ (dv_5 - dq_5)^{**} \\ (dv_6 - dq_6)^{**} \end{Bmatrix} = f_P^J \begin{Bmatrix} dM_z^I \\ dM_z^J \\ dM_y^I \\ dM_y^J \\ dM_x \\ dF \end{Bmatrix} \qquad (6.15b)$$

The quantities f_P^I and f_P^J are 4x6 matrices which contain the appropriately arranged coefficients of the hinge flexibility matrices $\tilde{f}_P^I$ and $\tilde{f}_P^J$.

As can be noted from Eqs. 6.4 and 6.15, the hinge at node I affects the degrees of freedom v_1, v_3, v_5 and v_6, while the hinge at node J affects the degrees of freedom v_2, v_4, v_5 and v_6. Therefore, the hinge flexibility coefficients of f_P^I and f_P^J can be simply added to the appropriate coefficients of the elastic beam flexibility matrix F in order to obtain the tangent flexibility matrix F_t for the complete element.

Thus, using Eqs. 6.8, 6.15 (a), and 6.15 (b) the action-deformation relationship is obtained for the complete element expressed in terms of the degrees of freedom v:

$$d\underline{v} = d\underline{q} + d\underline{w}_P^{\bullet}$$

$$= \underline{F}_t \cdot d\underline{S} \qquad (6.16)$$

where

$$dq + dw_p^* = \begin{Bmatrix} dq_1 + (dv_1 - dq_1) \\ dq_2 + (dv_2 - dq_2) \\ dq_3 + (dv_3 - dq_3) \\ dq_4 + (dv_4 - dq_4) \\ dq_5 + (dv_5 - dq_5)^* + (dv_5 - dq_5)^{**} \\ dq_6 + (dv_6 - dq_6)^* + (dv_6 - dq_6)^{**} \end{Bmatrix} = \begin{Bmatrix} dv_1 \\ dv_2 \\ dv_3 \\ dv_4 \\ dv_5 \\ dv_6 \end{Bmatrix}$$

and

$$d\underline{S}^T = \begin{bmatrix} dM_z^I, & dM_z^J, & dM_y^I, & dM_y^J, & dM_x, & dF \end{bmatrix}$$

Having determined the 6x6 tangent flexibility matrix $\underline{F}_t$, this matrix is inverted to obtain a 6x6 element tangent stiffness $\underline{K}_t$. That is:

$$\underline{K}_t = \begin{bmatrix} \underline{F}_t \end{bmatrix}^{-1} \tag{6.17}$$

The matrix $\underline{F}_t$ is positive definite because only deformation modes are represented by this matrix. Therefore $\underline{F}_t$ can be inverted.

6.2.4. Hinge Flexibility

From Eq. 6.10 it follows that the vector of actions $\tilde{\underline{S}}$ affecting the deformations of a hinge is defined as:

$$\tilde{\underline{S}}^T = \begin{bmatrix} M_z, & M_y, & M_x, & V_y, & V_z, & F \end{bmatrix} \tag{6.18}$$

Consider a subhinge i of a complete hinge, idealizing the subhinge as being rigid-plastic. Let $d\tilde{\underline{w}}_{spi}$ be the corresponding vector of the increment of plastic deformations, where

$$\begin{bmatrix} d\tilde{\underline{w}}_{spi} \end{bmatrix}^T = \begin{bmatrix} d\Theta_z, & d\Theta_y, & d\Theta_x, & d\gamma_z, & d\gamma_y, & d\delta \end{bmatrix}$$

in which $d\Theta_x$ and $d\delta$, respectively, are the increment in torsional deformation about the x-axis, and the axial deformation. It is necessary to obtain for the subhinge a flexibility rela-

tionship of the form:

$$d\widetilde{\underline{w}}_{spi} = \widetilde{\underline{f}}_{spi} \cdot d\underline{\widetilde{S}}$$ (6.19)

where $\widetilde{\underline{f}}_{spi}$ is the subhinge flexibility matrix. To achieve this, the following assumptions are made:

(1) Let $\Phi(\underline{\widetilde{S}})$ be the yield function defining a surface which translates in action space due to strain hardening. After some amount of hardening has taken place, the yield function is $\Phi(\underline{\widetilde{S}} - \underline{\alpha})$, where $\underline{\alpha}$ is the vector defining the location of the origin of the yield surface. This is illustrated in Fig. 6.7 for a two-dimensional action space. The direction of translation is governed by the hardening rule, to be discussed later.

(2) Drucker's postulate [77] applies, which states that the network done by an external agency acting over a cycle of stress is positive. Consequently, the following holds:

(a) The yield surface is convex for a stable work-hardening material.

(b) Any increment of plastic deformation is perpendicular to the yield surface, hence the equation for the yield surface, $\Phi(\underline{\widetilde{S}} - \underline{\alpha})$, is a plastic potential function.

(c) An increment of plastic deformation is linearly related to the action increment.

If the action point is on the yield surface, continued loading generates an increment of plastic deformation $d\widetilde{\underline{w}}_{spi}$. According to Drucker's postulate, this deformation is perpendicular to the yield surface, hence:

$$d\underline{\widetilde{w}}_{spi} = \underline{n} \cdot \lambda_i$$ (6.20)

where $\underline{n}$ is an outward normal unit vector from the yield surface at the point of action. λ_i is a scalar defining the magnitude of plastic deformation of the subhinge. Because the yield surface is considered to be a plastic potential function, the direction of the outward normal to the yield surface is the gradient of the yield function. Hence:

14

$$\underline{n} = \frac{\underline{\Phi},_{\tilde{S}}}{\sqrt{\underline{\Phi},_{\tilde{S}}^T \cdot \underline{\Phi},_{\tilde{S}}}} \tag{6.21}$$

in which $\underline{\Phi},_{\tilde{S}}$ is the gradient of the yield function. That is:

$$\underline{\Phi},_{\tilde{S}}^T = \left[\frac{\partial \Phi}{\partial M_z}, \frac{\partial \Phi}{\partial M_y}, \frac{\partial \Phi}{\partial M_x}, \frac{\partial \Phi}{\partial V_y}, \frac{\partial \Phi}{\partial V_z}, \frac{\partial \Phi}{\partial F} \right]$$

Consider an increment of action $d\underline{\tilde{S}}$ shown in Fig. 6.7. The component of $d\underline{\tilde{S}}$ in the direction of $\underline{n}$ is $d\underline{\tilde{S}}_n$, and is defined by:

$$d\underline{\tilde{S}}_n = \underline{n} \cdot (\underline{n}^T \cdot d\underline{\tilde{S}}) \tag{6.22}$$

Since by Drucker's postulate the plastic deformation increment is linearly related to the action increment, assume:

$$d\underline{\tilde{S}}_n = \underline{K}_{spi} \cdot d\underline{\tilde{w}}_{spi} \tag{6.23}$$

in which $\underline{K}_{spi}$ is a diagonal plastic stiffness matrix from the individual action-deformation relationships for the subhinge. That is, the off diagonal terms in $\underline{K}_{spi}$ are zero, with the diagonal terms defined as:

$$\underline{K}_{spi} = \left[K_{pM,i}, K_{pM,i}, K_{pM,i}, K_{pV,i}, K_{pV,i}, K_{pFi} \right] \tag{6.24}$$

The selection of the diagonal terms must be carefully specified in order to provide appropriate post-yield stiffness of the complete element. This will be discussed later.

If Eqs. 6.20 and 6.22 are substituted into Eq. 6.23, and the result premultiplied by $\underline{n}^T$, it follows that:

$$\underline{n}^T \cdot d\underline{\tilde{S}} = \underline{n}^T \cdot \underline{K}_{spi} \cdot \underline{n} \cdot \lambda_i \tag{6.25}$$

Therefore:

$$\lambda_i = \frac{n^T \cdot d\tilde{\underline{S}}}{\underline{n}^T \cdot \underline{K}_{spi} \cdot \underline{n}} \qquad (6.26)$$

With λ_i now defined, the increment of plastic deformation for the subhinge can be computed due to an increment of action. Upon substituting for λ_i into Eq. 6.20:

$$d\tilde{\underline{w}}_{spi} = \frac{n \cdot n^T}{\underline{n}^T \cdot \underline{K}_{spi} \cdot \underline{n}} \, d\tilde{\underline{S}} \qquad (6.27)$$

Therefore, by referring to Eq. 6.19 the required flexibility matrix of a yielded subhinge is obtained, reading:

$$\tilde{\underline{f}}_{spi} = \frac{n \cdot n^T}{\underline{n}^T \cdot \underline{K}_{spi} \cdot \underline{n}} \qquad (6.28)$$

As noted previously, the 6x6 flexibility matrix $\tilde{f}_p$ of a hinge is the sum of its yielded subhinges. Thus:

$$\tilde{\underline{f}}_P = \sum_{i=1}^{k} \tilde{\underline{f}}_{spi} \qquad (6.29)$$

where k represents the number of yielded subhinges.

After determining $\tilde{f}_p$ for the hinges at nodes I and J, the flexibility relationships are recast in terms of axial and flexural actions and the associated axial and total rotational deformations using Eqs. 6.12 to 6.14. In this manner the hinge flexibility matrices f_p^I and f_p^J of Eqs. 6.15 (a) and 6.15 (b) are obtained.

6.2.5. Hardening Rule

After initial yielding occurs, the behavior of a subhinge is assumed to obey the Mroz strain hardening rule for yield in metals [75,76]. In this analysis consider a hinge to have three subhinges. The location of the initial yield surface for each subhinge is plotted in a two-dimensional action space as shown in Fig. 6.8. Assume the current state, defined by $\tilde{S}_1$, has reached a point P1 on yield surface YS1, causing subhinge 1 to yield. Continued

loading will cause yield surface YS1 to translate towards yield surface YS2, in the direction defined by a vector from point P1 to the corresponding point P2. The point P2 lies on yield surface YS2 and is defined by $\tilde{\underline{S}}_2$. For points P1 and P2 to be corresponding, their outward normals $\underline{n}_1$ and $\underline{n}_2$ must be parallel, i.e.,

$$\underline{n}_1^T \cdot \underline{n}_2 = 1 \tag{6.30}$$

The translation of yield surface YS1 is depicted in Fig. 6.9(a). Yield surface YS2 does not begin to translate until subhinge 2 yields.

The vector of actions $\tilde{\underline{S}}_2$ at point P2 can be determined knowing the sizes and current positions of yield surfaces YS1 and YS2. In multi-dimensional space this is defined as:

$$\tilde{\underline{S}}_2 = \tilde{\underline{S}}_{u12}(\tilde{\underline{S}}_1 - \underline{\alpha}_1) + \underline{\alpha}_2 \tag{6.31}$$

in which $\underline{\alpha}_1$ and $\underline{\alpha}_2$, respectively, are the current positions of the origins of the yield surfaces YS1 and YS2. The matrix $\tilde{\underline{S}}_{u12}$ is square, whose off diagonal terms are zero. Each diagonal term of $\tilde{\underline{S}}_{u12}$ represents the relative size of yield surface YS2 to YS1 along the axes, i.e.:

$$diag\left[\tilde{\underline{S}}_{u12}\right] = \left[\frac{M_{zu2}}{M_{zu1}}, \frac{M_{yu2}}{M_{yu1}}, \frac{M_{xu2}}{M_{xu1}}, \frac{V_{yu2}}{V_{yu1}}, \frac{V_{zu2}}{V_{zu1}}, \frac{F_{u2}}{F_{u1}}\right]$$

Observing that the vector $\tilde{\underline{S}}_2 - \tilde{\underline{S}}_1$ defines a vector from point P1 to P2 in Fig. 6.9(a), it follows that the increment of translation $d\underline{\alpha}_1$ of yield surface YS1 is equal to:

$$d\underline{\alpha}_1 = (\tilde{\underline{S}}_2 - \tilde{\underline{S}}_1)d\alpha_1^* \tag{6.32}$$

where $d\alpha_1^*$ is a scalar defining the magnitude of translation of yield surface YS1. To determine $d\alpha_1^*$, Eq. 6.31 is substituted into 6.32 to obtain:

$$d\underline{\alpha}_1 = \left[(\tilde{\underline{S}}_{u12} - \underline{I})\tilde{\underline{S}}_1 - (\tilde{\underline{S}}_{u12}\underline{\alpha}_1 - \underline{\alpha}_2)\right]d\alpha_1^* \tag{6.33}$$

From the definition of the yield function, point P1 lies on yield surface YS1 when:

$$\Phi(\widetilde{\underline{S}}_1 - \underline{\alpha}_1) = 1 \tag{6.34}$$

The fact that the action point P1 must remain on the yield surface YS1 during translation requires that:

$$d\Phi = \underline{\Phi},{}^T_{\overline{S}}(d\widetilde{\underline{S}}_1 - d\underline{\alpha}_1) = 0 \tag{6.35}$$

Upon substituting Eqn. 6.33 into 6.35:

$$\underline{\Phi},{}^T_{\overline{S}}d\widetilde{\underline{S}}_1 - \underline{\Phi},{}^T_{\overline{S}}\left[(\widetilde{\underline{S}}_{u12} - \underline{I})\widetilde{\underline{S}}_1 - (\widetilde{\underline{S}}_{u12}\underline{\alpha}_1 - \underline{\alpha}_2)\right]d\alpha_1^* = 0 \tag{6.36}$$

Hence:

$$d\alpha_1^* = \cfrac{\underline{\Phi},{}^T_{\overline{S}}d\widetilde{\underline{S}}_1}{\underline{\Phi},{}^T_{\overline{S}}\left[(\widetilde{\underline{S}}_{u12} - \underline{I})\widetilde{\underline{S}}_1 - (\widetilde{\underline{S}}_{u12}\underline{\alpha}_1 - \underline{\alpha}_2)\right]} \tag{6.37}$$

Thus, yield surface YS1 undergoes an increment of translation $d\underline{\alpha}_1$ due to an increment of action $d\widetilde{\underline{S}}_1$, where:

$$d\underline{\alpha}_1 = \cfrac{\left[(\widetilde{\underline{S}}_{u12} - \underline{I})\widetilde{\underline{S}}_1 - (\widetilde{\underline{S}}_{u12}\underline{\alpha}_1 - \underline{\alpha}_2)\right]\underline{\Phi},{}^T_{\overline{S}} \cdot d\widetilde{\underline{S}}_1}{\underline{\Phi},{}^T_{\overline{S}}\left[(\widetilde{\underline{S}}_{u12} - \underline{I})\widetilde{\underline{S}}_1 - (\widetilde{\underline{S}}_{u12}\underline{\alpha}_1 - \underline{\alpha}_2)\right]} \tag{6.38}$$

If by the increment of action where yield surface YS1 translates that yield surface YS2 is reached, yield surfaces YS1 and YS2 will translate together towards a corresponding point P3 on yield surface YS3. This situation is illustrated in Fig. 6.9(b).

In the general case where subhinge i has yielded, yield surface YSi will translate towards yield surface YSj, where the translation increment is equal to:

$$d\underline{\alpha}_i = \cfrac{\left[(\underline{S}_{uij} - \underline{I})\widetilde{\underline{S}}_i - (\underline{S}_{uij}\underline{\alpha}_i - \underline{\alpha}_j)\right]\underline{\Phi},{}^T_{\overline{S}} \cdot d\widetilde{\underline{S}}_i}{\underline{\Phi},{}^T_{\overline{S}}\left[(\underline{S}_{uij} - \underline{I})\widetilde{\underline{S}}_i - (\underline{S}_{uij}\underline{\alpha}_i - \underline{\alpha}_j)\right]} \tag{6.39}$$

An exception to this rule occurs when the outermost yield surface YSN is reached. This occurs when all the subhinges of a hinge have yielded. For this situation the direction of translation is obtained by assuming that an additional infinitely large yield surface exists.

18

Thus, the diagonal terms in $\underline{S}_{uij}$ are infinite, and it can be shown that the translation of yield surface YSN is equal to:

$$d\underline{\alpha}_N = \frac{\left[\tilde{\underline{S}}_N - \underline{\alpha}_N\right]\Phi_{,\tilde{S}}^T \cdot d\tilde{\underline{S}}_N}{\Phi_{,\tilde{S}}^T\left[\tilde{\underline{S}}_N - \underline{\alpha}_N\right]} \qquad (6.40)$$

The translation of yield surface YSN represented by Eq. 6.40 occurs along the radial direction connecting the origin of YSN to the current action point $\tilde{\underline{S}}_N$. This is what is known as Ziegler's hardening rule [80].

6.2.6. Loading-Unloading Criteria

The loading-unloading criteria must be able to differentiate between plastic flow and elastic unloading from any plastic state for any specified deformation increment. Various criteria have been used by past researchers [78,79,80,81,82,83]. The procedure used herein was based on the criterion that the magnitude of plastic deformation defined by λ_i (Eq. 6.26) must be positive during continued loading from the yield surface.

Hence, given that the current state $\tilde{\underline{S}}$ is on the yield surface, that is:

$$\Phi(\tilde{\underline{S}} - \underline{\alpha}) = 1 \qquad (6.41)$$

the loading of a subhinge i continues to occur if the increment of action $d\tilde{\underline{S}}$ is such that

$$\lambda_i = \frac{\underline{n}^T \cdot d\tilde{\underline{S}}}{\underline{n}^T \cdot \underline{K}_{spi} \cdot \underline{n}} \geq 0 \qquad (6.42)$$

while unloading of subhinge i occurs if

$$\lambda_i = \frac{\underline{n}^T \cdot d\tilde{\underline{S}}}{\underline{n}^T \cdot \underline{K}_{spi} \cdot \underline{n}} < 0 \qquad (6.43)$$

If the unloading criterion is met for any yield surface, then the same holds for all remaining yield surfaces pertaining to active subhinges of the same hinge. If unloading occurs from more than one yield surface, then the surfaces are separated by an amount equal to $\epsilon \cdot \underline{n}$, as

shown in Fig. 6.10(b), where as a result, points Pi, Pj, and Pk each have a distinguishable state. A very small value of $\varepsilon = 1\times10^{-6}$ was used in the analyses. In a general case, points Pi, Pj, and Pk during previous loading correspond to the points on the yield surfaces YSi, YSj, and YSk, as shown in Fig. 6.10(a). Distinguishable states are necessary for reasons of numerical stability in the event that reloading occurs along the same normal $\underline{n}$ as unloading (See Fig 6.10(b)).

6.2.7. Determination of Plastic Stiffness

As noted previously, the post yield behavior of the complete element is governed by the plastic stiffness matrix $\underline{K}_{spi}$ of each subhinge. For each subhinge, the determination of the coefficients of $\underline{K}_{spi}$ requires a knowledge of the complete action-deformation relationships. Since the matrix $\underline{K}_{spi}$ is diagonal, each action-deformation relationship is uncoupled. Thus the individual coefficients in $\underline{K}_{spi}$ for all subhinges can be obtained from separate applied actions, as indicated in Figs. 6.11 and 6.12. The relationships for axial load, shear, and torsion are straightforward since the corresponding internal force is constant along the length of the member. However a complication arises in the case of bending moment, for the flexural stiffness at the end of a member depends on the variation of moment along the member. In a concentrated hinge model it is not possible to account for all possible moment variations which may occur, thus assumptions must be made regarding the hinge properties. Under seismic loading the links of EBFs have in-plane end moments which cause double curvature of the links. Thus, one could consider obtaining an action-deformation relationship where the link is subjected to equal magnitudes of end moments causing double curvature, as shown in Fig. 6.12(a). Equal end moments, as shown in Fig. 6.12(b), are plausible for out-of-plane bending.

To determine a plastic stiffness coefficient of $\underline{K}_{spi}$ for action quantity $\widetilde{S}$, the reciprocal of the slope of the action-deformation relationship for the current state is equated to the combined flexibilities of the elastic beam, K_{S_i}, and all yielded subhinges. Thus, if a

subhinge 1 yields due to the axial force F exceeding the yield strength F_{Y_1}, such that:

$$F_{Y_1} \le F < F_{Y_2}$$

then

$$\frac{1}{K_{F_2}} = \frac{1}{K_{F_1}} + \frac{1}{K_{pF_1}}$$ (6.44)

Whence, the plastic stiffness coefficient K_{pF_1} for the first subhinge associated with axial force is given as

$$K_{pF_1} = \frac{K_{F_1} K_{F_2}}{K_{F_1} - K_{F_2}}$$ (6.45)

where K_{F_1} and K_{F_2}, respectively, are the axial stiffness of the elastic beam, and slope of the action-deformation relationship between the strengths F_{Y_1} and F_{Y_2}, as shown in Fig. 6.11(a). If subhinge i yields,

$$F_{Y_i} \le F < F_{Y_{i+1}}$$ (6.46)

and

$$\frac{1}{K_{F_{i+1}}} = \frac{1}{K_{F_1}} + \sum_{j=1}^{i} \frac{1}{K_{pF_j}}$$ (6.47)

It can therefore be shown that the plastic stiffness coefficient K_{pF_i} for subhinge i associated with axial force is given as:

$$K_{pF_i} = \frac{K_{F_i} K_{F_{i+1}}}{K_{F_i} - K_{F_{i+1}}}$$ (6.48)

In the general case, the plastic stiffness coefficient K_{pS_i} for subhinge i associated with the action S is defined as

$$K_{pS_i} = \frac{K_{S_i} K_{S_{i+1}}}{K_{S_i} - K_{S_{i+1}}}$$ (6.49)

where

$$S_{Y_i} \leq S < S_{Y_{i+1}} \tag{6.50}$$

In Eq. 6.49, K_{S_i} and $K_{S_{i+1}}$, respectively, are the slope of the action-deformation relationship between the strengths $S_{Y_{i-1}}$ and S_{Y_i}, and the slope between the strengths S_{Y_i} and $S_{Y_{i+1}}$. Note that S must be one of the actions represented in the vector $\tilde{S}$ defined by Eq. 6.18.

6.3. Simplified Formulation

The general link model formulation discussed above was simplified in order to perform economical nonlinear dynamic analyses of EBFs. The simplifications involved introducing assumptions in the general formulation. These assumptions included the following:

(1)   Properly designed EBF framing should not permit the development of large axial link forces. Hence, the effects of axial forces can be neglected.

(2)   EBFs can be considered to be planar requiring only in-plane analysis of links.

(3)   Since previous research [7] indicated that shear yielding does not appear to be significantly influenced by the presence of bending moment, a rectangular yield surface was adopted for the subhinges, as shown in Fig. 6.13. Each hinge consisted of three subhinges.

6.3.1. Degrees of Freedom

As a consequence of assumptions 1 and 2, the deformation degrees of freedom include only rotation about the z-axis. Thus, for the elastic beam:

$$\underline{q}^T = \begin{bmatrix} q_1, q_2 \end{bmatrix} \tag{6.51}$$

and for the hinges

$$\begin{bmatrix} \underline{w}_P^I \end{bmatrix}^T = \begin{bmatrix} v_1 - q_1 \end{bmatrix} \tag{6.52a}$$

$$\begin{bmatrix} \underline{w}_P^J \end{bmatrix}^T = \begin{bmatrix} v_2 - q_2 \end{bmatrix} \tag{6.52b}$$

The external nodes each have three global degrees of freedom associated with the X-Y

plane. These are shown in Fig. 6.14, and include translations about the X and Y axes and rotation about the Z axis. Consequently, from Fig. 6.14:

$$\underline{r}^T = \begin{bmatrix} r_1, r_2, r_3, r_4, r_5, r_6 \end{bmatrix} \qquad (6.53)$$

6.3.2. Complete Element Stiffness

The elastic beam element stiffness relationships are:

$$\underline{S} = \underline{K} \cdot \underline{q} \qquad (6.54)$$

where

$$\underline{S}^T = \begin{bmatrix} M_z^I, M_z^J \end{bmatrix}$$

and

$$\underline{K} = \frac{EI_z}{L} \begin{bmatrix} K_{ii,} & K_{ij,} \\ K_{ij,} & K_{jj,} \end{bmatrix}$$

The 2x2 flexibility matrix of the elastic beam, which includes the effects of shear deformations, is easily obtained from:

$$\underline{F} = \underline{K}^{-1} + \underline{f}_{sz} = \begin{bmatrix} F_{ii} & F_{ij} \\ F_{ij} & K_{jj} \end{bmatrix} \qquad (6.55)$$

in which

$$\underline{f}_{sz} = \frac{1}{GA_z^*L} \begin{bmatrix} 1 & 1 \\ 1 & 1 \end{bmatrix}$$

The hinge flexibility relationship is affected only by shear and flexural deformations, resulting in rotations about the z-axis. For the hinge at node I:

$$d\underline{\widetilde{w}}_P^I = \left\{ \begin{matrix} d\Theta_z^I \\ d\gamma_z^I \end{matrix} \right\} = \widetilde{f}_P^I \left\{ \begin{matrix} dM_z^I \\ dV_y \end{matrix} \right\}$$

(6.56a)

and at node J:

$$d\underline{\widetilde{w}}_P^J = \left\{ \begin{matrix} d\Theta_z^J \\ d\gamma_z^J \end{matrix} \right\} = \widetilde{f}_P^J \left\{ \begin{matrix} dM_z^J \\ dV_y \end{matrix} \right\}$$

(6.56b)

where the hinge flexibility matrices are obtained by summing the flexibility matrices of yielded subhinges:

$$\widetilde{f}_P^I = \sum_i \widetilde{f}_{spi}^I = \begin{bmatrix} \widetilde{f}_{ii}^I & \widetilde{f}_{ij}^I \\ \widetilde{f}_{ji}^I & \widetilde{f}_{jj}^I \end{bmatrix}$$

(6.57a)

$$\widetilde{f}_P^J = \sum_i \widetilde{f}_{spi}^J = \begin{bmatrix} \widetilde{f}_{ii}^J & \widetilde{f}_{ij}^J \\ \widetilde{f}_{ji}^J & \widetilde{f}_{jj}^J \end{bmatrix}$$

(6.57b)

Since from Eqs. 6.12 and 6.13:

$$dv_1 - dq_1 = d\Theta_z^I + d\gamma_z^I$$

(6.58a)

$$dv_2 - dq_2 = d\Theta_z^J + d\gamma_z^J$$

(6.58b)

and from 6.14 (a):

$$dV_y = \frac{dM_z^I + dM_z^J}{L}$$

(6.14a)

Thus the flexibility relationship for the hinge at node I becomes:

$$dv_1 - dq_1 = \left[\left(\tilde{f}'_{ii} + \tilde{f}'_{ji} + \frac{\tilde{f}'_{ij} + \tilde{f}'_{jj}}{L} \right) \quad , \quad \left(\frac{\tilde{f}'_{ij} + \tilde{f}'_{jj}}{L} \right) \right] \left\{ \begin{matrix} dM'_z \\ dM^J_z \end{matrix} \right\} \tag{6.59a}$$

and at node J:

$$dv_2 - dq_2 = \left[\left(\frac{\tilde{f}^J_{ij} + \tilde{f}^J_{jj}}{L} \right) \quad , \quad \left(\tilde{f}^J_{ii} + \tilde{f}^J_{ji} + \frac{\tilde{f}^J_{ij} + \tilde{f}^J_{jj}}{L} \right) \right] \left\{ \begin{matrix} dM'_z \\ dM^J_z \end{matrix} \right\} \tag{6.59b}$$

Consequently, for the complete element:

$$\left\{ \begin{matrix} dv_1 \\ dv_2 \end{matrix} \right\} = \underline{F}_t \left\{ \begin{matrix} dM'_z \\ dM^J_z \end{matrix} \right\} \tag{6.60}$$

where $\underline{F}_t$ is the flexibility matrix of the complete element, reading:

$$\underline{F}_t = \left[\begin{matrix} \left(F_{ii} + \tilde{f}'_{ii} + \tilde{f}'_{ji} + \frac{\tilde{f}'_{ij} + \tilde{f}'_{jj}}{L} \right) & \left(F_{ij} + \frac{\tilde{f}'_{ij} + \tilde{f}'_{jj}}{L} \right) \\ \left(F_{ij} + \frac{\tilde{f}^J_{ij} + \tilde{f}^J_{jj}}{L} \right) & \left(F_{jj} + \tilde{f}^J_{ii} + \tilde{f}^J_{ji} + \frac{\tilde{f}^J_{ij} + \tilde{f}^J_{jj}}{L} \right) \end{matrix} \right] \tag{6.61}$$

The 2x2 tangent stiffness matrix $\underline{K}_t$ for the complete element is easily obtained by inverting the tangent flexibility matrix $\underline{F}_t$, that is:

$$\underline{K}_t = \left[\underline{F}_t \right]^{-1} \tag{6.62}$$

6.3.3. Hinge Flexibility

The yield surface for each subhinge can be idealized as being constructed of two vertical facets and two horizontal facets, as shown in Fig. 6.15(a). Among these facets, the adjacent horizontal and vertical facets a and b have been identified. Yield functions and the outward normal vectors of facets a and b are indicated in Fig 6.15(a). Similar functions

and outward normal vectors can be defined for the two other facets. The plastic stiffness matrix $\underline{K}_{spi}$ for each subhinge considers only moment and shear forces. Thus for subhinge i:

$$\underline{K}_{spi} = \begin{bmatrix} K_{pM,i} & 0 \\ 0 & K_{pV,i} \end{bmatrix}$$

(6.63)

in which

$K_{pM,i}$ = plastic flexural stiffness coefficient for subhinge i,

$K_{pV,i}$ = plastic shear stiffness coefficient for subhinge i.

The flexibility matrix of a yielded subhinge depends on which facet the current state lies. There are three possible variations of the flexibility matrix of a yielded subhinge. Consider cases (i), (ii) and (iii) below:

Case (i) - Current state lies only on facet **a**. Hence only moment yielding occurs. Since for facet **a** the outward normal $\left[\underline{n}_a\right]^T = [1,0]$, the flexibility matrix for subhinge i is equal to:

$$\widetilde{f}_{spi} = \frac{\underline{n}_a \cdot \underline{n}_a^T}{\underline{n}_a^T \cdot \underline{K}_{spi} \cdot \underline{n}_a} = \begin{bmatrix} \dfrac{1}{K_{pM,i}} & 0 \\ 0 & 0 \end{bmatrix}$$

(6.64)

Case (ii) - Current state lies only on facet **b**. Thus only shear yielding occurs. Since for facet **b** the outward normal $\left[\underline{n}_b\right]^T = [0,1]$, the flexibility matrix for subhinge i is equal to:

$$\widetilde{f}_{spi} = \frac{\underline{n}_b \cdot \underline{n}_b^T}{\underline{n}_b^T \cdot \underline{K}_{spi} \cdot \underline{n}_b} = \begin{bmatrix} 0 & 0 \\ 0 & \dfrac{1}{K_{pV,i}} \end{bmatrix}$$

(6.65)

Case (iii) - Current state lies on both facets **a** and **b**. Therefore, both moment and shear yielding occur. When the current state lies on the intersection of two facets, Eq. 6.20 must

hold for each of these facets. The increment of plastic deformation for a yielded subhinge is the sum of the contributions from each facet. That is:

$$d\underline{\tilde{w}}_{spi} = d\underline{\tilde{w}}_{spi_a} + d\underline{\tilde{w}}_{spi_b} \tag{6.66}$$

where for facet a, using Eq. 6.27:

$$d\underline{\tilde{w}}_{spi_a} = \frac{\underline{n}_a \cdot \underline{n}_a{}^T}{\underline{n}_a{}^T \cdot \underline{K}_{spi} \cdot \underline{n}_a} \left\{ \begin{matrix} dM_z \\ dV_y \end{matrix} \right\} \tag{6.67a}$$

and for facet b:

$$d\underline{\tilde{w}}_{spi_b} = \frac{\underline{n}_b \cdot \underline{n}_b{}^T}{\underline{n}_b{}^T \cdot \underline{K}_{spi} \cdot \underline{n}_b} \left\{ \begin{matrix} dM_z \\ dV_y \end{matrix} \right\} \tag{6.67b}$$

Consequently, for subhinge i:

$$d\underline{\tilde{w}}_{spi} = \left[\frac{\underline{n}_a \cdot \underline{n}_a{}^T}{\underline{n}_a{}^T \cdot \underline{K}_{spi} \cdot \underline{n}_a} + \frac{\underline{n}_b \cdot \underline{n}_b{}^T}{\underline{n}_b{}^T \cdot \underline{K}_{spi} \cdot \underline{n}_b} \right] \left\{ \begin{matrix} dM_z \\ dV_y \end{matrix} \right\} \tag{6.68}$$

Since from case (i), $\left[\underline{n}_a \right]^T = [1,0]$, and from case (ii), $\left[\underline{n}_b \right]^T = [0,1]$,

$$d\underline{\tilde{w}}_{spi} = \begin{bmatrix} \dfrac{1}{K_{pM,i}} & 0 \\ 0 & \dfrac{1}{K_{pV,i}} \end{bmatrix} \left\{ \begin{matrix} dM_z \\ dV_y \end{matrix} \right\} \tag{6.69}$$

the flexibility matrix for subhinge i from Eq. 6.69 is:

$$\underline{\tilde{f}}_{spi} = \begin{bmatrix} \dfrac{1}{K_{pM,i}} & 0 \\ 0 & \dfrac{1}{K_{pV,i}} \end{bmatrix} \tag{6.70}$$

If the current action point lies on ar of r ining facets of the yield surface, results for the subhinge are similar to one of the three cases discussed above. The complete subhinge flexibility matrix is then obtained by summing the subhinge flexibility matrices of all yielded subhinges. Thus, if the current action point lies on any vertical facet, then:

$$\tilde{f}_P = \begin{bmatrix} \sum_{i=1}^{k} \dfrac{1}{K_{pM,i}} & 0 \\ 0 & 0 \end{bmatrix} \tag{6.71a}$$

If the current action point lies on any horizontal facet, then:

$$\tilde{f}_P = \begin{bmatrix} 0 & 0 \\ 0 & \sum_{i=1}^{l} \dfrac{1}{K_{pV,i}} \end{bmatrix} \tag{6.71b}$$

If the current action point lies on the intersection of a horizontal and vertical facet, then:

$$\tilde{f}_P = \begin{bmatrix} \sum_{i=1}^{k} \dfrac{1}{K_{pM,i}} & 0 \\ 0 & \sum_{i=1}^{l} \dfrac{1}{K_{pV,i}} \end{bmatrix} \tag{6.71c}$$

In the above, k and l, respectively, are the number of active subhinges due to moment yielding, and shear yielding.

Note that because the outward normals of the intersecting facets are orthogonal, the hinge flexibility matrices are therefore diagonal. Upon substituting the above into Eq. 6.61, the complete element flexibility matrix for the general case reads:

$$\underline{F}_t = \begin{bmatrix} F_{ii} + \sum_{i=1}^{a} \left(\dfrac{1}{K_{pM,i}} \right)^I + \dfrac{1}{L} \sum_{i=1}^{b} \left(\dfrac{1}{K_{pV,i}} \right)^I & F_{ij} + \dfrac{1}{L} \sum_{i=1}^{b} \left(\dfrac{1}{K_{pV,i}} \right)^I \\ F_{ij} + \dfrac{1}{L} \sum_{i=1}^{c} \left(\dfrac{1}{K_{pV,i}} \right)^J & F_{jj} + \sum_{i=1}^{d} \left(\dfrac{1}{K_{pM,i}} \right)^J + \dfrac{1}{L} \sum_{i=1}^{c} \left(\dfrac{1}{K_{pV,i}} \right)^J \end{bmatrix} \tag{6.72}$$

where

I, J = node of the element to which the active subhinges correspond,

a = number of active subhinges due to moment yielding of hinge at node I,

b = number of active subhinges due to shear yielding of hinge at node I,

c = number of active subhinges due to shear yielding of hinge at node J,

d = number of active subhinges due to moment yielding of hinge at node J.

6.3.4. Hardening Rule

Both kinematic and isotropic hardening rules were incorporated into the shear link element. The kinematic hardening rule is similar to that described previously, where the Mroz hardening rule is used to translate the yield surfaces and the slope of strain hardening is determined from the plastic stiffness coefficients. The isotropic hardening rule is based on the anisotropic hardening rule by Mroz [76].

6.3.4.1. Kinematic Hardening

When the current state lies on only one facet the situation is treated as a one dimensional yield surface when calculating the yield surface translation using the Mroz hardening rule, Eq. 6.39. For example, if the current state lies on only facet a of yield surface YSi shown in Fig 6.15(a), then a horizontal translation will occur as shown in Fig 6.15(b).

The gradient $\Phi,_{M_i}$ of facet a is given by:

$$\Phi,_{M_i} = \frac{1}{Mu_i} \tag{6.73}$$

where Mu_i is the initial yield moment of yield surface YSi. From Eq. 6.39, the increment of translation $d\alpha_{M_n}$ due to the increment of bending moment dM_z is equal to:

$$d\alpha_{M_n} = \frac{\left[\left(\frac{Mu_j}{Mu_i} - 1\right)(Mu_i + \alpha_{M_n}) - \left(\frac{Mu_j}{Mu_i}\alpha_{M_n} - \alpha_{M_{ij}}\right)\right]\left(\frac{1}{Mu_i}\right)dM_z}{\left(\frac{1}{Mu_i}\right)\left[\left(\frac{Mu_j}{Mu_i} - 1\right)(Mu_i + \alpha_{M_n}) - \left(\frac{Mu_j}{Mu_i}\alpha_{M_n} - \alpha_{M_{ij}}\right)\right]} = dM_z \tag{6.74}$$

where

α_{M_n}, $\alpha_{M_{ij}}$ = current horizontal position of yield surface YSi, and the next subsequent yield surface YSj,

Mu_j = initial yield moment of yield surface YSj.

Hence, the translation vector in moment-shear action space for yield surface YSi is equal to:

$$d\underline{\alpha}_i = \begin{Bmatrix} dM_z \\ 0 \end{Bmatrix} \tag{6.75}$$

Similarly, if the current state lies on only facet **b** of yield surface YSi, the yield surface will translate vertically due to an increment of shear dV_y, as shown in Fig. 6.15(c). The gradient $\Phi,_{V_y}$ of facet **b** is equal to:

$$\Phi,_{V_y} = \frac{1}{Vu_i} \tag{6.76}$$

where Vu_i is the initial shear yield force of yield surface YSi. Hence, the increment of translation $d\alpha_{V_y}$ due to an increment in shear force dV_y is equal to:

$$d\alpha_{V_y} = \frac{\left[\left(\frac{Vu_j}{Vu_i} - 1 \right)(Vu_i + \alpha_{V_{yi}}) - \left(\frac{Vu_j}{Vu_i}\alpha_{V_{yi}} - \alpha_{V_{yj}} \right) \right] \left(\frac{1}{Vu_i} \right) dV_y}{\left(\frac{1}{Vu_i} \right) \left[\left(\frac{Vu_j}{Vu_i} - 1 \right)(Vu_i + \alpha_{V_{yi}}) - \left(\frac{Vu_j}{Vu_i}\alpha_{V_{yi}} - \alpha_{V_{yj}} \right) \right]} = dV_y \tag{6.77}$$

where

$\alpha_{V_{yi}}$, $\alpha_{V_{yj}}$ = current vertical position of yield surface YSi and the next subsequent yield surface YSj,

Vu_j = initial shear yield force of yield surface YSj.

The translation vector therefore in moment-shear action space for yield surface YSi is equal to:

$$d\underline{\alpha}_i = \begin{Bmatrix} 0 \\ dV_y \end{Bmatrix} \tag{6.78}$$

Note that the increment in translation of the yield surface facets is equal to the increment of action causing the translation. This is a property of the Mroz hardening rule, where a surface with a constant gradient will have the action point remain on the yield surface. For a curved yield surface, such as an ellipse, the gradient is not constant and as a result the action point will drift outside the translated yield surface. In order to achieve accurate

results this drift must be controlled.

When the action point lies on two facets simultaneously, the determination of the translation of the yield surface becomes complicated if the Mroz hardening rule is applied directly to the two-dimensional action space. Firstly, the gradient at the corners of the yield surface cannot be computed from the yield function. Secondly, unless the loading $d\tilde{\underline{S}}$ is in the direction of the yield surface translation, depicted in Fig. 6.16(a) as being the vector $\tilde{\underline{S}}_j - \tilde{\underline{S}}_i$ defined by points Pi and Pj, the action point will drift off the yield surface as shown in Fig. 6.16(b). Consequently if the vector $d\tilde{\underline{S}}$ is not parallel with $\tilde{\underline{S}}_j - \tilde{\underline{S}}_i$, then the action point must be returned to the yield surface. Therefore the forces in the yielded subhinge will not be equal to the forces of $\tilde{\underline{S}}_i + d\tilde{\underline{S}}$. As a result, unbalanced loads develop at the corresponding nodes of the element, requiring equilibrium correction. There have been many proposed procedures to correct the state determination for drift control [84,85,86,87,79,88]. For the link element the action point should logically be returned to the yield surface at the intersection of the two facets, since increased moment and shear loading should cause further moment and shear yielding. If this return rule were adopted, then the new action point would always be constrained to remain at the corner of the yield surface, whose direction of translation is parallel to $\tilde{\underline{S}}_j - \tilde{\underline{S}}_i$.

Rather than try to adopt a suitable gradient at the corners of the yield surface and attempt to control the drift phenomena, an approximation was made where Mroz's hardening rule was applied separately to each facet on which the current point may lie. Thus, in addition to yielding, the effect of moment-shear interaction was also ignored during strain hardening. Therefore, the components of yield surface translation are given by Eqs. 6.74 and 6.77. The yield surface translation is thus equal to the action increment. That is:

$$d\underline{\alpha}_i = \begin{Bmatrix} dM_z \\ dV_y \end{Bmatrix} \tag{6.79}$$

Note that no unbalanced loads develop in a hinge during yielding until another facet is reached, implying yielding of an additional subhinge.

6.3.4.2. Isotropic Shear Hardening

As was observed in the experimental behavior discussed in Chapter 4 and in previous experiments [3,5,6,7], both isotropic and kinematic hardening occur in links yielding predominantly in shear. For the cyclic link model an anisotropic rule was devised for each subhinge whereby isotropic and kinematic hardening occurred in shear, with moment yielding following only a kinematic hardening rule. That is, for moment:

$$\Phi(M_z - \alpha_{M_r}) = 1 \tag{6.80}$$

where α_{M_r} is the horizontal translation of the vertical facets of the yield surface due to moment yielding, while for shear:

$$\Phi(V_y - \alpha_{V_r}) = H(\varepsilon) \tag{6.81}$$

where α_{V_r} is the vertical translation of the horizontal facets of the yield surface due to shear yielding. $H(\varepsilon)$ is a function which represents the expansion of the yield surface due to shear yielding, where ε is a scalar parameter monotonically increasing in the course of cyclic plastic flow.

Following the suggestion of Mroz [76], ε was defined to be the length of the plastic shear deformation trajectory. That is:

$$\varepsilon = \int_0^t (d\gamma_p \bullet d\gamma_p)^{0.5} dt \tag{6.82}$$

in which $d\gamma_p$ is the increment of shear deformation of the complete hinge. The function $H(\varepsilon)$ was obtained by fitting a curve to the experimental data for isotropic hardening presented in Chapter 4. The following format was found to fit the trend of the experimental data:

$$2H(\varepsilon) = \Delta V_{max} - (\Delta V_{max} - 2V_{y_o})\exp(-a\varepsilon) \tag{6.83}$$

The parameters ΔV_{max} and V_{y_o} are defined in Fig. 6.17, where ΔV_{max} is the elastic shear force between the yield envelope at a large value of the plastic shear deformation, and V_{y_o}

32

is the initial shear yield strength. The coefficient a is a coefficient obtained by a regression analysis of the experimental data using the $H(\varepsilon)$ format.

Examples of function $H(\varepsilon)$ are shown plotted in Figs. 6.18 and 6.19 for a bare steel link (Specimen D1) and a composite link (Specimen B1). The use of function $H(\varepsilon)$ to expand the yield surface of a subhinge for shear yielding is illustrated by Fig. 6.20.

6.3.5. Loading-Unloading Criteria

The criteria for distinguishing plastic flow from elastic unloading discussed in Section 6.2.6 was applied separately to each facet of a yield surface involving the current state. For example, if the current state is on a facet indicating that moment yielding is occurring for subhinge i, then:

$$\underline{n}^T = \begin{cases} [1,0] & \text{if } M_z > 0 \\ [-1,0] & \text{if } M_z < 0 \end{cases}$$

and therefore,

$$\lambda_i = \frac{\underline{n}^T \cdot d\underline{\widetilde{S}}}{\underline{n}^T \cdot \underline{K}_{spi} \cdot \underline{n}} = \frac{\pm \, dM_z}{K_{pM,i}} \doteq \frac{M_z}{\sqrt{M_z M_z}} \, d\Theta_{pM,i} \tag{6.84}$$

where

$d\Theta_{pM,i}$ = calculated flexural rotation of subhinge i

Likewise for shear:

$$\underline{n}^T = \begin{cases} [0,1] & \text{if } V_y > 0 \\ [0,-1] & \text{if } V_y < 0 \end{cases}$$

and therefore,

$$\lambda_i = \frac{\pm\, dV_y}{K_{pV,i}} \doteq \frac{V_y}{\sqrt{V_y V_y}}\, d\gamma_{pV,i} \tag{6.85}$$

where

$d\gamma_{pV,i}$ = calculated shear deformation of subhinge i

Consequently, if the current state for subhinge i is on a facet which designates moment yielding, that is Eq. 6.80 holds, then unloading from this facet occurs if due to an increment of moment dM_z,

$$M_z \cdot d\Theta_{pM,i} < 0 \tag{6.86}$$

Likewise, if the current state for subhinge i is on a facet which designates shear yielding, that is Eq. 6.81 holds, then unloading from this facet occurs if due to an increment of shear dV_y,

$$V_y \cdot d\gamma_{pV,i} < 0 \tag{6.87}$$

The procedure of translating facets by a very small amount when concurrent unloading occurs was briefly discussed in Section 6.2.6.

6.3.6. Determination of Plastic Stiffness

The required plastic moment and shear stiffness coefficients can be determined from experimental action-deformation relationships using Eq. 6.49.

6.4. Effects of Composite Action

The simplified formulation presented in Section 6.3 is intended for modeling bare steel links. For the analysis of EBFs with composite floors a formulation for composite links is required. In this formulation an approach was adopted whereby the essential features of composite link behavior are accounted for in a gross sense. That is, items such as the cyclic stiffness and strength of the links and floor beams outside the links are modeled accurately, whereas the crack pattern and stress distribution in the floor slab are considered

to be of lesser importance.

6.4.1. Modeling of Composite Links

The analysis of the experimental data in Chapter 4 indicated that composite links had a greater initial elastic stiffness, initial shear yield strength, and ultimate shear strength compared to bare steel links. The interior composite links were found to exhibit a larger increase in these quantities then the exterior composite links. These phenomena are evident in Figs. 4.1 to 4.3, which compare cyclic shear response of the composite and bare steel links. From these figures it can also be seen that near the ultimate state of a link the plastic stiffness is greater for the composite specimens relative to the bare steel specimens. These figures also show no deterioration or pinching of the hysteretic loops. Analyses shown in Fig. 4.1(b) pertaining to an interior composite and bare steel link of the K-braced EBF subassemblies indicate that the latter specimen had a higher degree of isotropic hardening in shear.

The hysteretic moment behavior at the ends of a link, shown in Fig. 4.14, reveals that severe pinching of the hysteretic loops did not occur as in composite beams of moment resisting frames [22]. However, the composite links near the ultimate state had a greater rotational stiffness than the bare steel specimens. It was found by numerical experimentation that this effect is primarily due to the rotational stiffness of the composite floor beams outside the links. Furthermore, this rotational stiffness was also responsible for the increase in the initial elastic stiffness of the composite links.

Satisfactory results for the analyses of composite links were obtained by adopting the simplified formulation for bare steel links to model composite links. This involves using for the properties of the subhinges the corresponding greater shear strengths and plastic stiffnesses of the composite specimens. Furthermore, appropriate isotropic hardening parameters for composite specimens are also required, as well as the use of a newly developed composite beam-column element for modeling the cyclic rotational effects of the

floor beam outside the link. A summary of the action-deformation relationships for the bare steel and composite link specimens are given in Figs. 6.21 to 6.23. These relationships were obtained after studying the experimental data, and then performing several analyses using a range of different action-deformation subhinge relationships until a satisfactory correlation with the hysteretic behavior of the test specimens was achieved. The $H(\varepsilon)$ function to define isotropic hardening in shear were shown earlier in Figs. 6.18 and 6.19 for a bare steel and composite link. The composite beam-column element is described below.

6.4.2. Cyclically Loaded Beam-Column Element

As noted above, the flexural stiffness of a composite floor beam outside the link influences the moments which develop at the ends of a link as well as the elastic link stiffness. In Chapter 4 a study of the experimental moment-rotation cyclic behavior of the composite floor beams outside the link showed the response to be essentially elastic but with elastic moduli dependent on the sense of moment. Consequently, these members were modeled using a composite beam-column element that changes flexural stiffness with the reversal of moment.

The composite beam-column element, referred to as the complete element, consisted of the parallel component beam element [81] in series with a rigid-plastic rotational hinge at each end of the element, as shown in Fig. 6.24. Two beams are used in the parallel component beam element. The hinges are considered to be of zero length.

The behavior of a hinge depends on the load path. Generally the hinge is either rigid or has yielded, where yielding can occur only due to the effects of moment. Moment-axial load interaction is not considered to have an effect on the yielding of the hinges. The following rules define when a hinge is rigid or has yielded:

(1) For elastic cyclic loading where the parallel component beam element does not yield, a hinge will remain rigid under positive moment and will yield when subjected to a negative moment, resulting in a bilinear elastic moment-rotation response for the com-

plete element as shown in Fig. 6.25(a).

(2) When yielding of the parallel component beam element occurs, the hinge becomes rigid. The hinge will remain rigid while unloading from the plastic state of the parallel component beam element, as indicated in Fig. 6.25(b). If continued unloading results in a load reversal, then the hinge will yield, as shown in Fig. 6.25(b).

(3) Following yielding of the parallel component beam element and load reversal, a yielded hinge will continue to yield during any elastic cyclic loading of the parallel component beam element, resulting in the response of the complete element as shown in Fig. 6.25(c). Consequently, the hysteretic response of the complete element for continued cyclic loading would appear as shown in Fig. 6.25(d).

The elastic moment-rotation response of the complete element was based on the experimental behavior of the composite floor beams outside the links, as discussed in Chapter 4. The hysteretic behavior of the complete element is in reasonable agreement with some previous tests [22] of composite floor beams in a moment resisting frame (see Fig. 4.15). A properly designed short link could possibly have some yielding outside the link, but it should be small compared to the yielding in the link. Therefore most of the response of a complete element is expected to be elastic.

The parallel component beam element discussed here for the complete element is similar to that developed in Refs. 81, 86, and 89. In this approach first a yield surface is defined accounting for the interaction of moment and axial force. Such a yield surface is shown in Fig. 6.26, where the element is assumed to be elastic for action points within the surface. If the moment-axial load combination at an end of this element lies on or outside the surface, yielding occurs and a plastic hinge is introduced at the corresponding nodal point of the element. Solution points falling outside the yield surface are brought back to the yield surface by applying a corrective moment as shown in Fig 6.27. The effect of axial load on yielding can be ignored by specifying a yield surface that accounts only for moment, Fig 6.28.

6.4.2.1. Degrees of Freedom

The complete element has two external nodes and two internal nodes, as shown in Fig. 6.24 where the external nodes are identified as I and J. The internal nodes exist at the ends of the parallel component beam element. The hinges connect the internal nodes with the external nodes. The external nodes connect to the global structure and have three global degrees of freedom, namely translations about the X and Y axes, and rotation about the Z axis, as shown in Fig. 6.14. In the local xyz coordinate system, three deformation degrees of freedom exist for the complete element as shown in Fig. 6.29. Each hinge has only flexural deformation. The parallel component beam element has both axial and flexural deformations. The translation from global displacements $\underline{r}$ to the deformation degrees of freedom $\underline{v}$ of the complete element is accomplished by:

$$\underline{v} = \underline{a} \cdot \underline{r} \tag{6.88}$$

where

$$\underline{v}^T = \begin{bmatrix} v_1, v_2, v_3 \end{bmatrix}$$

$$\underline{r}^T = \begin{bmatrix} r_1, r_2, r_3, r_4, r_5, r_6 \end{bmatrix}$$

The displacement transformation matrix $\underline{a}$ is well known and is available in the literature [74].

The degrees of freedom $\underline{q}$ for the parallel component beam element are considered to act at the internal nodes, Fig. 6.30, and are defined as:

$$\underline{q}^T = \begin{bmatrix} q_1, q_2, q_3 \end{bmatrix} \tag{6.89}$$

Because the hinges are not affected by axial force,

$$v_3 = q_3 \tag{6.90}$$

The hinges at nodes I and J of the complete element each have degrees of freedom as follows; at node I:

$$\underline{w}_p^I = \left[v_1 - q_1 \right] \tag{6.91a}$$

and at node J:

$$\underline{w}_p^J = \left[v_2 - q_2 \right] \tag{6.91b}$$

6.4.2.2. Element Stiffness

In order to determine the element stiffness, a flexibility matrix is first formed for the parallel component beam element in terms of the degrees of freedom $\underline{q}$. The parallel component beam element consists of an elastic component with a parallel elastic-plastic component. Inelastic axial deformations are assumed not to occur in the parallel component beam element in order to simplify the problem of interaction between the axial load and flexural deformations after yield. This procedure is the same as that adopted by Powell [81,86,89], but is not strictly consistent. However, it is believed to be reasonable for most practical applications due to the fact that yielding in the floor beams outside the links is minor.

The force increment $d\underline{S}$ at the ends of the parallel component beam element can thus be expressed in terms of the increment of deformation $d\underline{q}$ by the element's stiffness relationship:

$$d\underline{S} = \underline{K}_b \cdot d\underline{q} \tag{6.92}$$

where

$$d\underline{S}^T = \left[dM_z^I, \ dM_z^J, \ dF \right]$$

in which

dM_z^I = increment in moment at end of the element adjacent to node I,

dM_z^J = increment in moment at end of the element adjacent to node J,

dF = increment in axial force,

$\underline{K}_b$ = stiffness matrix of parallel component beam element.

The stiffness matrix $\underline{K}_b$ of the parallel component beam element is equal to:

$$\underline{K}_b = \underline{K}_{el} + \underline{K}_{ep} \tag{6.93}$$

That is:

$$\underline{K}_b = \begin{bmatrix} K_{bii} & K_{bij} & 0 \\ K_{bij} & K_{bjj} & 0 \\ 0 & 0 & \dfrac{EA}{L} \end{bmatrix}$$

$$= \rho \begin{bmatrix} \dfrac{EI_z}{L}K_{ii} & \dfrac{EI_z}{L}K_{ij} & 0 \\ \dfrac{EI_z}{L}K_{ij} & \dfrac{EI_z}{L}K_{jj} & 0 \\ 0 & 0 & \dfrac{EA}{L} \end{bmatrix} + (1 - \rho) \begin{bmatrix} \dfrac{EI_z}{L}K_{ii}^* & \dfrac{EI_z}{L}K_{ij}^* & 0 \\ \dfrac{EI_z}{L}K_{ij}^* & \dfrac{EI_z}{L}K_{jj}^* & 0 \\ 0 & 0 & \dfrac{EA}{L} \end{bmatrix} \tag{6.94}$$

where

$\underline{K}_{el}$ = stiffness matrix of elastic component,

$\underline{K}_{ep}$ = stiffness matrix of elastic-plastic component,

K_{ii}, K_{ij}, K_{jj} = flexural stiffness factors of elastic component,

EI_z = bending rigidity,

EA = axial rigidity,

L = length of the parallel component beam element, as defined by nodes I and J,

K_{ii}^*, K_{ij}^*, K_{jj}^* = flexural stiffness factors for elastic-plastic component,

ρ = slope of strain hardening modulus as a proportion of elastic modulus.

The coefficients of $\underline{K}_{ep}$ depend on the state, and are computed as follows:

$$\underline{K}_{ii}^* = K_{ii}(1 - A) - K_{ij}C \tag{6.95a}$$

$$\underline{K}_{ij}^* = K_{ij}(1 - D) - K_{ii}B \tag{6.95b}$$

$$\underline{K}_{jj}^{\bullet} = K_{jj}(1 - D) - K_{ij}B \tag{6.95c}$$

where A, B, C and D are defined in Table 6.1.

If an effective shear area $A_z^{\bullet}$ is specified, the effects of shear deformations can be included in a procedure analogous to that for the link element (Eq. 6.55). Thus, the flexibility matrix $\underline{F}_b$ for the parallel component beam element which includes the effect of elastic shear deformations is equal to:

$$\underline{F} = \underline{K}_b^{-1} + \underline{f}_s \tag{6.96}$$

$$= \begin{bmatrix} F_{ii} & F_{ij} & 0 \\ F_{ij} & F_{jj} & 0 \\ 0 & 0 & \dfrac{L}{AE} \end{bmatrix}$$

where

$$\underline{f}_s = \frac{1}{GA_z^{\bullet}L} \begin{bmatrix} 1 & 1 & 0 \\ 1 & 1 & 0 \\ 0 & 0 & 0 \end{bmatrix}$$

In this manner, the parallel component beam element flexibility relationship is obtained which includes the effects of shear:

$$d\underline{q} = \underline{F} \cdot d\underline{S} \tag{6.97}$$

The incremental deformation relationship for the hinge at node I is equal to:

$$d\underline{w}_p^I = (dv_1 - dq_1) = f_s^I \cdot dM_z^I \tag{6.98a}$$

and at end J:

$$d\underline{w}_p^J = (dv_2 - dq_2) = f_s^J \cdot dM_z^J \tag{6.98b}$$

where

f_s^I, f_s^J = current flexibility of hinge at nodes I and J,

dM_p^I, dM_p^J = increment of moment at nodes I and J.

The increment of deformation $d\underline{v}$ is the sum of the parallel component beam element and hinge deformation increments. That is:

$$
\begin{Bmatrix} dv_1 \\ dv_2 \\ dv_3 \end{Bmatrix} = \begin{Bmatrix} dq_1 + d\underline{w}_P^J \\ dq_2 + d\underline{w}_P^J \\ dq_3 \end{Bmatrix} = \underline{F} \cdot d\underline{S} + \begin{bmatrix} f_s^I & 0 & 0 \\ 0 & f_s^J & 0 \\ 0 & 0 & 0 \end{bmatrix} d\underline{S} = \underline{F}_t d\underline{S}
\tag{6.99}
$$

where $\underline{F}_t$ is the flexibility matrix for the complete element.

The stiffness matrix $\underline{K}_t$ for the complete element is the inverse of $\underline{F}_t$:

$$
\underline{K}_t = \left[\underline{F}_t \right]^{-1}
\tag{6.100}
$$

It is possible that $\underline{K}_b$ is singular. This would be the situation when yielding occurs in the parallel component beam element followed by no strain hardening, or if a pin ended composite beam-column is being modeled. As a result, $\underline{F}_t$ cannot be computed by inverting $\underline{K}_b$. In such cases $\underline{K}_t$ is determined by:

$$
\underline{K}_t = \begin{bmatrix} K_{tii} & 0 \\ 0 & K_{tjj} \end{bmatrix}
\tag{6.101}
$$

where the coefficients K_{tii} and K_{tjj} are defined in Table 6.2.

6.4.2.3 Hinge Flexibility

The flexibility of a rigid hinge is considered to be null. A hinge develops flexibility when it yields under the conditions set forth in Section 6.4.2. A yielded hinge has a flexibility f_s equal to the inverse of its stiffness K_s. That is:

$$
f_s = \frac{1}{K_s}
\tag{6.102}
$$

The determination of K_s requires the knowledge of the action-deformation relationship for moment. As discussed in Section 6.2.7 it is not possible to account for all possible

moment variations which may occur. However, in EBFs for composite floor beams outside the link, it is believed that a bilinear flexural stiffness at the two ends of these members can be represented reasonably well by applying the two sets of moments, as shown in Fig. 6.31. These end moments are based on the moment diagrams of the floor beams from the non-linear analysis of K-braced and V-braced EBFs. The analyses involved subjecting these EBF models to static lateral loads to simulate inertia forces due to a seismic disturbance.

Knowing the bilinear elastic moment-rotation relationship (Fig 6.31) for each end of a member, the corresponding stiffness K_s of each hinge is determined individually. This is accomplished by equating the flexibility of a composite beam, subjected to negative moments, to the combined flexibilities of the parallel component beam element and a yielded hinge. That is:

$$\frac{1}{K^-} = \frac{1}{K^+} + \frac{1}{K_s}$$

(6.103)

where

K^- = negative elastic stiffness of composite floor beam outside the link (Fig. 6.31)

K^+ = positive elastic stiffness of composite floor beam outside the link (Fig. 6.31), equivalent to the elastic stiffness of the parallel component beam element.

Therefore, solving for K_s in Eq. 6.103 results in:

$$K_s = \frac{K^+ K^-}{K^+ - K^-}$$

(6.104)

6.4.2.4. Plastic Deformation and Loading-Unloading Criteria

Plastic deformations in the parallel component beam element are assumed to occur only as plastic rotations at either end of an element. For any increment of flexural deformations dq_1 and dq_2 of the parallel component beam element, the corresponding increments of plastic rotations $d\Theta_{p1}$ and $d\Theta_{p2}$ are given by:

$$\begin{Bmatrix} d\Theta_{p1} \\ d\Theta_{p2} \end{Bmatrix} = \begin{bmatrix} A & B \\ C & D \end{bmatrix} \begin{Bmatrix} dq_1 \\ dq_2 \end{Bmatrix} \qquad (6.105)$$

where A, B, C and D were defined previously in Table 6.1.

The deformations at the ends of the parallel component beam element are computed with the aid of Eqs. 6.98 (a) and 6.98 (b), after the deformations for the composite beam-column model $d\underline{v}$ have been determined using Eq. 6.88. That is:

$$dq_1 = dv_1 - f_s^I \cdot dM_z^I \qquad (6.106a)$$

and

$$dq_2 = dv_2 - f_s^J \cdot dM_z^J \qquad (6.106b)$$

Unloading from the plastic state at an end of the parallel component beam element occurs when the increment in plastic hinge rotation is opposite in sign to the bending moment. That is, unloading occurs if:

$$M_z \cdot d\Theta_p < 0 \qquad (6.107)$$

6.5. State Determination

6.5.1. General

It is necessary when dealing with inelastic analyses to perform a state determination after computing the increment in global displacements $d\underline{r}$ in order to determine the updated internal resisting forces $\underline{R}^I$ of the elements. As a result, the unbalanced global nodal loads $\underline{R}^U$ can be determined for the current state, where:

$$\underline{R}^U = \underline{R}^E - \underline{R}^I \qquad (6.108)$$

in which $\underline{R}^E$ are the external applied loads. If the specified norm of $\underline{R}^U$ is greater than an allowable tolerance, then an iteration is required as summarized in Fig. 6.32, in order to satisfy equilibrium to within the allowable tolerance.

44

The algorithm in Fig. 6.32 is for a static analysis, where depending on the solution approach the effective global structure stiffness matrix $\underline{K}_{eff}$ can be either the initial elastic stiffness or tangent stiffness matrix. Applications for nonlinear dynamic analyses are discussed in Chapter 7. Iteration with the initial elastic stiffness depicted in Fig. 6.33(a) is known as Modified Newton-Raphson iteration. Tangent stiffness iteration illustrated in Fig. 6.33(b) is known as Newton-Raphson iteration. The two methods can be combined, as illustrated in Fig. 6.33(c). These methods are not the only ones that are used to perform nonlinear structural analyses. There are many others [90,91,92,93,95], including a form of displacement control as well as secant stiffness.

6.5.2. Link Element State Determination

Having computed the increment of global displacements $\underline{dr}$ for the link element, it is necessary to compute $\underline{R}^{I}$ due to the associated element deformations $\underline{dv}$. The computational procedure is as follows:

(1)   Calculate the element deformation increment:

$$dv = \underline{a} \cdot \underline{dr} \tag{6.109}$$

where

$\underline{dv}$ = vector of element deformation increments,

$\underline{a}$ = displacement transformation matrix,

$\underline{dr}$ = vector of nodal displacement increments,

(2)   Calculate linear action increments for the element:

$$d\underline{S} = \underline{K}_{l} \cdot \underline{dv} \tag{6.110}$$

and determine the hinge action increments:

$$d\widetilde{\underline{S}} = \underline{h} \cdot d\underline{S} \tag{6.111}$$

where

$d\underline{S}$ = linear action increment of the element,

K_t = current element tangent stiffness matrix,

$d\underline{\tilde{S}}$ = linear action increment of the hinges,

$\underline{b}$ = action transformation matrix from $d\underline{S}$ to $d\underline{\tilde{S}}$.

(3)   Check for the occurrence of an event for each hinge, and calculate the corresponding event factor FAC for each complete hinge as a proportion of the deformation increment. Possible events are:

    (a)   Proportion of deformation increment to reach next yield surface. If this proportion is greater than one, then FAC is 1.0. Otherwise, an event occurs and FAC is set equal to the calculated proportion.

    (b)   Unloading from a facet of the yield surface, then FAC is set to zero.

(4)   Select the smallest event factor, FACM, from the event factors FAC of both complete hinges.

(5)   Compute for both hinges the plastic deformation increment $d\underline{\tilde{w}}_p$ from Eqs. 6.56 (a) and 6.56 (b), and the translation increment $d\underline{\alpha}_i$ of the yield surface of yielded subhinges.

(6)   Update the forces $d\underline{\tilde{S}}$, origins $\underline{\alpha}_i$ of the yield surfaces for all subhinges, total plastic deformations $\underline{\tilde{w}}_p$, and accumulated plastic shear deformation parameter ε of both hinges:

$$\underline{\tilde{S}} = \underline{\tilde{S}} + FACM \cdot d\underline{\tilde{S}} \tag{6.112a}$$

$$\underline{\alpha}_i = \underline{\alpha}_i + FACM \cdot d\underline{\alpha}_i \tag{6.112b}$$

$$\underline{\tilde{w}}_p = \underline{\tilde{w}}_p + FACM \cdot d\underline{\tilde{w}}_p \tag{6.112c}$$

$$\varepsilon = \varepsilon + FACM \cdot \sqrt{d\gamma_p \bullet d\gamma_p} \tag{6.112d}$$

(7)   Compute the complement of the event factor:

$$FACC = 1 - FACM \tag{6.113}$$

(8) If any event has occurred, reform the tangent stiffness matrix $\underline{K}_t$ for the element using Eqs. 6.72 and 6.62.

(9) Calculate the remaining element deformation increment:

$$d\underline{v} = FACC \cdot d\underline{v} \tag{6.114}$$

(10) If the deformation increment $d\underline{v}$ for the element has not been exhausted then go to Step 2.

(11) Compute the element action $\underline{S}$:

$$\underline{S} = \underline{b}^T \cdot \underline{\tilde{S}} \tag{6.115}$$

(12) Compute the internal resisting forces $\underline{R}^I$ for the element:

$$\underline{R}^I = \underline{a} \cdot \underline{S} \tag{6.116}$$

6.5.3. Composite Beam-Column Element State Determination

Having computed the increment of global displacements $d\underline{r}$ for the composite beam-column element (complete element), it is necessary to compute the internal resisting forces $\underline{R}^I$ due to the associated deformations $d\underline{v}$. The computational procedure is as follows:

(1) Calculate the deformation increment for the complete element:

$$d\underline{v} = \underline{a} \cdot d\underline{r} \tag{6.117}$$

where

$d\underline{v}$ = vector of deformation increment for the complete element,

$\underline{a}$ = displacement transformation matrix,

$d\underline{r}$ = vector of nodal displacement increment.

(2) Calculate the linear action increments for the complete element:

$$d\underline{S} = \underline{K}_t \cdot d\underline{v} \tag{6.118}$$

and determine the action increments for both hinges and the parallel component beam element:

$$dS_h = b \cdot dS \qquad (6.119)$$

$$dS_b = b_b \cdot dS \qquad (6.120)$$

where

dS = linear action increment of the complete element,

K_t = current tangent stiffness matrix of the complete element,

dS_h = linear action increment for the hinges,

b = action transformation vector from dS to dS_h,

dS_b = linear action increment for the parallel component beam element,

b_b = action transformation matrix from dS to dS_b.

(3)   Check for the occurrence of an event in each hinge and the parallel component beam element. Calculate the corresponding event factor FAC as a proportion of the deformation increment. Possible events are:

    (a)   Proportion of deformation to cause a hinge to yield or become rigid. If this proportion is greater than one, then FAC is 1.0. Otherwise, an event occurs and FAC is set equal to the calculated proportion.

    (b)   Proportion of deformation to cause yielding of the parallel component beam element. If this is greater than one, set FAC equal to 1.0. Otherwise, an event occurs and FAC is set equal to the calculated proportion.

    (c)   Unloading from the yield surface of the parallel component beam element, FAC is set to zero.

(4)   Select the smallest event factor, FACM, from the event factors FAC of both hinges and the parallel component beam element.

(5)   Compute the plastic deformation increment $d\Theta_p$ at both ends of the parallel component beam element, using Eq. 6.105.

(6) Update the forces $\underline{S}_b$ and $\underline{S}_h$ of the parallel component beam element and hinges, and the plastic deformation $\underline{\Theta}_p$ at both ends of the parallel component beam element:

$$\underline{S}_b = \underline{S}_b + FACM \cdot d\underline{S}_b \tag{6.121a}$$

$$\underline{S}_h = \underline{S}_h + FACM \cdot d\underline{S}_h \tag{6.121b}$$

$$\underline{\Theta}_p = \underline{\Theta}_p + FACM \cdot d\underline{\Theta}_p \tag{6.121c}$$

(7) Compute the complement of the event factor:

$$FACC = 1 - FACM \tag{6.122}$$

(8) If any event has occurred, reform the tangent stiffness matrix for the complete element using Eqs. 6.99 and 6.100, or if necessary Eq. 6.101.

(9) Calculate the remaining deformation increment for the complete element:

$$d\underline{v} = FACC \cdot d\underline{v} \tag{6.123}$$

(10) If the deformation increment $d\underline{v}$ for the complete element has not been exhausted then go to Step 2.

(11) Compute the action $\underline{S}$ for the complete element:

$$\underline{S} = \underline{b}_b^T \underline{S}_b \tag{6.124}$$

(12) Compute the internal resisting force $\underline{R}^I$ for the complete element:

$$\underline{R}^I = \underline{a} \cdot \underline{S} \tag{6.125}$$

6.6. Modeling of Experimental Specimens

6.6.1. General

ANSR-1 is a general purpose computer program [94] which was developed at the University of California at Berkeley for analysis of nonlinear structural response. Both the simplified link element formulation and the composite beam-column element formulation

were programmed into ANSR-1. Additional elements available in ANSR-1 include a three dimensional beam-column element, three dimensional truss element, and a continuum finite element for plane stress, plane strain, or axisymmetric analysis. ANSR-1 has both static and dynamic analysis capabilities, with the user having several alternatives for selecting a solution procedure.

6.6.2. Analysis of a Bare Steel Link

The bare steel link of the K-braced EBF subassembly (Specimen D1) was analyzed by modeling the test beam as shown in Fig. 6.34. The link element was used, along with the standard beam-column element already in ANSR-1. The element properties were based on the mechanical properties of Specimen D1 and the section properties summarized in Tables 2.3, 2.6, and 2.7. The area of the web was used as the effective shear area A_v^*.

The model of Specimen D1 was subjected to the first eight half cycles of the displacement history of Specimen D1. This involved applying nodal cyclic loads P_A and P_B at ends A and B of the link. The sign convention for the link deformation γ and link forces is given in Fig 6.35. Included in this figure is the identification of ends A and B of the link. The results of the analysis in terms of the link deformation γ and the link forces are compared with the measured response of Specimen D1 in Fig. 6.36 and 6.37.

Figures 6.36 and 6.37 indicate that the elastic stiffness of the model is in close agreement with the measured value for Specimen D1. The combined isotropic and kinematic hardening behavior of the model also correlates well with the experimental behavior. Furthermore, the model predicts shear yielding in the link, with moment yielding occurring at end A of the link during Cycle 2 when a γ of 0.04 rad. developed in the link. These results are similar to those observed during the testing of Specimen D1. In later cycles at the peak link shear force of each half cycle, the model has a greater plastic stiffness than the measured value for Specimen D1, resulting in a larger shear and end moments to develop in the link of the model. This discrepancy, however, is not too significant and could be minim-

ized by performing additional analyses where the action-deformation relationship is adjusted to give better results. Overall, it appears that the link element is capable of predicting reasonably well the cyclic response of bare steel links.

6.6.3. Analysis of a Composite Link

Specimen B1, an interior composite link, was analyzed by modeling the test beam as shown in Fig. 6.38. The link element was used along with the composite beam-column element. The element properties are based on mechanical properties of Specimen B1 and the section properties listed in Tables 2.3, 2.4, 2.6, and 2.7. Based on the experimental results given in Fig. 4.65, the effective moment of inertia I_{eff} equal to 2.6I was assigned to the composite beam-column element, where I is the moment of inertia of the bare steel specimens. The positive bending stiffness K^+ was established using this value of I_{eff} in the elastic expression for flexural stiffness of the composite beam-column element subjected to an end moment, i.e., from Eq. 4.8:

$$K^+ = \frac{3EI_{eff}}{L^*} = \frac{7.8EI}{L^*} \tag{6.126}$$

The quantity L^* is the length of the composite floor beam between the support and the end of the link. The value of the negative bending stiffness K^- was determined in a similar manner, requiring the use of 1.28I for the effective moment of inertia. These experimental results are summarized in Fig. 4.65. The required stiffness K_s for each hinge was then determined using Eq. 6.104. The measured effective width of 48 in. based on the stress distribution at the end of the link for Specimen B1 (Fig. 4.56) was used to estimate the positive moment and compressive axial load capacities for the composite beam-column element. The negative moment capacity and tensile capacity were set equal to the values of the bare steel beam specimens.

The analytical model of the composite beam specimen was subjected to the first eight half cycles of the displacement history of Specimen B1. This involved applying the nodal

cyclic loads P_A and P_B at ends A and B of the link. The model's response in terms of link deformation γ and link forces are compared with the measured values in Figs. 6.39 and 6.40. As before, the sign convention for the response is indicated in Fig 6.35.

Figure 6.39 shows that the shear hysteretic response of the model is in good agreement with the experimental results for elastic stiffness, shear yielding, as well as for kinematic and isotropic hardening phenomena. In Figure 6.40 the moment at link end A in the model shows some disagreement in later cycles, where the experimental results indicate a decrease in the moment during inelastic deformation. This experimental behavior was noted in Chapters 3 and 4 as being the consequence of damage to the concrete floor slab above the link. Therefore, by not including in the link element the cyclic deterioration of the moment capacity due to the effects of floor damage, there is a discrepancy with experimental results in terms of the distribution of link end moments. However, this discrepancy is not too large and the hysteretic response of the analytical model shows generally good agreement with the experimental behavior. Thus, the methods used to model the composite links and floor beams in EBFs are capable of predicting reasonable cyclic behavior of these members.

6.6.4. Analysis of a Three-Story EBF

An analysis was performed on a three-story EBF to examine how accurate the link model predicted global nonlinear response of an EBF. The three-story EBF analyzed was similar to the one tested in the laboratory by Roeder [6]. The geometry and member sizes of the test frame are shown in Fig 6.41. All of the connections in the test frame were moment resisting connections. The test frame subassemblage was a one-third scale model of a bay of the lower three stories of a 20-story EBF, see Fig. 6.42. The test frame was initially subjected to gravity loads P_G applied to the columns, followed by a cyclic lateral load H applied at the third floor which imposed a displacement history shown in Fig. 6.43. This displacement history was based on a simulation of estimated extreme response to 1.5 times

the El Centro earthquake (first 18 half cycles in Fig. 6.43), followed by the unscaled Pacoima Dam earthquake [6].

The model for the analysis used the section properties of the members shown in Fig. 6.41. The force-deformation relationships were based on experimentally determined behavior [6], and are summarized in Table 6.3. Moment-axial load interaction was accounted for in the elements modeling the beams, columns, and braces by a yield surface defined by Eq. 2.4-3 of the AISC Specification [20]. A schematic of the analysis model is given in Fig. 6.44, where a loading beam used in the experiment has also been modeled axially rigid. Four inch rigid offsets at the link ends adjacent to the column were introduced in order to maintain the proper length of the links and account for the depth of the columns. Hence, the column panel zones were modeled as being rigid.

The analysis model was initially subjected to the gravity loads P_G, followed by the first 27 half cycles of the displacement history shown in Fig. 6.43. The displacement history was imposed at the third floor of the model using a nodal force H, as shown in Fig. 6.44. Figures 6.45 to 6.47 show the lateral load-floor deflection for the three floors. The comparison between the experimental and analytical results is extremely good up to half cycle 25, indicated by the number 25 in these figures. Brace buckling was initiated in the test frame during half cycle 19 (see Fig. 6.47), causing the test frame's strength to begin to deteriorate. With further cycling of the test frame, the brace buckling became more pronounced, and the south link of the first floor (Fig. 6.41) experienced web tearing during half cycle 26. As a result, the test frame experienced a decrease in its strength in each of the cycles subsequent to cycle 19. Since the analytical model does not account for web tearing nor brace buckling, the analytical results show no deterioration in strength. Consequently, the analysis was stopped after completing the 27th half cycle because of the limited accuracy that would be expected during further cycles.

The relative vertical deflection between the ends of the model's first floor links are compared to the experimental results in Table 6.4. The comparison is by no means exact,

but it is good for inelastic analysis.

The hysteretic shear response of the first floor links of the model are shown in Fig. 6.48, indicating that the south link experienced more deformation. This magnitude of cyclic deformation would likely tear the links once the web buckled. The combined isotropic and kinematic hardening is evident in these figures. The corresponding moment-link deformation hysteretic response curves are shown in Figs. 6.49 and 6.50. Moment-shear force diagrams are shown in Figs. 6.51 and 6.52. These figures indicate that the link moment adjacent to the column is larger and became bounded near the moment capacity of M_p, while the smaller moment at the other end of the link kept increasing. This behavior is similar to the experimental response of short links tested by Kasai [7], using the setup shown in Fig. 6.53, where one end of the link (end A) was restrained from rotating. The hysteretic response of a short link (Specimen 7) is shown in Figs. 6.54 to 6.56, indicating a close resemblance to the behavior of the analysis results. Severe web tearing occurred during the last half cycle for this specimen.

Overall, the link element results in an accurate prediction of global response of EBFs if severe cyclic brace buckling and web tearing do not occur. The local response of the link element appears to resemble experimental cyclic behavior quite well up to the point when severe web tearing occurs.

CHAPTER 7

NONLINEAR DYNAMIC ANALYSIS METHOD FOR EBFs

7.1. General

Under strong seismic disturbances EBFs are designed to respond in an inelastic manner. In properly designed EBFs such activity occurs primarily in the links. In order to accurately assess the performance of EBFs for such conditions, nonlinear dynamic analyses are required. Important factors in a nonlinear dynamic analysis are the efficiency and stability of the solution procedure, in addition to the modeling assumptions which may have a significant effect on the calculated response.

This chapter presents a procedure to solve the incremental equations of motion for nonlinear dynamic analyses of EBFs. The procedure is based on a direct integration method. The effects of nonlinear deformations on the modeling of viscous damping are also examined. This chapter concludes with analyses of single degree of freedom systems in order to indicate general trends of simple systems and the effects of nonlinear deformations during earthquakes.

7.2. Source and Extent of Nonlinear Behavior

The major sources of nonlinearity in a structural system can be classified as follows:

(1) Material nonlinearity - This type of nonlinearity arises through the nonlinearity in the action-deformation relationships of the members of a structural system.

(2) Geometric nonlinearity - This type of nonlinearity arises through nonlinearity in the deformation-displacement relationships and through the need to formulate equilibrium conditions in the deformed configuration.

(3) Force nonlinearity - This type of nonlinearity occurs when the applied forces are a function of the displacements of the system. Examples are hydrodynamic loadings on

offshore platforms, and pressure loadings on thin membranes.

The choice of a solution scheme depends on the type and severity of nonlinearities affecting the behavior of the structural system. For the EBF analyses to be performed, which are presented in Chapter 8, material nonlinearity is the most predominant. These analyses involved medium height EBFs, consisting of three bays and six stories. For more slender and taller EBFs the geometric nonlinearity arising from the P-delta effect will likely become more significant than in the analyses of shorter, stockier EBFs. The nonlinearities that will be accounted for in the EBF nonlinear analysis procedure will consider material nonlinearity and the P-delta effect. As will be discussed later, the P-delta effect was considered by including a geometric structural stiffness in the analyses.

7.3. Incremental Equations of Motion

For a structural system subjected to dynamic loading, the equations of motion can be expressed in an incremental form relating the response to an applied load for a time step Δt. Such a format is presented below, where the damping of the system is being modeled assuming viscous damping:

$$\underline{M} \cdot \Delta \ddot{q} + \underline{C} \cdot \Delta \dot{q} + \underline{K}_t \cdot \Delta q = \underline{P}_{t + \Delta t} - (\underline{M} \cdot \ddot{q}_t + \underline{C} \cdot \dot{q}_t + \underline{R}_t) \tag{7.1}$$

The left hand side of Eq. 7.1 expresses the increment in response between time t and $t + \Delta t$ due to the unbalanced load occurring as a result of the applied load $\underline{P}_{t + \Delta t}$ at time $t + \Delta t$. The terms in Eq. 7.1 include:

$\underline{M}$ - structural mass matrix, which may be lumped or in consistent form,

$\underline{C}$ - damping matrix,

$\underline{K}_t$ - tangent stiffness matrix at time t, which may include a geometric stiffness,

$\Delta q, \Delta \dot{q}, \Delta \ddot{q}$ - increment of nodal displacements, velocities, and accelerations,

$\underline{P}_{t + \Delta t}$ - external applied loads at time $t + \Delta t$,

$\underline{R}_t$ - nodal loads in equilibrium with element forces at time t,

$\underline{\dot{q}}_t$, $\underline{\ddot{q}}_t$ - nodal velocities and accelerations at time t.

It will be assumed that the mass and damping matrices are constant. Viscous damping will be elaborated on later.

The inertia forces $\underline{f}_I(t)$ associated with the seismic ground motions are included in the $\underline{P}_{t + \Delta t}$ term. Typically, they are expressed as:

$$\underline{f}_I(t) = -\underline{M} \cdot \underline{r} \cdot \underline{\ddot{x}}_g(t) \tag{7.2}$$

where

$\underline{r}$ = influence coefficient vector or matrix expressing pseudostatic displacements result-

ing from support motions, see [99],

$\underline{\ddot{x}}_g(t)$ = ground accelerations of supports at time t.

For the present study, no relative support motion is assumed. Therefore, the effective earth-

quake forces are due to a ground acceleration $\ddot{x}_g(t)$, reading:

$$\underline{f}_I(t) = -\underline{M} \cdot \underline{r} \; \ddot{x}_g(t) \tag{7.3}$$

Note that the effects of soil structure interaction are not being considered, and there-

fore are not expressed in Eq. 7.1.

7.4. Solution of the Incremental Equations of Motion

The incremental equations of motion presented in Eq. 7.1 are typically solved using direct integration techniques. There are basically two methods for the direct integration of the equations of motion, namely explicit methods, in which the accelerations are found from the equations of motion and then integrated to obtain the displacements, and implicit methods, in which the equations of motion are combined with a time integration operator in order that displacements are found directly. The most widely used schemes of the two methods include:

(a) Explicit:

- Central Difference Method [100]

(b)   Implicit:

- Houbolt Method [101]

- Wilson-Θ Method [102]

- Newmark Method [103]

- Hilber-Hughes-Taylor Method [104]

- Hughes-Caughey-Liu Method [105]

To obtain a solution to the incremental equations of motion using an integration method, it is a requirement that the method possess stability and accuracy. Accuracy is assessed by measuring amplitude and frequency distortion as a function of time step size when the integration method is applied to an undamped linear oscillator. Stability is assessed by studying the amplitude growth of the computed solution.

The stability of integration methods have been established for linear systems [95,106,107]. However, for nonlinear systems the stability of the integration methods is generally problem dependent, and has not been fully established. In general, stability in a linear system is a numerical problem related to the spectral radius [95] of the integration operator for the different schemes. For a nonlinear system the source of instability is more complex, and basically is related to the accumulation of energy errors [118]. Sources of energy errors are due to equilibrium unbalance, and the work done by the unbalanced loads. To help control this, one should attempt to remove unbalanced loads within each time step and select a sufficiently small time step. Because of the complexity involved with nonlinear systems, the stability and accuracy of an integration algorithm can only be established by numerical experimentation.

The unconditional stability of many single step implicit integration methods in linear analysis has favored their use for practical nonlinear dynamic analysis. One which is addressed herein and used by the ANSR-1 computer program [94] is that of Newmark [103]. Newmark's method is an implicit two-parameter scheme in which it is assumed that

the increments in velocity $\Delta \dot{q}$ and acceleration $\Delta \ddot{q}$ are related to the increment in displacement Δq and state of motion at time t. That is:

$$\Delta \dot{q} = \frac{\gamma}{\beta \Delta t}\Delta q - \frac{\gamma}{\beta}\dot{q}_t + \Delta t \left(1 - \frac{\gamma}{2\beta}\right)\ddot{q}_t \qquad (7.4a)$$

$$\Delta \ddot{q} = \frac{1}{\beta (\Delta t)^2}\Delta q - \frac{1}{\beta \Delta t}\dot{q}_t - \frac{1}{2\beta}\ddot{q}_t \qquad (7.4b)$$

where

β, γ = integration parameters,

Δt = time step,

$\dot{q}_t, \ddot{q}_t$ = nodal velocities and accelerations at time t.

It has been shown [107] that for unconditional stability of Newmark's operator involving linear analysis that the integration parameters β and γ must satisfy the following criterion:

$$\gamma \geq 0.5 \qquad (7.5a)$$

$$\beta \geq 0.25(0.5 + \gamma)^2 \qquad (7.5b)$$

The *constant average acceleration* operator uses $\beta = 0.25$ and $\gamma = 0.50$. A number of other stable operators can be obtained by specifying appropriate values for the parameters β and γ which satisfy Eqs. 7.5 (a) and 7.5 (b). It is also possible to introduce numerical damping effects by specifying a damping parameter δ such that:

$$\gamma = 0.5 + \delta, \qquad \delta > 0 \qquad (7.6)$$

The incremental equations of motion can be solved for Δq by substituting Eq. 7.4 into 7.1, whereby the following results:

$$\underline{K}_t^* \cdot \Delta q = \underline{P}^* \qquad (7.7)$$

in which $\underline{K}_t^*$ is the effective stiffness matrix and $\underline{P}^*$ the effective load vector, where:

$$\underline{K}_t^* = \frac{1}{\beta(\Delta t)^2}\underline{M} + \frac{\gamma}{\beta\Delta t}\underline{C} + \underline{K}_t$$

and

$$\underline{P}^* = \underline{P}_{t+\Delta t} - \underline{M}\left[\left(1 - \frac{1}{2\beta}\right)\ddot{\underline{q}}_t - \frac{1}{\beta\Delta t}\dot{\underline{q}}_t\right] - \underline{C}\left[\Delta t\left(1 - \frac{\gamma}{2\beta}\right)\ddot{\underline{q}}_t + \left(1 - \frac{\gamma}{\beta}\right)\dot{\underline{q}}_t\right] - \underline{R}_t$$

Once $\Delta\underline{q}$ is determined, the motions are updated at time $t + \Delta t$. That is:

$$\underline{q}_{t+\Delta t} = \underline{q}_t + \Delta\underline{q} \tag{7.8a}$$

$$\dot{\underline{q}}_{t+\Delta t} = \left(1 - \frac{\gamma}{\beta}\right)\dot{\underline{q}}_t + \frac{\gamma}{\beta\Delta t}\Delta\underline{q} + \Delta t\left(1 - \frac{\gamma}{2\beta}\right)\ddot{\underline{q}}_t \tag{7.8b}$$

$$\ddot{\underline{q}}_{t+\Delta t} = \left(1 - \frac{1}{2\beta}\right)\ddot{\underline{q}}_t + \frac{1}{\beta(\Delta t)^2}\Delta\underline{q} - \frac{1}{\beta\Delta t}\dot{\underline{q}}_t \tag{7.8c}$$

Equilibrium will not be satisfied at time $t + \Delta t$ if during the time step Δt nonlinearities are developed. Consequently, an integration algorithm is required in which iterations are performed within the time step in order to satisfy equilibrium subject to a specified tolerance. Such an algorithm employing Newmark's integration method is given in Table 7.1. This algorithm is based on iterating with a constant effective stiffness for $\underline{K}_t^*$, as will be discussed below, and was the procedure adopted for the nonlinear dynamic analyses of EBFs using ANSR-1.

As noted in Chapter 6, two types of iterative procedures are commonly used, namely Newton-Raphson iteration and Constant Stiffness or Modified Newton-Raphson iteration. In Newton-Raphson iteration the structure tangent stiffness matrix $\underline{K}_t$ and hence the effective tangent stiffness matrix $\underline{K}_t^*$ are reformed at every iteration. Consequently, a large amount of computational effort may be required to form and decompose $\underline{K}_t^*$. In Constant Stiffness iteration $\underline{K}_t^*$ maintains its initial value, determined at the beginning of the analysis. Constant Stiffness iteration will converge more slowly than Newton-Raphson iteration, however,

this may offset the effort of reforming and decomposing $\underline{K}_i^*$ at every iteration. Generally, it is problem dependent. For the analyses of EBFs it was found that Constant Stiffness iteration was more efficient, therefore this type of iteration was incorporated into the algorithm shown in Table 7.1. The initial structure stiffness matrix $\underline{K}_0$, referred to in the initialization phase of the solution algorithm, includes a geometric stiffness based on gravity loads applied before the dynamic analysis.

Values for the integration parameters β, γ, and δ for the nonlinear EBF analyses were chosen whereby the *constant average acceleration* operator was employed. This operator was favored for nonlinear analysis because of its unconditional stability for linear analysis. The selection of the time step Δt is problem dependent. Therefore, for each EBF model several trial analyses were performed, where in each analysis a different time step size was chosen. The final choice for Δt was based on the value which resulted in no significant change in the response and energy calculations compared to the results obtained using a further reduced time step size of $0.5\Delta t$. Note that by employing the *constant average acceleration* method that δ is equal to zero, hence no numerical damping was present. In nonlinear dynamic response it is desirable to have some form of damping in order to filter out high frequency noise resulting from sudden changes in the structural stiffness. Therefore, viscous damping was used in the analyses. The effects of nonlinear deformations on viscous damping in EBFs are discussed next.

7.5. Viscous Damping

The damping matrix $\underline{C}$ of multi-degree of freedom systems is typically defined for linear problems to be proportional to the mass matrix $\underline{M}$ and elastic stiffness matrix $\underline{K}$. That is:

$$\underline{C} = a_0 \underline{M} + a_1 \underline{K} \tag{7.9}$$

This is referred to as Rayleigh damping [99], where $\underline{C}$ possesses the property that the gen-

eralized damping matrix $\underline{C}^*$ is diagonal. The generalized damping matrix is determined as follows:

$$\underline{C}^* = \underline{\Phi}^T \cdot \underline{C} \cdot \underline{\Phi} \tag{7.10}$$

in which $\underline{\Phi}$ are the eigenvectors of the elastic system. A structural system in which $\underline{C}^*$ is diagonal is said to be a classical damped system. The eigenvectors $\underline{\Phi}$ are obtained by solving the eigenvalue problem:

$$\underline{K} \cdot \underline{\Phi} = \underline{M} \cdot \underline{\Phi} \cdot \underline{\Lambda} \tag{7.11}$$

where $\underline{\Lambda}$ is a diagonal matrix which contains the eigenvalues of the system. Each eigenvalue in $\underline{\Lambda}$ represents the square of the frequency of vibration of a particular mode for the system. It is common practice to normalize $\underline{\Phi}$ with respect to the mass matrix $\underline{M}$, such that:

$$\underline{\Phi}^T \cdot \underline{M} \cdot \underline{\Phi} = \underline{I}$$

and:

$$\underline{\Phi}^T \cdot \underline{K} \cdot \underline{\Phi} = \underline{\Lambda}$$

where $\underline{I}$ is the identity matrix.

For a structural system whose generalized damping matrix is diagonal, the modal equations of motion for the system are uncoupled [99]. That is, for mode n, where the eigenvectors have been normalized with respect to the mass matrix, the modal equation of motion reads:

$$\ddot{y}_n(t) + 2\xi_n \omega_n \dot{y}_n(t) + \omega_n^2 y_n(t) = p_n(t) \tag{7.12}$$

where

$y_n(t)$, $\dot{y}_n(t)$, $\ddot{y}_n(t)$ = modal displacement, velocity, and acceleration,

ξ_n = modal damping ratio,

ω_n = vibration frequency of mode n,

$p_n(t)$ = generalized modal force.

Note that the motions $\underline{q}(t)$ in geometric coordinates are related to the modal motions by the following transformation:

$$\underline{q}(t) = \sum_n \underline{\Phi}_n y_n(t) \tag{7.13}$$

where $\underline{\Phi}_n$ is the eigenvector for mode n.

In elastic analyses the coefficients a_0 and a_1 of Eq. 7.9 are typically evaluated by assigning modal damping ratios for two elastic modes [99], where for mode n:

$$\xi_n = \frac{a_0}{2\omega_n} + \frac{a_1 \omega_n}{2} \tag{7.14}$$

Consequently, the modal damping ratio varies with frequency for an elastic system as shown in Fig. 7.1. The first term of Eq. 7.14 is related to mass proportional damping, while the second term corresponds to stiffness proportional damping. As evident in Fig. 7.1, stiffness proportional damping has higher damping at higher frequencies, whereas mass proportional damping has the opposite effect. Since in most linear seismic analyses the response is dominated by the lowest modes, either stiffness proportional or Rayleigh damping is typically used in order to filter out any noise created by high frequency response. In the past, researchers have preferred using stiffness proportional or Rayleigh damping to filter out the high frequency noise which can develop in a nonlinear system following a sudden change of the structural stiffness. ANSR-1 has adopted a similar approach for defining the damping matrix, in addition to allowing for tangent stiffness proportional damping. The structural damping matrix $\underline{C}$ in ANSR-1 is assembled from the global mass and the element stiffness matrices, reading:

$$\underline{C} = a_0 \underline{M} + \sum_i a_{1,} \underline{K}^{elm\ i} + \sum_i a_{2,} \underline{K}_t^{elm\ i} \tag{7.15}$$

where $\underline{K}^{elm\ i}$ and $\underline{K}_t^{elm\ i}$ are the elastic and tangent stiffness matrices for element i.

In nonlinear systems where there exist significant hysteretic energy dissipation the damping matrix is typically a linear combination of the mass and stiffness matrix. That is, either Rayleigh or stiffness proportional damping is used. This is based on the assumption that the response of an inelastic system is dominated by the hysteretic damping and that the change of the viscous damping properties due to nonlinear deformations is insignificant. This is generally true for analyses in which the viscous damping is small for all the participating modes.

Two nonlinear dynamic analyses were performed on the six-story EBF shown in Fig. 7.2. In both analyses the EBF was subjected to the NS component of the 1940 El Centro earthquake record which had been scaled by a factor of 1.5. In the first analysis Rayleigh damping was used to define the damping matrix for the EBF model where a five percent damping ratio was assigned to the first and fourth modes. In the second analysis no damping was used in the EBF model. The links in both analyses were modeled with elastic-perfectly plastic force-deformation relationships. The lumped masses used for the EBF model are given in Fig. 7.3. Figures 7.4(a) and 7.4(b) show the first floor brace response of both analyses. Included in these figures are the shear force time history of the link adjacent to the brace whose response is shown. A direct comparison of the first floor brace response for the two analyses was made by superimposing their axial force time histories on the same figure, as shown in Fig. 7.5. This figure indicates a similar axial brace force response for the two analyses during the first 1.5 seconds. During this time the response was linear elastic. However, there was a noticeable difference in the response of the two analyses after the elastic-perfectly plastic link reached the shear force V_p and yielded in shear at 1.6 seconds into the time history. The EBF model with Rayleigh damping developed a larger magnitude of axial brace force during link yielding than the EBF model without damping. This became a general trend, where the increase was as much as 48 percent, occurring at 2.2 seconds into the time history. The axial brace force of the analysis with Rayleigh damping was considerably larger than was warranted by the shear force in the link. How-

ever, the analysis without damping showed reasonable results for the axial force in the first floor brace. The same phenomenon of unusually large brace forces was also observed by Roeder [6], where the damping matrix was proportional to the initial stiffness matrix. Consequently, the assumption that nonlinear deformations do not significantly affect the viscous damping properties may not be valid for nonlinear analysis of EBFs.

To investigate the reliability of initial stiffness dependent viscous damping for EBFs, the modal damping ratios were studied for a one-story EBF at several assumed stages of structural yielding. The assumed stages of structural yielding are shown in Fig. 7.6, where the following points are identified:

A - Initial shear yielding in link,

B - Continued shear yielding in link with yielding in columns and braces at base of structure,

C - Full plastic shear yielding with moment yielding in link, continued yielding in columns and braces at base of structure.

The model of the one-story EBF is shown in Fig. 7.7, where the degrees of freedom have been reduced to the three generalized degrees of freedom r_1, r_2, and r_3. The damping matrix $\underline{C}$ for the model was based on Rayleigh damping, with initial modal damping ratios for the first three elastic modes of $\xi_1^I = 0.05$, $\xi_2^I = 0.05$, and $\xi_3^I = 0.065$. The vibration frequencies of the elastic structure for the first three modes were $\omega_1^I = 23.3$ rad/sec, $\omega_2^I = 40.5$ rad/sec, and $\omega_3^I = 69.6$ rad/sec.

The tangent stiffness $\underline{K}_t$ was determined for each stage of structure yielding corresponding to Fig. 7.6. The modal damping ratios were then determined for each stage from the generalized damping matrix $\underline{C}^*$, where:

$$\underline{C}^* = \tilde{\underline{\Phi}}^T \cdot \underline{C} \cdot \tilde{\underline{\Phi}} \qquad (7.16)$$

The matrix $\tilde{\underline{\Phi}}$ contains the eigenvectors for the tangent stiffness matrix $\underline{K}_t$. That is:

$$\underline{K}_I \cdot \tilde{\Phi} = \underline{M} \cdot \tilde{\Phi} \cdot \underline{\Lambda} \tag{7.17}$$

The generalized damping matrix for the yielded structure will not be diagonal. The modal damping ratio ξ of each inelastic mode was approximated by ignoring the off-diagonal terms of $\underline{C}^*$. Thus, for mode n:

$$\xi_n = \frac{C_{nn}^*}{2\omega_n} \tag{7.18}$$

where ω_n is the vibration frequency of inelastic mode n, obtained by the solution of the eigenvalue problem represented by Eq. 7.17, and C_{nn}^* the diagonal term of $\underline{C}^*$ corresponding to mode n. The accuracy of the above approximation for ξ_n has been examined in various studies. A criterion developed by Warburton and Soni [108] has indicated that this approximation is accurate as long as the vibration frequencies of the system are adequately spaced and the magnitudes of the off-diagonal terms of $\underline{C}^*$ are smaller than or of the same order as the diagonal terms. An examination of $\underline{C}^*$ for each stage of yielding of the model indicated that this criterion was met. Shing and Mahin [109] compared the above approximation for ξ_n with the exact solution for non-classical damped systems [110] and found the agreement was good. Thus, for this study the approximation should be accurate enough in order to provide reasonable results concerning the effect of nonlinear deformations on viscous damping of EBFs.

The effect of yielding on modal damping in the one-story EBF model is shown in Fig. 7.8. The fractional change of modal damping, $\xi_n - \xi_n^I$, with respect to initial modal damping, ξ_n^I, is plotted against that of ω_n for the first and third modes at the assumed stages of structural yielding. The viscous damping of the second mode appeared to be unaffected by the nonlinear effects, and therefore is not included in this figure. In the analysis, the progressive yield states resulted in an increase in modal periods. This is equivalent to a decrease in the modal frequencies ω_n. Figure 7.8 indicates that as link yielding progresses

the modal damping ratios increase while the modal frequencies decrease. This phenomenon is most prominent for the first mode. These results clearly indicate that the damping of the fundamental mode is significantly influenced by the yielding of the link. It was determined that the response of the six-story EBF models were primarily in the fundamental mode. Consequently, the large unwarranted axial brace forces in Fig. 7.4(a) developed by the Rayleigh damped EBF model during link yielding are due to the increase in modal damping.

To reduce the effects of nonlinear deformations on the viscous damping in EBF models, while working within the framework of ANSR-1, a form of nonproportional damping was used. That is, when forming the damping matrix using Eq. 7.15, Rayleigh damping was maintained for all elements excluding the links, while only mass proportional damping was used for the link elements. Tangent stiffness proportional damping was not used for any of the elements, thus the coefficients a_{2_i} were set equal to zero in Eq. 7.15. With this format for the damping matrix, the axial brace forces developed in the six-story EBF models were found to be more reasonable. A comparison between the response of models using Rayleigh damping and nonproportional damping, respectively, will be discussed in Chapter 8 for a six-story EBF.

Using the nonproportional damping format, the one-story EBF was reanalyzed for modal viscous damping behavior during nonlinear deformations. The results are shown in Fig. 7.9, where again the damping ratio of the first mode is shown to be most affected by the nonlinear deformations. A comparison with the previous case involving Rayleigh damping is shown in Fig. 7.10 for the first mode. This comparison indicates that the increase in the modal damping of the first mode is less for the nonproportional damped system, where this result is equal to about one-half the increase for the Rayleigh damped system.

7.6. Behavior of Simple Inelastic Systems

A simple structure system shown in Fig. 7.11, consisting of a single degree of freedom damped oscillator, was analyzed to illustrate phenomena associated with nonlinear dynamic

response. The purpose for the analyses of single degree of freedom, SDOF, systems was to gain additional insight into the phenomena associated with nonlinear response due to yielding before performing nonlinear dynamic analyses of multi-degree of freedom, MDOF, systems. The SDOF system analyzed was assigned a 5 percent viscous damping ratio and an initial elastic period T_0 of 0.2 seconds. A unit mass was assumed. The post yield stiffness of the oscillator was set at 1.5 percent of its elastic stiffness. A strength level factor η was defined for the oscillator as:

$$\eta = \frac{R_y}{m\ddot{x}_g\text{max}} \qquad (7.19)$$

where

m = mass of the system,

$\ddot{x}_g\text{max}$ = maximum ground acceleration of a selected earthquake record,

R_y = yield strength of the oscillator.

Two analyses were performed, one consisting of an elastic oscillator ($\eta = 4.0$) and the other an inelastic oscillator ($\eta = 0.48$). In both analyses, the systems were subjected to the first 20 seconds of the original NS component of the 1940 El Centro earthquake record. The displacement response history for the elastic and inelastic oscillators are shown in Fig. 7.12.

By comparing the responses of the two systems it is apparent that the inelastic oscillator develops an offset due to yielding, about which it oscillates. This nonlinear system also appears to develop a greater magnitude of maximum displacement due to yielding compared to the elastic oscillator. At the end of the analysis the nonlinear system developed a permanent deformation, characterized by the oscillations about the offset. A consequence of cyclic yielding resulting in plastic deformation is the dissipation of hysteretic energy. The dissipated hysteretic energy is the enclosed area shown in Fig. 7.13 of the force-deformation hysteretic loops for the inelastic system.

The input energy IE by an earthquake is equal to the total energy of the system, where for a nonlinear system:

$$IE = KE + PE + SE + DE + HE \tag{7.20}$$

where

KE = kinetic energy,

PE = change in potential energy of gravity and static loads on system,

SE = recoverable elastic strain energy,

DE = dissipated damping energy,

HE = dissipated hysteretic energy.

An elastic system does not dissipate hysteretic energy, therefore, the term HE would be deleted from Eq. 7.20 for such systems. The energy time histories for the elastic and inelastic systems discussed above are shown in Figs. 7.14(a) and 7.14(b). Since the analyses involved only inertia forces due to ground motions, no change in potential energy occurred. For the inelastic system most of the input energy is shown to be dissipated by hysteretic energy. The elastic system has a greater amount of dissipated damping energy compared to the inelastic system, however, the input energy is less compared to that of the inelastic system. For both systems the kinetic and recoverable strain energy remain relatively small throughout the response. Unlike the displacement time histories, which stop increasing after about 6 seconds, the hysteretic and damping energy continue to increase at an almost constant rate. Thus, for systems with limited energy dissipation capacity the duration of ground motion may have an important effect on the potential failure. Systems which are designed in order that they yield during strong seismic disturbances must possess ductility in order to assure that they can continue to dissipate hysteretic energy.

The two systems are a specific example for given properties of structural period, damping, and post yield behavior. The response of structural systems is particularly sensitive to the dynamic and mechanical characteristics of a structure [114]. This is evident in Figs. 7.15 to 7.17, where the indicated response quantities for the same El Centro

earthquake record have been plotted for systems with different initial periods T_0 and post yield behavior. In the long period range the systems tend to respond elastically. In the mid-range and shorter initial period range the systems are required to develop greater elastic resisting force, whereas systems with a reduced strength level will yield and dissipate energy. Figure 7.16 shows that the displacement ductility μ_D increases as the initial period decreases, where the effect is more pronounced for systems which possess less strain hardening. The displacement ductility μ_D is defined as:

$$\mu_D = \frac{q_{max}}{q_Y} \tag{7.21}$$

where

q_{max} = maximum displacement during the time history for a system,

q_Y = corresponding yield displacement.

Consequently, Fig. 7.16 implies that greater plastic deformations develop in inelastic systems which have smaller initial periods. The above results are for one earthquake record. It has been found [98] that the inelastic response of building structures is also sensitive to the excitation input. Therefore, different types of response can be expected for different earthquake motions.

7.7. Comments on the Treatment of MDOF Systems as Simple Nonlinear Systems

Often, an MDOF system is analyzed as an equivalent SDOF system. However, such an approach is not complete for nonlinear response. A MDOF system is typically transformed to a SDOF system using a mode shape or Ritz vector [111,112,113,117]. The mode shape or Ritz vector to transform the MDOF system to a SDOF system cannot express the participation of modes not represented by these vectors. Moreover, the mode shapes and frequencies will change during nonlinear deformations. The transformation vector is usually selected to represent the fundamental vibration mode. The accuracy of using these techniques depends to a great extent on the participation of the higher modes of the

MDOF system, in addition to the updating of the transformation vector during nonlinear deformations. Therefore, the conclusions concerning the analyses of SDOF systems discussed above must be carefully scrutinized before considering them appropriate for MDOF systems.

Applying the ductility levels of the SDOF systems to MDOF systems must be done with extreme caution. Ductility factors attempt to simplify a complex response, and in general there is little agreement on the precise definition of ductility [114]. MDOF systems may not exhibit definite yield points on a global basis, hence the definitions for ductility of SDOF systems with definite yield points will not hold.

As a final comment, it must be recognized that ductility based on local response (plastic hinge rotation, plastic shear deformation, plastic elongation) will be substantially larger than that based on global displacement. For MDOF systems, multiple internal member forces develop simultaneously, such as moment and axial load. It has been found that the interaction of these forces affects the ductility capacity of the members [115]. Therefore, required ductility factors for a design should be defined for the members, where the internal forces are reported in order to properly design the structure to survive a major earthquake.

CHAPTER 8

NONLINEAR DYNAMIC ANALYSES OF EBFs

8.1. General

In practice, the preliminary design of building structures for earthquake conditions is typically based on code defined seismic forces, where either equivalent lateral forces or inelastic response spectra are used [58,66,96]. The equivalent lateral force procedure consists of designing a structure to resist static lateral forces which represent the inertia forces resulting from seismic disturbances. These forces are largely associated with the first mode of dynamic response of typical structures. In an attempt to account for the effects of higher modes a concentrated force is introduced in some codes [96] at the roof level for tall frames. NEHRP [66] attempts to account for higher mode effects by increasing the magnitude of lateral force distribution near the roof level of tall frames. The inelastic response spectra are often based on the nonlinear dynamic response of a single degree of freedom oscillator, similar to that shown previously in Fig. 7.15. In such an approach, several spectra are usually obtained using different earthquake records and then the responses averaged and smoothed to obtain design spectra. Newmark and Hall [97] recommended a procedure for the construction of inelastic design spectra based on applying ductility factors to elastic spectra. The lateral forces representing the seismic inertia forces for the multi-degree of freedom structures are calculated from the inelastic response spectra using modal analysis procedures [99]. The code provisions concerning the equivalent lateral force and inelastic response spectra procedures have considered the fact that the structure will yield under strong seismic motions, whereby additional code provisions are recommended to account for ductility demands and strain hardening.

The use of the equivalent lateral force method has the advantage that it is practical for preparing preliminary designs, for it requires only that the general layout of the structure be

known. However, this method will admit some inaccuracies since it cannot take into account the detailed layout (distribution of stiffness, etc.) and characteristics (structural damping, stiffness degradation, ductility, etc.) of the structure being designed. On the other hand, inelastic response spectra attempt to account for ductility and the effects of damping. However, the use of inelastic response spectra requires that the detailed layout of the structure be known in order to determine the vibration properties. It has been shown by Mahin and Bertero [125] that inelastic response spectra cannot be viewed as being reliable in terms of limiting maximum ductility demands to specified values. Furthermore, Mahin and Bertero have indicated that the inelastic response of structures is particularly sensitive to the actual excitation input, as well as to the dynamic and mechanical characteristics of the structure [125]. In applying the inelastic response spectra method to multi-degree of freedom systems, such systems must be represented as single degree of freedom systems. This is not complete for determining the nonlinear response, as was noted in Chapter 7.

Using either of the above methods in a preliminary design procedure can therefore result in possible inaccuracies in the design result. Consequently, there is a need to assess the preliminary design procedure of EBFs, where the seismic forces are determined by one of these methods. This was accomplished by scrutinizing the response of code designed EBFs which had been subjected to strong ground motions. The responses were determined by conducting thorough nonlinear dynamic analyses of the EBFs.

The link element and composite beam-column element formulated in Chapter 6 were therefore implemented into the ANSR-1 program [94] with dynamic analysis capabilities. This enabled EBFs to be analyzed for response to strong seismic motions, where the links and floor beams could be modeled as either bare steel or composite links with user defined force-deformation relationships. Three different EBF designs of the same frame were made, where the provisions of NEHRP [66] were used as design guidelines. The seismic design forces were based on the equivalent lateral force procedure of NEHRP. Nonlinear dynamic analyses were then performed on each design, involving a total of 27 computer runs. The

same design was often reanalyzed for response to a different earthquake input record. Also, the effect of using different assumptions to model the EBFs were examined. Consequently the effects of strain hardening, geometric stiffness, composite action, Rayleigh versus nonproportional damping, and the use of pin connections in EBFs subjected to different ground motions were included in the assessment. The assessment of each EBF design involved examining the forces and deformations of the members, areas of plastic deformation in the EBF, in addition to energy dissipation and ductility of members obtained from the various analyses.

8.2. EBF Design Procedure

The structure selected for this study represented a six-story, three-bay exterior EBF of a symmetric building. A typical plan and elevation are shown in Fig. 8.1. This building was to provide office space in the San Francisco area. The exterior frames at the north and south ends of the building were both EBFs. All other frames were moment resisting frames. The two EBFs were assumed to resist all lateral seismic forces in the east-west direction. Each EBF had eccentric K-bracing in the upper three floors of the middle bay and eccentric D-bracing in the lower three floors of the exterior bays.

The three different EBF designs included the following:

Design 1 -   An EBF was designed where all connections were assumed to behave as moment type connections.

Design 2 -   An EBF was designed where all connections were assumed to behave as moment type connections. The link capacity at critical locations was increased, whereby the ratio of shear capacity to required shear strength V_p/V_{link} of each link was made more consistent among the floors compared to Design 1.

Design 3 -   An EBF was designed with pins at the beam and brace-to-column connections. All other connections, including those at the ends of the links adjacent

to the exterior columns and of the first floor braces which framed into the base of the EBF, were assumed to behave as moment type connections. An attempt was made to maintain the same distribution of the ratio of V_p/V_{link} among the links in the lower three floors as that of Design 2.

All links in the EBFs complied with the recommendations of Kasai and Popov [35] discussed in Chapter 1, for only short links were used in the designs. That is:

$$e \leq 1.6 \frac{M_p}{V_p} \tag{8.1}$$

where M_p and V_p, respectively, are the plastic moment and shear capacity of a wide flange steel section. The definition of the quantities M_p and V_p were given previously by Eqs. 1.1 and 1.3. It was decided to maintain the same length for all the links in the upper and lower three floors, respectively.

The gravity loads for the building were based on the recommendations of ANSI [126], where the dead and live load, respectively, were equal to 100 psf and 50 psf per floor with 100 psf and 20 psf for the roof. The facade of the building consisted of precast concrete cladding weighing 35 psf. An allowable reduction in live load per ANSI was used for the design of the individual members. The beams were considered to have been fabricated from A36 steel, the columns from A572 grade 50 steel, and the braces from A441 structural steel tubing.

As noted above, the building was designed to resist earthquakes using the equivalent lateral force provisions of NEHRP, which is an ultimate strength code. The equivalent lateral forces were based on the effective weight of the building, consisting of full dead and cladding load in addition to 25 percent of the live load. Thus, the design base shear V_B was calculated according to the following [66]:

$$V_B = C_s W \tag{8.2}$$

where W is the building's effective weight. The coefficient C_s is the seismic design coefficient, defined by the following relationship [66]:

$$C_s = 1.2 \frac{A_v S}{RT^{2/3}}$$ (8.3)

where

A_v = effective peak velocity-related acceleration coefficient,

S = soil profile coefficient,

R = response modification factor,

T = fundamental period of structure.

For the location and type of building being designed, the NEHRP provisions required an A_v value equal to 0.4, with S equal to 1.2. The building's fundamental period T was estimated using Eq. 4.5 in NEHRP, which reads:

$$T = \frac{0.05 h_n}{\sqrt{L}}$$ (8.4)

where

h_n = height in feet above the base to the highest level of the building,

L = overall length (in feet) of the building at the base in the direction under consideration.

In the east-west direction, corresponding to the plane of bending for the EBFs (see Fig 8.1), the estimation of the fundamental period was 0.45 seconds. For the two EBF designs with all moment connections (Designs 1 and 2) the NEHRP provisions require a value of 7 for the response modification factor R. The EBF design with pin connections (Design 3) required a 17 percent reduction in the the response modification factor. This is necessary in order to comply with the NEHRP requirement that the design base shear be increased by 20 percent for braced frames with pinned connections.

The total effective weight of the building for determining the design base shear V_B was equal to 4542 kips. This resulted in a value of V_B equal to 636 kips for Designs 1 and 2, and 763 kips for Design 3. Each of the EBFs was assumed to resist equal amounts of

V_B. Hence the required base shear capacity V_B^{EBF} of each EBF was 318 kips for Designs 1 and 2, and 381.5 kips for Design 3. These values of V_B^{EBF} are a result of accumulating the lateral story shear forces. The lateral seismic force F_x at each floor level was determined using Eq. 4.6 of NEHRP, where for story level x:

$$F_x = C_{Vx}V_B^{EBF} \qquad (8.5)$$

where

$$C_{Vx} = \frac{w_x h_x}{\sum_{i=1}^{6} w_i h_i} \qquad (8.6)$$

in which

w_x, w_i = portion of effective weight located at story level x or i.

h_x = height above base to level x.

The resulting vertical distribution of lateral seismic forces for the EBFs is shown in Fig 8.2.

In order to predict member forces in an EBF at the preliminary design stage, the use of a plastic analysis technique is the most rational approach. Using such an approach the required strength and desired energy dissipation mechanisms for a frame can best be achieved. To assure good performance, EBFs should be designed such that inelastic activity is confined primarily to the links. For such behavior the link shear resisting capacity governs the plastic capacity of the frame. Therefore, the primary objective in EBF design is to select a link with an appropriate shear resisting capacity V_p that satisfies the required plastic capacity of the EBF, followed by the selection of the other members in such a manner that they remain elastic in order to assure the plastic activity of the link.

All members were designed considering bare steel behavior, and satisfied the compactness requirements of the AISC Specification [20]. The floor beams in braced bays were designed first, using the plastic design procedure by Kasai [7,119]. This method is analogous to that of Popov and Engelhardt [127]. In order to use this procedure an

approximation of the amount of story shear developed at each story level was required for the braced bays. For the EBF designs using all moment connections (Designs 1 and 2) it was assumed that the braced bay in each of the upper three floors developed 80 percent of the story shear, while each braced bay in the lower three floors developed 45 percent of the story shear. For the EBF design with pin connections (Design 3) these corresponding values were assumed equal to 92.5 percent in the upper three floors and 48.75 percent in the lower three floors. An analysis of each of the final designs for Designs 1, 2, and 3 indicated that these approximations were reasonable. The required shear force V_{link} in each link was then established, where the following expression [7] was used for each floor:

$$V_{link} = \frac{h}{L} V_{cum} \tag{8.7}$$

where

V_{link} = required link shear force at a particular floor level,

V_{cum} = static design shear force accumulated from the roof to the corresponding floor level,

h,L = story height and braced bay width, respectively, associated with the floor level.

This approach is illustrated in Fig. 8.3 for K and D-braced one bay EBFs. For the K-braced EBF, Eq. 8.7 can be derived by writing a moment equilibrium relationship around the column base at point A, in Fig. 8.3(a), where the significance of moments acting at the upper and lower ends of the EBF panel are assumed negligible. For the D-braced EBF it has been shown [7] that Eq. 8.7 remains reasonably accurate. Popov and Engelhardt [127] derived Eq. 8.7 by considering moment equilibrium of a simplified free-body diagram of an EBF with points of inflection at midheight of the braces and columns, and at midspan of the links.

The required axial force in the braces P_{br} and floor beams outside the link P_{bm} were then determined by statics. These forces were based on the ultimate link state. As discussed in Chapter 1 and supported by the results of the experimental study presented in

Chapter 4, the ultimate link shear force V_{ult} should be at least equal to the following:

$$V_{ult} = 1.5 V_p \qquad (8.8)$$

where V_p is the actual plastic shear capacity of the beam section used for the link which satisfies Eq. 8.7. Based on the experimental behavior of short links [119], the link end moments M_A and M_B at the ultimate state were assumed to be equal to the following:

$$\text{K-braced EBF,} \qquad M_A = M_B = \frac{e \cdot V_{ult}}{2} \qquad (8.9a)$$

$$\text{D-braced EBF,} \qquad M_A = M_p$$
$$M_B = e \cdot V_{ult} - M_p \qquad (8.9b)$$

where for the D-braced EBF M_A and M_B, respectively, are the link moments at the column face and at the opposite end of the link. Using the free body diagrams of the beam-brace subassemblage shown in Figs 8.4(a) and (b), estimates for the axial forces of the braces and floor beams outside the links in K-braced and D-braced panels of Designs 1, 2, and 3 were determined corresponding to the ultimate state of each link.

The moments in the braces and floor beams outside the links corresponding to the ultimate link state were then determined. By numerical experimentation it was found, depending on the relative stiffness of the adjoining floor beam and brace, that a brace above the first floor with a moment connection developed 15 to 25 percent of the adjacent link end moment M_b. The design moments for braces above the first floor were therefore assumed to be equal to $0.2 M_b$. For Designs 1 and 2, equal end moments were assumed for all braces above floor 1. Due to the arrangement of the pin and moment connections in Design 3, a moment developed at only the upper end of each brace above the first floor, which was attached to a link. This moment was assumed to be equal to $0.2 M_b$. In all three designs, moment connections were used at both ends of the first floor brace. The brace moment at the lower fixed end was assumed to be equal to $0.4 M_b$, while the brace moment at the link was assumed to be equal to $0.2 M_b$.

The beam outside the link was assigned a design moment to resist the beam moment M_c developed at the end of the gusset plate, see Fig. 8.5. The gusset plates were assumed to have a length L_g of 20 in. along the floor beam. It was found that the axial forces generated in the braces and floor beams outside the links were large, consequently these members had to be designed as beam-columns. Therefore, Eqs. 2.4-2 and 2.4-3 of the AISC Specification were employed to design for moment and axial force interaction, considering both strength and stability.

The floor beams in the unbraced panels of Designs 1, 2, and 3 were then designed. The effect of axial force was ignored for these members. Required moment capacities were determined by equating the internal work to the external work done by the seismic forces F_x and gravity loads for the assumed collapse mechanism of the EBF. The assumed mechanism for Designs 1 and 2 is shown in Fig. 8.6 (a), while that of Design 3 is shown in Fig. 8.6 (b). The internal work was expressed in terms of the unknown capacity $M_{p_{beam}}$ of the floor beams of unbraced panels, as shown in Figs. 8.6(a) and (b), by assuming proportionality factors α_i for the capacity of each floor beam in the unbraced panels. The internal work done by columns yielding at the base is generally small compared to that of the links [120], and therefore was ignored. The capacities of the floor beams selected for each unbraced panel equaled or exceeded the required capacity for a local beam mechanism, Fig. 8.7, based on factored gravity loads [66].

The columns of the EBF were designed as beam-columns using Eqs. 2.4-2 and 2.4-3 of the AISC Specification. The moment capacity of all floor beams and links framing into columns were increased to $1.25M_p$ to account for possible overstrengthen floor beams, as required by NEHRP for column design. In addition, the shear force in all of the links was assumed to have reached V_{ult}. The column axial design forces accounted for the combined effect of seismic forces and gravity loads, using the NEHRP load factors. The column design moments for Designs 1 and 2 were determined using the weak beam-strong column concept. As will be discussed later in the analyses results, the point of inflection in the

columns of EBFs with beam-to-column moment connections can have widely varying positions during an earthquake, particularly in columns which are adjacent to links. This phenomenon is associated with the floor beam and link moments at a beam-column joint being unevenly distributed to the adjoining columns above and below the floor. Hence, an allowance must be made if plastic hinge development at the top and bottom end of a column in a story is to be avoided. Using the recommended column design procedure of Paulay [121,122], this allowance was made by introducing a dynamic magnification factor ω. Therefore, for Designs 1 and 2 the required flexural capacity M_{col} of the columns was based on the following:

$$M_{col} = \omega M_{code} \tag{8.10}$$

where M_{code} is the required column moment capacity determined by the weak beam-strong column concept. In the weak beam-strong column concept the beam moments are distributed equally to the columns above and below the particular floor. That is for a particular floor level where moment-connections exist, the column moment M_{code} based on the weak beam-strong column concept is in general equal to:

$$M_{code} = 0.5 \left[\sum 1.25 M_{p_{beam}} + \sum 1.25 M_{p_{link}} + \sum M_{brace} + \sum M_{D_{beam}} \right] \tag{8.11}$$

where $M_{p_{beam}}$ and $M_{p_{link}}$, respectively, are the flexural capacities of the floor beam and link which frame into the column. The moment M_{brace} is the brace end moment adjacent to the column, which was assumed previously to be equal to $0.2 M_b$ for Designs 1 and 2. The moment $M_{D_{beam}}$ is associated with the floor beam end moment adjacent to the columns in the braced panels, as shown in Fig. 8.8. Numerical experimentation indicated that $M_{D_{beam}}$ for Designs 1 and 2 could be approximated by:

$$M_{D_{beam}} = 0.20 M_b \tag{8.12}$$

Equation 8.10 is used at each floor level to establish the required moment capacity at the ends of adjoining columns. The column moment at the base was assumed to be equal to

twice the moment developed at the top of the first floor column. Because only one column frames into a beam-column joint at the roof, no dynamic amplification factor was applied to the these column moments. Therefore, the required column moment capacity M_{col} for Designs 1 and 2 at the roof was in general equal to the following:

$$M_{col} = \sum 1.25 M_{P_{beam}} + \sum M_{D_{beam}} \qquad (8.13)$$

Because of the arrangement of the pin connections in Design 3, the entire length of each interior column was assumed to be a cantilever fixed at the base of the EBF. In addition, each exterior column in the upper three floors was idealized as a cantilever fixed at the third floor. The design envelope for end moments in these columns was then established by estimating the shear force developed in these members. This is recognized to be a very severe criterion for sizing the column. In any event some provision for moment capacity must be included in the preliminary design. Each interior column of Design 3 was assumed to develop 1.25 percent of the story shear through cantilever action, while each exterior column in the upper three floors was assumed to develop 2.5 percent of the story shear through cantilever action. These values were based on examining the results of previous static analyses of EBFs. The moments in the columns idealized as cantilevers were not amplified by ω, for these column moments were determinate for a given vertical distribution of lateral force along the corresponding column. In the remaining exterior columns, located in the lower three floors, moment connections attached the links to the columns. Therefore, the required moment capacity at each end of these columns was determined, as in Designs 1 and 2, using the strong column-weak beam concept and the dynamic amplification factor ω.

After completing the preliminary design, the story drift, link deformation, and member forces were checked for compliance with NEHRP provisions. This involved performing an elastic analysis of the designed frame, where the gravity loads and lateral forces F_x were applied to the structure using the appropriate load combination factors [66]. The calculated displacements and deformations were then scaled to simulate ultimate conditions. That is,

the story drift for ultimate conditions in EBFs is assumed by NEHRP to be equal to the elastic story drift multiplied by a deflection amplification factor C_d of 5. The corresponding plastic deformation in the links at ultimate conditions is assumed by NEHRP to be equal to the elastic link deformation multiplied by the factor $(C_d - 1)$. These scaled deformations were then compared with the limits recommended by NEHRP, where the maximum allowable story drift is 1.5 percent, and the maximum allowable plastic link deformation is 0.06 radians. Member forces were examined for compliance with NEHRP by comparing the calculated elastic link shear forces with the recommended limit of V_p. The other members were checked to assure their stability and strength allowed the ultimate link state to be obtained. Two additional requirements besides those of NEHRP were considered which the EBF designs had to satisfy. Firstly, if the elastic analysis indicated that yielding outside the links would occur then the design was considered inappropriate. Secondly, the vertical floor deflection of the floor beams under serviceability conditions had to meet deflection limits of the AISC Specification. If the preliminary design did not meet the NEHRP and the two additional requirements, then the plastic design procedure was repeated, where questionable members were replaced followed by another design check. It was found that if a preliminary design had to be repeated it was due to excessive link deformation.

The result for Designs 1, 2, and 3 are shown in Figs. 8.9 to 8.11. Recommended link and connection details for typical EBFs can be found in Refs. [7,18,119,127].

8.3. Program of Investigation

As noted previously, the three designs were analyzed for nonlinear response to strong motion earthquake records. It was decided to use more then one earthquake record in order that the performance of the EBF designs could be assessed for response involving several cycles of significant link yielding, in addition to large excursions of plastic link deformation, respectively. When subjecting the EBF designs to the south-east component of the 1940 El Centro earthquake record which had been scaled by a factor of 1.5, several cycles

of significant link yielding occurred. The original El Centro earthquake record was recorded in the epicentral area of the earthquake, and is considered to be a strong motion earthquake [123]. The scaled El Centro earthquake record had a magnitude of peak ground acceleration equal to 0.5 g, as indicated by the scaled accelerogram shown in Fig. 8.12. When subjecting the EBF designs to the north-east component of the 1966 Parkfield earthquake, the responses contained large excursions of plastic link deformation. The Parkfield earthquake record was recorded 200 feet from the ruptured fault, resulting from a lesser magnitude earthquake than El Centro. However, the Parkfield accelerogram possessed a magnitude of peak ground acceleration equal to 0.49 g, as shown in Fig. 8.13. The response to other earthquake records was also examined (Taft, Pacoima Dam), however, it was determined that the El Centro and Parkfield earthquake records were the most representative. Therefore, the discussion will focus on the response of the three EBF designs to the scaled El Centro and original Parkfield earthquake records.

A summary of the nomenclature to identify the results of the analyses using the scaled El Centro and original Parkfield earthquake records is given in Table 8.1. Each design was initially analyzed for the first 15 seconds of one of the earthquake records as a bare steel frame with representative strain hardening. The damping matrix was based on nonproportional damping. The effects of modeling assumptions were then examined, where the duration of the input earthquake record was again 15 seconds.

Design 1 was thus reanalyzed (scaled El Centro record) assuming elastic-perfectly plastic behavior (EPP) in order to study the effects of strain hardening. Design 1 was also analyzed assuming Rayleigh damping (scaled El Centro record) in order to examine the sensitivity of the response to different forms of modeling viscous damping.

To determine if the P-delta effect were significant, the results of one of the initial analyses of Design 2 was compared with the results of an additional analysis which did not include a geometric stiffness. The analysis used to assess the P-delta effect involved the EBF model subjected to the Parkfield earthquake record. To assess the effects of composite

floor slabs in EBFs, Design 2 was modeled using composite floor beams with representative strain hardening. Thus, the composite beam properties were determined for an exterior and an interior EBF with composite floor slabs. An exterior EBF is located at a parameter of the building. Such a frame was part of the original building plan. An interior EBF is situated at the interior of the building. Such an arrangement was not part of the original building plan. The intent of modeling an interior EBF with composite floor slabs was to assess the response of an EBF with increased composite action compared to an exterior EBF with composite floor slabs. In addition to comparing the responses of EBFs with composite floor slabs to the responses of the bare steel EBFs, the bare steel based design procedure was compared with the responses of the EBFs with composite floor slabs. Consequently, it could then be established whether the effects of composite action should be incorporated into the design procedure for EBFs. This involved performing four more analyses of Design 2, whereby the response of EBFs with different degrees of composite action to different earthquake records was assessed.

Originally, Design 3 was analyzed assuming that the pin connections did behave as true pins. Since in practice a pin connection, also referred to as a shear connection, will likely develop some bending moment, Design 3 was reanalyzed using all moment type connections. This enabled an assessment to be made concerning the effects of developing bending moment at the pin connections, and also the use of pin connections versus moment connections in EBFs.

The response quantities examined included those which would enable a comparison of the responses with the design procedure, and give an indication of the effects of the earthquake record and modeling assumptions. Therefore, the response quantities included the following: member forces, areas of inelastic activity in the EBFs, link deformation, plastic deformation demand outside the links, member energy dissipation, the stability of braces and columns, the point of inflection in columns, story drift and displacement, and the story shears.

8.4. ANSR Model

As indicated previously, the ANSR-1 program was used to perform the nonlinear dynamic analyses of the EBF designs. The model of each EBF consisted of two-dimensional elements, where in the plane of the EBF horizontal, vertical, and rotational degrees of freedom were defined for each node. The nodal degrees of freedom at the supports were fully restrained to simulate fixed boundary conditions. Centerline dimensions between members were used. Rigid offsets were included in the model to simulate rigid gussets plates at the ends of the links and also eccentricities between the column centerlines and the pin connections. The total mass of the building was based on the effective weight W. Since only the EBFs of the building were assumed to resist the lateral seismic forces, the total mass of the building was divided equally among its two EBFs. In each floor of the EBF model the mass associated with that floor was lumped at the nodes based on the tributary length of the floor beams. Since in the experimental study (Chapter 4) significant uplift of the floor slab was found to occur at the ends of the links, lumped mass associated with vertical inertia forces was defined at the corresponding nodes of the EBF models. These lumped masses were based on the tributary area of the floor slab. No rotational inertia force at the nodes was considered. A summary of the lumped masses for the EBF models is given in Fig. 8.14.

The links were modeled using the newly implemented link element. The AISC Manual [124] was consulted for the section properties, where the effective shear area A_v^* was based on the area of the web. The action-deformation relationships for the links of the various analyses are given in Fig. 8.15. These relationships were used to establish the subhinge stiffnesses. The parameters to define the effect of isotropic shear hardening (Eq. 6.83) are also given in Fig. 8.15. Both the action-deformation relationships and the isotropic shear hardening parameters were based on experimental data presented in Chapter 4 (Figs. 6.18 and 6.19, and Figs. 6.21 to 6.23) which had been normalized by their respective yield forces. A set of preliminary analyses indicated that the amount of axial force

developed in the links was small and could be ignored in determining the link capacity.

The braces, columns, and bare steel floor beams outside the links were modeled using the standard two-dimensional beam-column element in ANSR. The composite floor beams outside the links were modeled with the newly implemented composite beam-column element. Both of these elements considered moment-axial force interaction, accounting for inelastic flexural deformations but not buckling. The interaction surface was based on the AISC moment-axial force interaction formula, Eq. 2.4-3, and is shown in Fig 8.16. The stability of each member was checked after the completion of an analysis, using Eq. 2.4-2 of the AISC Specification and the member forces developed during the analysis. The assumed action-deformation relationship for the bare steel beam-column element is shown in Fig. 8.17. The effective moment of inertia I_{eff} and effective width b_{eff} based on stress distribution were determined for the composite beam-column elements using the procedure discussed in Chapter 5. This involved using the loading conditions shown in Fig. 8.18 to approximate the conditions of the composite floor beams in the EBFs. The floor slab was assumed to be constructed of a metal deck with a 6.5 in. thick concrete slab, and behave as an orthotropic plate. The degree of orthotropic behavior was the same as that measured in the experimental specimens (see Chapter 5). With I_{eff} and b_{eff} established, the action-deformation relationships were defined for the composite beam-column elements, see Fig. 8.19, where the hinge stiffness K_s for each composite beam-column element was determined by Eq. 6.104. The composite positive moment and compressive axial load capacities, M_p^+ and P_y^-, were determined using b_{eff}. A summary of the properties to define the action-deformation relationships and interaction surfaces for the composite beam-column elements is given in Tables 8.2 and 8.3. The moment of inertia I, moment capacity M_p^-, and tension axial load capacity P_y^+ in these tables are based on the properties of the bare steel section of the composite floor beam, available in the AISC Manual.

In Chapter 5 it was shown that b_{eff} varies along the floor beam outside the link for

seismic conditions. Consequently, for the present case the floor beam will not likely have the same value of $b_{\textit{eff}}$ at the column and at the end of the link, points D and B in Fig 8.18. This is also true for $I_{\textit{eff}}$. Because point B of the floor beam is adjacent to the link, it develops a larger moment and deformation compared to that at point D. Therefore, the properties at point B of the floor beam will have a greater influence on the response of the EBF. Consequently, using similar properties at both ends of the floor beams outside the links should give reasonable results, where the properties at the end adjacent to the link are used.

The local force effect due to the distributed gravity loads along the beams and links was accounted for by assigning initial forces to the elements involved. The initial forces of a beam or link were equal to the fixed end forces developed in the members under gravity load.

The damping matrix $\underline{C}$ for the EBF models required the determination of the natural periods of the elastic structure. A summary of the natural periods for the first five elastic modes is given in Table 8.4 for the models of the three EBF designs. For each model the coefficients a_0 and a_1, were calculated using Eq. 7.14 of Chapter 7 in order to define the damping matrix using Eq. 7.15. For the EBF models with Rayleigh damping, the first and fourth elastic modes were assumed to have a 5 percent damping ratio. As noted in Chapter 7, the damping matrix based on nonproportional damping was obtained by ignoring the contribution of the initial link stiffness to $\underline{C}$ in Eq. 7.15. That is:

$$\underline{C} = a_0\underline{M} + \sum_i a_{1,}\underline{K}^{elm\ i} \qquad (8.14)$$

where $a_{1,} = 0$ for the link elements. For the EBF model with nonproportional damping the coefficient a_0, as well as the coefficients $a_{1,}$ of the elements excluding the links, were determined using a 5 percent damping ratio for the first and fourth elastic modes. Based on this value of a_0, the damping ratio for the first elastic mode was equal to 4.1 percent for the link elements.

8.5. Analysis Procedure

Each of the analyses was initiated by applying the gravity loads and then calculating the structural response. A geometric stiffness was then determined based on the member axial forces due to these gravity loads. This geometric stiffness was added to the initial elastic stiffness of the model. The nonlinear dynamic analysis was then performed using the procedure described in Section 7.4 of Chapter 7, which involved Constant Stiffness iteration. Therefore, the geometric stiffness was not updated during a dynamic analysis. This should not have a significant effect on the results, for it was found that the P-delta effect was not pronounced for the EBF designs being analyzed.

The dynamic analyses were performed using a constant time step size of 0.005 seconds. Hence 3,000 time steps were required to analyze the EBF designs for the first 15 seconds of a selected earthquake record. The time step size of 0.005 seconds was selected using the criteria discussed in Section 7.4.

8.6. Analysis Results

8.6.1. Response of EBF Design 1

Design 1 was designed on the premise that all links be W18 beam sections, as shown in Fig. 8.9. As in a real situation, members sizes were repeated in order to have an economical design.

To facilitate the discussion of Design 1, as well as the other designs, the various analyses will be referenced by the nomenclature defined in Table 8.1. Furthermore, the link end moments M_A and M_B will have the positive sign convention shown in Fig. 8.20. The results to be discussed concerning Design 1 will include EC1, EC2, and EC3 from the scaled El Centro analyses, and PA1 from the Parkfield analyses. Hence, the effects of strain hardening, damping model, and earthquake record will be examined.

The areas in which yielding occurred in these four analyses of Design 1 are shown in

Fig. 8.21. From this figure it can be seen that the locations of links yielding in shear are similar for all four analyses. Furthermore, moment yielding developed adjacent to the exterior columns in the links. It appears that Design 1 developed more yielding outside the links when subjected to the Parkfield earthquake record, for in analysis PA1 additional plastic hinges developed at the ends of several floor beams adjacent to the ends of links, at the base of an exterior column, and in the floor beams of unbraced panels at floors 3 and 4 compared to analysis EC1.

The time histories for the lateral floor displacements from the four analyses of Design 1 are shown in Fig. 8.22. The response to the scaled El Centro earthquake record of the models with strain hardening but with different damping assumptions (analyses EC1 and EC3) had a similar displacement history, where all floors tended to oscillate about their original positions. On the other hand, the elastic-perfectly plastic model (analysis EC2) developed more of a one-sided lateral floor displacement time history, leading to larger magnitudes of lateral displacement than the analyses with strain hardening. The one-sided displacement is an indication of permanent link deformation resulting from link yielding. The response to the Parkfield earthquake record (analysis PA1) included sustained displacements with intermediate unloading and reloading from time $t = 4.0$ to 5.0 seconds. This was followed by oscillations about a non-zero reference for all floors above floor 1. Design 1, when modeled with strain hardening, appears to have developed more permanent deformation when subjected to the Parkfield earthquake record.

The maximum story drift during the El Centro analyses are shown in Fig. 8.23(a). This figure indicates that compared to the upper floors, the lower floors developed greater story drift, where slightly larger magnitudes occurred in the elastic-perfectly plastic model compared to the models with strain hardening. The maximum story drift developed during the Parkfield earthquake record is shown in Fig. 8.23(b), where it is apparent that the story drift is greater than that due to the scaled El Centro earthquake record. Furthermore, during the Parkfield earthquake the story drift in the first and second floors approached the code

limit of 1.5 percent.

The limited resistance of the model without strain hardening is evident in the base shear time history shown in Fig. 8.24(a), where it is compared to the results of the model with strain hardening. For completeness, base shear time histories for the other analyses of Design 1 are shown in Figs. 8.24(b) and (c). A summary of the maximum base shear for these analyses, as well as those of Designs 2 and 3, is given in Tables 8.5 and 8.6. The story shear envelopes for Design 1 are shown in Figs. 8.25(a) and (b). From Fig. 8.25(a) it is apparent that the strain hardening effect caused larger story shears, with a greater increase occurring in the lower floors. By including strain hardening, the base shear increased by 30 percent in the model with nonproportional damping. This figure also indicates that Rayleigh damping apparently adds greater resistance than nonproportional damping. The story shears were generally six percent greater in the model with Rayleigh damping compared to the model with nonproportional damping. The story shear envelope for the response to the Parkfield earthquake record (analysis PA1) is shown in Fig. 8.25(b), where it is compared to the maximum story shear forces developed during the scaled El Centro earthquake record (analysis EC1). This figure indicates that greater story shear forces developed during the Parkfield earthquake, where the maximum base shear of analysis PA1 is 12 percent greater than that of analysis EC1.

The maximum shear forces developed in the links are shown in Fig. 8.26. The fourth floor link developed a slightly greater maximum shear force than some of the links in the lower floors, particularly during the Parkfield earthquake. This phenomenon is attributed to the sudden change of the bracing configuration at floors 3 and 4. However, a general trend exists where larger shear forces developed in the links of the first floor, particularly in the analyses involving strain hardening. Larger shear forces were also found to exist in the links of lower floors in the preliminary design. However, as shown in Fig. 8.26, the analyses results are greater than the preliminary design link shear forces. This can be attributed to the fact that the selected sections for the links had greater capacities than the

required design forces. Strain hardening is not included in the link shear design forces, therefore the results of the analyses with strain hardening show an even bigger discrepancy compared to the design forces.

Greater amounts of link strain hardening developed in the lower floors, as shown in Fig. 8.27 by the increase in the link shear force beyond the yield strength V_p. Figure 8.27 indicates that the first floor links developed a maximum shear of 1.55 V_p during both the scaled El Centro and original Parkfield earthquakes. Figure 8.27(b) indicates that the Parkfield earthquake record causes greater link strain hardening in the upper floors than the scaled El Centro earthquake record. The El Centro analyses using different damping models (analysis EC1 and EC3) appear to have developed similar magnitudes of strain hardening and thus maximum link shear forces, as shown in Figs. 8.26 and 8.27. Therefore the use of the different damping modeling does not appear to have significantly influenced the shear force in the links.

Shear-deformation hysteretic loops for links in floors 1 and 4 are shown in Fig. 8.28 from analysis EC1. Corresponding results are shown in Fig. 8.29 for the same EBF model (analysis PA1) subjected to the Parkfield earthquake record. These figures indicate that a greater number of yield excursions occurred during the response to the scaled El Centro earthquake, however, greater link deformations occurred during the Parkfield earthquake. Furthermore, the link deformation in the first floor link is greater than that of the fourth floor link for both analyses. The link deformation envelopes for all of the floors are given in Fig. 8.30. This figure indicates that the links of the lower floors generally developed greater deformation. Strain hardening apparently decreased the amount of link deformation, as shown in Fig. 8.30(a). However, the code limit of 0.06 radians for link deformation is exceeded by the first floor link during the scaled El Centro earthquake (Fig. 8.30(a)), and by the lower three floors during the Parkfield analysis (Fig. 8.30(b)). Apparently the Parkfield earthquake record results in a significant increase in the link deformation of all floors.

Moment-deformation hysteretic loops for the first and fourth floor links are shown in

Fig. 8.31 for analysis EC1, and in Fig. 8.32 for analysis PA1. From these figures it is apparent that the end moments of the links adjacent to a column are not equal. In Figs. 8.31(a) and 8.32(a) the link end moment M_B next to the column was as much as four times the end moment M_A at the other end of the link during elastic loading. After strain hardening, M_B was equal to $2M_A$. Therefore, full equalization of end moments did not occur in this link. This was found to also have occurred in the other links which were adjacent to the columns. Figures 8.31(b) and 8.32(b) indicate that the link at the fourth floor had approximately equal magnitudes of end moment. This was found to occur in all of the links in the K-braced panels. With strain hardening, the link end moments adjacent to columns developed a maximum moment as large as 1.15 M_p, as shown in Fig. 8.33, indicating a desirability of using 1.25M_p as suggested in the code for column design. This figure also illustrates that the use of a different damping model (analyses EC1 and EC3) did not appear to significantly influence the amount of end moment developed in the links.

Figure 8.34 shows the maximum relative vertical displacements Δ_r developed between the ends of each link. Consistent with the link deformation envelopes, Δ_r increased in the lower floors, with greater values of Δ_r occurring during the Parkfield earthquake. For the results shown in Fig. 8.34(b), in which the links were modeled with strain hardening, the maximum value of Δ_r during the Parkfield earthquake (analysis PA1) and the scaled El Centro earthquake (analysis EC1), respectively, was nine percent and seven percent of the link's length. The permanent relative vertical displacement Δ_{rp} of the links was determined at the end of the time histories for floors 1, 2, and 4 shown in Figs. 8.35 through 8.37. The values of Δ_{rp} are summarized in Tables 8.7 and 8.8. It was found that larger values of Δ_{rp} occurred in floors 2 and 4 compared to floor 1, with the Parkfield earthquake record causing a Δ_{pr} of 0.77 inches in floor 4. This was the largest value of Δ_{pr} developed in Design 1, and was equal to about three percent of the link's length.

An examination of the zones of yielding during the analyses of Design 1 was presented earlier in Fig. 8.21. As was noted then, yielding outside the links was more pro-

nounced during the Parkfield earthquake (analysis PA1), where yielding in floor beams of braced panels occurred outside the links. Figure 8.38 shows for these members the maximum moment and axial force corresponding to the EBF model with strain hardening and nonproportional damping. These results are from the response to the scaled El Centro (analysis EC1) and original Parkfield earthquake records (analysis PA1). The maximum forces shown in Fig. 8.38 indicate that the design forces are more reasonable for the upper floors. During the Parkfield earthquake the calculated response exceeded the design forces in the lower three floors, resulting in yielding. The maximum plastic rotation Θ_p of these members however was found to be less than one-half the rotation Θ_Y, where Θ_Y is the rotation at yield of the floor beam outside the link determined by:

$$\Theta_Y = \frac{M_Y L}{3EI} \qquad (8.15)$$

where

M_Y = yield moment of floor beam,

L = length of floor beam between the column and the end of the link,

EI = bending rigidity of floor beam.

It is not expected that this yielding would result in local buckling which will limit the ductility of these members, for Θ_p is in the range where the compact floor beams can control local buckling [115].

The maximum moments developed in the floor beams of unbraced panels are shown in Fig. 8.39 from the analyses of Design 1. An examination of Fig. 8.39(a) indicates that the analyses with strain hardening developed approximately the same maximum floor beam moments as the elastic-perfectly plastic analysis. Figure 8.39(b) indicates that the Parkfield earthquake record produced larger moments in these floor beams than the scaled El Centro earthquake record. Although the results in Fig. 8.39(b) correspond to models with strain hardening, there was not a significant increase in the moment beyond M_p.

The use of $1.25M_p$ for column design however is still justified, for it serves as a safe-guard against situations where the floor beams have overstrength and columns understrength due to the varying yield strength of structural steel. The axial force in the floor beams of unbraced panels was found to be small, where the maximum member axial force was less than seven percent of the member axial yield force. The yielded floor beams of unbraced panels developed larger amounts of Θ_p compared to other members in the EBF models. The maximum amount of Θ_p developed in the floor beams of the unbraced panels was found to be equivalent to 1.5 times the rotation Θ_Y, where Θ_Y is the rotation at yield of the floor beam as determined by:

$$\Theta_Y = \frac{M_Y L}{6EI} \tag{8.16}$$

where

M_Y = yield moment of the floor beam,

L = length of the floor beam,

EI = bending rigidity of the floor beam.

This amount of ductility demand is reasonable, and likely can be supplied by the floor beams [115].

The braces of the models were checked after the completion of each analysis and found to have developed no stability problems. Axial force time histories for a first floor brace are shown in Fig. 8.40. The results in Fig. 8.40(a) correspond to the models with and without strain hardening, using nonproportional damping. From this figure it is apparent that the link with strain hardening caused a greater axial force to develop in the adjoining brace. This was found to occur in all braces framing into links which developed yielding, as shown in the axial brace force envelopes plotted in Fig. 8.41(a). These results are from the response to the scaled El Centro earthquake record, where all of the links except for the one at the roof (see Fig. 8.21) developed yielding. The increase in the axial brace force due to link strain hardening is shown in Fig. 8.41(a) to be more pronounced in the lower floors,

where a 25 percent increase in the axial brace force occurred in the first floor. However, the design envelope appears to be satisfactory for these two analyses. On the contrary, Fig. 8.41(b) indicates that the Parkfield earthquake record caused greater axial brace forces than the scaled El Centro earthquake record in models with strain hardening. Consequently, the axial force in the braces of the lower three floors during the Parkfield earthquake exceeded the compressive design force. At the first floor the Parkfield analysis results were 10 percent greater than the design force.

As discussed in Chapter 7, Rayleigh damping compared to nonproportional damping leads to larger brace forces. It was shown that this was due to the increase in damping of the lower modes during inelastic deformations. A time history of the axial force for a first floor brace is shown in Fig. 8.42(a) corresponding to the model with Rayleigh damping. These results are based on the response to the scaled El Centro earthquake record (analysis EC3). The shear force time history for the link adjacent to this brace is shown in Fig. 8.42(b). Superimposed on these two figures is the response for the model with nonproportional damping which was subjected to the scaled El Centro earthquake record (analysis EC1). The increase in the axial brace force in the model with Rayleigh damping is evident compared to that in the model with the nonproportional damping. The shear force in the first floor link of the two models however is similar at the instances when the maximum magnitudes of axial brace force develops. The axial brace force envelope corresponding to these two analyses is shown in Fig. 8.43. This figure illustrates the fact that the braces next to yielded links (floors 1 through 5) developed larger axial forces when the EBF was modeled with Rayleigh damping as opposed to nonproportional damping. The increase is more pronounced in the braces of the lower floors, whose links happen to develop the most strain hardening. An 11 percent increase in the maximum axial force was found in the first floor brace. This increase is enough to cause the axial force in the first floor brace to exceed the design envelope by 10 percent during the analysis involving Rayleigh damping.

The phenomenon of the axial brace forces increasing when higher damping develops

in the link can be explained by considering a free body diagram of a floor beam and brace in an EBF. This free body diagram must include the members' damping forces f_D and the vertical inertia force f_I which develops at the end of the link. Such a free body diagram is shown in Fig. 8.44. Considering the vertical equilibrium of the node at the end of the link, an expression for the axial brace force P_{br} and axial damping brace force $f_{D_{br}}$ can be written, reading:

$$P_{br} + f_{D_{br}} = \frac{V_{link} + V_{bm}}{\sin\Theta} + \frac{f_I + f_{D_L} + f_{D_{bm}} + f_{D_m}}{\sin\Theta} \tag{8.17}$$

where

V_{link}, V_{bm} = shear forces of the floor beam in the link and outside the link,

f_I = vertical inertia force associated with the lumped mass,

f_{D_L}, $f_{D_{bm}}$ = damping shear forces of the floor beam in the link and outside the link,

f_{D_m} = damping force associated with the lumped mass,

Θ = angle of inclination between the brace and floor beam, see Fig. 8.44.

It is believed that the term $f_{D_{br}}$ is small relative to P_{br} because the velocity associated with the axial extension of the brace is small. Hence, Eq. 8.17 clearly illustrates that the effect of inertia and damping forces leads to an increased brace force P_{br} during the dynamic response. It was determined that the inertia and damping forces increased the maximum value of P_{br} of the first floor brace by 3 to 5 percent in the El Centro analysis with nonproportional damping and strain hardening (analysis EC1). In the El Centro analysis with Rayleigh damping and strain hardening (analysis EC3) the damping and inertia forces increased the maximum value of P_{br} of the first floor brace by 11 to 15 percent, while the Parkfield analysis with nonproportional damping (analysis PA1) had an 8 to 11 percent increase in the maximum value of P_{br} of the first floor brace.

The maximum end moments developed in the braces are shown in Fig. 8.45. This figure indicates that the maximum magnitude of brace moments which developed above the first floor were approximately equal for the analyses. There was a noticeable increase in the

moment of the first floor brace, which developed at the fixed end of the brace. Strain hardening and damping modeling did not appear to influence the development of the brace moments. A small increase in the brace moments occurred during the Parkfield earthquake record compared to the scaled El Centro earthquake record, where the increase is greater in the braces of the lower floors. With the increase in the brace moment at the first floor during the Parkfield earthquake, the brace design moment envelope was exceeded at the first floor by approximately 20 percent. At other floors, the design envelope for the brace moments appears to have been reasonable for all analyses of Design 1.

A review of the response of the columns indicated that all of the columns remained stable during the analyses. As noted previously, the first floor exterior column yielded at the base during the Parkfield earthquake, however the maximum plastic rotation was less than one-fourth the rotation Θ_Y, where Θ_Y is the rotation at yield of the column determined by:

$$\Theta_Y = \frac{M_Y h}{6EI} \tag{8.18}$$

where

M_Y = yield moment of the column,

h = height of the column,

EI = bending rigidity of the column.

It is expected that this will not result in any ductility problems, for only one yield excursion occurred and the plastic deformation is in the range where the compact section selected for the first floor column can control local buckling [115].

The column axial force envelopes are shown in Fig. 8.46. The effect of link strain hardening on the column axial force is evident in Fig. 8.46(a). In this figure the maximum column axial force was 700 kips in the exterior columns and 650 kips in the interior columns for the model with strain hardening. This amounts to an increase of 22 percent and 13 percent compared to the elastic-perfectly plastic model. These results correspond to

a compression force. The use of Rayleigh damping compared to nonproportional damping resulted in an increase in the maximum axial force by 100 kips and 50 kips in the exterior and interior columns, respectively, as shown in Fig. 8.46(b). This amounts to a 13 percent and 8 percent increase in the maximum column axial forces, and were compressive axial forces. The column axial force envelope shown in Fig. 8.47 indicates that the Parkfield earthquake record produced larger column axial forces than the scaled El Centro earthquake record. This is most noticeable in the exterior columns adjacent to the links of the lower three floors. An increase of 10 to 15 percent in the axial force was found to have occurred in these columns. For all of the analyses of Design 1, the column axial force preliminary design envelope appears to have served well for determining the design forces.

For the columns, a moment diagram was drawn corresponding to the maximum moments developed in each column, as shown in Figs. 8.48 to 8.51. Considering strain hardening, Figs. 8.48 and 8.49 show that the column moments based on the weak beam-strong column concept (indicated by M_{code}) need to be amplified by Paulay's procedure [121] in order to give an appropriate design envelope for the columns adjacent to the links (exterior columns of floors 1 through 3). Elsewhere in the EBF, the use of M_{code} for column design would appear to have been sufficient. Figure 8.50 indicates that the elastic-perfectly plastic link response causes the columns to develop greater moments, particularly in the lower floors. This is an indication that the additional lateral load carrying capacity of the EBF models with strain hardening was developed through the truss action of the EBFs, as opposed to bending of the columns. This same phenomenon is also present when comparing the results in Fig. 8.51 from the two analyses corresponding to Rayleigh damping and nonproportional damping. The former analysis developed a greater base shear (see Fig. 8.25(a)) compared to the analysis with nonproportional damping, where the additional lateral load was resisted by truss action.

Figures 8.52 and 8.53 show the energy time histories for the analyses of Design 1. Note the resemblance with the results for the inelastic single degree of freedom system dis-

cussed in Chapter 7 (see Fig. 7.14), where a majority of the input energy was dissipated by hysteretic energy. The energy time histories shown in Fig. 8.52 indicate that the cyclic response to the scaled El Centro earthquake record resulted in a greater amount of energy dissipation compared to the response to the Parkfield earthquake record. This occurred in spite of the fact that the Parkfield earthquake record caused larger member forces and a base shear to develop, as well as yielding in more of the members than the scaled El Centro earthquake record. The scaled El Centro earthquake record resulted in a greater amount of energy dissipation because of the greater number of yield excursions occurring in the links of the model. Most of the energy dissipated during the response to the Parkfield earthquake record occurred between 4 and 5 seconds when large sustained displacements developed in the links.

Tables 8.9 and 8.10 summarize the energy results, showing that the input energy IE was not a constant, nor was the dissipated hysteretic energy HE and damping energy DE of the models. These values were found to vary for different earthquakes and modeling assumptions. For similar models (analyses EC1 and PA1), the scaled El Centro earthquake record resulted in a larger amount of input energy to the EBF, compared to the Parkfield earthquake record. Tables 8.9 and 8.10 also indicate that the links dissipated almost all the hysteretic energy, where the links in the lower floors dissipated larger portions of energy. Considering strain hardening (analyses EC1 and PA1), the two links in the first floor dissipated about 67 percent of the total hysteretic energy dissipated by the EBF during the scaled El Centro earthquake record, and about 57 percent during the Parkfield earthquake record. The elastic-perfectly plastic and Rayleigh damped models, when subjected to the scaled El Centro earthquake record, responded in a manner where the first floor links dissipated about the same percentage of the EBF's hysteretic energy as in analyses EC1 and PA1. The amount of hysteretic energy dissipated per link is shown in Fig. 8.54.

It is apparent that the links in the first floor are severely taxed compared to the links in the other floors. A more uniform distribution of energy dissipation among the links is

desirable in order to maintain the efficiency of the EBF. With a majority of the inelastic activity occurring in one link, the energy dissipation capacity of the EBF becomes limited by the energy dissipation capacity of that link.

8.6.2. Response of EBF Design 2

Design 2 was a modification of Design 1, where the links of the first and second floors were replaced by links of a larger section size. This was done in order to force the links in the upper floors to develop greater amounts of plastic deformation, and therefore dissipate more hysteretic energy. As a result, the first floor links of Design 2 would likely dissipate less energy than Design 1, thereby resulting in a more uniform distribution of energy dissipation among all links. The ensuing link shear strength to required shear strength ratio V_p/V_{link} for the floors is shown in Fig. 8.10. With the increased link capacity in floors 1 and 2, larger section sizes were required for the braces and exterior columns of floors 1 and 2.

With the changing of the section sizes, the elastic fundamental period of vibration became equal to 0.69 seconds (see Table 8.4). Hence, the elastic fundamental period of vibration for Design 2 was about 4 percent shorter than that of Design 1. The higher elastic vibration periods for Design 2 show a smaller change with respect to those of Design 1. Therefore, the initial vibration periods of Designs 1 and 2 appear to be very similar.

8.6.2.1. Comparison of Design 2 with Design 1

A comparison of Design 1 and 2 is appropriate in order to evaluate whether the design modifications served their purpose. Therefore, Design 2 was subjected to the scaled El Centro earthquake record as well as the Parkfield earthquake record. The results to be discussed in the comparison of Design 2 with Design 1 pertain to the model which considered strain hardening with nonproportional damping. The two ensuing analyses of Design 2 are identified in Table 8.1 as EC5 and PA2.

The maximum shear forces developed in the links of Designs 1 and 2 are shown in Fig. 8.55. Normalized results with respect to the link shear capacity V_p are shown in Fig. 8.56. These figures indicate that although larger shear forces developed in all of the links of Design 2 compared to Design 1, less strain hardening developed in the first and second floor links of Design 2. Furthermore, in Design 2 greater amounts of strain hardening developed in the links above the second floor than in Design 1. In Design 2 the links of floors 1 through 3 have about the same amount of strain hardening, reaching a maximum shear force of $1.46V_p$ during analysis EC5 and $1.5V_p$ during analysis PA2. The corresponding link deformation envelopes are shown in Fig. 8.57. This figure indicates that the maximum magnitude of link deformation in Design 2, while having decreased in floors 1 and 2, increased in floors 3 through 5 compared to Design 1. Consequently, during the Parkfield earthquake the link deformation in floors 1 through 4 exceeded the code limit of 0.06 rad. [66].

The energy time histories of Designs 1 and 2 were found to be similar in form for corresponding earthquake records, and therefore are not shown for Design 2. Figure 8.58 shows the amount of hysteretic energy dissipated by the links of Designs 1 and 2 due to the scaled El Centro and original Parkfield earthquake records, respectively. These results indicate that the links of floors 3 through 5 of Design 2 dissipated more hysteretic energy than those of Design 1, while the first floor links of Design 2 dissipated less energy than those of Design 1. The percentage of hysteretic energy dissipated per link and the total amount dissipated by the EBF model of Design 2 are included in Tables 8.9 and 8.10. These tables shows that the links of floors 3 through 5 accounted for a larger percentage of the hysteretic energy dissipated by the EBF model of Design 2 compared to Design 1. The first floor links of Design 2 accounted for about 42 percent of the hysteretic energy dissipated by the EBF model during the scaled El Centro earthquake record, and about 46 percent during the Parkfield earthquake record. It therefore appears that by having increased the link shear capacity of the lower two floors, a greater amount of hysteretic energy was dissipated by

the upper floor links. Consequently a more desirable distribution of energy dissipation was achieved among the floors.

The story drift for Designs 1 and 2 are compared to each other in Fig. 8.59. As a result of strengthening the first and second floor links, the maximum story drift was reduced by 43 percent in the El Centro analysis and 12 percent in the Parkfield analysis. Base shear time histories for Designs 1 and 2 are shown in Fig. 8.60. This figure indicates that Design 2 achieved a greater lateral load resistance for almost all cycles of vibration. The maximum base shears for Designs 1 and 2, summarized in Tables 8.5 and 8.6, indicate that Design 2 developed a 10 percent greater base shear compared to Design 1 during the response to the scaled El Centro earthquake record, and a 19 percent greater base shear during the response to the Parkfield earthquake record.

8.6.2.2. Effect of Composite Floor Slabs

As noted previously, Design 2 was analyzed accounting for the effect of composite floor slabs. To facilitate the discussion, an interior EBF with composite floor slabs will be referred to as a composite interior EBF. Likewise, an exterior EBF with composite floor slabs will be referred to as a composite exterior EBF. The effects of composite floor slabs on the response of EBFs were evaluated by comparing responses of the composite exterior EBF model (analyses EC7 and PA5) and composite interior EBF model (analyses EC8 and PA6), respectively, with the previously presented results of the bare steel model for Design 2 (analyses EC5 and PA2). All analyses of Design 2 for composite action included strain hardening and nonproportional damping, where the models were subjected to both the scaled El Centro and original Parkfield earthquake records. The periods of vibration for the first five elastic modes of the models with composite floors are included in Table 8.4. The period of vibration for the first and second elastic modes for the composite exterior EBF model were about 1 and 3 percent shorter than those for the corresponding bare steel EBF model. A decrease of about 2 and 3 percent occurred for the composite interior EBF

model. Smaller changes in the periods of the higher elastic modes are noted for the composite EBF models relative to those of the bare steel EBF model. Consequently, the elastic periods of vibration appear to be very similar for the composite and bare steel EBF models.

The yielded members of the bare steel and composite EBF models are shown in Figs. 8.61 and 8.62. These figures indicate that the composite and bare steel EBF models had similar patterns of link shear yielding among the floors. Furthermore, additional moment yielding occurred in the fourth floor link of the composite interior EBF model when subjected to both the scaled El Centro and Parkfield earthquake records. Additional yielding also appears to have developed outside the links in the interior composite EBF model compared to the bare steel EBF model. It has been determined that this yielding occurred when the composite members developed tension in the floor slab. It was assumed that the concrete floors offered no tensile capacity, and therefore composite members under such conditions had capacities of only the bare steel sections.

The floors' lateral displacement time histories for the bare steel and composite EBF models are shown in Figs. 8.63 and 8.64. For each respective earthquake record, the lateral floor displacement time histories appear to be nearly identical. As in Design 1, the response of Design 2 to the scaled El Centro earthquake record was more cyclically symmetric compared to the response of Design 2 to the Parkfield earthquake record. The latter response was more one sided, implying permanent deformation. The maximum story drift, shown in Fig. 8.65, indicates that the story drift developed in the composite and bare steel EBF models were very similar. However, in the bottom three floors the composite EBF models had a slightly greater story drift than the bare steel EBF model for both the El Centro and Parkfield earthquake records. The increase in the story drift of the composite EBF models was not enough to cause the code limit of 1.5 percent to be exceeded. The story shear forces were also found to be greater in the composite EBF models than the bare steel EBF model, as shown in the story shear envelopes plotted in Fig. 8.66. The base shear time histories for the composite EBF models are compared to the bare steel EBF model in Figs.

8.67 and 8.68. The maximum base shear was found to be about 3 percent greater for the composite exterior EBF model and 10 percent greater for the composite interior EBF model compared to the bare steel EBF model (see Tables 8.5 and 8.6).

The shear-deformation hysteretic loops for the first and fourth floor links are shown in Figs. 8.69 and 8.70, and correspond to the bare steel and composite interior EBF models. These results indicate that the composite links hysteretic shear response resembles that of the bare steel links, although the shear force of the composite links is slightly greater. The maximum shear forces developed in the links of the bare steel and composite EBF models are shown in Fig. 8.71. These results were normalized by their respective shear yield strengths V_Y, and plotted in Fig. 8.72. Apparently, larger shear forces developed in the composite links (Fig. 8.71), where for the first floor link the composite interior EBF had a 9 percent greater shear force than that of the bare steel EBF, and the composite exterior EBF a 3 percent greater shear force compared to that of the bare steel EBF. The composite link shear forces correspond to $1.63V_p$ and $1.55V_p$, where V_p is the shear capacity of the bare steel section. The corresponding bare steel link of the first floor reached a maximum shear of $1.5V_p$. As in Design 1, the link shear forces from the analyses of Design 2 exceeded the preliminary design shear forces. This is due to the link capacity of the selected section sizes exceeding the required design values, as well as the preliminary design link shear forces not considering the affects of strain hardening and composite action. Although the composite links developed a greater shear force than the bare steel links, the composite links developed less strain hardening, as indicated by Fig. 8.72. This is due to the fact that the composite link elements were assigned a greater yield strength V_Y than the bare steel link elements. The link properties for the composite link elements were summarized previously in Fig. 8.15, and are based on the experimental data of the test program discussed in Chapter 4. Hence, referring to Fig. 8.15, the links of the composite exterior and interior composite EBF models, respectively, were assigned a 5 and 17 percent greater shear yield strength (indicated as V_{y_1} in Fig. 8.15) than the links of the bare steel EBF model.

The link deformation envelopes corresponding to the bare steel and composite EBF analyses of Design 2 are given in Fig. 8.73. This figure indicates that the maximum link deformation for the bare steel and composite EBF models are very similar, where greater amounts of link deformation develop in the lower floors. The largest discrepancy between the maximum link deformations of the bare steel and composite EBF models was eight percent, which occurred at the second floor during the Parkfield earthquake. While the maximum link deformation was satisfactory for the El Centro analyses, the code limit of 0.06· rad. was exceeded by the bare steel and composite links at floors 1, 2, and 3 when subjecting Design 2 to the Parkfield earthquake record.

The maximum moments developed in the links are shown in Fig. 8.74. With respect to the bare steel link moments, the composite links of the K-braced panels (floors 4 to the roof) show a greater increase in the link end moment than the composite links of the D-braced panels (floors 1 through 3). For the composite links in the K-braced panels, this increase was from 10 to 15 percent. The maximum amount of moment strain hardening in the composite links occurred at the end of the link which was connected to the, exterior columns. The bare steel link was found to behave in a similar manner. The second floor link of the composite interior EBF model developed the largest amount of strain hardening, where the end moment reached $1.14M_p$. However, this moment was only four percent larger than that of the corresponding bare steel link. Hence, it appears that composite action did not significantly influence the amount of moment strain hardening in the links.

Moment-deformation hysteretic loops for first and fourth floor links of the composite interior EBF model are shown in Figs. 8.75 and 8.76. For the first floor composite link, during elastic deformations the end moment M_B at the column was found to be three to four times larger than the moment M_A at the other end of the link. After significant strain hardening, M_B was two to three times larger than M_A. This was found to be consistent with the results of the other links which were adjacent to columns in the composite interior EBF model. It was also found that the links adjacent to the columns in the composite exterior

and bare steel EBF models had similar ratios for the end moments as the above results for the composite interior EBF model. Therefore, an equalization of the end moments of links adjacent to the columns did not occur. From the fourth floor composite link response shown in Figs. 8.75(b) and 8.76(b), it is apparent that these link end moments were also not equal. This was found to have occurred in all of the composite links of the K-braced panels (floors 4, 5, and the roof). The composite links of these upper three floors were found to have developed a greater end moment at the end of the link where the floor slab was in compression. This phenomenon was more pronounced in links of the composite interior EBF model. As noted in the experimental results, this is due to the effect of the floor beam outside the link developing an increase in its flexural stiffness when compression developed in the floor slab. Although the end moments of the composite links of the K-braced panels were not equal, the ratio of the end moments for these links was closer to unity than for the links adjacent to the exterior columns. The ratio of end moments for the composite links in the K-braced panels ranged from 1.25 to 1.5 for the composite interior EBF, and from 1.2 to 1.3 for the composite exterior EBF. Based on the above observations with regard to the links adjacent to columns and in K-braced panels, it appears that composite action did not have a significant effect on the link end moments.

The values of the maximum relative vertical displacement Δ_r between the ends of the links are shown in Fig. 8.77. Composite action does not appear to have significantly influenced Δ_r. The time histories for Δ_r for links of floors 1, 2, and 4 are shown in Figs. 8.78 and 8.79, corresponding to the responses of the bare steel and composite interior EBF models subjected to the scaled El Centro and original Parkfield earthquake records. These results, as well as time histories for the composite exterior EBF model (not shown), were used to determine the permanent relative vertical displacement Δ_{rp} in the links at the end of the analyses. The ensuing results for Δ_{rp} are summarized in Tables 8.7 and 8.8. These results indicate that Δ_{rp} was not consistently greater for the bare steel model (analyses EC5 and PA2) relative to the models with composite floors (analyses EC7, PA5 and EC8, PA6).

For corresponding earthquake records Δ_{rp} of the composite EBF models appears to have decreased at some floors, while at other floors to have increased relative to the bare steel EBF model's results. This phenomenon also appears to be affected by the use of different earthquake records. Overall, Δ_{rp} remained small compared to the length of the links. For the composite EBF analyses the maximum value of Δ_{rp} was about 0.9 in., which occurred in the second floor link of the composite interior EBF model during the Parkfield earthquake. This result was about 3.5 percent of the link's length. For the bare steel EBF model the maximum value of Δ_{rp} was 3.5 percent of the link's length, which occurred in the fourth floor link.

Higher degrees of composite action were found to have caused slightly greater end moments of the floor beams outside the links in the K-braced panels. This was more evident at the ends of these members which were adjacent to links, as shown in Fig 8.80(a) for the Parkfield earthquake. The maximum end moments of the floor beams of the D-braced panels (floors 1, 2, and 3) are shown to have been nearly equal for both the composite and bare steel EBF models. Due to the larger shear forces associated with the composite links, the axial forces which developed in the floor beams outside the links increased in the EBF models with composite floors. This is evident in Fig. 8.80(b), which shows the maximum axial forces of these members corresponding to the response to the Parkfield earthquake record. Consequently, the composite interior EBF model developed larger axial forces outside the links than the bare steel and composite exterior EBF models, resulting in the axial design forces being exceeded in floors 1 through 4. These axial forces for the composite interior EBF model, however, were only about 10 percent greater than the result for the bare steel EBF model. As noted in Figs. 8.61 and 8.62, yielding did occur in some of the floor beams outside the links of the bare steel and composite EBF models. This yielding occurred in the EBF models with composite floors when the axial force and bending moment resulted in tension in the concrete floor slab. As noted previously, the composite sections had the capacity of only a bare steel section under these conditions. However, the

yielding of the floor beams outside the links did not result in a significant amount of plastic deformation. The maximum plastic deformation of these members was found to be relatively minor, being less than the rotation Θ_Y defined by Eq. 8.15. It therefore appears that the design procedure for the floor beams outside the links does not have to be modified to account for the effects of composite action.

The maximum moments developed in the floor beams of unbraced panels is shown in Fig. 8.81. Composite action does not appear to have significantly influenced these results. The composite floor beams were found to have yielded when the floor slab developed tension. The axial force of the floor beams in unbraced panels for both the bare steel and composite EBF models was relatively small. A maximum value equivalent to seven percent of the bare steel section's axial yield strength was observed. Like Design 1, the majority of the plastic deformation occurring outside the links developed in the floor beams of unbraced panels, particularly during the Parkfield earthquake. The composite floor beams experienced greater plastic deformation than the bare steel floor beams, however, the maximum plastic deformation of the composite floor beams was only $1.3\Theta_Y$, where Θ_Y is the rotation defined by Eq. 8.16. This amount of plastic deformation is considered relatively minor.

It is expected that since larger shear forces developed in the composite links, greater axial brace forces would also develop in the composite EBF models compared to the bare steel EBF model. The axial force envelopes for the braces are shown in Fig. 8.82. This figure indicates that the axial forces in the braces of the composite interior EBF model were indeed greater compared to those of the bare steel EBF model. Axial brace force time histories for the first floor are given in Fig. 8.83 for the bare steel and composite interior EBF models. These results indicate that the axial brace force of the composite interior EBF model exceeded that of the bare steel EBF model several times during the analysis. It was found that the braces of the composite interior EBF model developed axial brace forces in floors 1 through 4 which were approximately 12 percent greater than those of the bare steel EBF model. The maximum axial brace forces in floors 1 through 4 of the composite exte-

rior EBF model (not shown) were found to be about four percent greater than those of the bare steel EBF model.

The axial brace force design envelopes in Fig. 8.82 appear to have been satisfactory for the bare steel analysis, although the first floor brace axial force exceeded the design force by about five percent during the Parkfield earthquake. The shear force in the link corresponding to this brace force was $1.5V_p$ (see Fig. 8.72(b)). The phenomenon of the axial brace force in the bare steel EBF model exceeding the design envelope is attributed to the effect of the inertia and damping forces, as discussed previously. For the composite exterior EBF model, the axial force of the first floor brace (not shown) also exceeded the design envelope. This occurred during the Parkfield earthquake, where the axial force was about nine percent greater than the design value. The design envelope in Fig. 8.82 appears to also have been satisfactory for braces of the composite interior EBF model when subjected to the scaled El Centro record. However, during the Parkfield earthquake the axial brace forces in floors 1 through 4 of this model exceeded the design envelope. For this analysis the axial forces exceeded their design loads by 14 percent at the first floor, 9 percent at the second floor, 10 percent at the third floor, and less than 4 percent at the fourth floor. The phenomenon of the axial brace forces of the composite interior EBF model exceeding the design loads is attributed to the effect of the inertia and damping forces, in addition to the increased shear capacity of the composite links.

The effect of composite floors also resulted in larger moments in some of the braces, as shown in Fig. 8.84. The design moments, while satisfactory for the El Centro analyses, do not appear to have been satisfactory for the first and second floor braces of the Parkfield analyses. Fortunately, the capacity of selected structural tubes for the braces exceeded the required design moments, and consequently the braces did not yield nor buckle.

The columns of the composite EBF models developed greater axial forces compared to the columns of the bare steel EBF model. Columns of the composite interior EBF model were found to have developed the largest increase of axial force relative to the results for

the bare steel EBF model. Column axial force envelopes for the composite interior and bare steel EBF models are shown in Fig. 8.85. From this figure it was determined that column axial forces of the composite interior EBF model were greater than those of the bare steel EBF model by as much as 10 percent in the exterior columns, and 12 percent in the interior columns. However, the column axial design forces, which were based on a bare steel frame, appear to have been satisfactory for the composite EBF.

The individual moment diagrams corresponding to maximum moments of each column for the bare steel and composite interior EBF models are shown in Figs. 8.86 to 8.89. From Figs. 8.86 and 8.87 it is evident that composite action caused larger column moments. A comparison of the bare steel analyses results with the design forces, Figs. 8.88 and 8.89, indicates that the use of column moments M_{code} based on the weak beam-strong column concept appears to have been satisfactory for the interior columns. However, for the exterior columns adjacent to the links (floors 1, 2, and 3), the bare steel analyses results exceeded M_{code}. Fortunately, as was noted previously, the column design moments were based on magnified moments ωM_{code}.

Moments developed in the exterior and interior columns of the bare steel EBF model at selected times are shown in Figs. 8.90 to 8.93. These results indicate that the sum of floor beam moments are not equally distributed to the columns above and below the floors. This is quite evident in the exterior columns at the second and third floors at time $t = 5.4$ seconds during the El Centro analysis (Fig. 8.90), and also at the first and second floors at time $t = 4.5$ and 5.0 seconds during the Parkfield analysis (Fig. 8.92). As a result, the moments at the top of the exterior columns between the first and second floors and also the ground level and first floors exceeded the moment M_{code} at $t = 4.5$ and 5.0 seconds during the Parkfield analysis. During the same analysis, at $t = 4.5$ seconds the exterior column moments at the base of the EBF also exceeded M_{code}. The moments of the interior columns compared to the exterior columns remained relatively small above the first floor, but unlike the exterior columns, some of the interior columns developed single curvature. The

moment diagrams of Figs. 8.90 to 8.93 also indicate that the point of inflection for the columns cannot be considered as a stationary point. This fact should be accounted for when designing the column splices of EBF, since it is likely that a column splice will be subjected to a bending moment during an earthquake regardless of where it is placed along a column.

Based on an examination of the above results for the column moments, it was concluded that magnifying the moments M_{code} based on the weak beam-strong column philosophy was appropriate for the design of the exterior columns adjacent to links. This compensates for the unequal distribution of floor beam moments to columns above and below the floors, in addition to the increased column moments in the EBFs due to the effects of composite floors. For the interior columns, as well as the exterior columns not adjacent to links, it was determined that the use of unmagnified moments M_{code} based on the weak beam-strong column philosophy is appropriate for design. Design envelopes based on these concepts are compared in Figs. 8.94 and 8.95 with the analysis results. As indicated in these figures, a magnification factor of 1.8 was used to obtain the design moments M_{col} for the exterior columns supporting floors 1, 2, and 3. Although all of the columns in Design 2 were actually designed using the magnified moments ($1.8M_{code}$), yielding developed at the base of the first floor exterior column. However, the maximum plastic rotation was small, being equal to $0.25\Theta_y$, where Θ_y is the rotation defined by Eq. 8.18. Furthermore, all of the columns were checked for stability using the analyses results and found not to develop any potential instabilities.

The summary of the hysteretic, damping, and total energy dissipated by the EBF models of Design 2 are included in Tables 8.9 and 8.10. From these tables, it is apparent that the amount of hysteretic energy dissipated by the EBF models of Design 2 was at least 3.5 times more than that due to viscous damping. Furthermore, the links accounted for practically all of the energy dissipated by the EBFs. The hysteretic energy dissipated by the links of each floor is shown in Fig. 8.96 for the bare steel and composite EBF models.

From this figure, as well as Tables 8.9 and 8.10, it is apparent that for corresponding earthquake records the amount of hysteretic energy dissipated by the links of EBF models with composite floors was practically equal to that of the bare steel EBF model. Hence, the amount of hysteretic energy dissipated by the links appears not to have been significantly influenced by the effects of composite action.

8.6.2.3 P-Delta Effect

As noted previously, a bare steel model of Design 2 was also subjected to the Parkfield earthquake record, where the geometric stiffness was not included in the model. A comparison of the ensuing results (analysis PA4) with those of the analysis with a geometric stiffness (analysis PA2) helped to establish the extent the P-delta effect had on the response.

It was found that the yielded members of analysis PA4 were identical to those of analysis PA2, shown previously in Fig. 8.62(a). It was also found that the maximum story drift and story shear force envelopes, shown in Figs. 8.97 and 8.98, for analyses PA2 and PA4 were very similar, except for a slightly greater story drift at the third floor in the analysis without a geometric stiffness. Furthermore, the link forces (shown in Fig. 8.99), the forces in the floor beams outside the links (not shown), and forces in the floor beams of the unbraced panels (also not shown) were found to be nearly identical for corresponding members of the two analyses.

The envelopes for link deformation and the maximum relative vertical displacement Δ_r developed between the ends of the links are shown in Fig. 8.100 for analyses PA2 and PA4. This figure is analogous to the maximum story drift, where although corresponding results for both analyses are similar, the analysis with no P-delta effect tended to have a slightly greater link deformation and a Δ_r at the third floor. This is partially attributed to the effects of changing the bracing configuration and hence story stiffness between floors 3 and 4.

The braces and columns in EBFs under combined gravity and seismic loading were

found in the previously discussed analyses to develop large axial forces. Consequently, these members are susceptible to the P-delta effect if significant transverse displacement develops in these members. The axial force envelopes and maximum moments of the braces are shown in Fig. 8.101 for analyses PA2 and PA4. This figure indicates that the axial force and moment in the braces are not significantly influenced by the P-delta effect. There is however evidence in Fig. 8.101(a) that the compression axial force is increased by the P-delta effect, but it was determined that this increase was less than six percent. The axial force envelopes and maximum individual column moments, respectively, are shown in Figs. 8.102 and 8.103. These figures indicate that the columns also are not significantly influenced by the P-delta effect. The axial force in the columns did increase due to the P-delta effect, but this increase was less than six percent.

An examination of Table 8.10 indicates that the hysteretic and damping energy dissipated by the EBFs were nearly identical for analyses PA2 and PA4. Apparently, the energy dissipated by the EBFs was not significantly influenced by the P-delta effect.

8.6.3. Response of EBF Design 3

As noted previously, Design 3 consisted of an EBF with pins at the beam and brace-to-column connections. Hence by NEHRP provisions a 20 percent increase in the design base shear was required [66]. The reason for designing an EBF with pin connections is that during construction it eases the erection of the frame.

In Design 3 an attempt was made to choose the section sizes for the links in such a manner that the phenomenon of one or two links dissipating a major portion of the hysteretic energy was avoided. Therefore, the ratio of link shear strength to required shear strength V_p/V_{link} for each of the floors was given careful consideration. An attempt was made to match the V_p/V_{link} ratios in the lower three floors of Design 2, and use smaller ratios of V_p/V_{link} in the remaining upper three floors of Design 3 compared to Design 2. In selecting the section sizes for the links, consideration was also given to the eV_p/M_p ratio of

each link, where it was desired to use values similar to those of Design 2. Available section sizes resulted in the use of the members shown in Fig. 8.11. Compared to Design 2, shown in Fig. 8.10, the V_p/V_{link} ratios of Design 3 were nearly equal for the first floor, greater in the second and third floors, and smaller in the remaining floors.

Design 3, with its pin connections, was analyzed using the scaled El Centro earthquake record (analysis EC10) and original Parkfield earthquake record (analysis PA8). As noted previously, to examine the effect of pin connections acting as semi-rigid connections, full moment connections were assumed and Design 3 was reanalyzed using the scaled El Centro earthquake record (analysis EC9) and original Parkfield earthquake record (analysis PA7).

The initial elastic periods of vibration for Design 3 are included in Table 8.4. These values indicate that the first and second elastic modes of the EBF model with pin connections had about a one and five percent longer period, respectively, than the corresponding EBF model with all moment connections. The periods of the higher elastic modes showed an even smaller discrepancy between the two EBF models. Therefore, the use of the pin connections in the EBF did not appear to significantly affect the elastic periods of vibration.

For corresponding earthquake records the yielding of links was similar for both EBF models of Design 3, as shown in Figs. 8.104 and 8.105. The EBF model with all moment connections developed yielding in some of the floor beams of the lower unbraced panels. Compared to the response to the scaled El Centro earthquake record, the Parkfield earthquake record resulted in more inelastic activity, where yielding occurred in the link at the roof and at the base of the exterior first floor columns. Although the links at the roof in the bare steel EBF models of Design 1 and 2 did not yield, Designs 1 and 2 tended to have more yielding in the floor beams outside the link and also in the floor beams of unbraced panels compared to Design 3.

The lateral floor displacement time histories for the two EBF models of Design 3 were similar for corresponding earthquake records, as shown in Figs. 8.106 and 8.107. As in the

analysis of Designs 1 and 2, the scaled El Centro earthquake record resulted in both of the EBF models of Design 3 to respond in a more cyclically symmetric manner compared to that of the response to the Parkfield earthquake record. However, unlike the responses of Designs 1 and 2 to the Parkfield earthquake, the lateral roof displacement of Design 3, following the large sustained displacements from $t = 3.5$ to 5.0 seconds, was less than the lateral displacements of some of the lower floors. Figure 8.107 indicates that the lateral displacements of the fourth and fifth floors were consistently larger than the lateral roof displacement.

The story drift envelopes for the EBF model with pin connections and the EBF model with all moment connections were practically identical, as shown in Fig. 8.108. Similar to Designs 1 and 2, both EBF models of Design 3 developed a greater story drift in the lower floors compared to the upper floors. Furthermore, the story drift of Design 3 satisfied the code limit of 1.5 percent.

Base shear time histories for the two EBF models, shown in Fig. 8.109, indicate that the backup moment frame created by using all moment connections did not add much additional resistance to the EBF model with pin connections. Tables 8.5 and 8.6 reveal that the maximum base shear was only three to four percent greater in the EBF model with all moment connections. In fact, the maximum shear of all stories of this EBF model were also only slightly greater than those of the EBF model with pin connections, as shown in the story shear envelopes presented in Fig. 8.110.

It was found that for the same earthquake record, the hysteretic behavior of corresponding links of the two EBF models were almost identical. The maximum shear forces developed in the links and the corresponding normalized shear forces, respectively, are shown in Figs. 8.111 and 8.112. These results show the similarity with respect to shear force between corresponding links of the two EBF models. Like Design 2, the first floor links of Design 3 strain hardened to a maximum shear force of $1.45V_p$ during the scaled El Centro earthquake and to $1.5V_p$ during the Parkfield earthquake. However, unlike Design 2,

the third floor link of Design 3 developed slightly less strain hardening than the fourth and fifth floor links. The associated maximum link deformations for each floor are shown in Fig. 8.113, indicating the similarity between corresponding links of the two EBF models of Design 3. Like the bare steel EBF models of Designs 1 and 2, greater magnitudes of link deformation developed in the lower floor links in both EBF models of Design 3. While the maximum link deformation of the lower three floors of Designs 1 and 2 exceeded the code limit of six percent, only the link deformation of the first and second floors of Design 3 exceeded this code limit for the Parkfield earthquake.

The maximum link end moments corresponding to the response of the two EBF models of Design 3 are shown in Fig. 8.114, where they have been normalized by their respective plastic capacities M_p. These results indicate the similarity with regards to moment between corresponding links of both EBF models. From this figure it is apparent that the links in the lower floors developed greater end moments. These link end moments developed at the face of the exterior columns, reaching a moment of approximately $1.07M_p$ in the first and second floor links during the Parkfield earthquake. Designs 1 and 2 had similar characteristics. During the Parkfield earthquake, Designs 1 and 2 developed a moment of $1.15M_p$ and $1.1M_p$ at the face of the exterior columns in the first floor links (see Figs. 8.33(b) and 8.74(b)). It was found that the ratio of end moments of the links adjacent to columns in both EBF models of Design 3 were similar, where during elastic deformations the moment M_B at the column was 2 to 3 times larger than the moment M_A at the other end of the link. After significant strain hardening developed in the link, M_B was 1.5 to 3 times larger than M_A. Thus, as in the analyses of Designs 1 and 2, the link end moments next to the exterior columns in Design 3 did not equalize. On the other hand, the link end moments of the K-braced panels (floors 4, 5, and the roof) remained nearly equal in magnitude for Design 3.

The maximum relative vertical displacement Δ_r between the ends of the links are shown in Fig. 8.115. For corresponding earthquake records, these results appear to have

also been similar for both EBF models of Design 3. The permanent relative vertical displacement Δ_{rp} between the ends of the links of floors 1, 2, and 4 were obtained from Δ_r time histories. These results are summarized in Tables 8.7 and 8.8. The EBF model with pin connections subjected to the scaled El Centro earthquake record (analysis EC10) was found to have developed values of Δ_{rp} which were greater than or equal to Δ_{rp} for the corresponding links of the EBF model with all moment connections (analysis EC9). Such consistency however was not evident in the response to the Parkfield earthquake record. However, Δ_{rp} of the fourth floor link for the Parkfield analyses of Design 3 was significantly less (0.07 and 0.09 inches) than that from the corresponding analyses of Designs 1 (0.77 inches) and 2 (1.04 inches).

The maximum moments developed in the floor beams outside the links are shown in Fig. 8.116. From this figure it is apparent that for corresponding earthquake records the maximum moments adjacent to the links of floors 1, 2, and 3 were nearly equal in the two EBF models. In the remaining upper three floors, these moments were about 10 percent greater in the EBF model with pin connections. The maximum axial forces developed in the floor beams outside the links are shown in Fig. 8.117. From this figure it is apparent that the maximum axial forces which developed in the floor beams outside the links were invariant with respect to the type of connection used to attach the braces and floor beams to the columns. Furthermore, the axial design forces appear to have been satisfactory. The design moments appear to also have been reasonable in the upper three floors (Fig. 8.116). Although in the lower three floors the design moments were exceeded during the Parkfield earthquake, yielding did not occur in these members under the combined action of moment and axial force since the floor beams had adequate capacity.

The maximum moments which developed in the floor beams of the unbraced panels in the EBF model with all moment connections are shown in Fig. 8.118. The largest floor beam end moments were developed at the first floor during the Parkfield earthquake, where the moment was equal to approximately $1.03 M_p$. This indicates that minimal strain harden-

ing occurred in the floor beams of the unbraced panels. The axial force in these members was found to be less than six percent of the axial yield strength of their steel sections. While yielding occurred in these members at the first and second floors during the Parkfield earthquake (see Fig. 8.105(b)), the ensuing maximum plastic deformation was equivalent to $1.4\Theta_Y$, where Θ_Y is the rotation defined by Eq. 8.16. Therefore, for the EBF model with all moment connections, the maximum ductility demand in the floor beams of the unbraced panels was about the same as that of Designs 1 and 2.

The maximum axial brace forces for the two EBF models of Design 3 were found to be nearly identical, as shown in Fig. 8.119. The axial design forces appear to have been satisfactory, although during the Parkfield earthquake the maximum axial force in the first floor brace of the EBF model with all moment connections exceeded the corresponding design force by about three percent. At this instant the first floor link developed a shear force of $1.5V_p$. The first floor brace exceeding the design envelope is attributed to the effect of the damping and vertical inertia forces, as discussed previously. Maximum moments developed in the braces of both EBF models are shown in Fig. 8.120. The maximum brace moments developed during the scaled El Centro earthquake record appear to have been nearly identical for the two EBF models of Design 3. However, during the Parkfield earthquake record the model with all moment connections had a tendency to develop significantly larger moments in the braces of the third and fourth floors than the EBF model with pin connections. The corresponding moments of the third and fourth floor braces were 46 percent greater than the brace maximum moments of the EBF model with pin connections. Although the design moments appear to have been satisfactory for the brace moments developed during the scaled El Centro earthquake, both EBF models developed brace moments at the base of the EBF during the Parkfield earthquake which exceeded the design envelope. The third floor brace moment of the EBF model with all moment connections also exceeded the design envelope, however, the amount by which it exceeded the design envelope was considerably less than that at the base. Fortunately,

Design 3 used structural tubing sizes for the braces which had enough capacity that failure did not occur. A check of brace stability found no indications of brace buckling occurring during the analyses of Design 3.

The maximum axial forces developed in the columns were found to be similar for corresponding columns of the two EBF models. This phenomenon is illustrated by the column axial force envelopes shown in Fig. 8.121. In this figure the axial design forces are shown to have been satisfactory for the exterior columns, and all interior columns except for the first floor. The interior first floor column of the EBF model with pin connections exceeded its axial design force by about 13 percent during the Parkfield earthquake. In all previous analyses the axial design forces were always found to be satisfactory. The reason for the axial force exceeding the design force in the present case is attributed to the fact that the design envelope was based on the assumption that all links simultaneously reached a shear force of $1.5V_p$.

The behavior of the EBF in the present study is such that when the braces of the upper three floors develop compressive axial force due to lateral seismic forces, an accumulation of compressive axial force occurs in the interior columns of the upper three floors, as idealized in Fig. 8.122. The braces of the lower three floors will in turn develop tension, relieving the interior columns of some of the compressive axial force. The situation of column compressive axial force as opposed to tension was chosen for discussion for two reasons. Firstly, columns resist dead load by developing compressive axial force, and therefore, when combined with the column seismic axial forces created by the braces, develop greater compression than tension axial forces. Secondly, the resistance in compression is less than in tension for columns in which stability controls. In the Parkfield analysis of Design 3, the axial brace forces which developed in the upper three floors resulted in larger compressive axial forces in the interior columns between the second and third floors compared to Designs 1 and 2. However, the third floor link of Design 3 developed a maximum shear force of only $1.25V_p$ compared to approximately $1.45V_p$ for Designs 1 and 2. This is attri-

buted to the fact that the third floor link of Design 3 had about a 24 percent greater V_p/V_{link} ratio than Designs 1 and 2 (see Figs. 8.9 to 8.11). As a result, the compressive axial force in the interior columns below the second floor were larger than anticipated because a tension force corresponding to $1.25V_p$ instead of $1.5V_p$ developed in the second floor braces of Design 3. Apparently, in Designs 1 and 2 the link shear force of $1.45V_p$ at the third floor was close enough to $1.5V_p$ that the axial force in the interior columns below the second floor did not exceed the design force. Therefore, in designing the columns of EBFs where the braces in tension are relied upon to relieve the accumulation of column compressive axial force, the designer must consider very carefully the V_p/V_{link} ratios of the floors and thereby determine whether these braces in tension will likely be resisting link shear forces of $1.5V_p$. Fortunately, the section size selected for the first and second floor interior columns provided enough capacity that failure did not occur. A stability check of all columns was made. The results indicated that buckling of the columns did not occur during the analyses.

The moment diagrams for individual columns corresponding to maximum moments for each column of both models of Design 3 are shown in Figs. 8.123 and 8.124. These figures indicate that the maximum moments developed in the exterior columns of the bottom three floors were nearly identical for corresponding columns of the two EBF models. However, the interior columns of the EBF model with all moment connections developed larger moments than the columns of the EBF model with pin connections. This phenomenon also occurred in the exterior columns above the third floor. Moment diagrams for the exterior and interior columns at selected times during the analyses are shown in Figs. 8.125 to 8.132. These figures indicate that the moments of the corresponding columns of the two EBF models had a close resemblance. This was particularly true for the exterior columns of the lower three floors. This was expected, since links with moment connections framed into the exterior columns at the bottom three floors in both EBF models. The phenomena of unequal distribution of beam moments to columns above and below the corresponding

floors, and the point of inflection not being stationary is evident in these moment diagrams. These observations were most pronounced in the exterior columns between the second and third floors at time $t = 4.5$ seconds, and between the first and second floors at time $t = 5$ seconds during the Parkfield analyses.

The design moment envelope M_{col} for the columns based on cantilever action are shown in Figs. 8.123 and 8.124 (all interior columns and the exterior columns above the third floor). As noted previously, no dynamic amplification factor was used for these design moments. The design moment envelope M_{col} appears to have been satisfactory for these members in the EBF model with pin connections. For the EBF model with all moment connections, M_{col} for the same columns, excluding the interior column below the first floor, was also satisfactory. However, as seen in these figures as well as the moment diagrams of Figs. 8.125 to 8.132, these columns in the EBF model with pin connections did not always develop single curvature. This is due to two reasons. Firstly, eccentric pin connections with respect to the centerline of the columns were assumed and accounted for in the EBF model by using offsets from the column centerline. As a result, these eccentricities developed moments in the columns of the EBF models with pin connections. Secondly, participation of the higher modes resulted in the lateral inertia loads at the different floor levels to act sometimes in opposite directions. This led to double curvature of the columns.

It is seen in Figs. 8.123 and 8.124 that the maximum moments of the exterior columns of the lower three floors all exceeded the design value M_{code} during the scaled El Centro and Parkfield earthquakes. The design moments for the exterior columns of the three lower floors based on the amplified moments $1.8M_{code}$ therefore appear to be more practical than the moments M_{code}, where M_{code} was derived from the weak beam-strong column concept. Although during the Parkfield earthquake yielding occurred at the base of the first floor columns (see Fig. 8.105), which were designed using moments $1.8M_{code}$, the ensuing plastic deformation was less than $0.5\Theta_Y$, where Θ_Y is the rotation defined by Eq. 8.18.

The amounts of hysteretic energy dissipated by the links are shown in Fig. 8.133, indi-

cating that these results of both EBF models were nearly identical. An examination of Tables 8.9 and 8.10 indicates that the links accounted for practically all of the energy dissipated by the EBF models of Design 3. The hysteretic energy dissipated by both of the first floor links accounted for over 60 percent and 56 percent of the total hysteretic energy dissipated during the El Centro and Parkfield earthquakes, respectively. This result is more consistent with the response of Design 1 than Design 2. It appears that although it was intended to have the links above the first floor participate in a manner similar to Design 2, Tables 8.9 and 8.10 show the distribution of energy dissipated by the links of Design 3 was more similar to that of Design 1. As noted in the discussion of Design 2, this phenomenon is influenced by the distribution of the link shear strength to required shear strength ratio V_p/V_{link} among the floors. In Design 3, the second and third floor links had V_p/V_{link} ratios that were 7 and 24 percent greater than the corresponding links of Design 2. For Design 3, a more desirable performance could be achieved by reducing the capacity of the third floor links.

8.7. Summary and Conclusions of EBF Analyses

From the above discussion, the following conclusions are noted with respect to the design and nonlinear analyses of the 6-story EBFs:

(1)   Strain hardening in the links and other members of the EBFs resulted in less link deformation and story drift compared to an elastic-perfectly plastic response. Furthermore, the effect of link strain hardening resulted in greater brace forces, as well as forces in the beams and columns. Through strain hardening, the links developed a maximum shear force of $1.5V_p$ in the bare steel EBF models, and $1.63V_p$ in the interior EBF models with composite floor slabs. In both cases these maximum link shear forces developed in the lower floors.

(2)   Including the effect of composite action in the EBF models resulted in an increase of the ultimate link shear forces. The links of the interior EBF model with composite

floor slabs developed maximum shear forces which were as much as 10 percent greater than the corresponding link shear forces of the bare steel EBF model. In the exterior EBF model with composite floor slabs this increase was as much as 4 percent. The increase in the link shear forces resulted in larger forces developing in the other members of the EBF models. For the interior EBF model with composite floor slabs the axial forces in the columns and braces, respectively, were as much as 10 and 12 percent greater than the corresponding member forces of the bare steel EBF model. Likewise, the moments in the columns and braces, respectively, were as much as 14 percent and 40 percent greater than those of the bare steel model. A smaller increase in the member forces occurred in the exterior EBF model with composite floor slabs relative to those of the bare steel EBF model. The column and brace axial forces increased as much as 4 percent, while the moments in the columns and braces, respectively, increased as much as 5 and 25 percent for this model relative to the bare steel EBF model. Although greater forces developed in the members of the EBF models with composite floor slabs, the amount of hysteretic energy dissipated by these EBF models was almost identical to that of the bare steel EBF model.

(3) The dynamic excitation of EBFs led to vertical inertia forces and damping forces in the links and other members as the links deformed and the floors developed uplift. The link damping forces increased as the links yielded due to the effect of yielding on viscous damping and the increased relative vertical motion between the ends of the links. Including the elastic stiffness of the links in the viscous damping matrix through initial stiffness proportional damping resulted in larger link damping forces than if the elastic stiffness of the links were not included. Axial forces in the braces were increased due to the vertical inertia and the damping forces. As a result, the axial force of some of the braces exceeded the design forces that were established considering static equilibrium based on link shear forces of $1.5V_p$. The combined effects of the vertical inertia and damping forces, and the increased shear capacity of

links with composite floors resulted in a axial brace force which exceeded the design force by as much as 14 percent. Considering these phenomena in addition to the possibility that the webs of links may be stronger and the braces weaker than anticipated due to the variation in material strengths, it is recommended that at critical locations where significant inelastic activity is expected that the axial design force for the braces be increased to where they are based on link shear forces of $1.7V_p$ instead of the current value of $1.5V_p$.

(4) The preliminary design assumption of using 20 percent of the link end moment as the design moment for braces with moment connections was not satisfactory in the lower three floors for all analyses. It is at these floors where the maximum story drift and yielding outside the link in the floor beam developed. These phenomena have been determined to cause an increase in the brace moment. In order to ensure that a safe EBF design exist the moment capacity of each brace considering axial force effects must balance the moments developed at the ends of the adjoining link and floor beam outside the link. Therefore analysis of preliminary EBF designs are required in order to assess whether the braces will be able to resist the forces developed in the adjoining floor beam and link. At critical locations where major inelastic activity and strain hardening are expected in the link, consideration must be given to the fact that the floor beams could possibly yield outside the links thereby forcing the adjoining brace to resist any additional increase in link end moment. It is recommended that a pin connection for braces be used at the base of the EBF in order to avoid potential problems associated with the large brace moments which were found to develop at the lower end of such braces.

(5) Accounting for the P-delta effect did not result in any significant change in the response. The most pronounced effects were a six percent increase in the brace and column axial forces when the P-delta effect was accounted for.

(6) The use of pin connections in an EBF resulted in a response that was almost identi-

cal to the response of the corresponding EBF with all moment connections. However, the increase in the equivalent lateral loads for designing EBFs with pin connections is necessary because of the associated loss of redundancy.

(7)   A major portion of yielding and strain hardening of the EBF models occurred in the links, with the links accounting for practically all the hysteretic energy dissipated by the EBF models. The effect of viscous damping energy was found to be smaller compared to the hysteretic energy where the damping accounted for an average of 20 percent of the total energy dissipated by the system.

(8)   The maximum story drift was within the code limit of 1.5 percent. However, the deformation of the lower floor links in the EBF models with strain hardening and nonproportional damping often exceeded the code limit of 0.06 rad. during the Parkfield earthquake. In Design 1 the first floor link developed a deformation as large as 0.11 rad. The improved designs, Designs 2 and 3, experienced maximum link deformations of about 0.10 and 0.08 rad. during the Parkfield earthquake. The maximum link deformation developed during the scaled El Centro earthquake was 0.075 rad. (Design 1), while Designs 2 and 3 both developed 0.04 rad. Therefore, even though the preliminary design was found to satisfy the code limit for link deformation, this limit was exceeded during the nonlinear analyses of the EBFs. Experimental data summarized in Chapter 4 and by Kasai [7] noted that an important aspect of link deformation is the measurement of the maximum link deformation γ_u, where γ_u is the deformation measured from the point of zero shear during a half cycle (see Fig. 4.25). This experimental data indicated that links had been able to sustain values of γ_u equal to 0.13 to 0.15 rad. before web buckling occurred. Values of γ_u related to the EBF analyses involving the Parkfield earthquake were determined from the link hysteretic loops and found to be no more than 0.15 rad. for Design 1, 0.11 rad. for Design 2, and 0.10 rad. for Design 3. For the scaled El Centro earthquake record, these values were 0.09 rad. for Design 1, 0.05 rad. for Design 2, and

0.06 rad. for Design 3. Thus, while the three designs did not always satisfy the code limit of 0.06 rad. of link deformation, experimental data indicates that the deformation developed in the links during the analyses was possible if appropriate link details are used.

(9)   In designing EBFs, careful consideration must be given to the selection of section sizes for the links. This includes observing the relative values of the link shear resistance to required design shear strength ratios V_p/V_{link} among the floors. To prevent the occurrence of one or two links dissipating a majority of the hysteretic energy (soft stories), the V_p/V_{link} ratio of the links in all floors should be as close as possible to the same value, where this ratio is established using the plastic design procedure described herein. A smaller V_p/V_{link} ratio for the upper floor links relative to the lower floor links is more advantageous than having a larger V_p/V_{link} ratio for the upper floor links relative to the lower floor links. Using these guidelines soft stories can be avoided, resulting in a more uniform distribution of energy dissipation among the links. This will also aid in decreasing the maximum story drift as well as the link deformation which would otherwise occur in the links of a soft story.

(10) Links that were adjacent to columns developed unequal initial elastic end moments. The link end moment at the column, M_B, was 2 to 4 times greater than the other end moment of the link, M_A. If strain hardening occurred in the link following shear yielding, the moment M_A increased more than M_B, however, equalization of the link end moments did not occur. The moment M_B often reached M_p, the plastic capacity of the section, and by strain hardening in flexure developed a moment as large as $1.15M_p$. The moment M_A remained less than M_p. The links which were not adjacent to columns (links in the K-braced panels) had approximately equal end moments in the bare steel EBF analysis. The maximum end moments in these links were less than M_p. Composite action resulted in a larger moment at the end of the links in the K-braced panels where the slab was in compression due to the bending

moment. These end moments were about 1.2 to 1.5 times larger than the end moments at the other end of the links. The maximum moments developed in these links at the third floor was about $1.1M_p$.

(11) The plastic deformation imposed on yielded members outside the links was small relative to that in the links. Of the yielded members outside the links, the floor beams of the unbraced panels developed the most plastic deformation. The maximum plastic deformation of these members was less than 1.5 times the yield rotation of similar members subjected to equal end moments. Since these members are compact sections and the axial force was less than six percent of the yield force, no ductility problems would be expected. The floor beams outside the links and the exterior columns at the base had even smaller ductility demands. It is anticipated that ductility problems would also not occur in these members. Current ongoing research [41] will attempt to set guidelines for ductility capacity of such members.

(12) The design values for moment and axial load of the floor beams outside the links were exceeded by the forces developed during the response to the earthquake records. However, as noted above, yielding outside the links in these floor beams did not impose excessive ductility demands. Furthermore, EBFs with composite floors have increased resistance. As a result, the design procedure used herein appears to be satisfactory for these members.

(13) The maximum moment developed adjacent to columns in the floor beams of unbraced panels was $1.03M_p$. As noted previously, for links next to columns the maximum end moment was $1.15M_p$. These values were less than the recommended value of $1.25M_p$ for column design. However, due to the variation in material properties which could result in a higher nominal beam strength and a lower nominal column strength, the use of the 1.25 factor is warranted.

(14) Applying the weak beam-strong column design philosophy to columns adjacent to links without a dynamic amplification factor is not satisfactory. Under dynamic

excitation the link end moment at the columns is often not distributed equally to the columns above and below a yielded link. As a result, the point of inflection was found not to be stationary in these columns. The use of a dynamic amplification factor is also justified by the fact that composite action in EBFs resulted in larger column moments compared to a bare steel EBF. In view of the above, great care must be taken in designing column splices.

(15) When designing columns where braces are relied upon to relieve the accumulation of axial compressive force in the column, one must carefully consider whether the links that are connected to these braces will develop a shear force of $1.5V_p$. Examining the relative values of the V_p/V_{link} ratios among the links will be helpful in making such decisions.

Each earthquake has unique ground motions, and as a result an EBF subjected to different earthquake records will develop unique responses. A major portion of the inelastic response of the EBF designs to the Parkfield earthquake record occurred during one cycle of sustained plastic link deformation. The scaled El Centro earthquake record produced many yield excursions, which resulted in more cyclically symmetric plastic deformations. Consequently, while the Parkfield earthquake record generally caused larger member forces and deformation, the scaled El Centro earthquake record resulted in more energy dissipation. By using a plastic preliminary EBF design procedure with equivalent seismic lateral forces, and then performing nonlinear dynamic analyses on the design result, it was demonstrated that the energy dissipation can be designed to remain mostly in the links. This involved designing the EBF where the links yield, with all of the other members remaining essentially elastic. Consequently, only minor inelastic activity, if any, develops outside the links as they strain harden.

The analytical results reported in this chapter should help to further the design developments of EBFs. While the element formulations were based on cyclic static response of experimental specimens, the nonlinear dynamic analyses results are believed to

be reasonable. However, there is still a need to verify the responses through experimental investigation of EBFs under dynamic loading. The conclusions reached with regards to the nonlinear dynamic analyses are appropriate for the EBFs analyzed. In these analyses, it was assumed that the structural detailing of the links, connections, and other members was adequate for seismic resistant design. General EBF designs must be carefully scrutinized before considering whether the conclusions of this study are applicable to such designs. The reader is reminded that the conclusions reported herein are based on results obtained from EBF models where the effects of soil structure interaction are not included in the analysis.

130

BIBLIOGRAPHY

[1]   Krawinkler, H., Bertero, V.V., and Popov, E.P., "Inelastic Behavior of Steel Beam to Column Subassemblages," *EERC Report No. 71-7*, Earthquake Engineering Research Center, University of California, Berkeley, CA, Oct. 1971.

[2]   Popov, E.P. and Black, R., "Steel Struts Under Severe Cyclic Loadings," *Journal of the Structural Division*, ASCE, Vol. 107, No. ST9, Sept. 1981.

[3]   Hjelmstad, K.D. and Popov, E.P., "Seismic Behavior of Active Beam Links in Eccentrically Braced Frames," *EERC Report No. 83-15*, Earthquake Engineering Research Center, University of California, Berkeley, CA, July 1983.

[4]   Kasai, K., "A Plastic Design Method of Eccentrically Braced Frames," CE 299 Report Submitted to University of California, Berkeley, SESM.

[5]   Malley, J.O. and Popov, E.P., "Design Considerations for Shear Links in Eccentric Braced Frames," *EERC Report No. 83-24*, Earthquake Engineering Research Center, University of California, Berkeley, CA, November 1983.

[6]   Roeder, C.W. and Popov, E.P., "Inelastic Behavior of Eccentric Braced Steel Frames Under Cyclic Loadings," *EERC Report No. 77-18*, Earthquake Engineering Research Center, University of California, Berkeley, CA, August 1977.

[7]   Kasai, K. and Popov, E.P.,"A Study of Seismically Resistant Ecccentrically Braced Steel Frame Systems," *EERC Report No. 86-01*, Earthquake Engineering Research Center, University of California, Berkeley, CA, January 1986.

[8]   Manheim, D., "On The Design of Eccentrically Braced Frames," Thesis presented to the University of California, Berkeley, in partial fulfillment for the degree of Doctor of Engineering, 1982.

[9]   Fisher, J., "Design of Composite Beams With Formed Metal Deck," *AISC Engineering Journal*, Vol. 7, No. 3, July 1970.

[10]   Grant, J., Fisher, J., and Slutter, R.O., "Composite Beams With Formed Steel Deck," *AISC Engineering Journal*, Vol. 14, No. 1, 1st Quarter, 1977.

[11]   Slutter, R., Driscoll, G., "Flexural Strength of Steel-Concrete Composite Beams," *Journal of the Structural Division, ASCE*, Vol. 91, No. ST2, April, 1965.

[12]   Ollgaard, J.G., Slutter, R.G., and Fisher, J.W., "Shear Strength of Stud Connectors in Lightweight and Normal-Weight Concrete," *Engineering Journal of the American Institute of Steel Construction*, Vol. 8, No. 2, 1971.

[13]   Robinson, H., "Tests on Composite Beams With Cellular Deck," *Journal of the Structural Division, ASCE*, Vol. 93, No. ST4, August 1967.

[14]   Robinson, H., "Composite Beam Incorporating Cellular Steel Decking," *Journal of the Structural Division, ASCE*, Vol. 95, No. ST3, March 1979.

[15]   Robinson, H., "Preliminary Investigation of a Composite Beam With a Ribbed Slab formed by Cellular Steel Decking," *Engineering Dept. Report No. 35*, McMaster University, October 1961.

[16]   Iyengar, H.S.,"State of the Art Report on Composite or Mixed Steel-Concrete Construction for Buildings," Structural Specification Liaison Committee, ASCE, 1977.

[17]   Goel, S.C., Foutch, D.A., "Preliminary Studies and Test Results of Eccentrically Braced Full-Size Steel Structure," U.S.-Japan Cooperative Earthquake Research Program Sixteenth Joint Meeting, May 15-18, Washington D.C., 1984.

[18]   Popov, E.P., Malley, J.O., "Design of Links and Beam-to-Column Connections for Eccentrically Braced Steel Frames," *EERC Report No. 83-03*, Earthquake Engineering Research Center, University of California, Berkeley, CA, January, 1983.

[19]   Neal, B.G.,"Effect of Shear Force on the Fully Plastic Moment of an I-Beam," *Journal of Mechanical Engineering Science*, Vol. 3(3), 1961.

[20]   Specification for the Design, Fabrication and Erection of Structural Steel for Buildings, 8th ed., American Institute of Steel Construction, New York, 1980.

[21]   Siess, C.P., Viest, I.M., and Newmark, N.M., "Small-Scale Tests of Shear Connectors and Composite T-Beams," *Bulletin No. 396*, Experimental Station, University of Illinois, Urbana, Illinois, 1952.

132

[22]   Humar, J.L., "Composite Beams Under Cyclic Loading," *Journal of the Structural Division, ASCE*, Vol. 105, No. ST10, October, 1979.

[23]   Hawkins, N.M., Mitchell, D., "Seismic Response of Composite Shear Connections," *Journal of Structural Engineering, ASCE*, Vol. 110, No. 9, September, 1984.

[24]   Moffat, K.R., "An Analytical Study of the Longitudinal Bending Behavior of Composite Box Girder Bridges Having Incomplete Interaction," *CESLIC Report CB1*, Civil Engineering Structures Laboratory, Imperial College of Science and Technology, London, England, 1976.

[25]   Moffat, K.R., "Shear Lag in Steel Box Girder Bridges," *The Structural Engineer*, London, England, Vol. 53, October, 1975.

[26]   Kato, B., Aoyama, H., Okada, T., Uchida, N., "Composite Steel and Concrete Beams in the Building Structure in Japan," Regional Conference on Planning and Design of Tall Buildings, August 28-30, 1973, Tokyo, Japan.

[27]   Johnson, R.P., Willmington, R.T., "Vertical Shear in Continuous Composite Beams," *Proceedings, Institution of Civil Engineers*, 1972.

[28]   H.H. Robertson Company, *Technical Data Book*, Pittsburgh, Pennsylvania.

[29]   "Embedment Properties of Head Studs," TRW Nelson Division, Ohio, January, 1983.

[30]   American Society for Testing and Materials, Standard Methods of Tension Testing of Metallic Materials, ASTM Designation E8-79, Philadelphia, 1980.

[31]   American Society for Testing and Materials, Standard Methods for Compressive Strength of Cylindrical Concrete Specimens, ASTM Designation C39-72, Philadelphia, 1980.

[32]   American Society for Testing and Materials, Standard Method for Splitting Tensile Strength of Cylindrical Concrete Specimens, ASTM Designation C496-71, Philadelphia, 1980.

[33]   American Society for Testing and Materials, Standard Method for Flexural Strength of Concrete, ASTM Designation C78-75, Philadelphia, 1980.

[34]   American Society for Testing and Materials, Standard Method for Unit Weight of Structural Lightweight Concrete, ASTM Designation C567-71, Philadelphia, 1980.

[35]   Kasai, K., Popov, E.P., "General Behavior of WF Steel Shear Link Beams," *Journal of Structural Engineering, ASCE*, Vol. 112, No. 2, February 1986.

[36]   Kasai, K., Popov, E.P., "Cyclic Web Buckling Control for Shear Link Beams," *Journal of Structural Engineering, ASCE*, Vol. 112, No. 3, March 1986.

[37]   Wakabayashi, M., "Inelastic Behavior of Full-Scale Steel Frames with and without Bracings," *Bulletin of the Disaster Prevention Research Institute*, Vol. 24, Part 1, Kyoto University, Kyoto, Japan, March 1974.

[38]   Popov, E.P., Amin, N.R., Louie, J.J.C., and, Stephen, R.M., "Cyclic Behavior of Large Beam-Column Assemblies", *Earthquake Spectra*, Vol. 1, No. 2, Feb. 1985, pp. 3-38.

[39]   Maison, B.F.and Popov, E.P., "Cyclic Response prediction for Braced Steel Frames", *Journal of the Structural Division*, ASCE, 106, No. ST7, Proc. Paper 15534, 1401-1416, July 1980.

[40]   Nigam, N.C., "Inelastic Interactions in the Dynamic Response of Structures," Earthquake Engineering Laboratory, California Institute of Technology, Pasadena, CA 1967.

[41]   Engelhardt, M.D., Thesis to be presented to the University of California, Berkeley in Partial Fulfillment for the Degree of Doctor of Philosophy in 1988.

[42]   Boutros, M.K., Goel, S.C., "Analytical Modelling of Braced Steel Structures," *Report No. UMCE 85-7*, Department of Civil Engineering, University of Michigan, Ann Arbor, Michigan, August 1985.

134

[43] Hodge, P.G., "Plastic Analysis of Structures," McGraw-Hill Book Company, Inc., New York, 1959.

[44] Leth, C.F., "Effect of Shear Stresses on the Carrying Capacity of I-Beams," *Technical Report No. A-11-107*, Brown University, 1954.

[45] ASCE-WRC, "Plastic Design in Steel", *ASCE Manual 41*, 2nd Edition, Welding Research Council and American Society of Civil Engineers, New York, 1971.

[46] Timoshenko, S.P., "Strength of Materials," Part II, Second Edition, D. Van Nostrand Company Inc., New York, August 1941.

[47] Roark, R.J., Young, W.C., "Formulas for Stress and Strain," Fifth Edition, McGraw-Hill Book Company, New York, 1975.

[48] Karsan, I.D., Jirsa, J.O., "Behavior of Concrete under Compressive Loadings," *Journal of Structural Division, ASCE*, Vol. 95, ST12, December 1969.

[49] Sinha, B.P., Gerstle, K.H., and Tulin, L.G., "Stress-Strain Relationships for Concrete under Cyclic Loading," *Journal ACI*, Vol. 61, No. 2, February 1964.

[50] Hognestad, E., "A Study of Combined Bending and Axial Load in Reinforced Concrete Members," *Bulletin Series No. 399*, University of Illinois Engineering Experimental Station, November 1951.

[51] Salmon, C.G., Johnson, J.E., "Steel Structures - Design and Behavior," Harper and Row Publishers, New York, New York, 1971.

[52] Bleich, F., "Strength of Metal Structures," 1st Edition, McGraw-Hill Book Company, Inc., New York, 1952.

[53] Timoshenko, S.P., Gere, J.M., "Theory of Elastic Stability," McGraw-Hill Book Co., New York, New York, 1969.

[54] Hechtman, R.A., Hattrup, J.S., Styer, E.F., and Tiedemann, J.L., "Lateral Buckling of Rolled Steel Beams," *Proceedings, ASCE*, Vol. 81, Paper 797, 1955.

[55] Gaylord, E.H., Gaylord, C.N., "Design of Steel Structures," McGraw-Hill Book Co., New York, New York, 1972.

[56] Johnson, R.P., Van Dolen, K., and Kemp, A.R., "Ultimate Strength of Continuous Composite Beams," *Proceedings, Conference on Structural Steelwork*, British Constructional Steelwork Association, November 1967.

[57] Hamada, S., Longworth, J., "Buckling of Composite Beams in Negative Bending," *Journal of the Structural Division, ASCE*, Vol. 100, No. ST11, November, 1974.

[58] SEAOC Tentative Lateral Force Requirements, Seismology Committee, Structural Engineers Association of California, Sacramento/San Francisco/Los Angeles, California, 1985

[59] Kusuda, T., and Thurlimann, B., "Strength of Wide-Flange Beams Under Combined Influence of Moment, Shear, and Axial Force", *Report No. 248.1*, Fritz Engineering Laboratory, Lehigh University, Bethlehem, Pennsylvania, 1958.

[60] Fung, Y.C., "Foundations of Solid Mechanics," Prentice-Hall, Inc., Englewood Cliffs, N.J., 1965.

[61] Timoshenko, S.P., "Theory of Elasticity," Third Edition, McGraw-Hill Book Company, Inc., New York, 1970.

[62] Szilard, R., "Theory and Analysis of Plates," Prentice-Hall Inc., Englewood Cliffs, N.J., 1974.

[63] Timoshenko, S.P., "Theory of Plates and Shells," Second Edition, McGraw-Hill Book Company, New York, 1959.

[64] Allen, D.N., Severn, R.T., "Composite Action Between Beams and Slabs under Transverse Load," *The Structural Engineer*, Vol. 39, No. 5, May 1961.

[65] Popov, E.P., "Introduction to Mechanics of Solids," Prentice-Hall, Englewood Cliffs, N.J., 1968.

136

[66]   NEHRP (National Earthquake Hazards Reduction Program), *Recommended Provisions for the Development of Seismic Regulations for New Buildings*, Building Seismic Safety Council, Federal Emergency Management Agency, Washington, D.C., 1985.

[67]   Girkmann, K., "Flächentragwerke," Springer-Verlag, Austria, 1946 (in German).

[68]   Troitsky, M.S., "Orthotropic Bridges -- Theory and Design," James F. Lincoln Arc Welding Foundation, Cleveland, Ohio, August 1967.

[69]   Plantema, F.J., "Sandwich Construction: The Bending and Bucking of Sandwich Beams, Plates, and Shells," John Wiley and Sons, Inc., New York, 1966.

[70]   Giberson, M.F., "Two Nonlinear Beams with Definitions of Ductility," *Journal of the Structural Division, ASCE*, Vol. 95, No. ST2, February 1969.

[71]   Clough, R.W., Benuska, K.L., and Lin, T.Y., "FHA Study of Seismic Design Criteria for High-Rise Buildings," *HUDTS-3*, Federal Housing Administration, Washington, D.C. August 1966.

[72]   Yang, M.S., "Seismic Behavior of an Eccentrically X-Braced Steel Structure," *EERC Report 82-14*, Earthquake Engineering Research Center, University of California, Berkeley, CA, September 1982.

[73]   Neal, G.G., "The Effect of Shear and Normal Force on the Fully Plastic Moment of a Beam of Rectangular Cross Section," *Journal of Applied Mechanics*, Vol. 28, No. 2, 1961.

[74]   Bathe, K.J., and Wilson, E.L., "Numerical Methods in Finite Element Analysis," Prentice-Hall, Englewood Cliffs, N.J., 1976.

[75]   Mroz, Z., "An Attempt to Describe the Behavior of Metals under Cyclic Loads using a More General Workhardening Model," *Acta Mechanica*, Vol. 7, 1969.

[76]   Mroz, Z., "On the Description of Anisotropic Workhardening," *Journal Mech. Phys. Solids,* Vol. 15, Pergammon Press, Ltd., Great Britain, 1967.

[77]   Naghdi, A., "Plasticity," Office of Naval Research, Pergammon Books, 1960.

[78]   Porter, F.L., and Powell, G.H., "Static and Dynamic Analysis of Inelastic Frame Structures," *EERC Report No. 71-3,* Earthquake Engineering Research Center, University of California, Berkeley, CA, June 1971.

[79]   Chen, P.F., and Powell, G.H., "Generalized Plastic Hinge Concepts for 3D Beam-Column Elements," *EERC Report No. 82-20,* Earthquake Engineering Research Center, University of California, Berkeley, CA, November 1982.

[80]   Ziegler, H., "A Modification of Prager's Hardening Rule," *Quarterly of Applied Mathematics,* Vol. 17, No. 55, 1959.

[81]   Riahi, A., Row, D., and Powell, G.H., "Three Dimensional Inelastic Frame Elements for the ANSR-I Program," *EERC Report No. 78-06,* Earthquake Engineering Research Center, University of California, Berkeley, CA, 1978.

[82]   Nigam, N.C., "Yielding in Framed Structures under Dynamic Loads," *Journal of Engineering Mechanics Division, ASCE,* Vol. 96, No. EM5, October, 1970.

[83]   Argyris, J.H., "Finite Element Analysis of Two and Three-Dimensional Elasto-Plastic Frames -- The Natural Approach," *Computer Methods in Applied Mechanics and Engineering,* Vol. 35, 1982.

[84]   Wen, R.K., "Dynamic Analysis of Inelastic Space Frames," *Journal of Engineering Mechanics Division, ASCE,* Vol. 96, No. EM5, 1970.

[85]   Orbison, J.G., "Nonlinear Static Analysis of Three-Dimensional Steel Frames," Dissertation Submitted in Partial Fulfillment of the Degree of Doctor of Philosophy, Cornell University, Ithaca, New York, May 1982.

138

[86]   Row, D.G., Powell, G.H., and Mondkar, D.P., "2D Beam Column Element (Type 5 - Parallel Element Theory) for the ANSR-II Program," *EERC Report No. 79-30*, Earthquake Engineering Research Center, University of California, Berkeley, CA, 1979.

[87]   Uzgider, E.U., "Inelastic Response of Space Frames to Dynamic Loads," *Computers and Structures*, Vol. 11, 1980.

[88]   Hilmy, S.I., "Adaptive Nonlinear Dynamic Analysis of Three-Dimensional Steel Framed Structures with Interactive Computer Graphics," *Report No. 84-8*, Department of Structural Engineering, Cornell University, Ithaca, New York, June 1984.

[89]   Powell, G.H., "DRAIN-2D User's Guide," *EERC Report No. 73-22*, Earthquake Engineering Research Center, University of California, Berkeley, CA, 1973.

[90]   Bergan, P., "Solution Algorithms for Nonlinear Structural Problems," *Proceedings, International Conference on Engineering Applications of the Finite Element Methods*, Hovik, Norway, May 1979.

[91]   Mattheis, H. and Strang, G., "The Solution of Nonlinear Finite Element Equations," *International Journal of Numerical Methods in Engineering*, Vol. 14, 1979.

[92]   Powell, G., and Simmons, J., "Improved Iteration Strategy for Nonlinear Structures," *International Journal of Numerical Methods in Engineering*, Vol. 17, 1981.

[93]   Riks, E., "An Incremental Approach to the Solution of Snapping and Buckling Problems," *International Journal of Solids and Structures*, Vol. 15, 1979.

[94]   Mondkar, D.P., and Powell, G.H., "ANSR-I General Purpose Computer Program for Analysis of Non-Linear Structural Response", *EERC Report No. 75-37*, Earthquake Engineering Research Center, University of California, Berkeley, CA, 1975.

[95]   Bathe, K.J., "Finite Element Procedures in Engineering Analysis," Prentice-Hall, Englewood Cliffs, N.J., 1982.

[96]   UCB, Uniform Building Code, International Conference of Building Officials, Whittier, California, 1982.

[97]   Newmark, N.M., and Hall, W.J., "Earthquake Spectra and Design", EERI (Earthquake Engineering Research Institute), Berkeley, CA.

[98]   Zienkiewicz, O.C.,"The Finite Element Method," 3rd Edition, McGraw-Hill Book Company, Inc., 1977.

[99]   Clough, R.W., and Penzien, J., *Dynamics of Structures*, McGraw-Hill Book Company, Inc., New York, 1975.

[100]   Collatz, L., "The Numerical Treatment of Differential Equations," Springer-Verlag, New York, New York, 1966.

[101]   Houbolt, J.C., "A Recurrence Matrix Solution for the Dynamic Response of Elastic Aircraft," *Journal of Aeronautic Science*, Vol. 17, 1950.

[102]   Wilson, E.L., Farhoomad, I., and Bathe, K.J., "Nonlinear Dynamic Analysis of Complex Structures," *International Journal of Earthquake Engineering and Structural Dynamics*, Vol. 1, 1973.

[103]   Newmark, N.M., "A Method of Computing for Structural Dynamics," *Journal of Engineering Mechanics Division, ASCE*, Vol. 85, 1959.

[104]   Hilber, H.M., Hughes, T.J.R., and Taylor, R.L., "Improved Numerical Dissipation of Time Integration Algorithms in Structural Dynamics," *Earthquake Engineering and Structural Dynamics*, Vol. 5, 1977.

[105]   Hughes, T.J.R., Caughey, T.K., and Liu, W.K., "Finite Element Methods for Nonlinear Elastodynamics which Conserve Energy," *Journal of Applied Mechanics*, Vol. 45, 1978.

[106]   Nickell, R.E., "On the Stability of Approximation Operators in problems of Structural Dynamics," *International Journal of Solids and Structures*, Vol. 7, 1971.

140

[107] Goudreau, G.L., and Taylor, R.L., "Evaluation of Numerical Integration Methods in Elastodynamics," *Computer Methods in Applied Mechanics and Engineering,* Vol. 2, 1972.

[108] Warburton, G.B., and Soni, S.R., "Errors in Response Calculations for Non-Classically Damped Structures," *Earthquake Engineering and Structural Dynamics,* Vol. 5, 1977.

[109] Shing, P.B., and Mahin, S.A., "Elimination of Spurious Higher-Mode Response in Pseudodynamic Tests," *to be published in Earthquake Engineering and Structural Dynamics in 1987.*

[110] Meirovitch, L, "Analytical Methods in Vibrations," Macmillan, New York, 1967.

[111] Saiidi, M., and Sozen, M.A., "Simple Nonlinear Seismic Analysis of Reinforced Concrete Structures," *Journal of the Structural Division, ASCE,* Vol. 107, No. ST5, May 1981.

[112] Shibata, A., and Sozen, M., "Substitute - Structure Method for Seismic Design in Reinforced Concrete," *Journal of the Structural Division, ASCE,* Vol. 102, No. ST1, January 1976.

[113] Tansirikongkol, V., and Pecknold, D.A., "Approximate Model Analysis of Bilinear MDF Systems Subjected to Earthquake Motions," *Civil Engineering Studies, Structural Research Series, No. 449,* University of Illinois, Urbana, August 1978.

[114] Mahin, S.A., and Lin, J., "Construction of Inelastic Response Spectra for Single Degree of Freedom Systems," *EERC Report No. 83-17,* Earthquake Engineering Research Center, University of California, Berkeley, CA, 1983.

]115] Galambos, T.V., "Deformation and Energy Absorption Capacity of Steel Structures in the Inelastic Range," *AISC Bulletin No. 8,* New York, New York, 1968.

[116] Hurty, W.C., Rubinstein, M.F., "Dynamics of Structures," Prentice-Hall, Inc.,

Englewood cliffs, N.J., 1964.

[117] Leger, P., Wilson, E.L., and Clough, R.W., "The Use of Load Dependent Vectors for Dynamic and Earthquake Analyses," *EERC Report No. 86-04*, Earthquake Engineering Research Center, University of California, Berkeley, CA, 1986.

[118] Golafshani, A., and Powell, G.H., "DRAIN-2D2: A Computer Program for Inelastic Seismic Response of Structures," Ph.D., Dissertation, University of California, Berkeley, 1974.

[119] Popov, E.P., Kasai, K., and Engelhardt, M.D., "Advances in Design of Eccentrically Braced Frames," *Proceedings, Pacific Structural Steel Conference*, New Zealand, August 1986.

[120] Kasai, K., and Popov, E.P., "On Seismic Design of Eccentrically Braced Steel Frames," *Proceedings 8WCEE*, San Francisco, California, Vol. 5, July 21-28, 1984, pp.387-394.

[121] Paulay, T., "Deterministic Seismic Design Procedures for Reinforced Concrete Buildings," *Engineering Structures*, Vol. 5, No. 1, January 1983.

[122] Standards Association of New Zealand, "Code of Practice for the Design of Concrete Structures," Draft, New Zealand Standard NZS 3101, Parts 1 and 2, 1982.

[123] Jennings, P.C., Housher, G.W., and Tsai, N.C., "Simulated Earthquake Motions," California Institute of Technology, Pasadena, California, 1968.

[124] AISC, "Specifications for the Design, Fabrication and Erection of Structural Steel for Buildings with Commentary," *Manual of Steel Construction*, 8th Edition, American Institute of Steel Construction, 1980.

[125] Mahin, S.A., and Bertero, V.V., "An Evaluation of Inelastic Seismic Design Spectra," *Journal of the Structural Division, ASCE*, Vol. 107, No. ST9, September 1981.

142

[126] ANSI, "American National Standard Minimum Design Loads for Buildings and other Structures," ANSI A58.1-1982, New York, New York, 1982.

[127] Popov, E.P., and Engelhardt, M.D., "Seismic Eccentrically Braced Frames," *to be published in Journal of Construction Steel Research,* United Kingdom, 1987.

[128] Ricles, J.M., and Popov, E.P., "Experiments on Eccentrically Braced Frames with Composite Floors," *EERC Report No. 87-06,* Earthquake Engineering Research Center, University of California, Berkeley, CA, 1987.

TABLES

Yield Condition	A	B	C	D
Elastic	0	0	0	0
Plastic Hinge at Node I Only	1	K_{ij}/K_{ii}	0	0
Plastic Hinge at Node J Only	0	0	K_{ij}/K_{jj}	1
Plastic Hinges at Nodes I and J	1	0	0	1

Table 6.1   Coefficients for Determining Stiffness Matrix and Plastic Hinge Rotation of Parallel Component Beam Element [81].

Singularity Condition	K_{tii}	K_{tjj}
No Flexural Stiffness at Node I, $K_{bii} = K_{bij} = 0$	0	$\dfrac{1}{\dfrac{1}{K_{bjj}} + \dfrac{1}{GA_z^*L} + f_s^j}$
No Flexural Stiffness at Node J, $K_{bjj} = K_{bij} = 0$	$\dfrac{1}{\dfrac{1}{K_{bii}} + \dfrac{1}{GA_z^*L} + f_s^i}$	0
No Flexural Stiffness at Nodes I and J, $\underline{K}_b = \underline{0}$	0	0

Table 6.2   Stiffness Coefficients for Complete Element when Stiffness Matrix of Parallel Component Beam Element is Singular.

Beam-Column Elements			
Member [1]	Strain Hardening Ratio ρ [2]	P_y (kip) [3]	M_y (kip-in) [4]
W 6 x 12 Beams	0.03	173	350
W 6 x 25 Beams	0.03	358	797
W 8 x 25 Columns	0.03	367	1259
2-C 5 x 6.7 Braces	0.03	158	282

Link Elements							
Member [1]	Isotropic Hardening a [2]	ΔV_{max} [3]	Subhinge [4]	M_y (kip-in) [5]	V_y (kip) [6]	K_{pM} (kip-in) [7]	K_{pV} (kip) [8]
W 6 x 12	8.34	2.2 Vy_o	1	350	33	9298	442
			2	396	41	9028	429
			3	420	46	692	33
W 6 x 25	8.34	2.2 Vy_o	1	797	45	22466	614
			2	900	57	21812	595
			3	956	64	778	46

Table 6.3   Force-Deformation Properties of Elements for Modeling the Bottom Three Stories of 20 Story EBF.

Half Cycle	Lateral Load (kips)		3rd Floor Lateral Displacement (inches)		North Link 1st Floor Vertical Deflection (inches)		South Link 1st Floor Vertical Deflection (inches)	
	Test	ANSR	Test	ANSR	Test	ANSR	Test	ANSR
[1]	[2]	[3]	[4]	[5]	[6]	[7]	[8]	[9]
1	64.3	66.9	0.50	0.49	0.06	0.02	0.14	0.08
7	83.2	90.5	0.99	0.99	0.17	0.12	0.32	0.24
13	100.0	106.2	1.49	1.49	0.23	0.20	0.53	0.47
19	113.6	114.1	3.00	2.99	0.52	0.34	1.16	1.20
23	113.0	116.9	4.53	4.50	0.82	0.57	1.79	1.82

Table 6.4 Maximum Relative Displacement Between Ends of Links at Selected Half Cycles.

TABLE 7.1 NONLINEAR DYNAMIC ANALYSIS SOLUTION ALGORITHM.

I. Initialization of Algorithm

(1) Specify parameters β, γ, time step size Δt, and convergence tolerance TOL.

(2) Compute intergration parameters:

$$a_1 = \frac{1}{\beta(\Delta t)^2} \qquad a_2 = \frac{1}{\beta \Delta t} \qquad a_3 = \frac{1}{2\beta}$$

$$a_4 = \frac{\gamma}{\beta \Delta t} \qquad a_5 = \frac{\gamma}{\beta} \qquad a_6 = \Delta t \left(1 - \frac{\gamma}{2\beta}\right)$$

(3) Form the effective stiffness matrix:

$$\underline{K}_t^* = a_1 \underline{M} + a_4 \underline{C} + \underline{K}_0$$

(4) Perform decomposition of effective stiffness matrix:

$$\underline{L} \, \underline{D} \, \underline{L}^T = \underline{K}_t^*$$

(5) Specify initial conditions for the analysis, e.g. $\underline{q}_t$, $\underline{\dot{q}}_t$, and $\underline{\ddot{q}}_t$ at time = 0.

II. Iteration Within Time Step

(1) Determine load vector $\underline{P}_{t+\Delta t}$.

(2) Set iteration index i= 0 and initialize the motion vectors:

$$\underline{q}^{(i)}_{t+\Delta t} = \underline{q}_t$$

$$\underline{\dot{q}}^{(i)}_{t+\Delta t} = (1 - a_5)\underline{\dot{q}}_t + a_6\underline{\ddot{q}}_t$$

$$\underline{\ddot{q}}^{(i)}_{t+\Delta t} = (1 - a_3)\underline{\ddot{q}}_t - a_2\underline{\dot{q}}_t$$

(3) Perform state determination for current configuration to determine equivalent nodal

forces $\underline{R}_t^{(i)}$ in equilibrium with the element internal forces.

148

(4) Solve for incremental displacement $\Delta q^{(i+1)}$ for iteration i:

$$\underline{L}\,\underline{D}\,\underline{L}^{T}\cdot\Delta\underline{q}^{(i+1)} = \underline{P}_{t+\Delta t} - \left[\underline{M}\cdot\ddot{\underline{q}}^{(i)}_{t+\Delta t} + \underline{C}\cdot\dot{\underline{q}}^{(i)}_{t+\Delta t} + \underline{R}^{(i)}_t\right]$$

(5) Update motions:

$$\underline{q}^{(i+1)}_{t+\Delta t} = \underline{q}^{(i)}_{t+\Delta t} + \Delta\underline{q}^{(i+1)}$$

$$\dot{\underline{q}}^{(i+1)}_{t+\Delta t} = \dot{\underline{q}}^{(i)}_{t+\Delta t} + a_4\Delta\underline{q}^{(i+1)}$$

$$\ddot{\underline{q}}^{(i+1)}_{t+\Delta t} = \ddot{\underline{q}}^{(i)}_{t+\Delta t} + a_1\Delta\underline{q}^{(i+1)}$$

(6) Perform state determination for updated configuration to determine $\underline{R}^{(i+1)}_t$ corresponding to $\underline{q}^{(i+1)}_{t+\Delta t}$.

(7) Compute the residual load vector:

$$\hat{\underline{f}} = \underline{P}_{t+\Delta t} - \left[\underline{M}\cdot\ddot{\underline{q}}^{(i+1)}_{t+\Delta t} + \underline{C}\cdot\dot{\underline{q}}^{(i+1)}_{t+\Delta t} + \underline{R}^{(i+1)}_t\right]$$

(8) Check convergence:

If $\dfrac{\|\hat{\underline{f}}\|}{\|\underline{P}_{t+\Delta t}\|} < $ TOL   then proceed to next time step.

If $\dfrac{\|\hat{\underline{f}}\|}{\|\underline{P}_{t+\Delta t}\|} \geq $ TOL   then i = i +1, go to Step 4.

ANALYSIS DESCRIPTION	1.5*EL CENTRO 1940 SE			PARKFIELD 1966 NE		
[1]	DESIGN 1 [2]	DESIGN 2 [3]	DESIGN 3 [4]	DESIGN 1 [5]	DESIGN 2 [6]	DESIGN 3 [7]
1. Bare Steel Frame, Strain Hardening, P-delta Effect, Nonproportional Damping	EC1	EC5	EC9	PA1	PA2	PA7
2. Bare Steel Frame, Elas. Perfectly Plastic, P-delta Effect, Nonproportional Damping	EC2	EC6			PA3	
3. Bare Steel Frame, Strain Hardening, P-delta Effect, Rayleigh Damping	EC3					
4. Bare Steel Frame, Elas. Perfectly Plastic, P-delta Effect, Rayleigh Damping	EC4					
5. Bare Steel Frame, Strain Hardening, No P-delta Effect, Nonproportional Damping					PA4	
6. Composite Exterior Frame, Strain Hardening, P-delta Effect, Nonproportional Damping		EC7			PA5	
7. Composite Interior Frame, Strain Hardening, P-delta Effect, Nonproportional Damping		EC8			PA6	
8. Bare Steel Frame, Strain Hardening, Pin Beam & Brace Connection, P-delta Effect, Nonproportional Damping			EC10			PA8

Table 8.1 Summary of Nonlinear Dynamic EBF Analyses.

150

SECTION [1]	I_{eff} (in⁴) [2]	b_{eff} (in) [3]	$\dfrac{I_{eff}}{I}$ [4]	Ks (k-in) [5]	M_p^+ (k-in) [6]	M_p^- (k-in) [7]	P_y^- (kips) [8]	P_y^+ (kips) [9]
W18x65 link beam, exterior bay	1721	13.3	1.61	1167910	6648	4788	857	688
W18x46 link beam, exterior bay	1246	12.8	1.75	687050	4936	3265	649	486
W18x46 link beam, interior bay	1189	13.5	1.67	951878	5001	3265	658	486
W18x40 link beam, exterior bay	1095	12.6	1.79	573462	4393	2822	586	425
W18x40 link beam, interior bay	1053	13.4	1.72	784162	4449	2822	595	425
W18x35 link beam, interior bay	908	13.2	1.78	624246	3963	2394	539	371
W18x35 link beam, interior bay	903	7.7	1.77	576399	3455	2394	469	371
W16x26 link beam, exterior bay	536	6.2	1.78	506587	2370	1591	356	277

Table 8.2 Composite Beam Properties for EBF Design 2, Exterior Composite Frame.

SECTION [1]	I_{eff} (in⁴) [2]	b_{eff} (in) [3]	$\dfrac{I_{eff}}{I}$ [4]	Ks (k-in) [5]	M_p^+ (k-in) [6]	M_p^- (k-in) [7]	P_y^- (kips) [8]	P_y^+ (kips) [9]
W18x65 link beam, exterior bay	2111	31.8	1.97	897279	8034	4788	1093	688
W18x46 link beam, exterior bay	1518	30.4	2.13	554565	6193	3265	878	486
W18x46 link beam, interior bay	1454	32.9	2.04	749094	6314	3265	905	486
W18x40 link beam, exterior bay	1335	30.4	2.18	467214	5595	2822	813	425
W18x40 link beam, interior bay	1280	32.6	2.09	629404	5721	2822	840	425
W18x35 link beam, interior bay	1106	32.2	2.17	507346	5064	2394	781	371
W18x35 link beam, interior bay	1098	18.5	2.15	468389	4352	2394	607	371
W16x26 link beam, exterior bay	650	15.0	2.16	413280	3043	1591	467	277

Table 8.3 Composite Beam Properties for EBF Design 2, Interior Composite Frame.

EBF Model [1]	Natural Periods (Seconds)				
	Mode 1 [2]	Mode 2 [3]	Mode 3 [4]	Mode 4 [5]	Mode 5 [6]
Design 1 - Bare Steel EBF	0.713	0.275	0.168	0.161	0.136
Design 2 - Bare Steel EBF	0.688	0.271	0.164	0.160	0.133
Design 2 - Composite Exterior EBF	0.680	0.264	0.161	0.160	0.132
Design 2 - Composite Interior EBF	0.678	0.262	0.161	0.160	0.132
Design 3 - Bare Steel EBF, Pin Connections	0.627	0.265	0.153	0.152	0.126
Design 3 - Bare Steel EBF, All Moment Connections	0.621	0.253	0.152	0.149	0.125

Table 8.4 Natural Periods of First Five Elastic Modes of EBF Models.

[1]	Analysis									
	Design 1				Design 2				Design 3	
	EC1 [2]	EC2 [3]	EC3 [4]	EC4 [5]	EC5 [6]	EC6 [7]	EC7 [8]	EC8 [9]	EC9 [10]	EC10 [11]
V_{max} (kips)	650	497	694	556	718	572	739	796	910	880
$\dfrac{V_{max}}{V_{Design}}$	2.04	1.56	2.18	1.74	2.26	1.79	2.33	2.50	2.39	2.31

V_{max} = Maximum Base Shear, Analysis

V_{Design} = Design Base Shear

Table 8.5   Maximum Base Shear for EBF Design Subjected to First 15 Seconds of 1.5 * El Centro Earthquake Record.

[1]	Analysis							
	Design 1	Design 2					Design 3	
	PA1 [2]	PA2 [3]	PA3 [4]	PA4 [5]	PA5 [6]	PA6 [7]	PA7 [8]	PA8 [9]
V_{max} (kips)	727	862	612	857	880	940	983	946
$\dfrac{V_{max}}{V_{Design}}$	2.29	2.71	1.93	2.69	2.77	2.96	2.58	2.48

V_{max} = Maximum Base Shear, Analysis

V_{Design} = Design Base Shear

Table 8.6   Maximum Base Shear for EBF Design Subjected to First 15 Seconds of Parkfield Earthquake Record.

	Permanent Relative Link Displacement - Inches									
	Design 1				Design 2				Design 3	
Floor [1] Analysis	EC1 [2]	EC2 [3]	EC3 [4]	EC4 [5]	EC5 [6]	EC6 [7]	EC7 [8]	EC8 [9]	EC9 [10]	EC10 [11]
1	0.14	0.24	0.07	0.17	0.10	0.09	0.07	0.05	0.19	0.19
2	0.42	0.29	0.14	0.33	0.10	0.02	0.10	0.23	0.04	0.09
4	0.28	0.49	0.28	0.33	0.21	0.77	0.35	0.17	0.25	0.50

Table 8.7   Permanent Relative Displacement Between Ends of Links, 1.5*El Centro Earthquake Record.

	Permanent Relative Link Displacement - Inches							
	Design 1	Design 2					Design 3	
Floor [1] Analysis	PA1 [2]	PA2 [3]	PA3 [4]	PA4 [5]	PA5 [6]	PA6 [7]	PA7 [8]	PA8 [9]
1	0	0.28	0.56	0.26	0.25	0.33	0.12	0.02
2	0.59	0.77	1.18	0.79	0.89	0.90	0.66	0.79
4	0.77	1.04	1.94	1.10	0.89	0.69	0.07	0.09

Table 8.8   Permanent Relative Displacement Between Ends of Links, Parkfield Earthquake Record.

(DISSIPATED HYSTERETIC LINK ENERGY/TOTAL DISSIPATED HYSTERETIC ENERGY) * 100									
DESIGN 1				DESIGN 2				DESIGN 3	
ANALYSIS FLOOR									
EC1	EC2	EC3	EC4	EC5	EC6	EC7	EC8	EC9	EC10
R									
0	0	0	0	0	0	0	0	0	0
5									
1.9	0.6	2.3	1.3	4.6	3.4	4.1	3.5	4.7	5.3
4									
2.7	1.0	3.5	1.7	6.8	3.8	7.1	6.5	5.0	5.9
3									
3.9+3.9	1.9+2.1	5.6+5.7	3.9+4.0	11.5+11.3	11.4+11.0	11.5+11.2	11.8+11.7	3.2+3.2	3.0+3.1
2									
10.2+10.1	9.3+9.1	10.8+10.8	9.8+9.8	11.7+11.6	8.7+8.6	11.5+11.6	10.9+11.2	10.7+10.8	10.8+10.9
1									
33.4+33.5	37.8+37.9	30.6+30.6	34.6+34.5	21.2+21.2	26.5+26.5	21.5+21.4	22.1+22.0	31.1+31.3	30.3+30.7
ΣFLOORS									
99.6	99.7	99.9	99.6	99.9	99.9	99.9	99.7	100.0	100.0

	DESIGN 1				DESIGN 2				DESIGN 3	
ANALYSIS ENERGY	EC1	EC2	EC3	EC4	EC5	EC6	EC7	EC8	EC9	EC10
TOTAL DHE (kip-in)	8359	7688	7262	6793	7828	7918	7662	7380	6767	6609
DDE (kip-in)	2268	1445	1387	270	2236	1783	2071	2109	1700	1605
IE @ t=15s (kip-in)	10782	9319	8809	7257	10362	10014	10046	9823	8909	8661

DHE = Dissipated Hysteretic Energy
DDE = Dissipated Viscous Damping Energy
IE = Input Earthquake Energy

Table 8.9 Energy Tabulations for EBF Designs Subjected to 1.5*El Centro Earthquake Record.

FLOOR \ ANALYSIS	(DISSIPATED HYSTERETIC LINK ENERGY/TOTAL DISSIPATED HYSTERETIC ENERGY) * 100							
	DESIGN 1	DESIGN 2					DESIGN 3	
	PA1	PA2	PA3	PA4	PA5	PA6	PA7	PA8
R	0	0	0	0	0	0	0.2	0.1
5	2.5	4.7	2.8	4.1	4.0	3.7	6.4	5.6
4	2.9	6.5	6.1	6.4	6.2	5.9	5.4	4.6
3	4.9+4.8	8.6+8.4	11.6+11.1	9.9+9.7	9.5+9.4	9.5+9.4	2.9+2.9	2.9+3.1
2	13.6+13.7	12.5+12.5	13.5+13.5	12.9+13.1	13.1+13.1	12.9+12.9	12.8+13.0	11.8+11.9
1	28.0+27.9	22.9+22.8	19.9+19.9	21.4+21.3	21.6+21.6	22.2+22.2	28.0+28.1	29.2+29.4
ΣFLOORS	98.3	98.9	98.4	98.8	98.5	98.7	99.7	98.6

ENERGY \ ANALYSIS	DESIGN 1	DESIGN 2					DESIGN 3	
	PA1	PA2	PA3	PA4	PA5	PA6	PA7	PA8
TOTAL DHE (kip-in)	6365	6554	5961	6529	6571	6712	6438	6628
DDE (kip-in)	1401	1445	1090	1459	1484	1543	1535	1469
IE @ t=15s (kip-in)	7898	8101	7179	8093	8121	8358	8079	8201

DHE = Dissipated Hysteretic Energy

DDE = Dissipated Viscous Damping Energy

IE = Input Earthquake Energy

Table 8.10 Energy Tabulations for EBF Designs Subjected to Parkfield Earthquake Record.
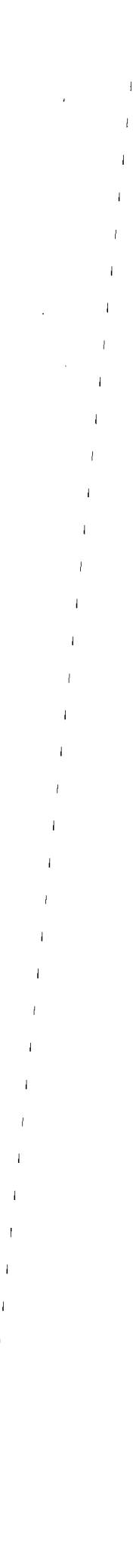
FIGURES
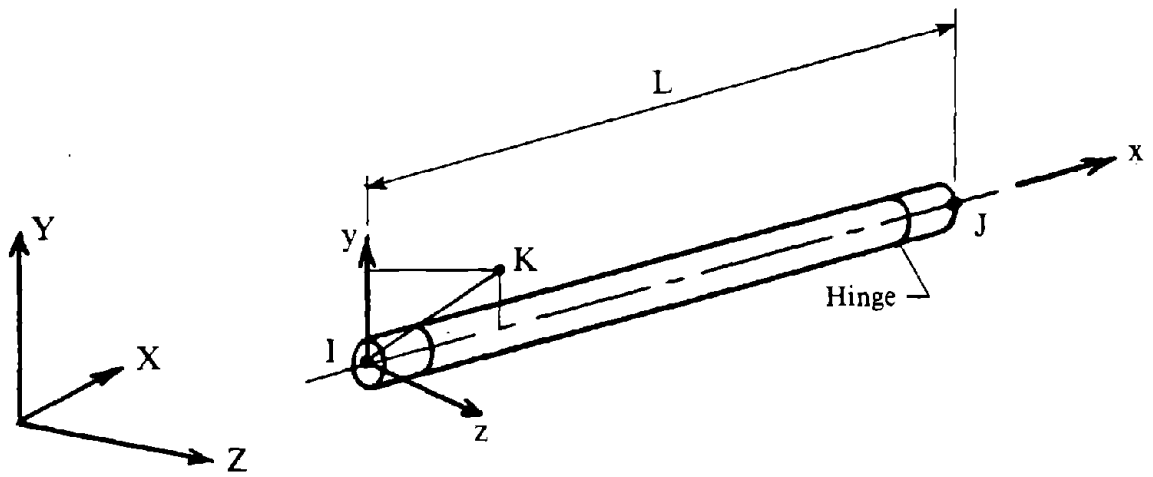
Fig. 6.1   Defining Position of Beam-Column Element in Space.
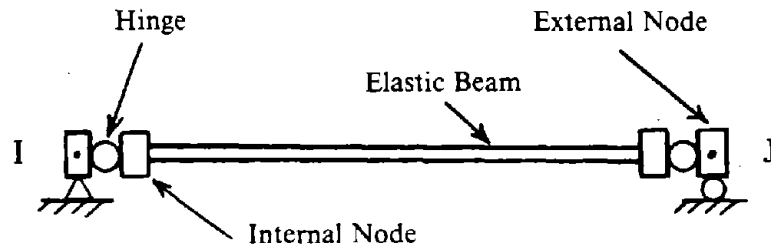
Fig. 6.2   Beam-Column Element Components.
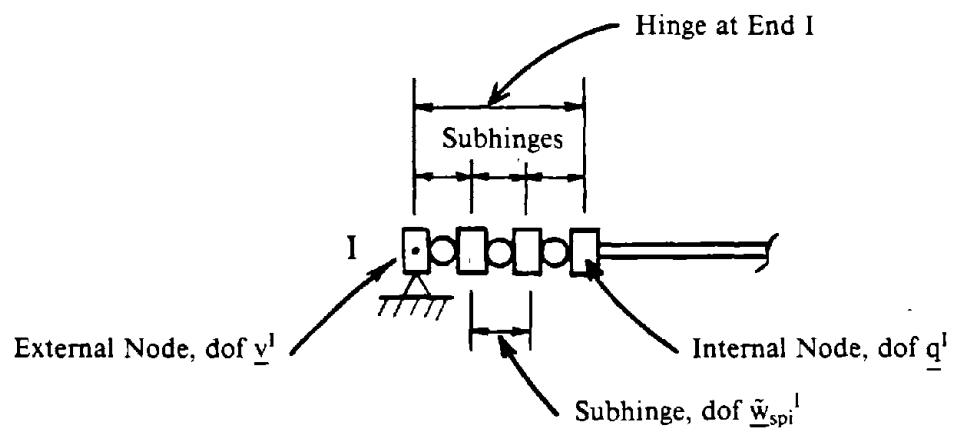
Fig. 6.3   Hinge and Subhinges at End I.
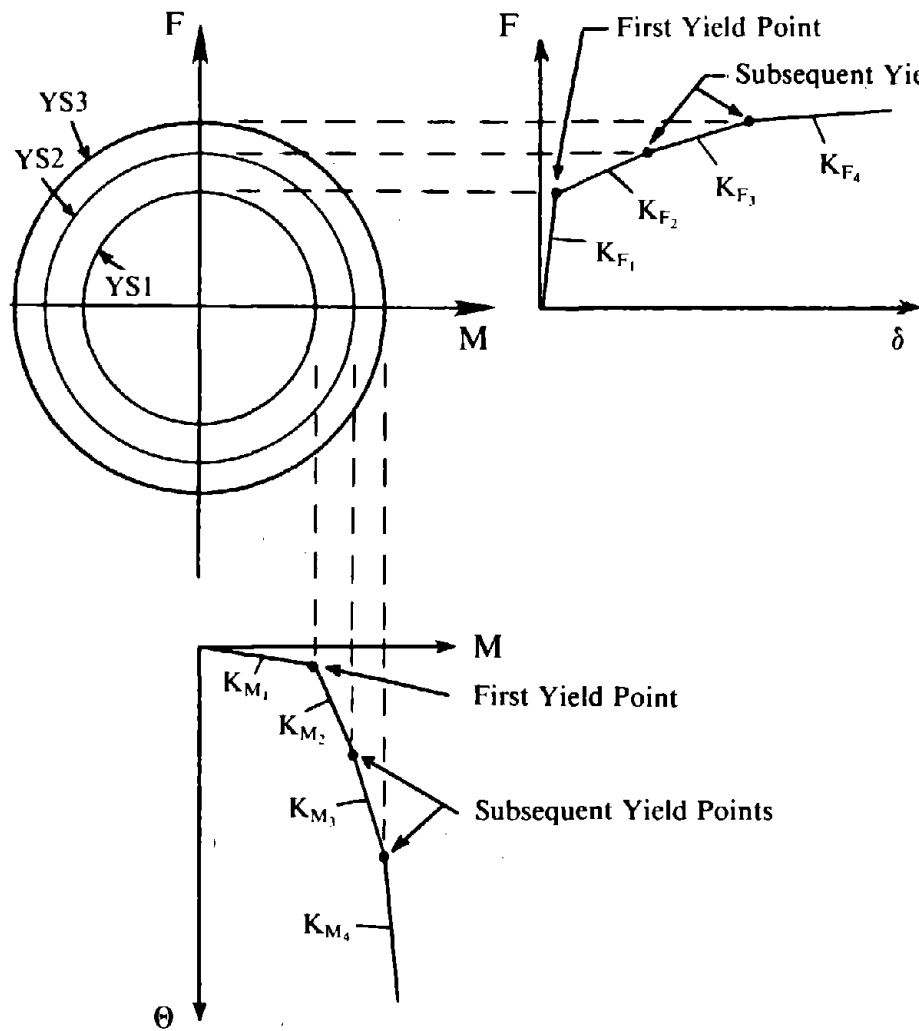
(a) Initial Position of Subhinge Yield Surfaces
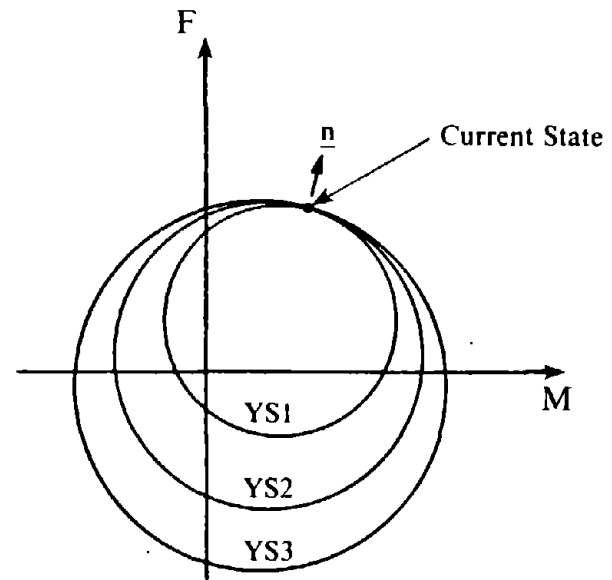
(b) Translation of Yield Surfaces After Hardening

Fig. 6.4   Strain Hardening Behavior of Hinges.
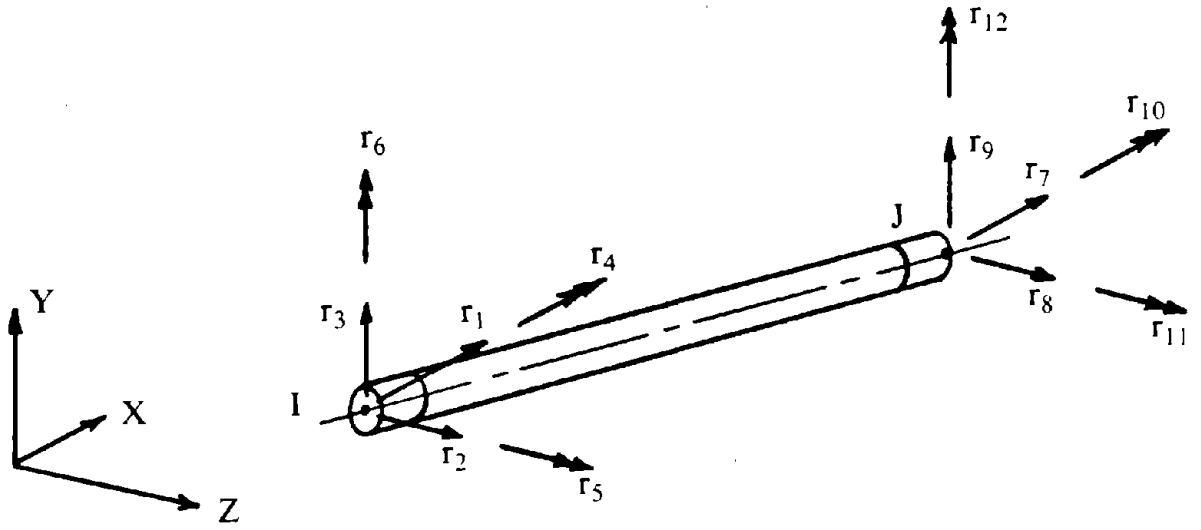
(a) Global Displacements
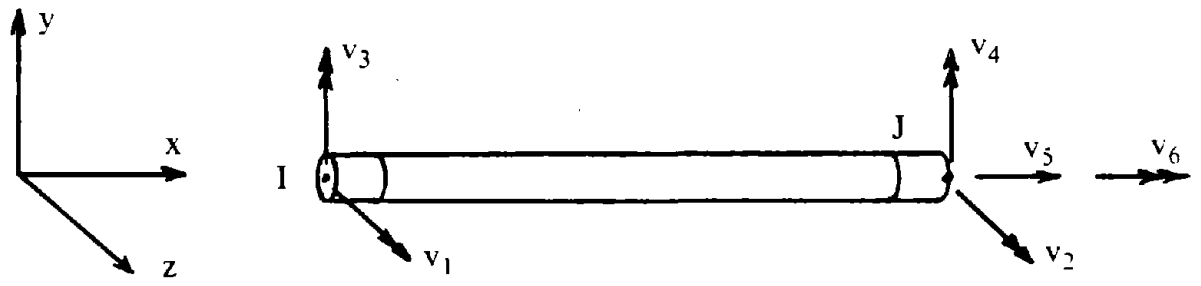
(b) Local Deformations

Fig. 6.5   .   Degrees of Freedom. 3-D Beam-Column Element.
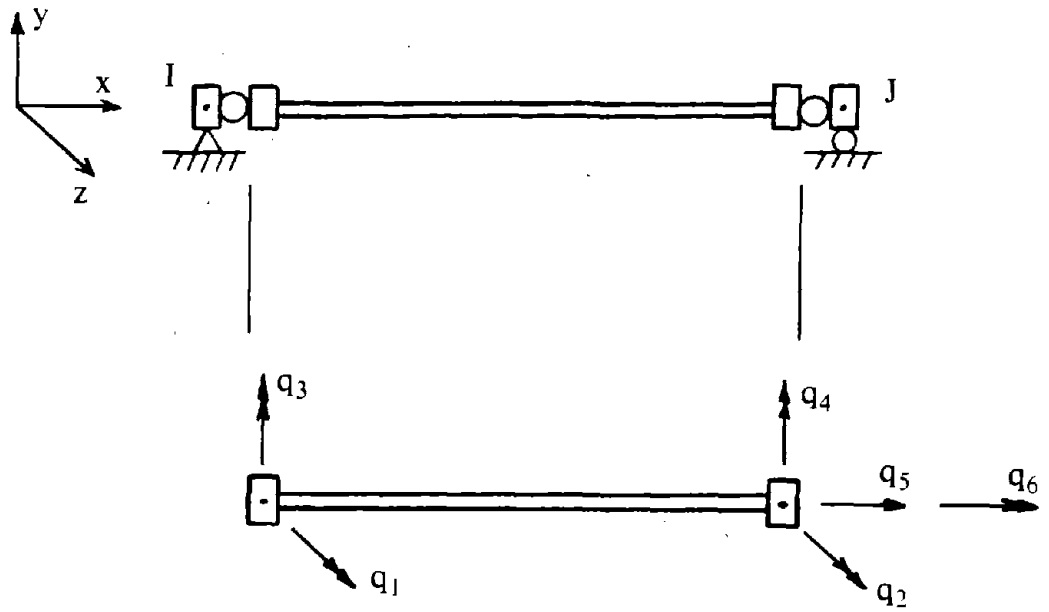
Fig. 6.6   Elastic Beam Deformation Degrees of Freedom.

(a) Initial Position of Yield Surface

(b) Translated Yield Surface
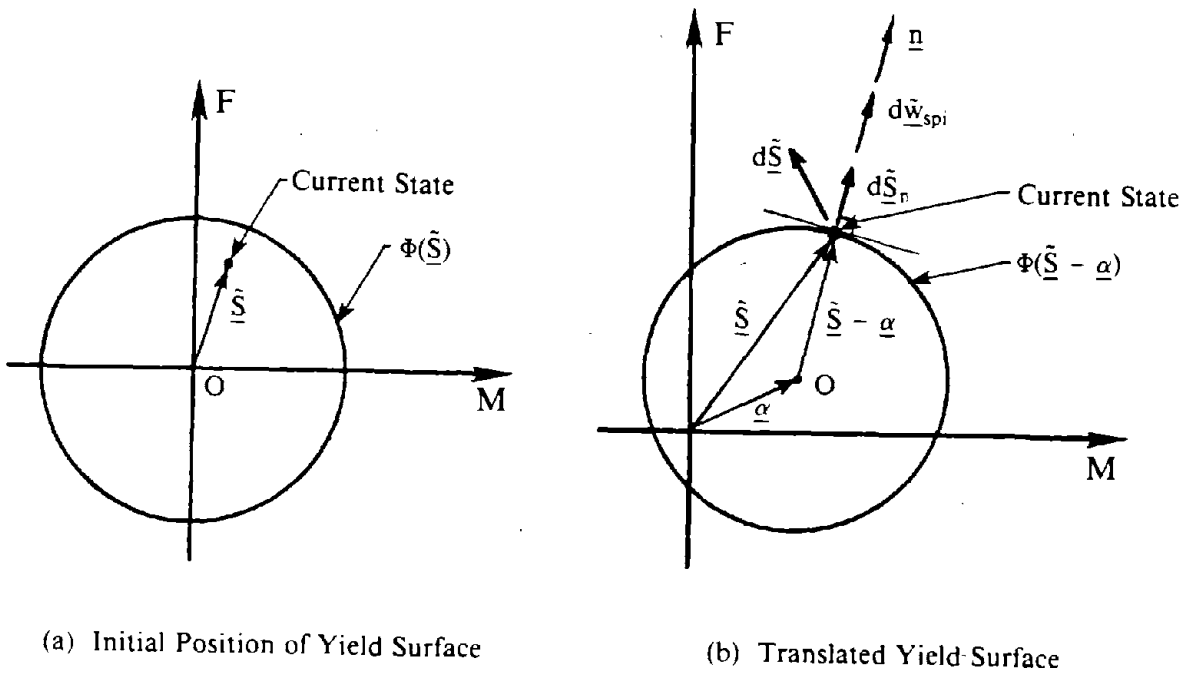
Fig. 6.7   Defining Yield Surfaces by Yield Functions.
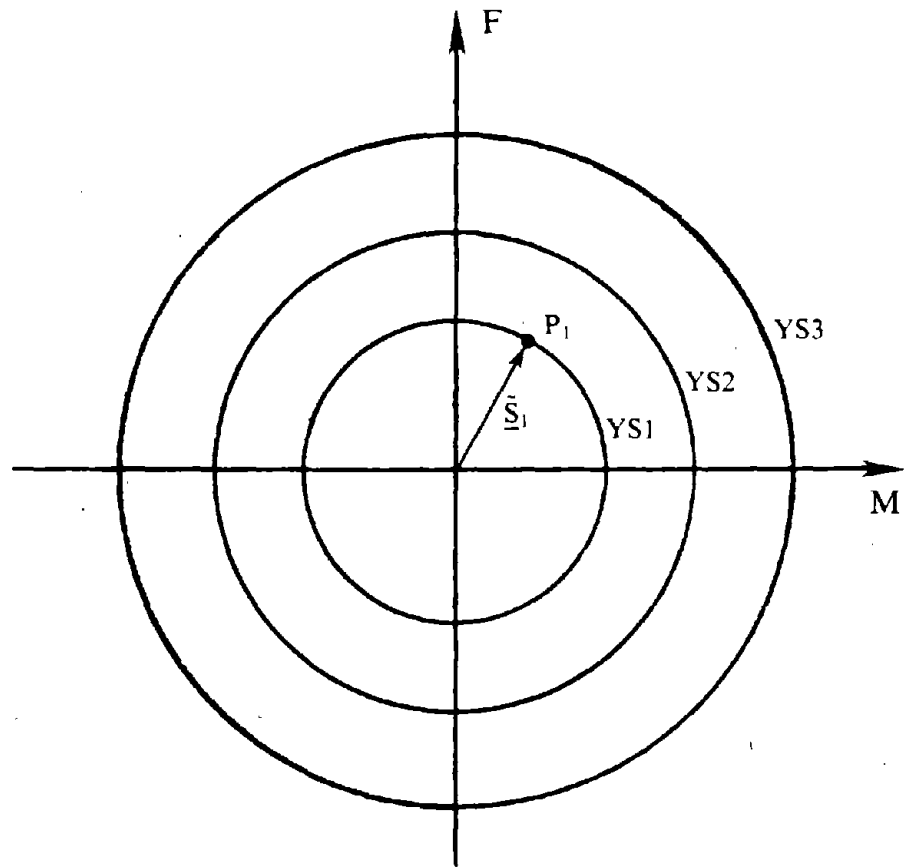
Fig. 6.8   Subhinge Yield Surfaces Prior to Yielding.

(a)

(b)
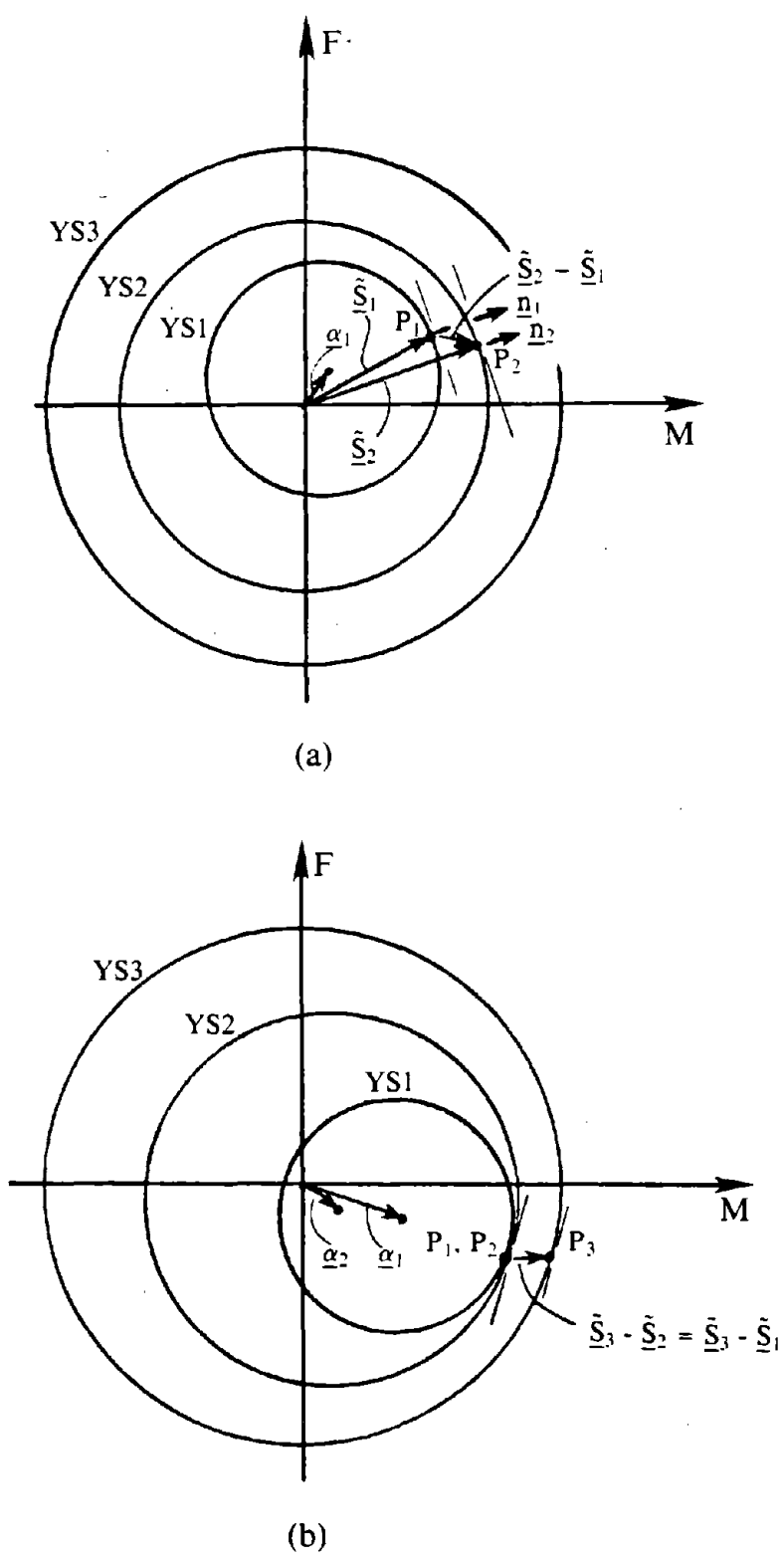
Fig. 6.9   Translation of Yield Surfaces Following Mroz's Rule.

164

F

$\underline{n}$

P_i, P_j, P_k

$\tilde{\underline{S}}$

$\underline{\alpha}_i$

$\underline{\alpha}_j$

$\underline{\alpha}_k$

M

YSi

YSj

YSk
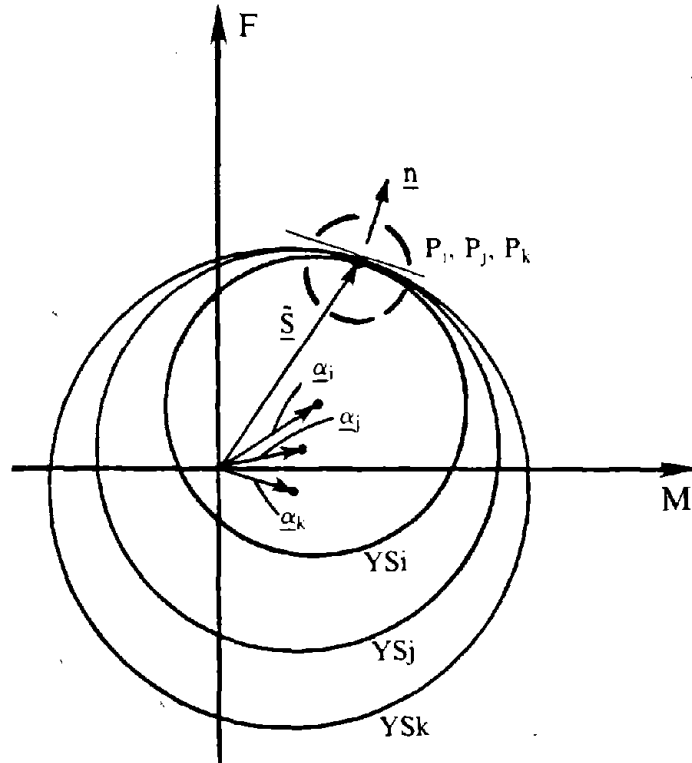
(a) State Prior to Unloading

$\underline{n}$

P_k

P_j

P_i

YSk

YSi

YSj

$YSi = \Phi_i(\tilde{\underline{S}} - \underline{\alpha}_i - 2\epsilon \cdot \underline{n})$

$YSj = \Phi_j(\tilde{\underline{S}} - \underline{\alpha}_j - \epsilon \cdot \underline{n})$

$YSk = \Phi_k(\tilde{\underline{S}} - \underline{\alpha}_k)$

$\epsilon \doteq 10^{-6}$
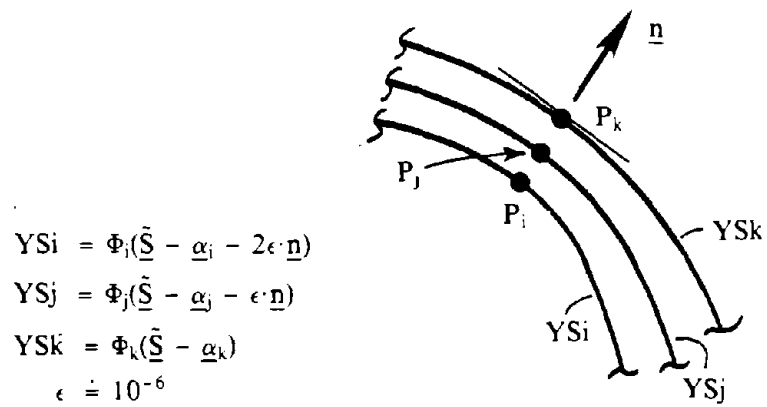
(b) Defining Unique Points P_i, P_j, and P_k While Unloading

Fig. 6.10   Unloading From Concurrent Yield Surfaces.
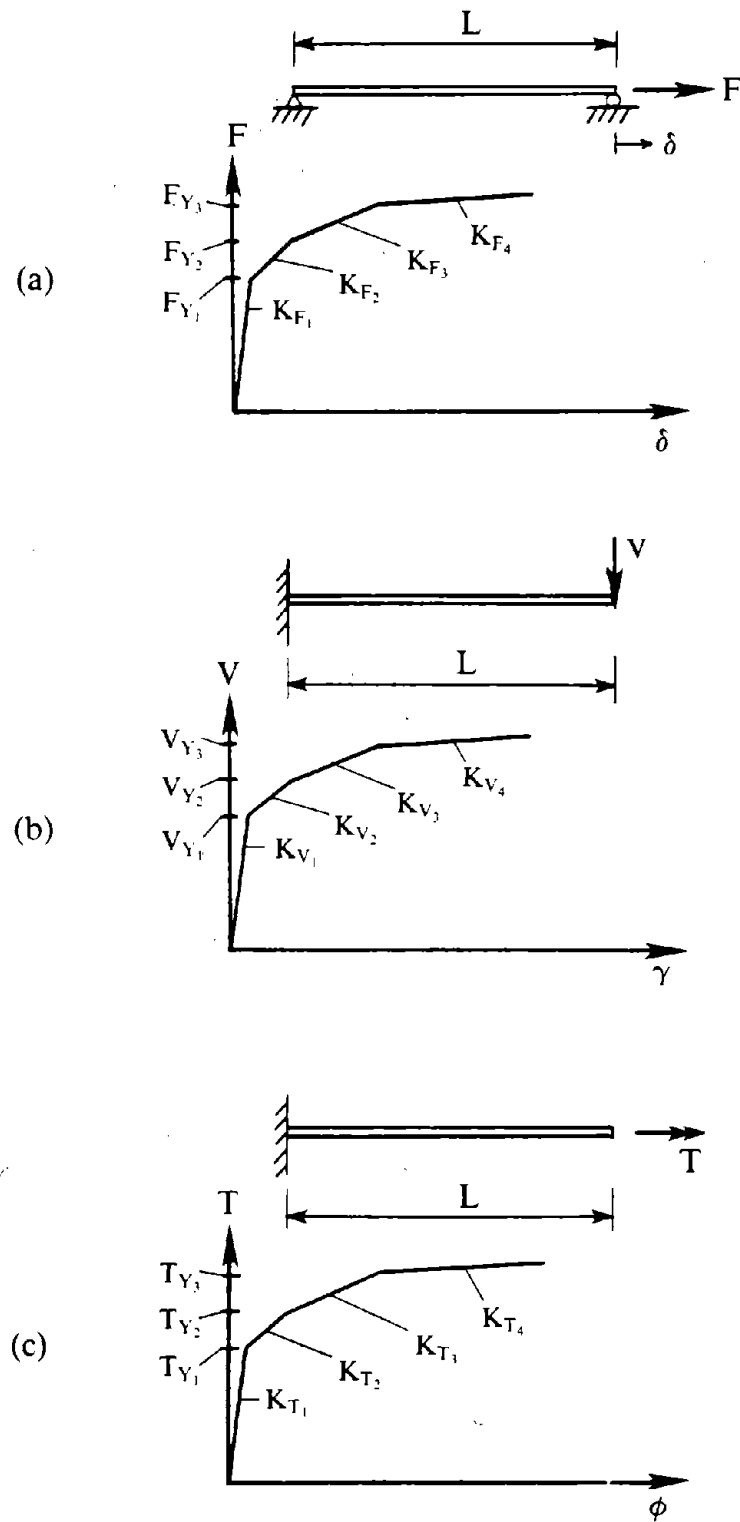
Fig. 6.11   Determining Action-Deformation Relationships for
(a) Axial Force, (b) Shear, and (c) Torsion.
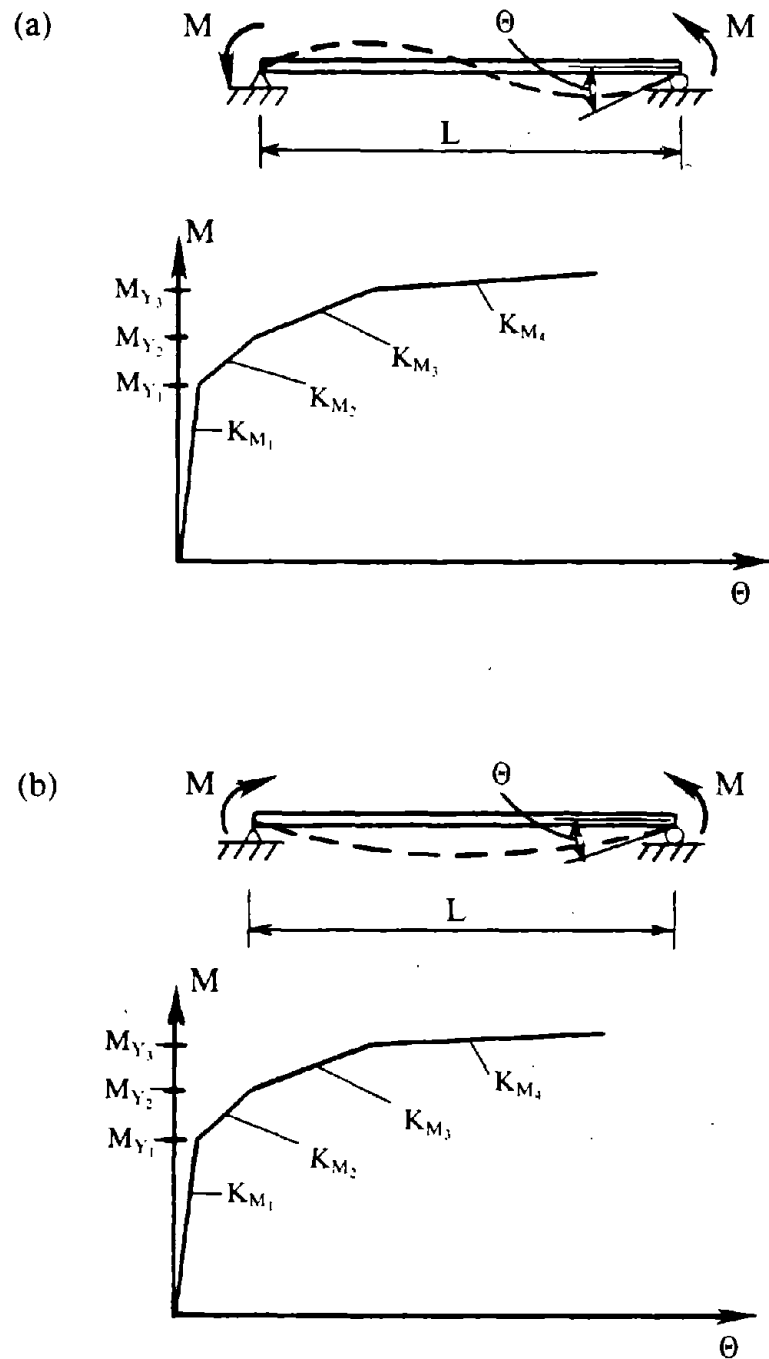
Fig. 6.12   Determining Action-Deformation Relationships for Moment, Involving
(a) In-Plane Bending, and (b) Out-of-Plane Bending of Links.
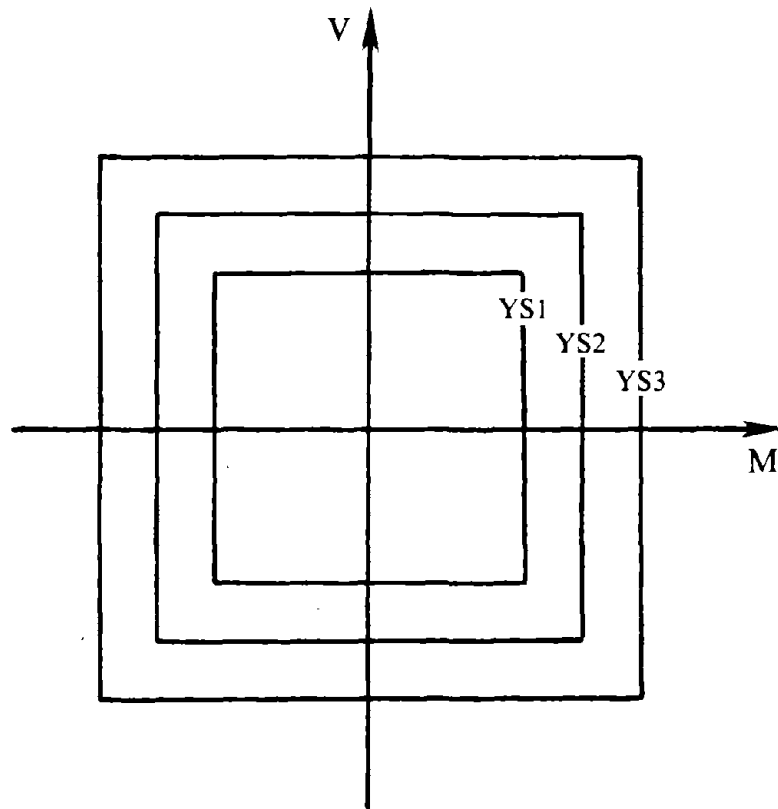
Fig. 6.13   Yield Surfaces for Subhinges of Planar Link Element.
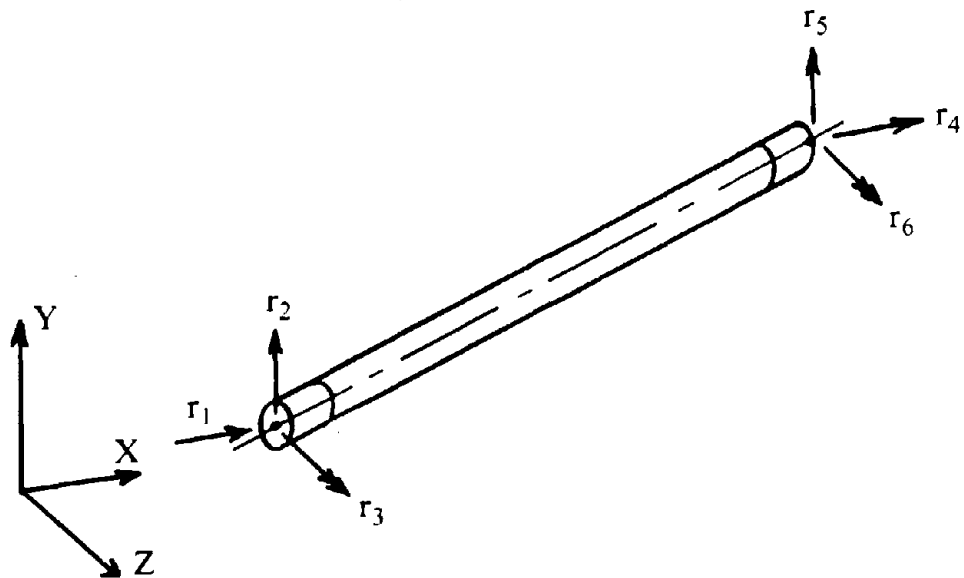
Fig. 6.14   Global Degrees of Freedom, Planar Link Element.

$$\underline{n}_b = \begin{Bmatrix} 0 \\ 1 \end{Bmatrix}$$

facet b

Vu_i

$$\underline{n}_a = \begin{Bmatrix} 1 \\ 0 \end{Bmatrix}$$

M

O

facet a

YSi

Mu_i

(a) Facets **a** and **b** of Yield Surface

$$\Phi_a = \left| \frac{M - \alpha_{M_{zi}}}{Mu_i} \right|$$

$$\Phi_b = \left| \frac{V - \alpha_{V_{yi}}}{Vu_i} \right|$$

V

P_i → P_j

O

M

YSi

YSj

(b) Horizontal Translation Due to Moment Hardening

$d\alpha_{M_{zi}}$

YSj

V

P_j

YSi

P_i

O

M

$d\alpha_{V_{yi}}$

(c) Vertical Translation Due to Shear Hardening
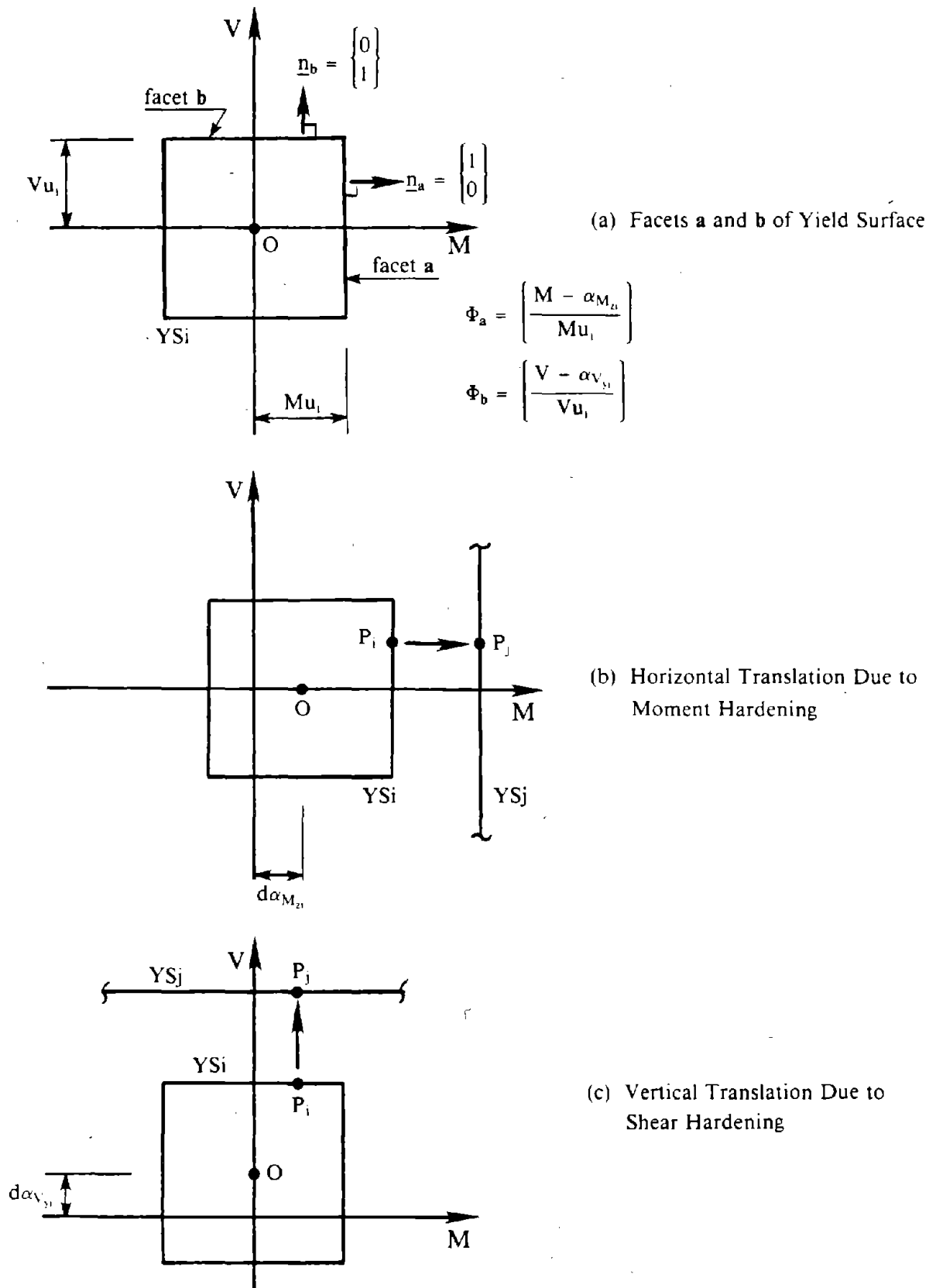
Fig. 6.15   Description and Hardening Behavior of a Yield Surface. Planar Link Element.
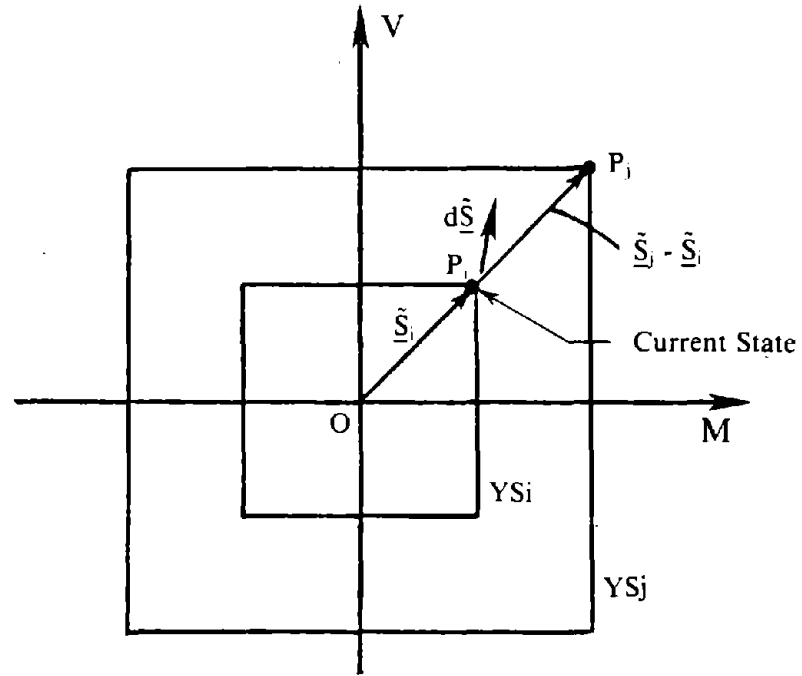
(a) Load Increment Causing Hardening
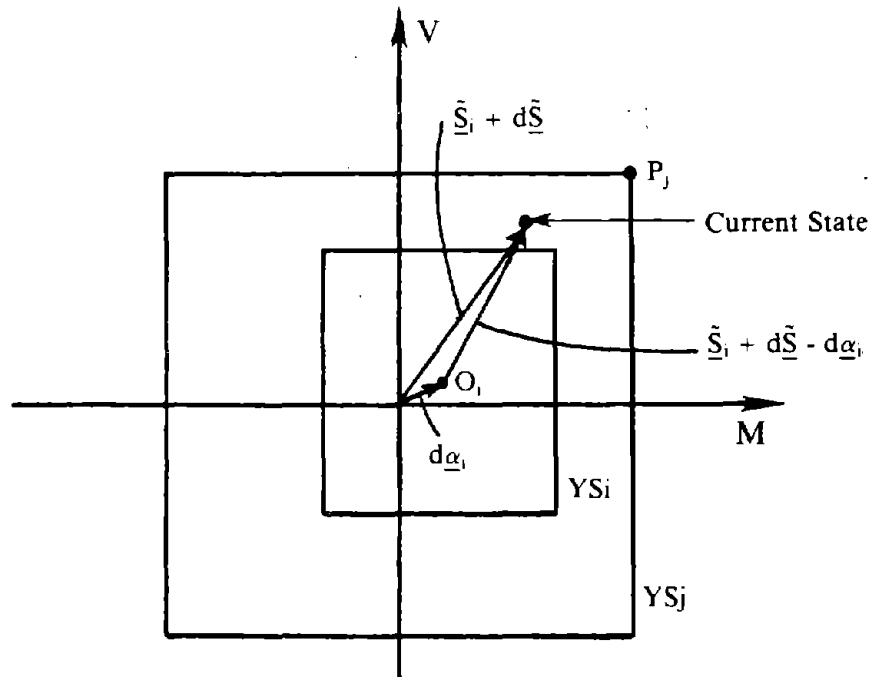
(b) Updated State

Fig. 6.16   Drift of State From Yield Surface.

V (KIPS)

100

0

-100

ΔV_{max}

ΔV_o

2H (KIPS)

$$2H(\epsilon) = 217.2 - 55.2\exp(-8.34\epsilon)$$

o Measured

—— Regression Analysis

ϵ (RAD)
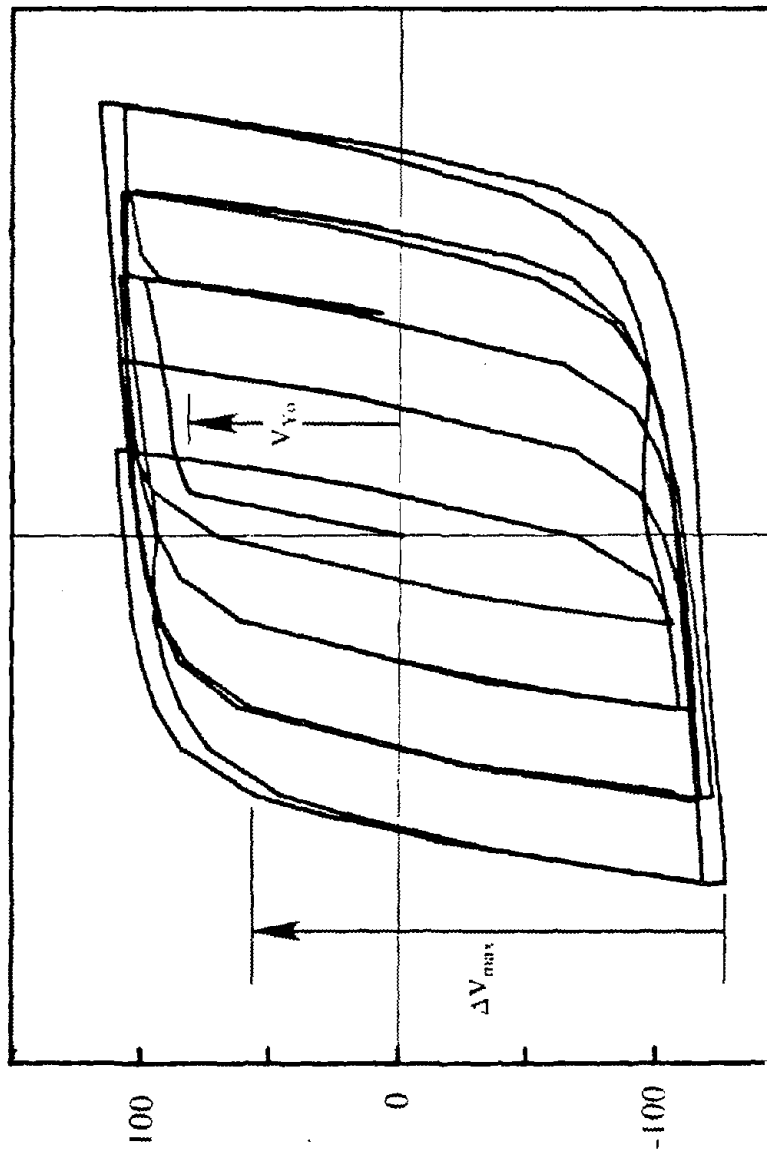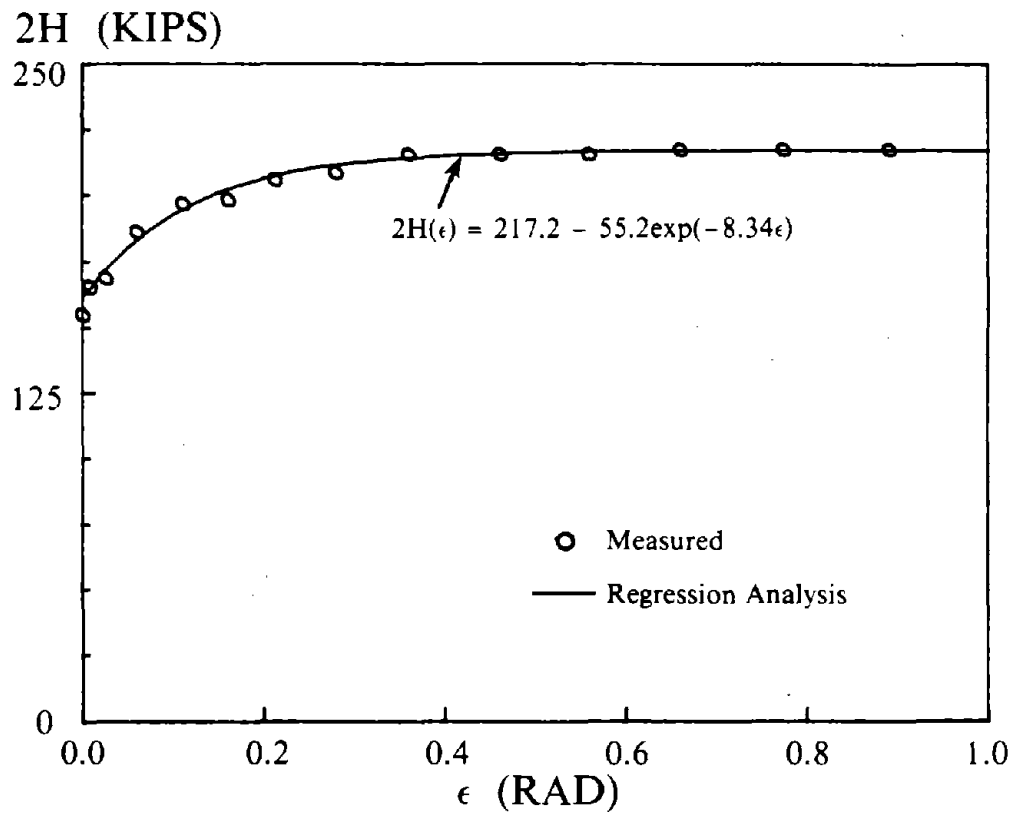
Fig. 6.18   Isotropic Hardening Effect on Cyclic Shear Yield Strength, Specimen D1.

2H (KIPS)

$$2H(\epsilon) = 225.0 - 35.0\exp(-5.67\epsilon)$$

o Measured

—— Regression Analysis

ϵ (RAD)
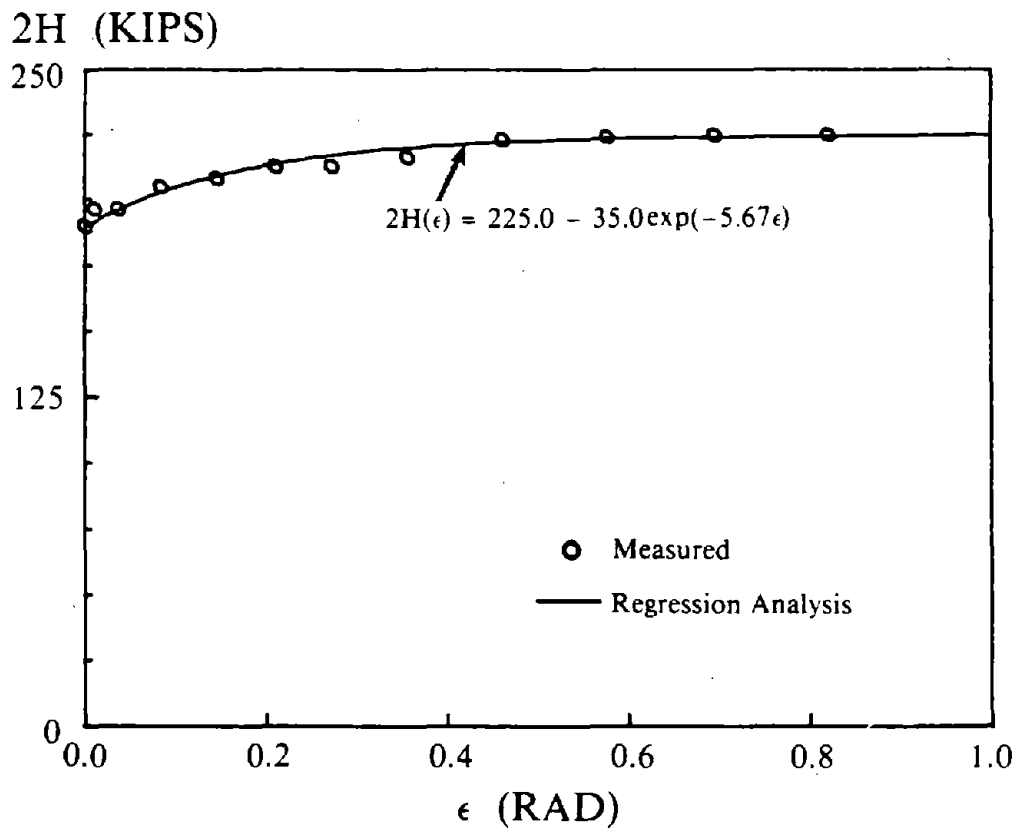
Fig. 6.19   Isotropic Hardening Effect on Cyclic Shear Yield Strength, Specimen B1.

(a) Before Yielding

(b) After Isotropic and Kinematic Hardening
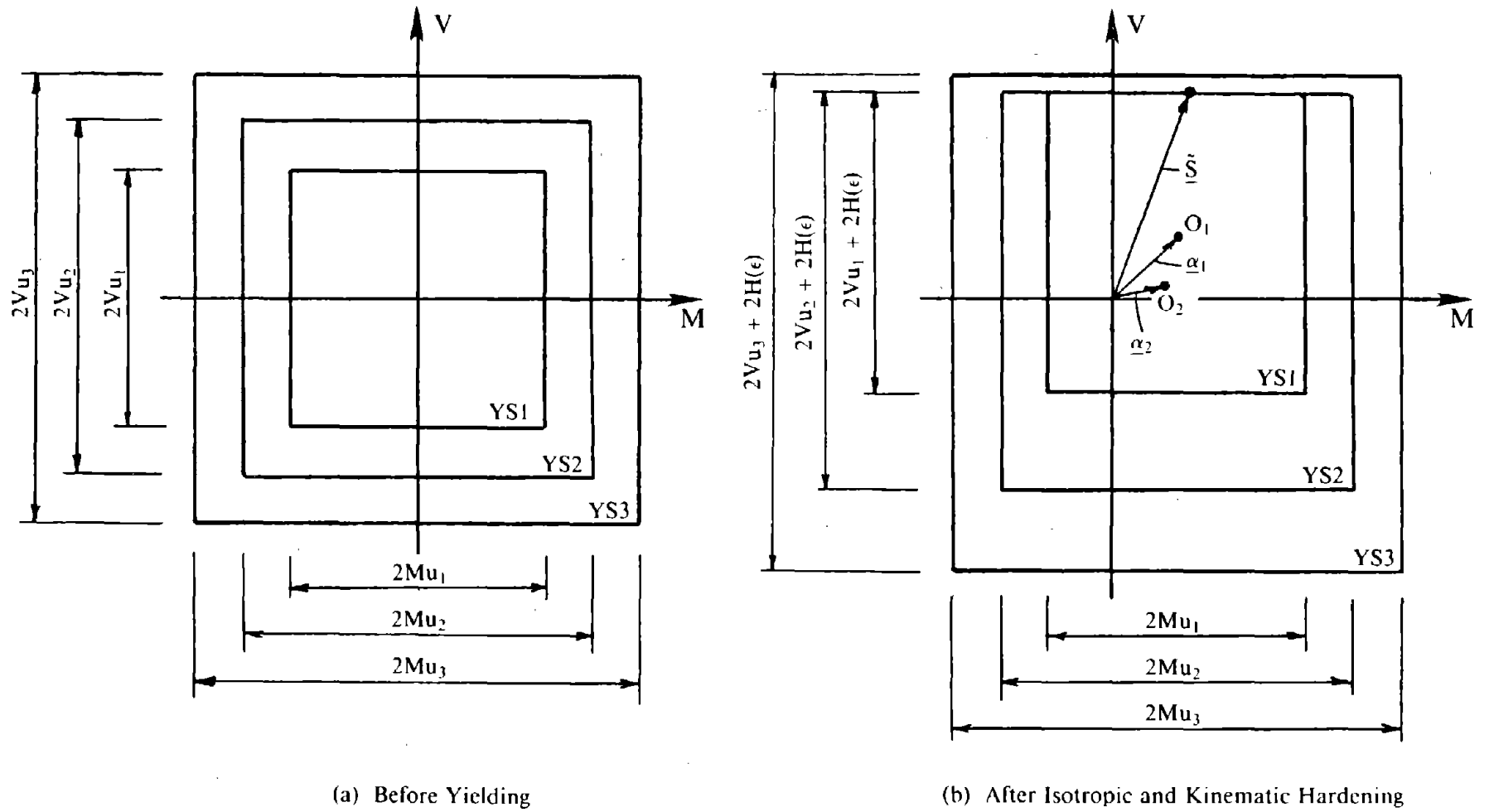
Fig. 6.20   Behavior of Yield Surfaces Due to Isotropic and Kinematic Hardening.

$V_Y = 81$ kips

$1.40V_Y$

$1.26V_Y$

V_Y

K_{V_2}

K_{V_3}

K_{V_4}

$K_{V_1} \doteq \dfrac{GA_l^*}{e} = 1706$ k/in

$K_{V_2} = 0.03K_{V_1}$

$K_{V_3} = 0.015K_{V_1}$

$K_{V_4} = 0.002K_{V_1}$

K_{V_1}

$\gamma \bullet e$

Sym.

$M_Y = 1192$ k – in

$1.20M_Y$

$1.13M_Y$

M_Y

K_{M_2}

K_{M_3}

K_{M_4}

$K_{M_1} \doteq \dfrac{6EI_l}{e} = 1.211 \times 10^6$ k – in

$K_{M_2} = 0.03K_{M_1}$

$K_{M_3} = 0.015K_{M_1}$

$K_{M_4} = 0.002K_{M_1}$

K_{M_1}

Θ

Sym.
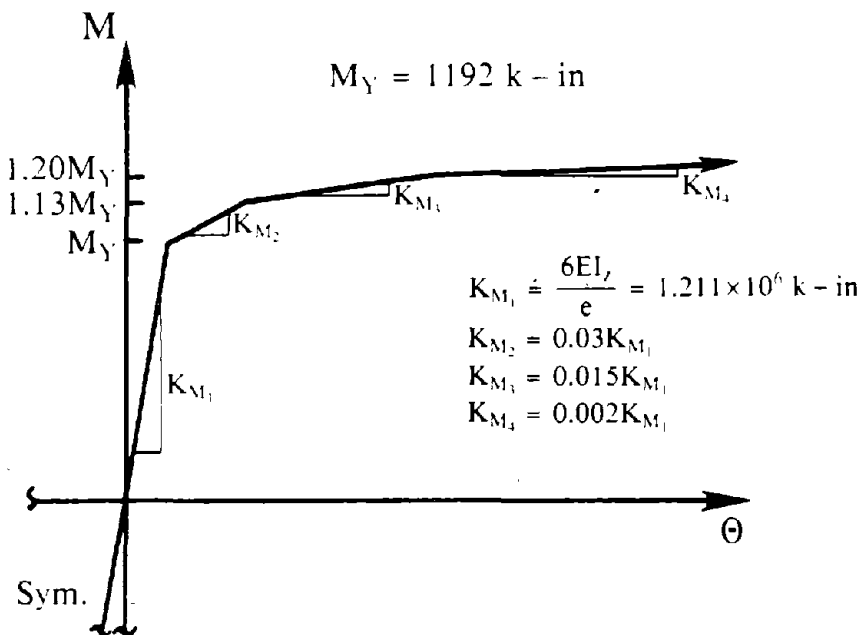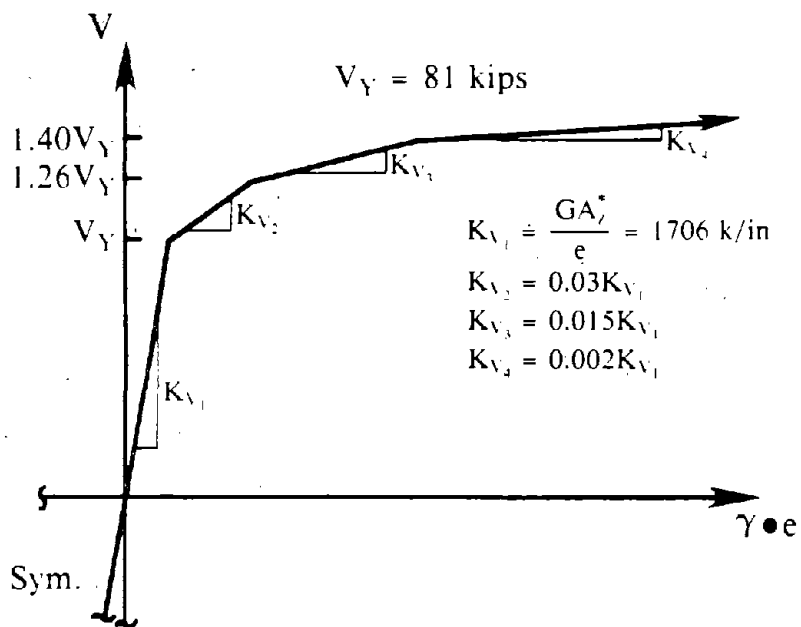
Fig. 6.21   Force-Deformation Relationships for (a) Shear, and
(b) Moment to Model Bare Steel Links.

174
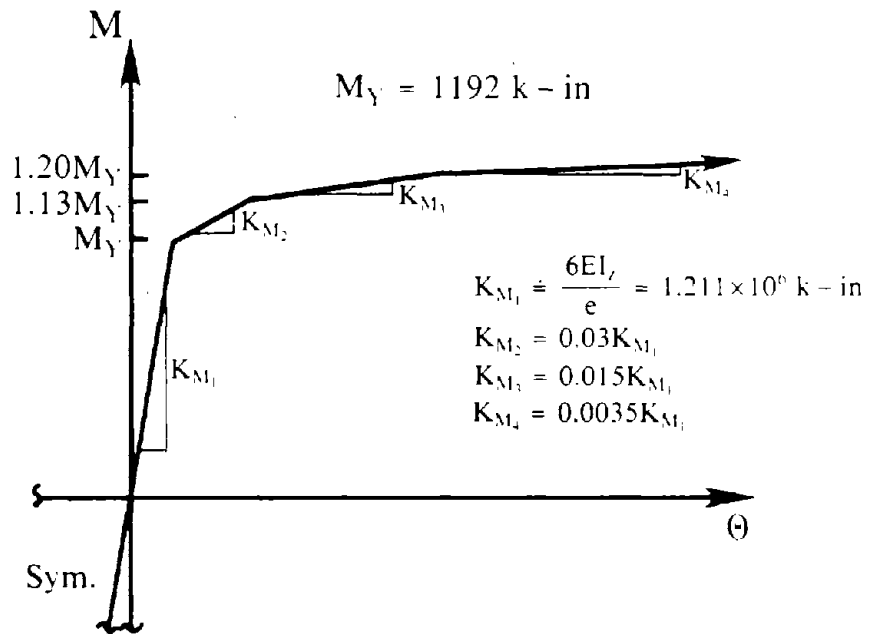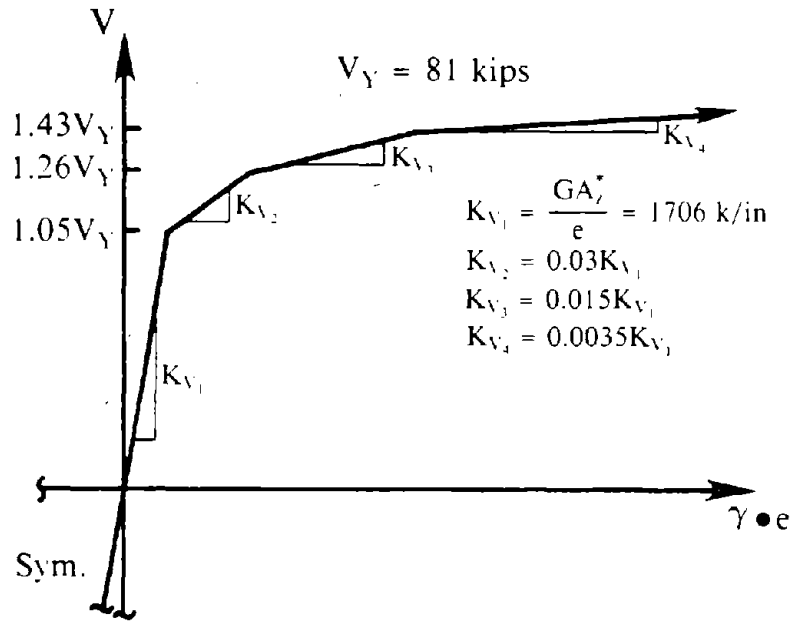
Fig. 6.22   Force-Deformation Relationships for (a) Shear, and
(b) Moment to Model Composite Links in Exterior EBFs.
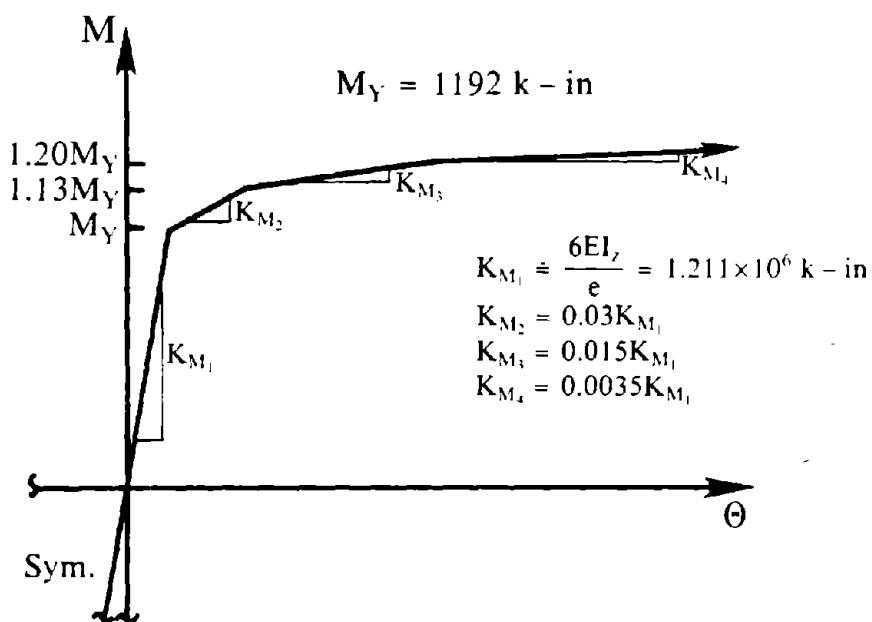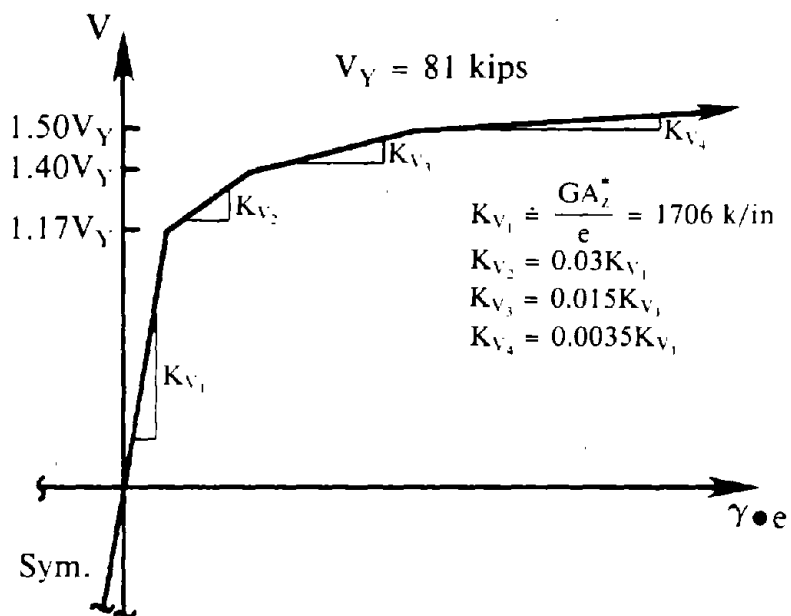
Fig. 6.23   Force-Deformation Relationships for (a) Shear, and
(b) Moment to Model Composite Links in Interior EBFs.
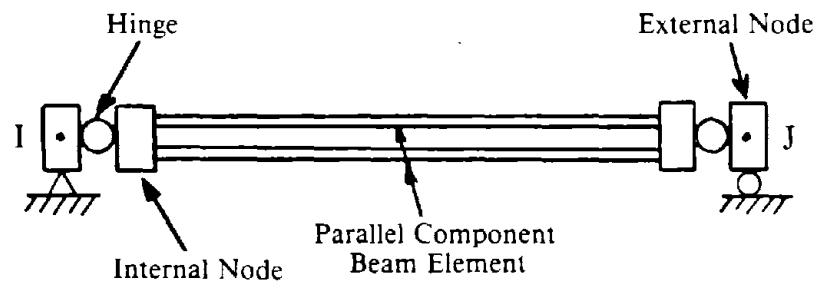
Fig. 6.24   Composite Beam-Column Element Components.
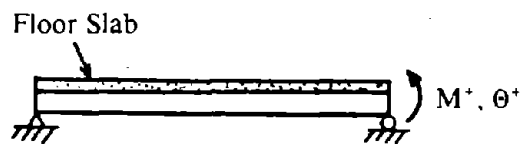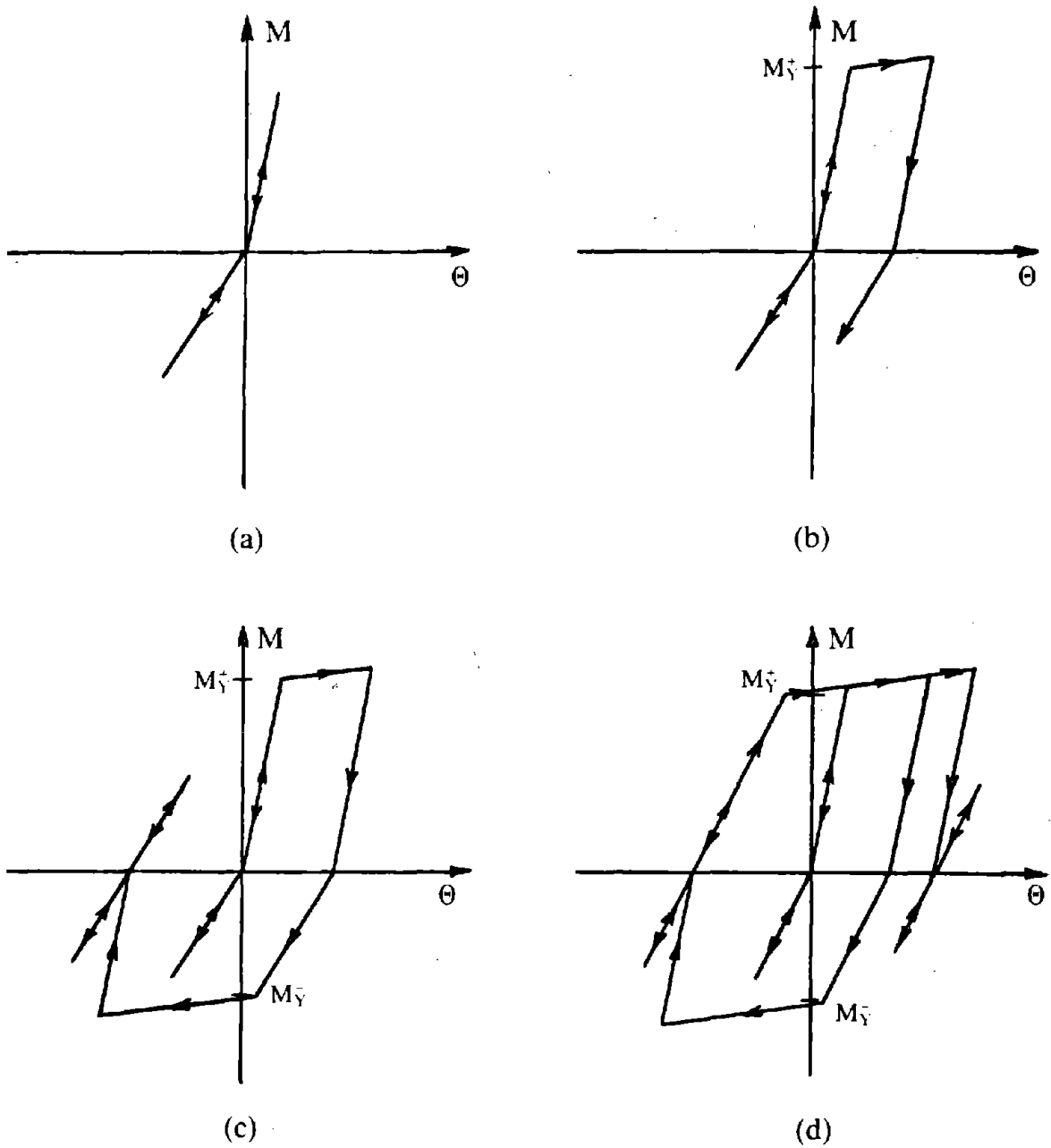
Fig. 6.25   Hysteretic Behavior of Composite Beam-Column Element.
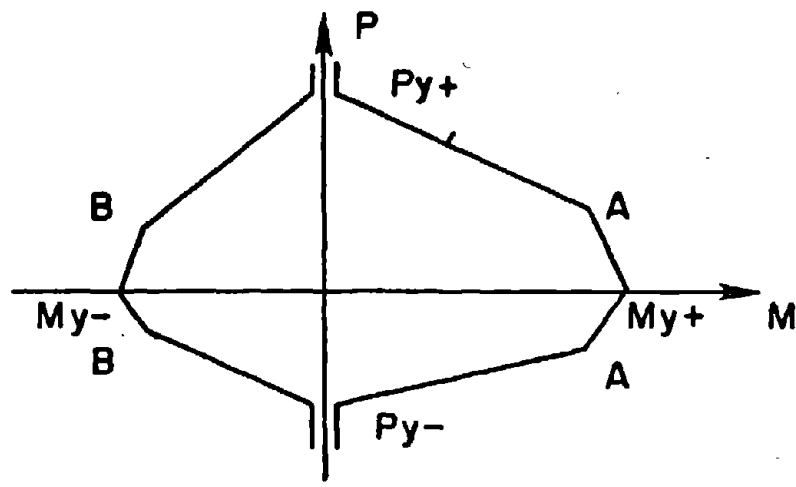
Fig. 6.26   Yield Interaction Surface [81].

(a)
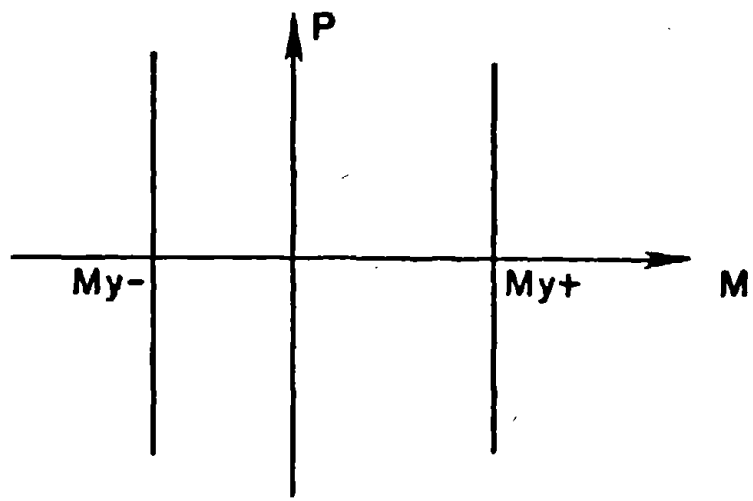
Fig. 6.28   Yield Surface, Ignoring Effect of Axial Load [81].
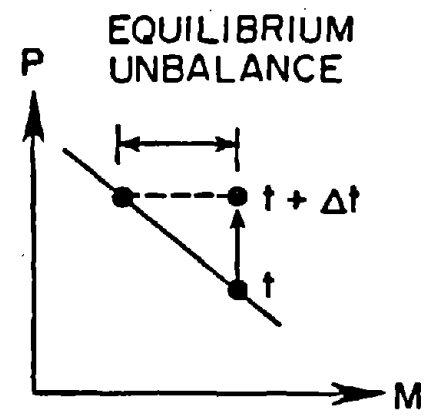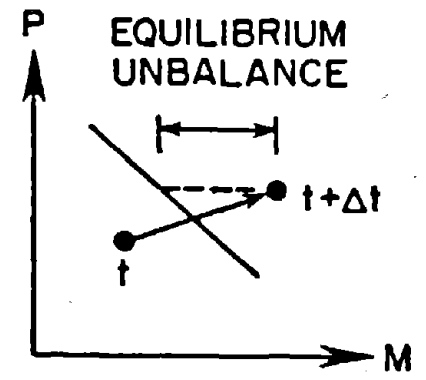
(b)

Fig. 6.27   Equilibrium Correction for Yield Surface
Overshoot [81].
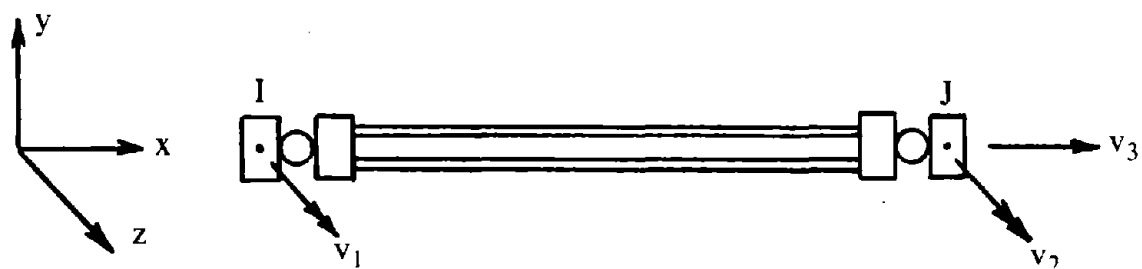
Fig. 6.29   Deformation Degrees of Freedom, Composite Beam-Column Element.
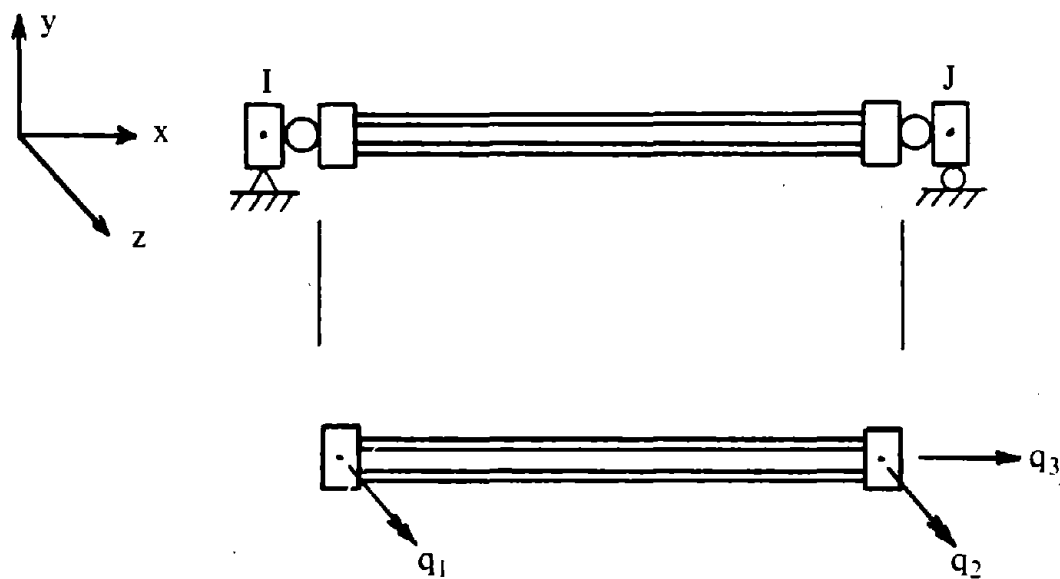
Fig. 6.30   Parallel Component Beam Element Deformation Degrees of Freedom.

$K^+:$

$M_a = M$ ⤸ Θ_a Θ_b ⤸ $M_b = 5M$

$K^-:$

$M_a = -M$ ⤸ Θ_a Θ_b ⤸ $M_b = -5M$
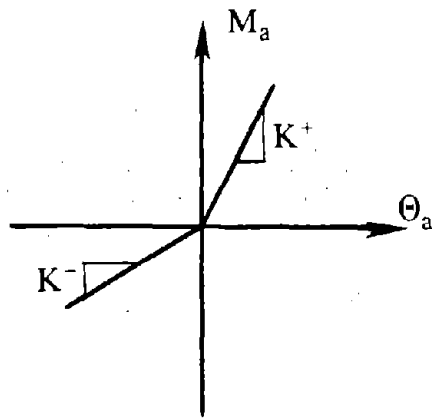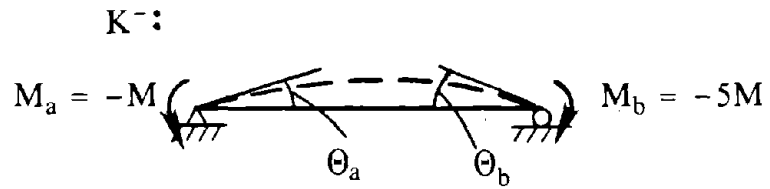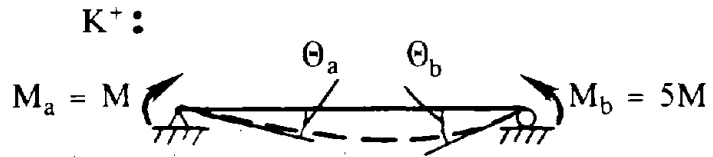
(a) Adjacent to Column
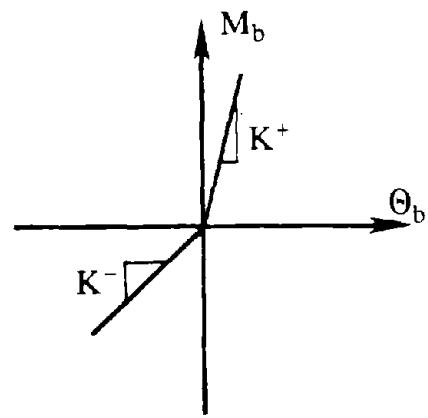
(b) Adjacent to Link.

Fig. 6.31   Determining Elastic Bilinear Moment-Rotation Relationship.

1) $\underline{K}_{eff}\ d\underline{r}\ =\ \underline{R}^U$

2) $\underline{R}^U\ =\ \underline{R}^E\ -\ \underline{R}^I$

3) $\underline{r}\ =\ \underline{r}\ +\ d\underline{r}$

—No——— 4) $\|\underline{R}^U\|\ <\ tol$

|
YES
↓

5) STOP
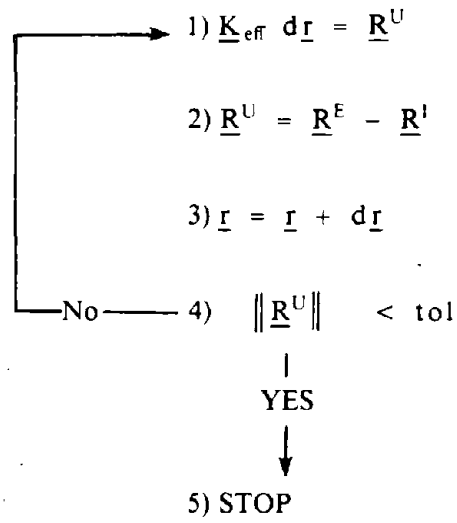
Fig. 6.32 Computing Global Displacements for a Nonlinear Statics Problem.

(a) Modified Newton-Raphson

(b) Newton-Raphson

(c) Combination of (a) and (b)
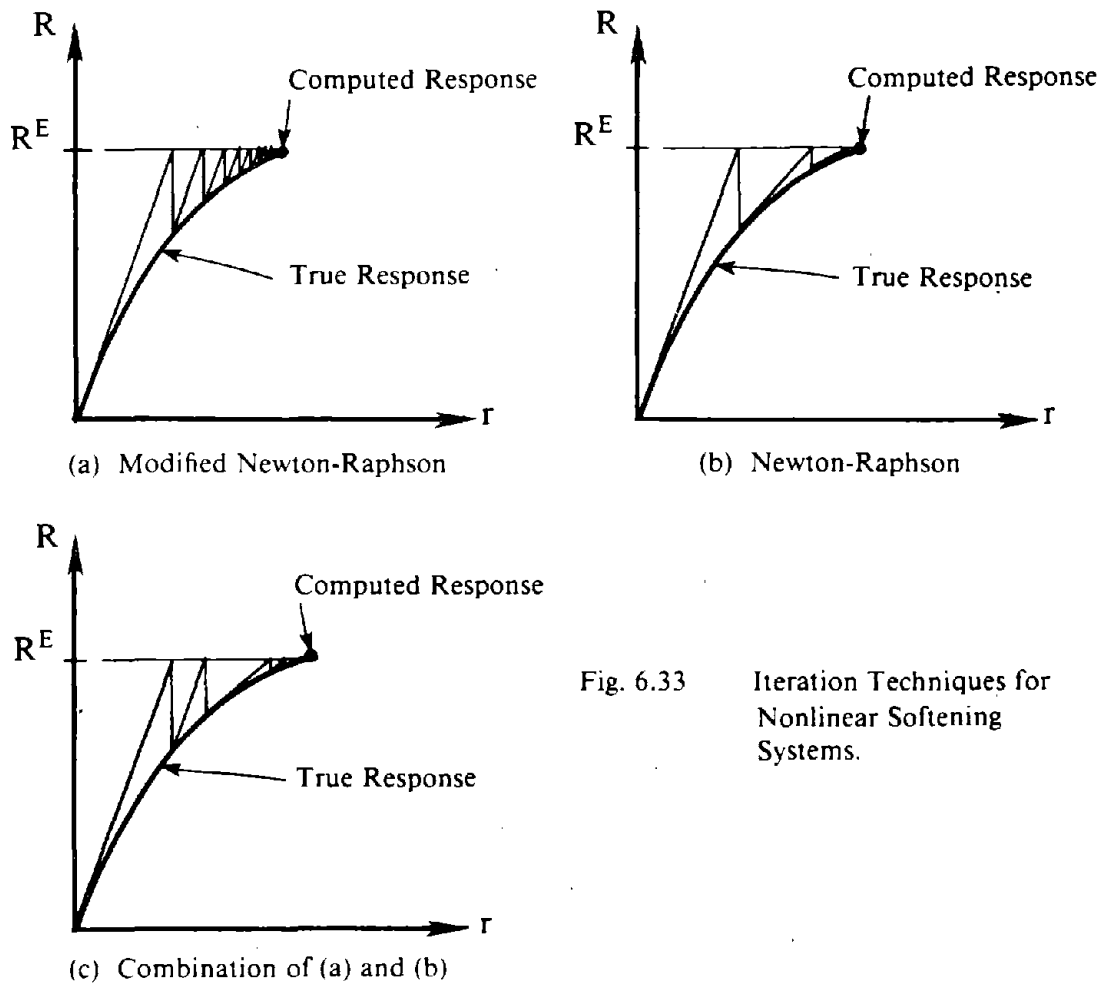
Fig. 6.33 Iteration Techniques for Nonlinear Softening Systems.
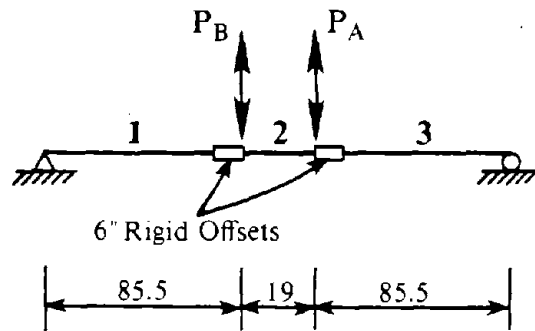
Elements 1 , 3 : Standard ANSR-1 Beam-Column Element
- Strain Hardening Proportion, $\rho = 0.015$
- A = 5.72 in^2
- A_z^* = 2.88 in^2
- I = 128.1 in^4
- E = 28783 ksi
- ν = 0.33
- M_y = 1192 k-in
- P_y = 284 kip

Element 2 : Link Element
- A = 5.72 in^2
- A_z^* = 2.88 in^2
- I = 128.1 in^4
- E = 28783 ksi
- ν = 0.33
- Action-Deformation Relationship from Fig. 6.21.
- Isotropic Hardening Coefficient, a = 8.336

$$\Delta V_{max} = 2.68 \ V_{yo}$$

Fig. 6.34   Modeling of Specimen D1.
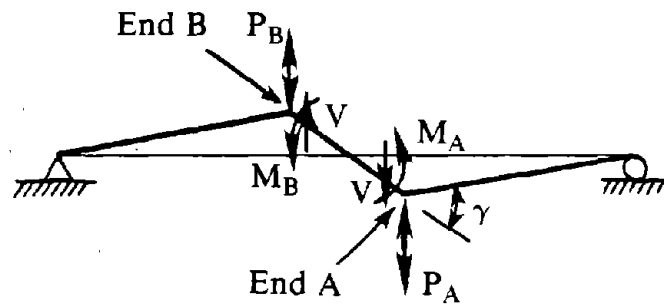
Fig. 6.35   Positive Sign Convention for Link Response.
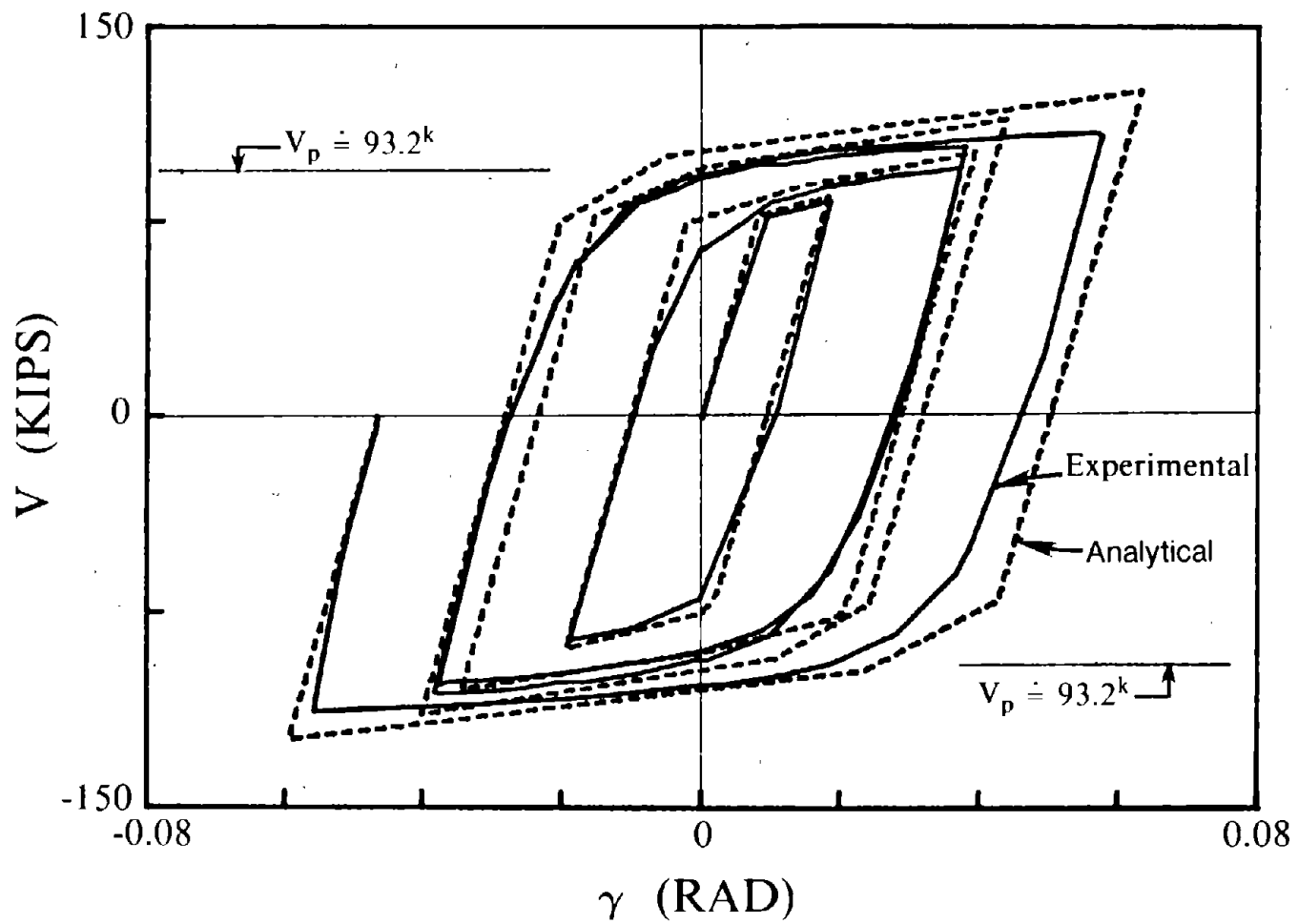
Fig. 6.36   Shear-Deformation Response of Link, Specimen D1.
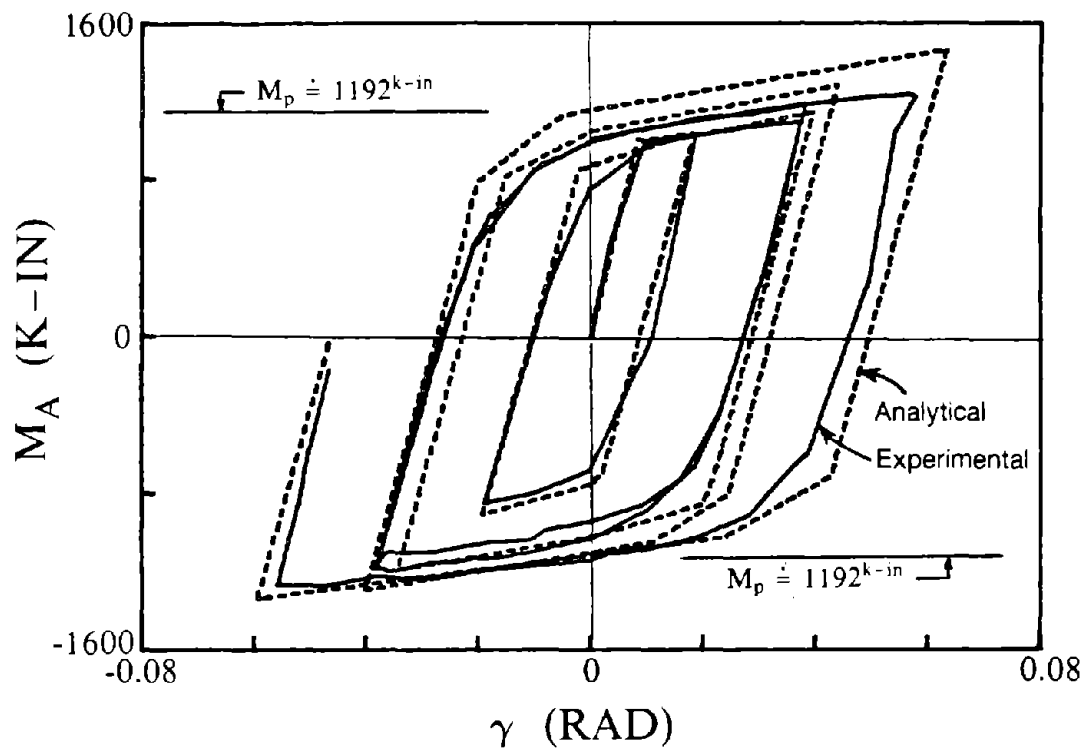
(a)
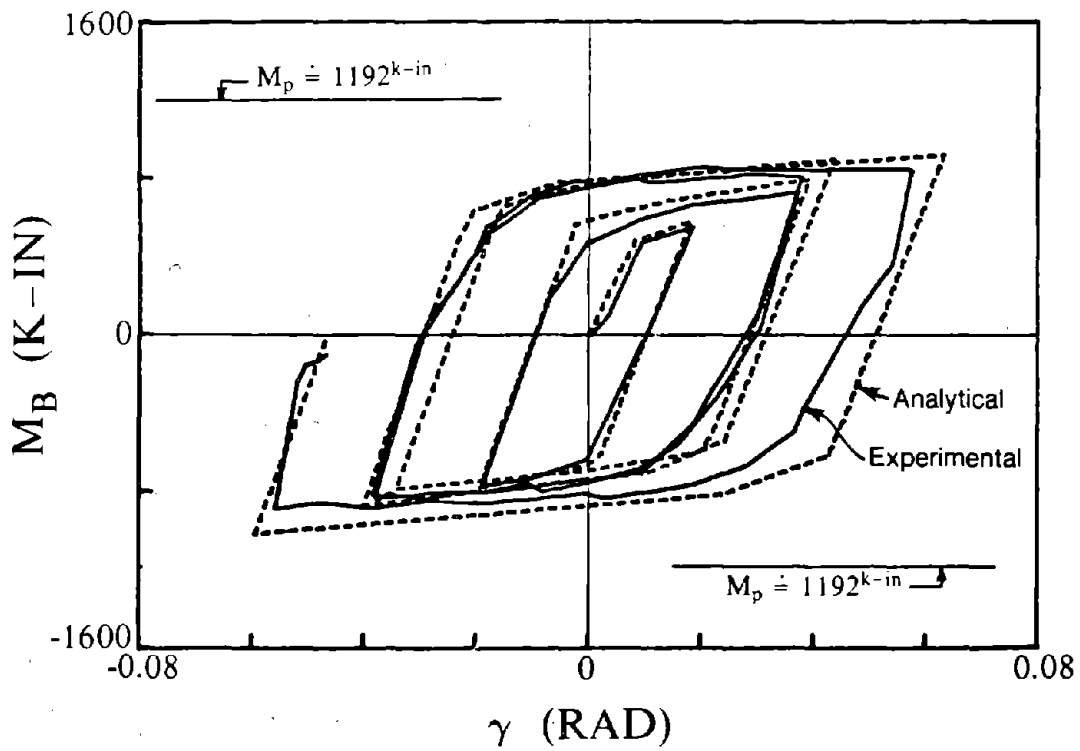
(b)

Fig. 6.37   Moment-Deformation Response of Link, Specimen D1.

P_B P_A

6" Rigid Offsets

| 85.5" | 19" | 85.5" |
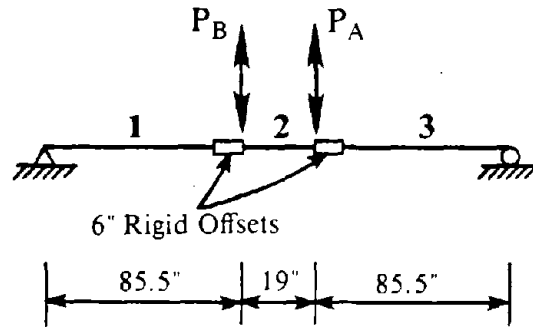
Elements 1 , 3 : Standard Composite Beam-Column Element

- Strain Hardening Proportion, $\rho = 0.03$
- $A = 5.72 \ in^2$
- $A_z^{\bullet} = 2.88 \ in^2$
- $I_{eff} = 333 \ in^4$, where $I_{eff} = 2.61$ [Fig. 4.65]
- $E = 28783 \ ksi$
- $\nu = 0.33$
- $b_{eff}^{\sigma} = 48 \ in$, [Fig. 4.56]

  - $M_y^{+} = 2451 \ k-in$

  - $M_y^{-} = 1192 \ k-in$

  - $P_y^{+} = 284 \ kip$

  - $P_y^{-} = 939 \ kip$

- K^{-} based on Fig. 4.60, $K_s = 2.644 \times 10^5 \ kip-in$

Element 2 : Link Element

- $A = 5.72 \ in^2$
- $A_z^{\bullet} = 2.88 \ in^2$
- $I = 128.1 \ in^4$
- $E = 28783 \ ksi$
- $\nu = 0.33$
- Action-Deformation Relationship from Fig. 6.23.

- Isotropic Hardening Coefficient. $a = 5.668$

$$\Delta V_{max} = 2.38 \ V_{yu}$$

Fig. 6.38   Modeling of Specimen B1.
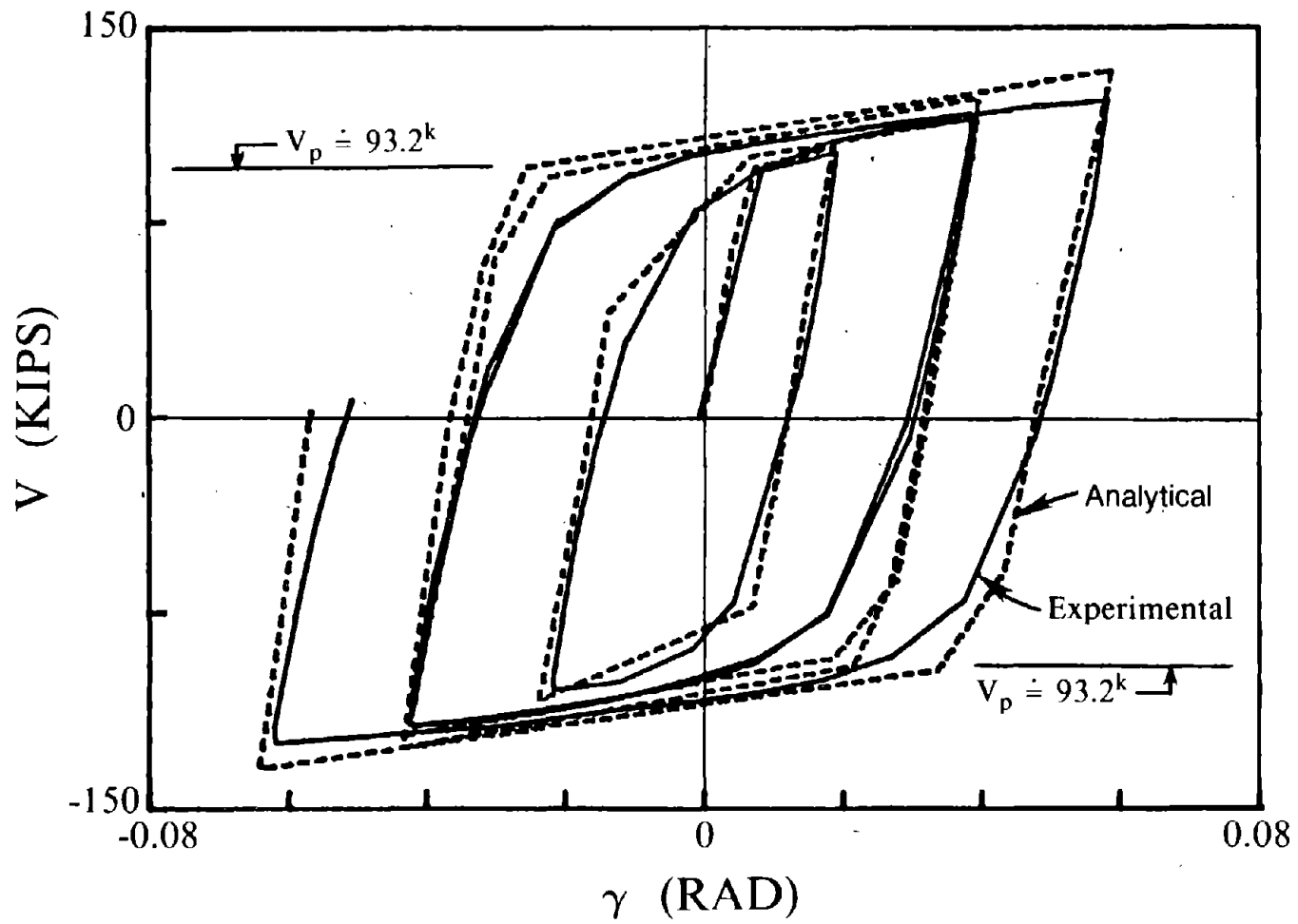
Fig. 6.39   Shear-Deformation Response of Link, Specimen B1.

188
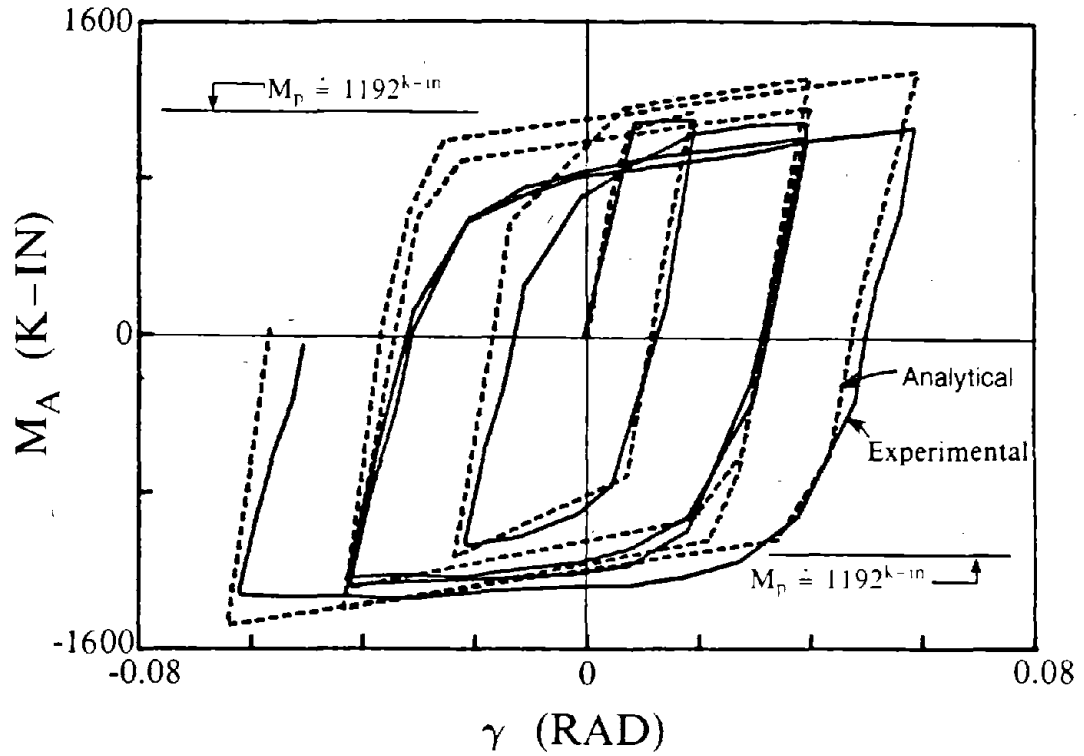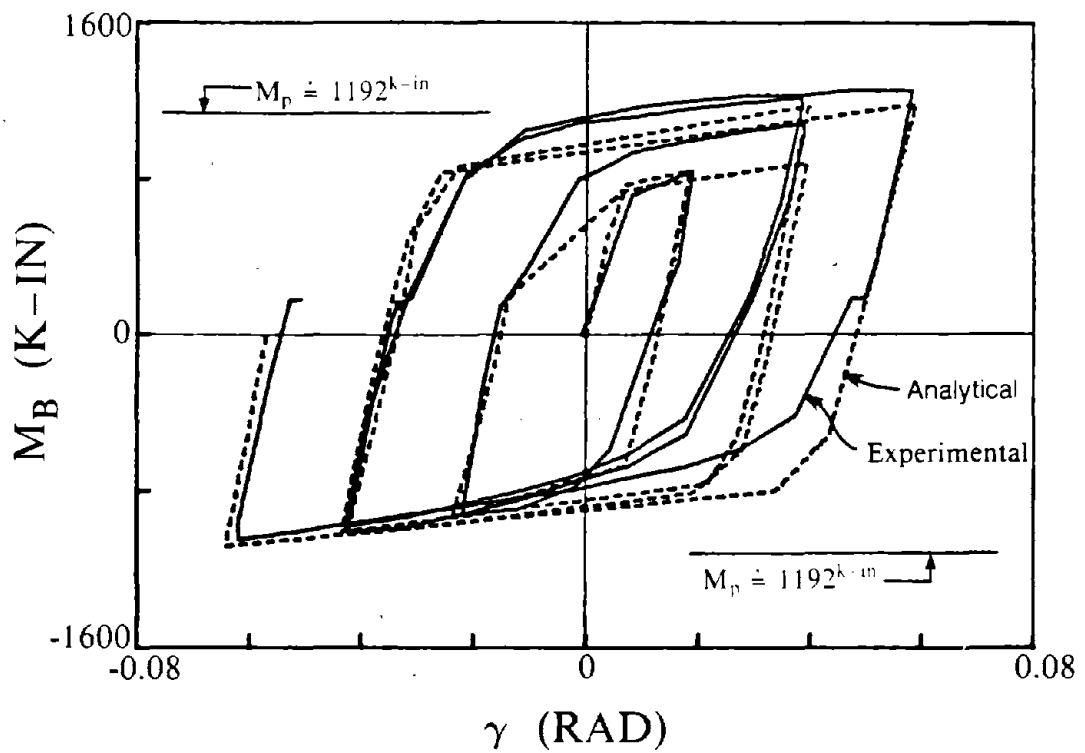
Fig. 6.40   Moment-Deformation Response of Link. Specimen B1.
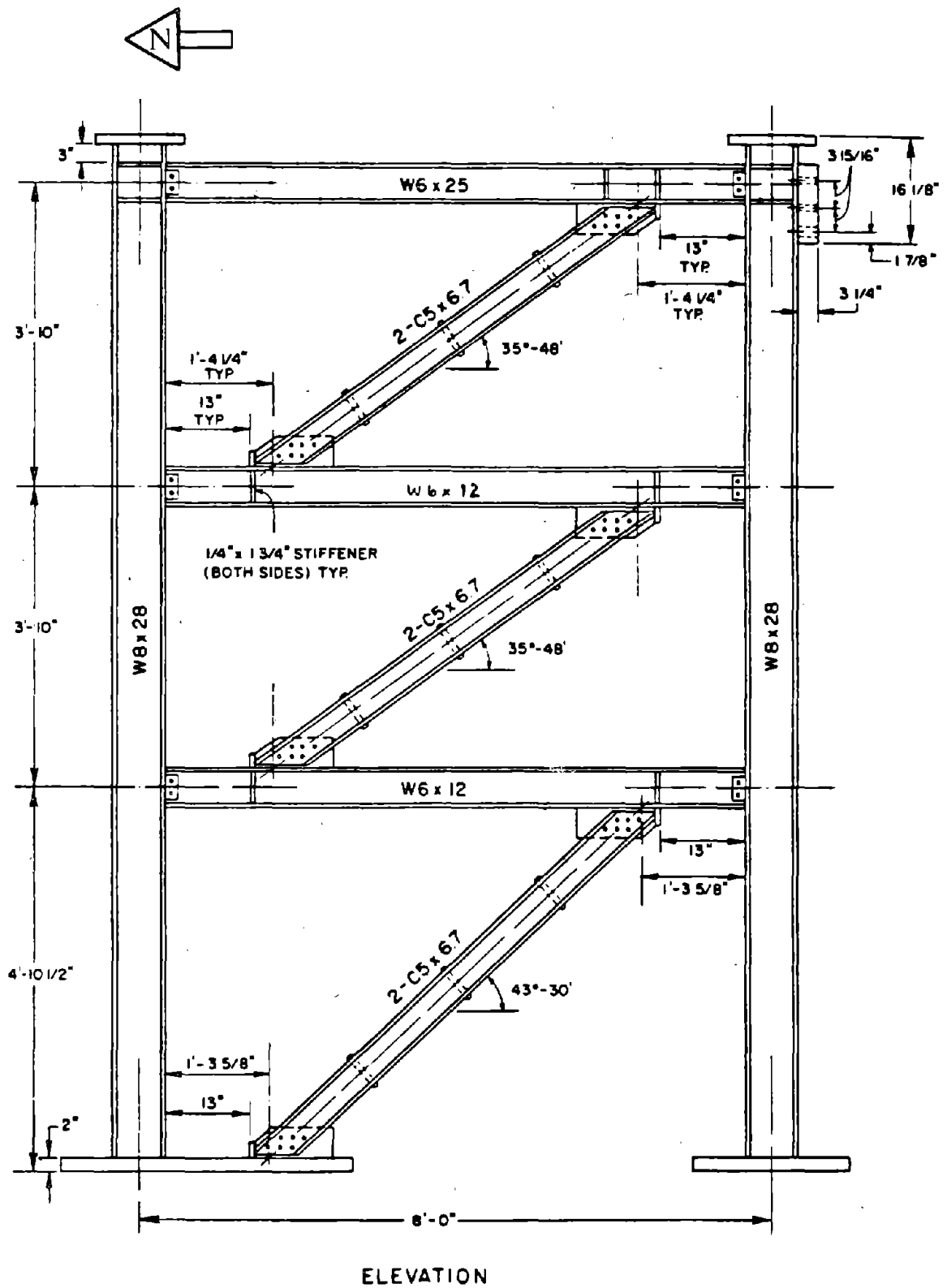
Fig. 6.41　　General Design of Test Frame 2 [6].
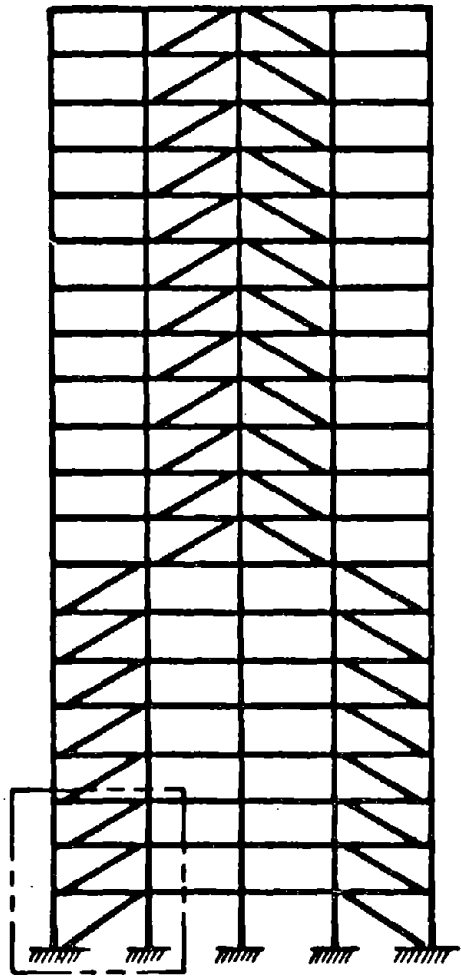
(a) LOCATION OF TEST FRAME   (b) FREEBODY OF TEST FRAME
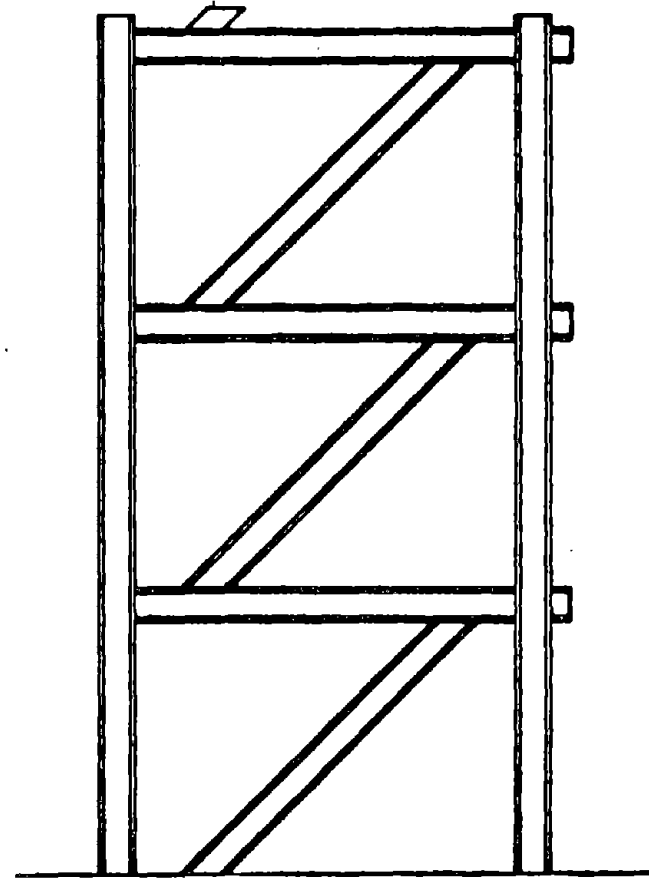
Fig. 6.42   Location and Free Body of the Test Frame [6].
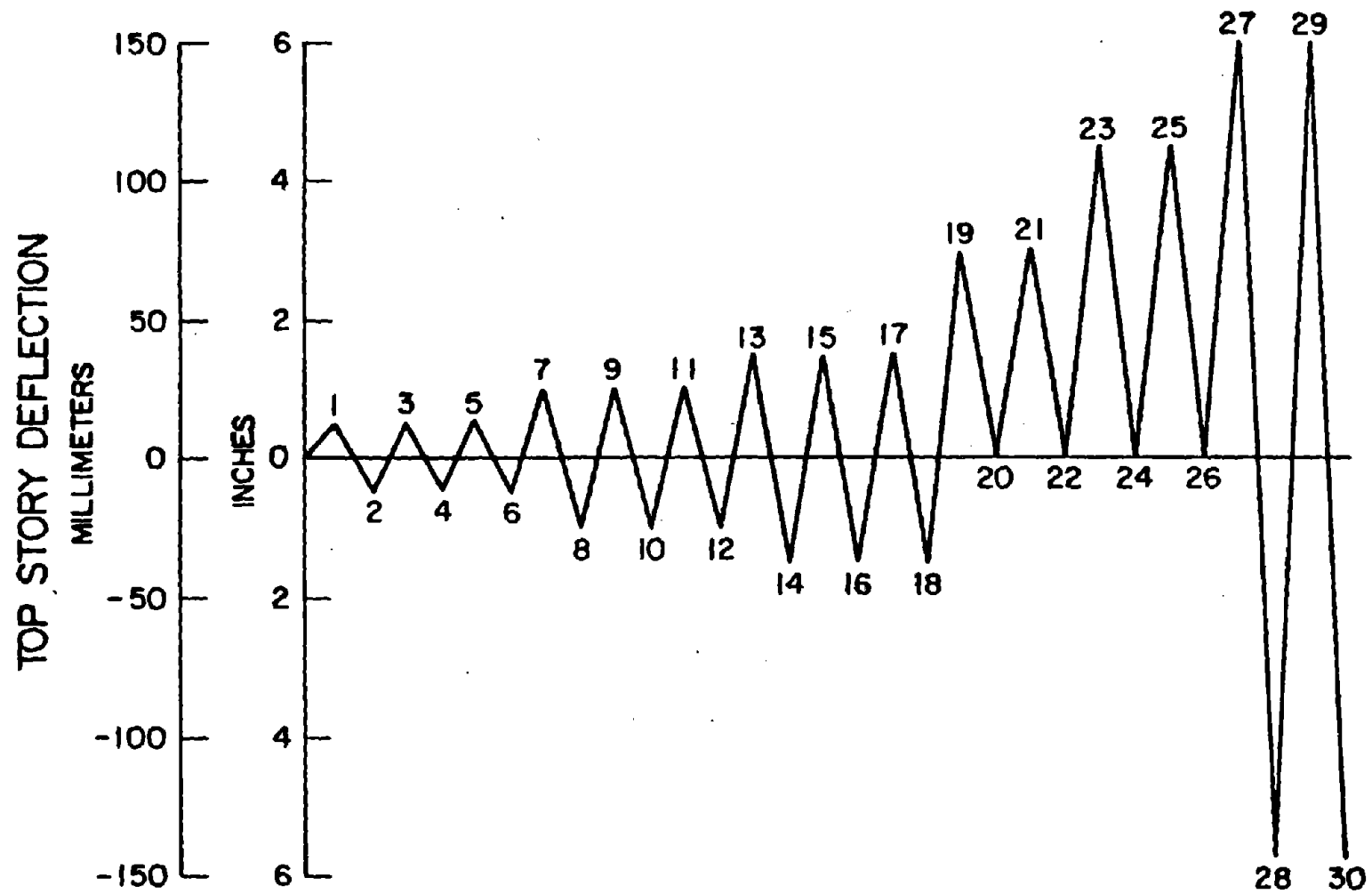
Fig. 6.43   Load Program for the Inelastic Cycles of Testing [6].
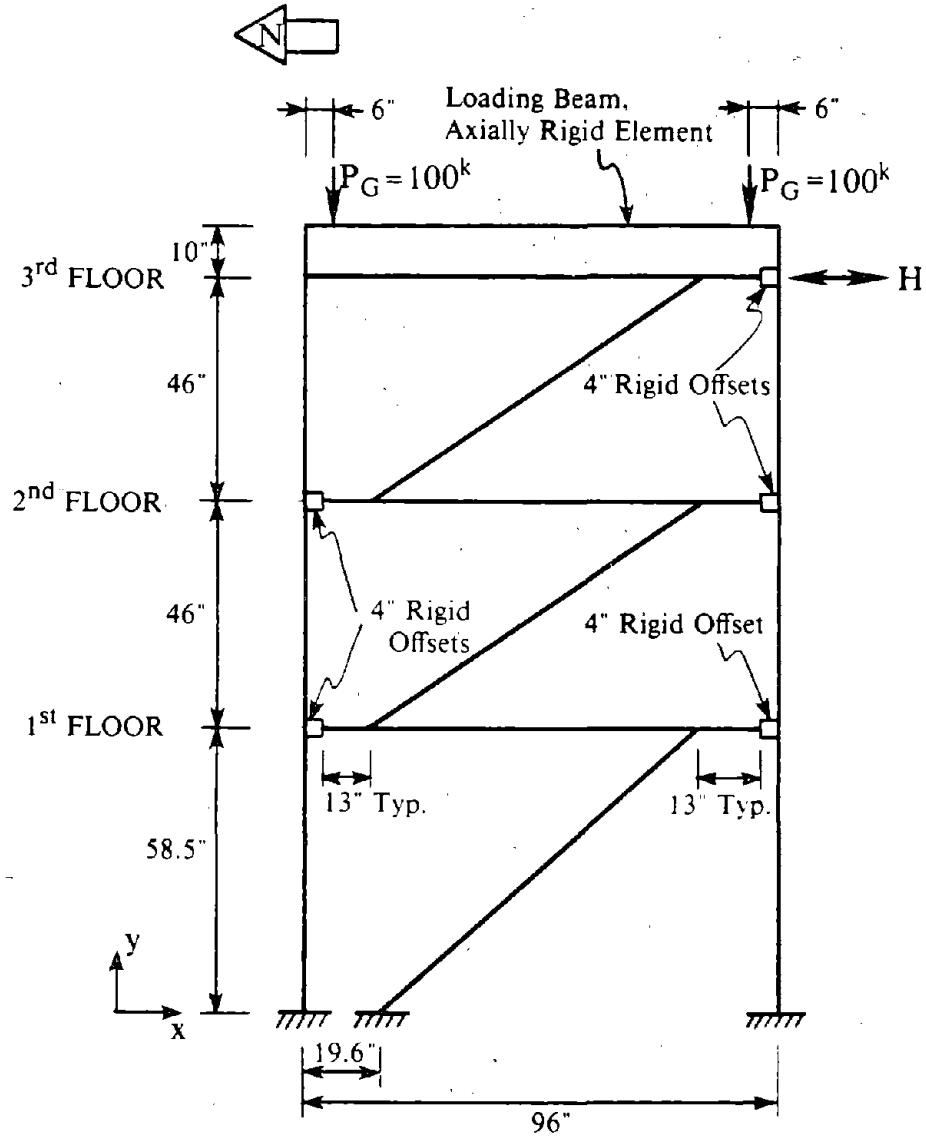
Fig. 6.44   Schematic of Analysis Model.
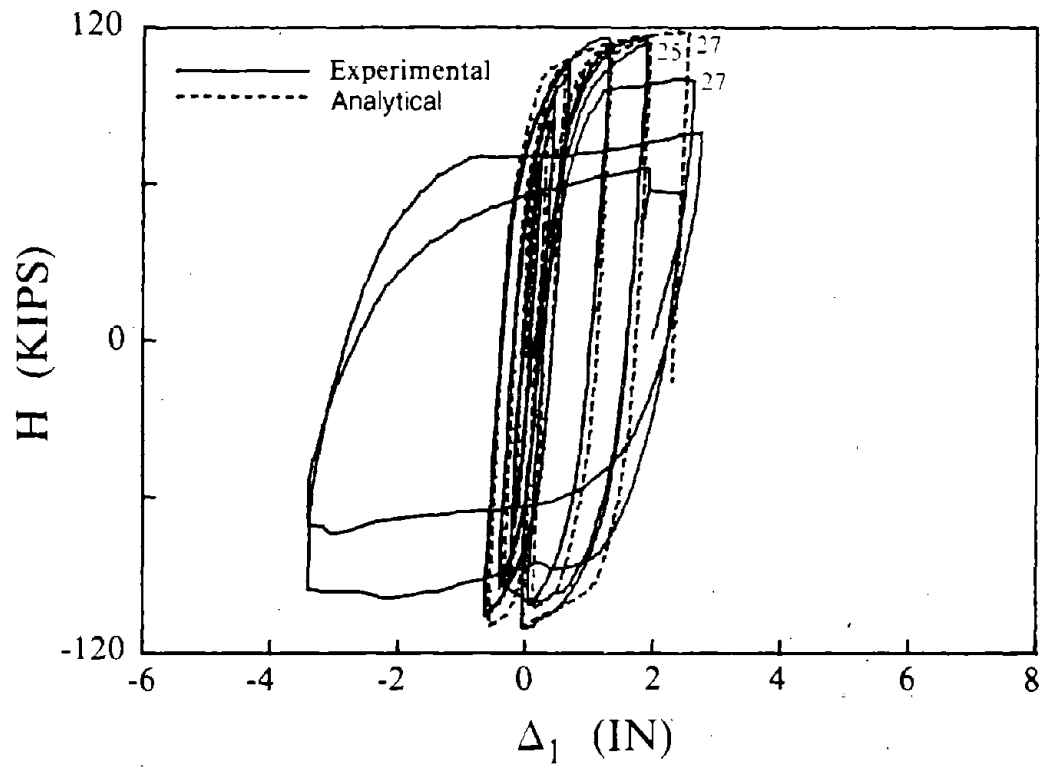
Fig. 6.45   Lateral Load - First Floor Deflection Hysteretic Behavior.
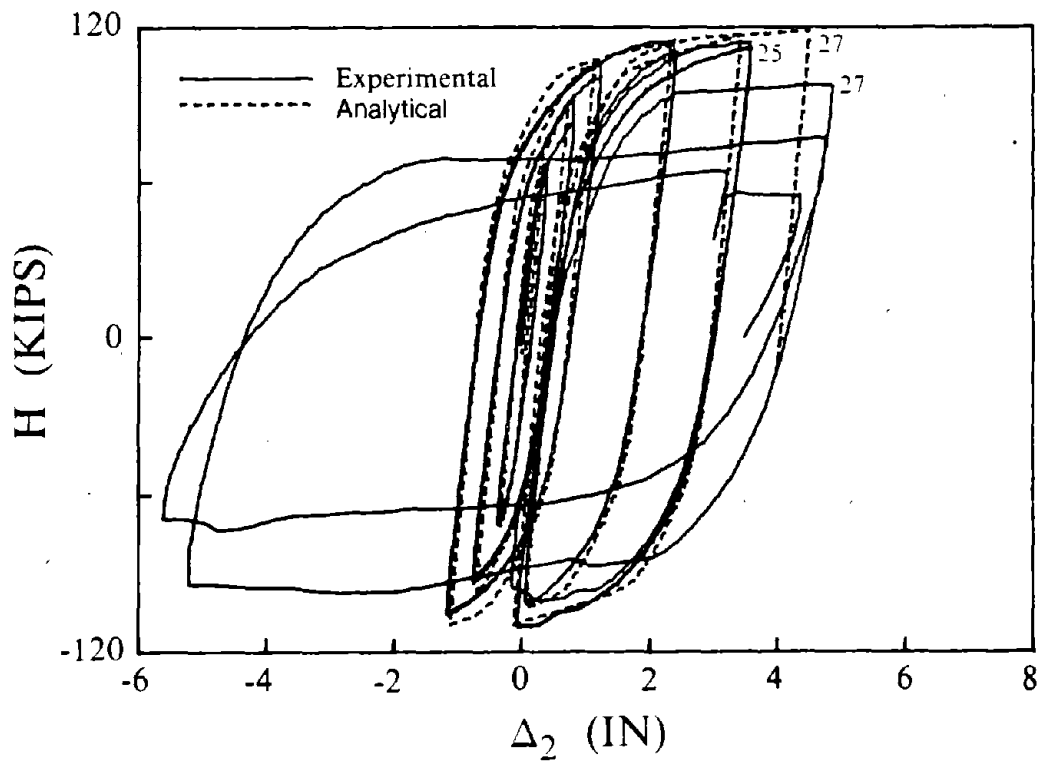
Fig. 6.46   Lateral Load - Second Floor Deflection Hysteretic Behavior.
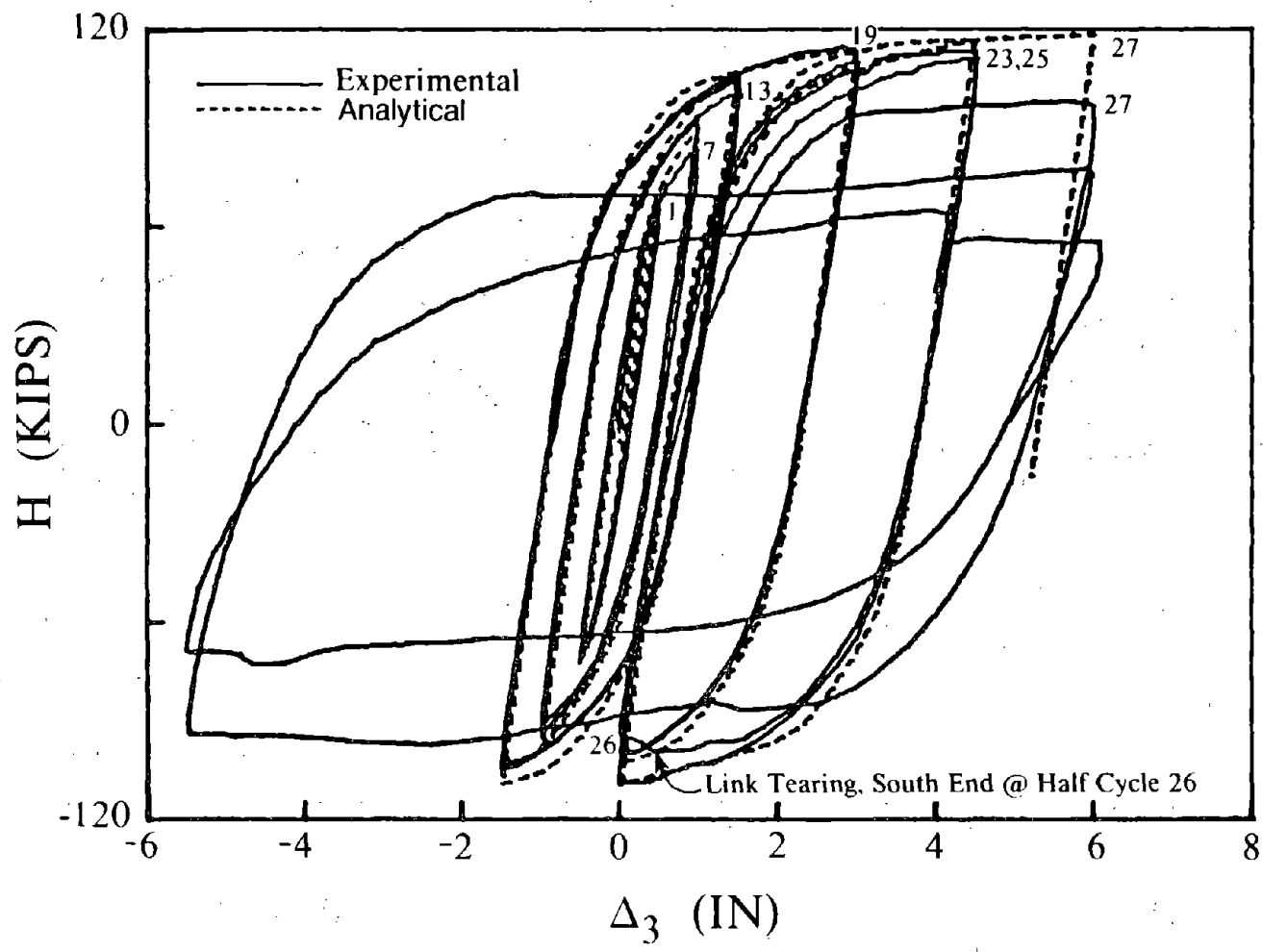
Fig. 6.47   Lateral Load - Third Floor Deflection Hysteretic Behavior.
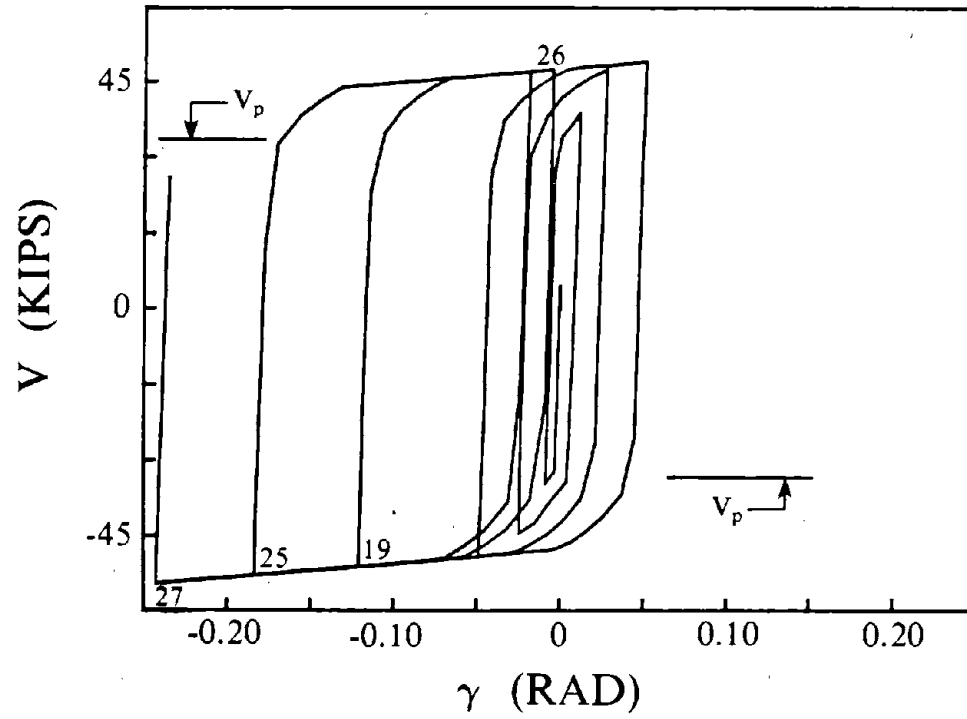
(a) South Link
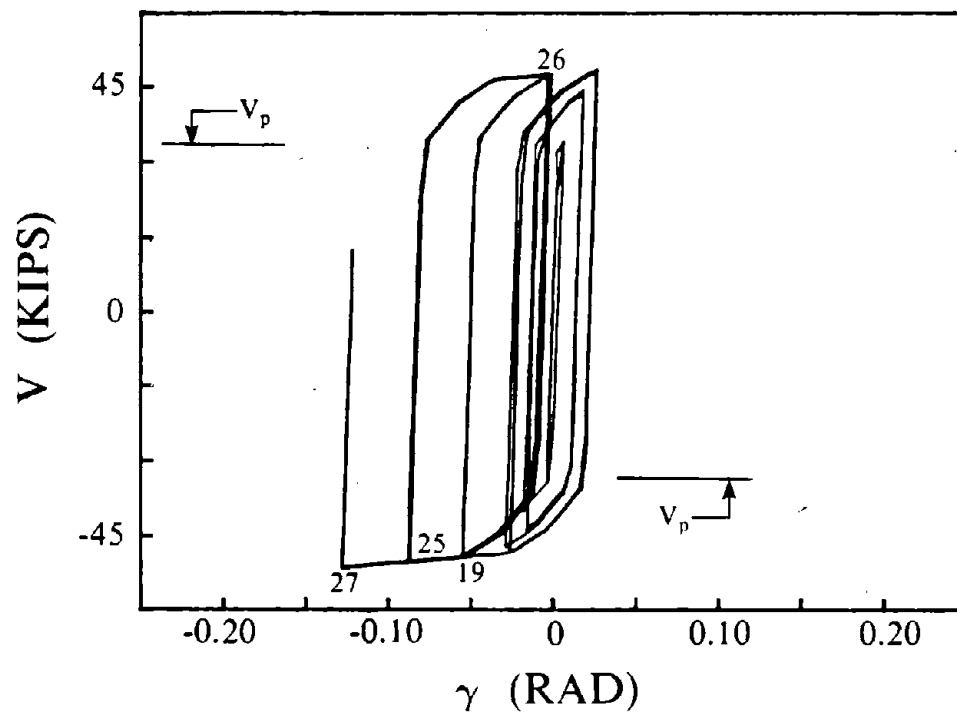
(b) North Link

Fig. 6.48   Hysteretic Response of Model, First Floor Links.
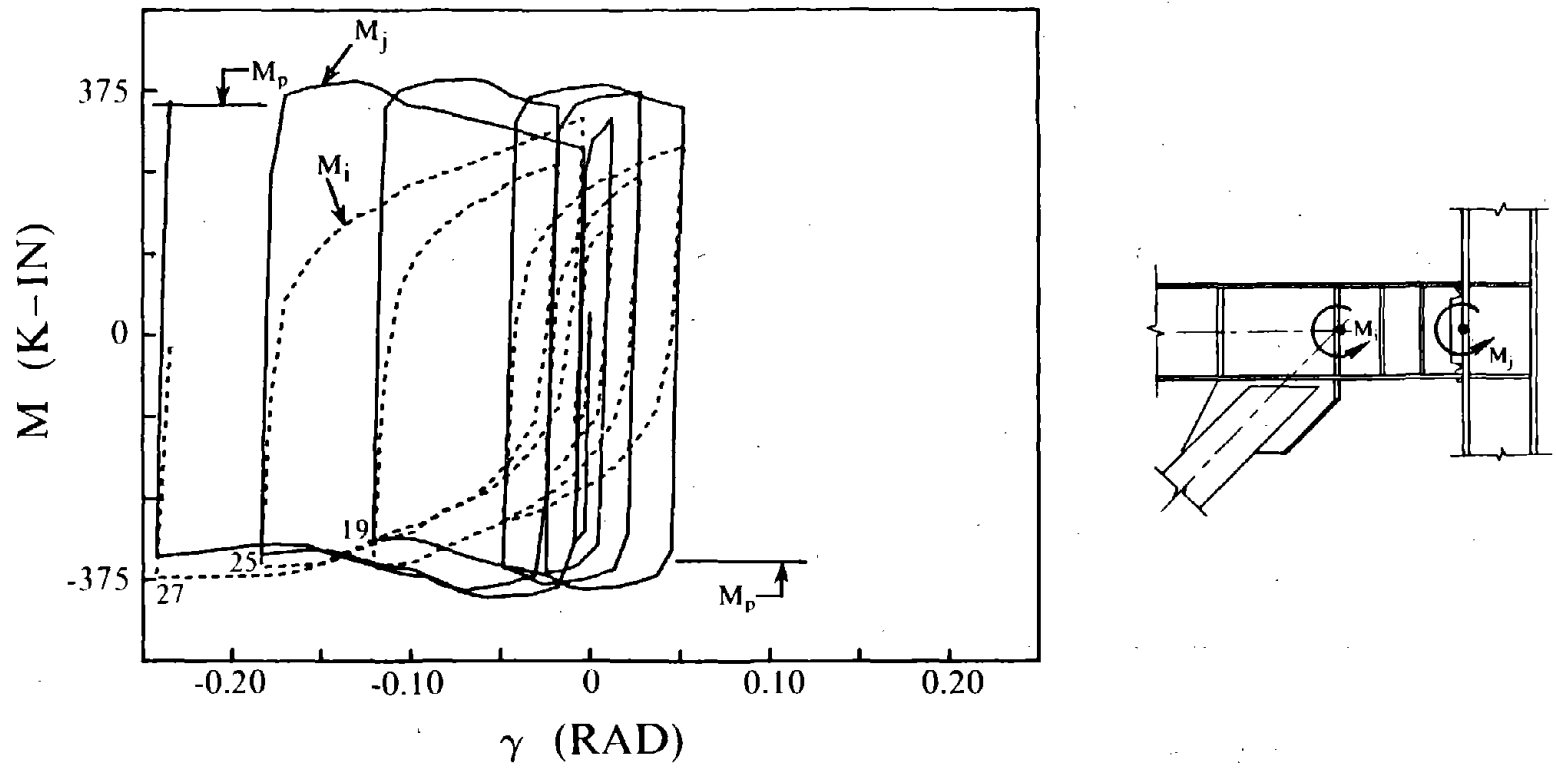
Fig. 6.49   Moment-Deformation Response of Model's First Floor South Link.
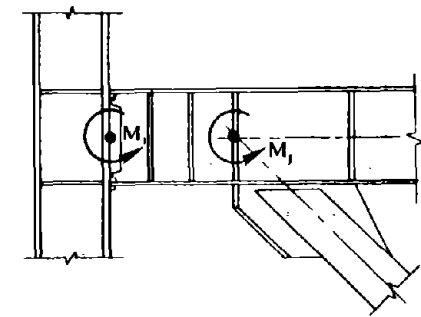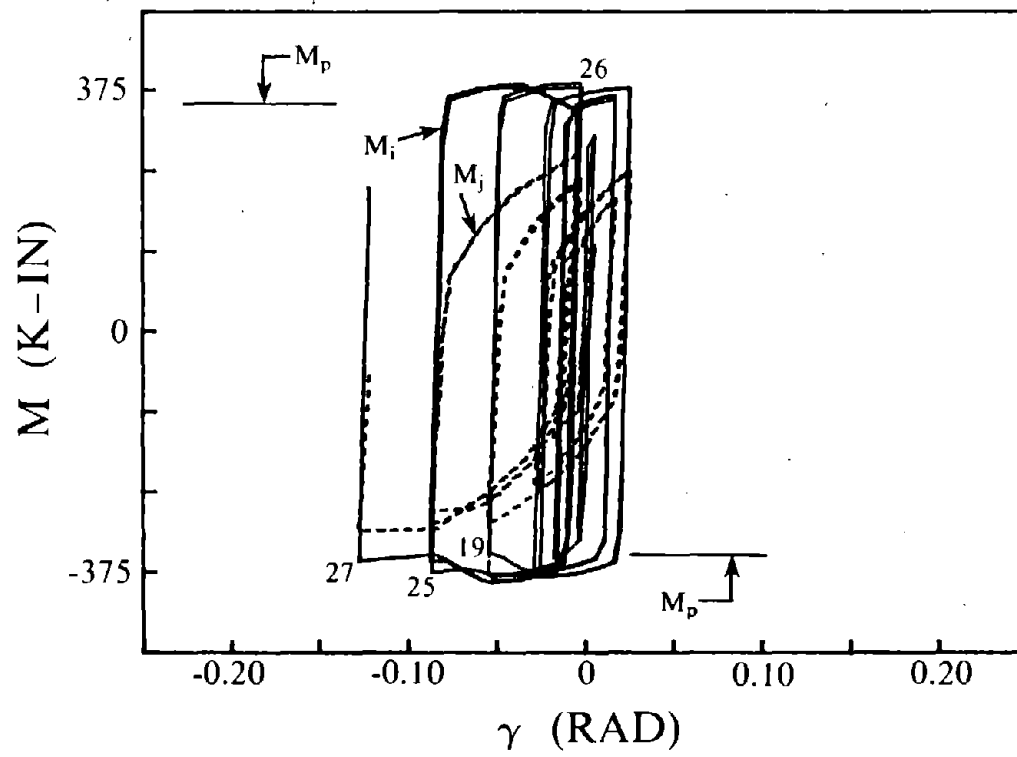
Fig. 6.50   Moment-Deformation Response of Model's First Floor North Link.

198
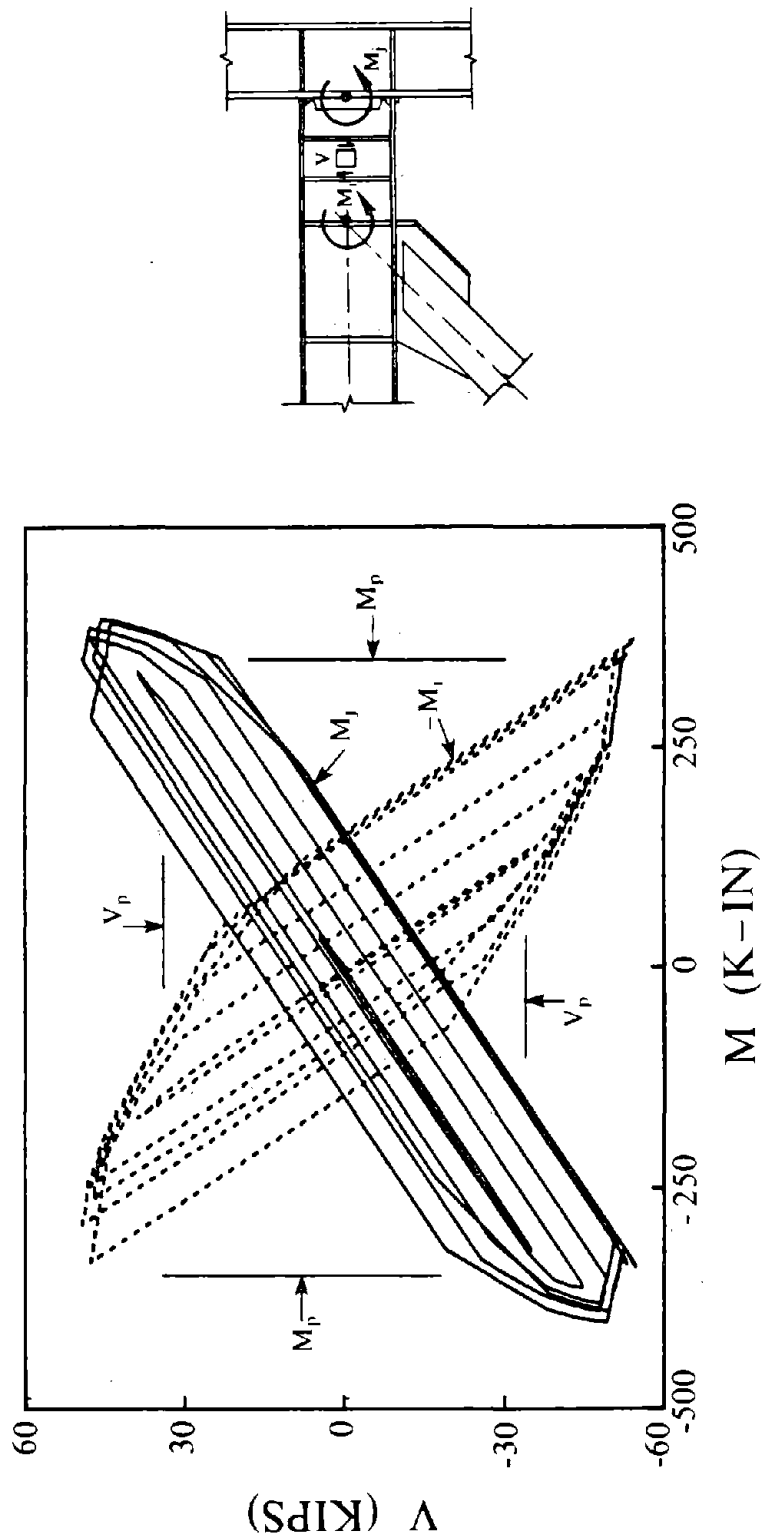
Fig. 6.51   Moment-Shear Behavior of Model's First Floor South Link.
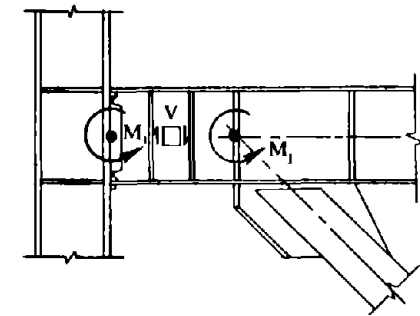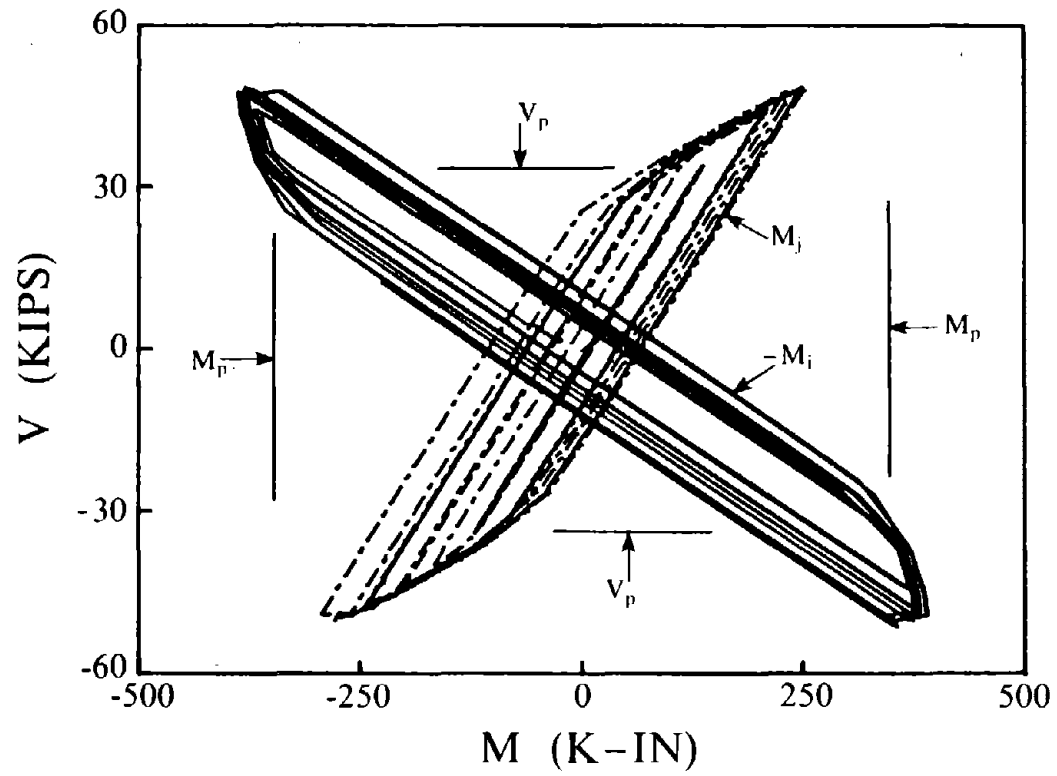
Fig. 6.52   Moment-Shear Behavior of Model's First Floor North Link.
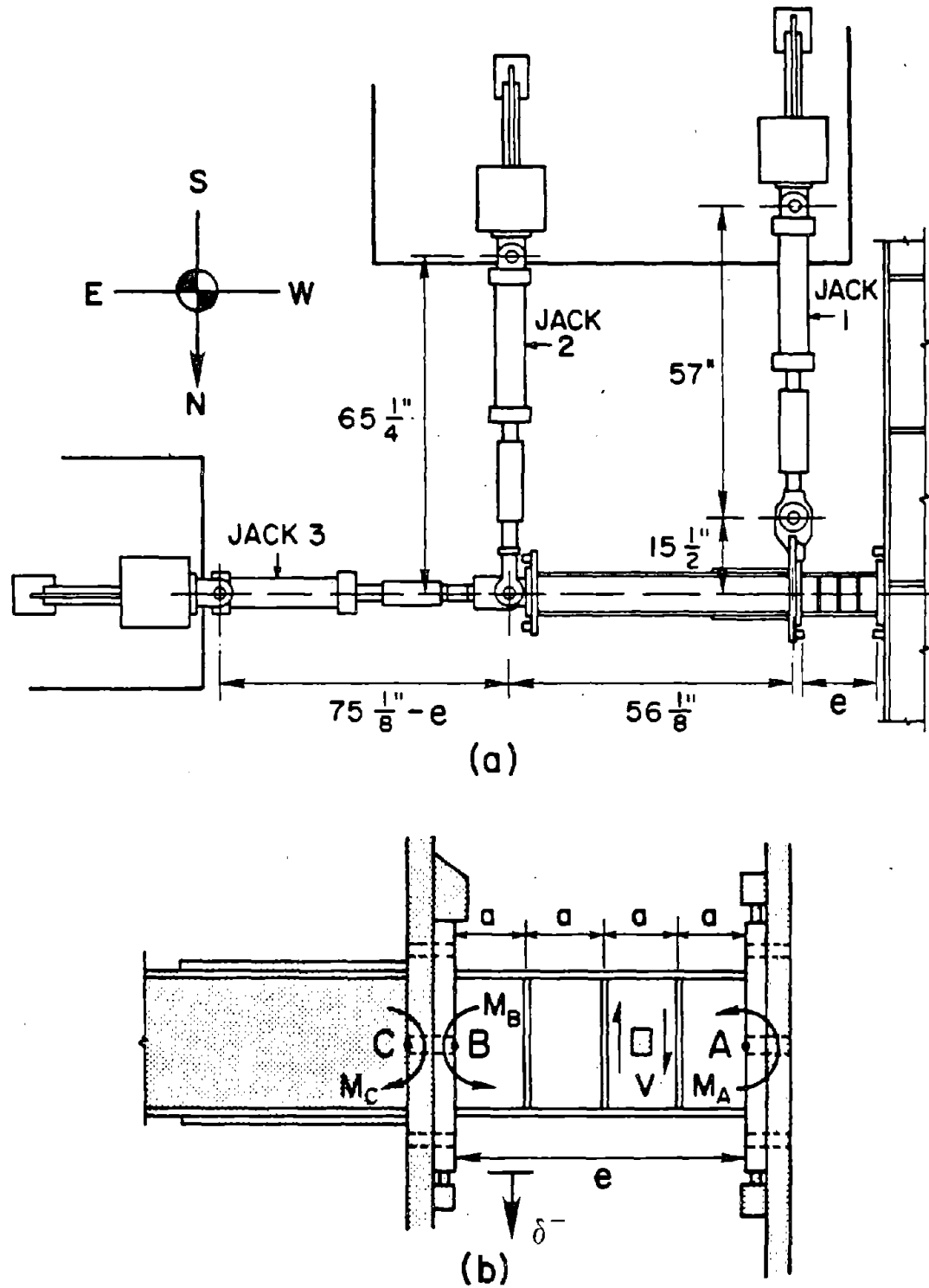
Fig. 6.53   Experimental Setup for Testing of Links by Kasai [7].
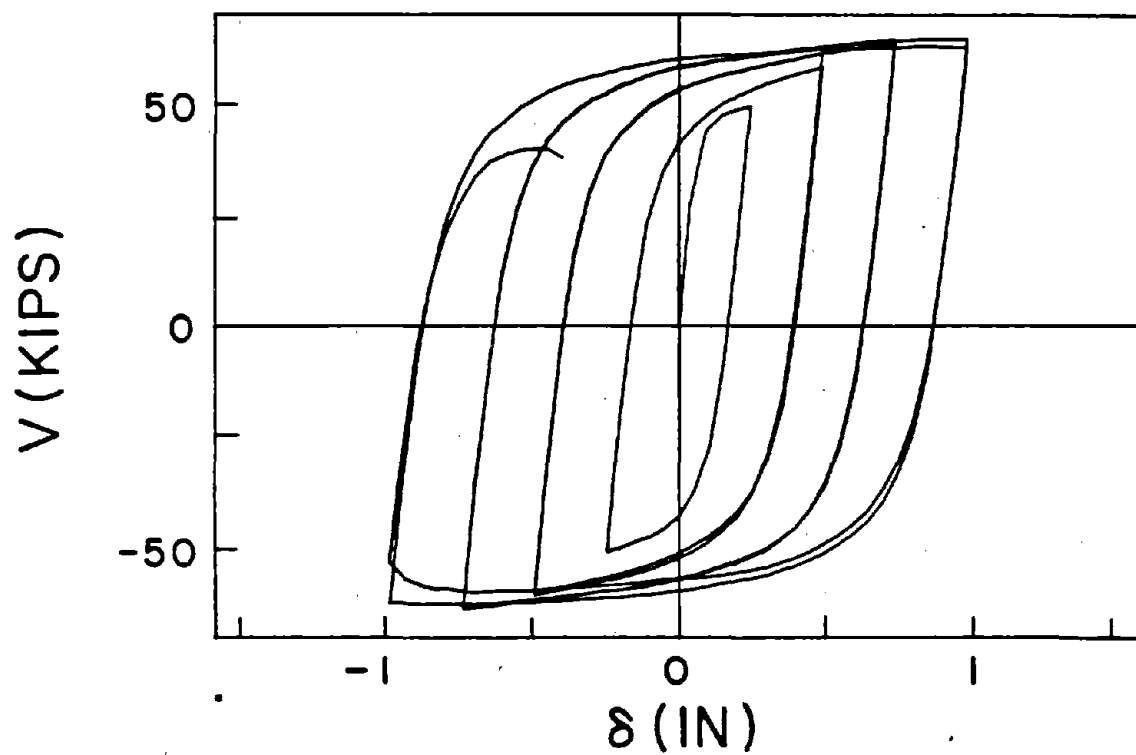
Fig. 6.54   Shear-Displacement Relationship of Specimen 7, After Kasai [7].
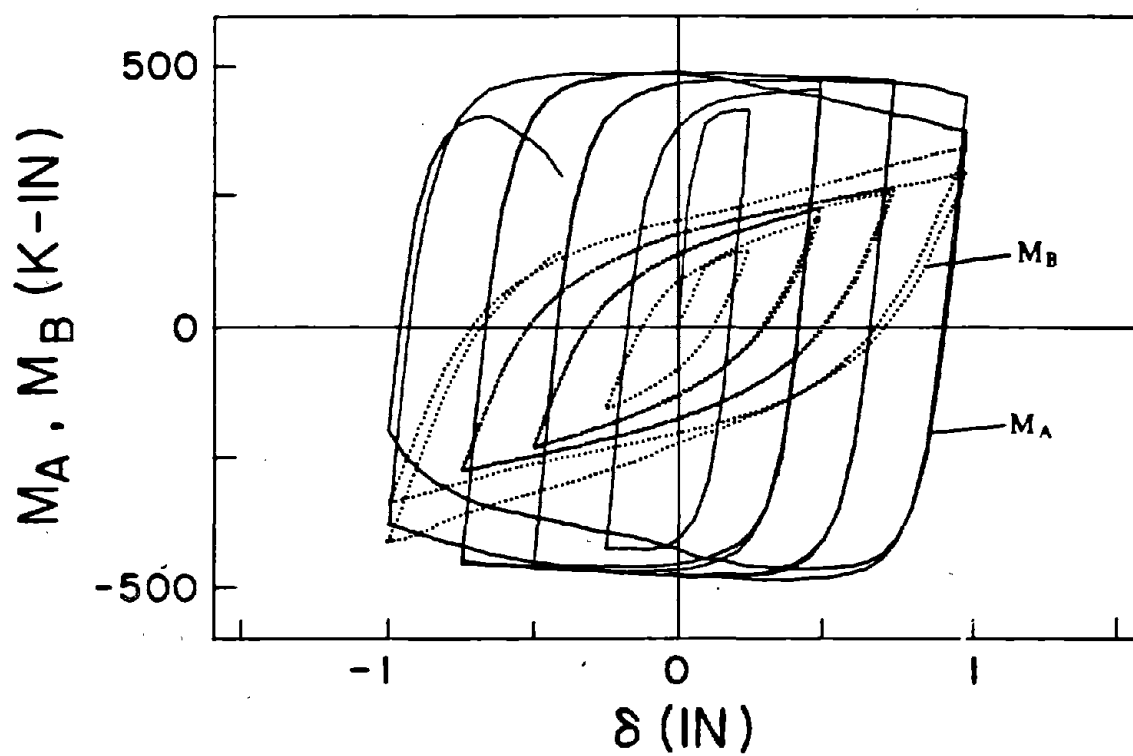
Fig. 6.55   Moment-Displacement Relationship of Specimen 7, After Kasai [7].
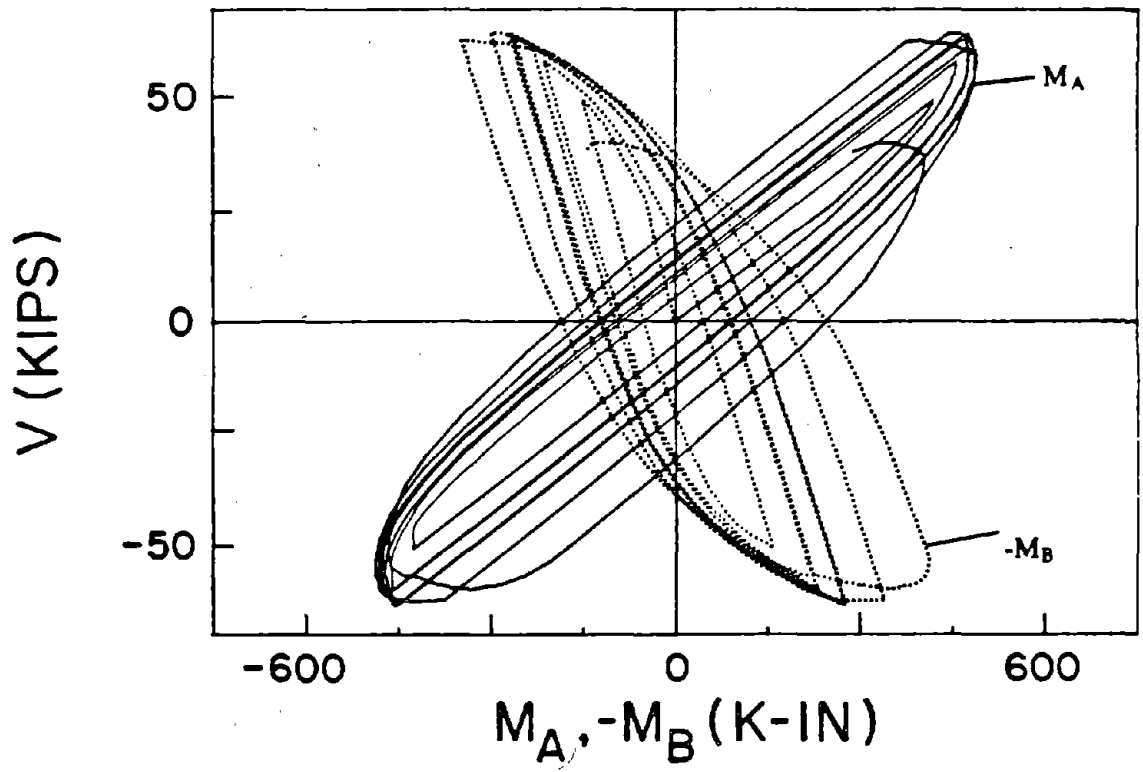
Fig. 6.56   Moment-Shear Relationship of Specimen 7, After Kasai [7].
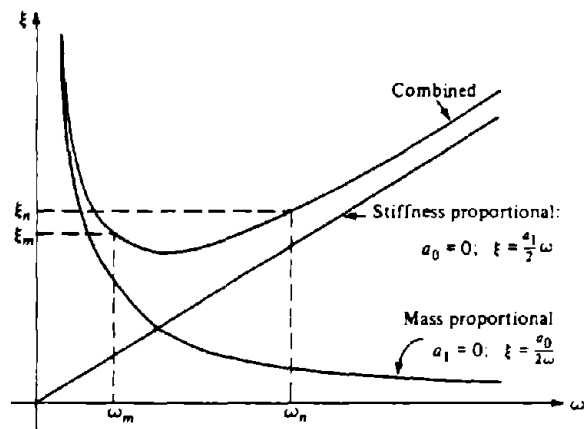
Fig. 7.1   Relationship Between Damping Ratio and Frequency [99].
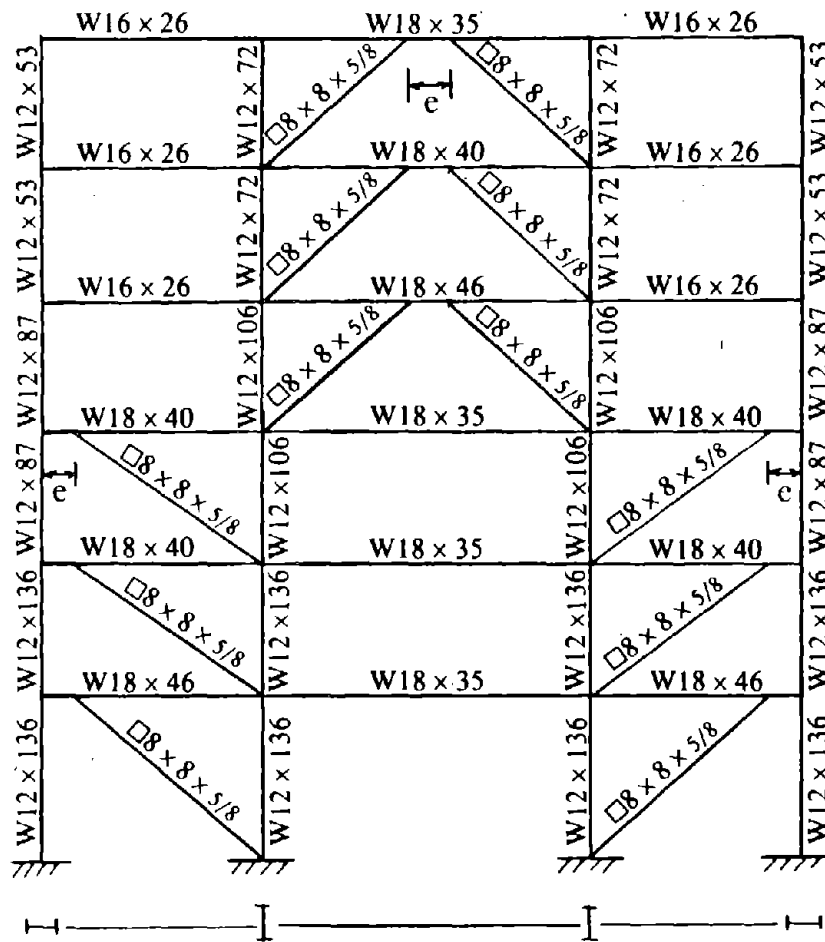
Floor	e	$\dfrac{V_p}{V_{LINK}}$	$\dfrac{e \cdot V_p}{M_p}$
Roof	30"	4.04	1.38
5	30"	2.29	1.24
4	30"	1.92	1.24
3	26"	1.47	1.08
2	26"	1.31	1.08
1	26"	1.13	1.08

Note:
- A36 Steel Beams
- A572, Grade 50 Columns
- A441 Structural Steel Tube Braces (F_Y = 46 ksi)
- All Moment Connections

Fig. 7.2   6-Story EBF Analyzed.

Fig. 7.3   Lumped Mass Description for EBF Model.

| | Mass - (kip-sec^2/in) | | |
Floor	m_1	m_2	m_3
Roof	0.135	0.158	0.076
5	0.193	0.186	0.089
4	0.193	0.186	0.089
3	0.095	0.110	0.264
2	0.095	0.110	0.264
1	0.158	0.127	0.303
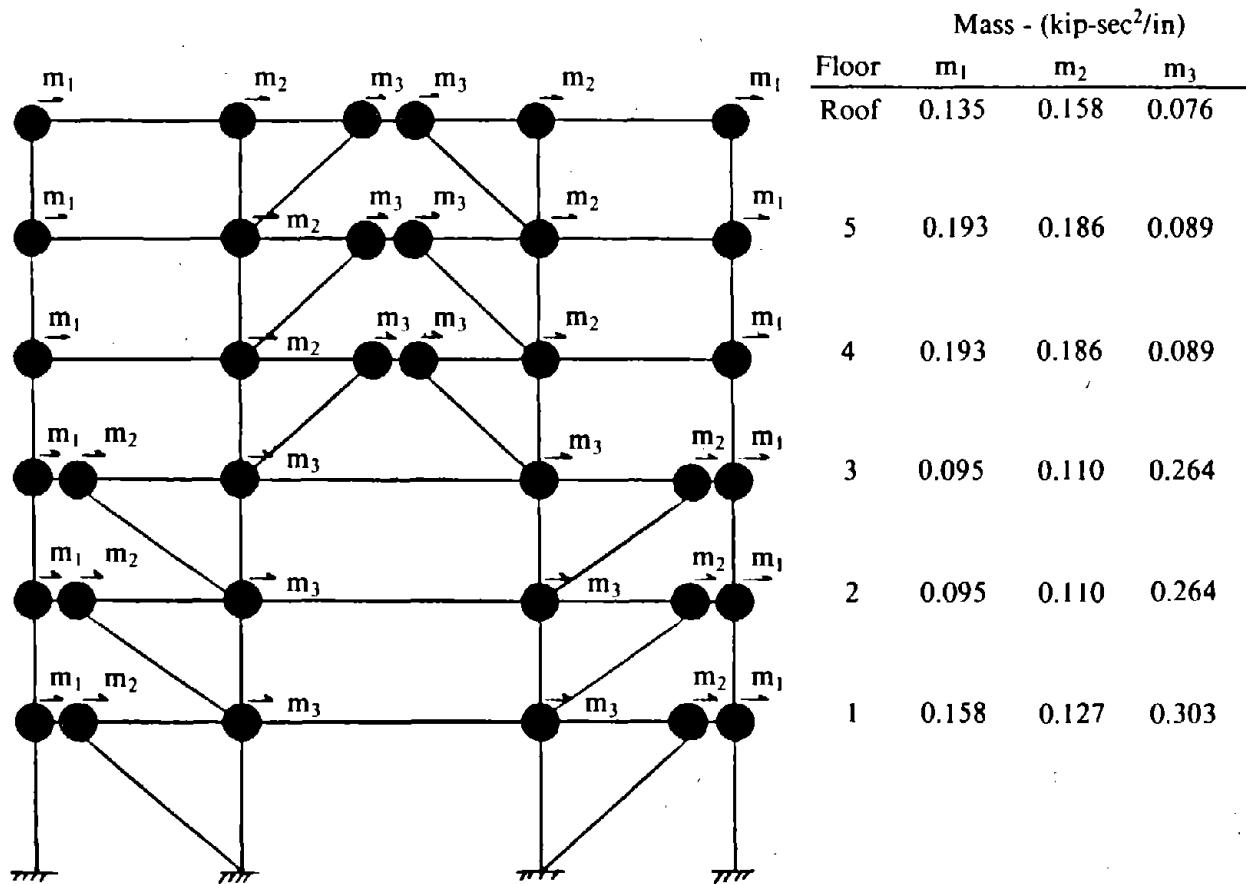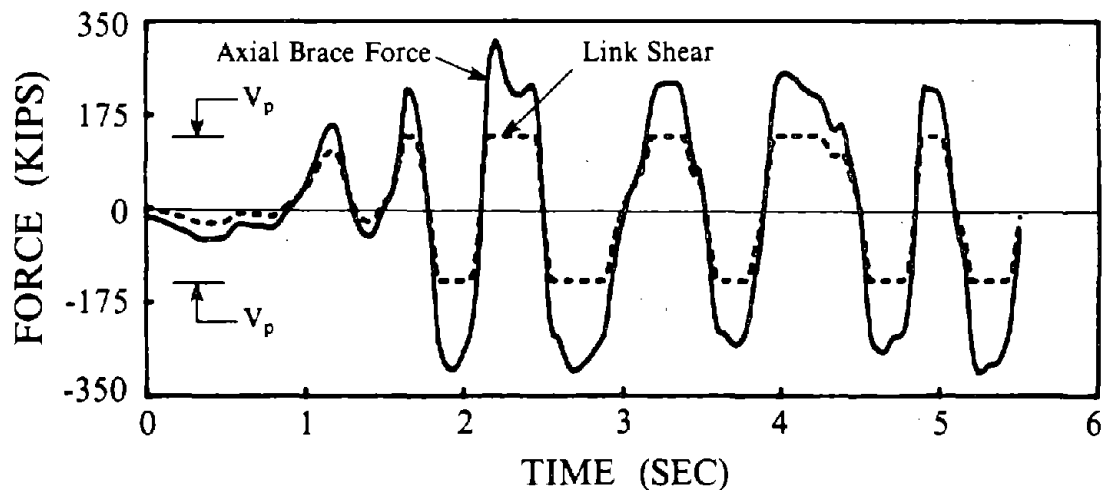
(a) 6-Story EBF With Rayleigh Damping
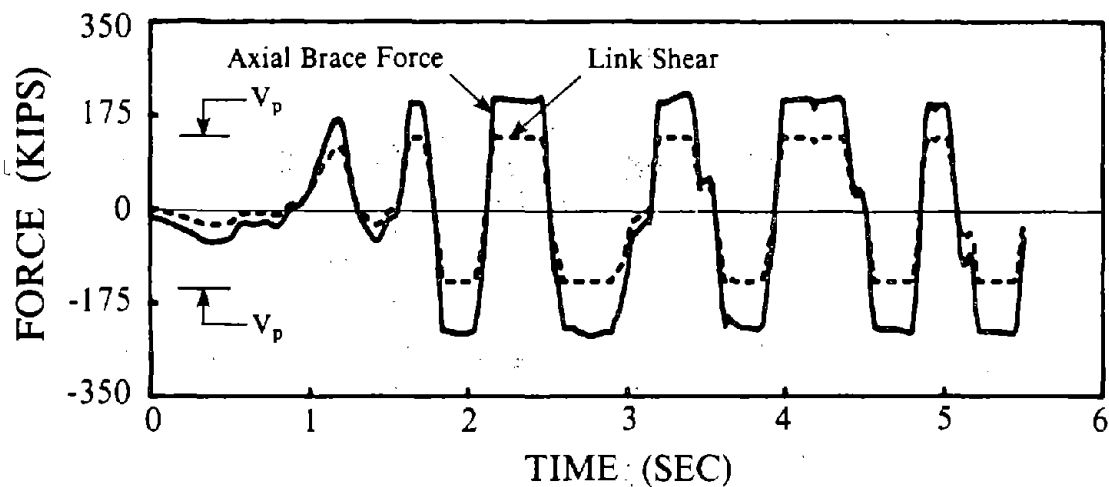
(b) 6-Story EBF Without Damping

Fig. 7.4   Response of First Floor Brace and Link of 6-Story EBF
Subjected to 1940 El Centro (S00E) Earthquake Record.
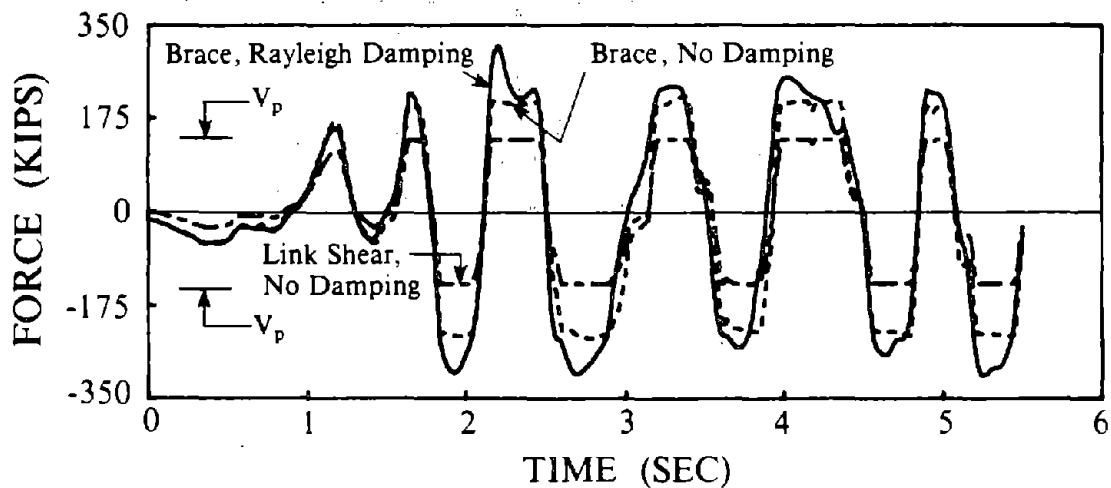
Fig. 7.5   Comparison of Axial Forces of First Floor Brace, 6-Story EBF.

(a)

A   B   C
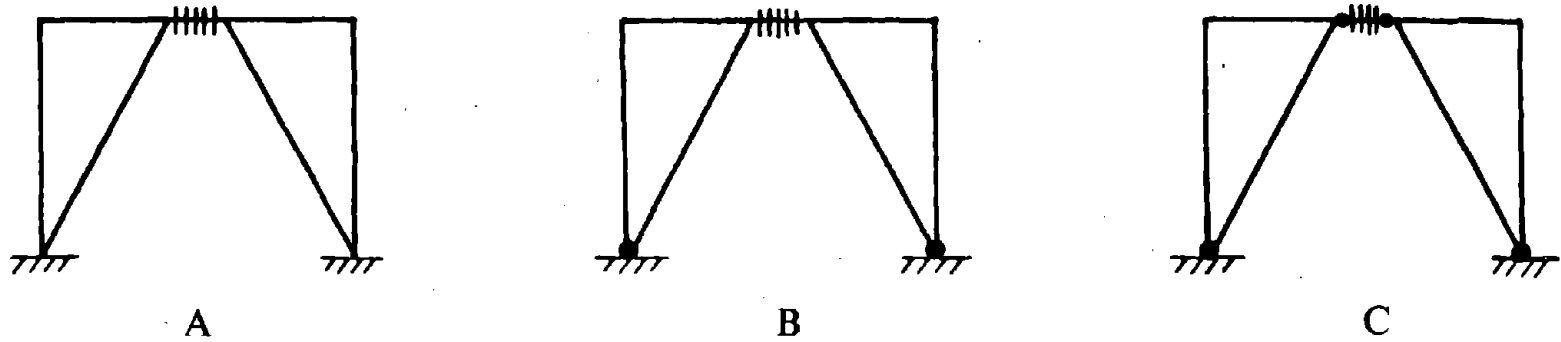
(b)
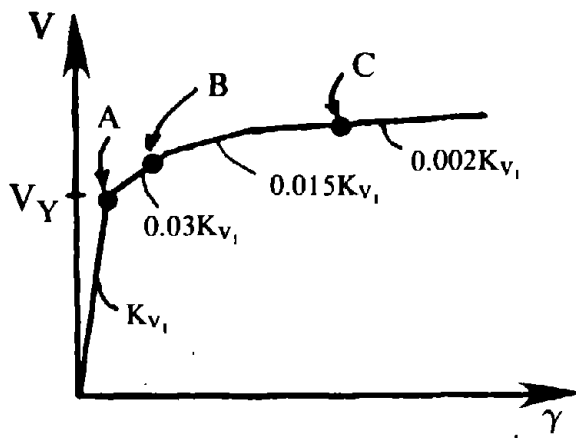
Link Action-Deformation
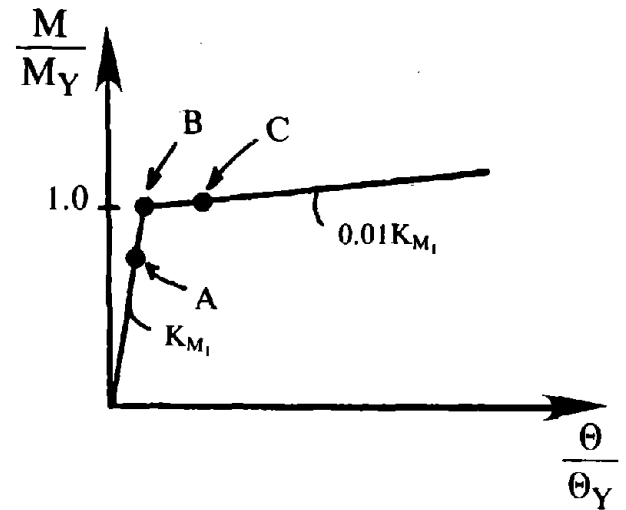
Brace and Column Action-Deformation

Fig. 7.6   Assumed Stages of Yielding A, B, and C as Indicated on
             (a) Structure, and (b) Member Force-Deformation Relationships.
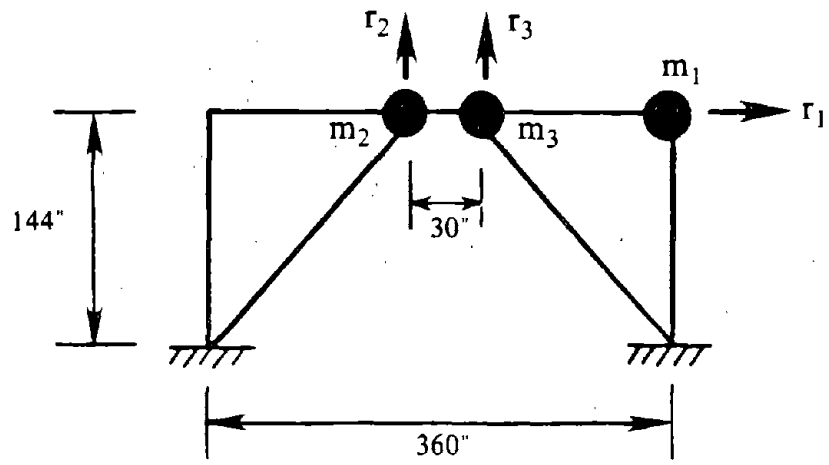
Fig. 7.7   One-Story EBF Model for Modal Damping Analysis.
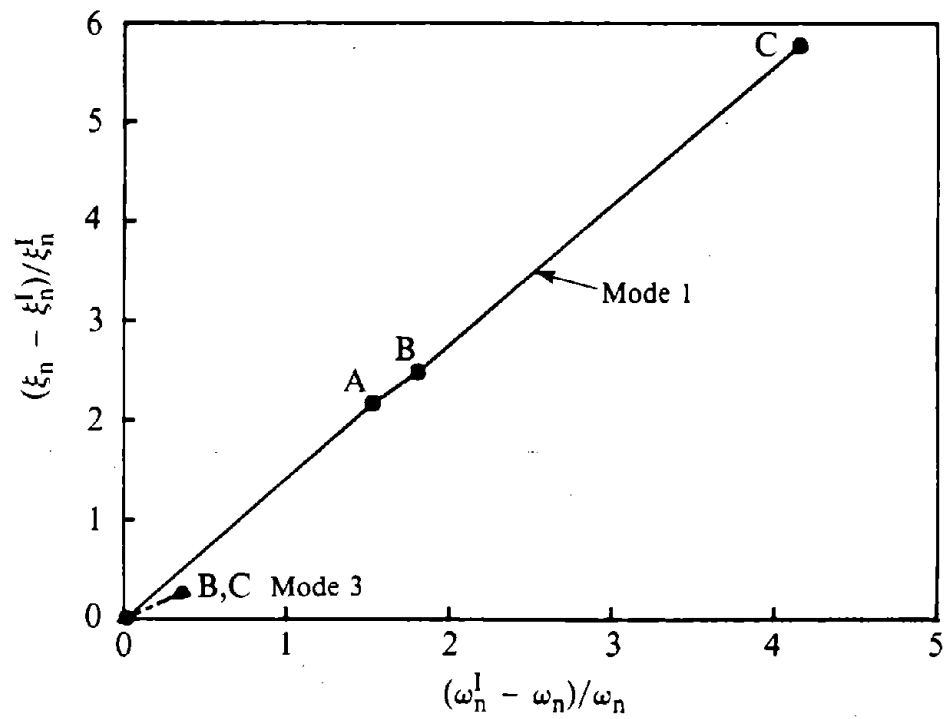
Fig. 7.8   Nonlinear Deformation Effect on Modal Damping,
One-Story EBF Model With Rayleigh Damping.
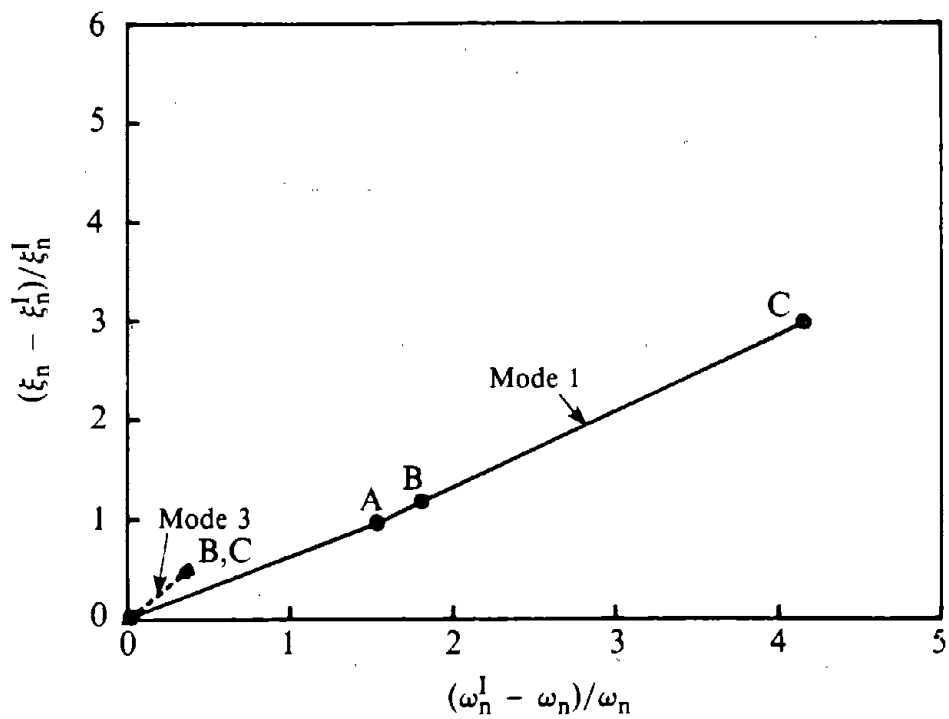
Fig. 7.9   Nonlinear Deformation Effect on Modal Damping.
One-Story EBF Model With Nonproportional Damping.
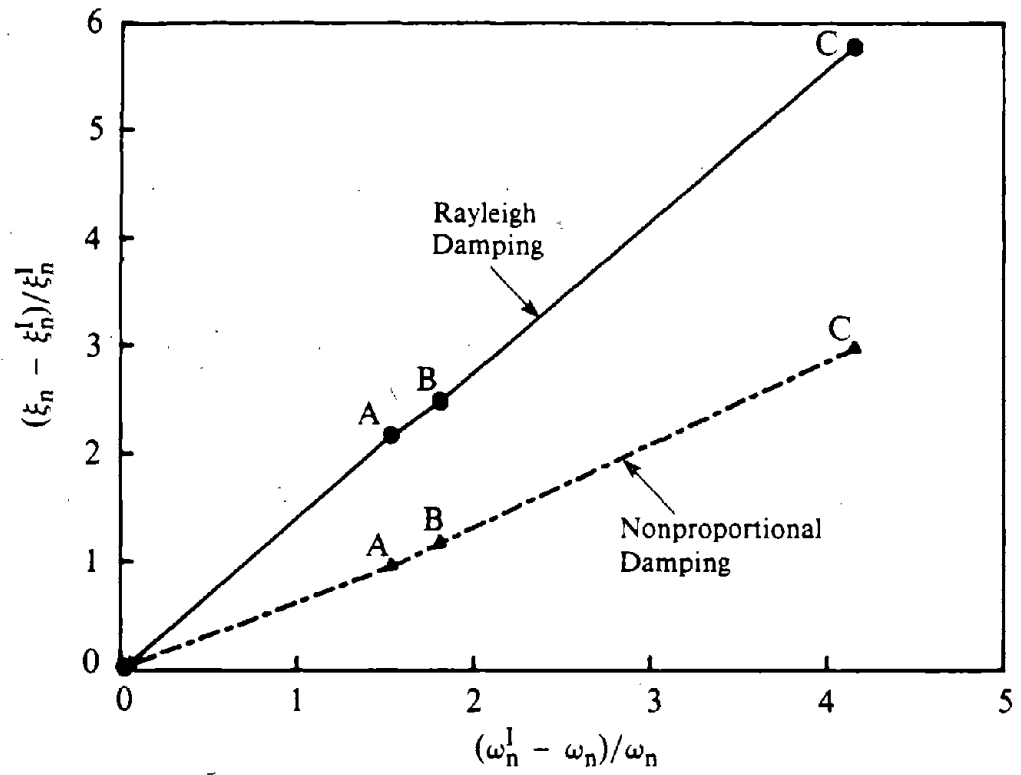
Fig. 7.10   Comparison of Increases in First Mode Damping, One-Story EBF Model.

$$m = 1 \text{ kips} - \text{sec}^2/\text{in}$$
$$c = 2\xi\omega m$$
$$\xi = 0.05$$
$$T_0 = 0.2 \text{ sec}$$

(a) SDOF Oscillator

$$K_Y = 0.015 K_0$$
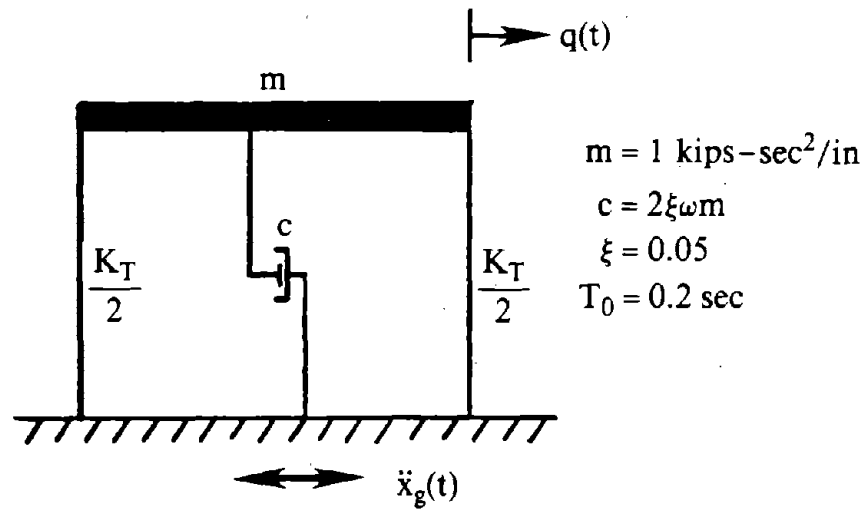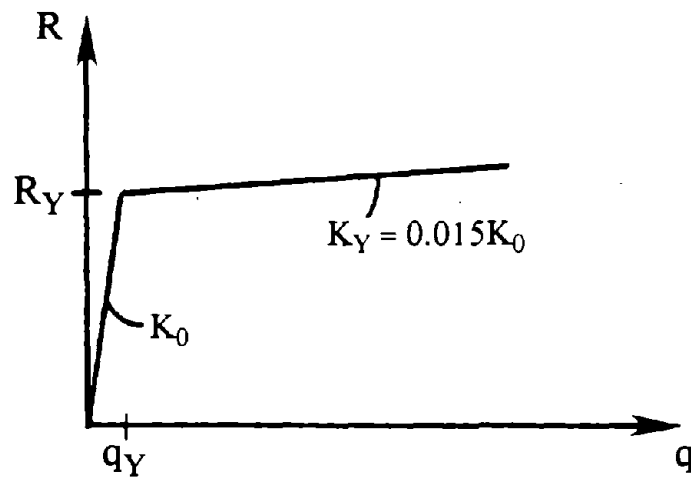
(b) Force-Deformation Relationship of Oscillator

Fig. 7.11   Simple Structural System for Dynamic Analyses.

212

(a) Elastic Oscillator, $\eta = 4.0$

(b) Inelastic Oscillator, $\eta = 0.48$
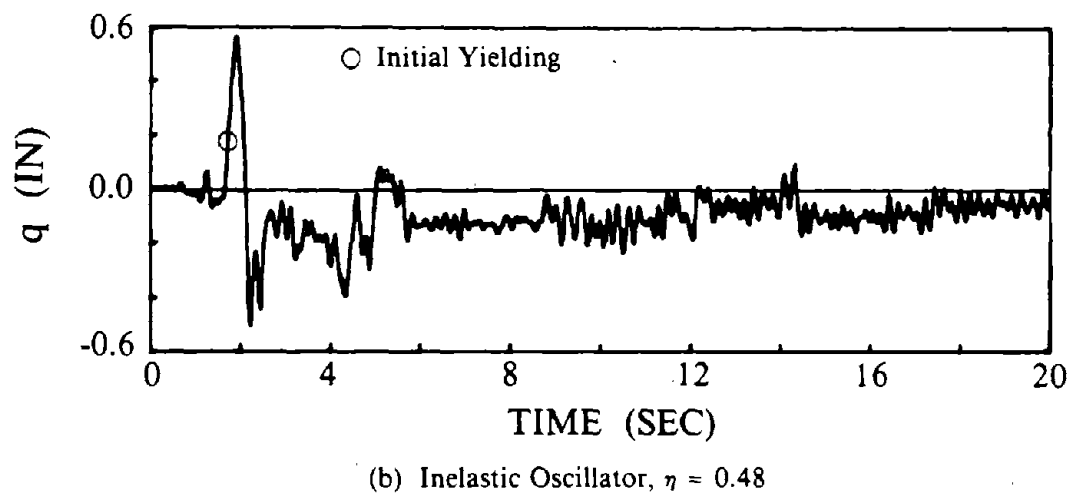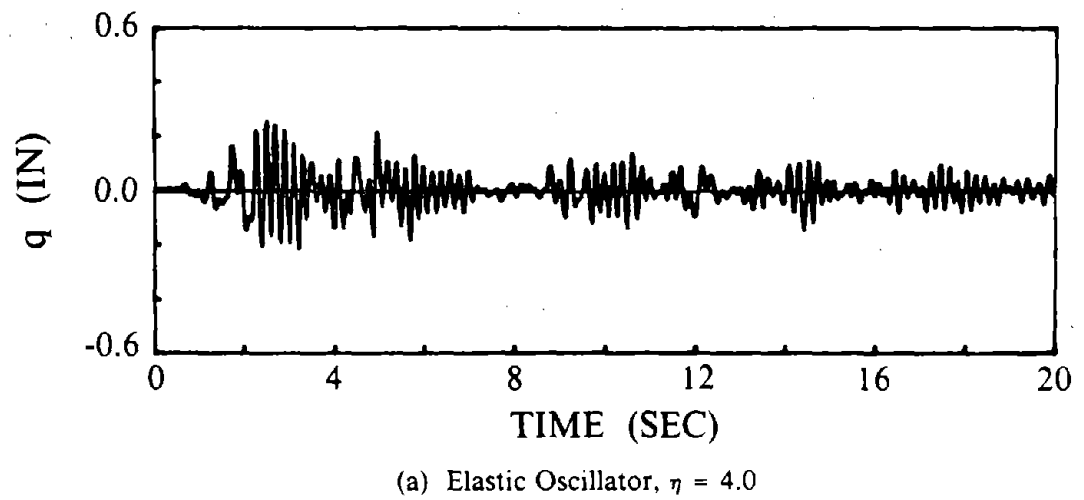
Fig. 7.12   Displacement Response Time Histories of Systems Subjected to 1940 El Centro (S00E) Earthquake Record.
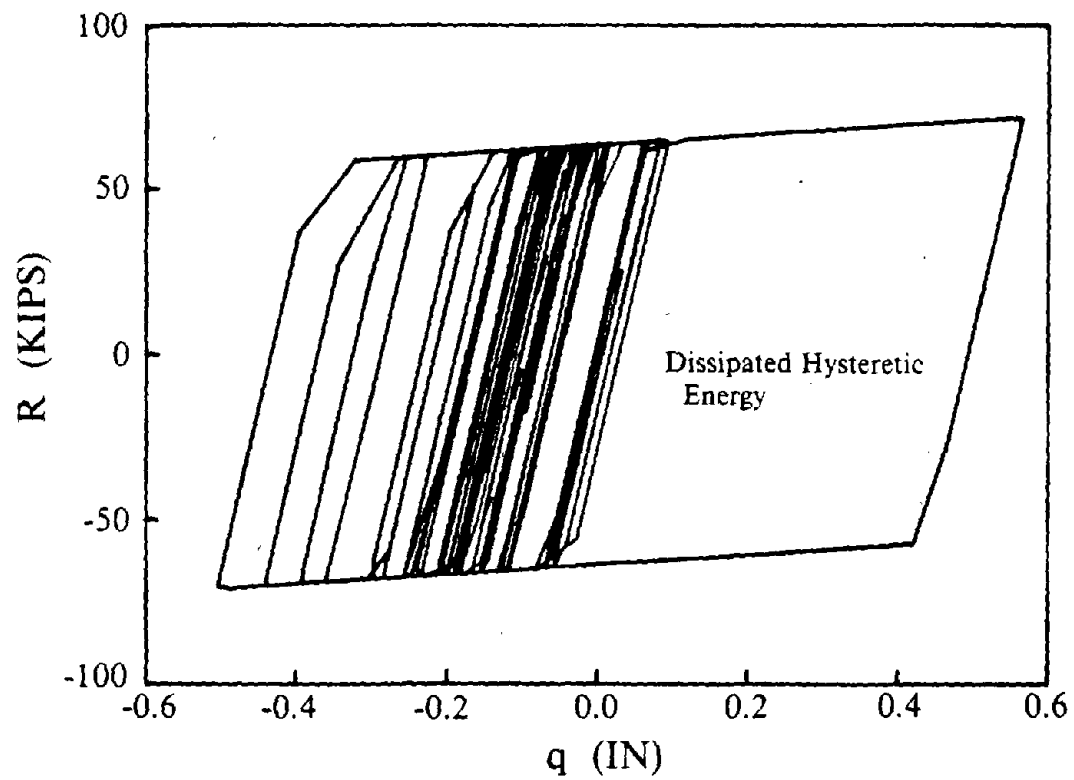
Fig. 7.13   Force-Deformation Hysteretic Response of Inelastic Oscillator, $\eta = 0.48$.
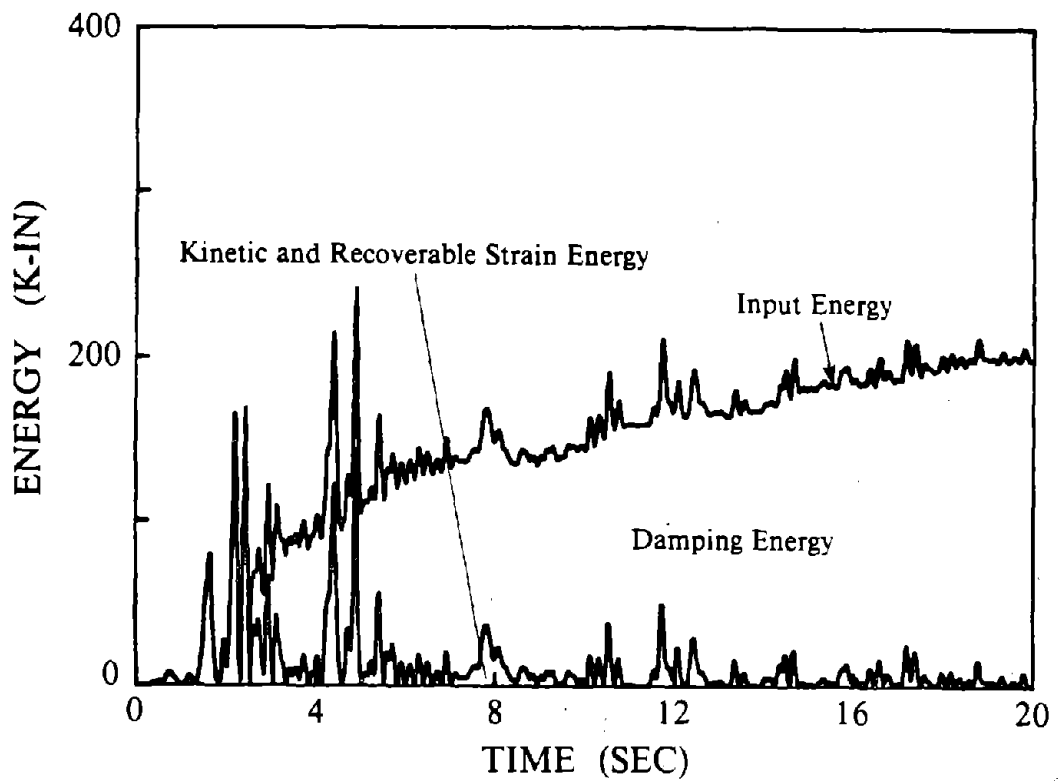
(a) Elastic Oscillator, $\eta = 4.0$
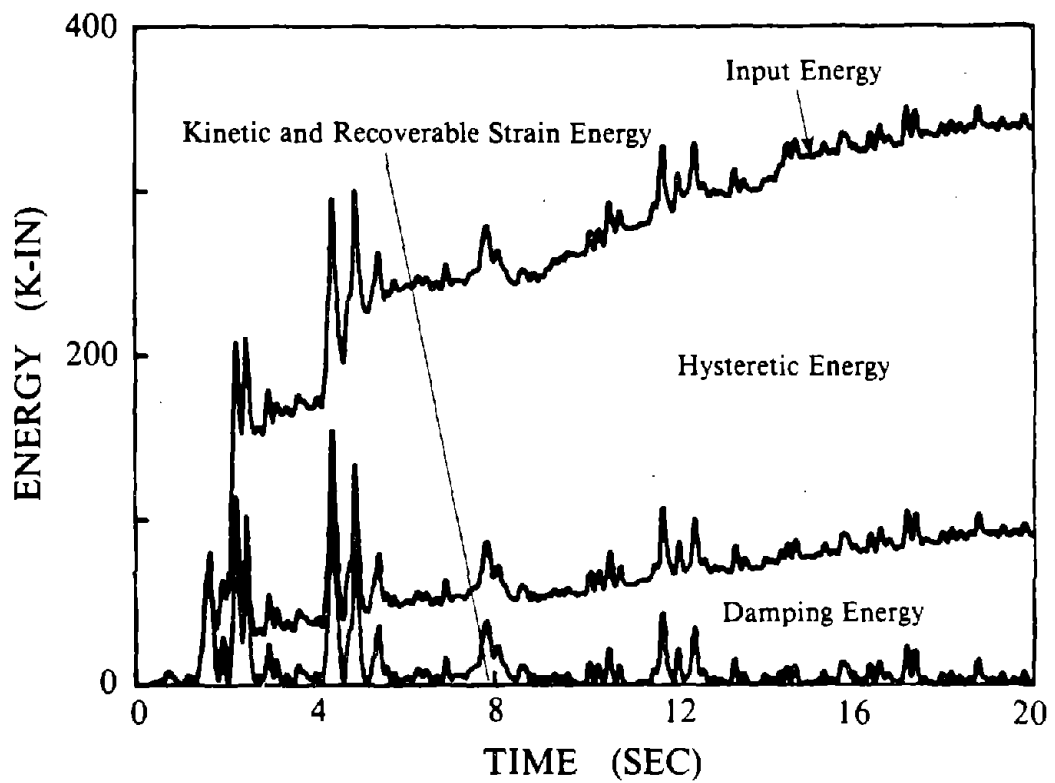
(b) Inelastic Oscillator, $\eta = 0.48$

Fig. 7.14   Energy Time Histories of Systems Subjected to 1940 El Centro (S00E) Earthquake Record.
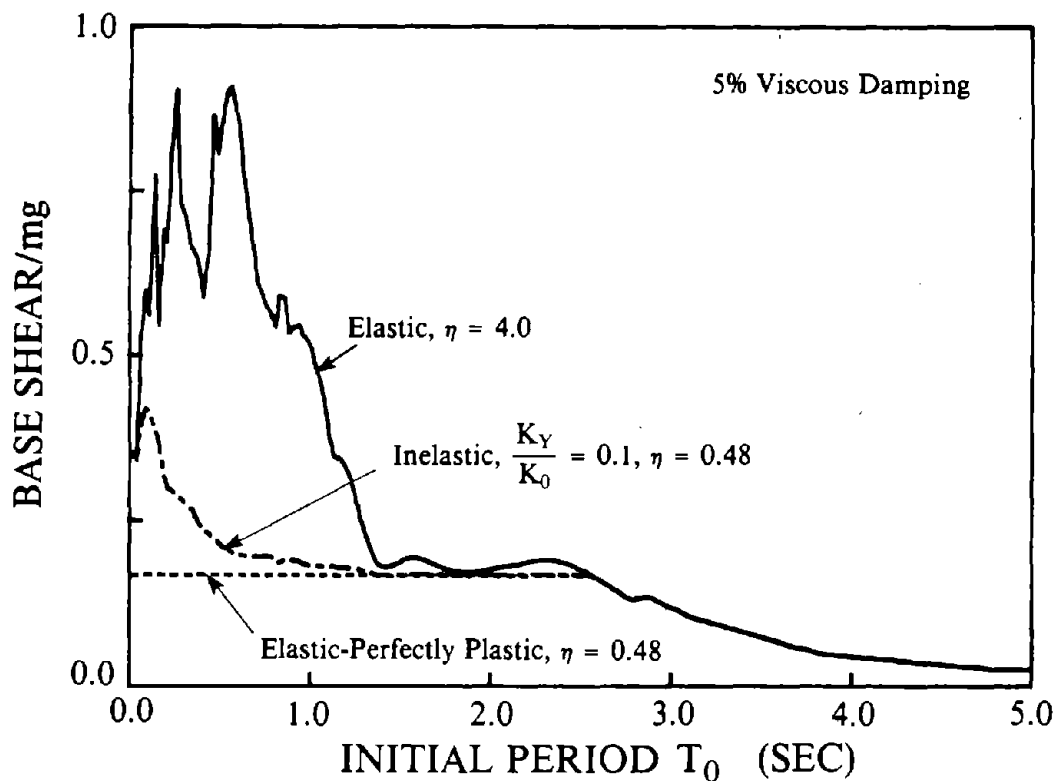
Fig. 7.15   Base Shear Response Spectra for 1940 El Centro (S00E) Earthquake Record.
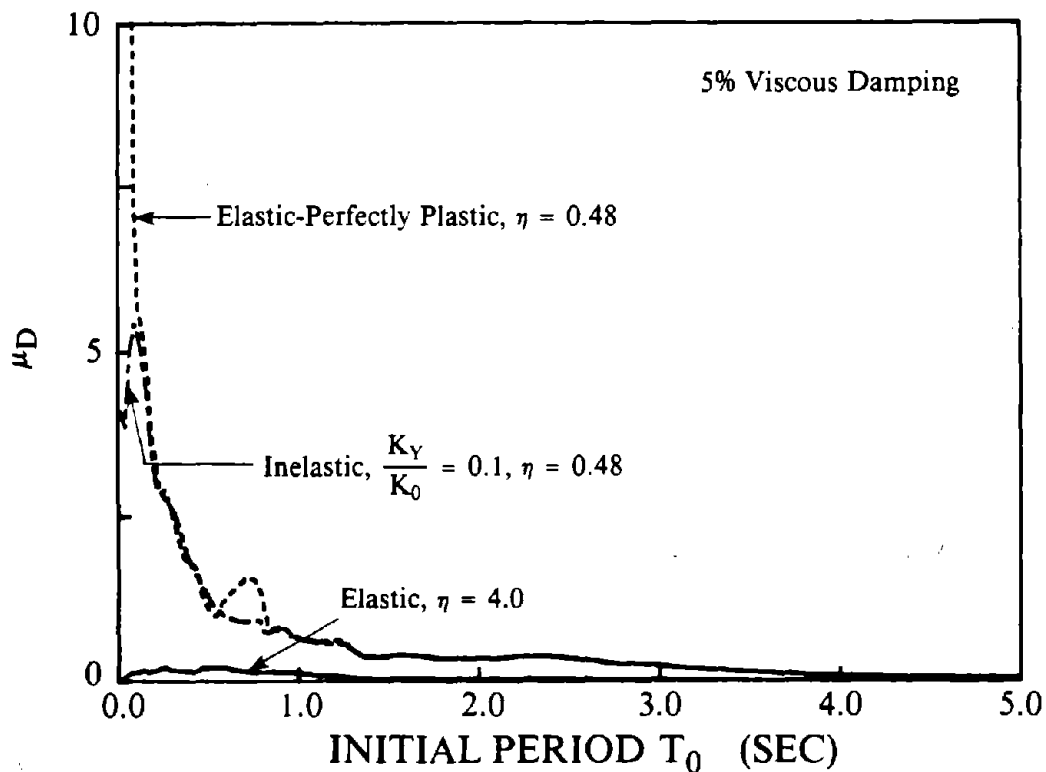
Fig. 7.16   Maximum Displacement Ductility Spectra for
1940 El Centro (S00E) Earthquake Record.
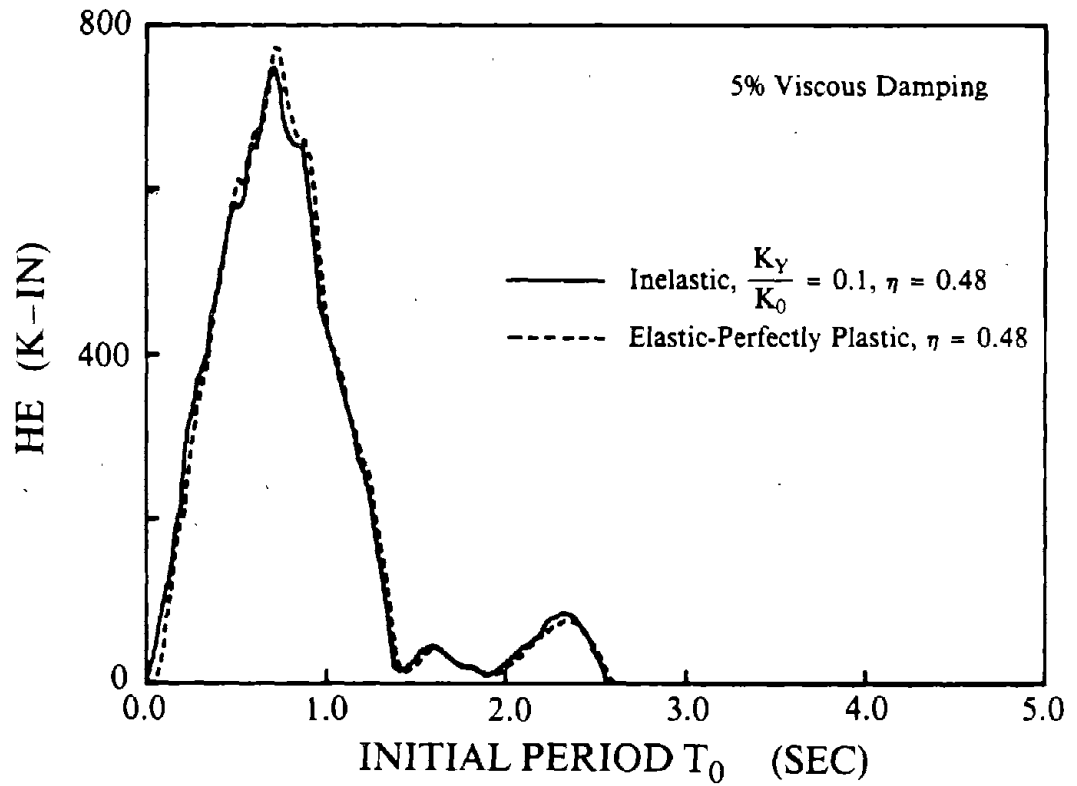
Fig. 7.17   Hysteretic Energy Dissipation Spectra for
1940 El Centro (S00E) Earthquake Record.

(a) Plan of Building

(b) Elevation of EBF
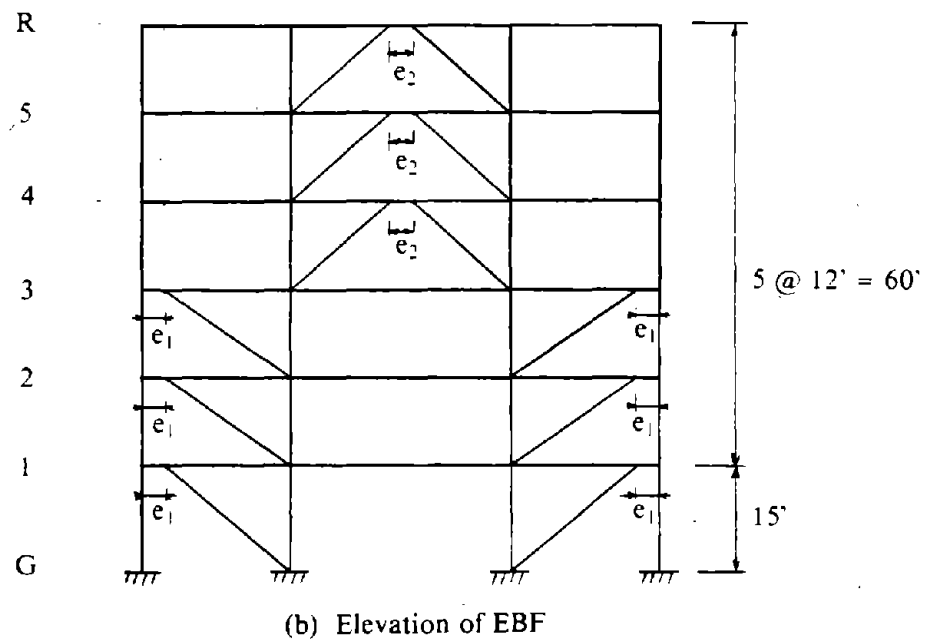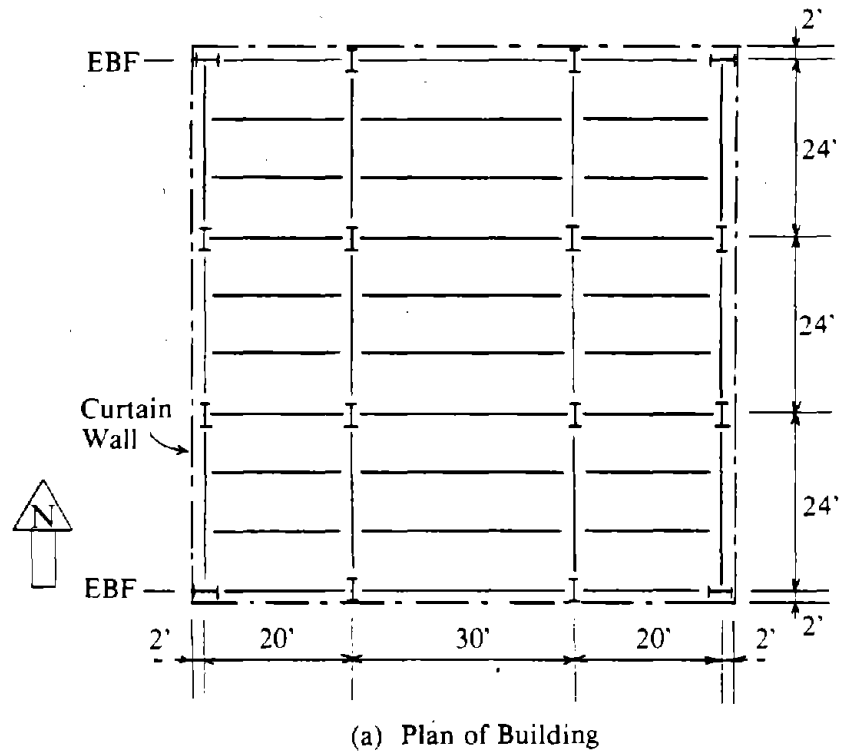
Fig. 8.1   Schematic of Building with Two Exterior EBFs used in Study.

218
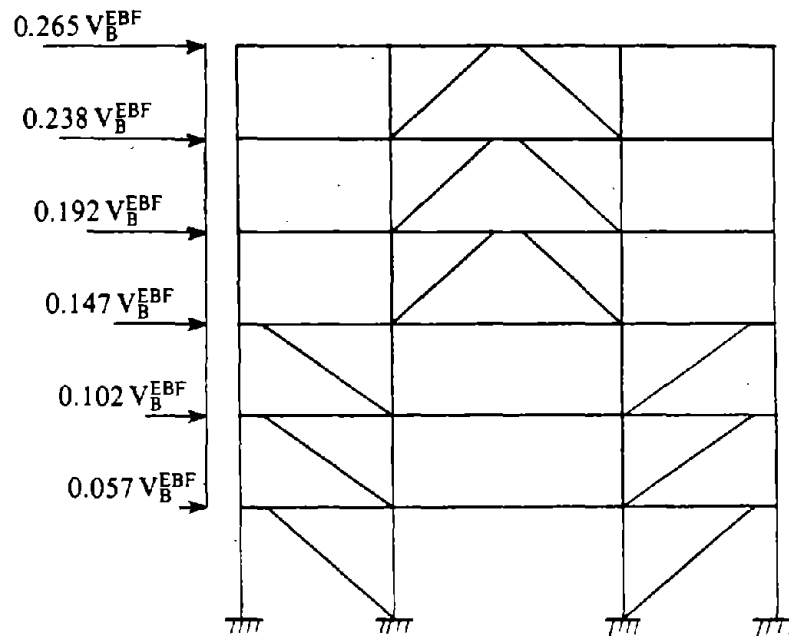
Fig. 8.2   Vertical Distribution of Base Shear V_B^{EBF} to Floors per NEHRP.

(a)   (b)
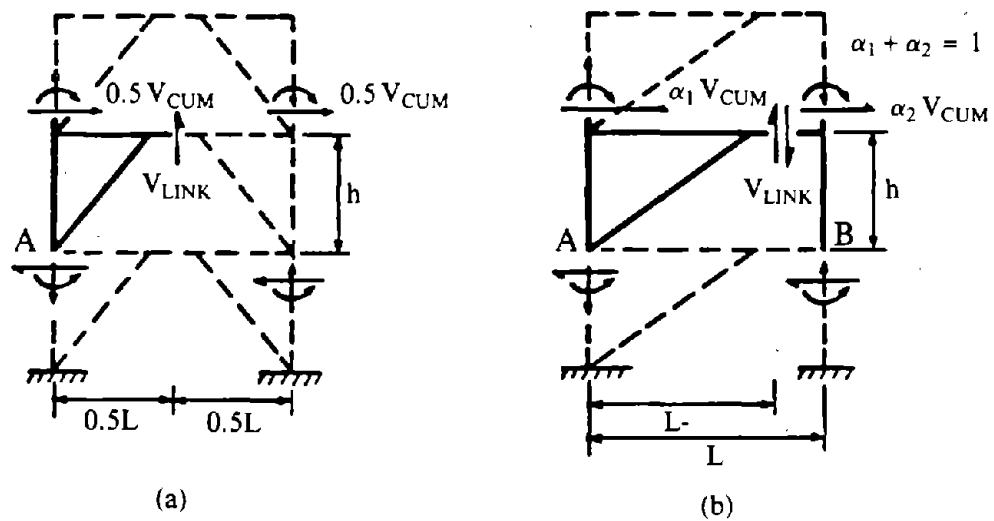
Fig. 8.3   Approximate Free-Body Diagrams of (a) Eccentric K-Braced Frame,
and (b) Eccentric D-Braced Frame.

(a) K-Braced EBF   (b) D-Braced EBF
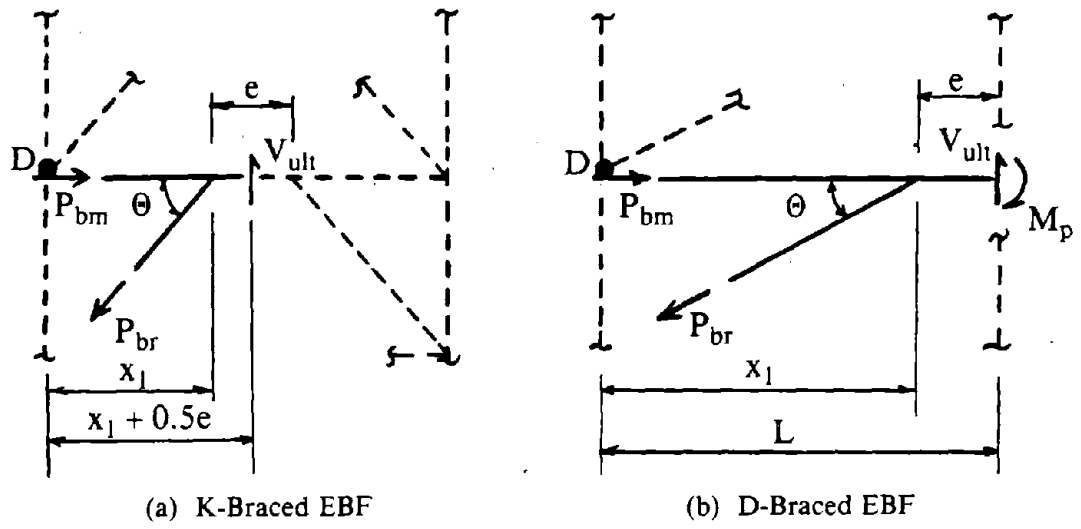
Fig. 8.4   Beam-Brace Subassemblies to Determine Axial Forces in Brace and Floor Beam.
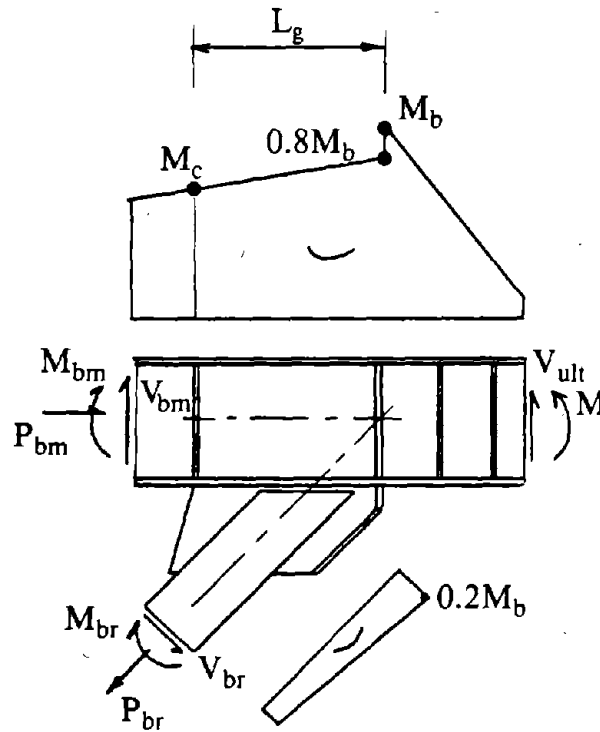
Fig. 8.5   Determination of Design Moment M_c in Floor Beam at End of Gusset Plate.
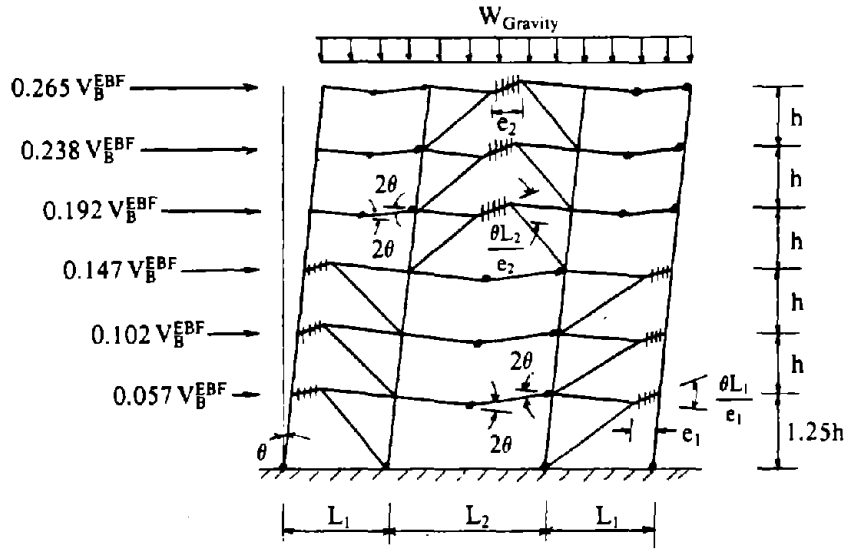
$$W_{EXT} = 4.50\, V_B^{EBF}\, h\theta + \frac{W_G}{4}\,(2L_1^2 + 2L_2^2)\theta$$

$$W_{INT} = 4\theta M_{P_{bm}} \sum_1^9 \alpha_i + \theta L_1 \sum_j^6 V_{P_j} + \theta L_2 \sum_k^3 V_{P_k}$$

a) Designs 1 and 2
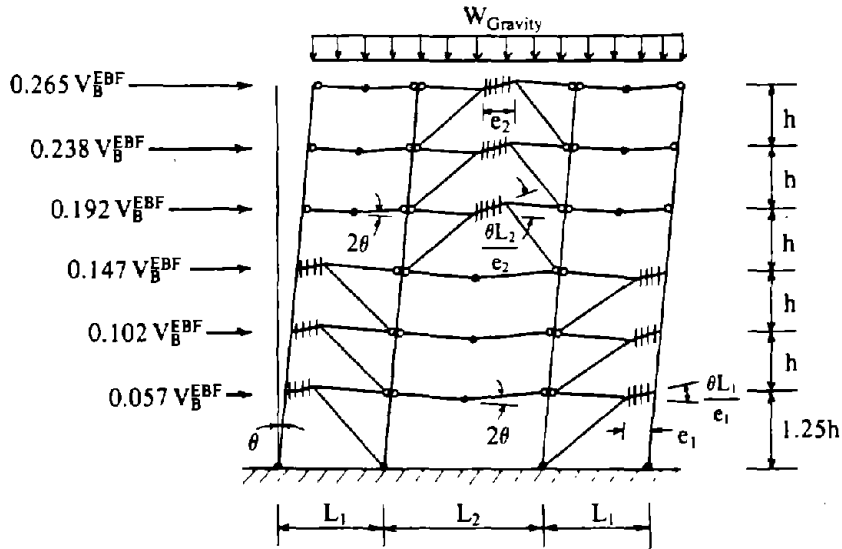
$$W_{EXT} = 4.50\, V_B^{EBF}\, h\theta + \frac{W_G}{4}\,(2L_1^2 + 2L_2^2)\theta$$

$$W_{INT} = 2\theta M_{P_{bm}} \sum_1^9 \alpha_i + \theta L_1 \sum_j^6 V_{P_j} + \theta L_2 \sum_k^3 V_{P_k}$$

(b) Design 3 with Pin Connections

Fig. 8.6   EBF Collapse Mechanism for Designing the Floor Beams of Unbraced Panels.
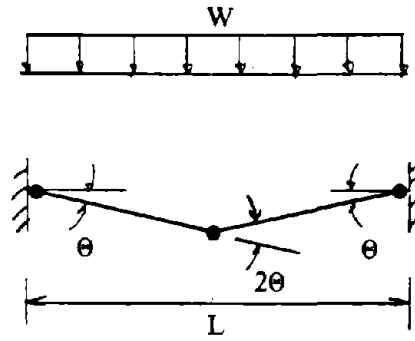
(a) Floor Beam with Moment Connections
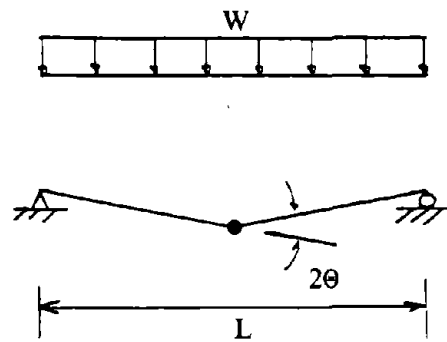
$$M_{p_{bm}} \geq \frac{WL^2}{16}$$

(b) Floor Beam with Pin Connections

$$M_{p_{bm}} \geq \frac{WL^2}{8}$$

Fig. 8.7   Local Beam Mechanisms.
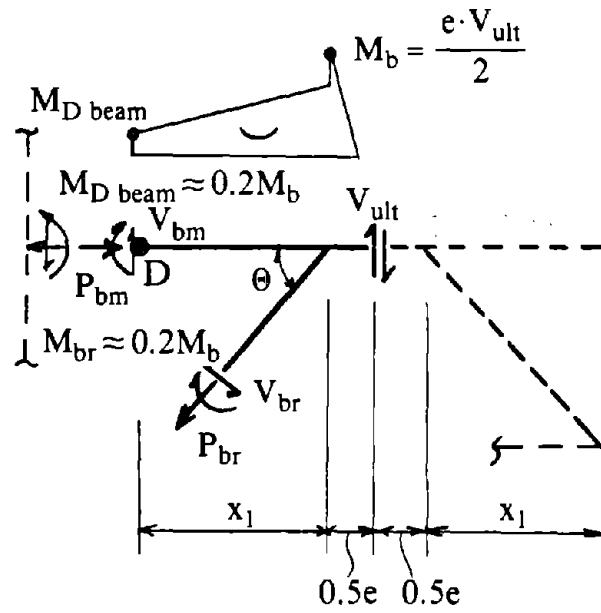
(a) K-Braced Panel
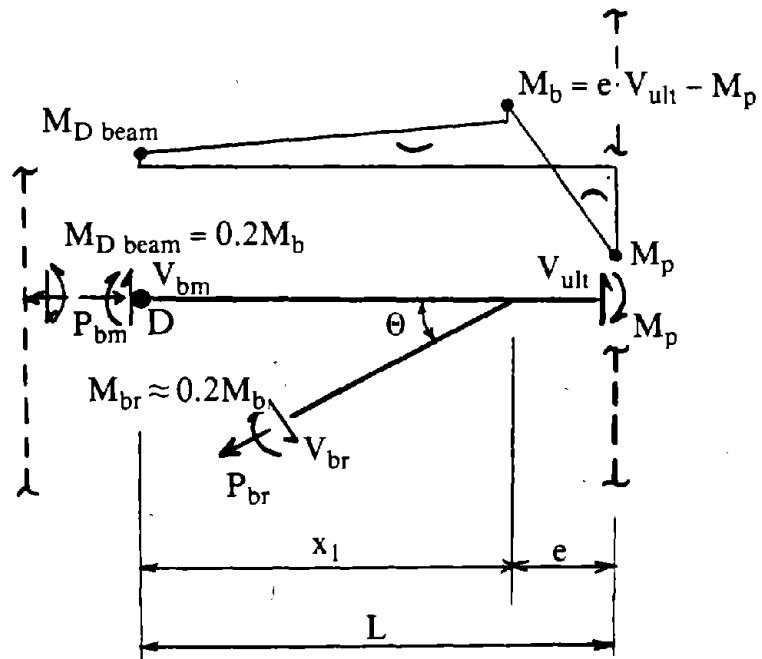
(b) D-Braced Panel

Fig. 8.8   Approximation of Floor Beam Moment $M_{D_{beam}}$ at Column.

Floor	e	$\dfrac{V_p}{V_{LINK}}$	$\dfrac{e \cdot V_p}{M_p}$
Roof	30"	4.04	1.38
5	30"	2.29	1.24
4	30"	1.92	1.24
3	26"	1.47	1.08
2	26"	1.31	1.08
1	26"	1.13	1.08

Note:
- A36 Steel Beams
- A572, Grade 50 Columns
- A441 Structural Steel Tube Braces (F_Y = 46 ksi)
- All Moment Connections

Fig. 8.9   Design 1 - All Moment Connections.
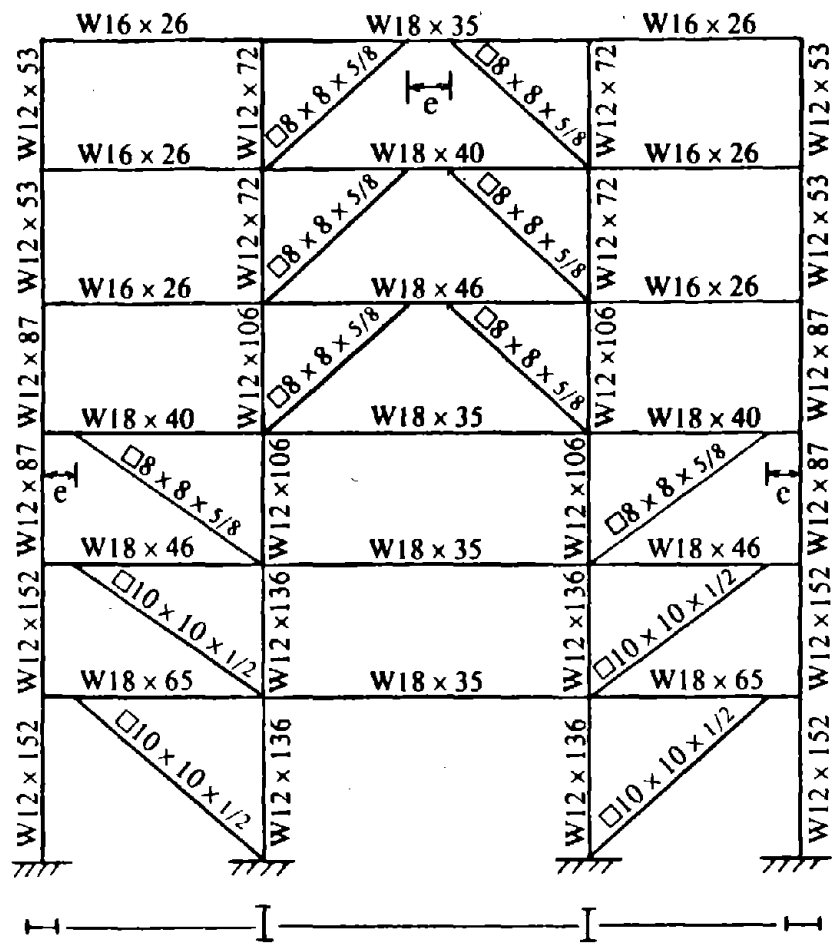
Floor	e	$\dfrac{V_p}{V_{LINK}}$	$\dfrac{e \cdot V_p}{M_p}$
Roof	30"	4.04	1.38
5	30"	2.29	1.24
4	30"	1.92	1.24
3	26"	1.47	1.08
2	26"	1.51	1.08
1	26"	1.44	0.94

Note:
- A36 Steel Beams
- A572, Grade 50 Columns
- A441 Structural Steel Tube Braces (F_Y = 46 ksi)
- All Moment Connections

Fig. 8:10   Design 2 - Increased Link Capacity at Floors 1 and 2, All Moment Connections.
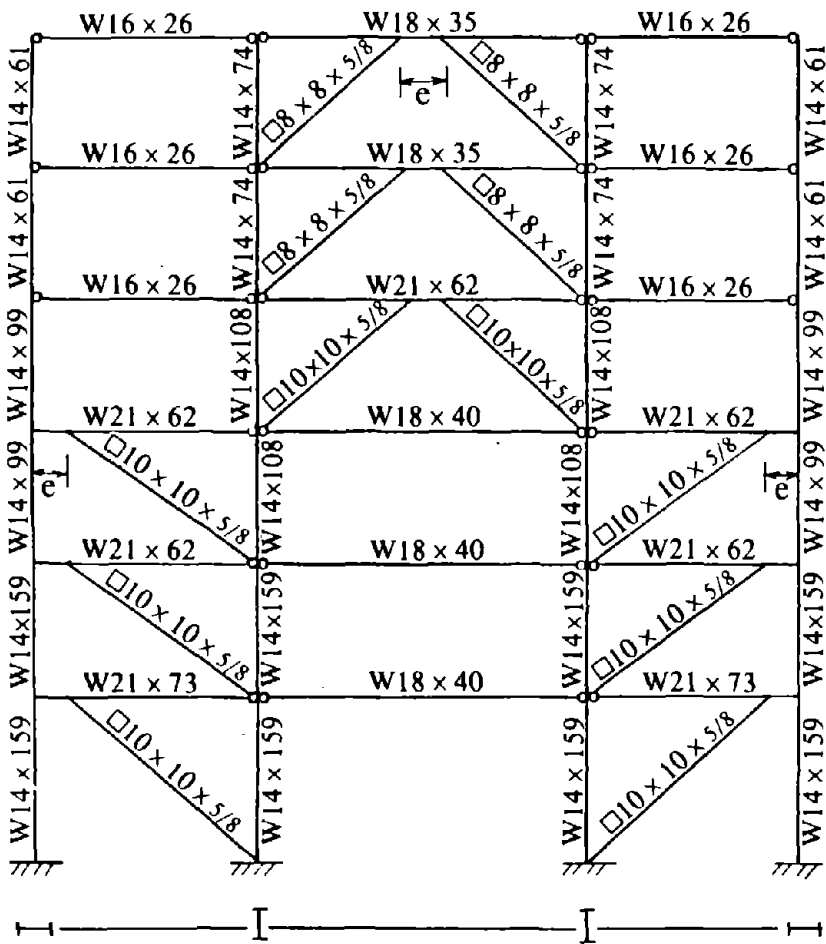
Floor	e	$\dfrac{V_p}{V_{LINK}}$	$\dfrac{e \cdot V_p}{M_p}$
Roof	34"	2.69	1.59
5	34"	1.91	1.25
4	34"	1.65	1.17
3	30"	1.82	1.02
2	30"	1.62	1.02
1	30"	1.41	0.98

Note:
- A36 Steel Beams
- A572, Grade 50 Columns
- A441 Structural Steel Tube Braces ($F_Y = 46$ ksi)
- Use of Pin Connections as Shown

Fig. 8.11   Design 3 - Pin Connections at Beam-to-Column and Brace-to-Column Connections.
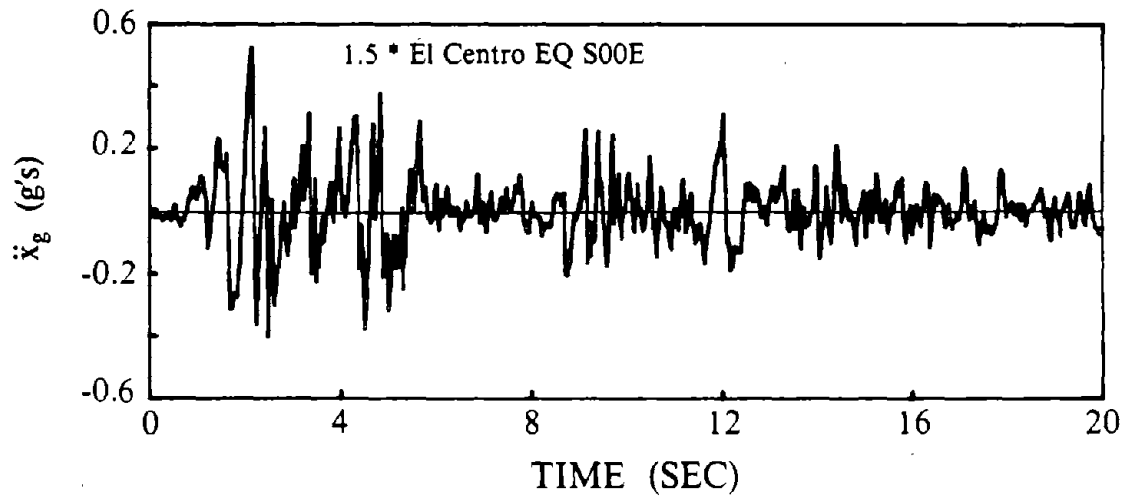
Fig. 8.12   Accelerogram for the 1940 El Centro Earthquake Record Scaled to O.5g.
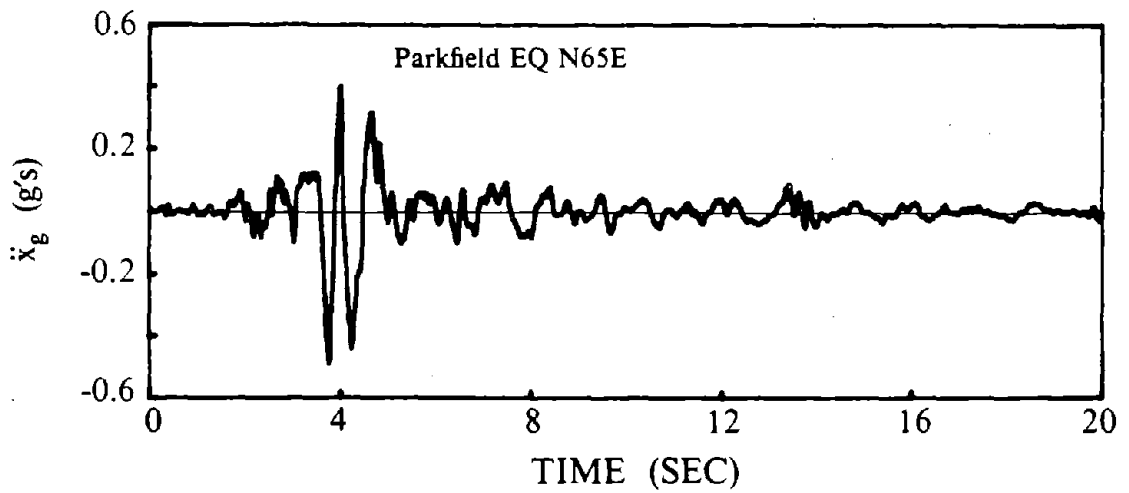
Fig. 8.13   Accelerogram for the Original 1966 Parkfield Earthquake Record.

Mass - (kip-sec^2/in)

Floor	m_1	m_2	m_3	m_4
Roof	0.135	0.158	0.076	0.076
5	0.193	0.186	0.089	0.089
4	0.193	0.186	0.089	0.089
3	0.095	0.110	0.264	0.110
2	0.095	0.110	0.264	0.110
1	0.158	0.127	0.303	0.127
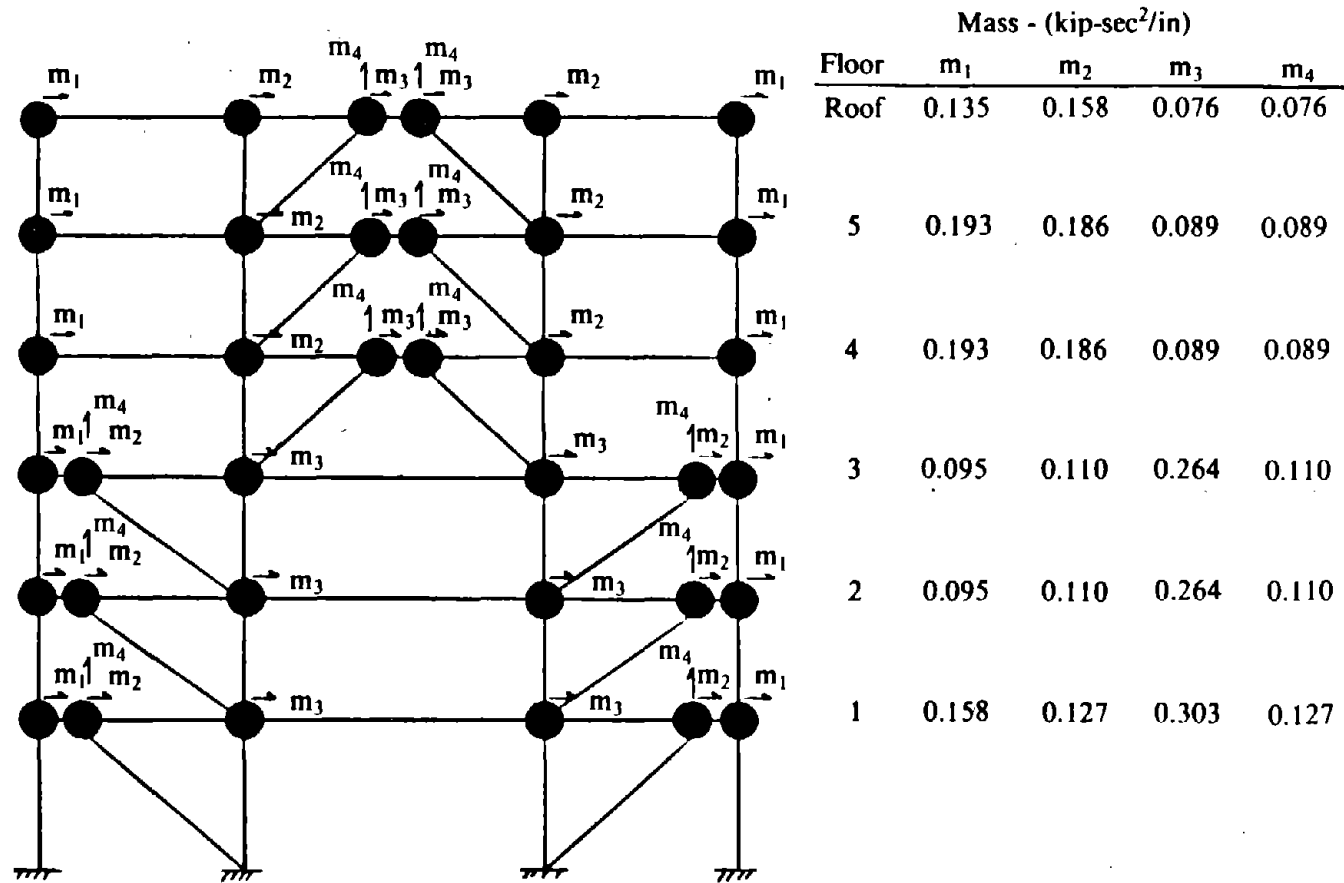
Fig. 8.14   Lumped Mass Description for EBF Models.

228

(a) Shear   (b) Moment
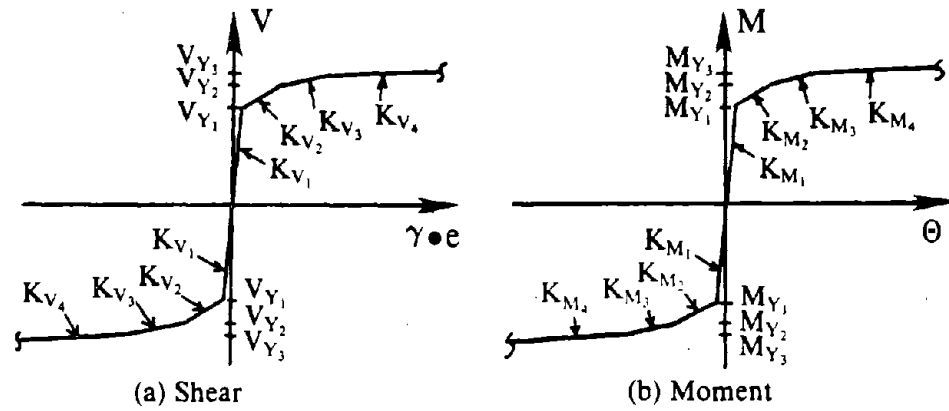
Parameter	Bare Steel, Strain Hard.	Bare Steel, EPP	Composite Ext., Strain Hard.	Composite Int., Strain Hard.
Shear				
V_{Y_1}	V_p	V_p	$1.05V_p$	$1.17V_p$
V_{Y_2}	$1.26V_p$	$1.26V_p$	$1.26V_p$	$1.40V_p$
V_{Y_3}	$1.40V_p$	$1.40V_p$	$1.43V_p$	$1.50V_p$
K_{V_1}	$\dfrac{GA_z^*}{e}$	$\dfrac{GA_z^*}{e}$	$\dfrac{GA_z^*}{e}$	$\dfrac{GA_z^*}{e}$
K_{V_2}	$0.03K_{V_1}$	$0.0001K_{V_1}$	$0.03K_{V_1}$	$0.03K_{V_1}$
K_{V_3}	$0.015K_{V_1}$	$0.0001K_{V_1}$	$0.015K_{V_1}$	$0.015K_{V_1}$
K_{V_4}	$0.002K_{V_1}$	$0.0001K_{V_1}$	$0.0035K_{V_1}$	$0.0035K_{V_1}$
V_{Y_0}	V_{Y_1}	V_{Y_1}	V_{Y_1}	V_{Y_1}
ΔV_{max}	$2.68V_{Y_1}$	$2V_{Y_1}$	$2.38V_{Y_1}$	$2.38V_{Y_1}$
a	8.336	0	5.668	5.668
Moment				
M_{Y_1}	M_p	M_p	M_p	M_p
M_{Y_2}	$1.13M_p$	$1.13M_p$	$1.13M_p$	$1.13M_p$
M_{Y_3}	$1.20M_p$	$1.20M_p$	$1.20M_p$	$1.20M_p$
K_{M_1}	$\dfrac{6EI}{e}$	$\dfrac{6EI}{e}$	$\dfrac{6EI}{e}$	$\dfrac{6EI}{e}$
K_{M_2}	$0.03K_{M_1}$	$0.0001K_{M_1}$	$0.03K_{M_1}$	$0.03K_{M_1}$
K_{M_3}	$0.015K_{M_1}$	$0.0001K_{M_1}$	$0.015K_{M_1}$	$0.015K_{M_1}$
K_{M_4}	$0.002K_{M_1}$	$0.0001K_{M_1}$	$0.0035K_{M_1}$	$0.0035K_{M_1}$

Fig. 8.15   Force-Deformation Relationships for the Various Hardening and Composite Link Models.
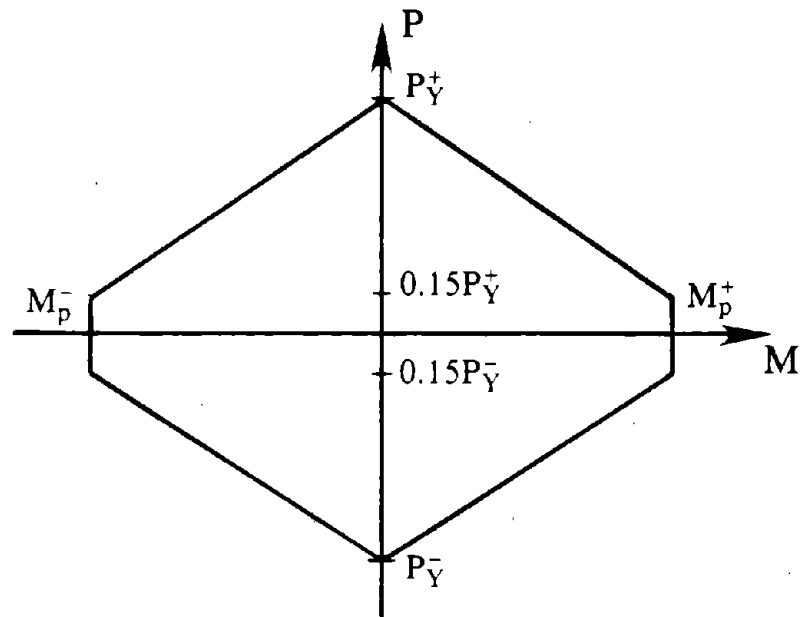
Fig. 8.16   Moment-Axial Load AISC Interaction Surface.
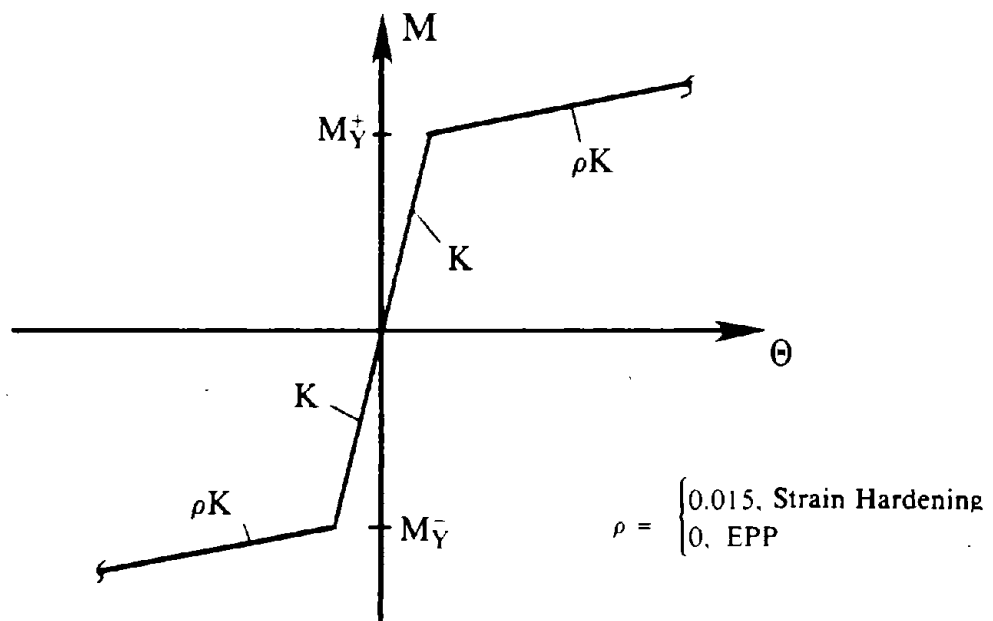
Fig. 8.17   Action-Deformation Relationship for Bare Steel Beam-Column Element.

$$K^+ = \frac{3EI_{eff}}{L^*} = \frac{M^+}{\Theta^+}$$

$$K^- = \frac{3EI}{L^*}$$

$$K^+ = \frac{3EI_{eff}}{L^*} = \frac{M^+}{\Theta^+}$$

$$K^- = \frac{3EI}{L^*}$$

$$K^+ = \frac{6EI_{eff}}{L} = \frac{M^+}{\Theta^+}$$

$$K^- = \frac{6EI}{L}$$
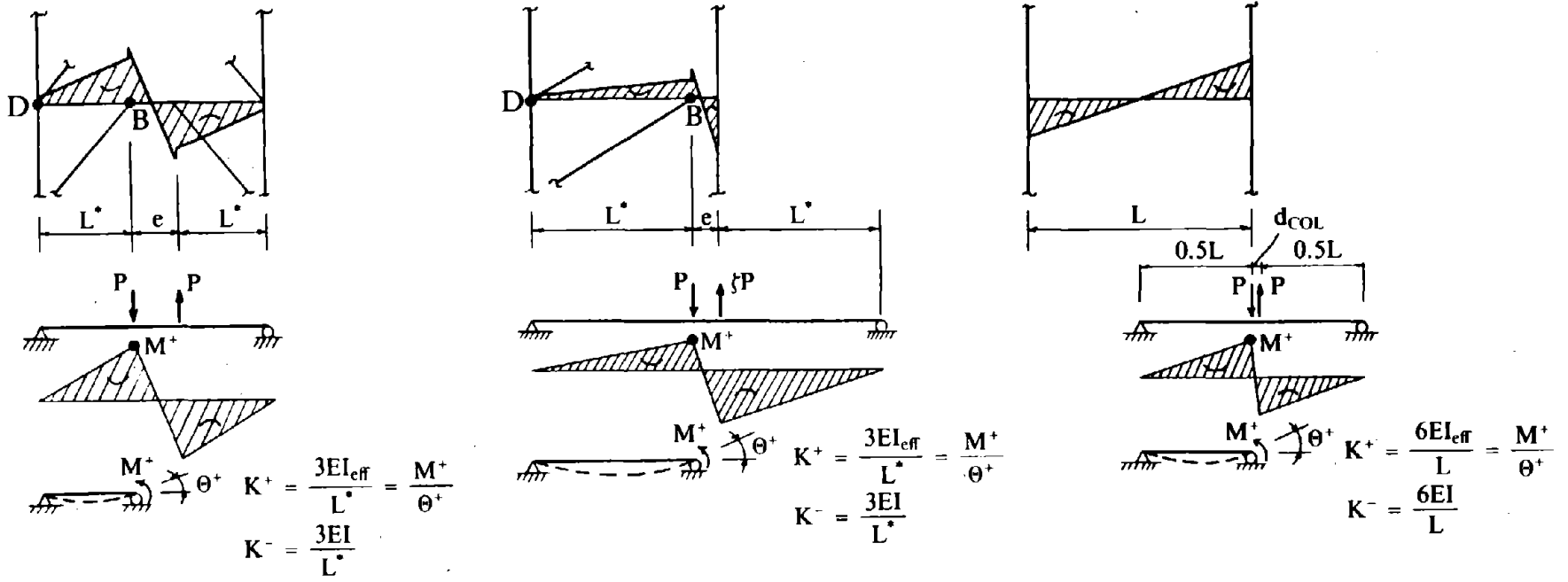
(a) Floor Beam Outside the Link
of K-Braced Panels

(b) Floor Beam Outside the Link
of D-Braced Panels

(c) Floor Beam of Unbraced Panels

Fig. 8.18 Load Conditions for Simply Supported Beams to Determine Effective Moment
of Inertia I_{eff} and Positive Flexural Stiffness K^+ of Composite Floor Beams
Using Slab-Girder Interaction Analysis.
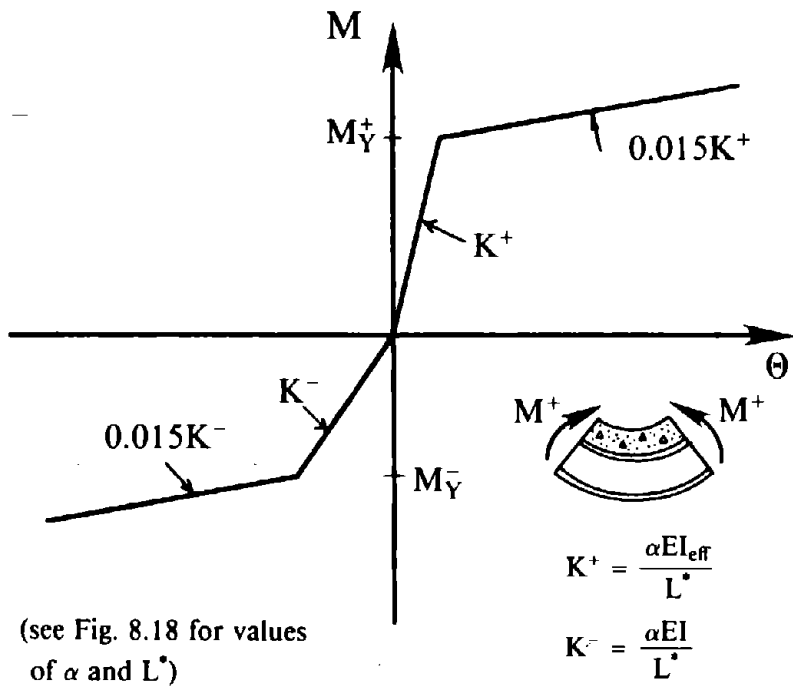
Fig. 8.19   Action-Deformation Relationship for Composite
Beam-Column Element.

$$K^+ = \frac{\alpha EI_{eff}}{L^*}$$

$$K^- = \frac{\alpha EI}{L^*}$$

(see Fig. 8.18 for values
of α and L^*)

(a) Link Adjacent to Column

(b) Link in K-Braced Panel
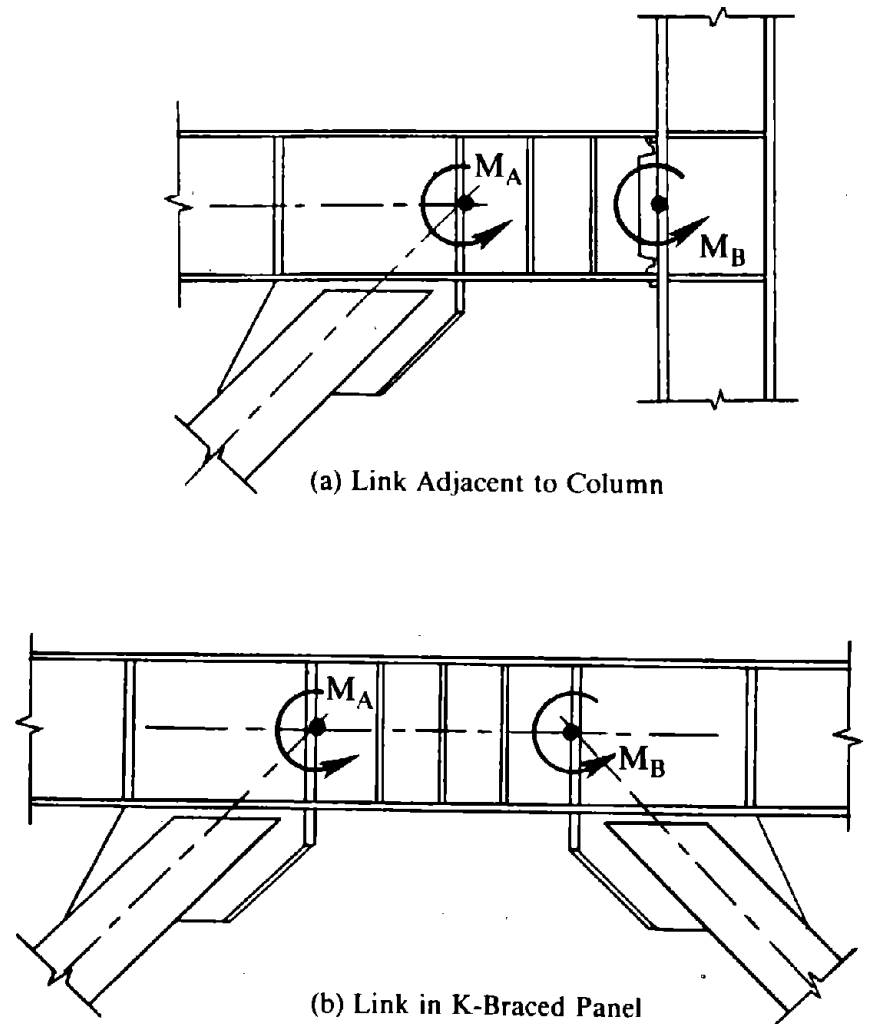
Fig. 8.20   Positive Sign Convention for Link End Moments.
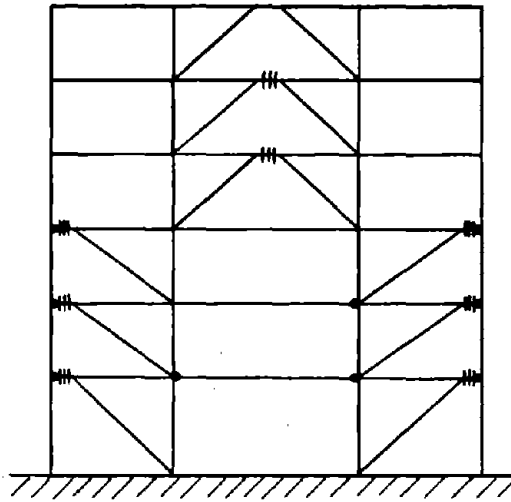
232

(a) Strain Hardening with Nonproportional
Damping. 1.5 * El Centro Earthquake
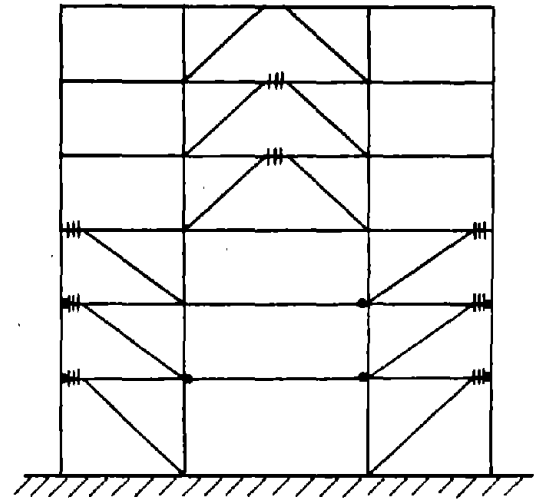
(b) Elastic-Perfectly Plastic with
Nonproportional Damping.
1.5 * El Centro Earthquake
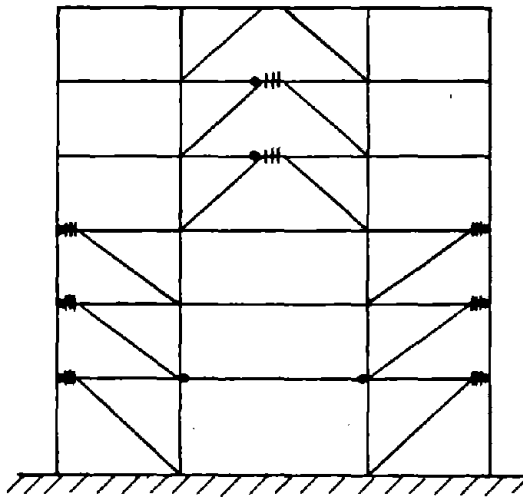
(c) Strain Hardening with Rayleigh
Damping. 1.5 * El Centro Earthquake
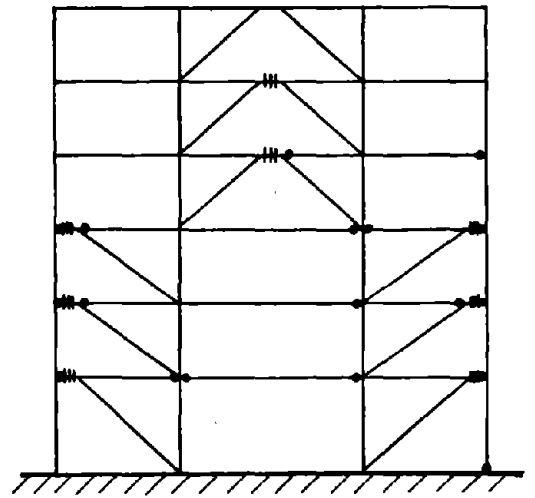
(d) Strain Hardening with Nonproportional
Damping. Parkfield Earthquake

Fig. 8.21 Yielded Members of EBF Models for Design 1.
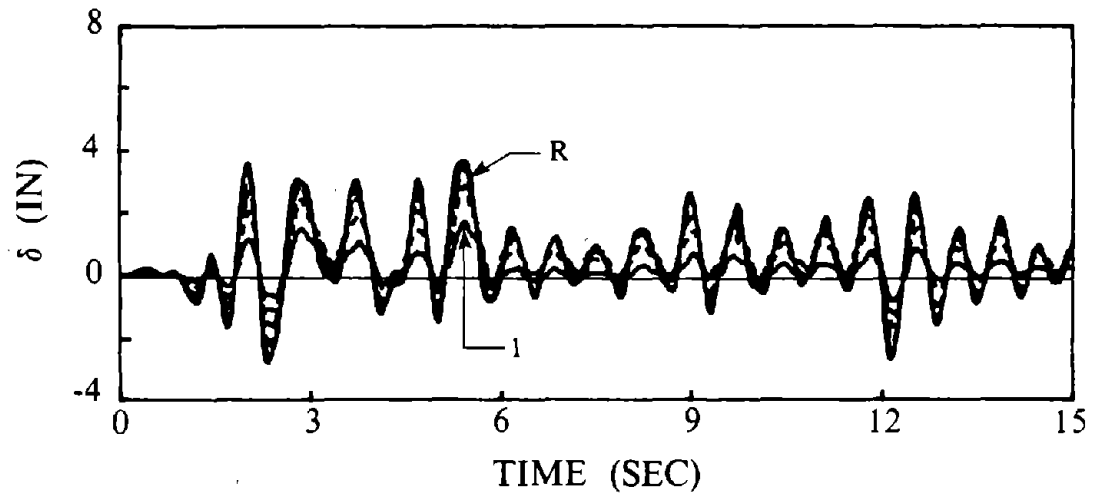
(a)   Strain Hardening with Nonproportional Damping, 1.5 * El Centro Earthquake
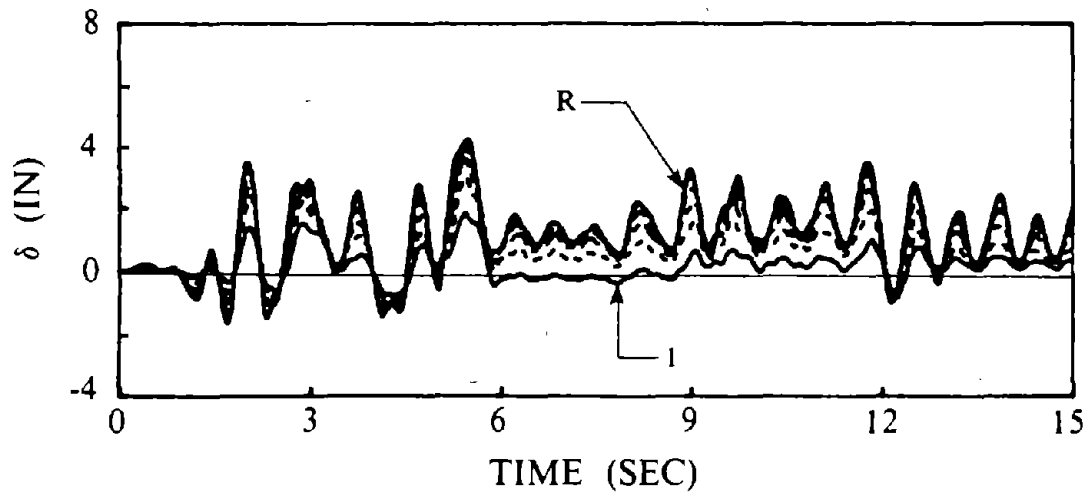
(b)   Elastic-Perfectly Plastic with Nonproportional Damping. 1.5 * El Centro Earthquake

Fig. 8.22   (Continued) Lateral Floor Displacements for EBF Models of Design 1.
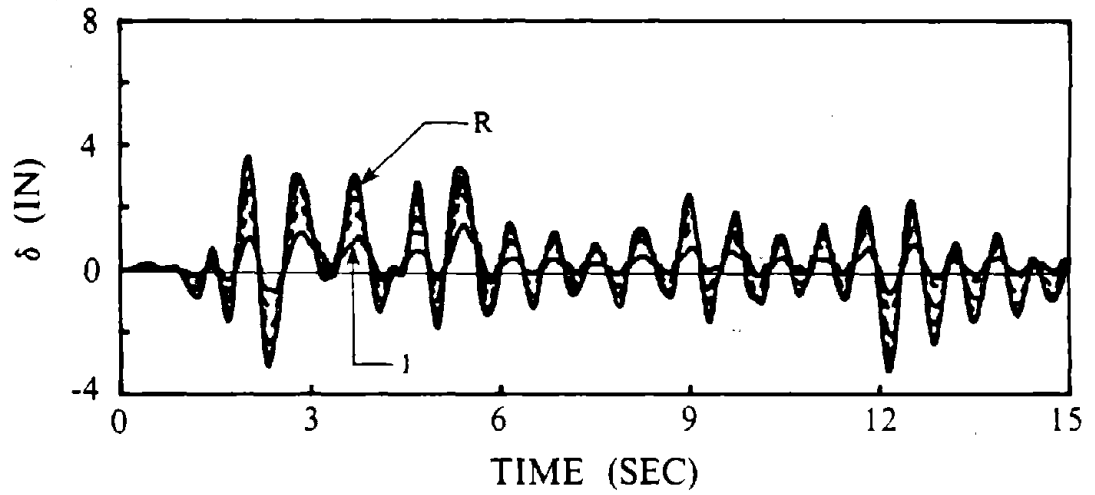
234

(c) Strain Hardening with Rayleigh Damping, 1.5 * El Centro Earthquake
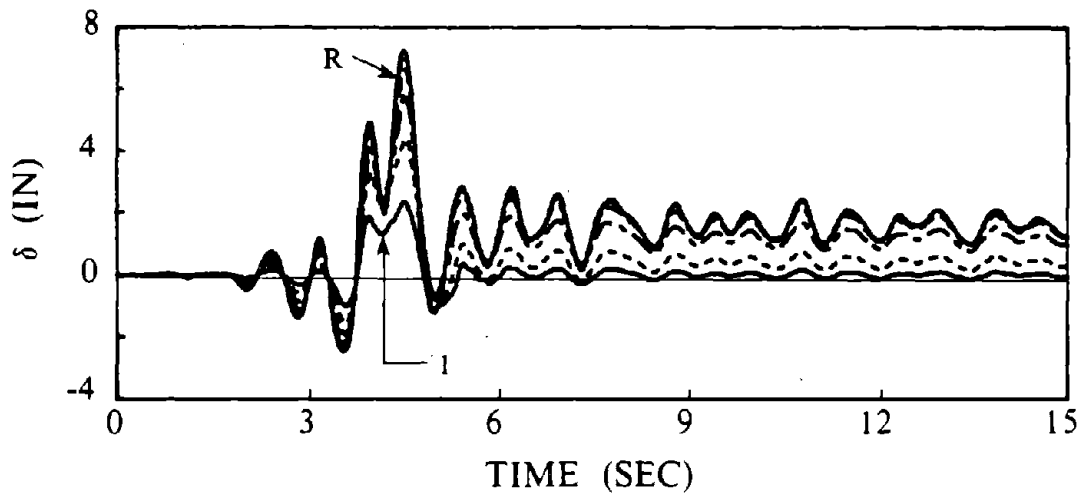
(d) Strain Hardening with Nonproportional Damping, Parkfield Earthquake

Fig. 8.22   Lateral Floor Displacements for EBF Models of Design 1.
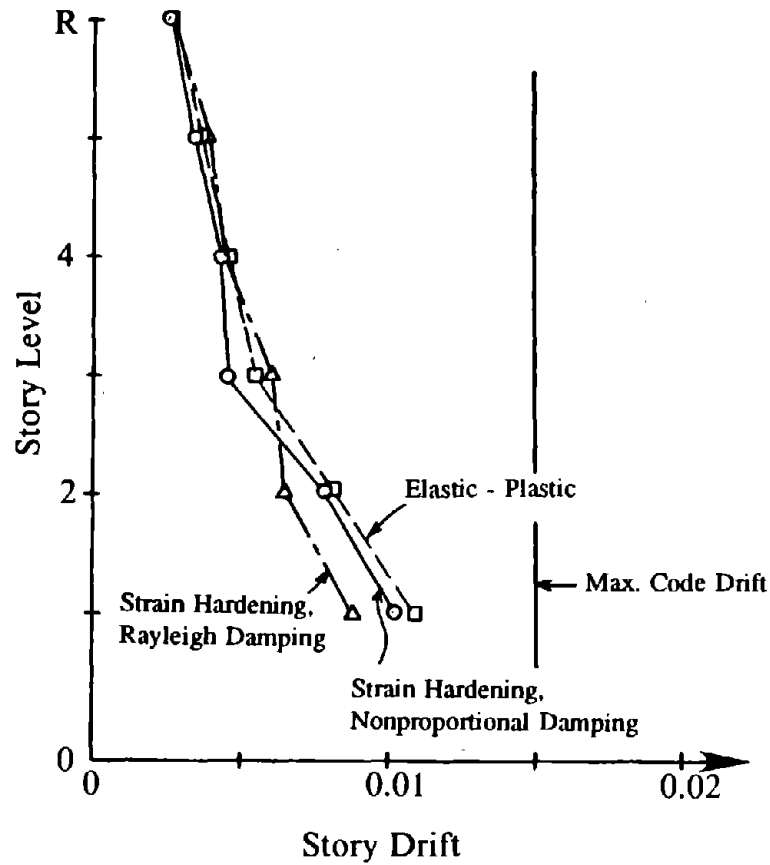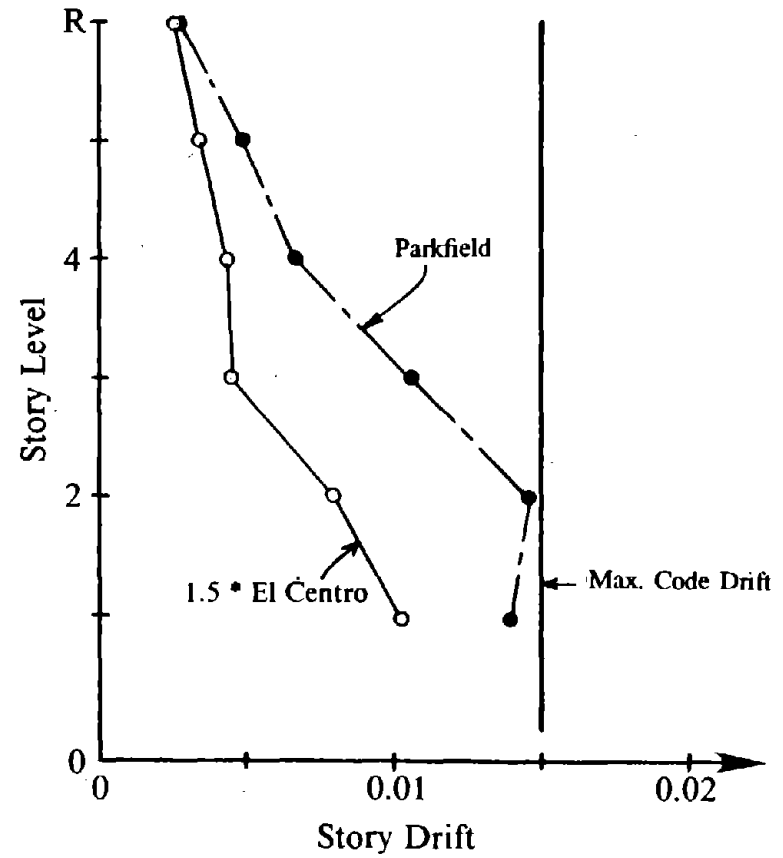
(a) 1.5 * El Centro Earthquake

(b) 1.5 * El Centro Earthquake and Parkfield Earthquake,Strain Hardening with Nonproportional Damping

Fig. 8.23 Maximum Story Drift for EBF Models of Design 1.

236
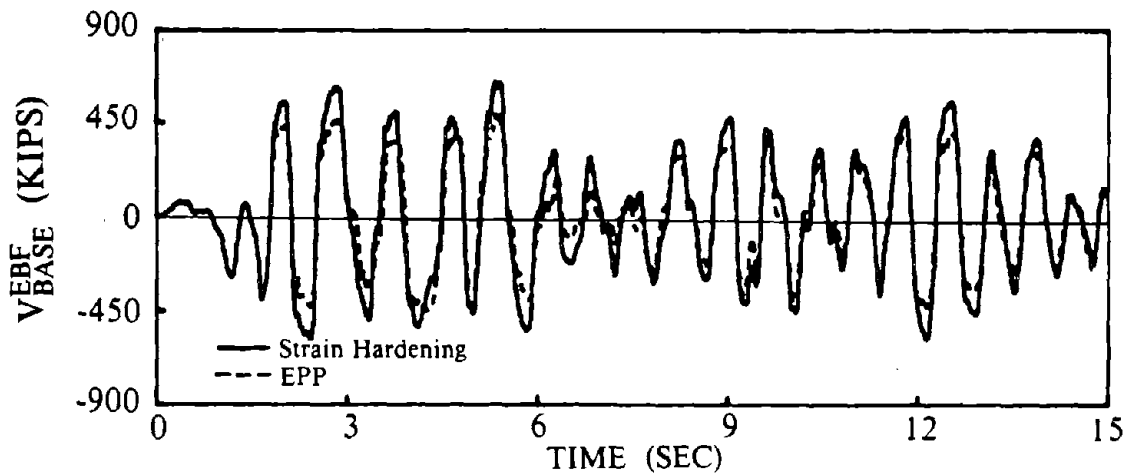

(a) EPP and Strain Hardening Models with Nonproportional Damping, 1.5 * El Centro Earthquake
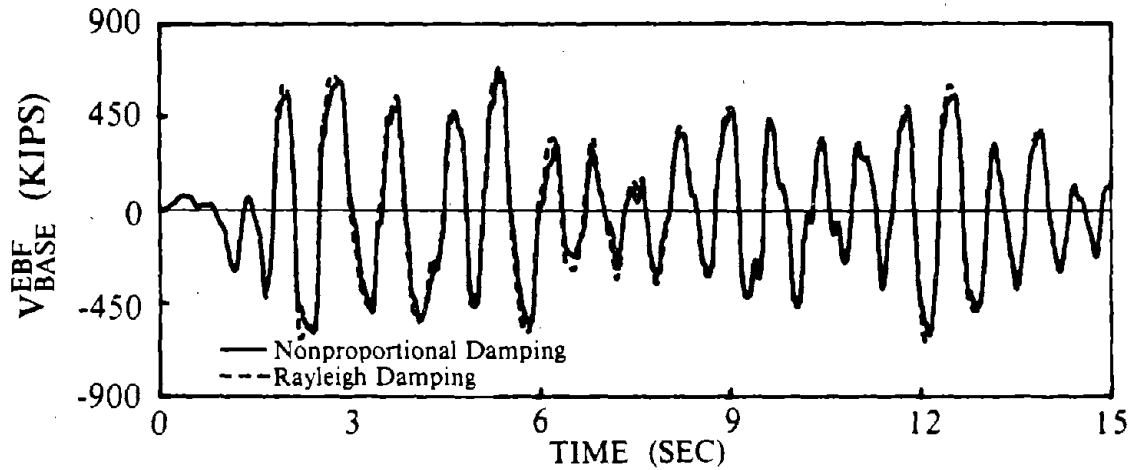
(b) Nonproportional and Rayleigh Damped Models with Strain Hardening, 1.5 * El Centro Earthquake.
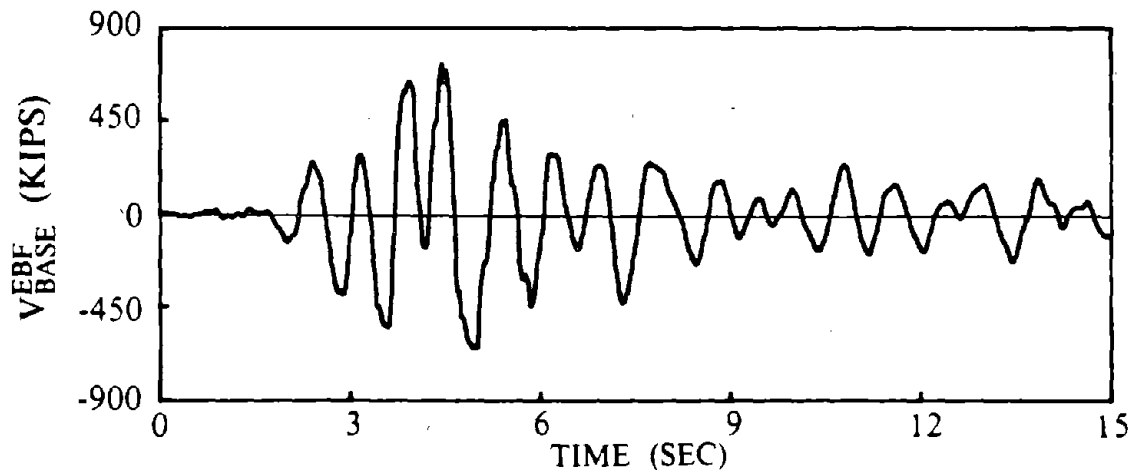
(c) Nonproportional Damped Model with Strain Hardening, Parkfield Earthquake

Fig. 8.24 Base Shear Time Histories for EBF Models of Design 1.
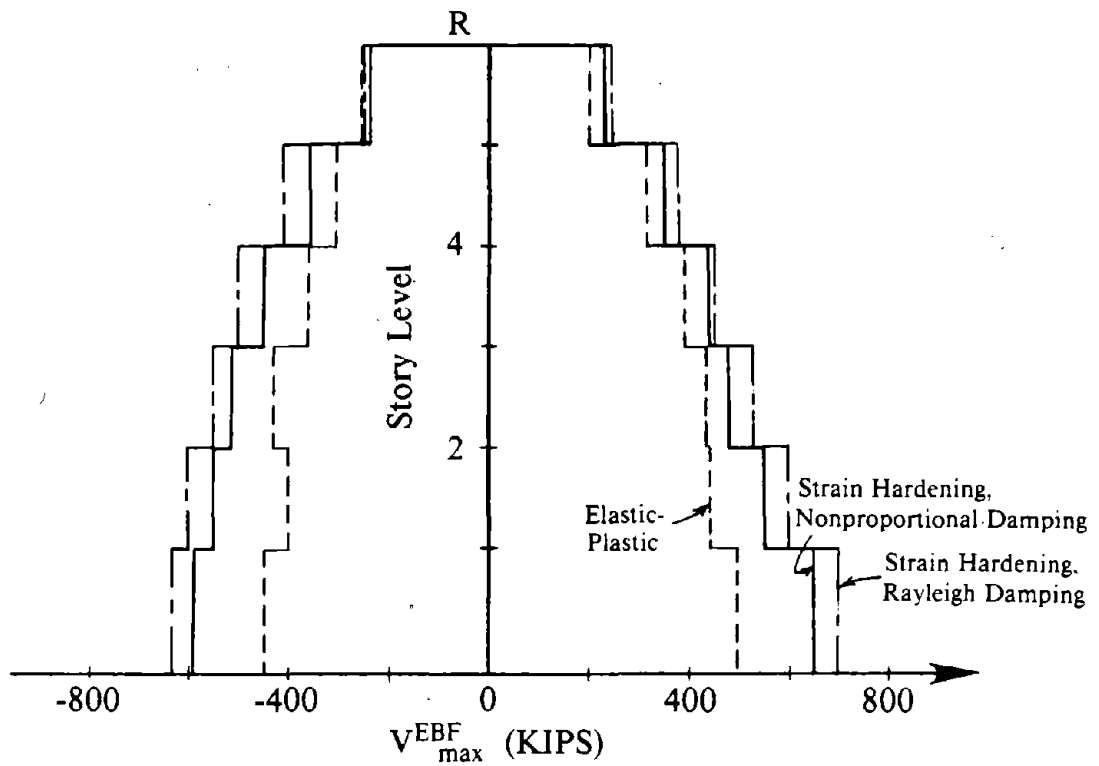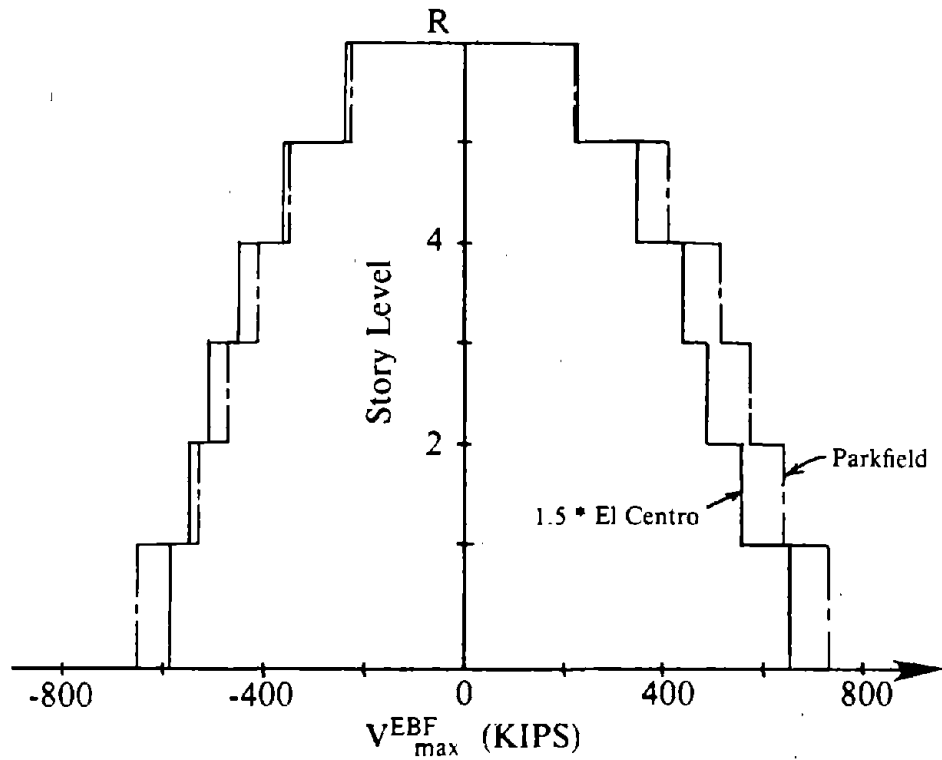
(a) 1.5 * El Centro Earthquake

(b)   1.5 * El Centro Earthquake and Parkfield Earthquake, Strain Hardening with Nonproportional Damping

Fig. 8.25   Story Shear Envelopes for EBF Models of Design 1.
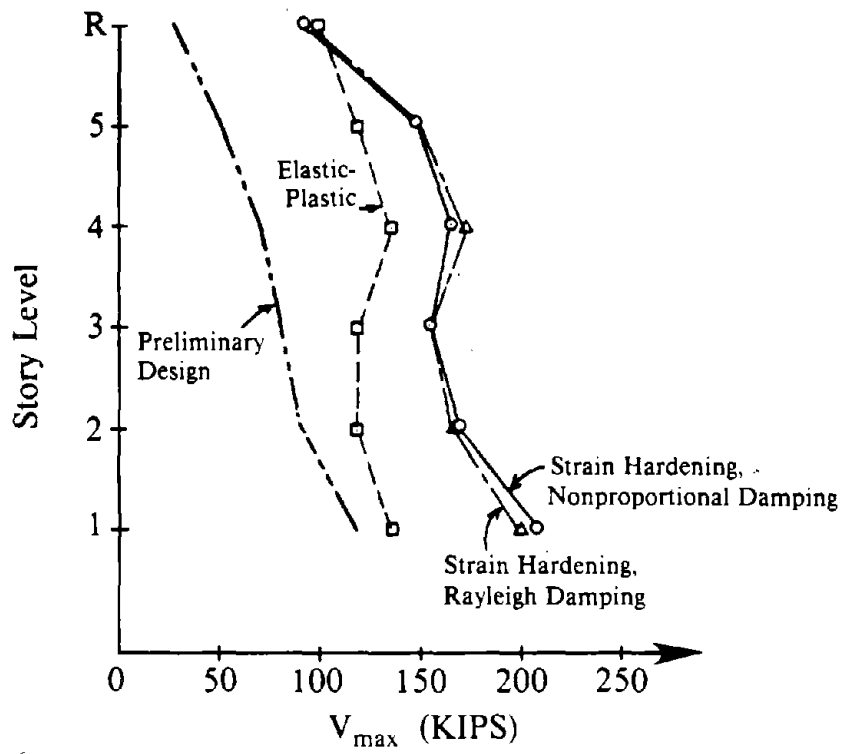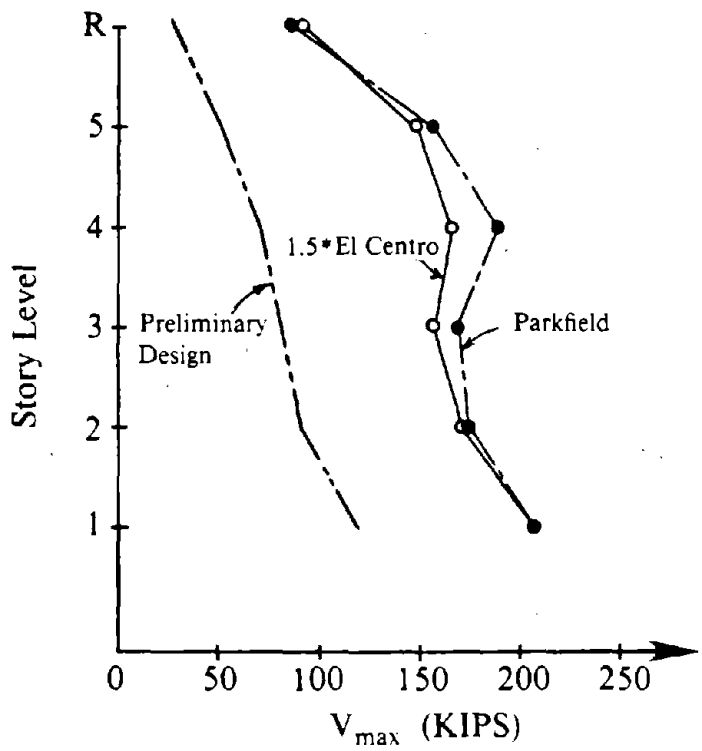
(a) 1.5 * El Centro Earthquake

(b) 1.5 * El Centro Earthquake and Parkfield Earthquake, Strain Hardening with Nonproportional Damping

Fig. 8.26   Maximum Link Shear Forces for EBF Models of Design 1.
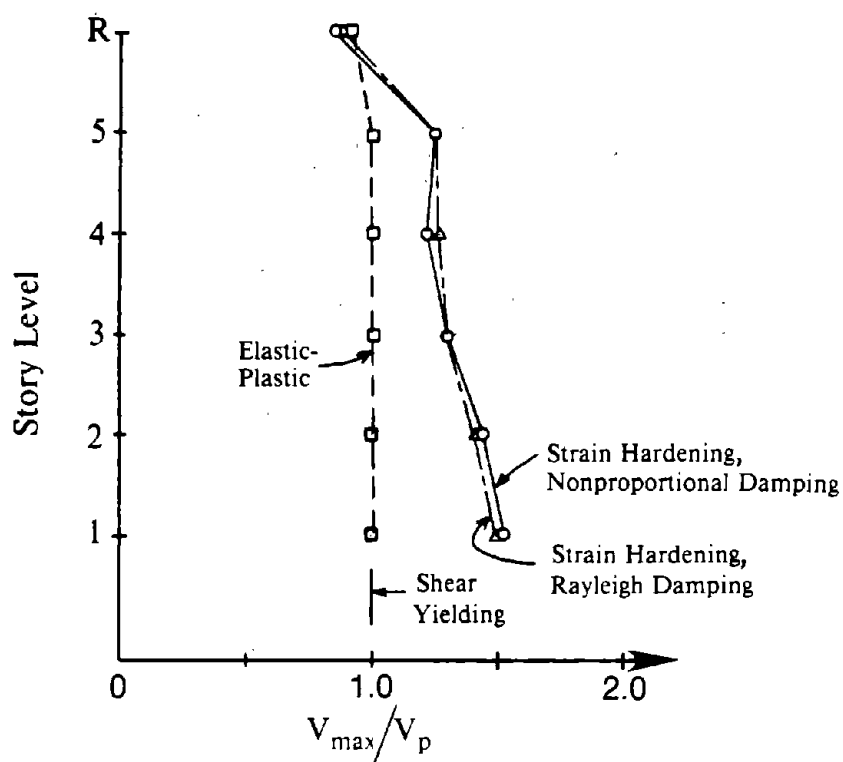
(a) 1.5*El Centro Earthquake
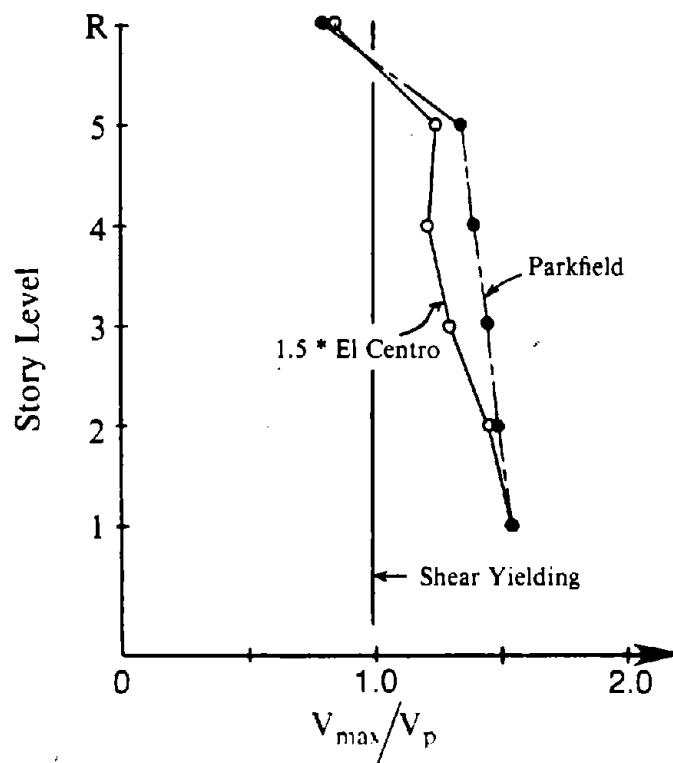
(b)   1.5 * El Centro Earthquake and Parkfield Earthquake, Strain Hardening with Proportional Damping

Fig. 8.27   Normalized Maximum Link Shear Forces for EBF Models of Design 1.
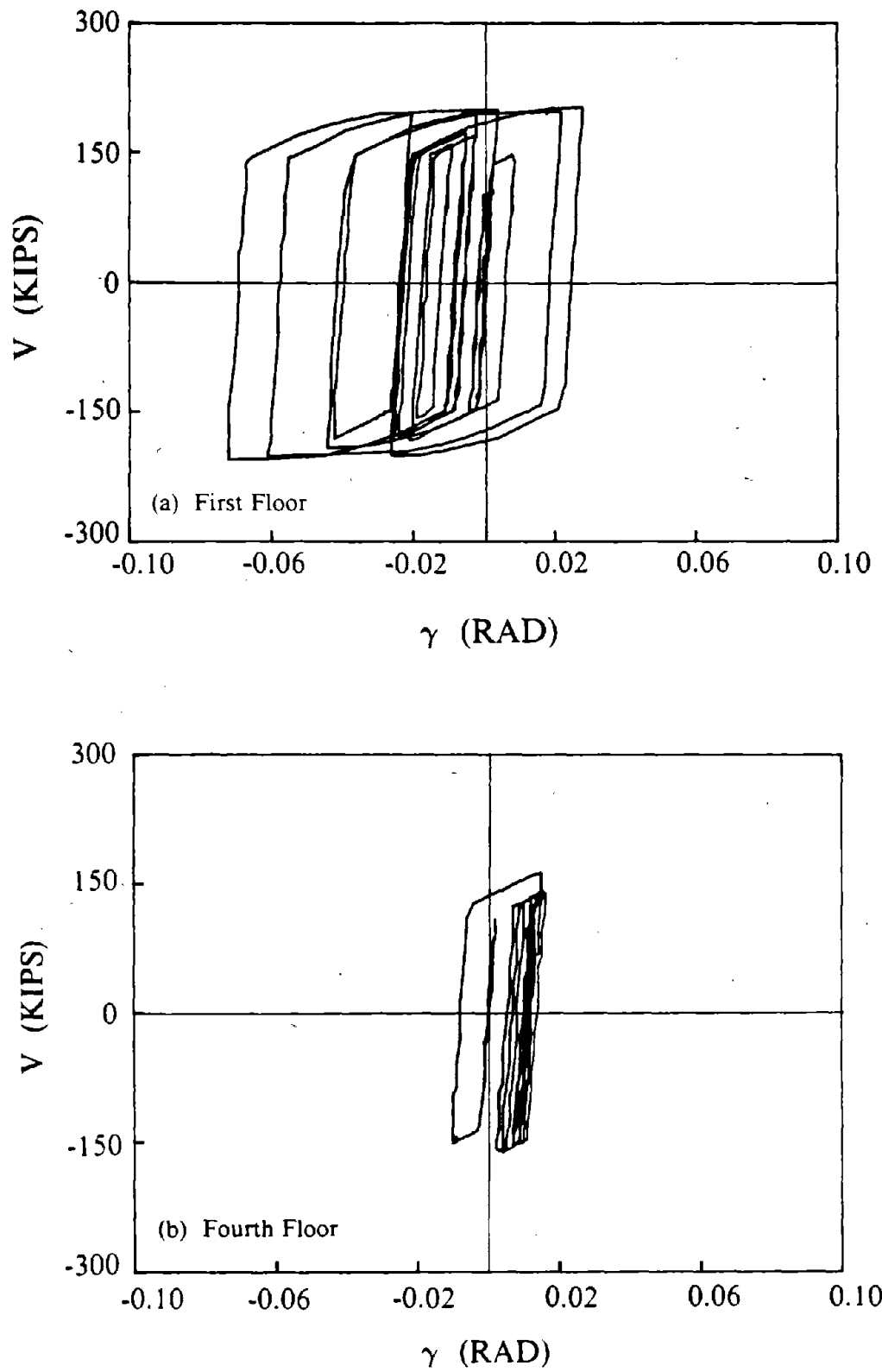
Fig. 8.28 Shear-Deformation Hysteretic Response of Links for Design 1 Subjected to 1.5* El Centro Earthquake, Strain Hardening with Nonproportional Damping.
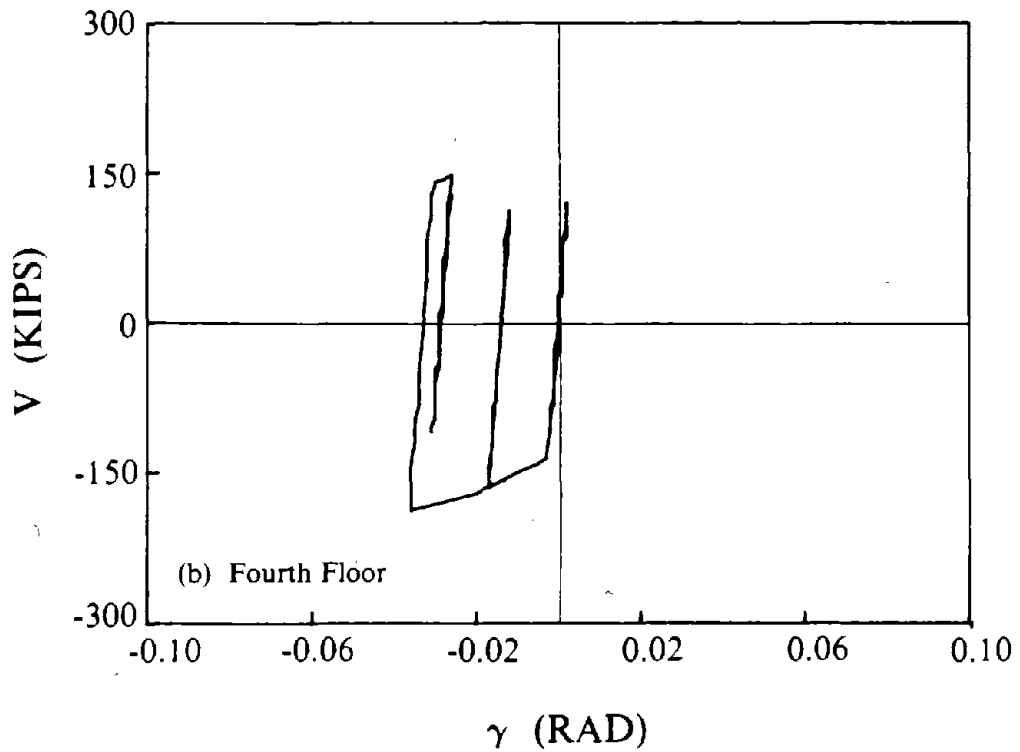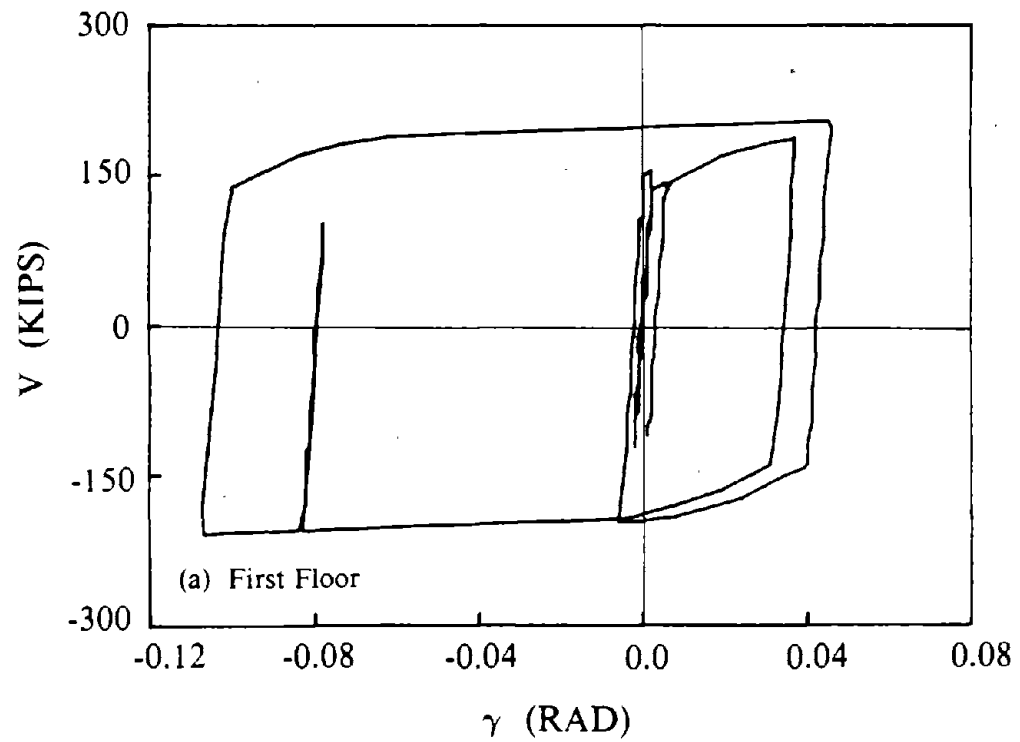
Fig. 8.29   Shear-Deformation Hysteretic Response of Links for Design 1 Subjected to Parkfield Earthquake, Strain Hardening with Nonproportional Damping.
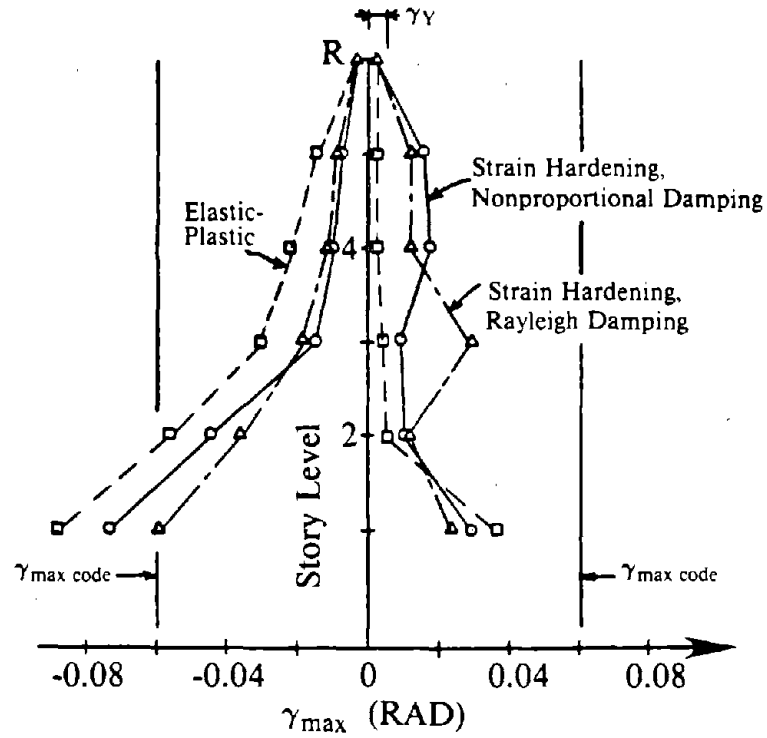
(a) 1.5 * El Centro Earthquake
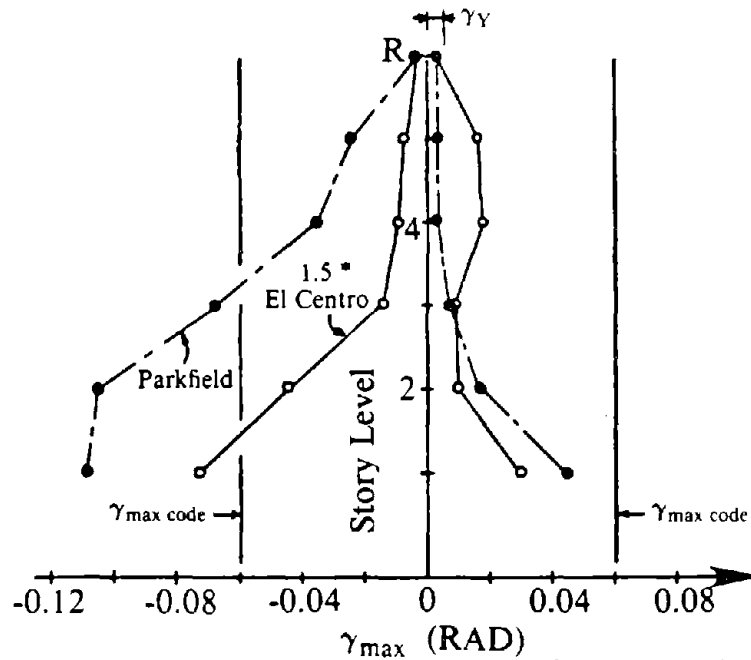
(b) 1.5 * El Centro Earthquake and Parkfield Earthquake.
Strain Hardening with Nonproportional Damping

Fig. 8.30 Link Deformation Envelopes for EBF Models of Design 1.
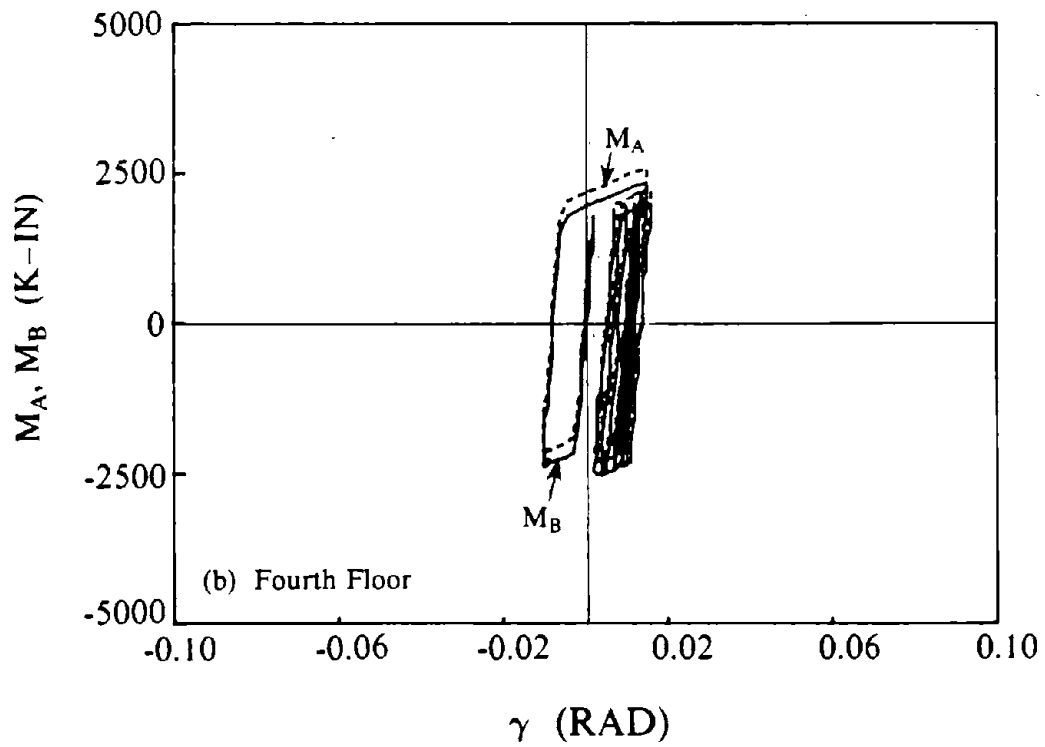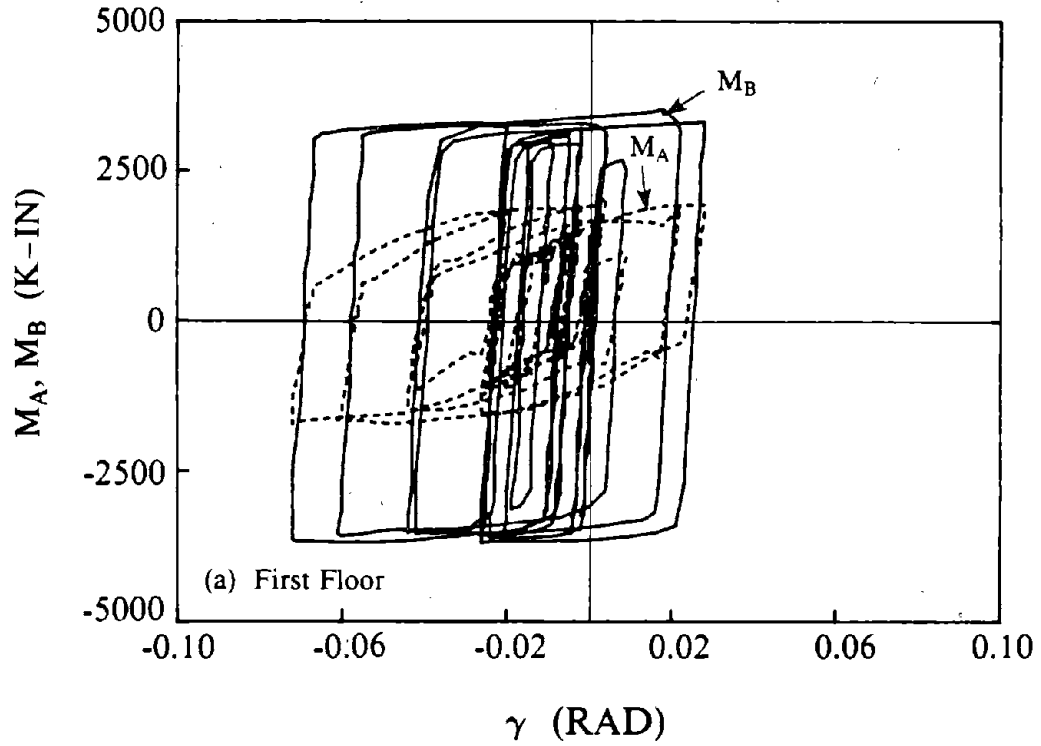
Fig. 8.31   Moment-Deformation Hysteretic Response of Links for Design 1 Subjected to 1.5 * El Centro Earthquake, Strain Hardening with Nonproportional Damping.
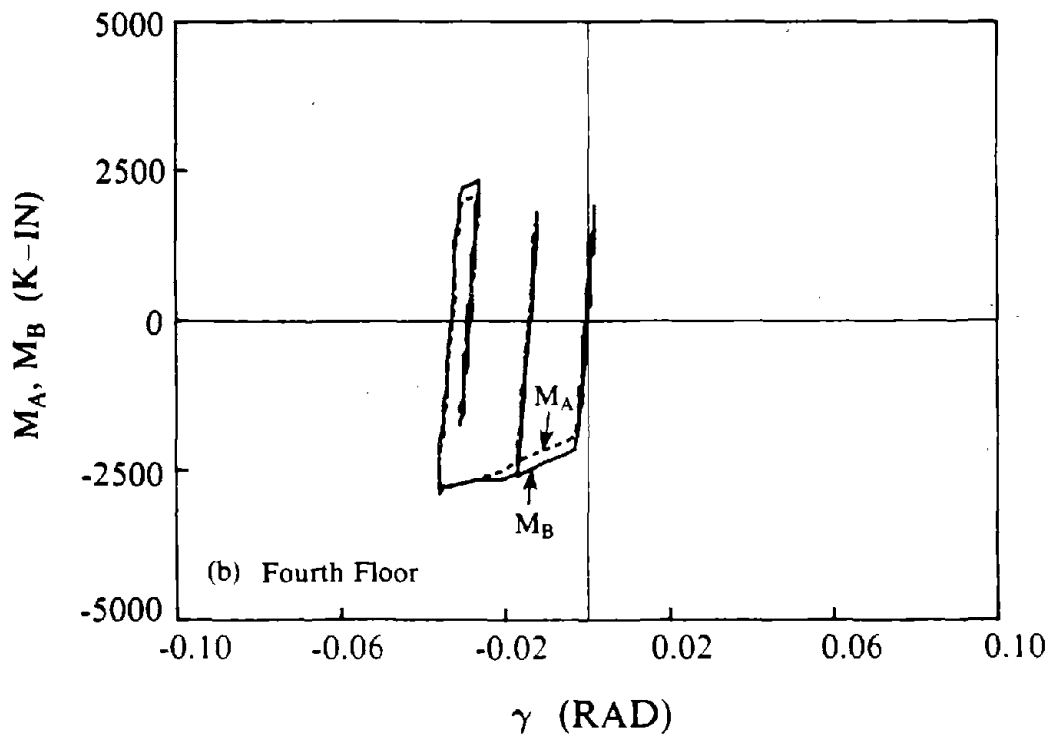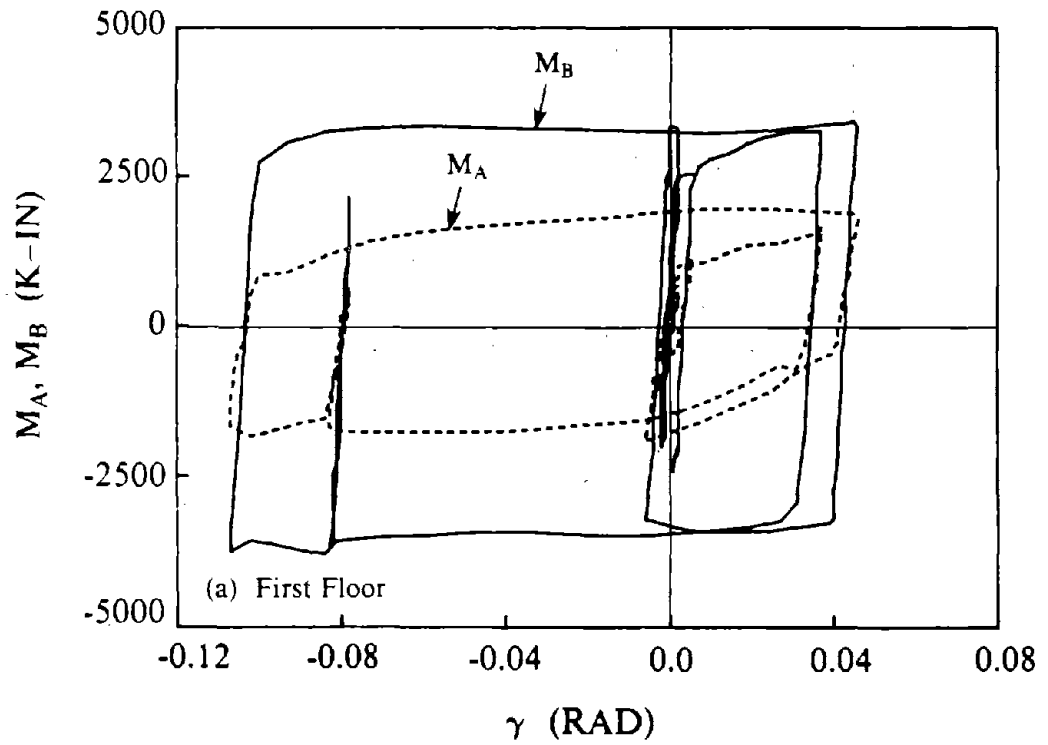
Fig. 8.32 Moment-Deformation Hysteretic Response of Links For Design 1 Subjected to Parkfield Earthquake, Strain Hardening with Nonproportional Damping.
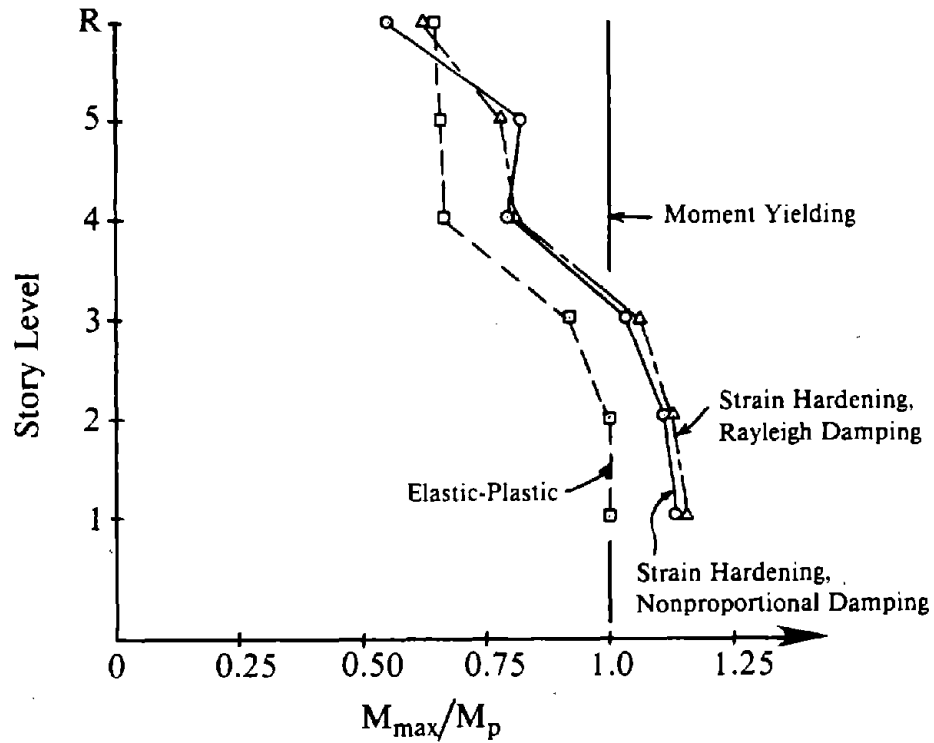
(a) 1.5 * El Centro Earthquake
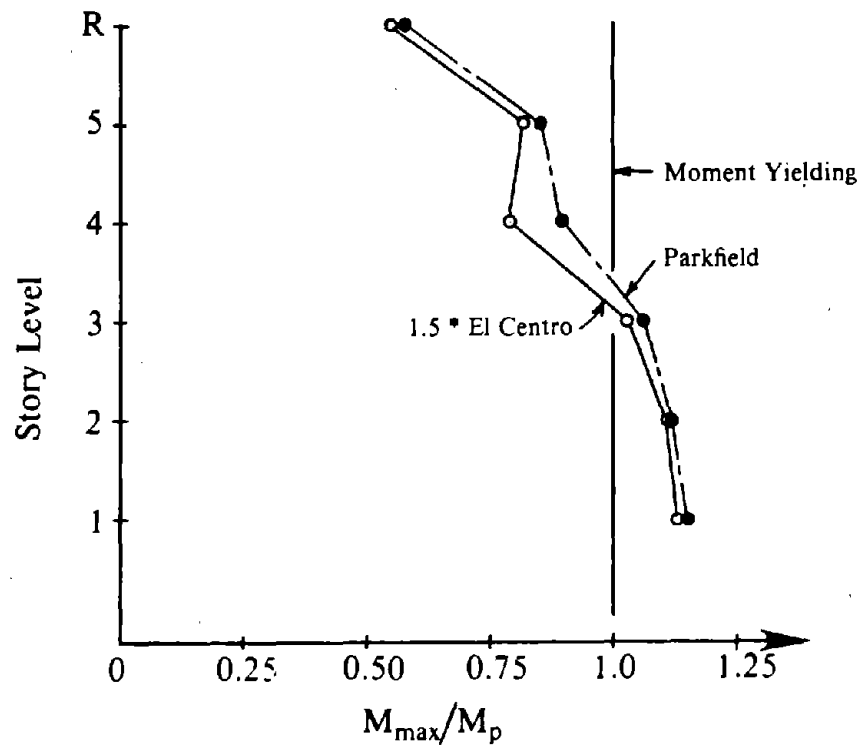
(b) 1.5 * El Centro Earthquake and Parkfield Earthquake,
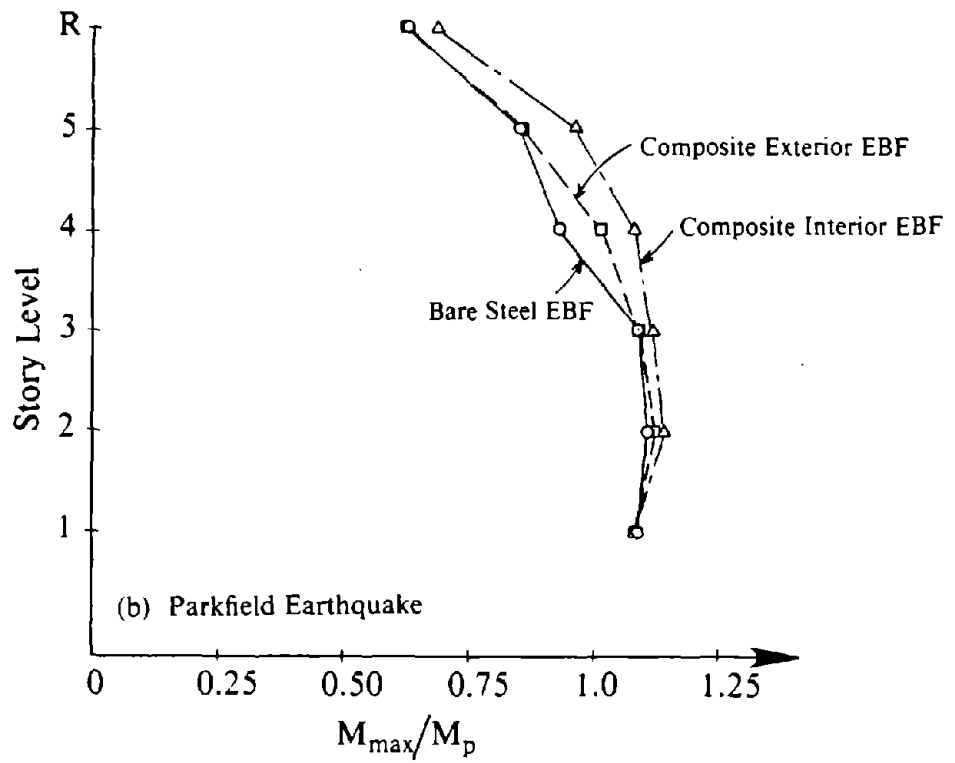Strain Hardening with Nonproportional Damping.

Fig. 8.33   Normalized Maximum Link End Moments for EBF Models of Design 1.
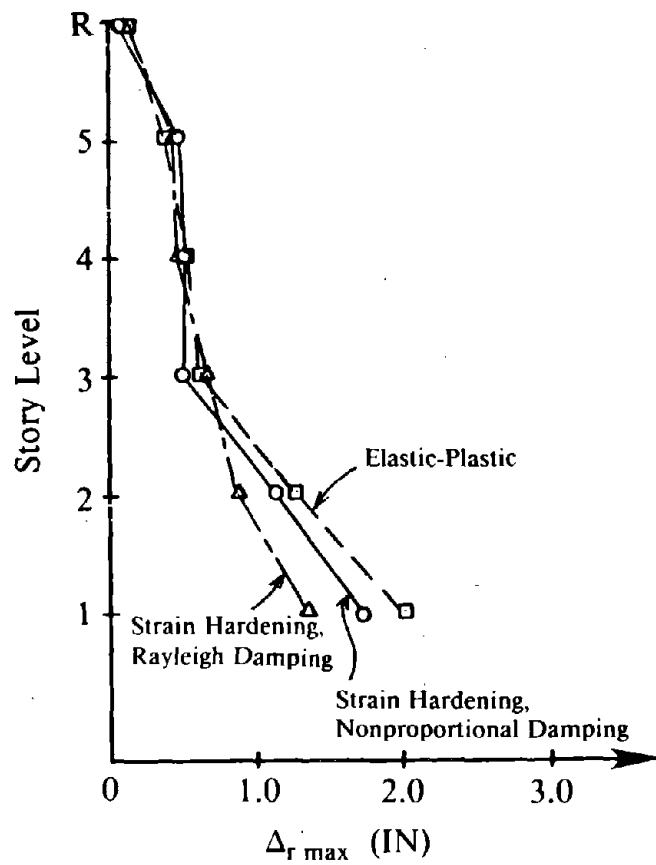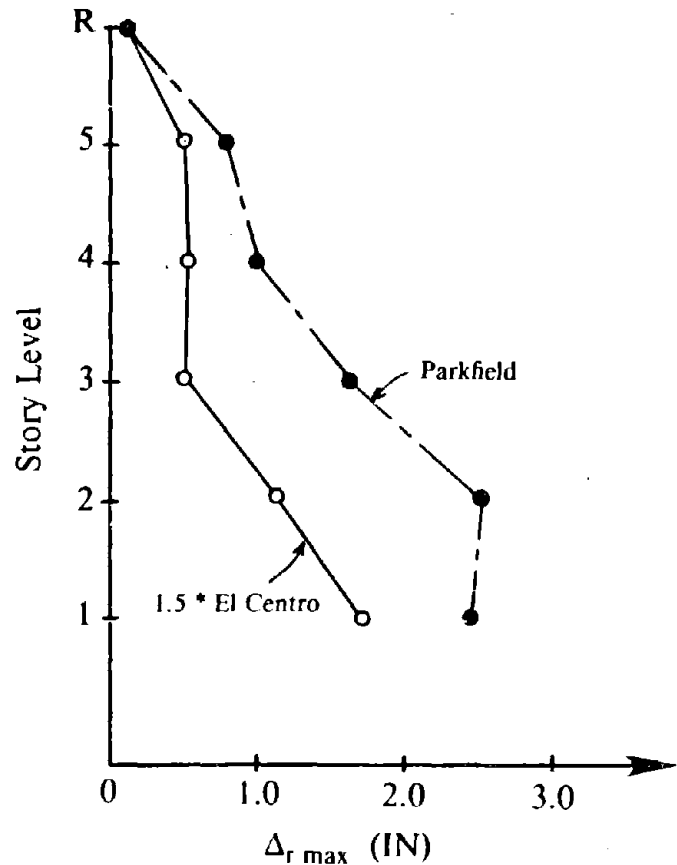
(a)   1.5 * El Centro Earthquake

(b)   1.5 * El Centro Earthquake and Parkfield Earthquake,
Strain Hardening with Nonproportional Damping

Fig. 8.34   Maximum Relative End Displacement of Links in EBF Models of Design 1.
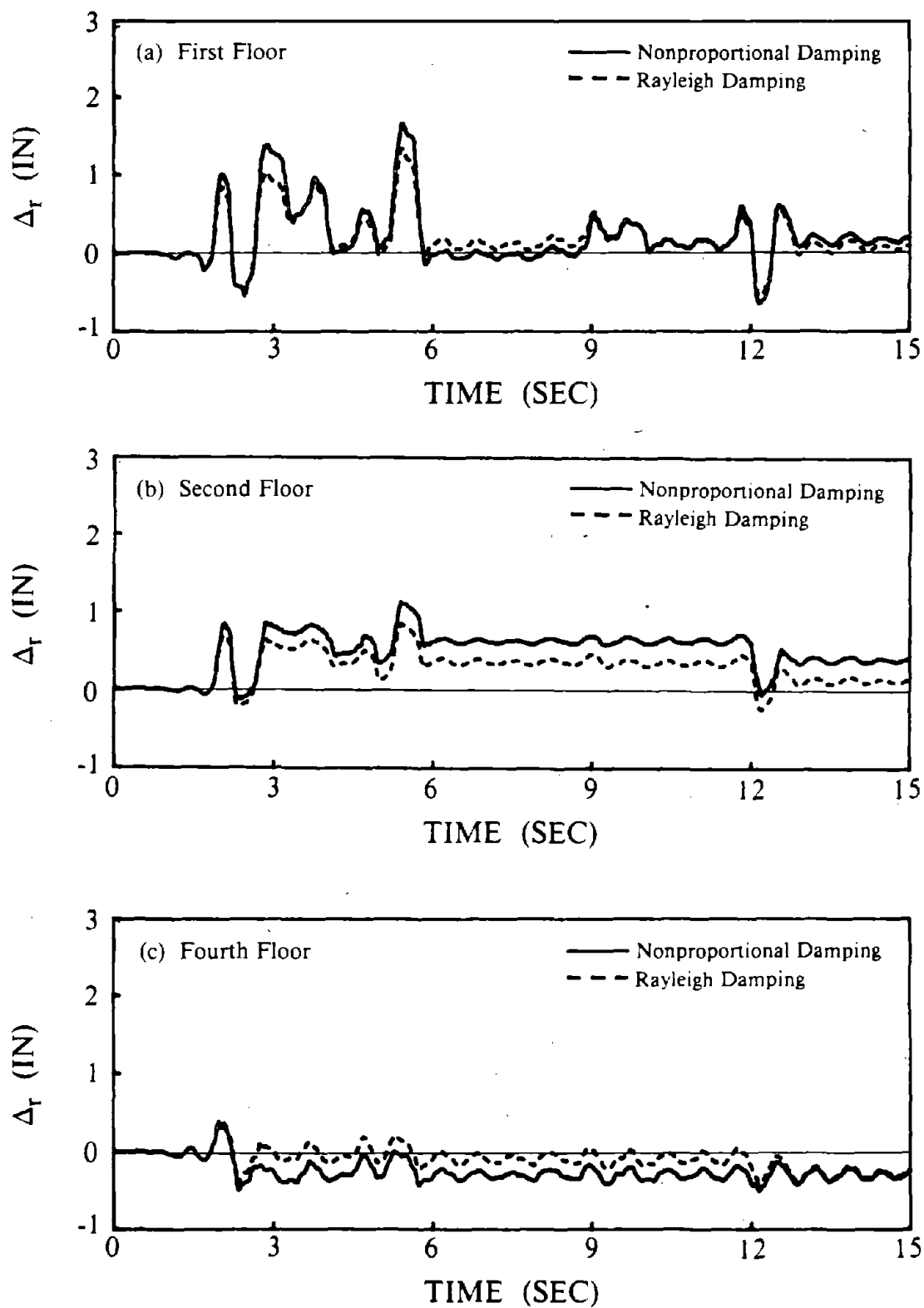
Fig. 8.35   Relative End Displacement Time Histories for Links of Design 1 with Strain Hardening, 1.5 * El Centro Earthquake.
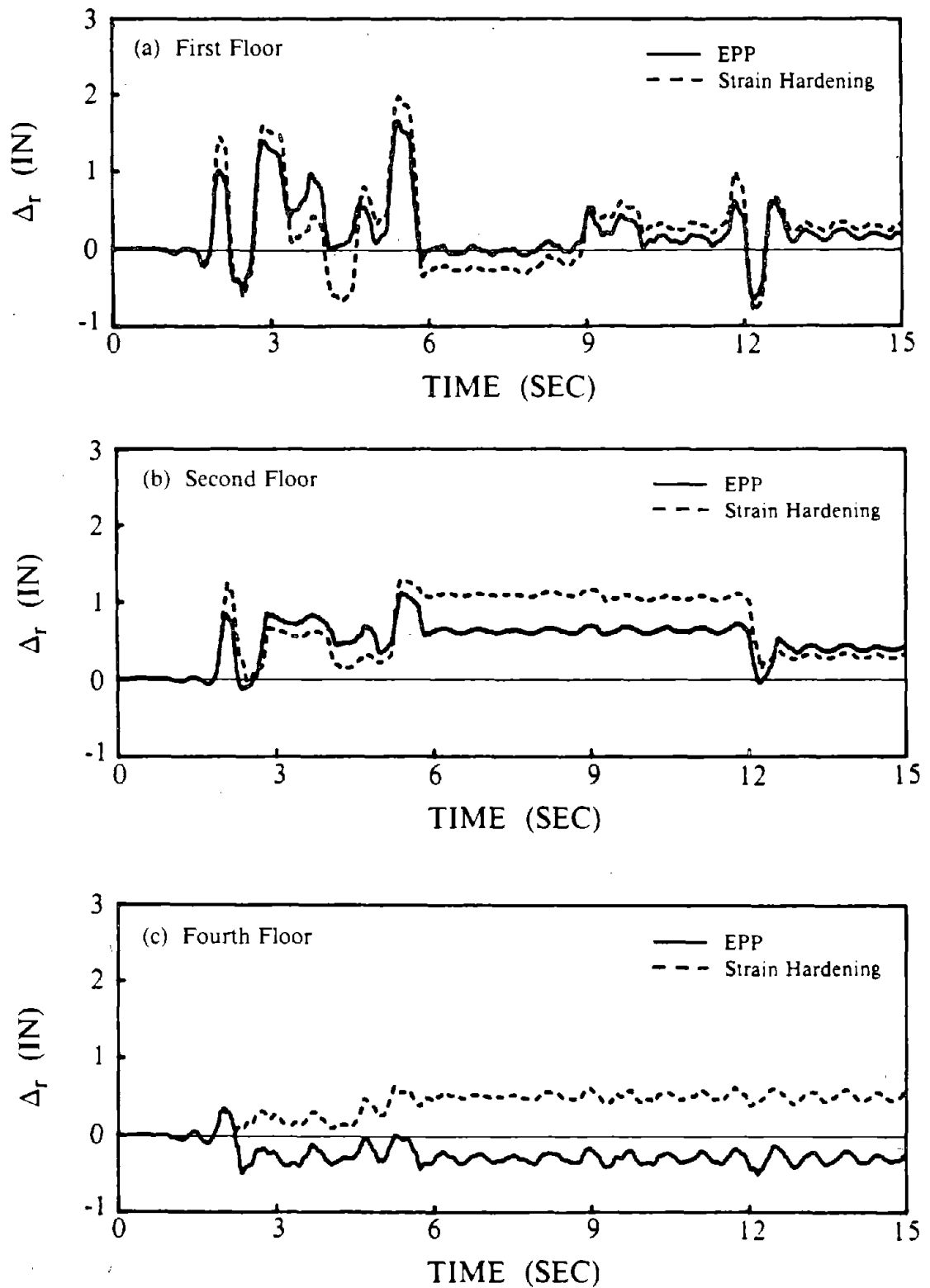
Fig. 8.36   Relative End Displacement Time Histories for Links of Design 1 with Nonproportional Damping, 1.5 * El Centro Earthquake.
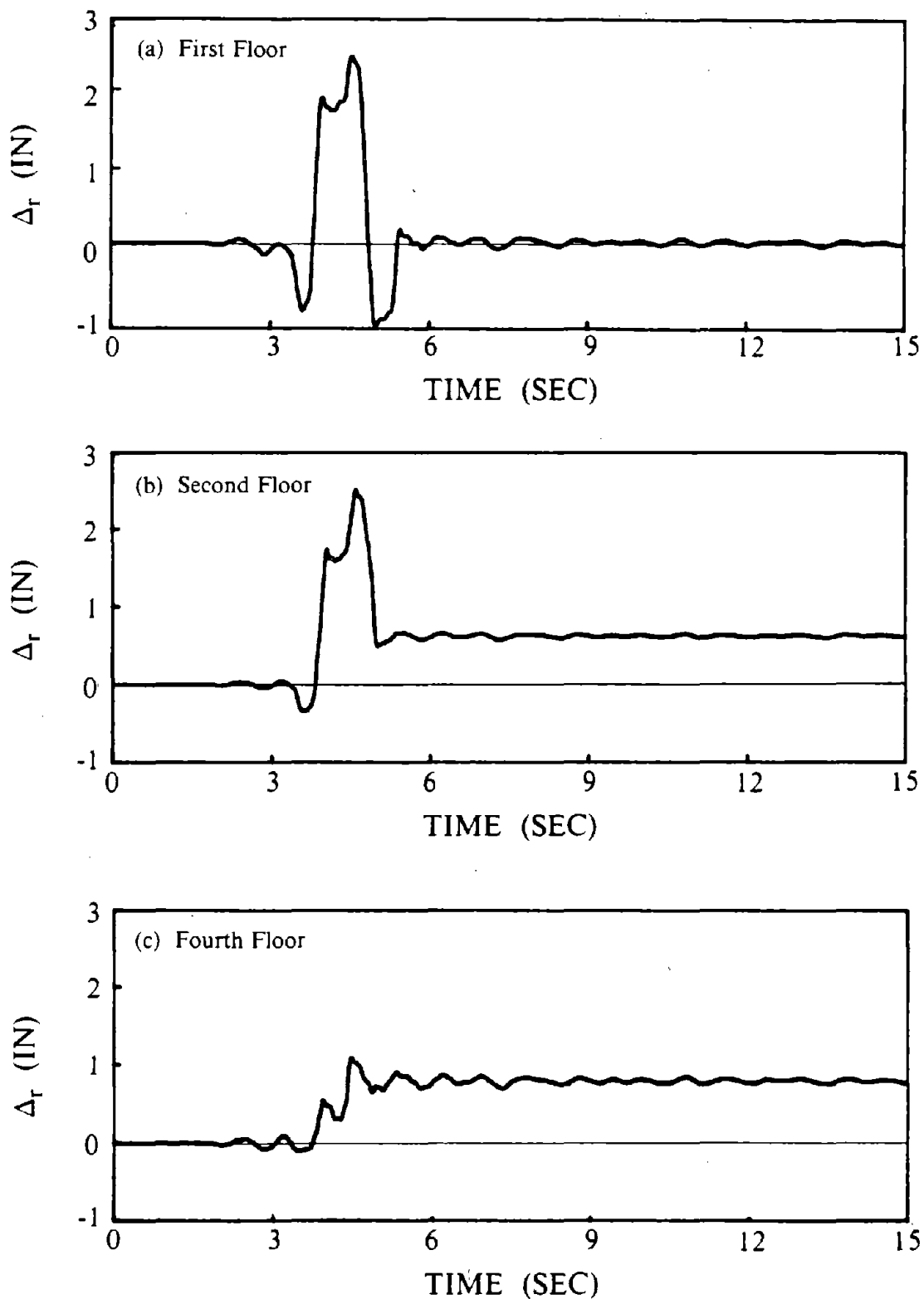
Fig. 8.37   Relative End Displacement Time Histories for Links of Design 1 with Strain Hardening, Parkfield Earthquake.

250
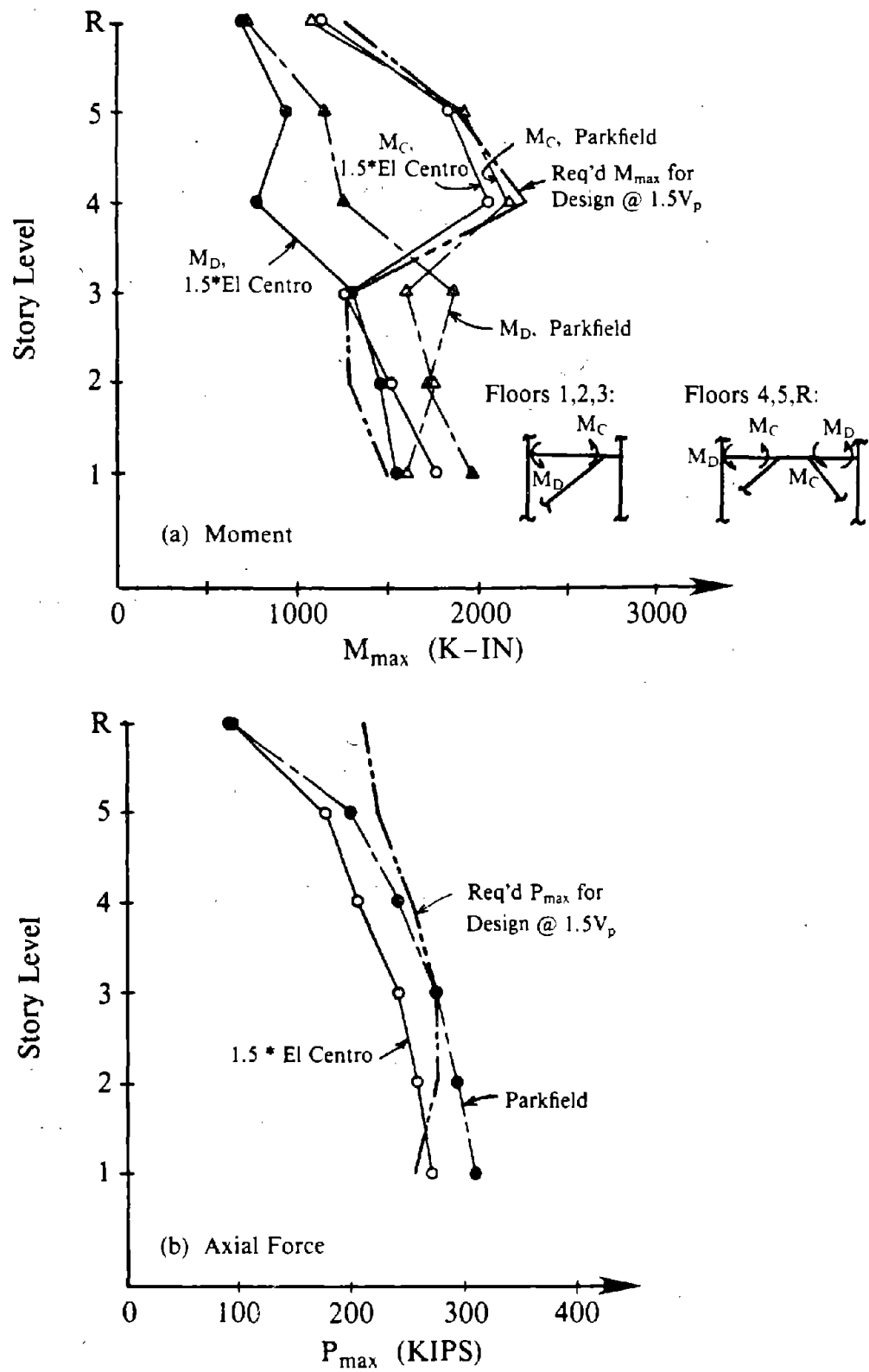
Fig. 8.38   Maximum Forces in Floor Beams Outside the Links for EBF Model with Strain
Hardening and Nonproportional Damping. Design 1.
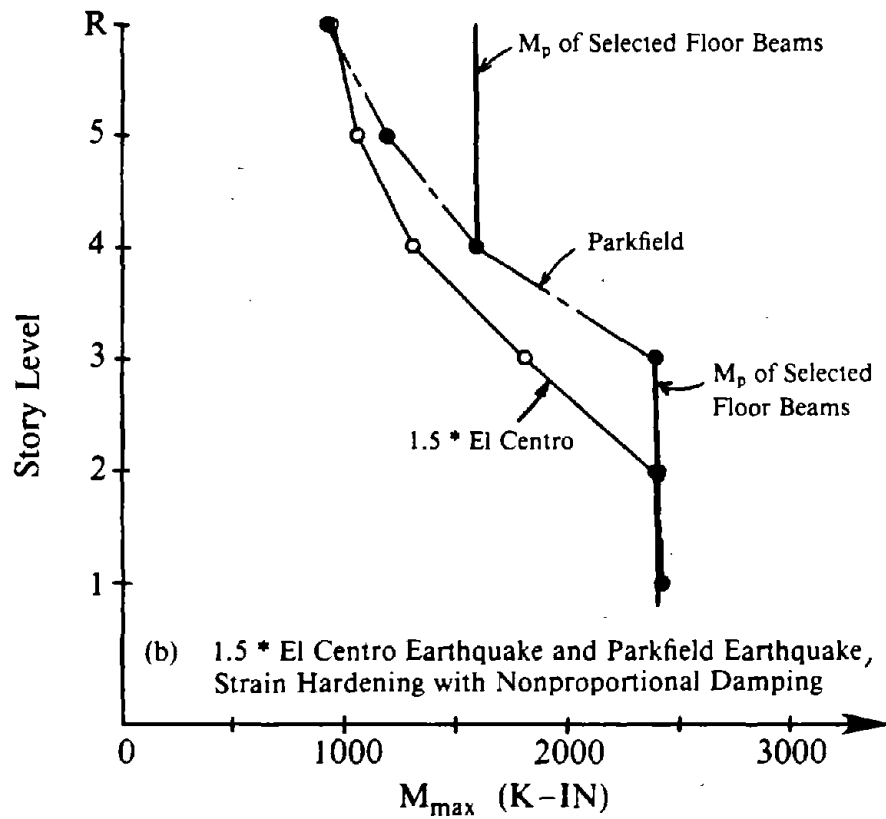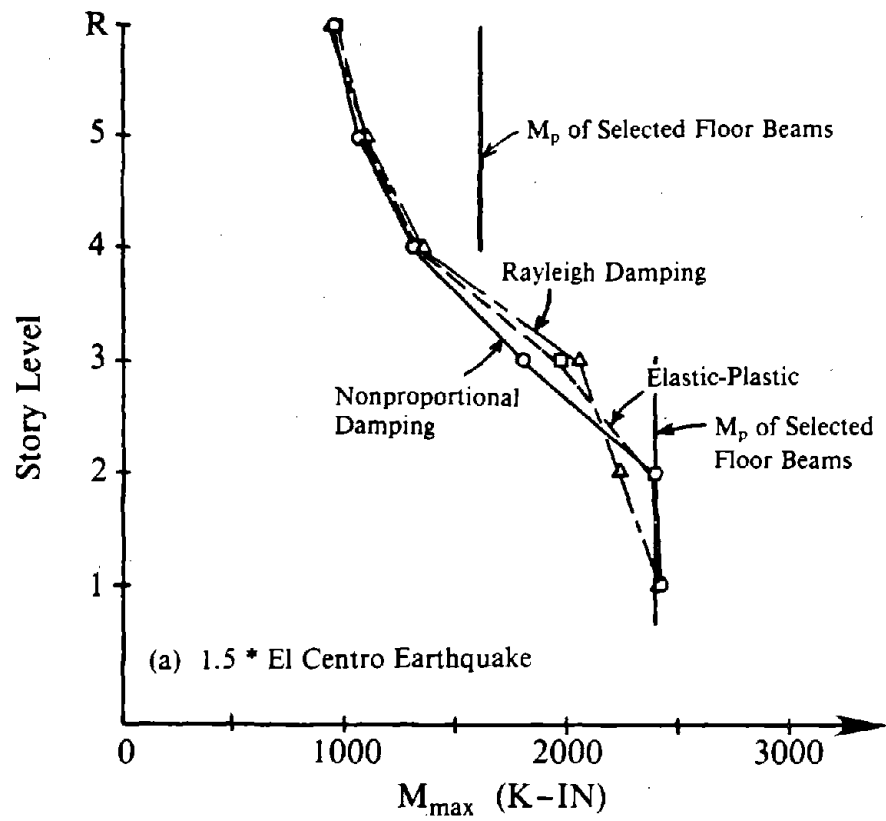
Fig. 8.39   Maximum Moments Developed in Floor Beams of Unbraced Panels for Design 1.
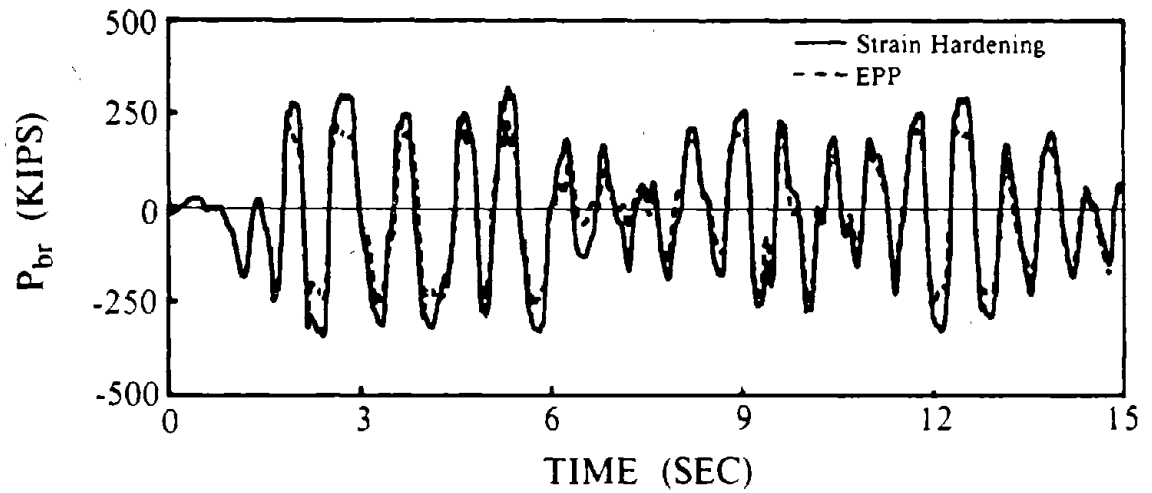
(a) 1.5 * El Centro Earthquake, Nonproportional Damping
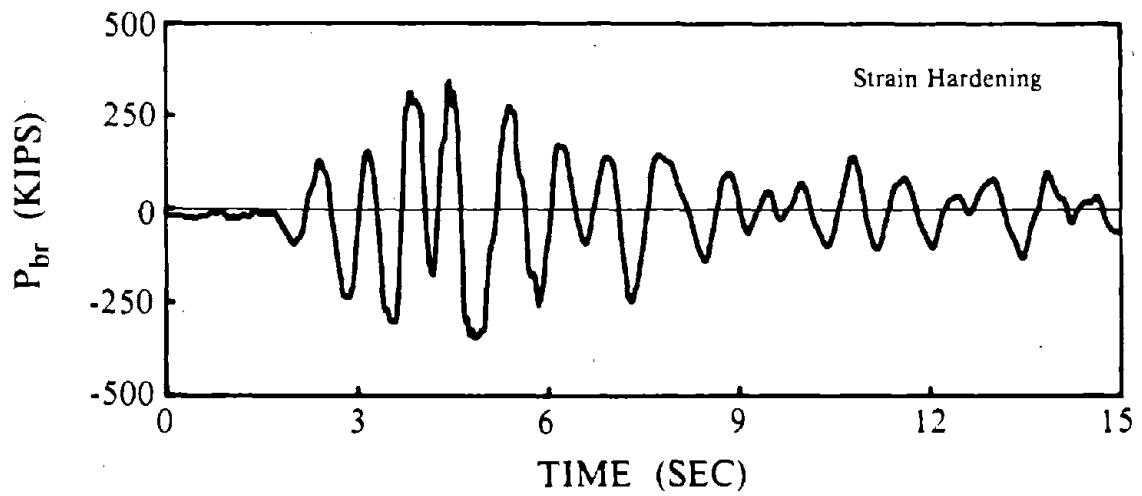
(b) Parkfield Earthquake, Nonproportional Damping

Fig. 8.40   Axial Force Time Histories of First Floor Brace, Design 1.
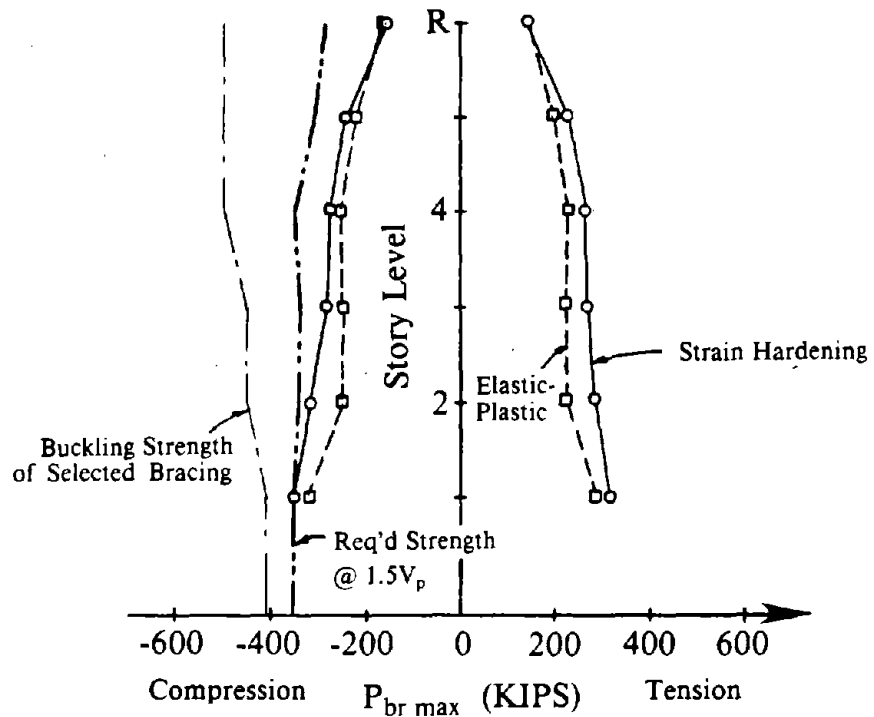
(a) 1.5 * El Centro Earthquake
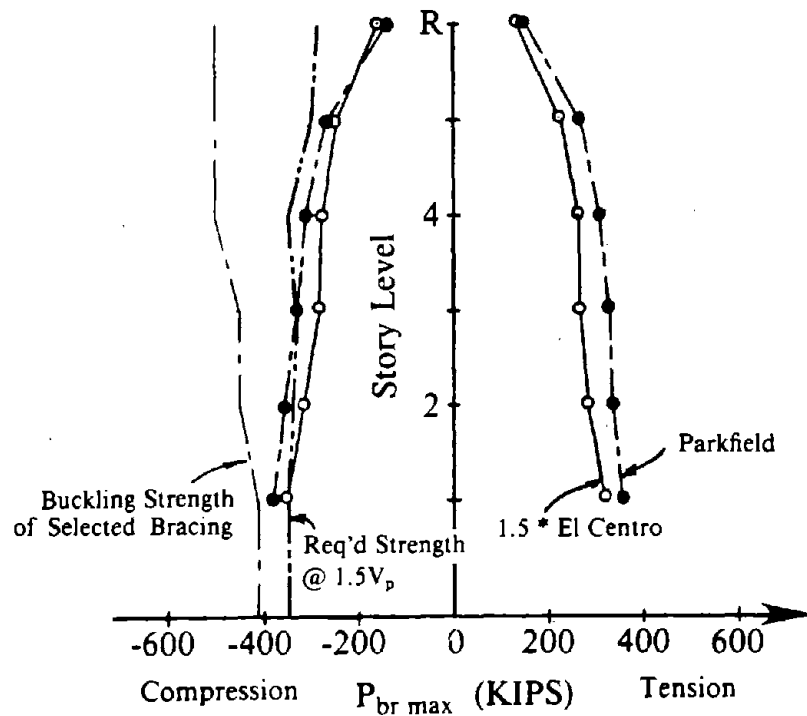
(b) 1.5 * El Centro Earthquake anJ Parkfield Earthquake, Strain Hardening

Fig. 8.41   Axial Brace Force Envelopes for Models with Nonproportional
Damping. Design 1.
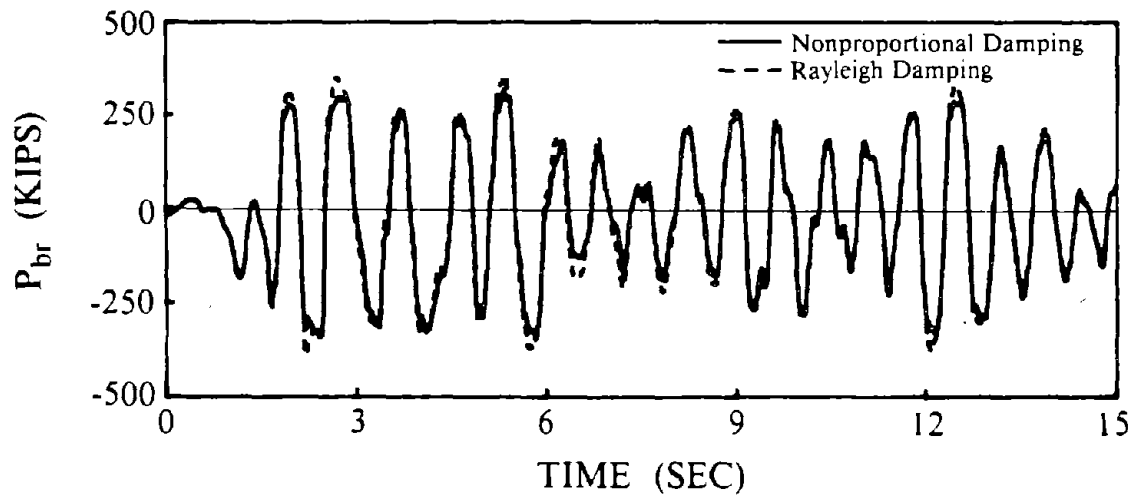
(a) Axial Brace Force
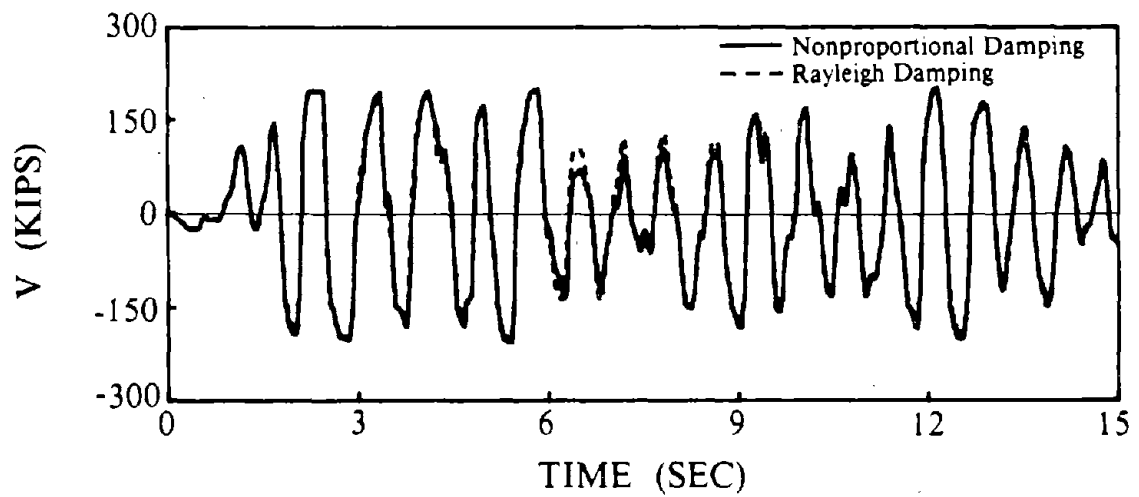
(b) Link Shear Force

Fig. 8.42   Response of First Floor Brace and Link of Design 1, EBF Model with Strain Hardening Subjected to 1.5 * El Centro Earthquake.
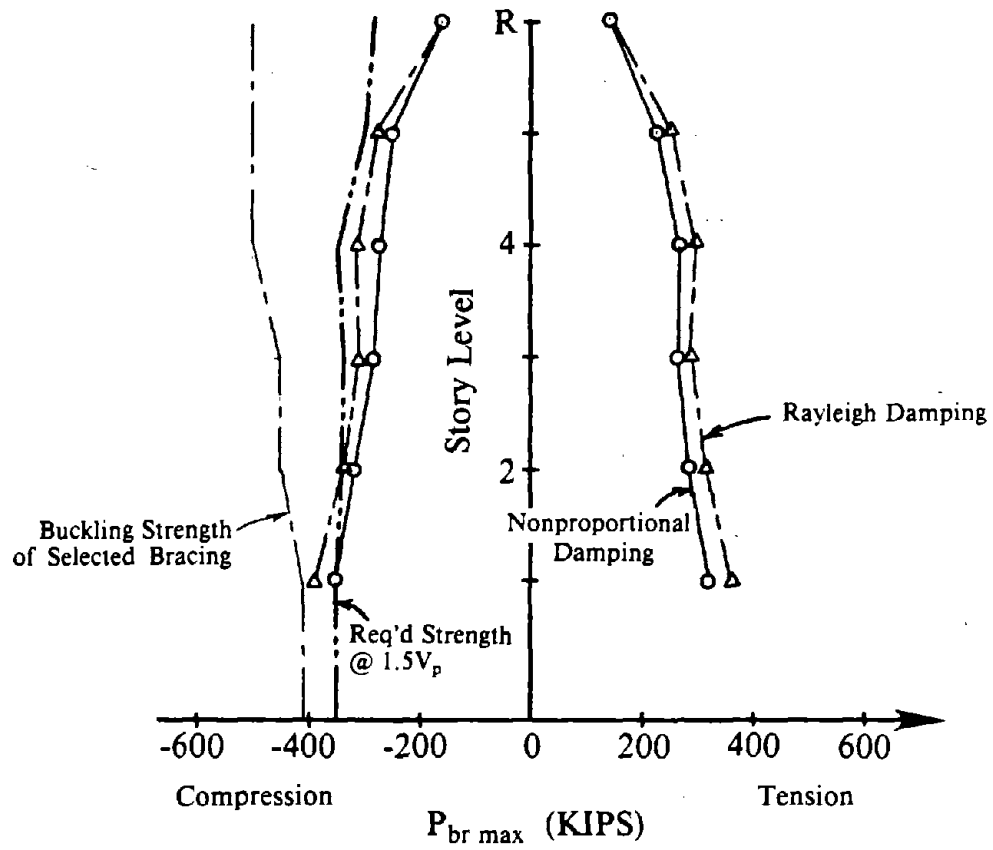
Fig. 8.43   Axial Brace Force Envelopes for Models with Strain Hardening Subjected to 1.5
            * El Centro Earthquake, Design 1.
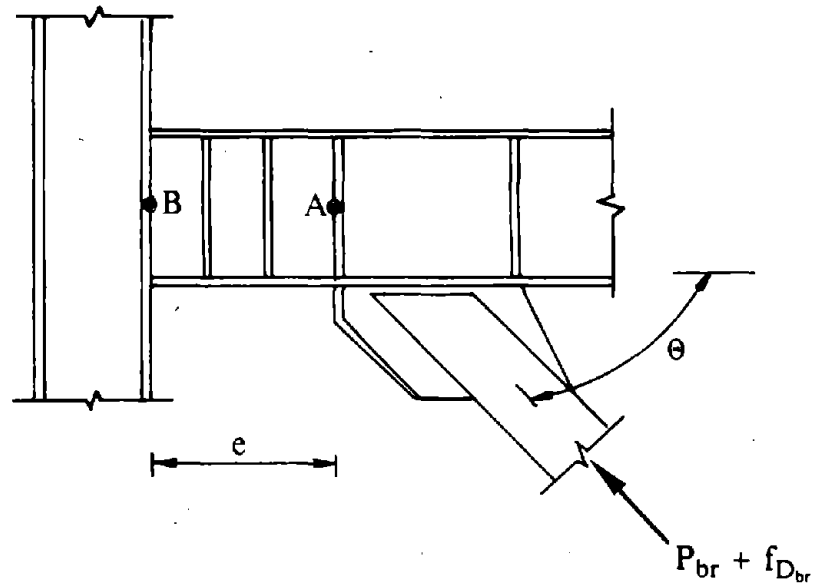
Proportional Damping is Assumed,

$$\underline{C} \doteq b_0 \underline{M} + b_1 \underline{K}$$

$$f_{D_{br}} + P_{br} = \frac{V_{LINK} + V_{bm}}{\sin\Theta} + \frac{f_I + f_{D_L} + f_{D_{bm}} + f_{D_m}}{\sin\Theta}$$
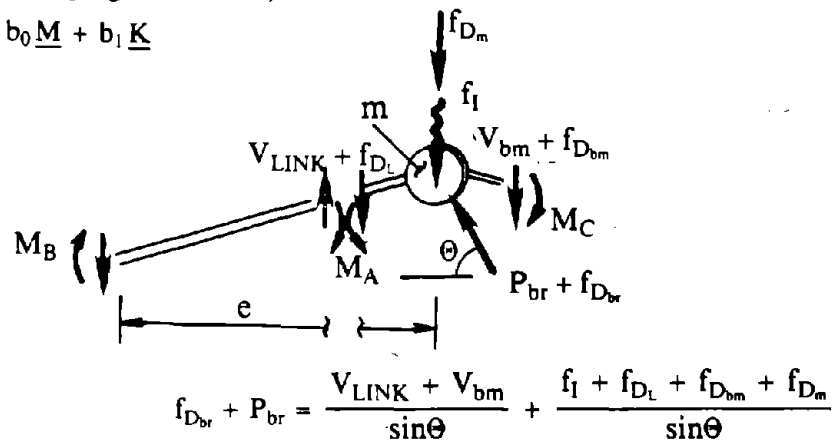
Fig. 8.44   Free Body Diagram to Determine Effect of Inertia
and Damping Forces on Axial Brace Force.
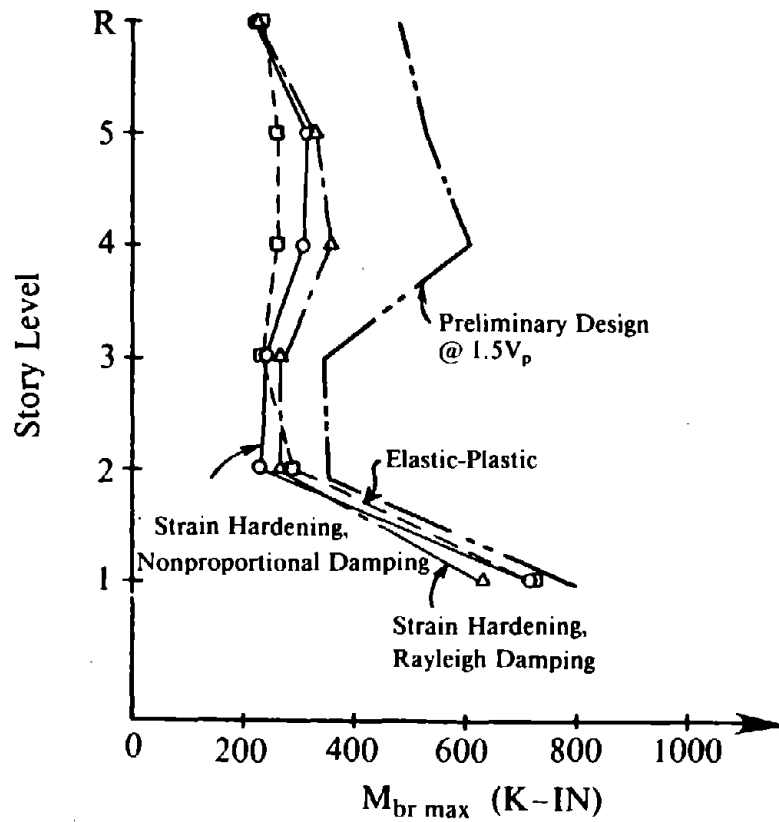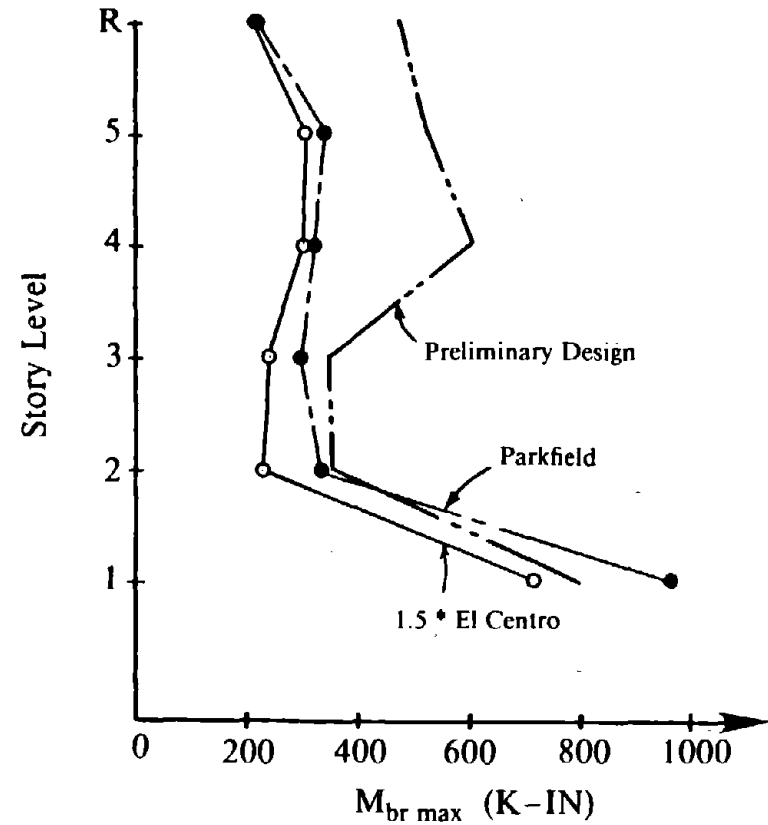
Fig. 8.45   Maximum Brace Moments for EBF Models of Design 1.

(a) 1.5 * El Centro Earthquake

(b) 1.5 * El Centro Earthquake and Parkfield Earthquake, Strain Hardening with Nonproportional Damping

R

Interior Col..
Req'd Design
Envelope @ 1.5V_p

Interior Columns.
Elastic-Plastic

Interior Columns,
Strain Hardening

4

Story Level

Exterior Col..
Req'd Design
Envelope @ 1.5V_p

Exterior Columns,
Strain Hardening

2

Exterior Columns.
Elastic-Plastic

-800   -600   -400   -200   0   200   400   600   800

Compression $P_{col\ max}$ (KIPS)   Tension

(a) 1.5 * El Centro Earthquake, Nonproportional Damping

R

Interior Col.,
Req'd Design
Envelope @ 1.5V_p

Interior Columns.
Nonproportional Damping

Interior Columns.
Rayleigh Damping

4

Story Level

Exterior Col.,
Req'd Design
Envelope @ 1.5V_p

Exterior Columns,
Rayleigh Damping

2

Exterior Columns,
Nonproportional Damping

-800   -600   -400   -200   0   200   400   600   800

Compression $P_{col\ max}$ (KIPS)   Tension

(b) 1.5 * El Centro Earthquake, Strain Hardening
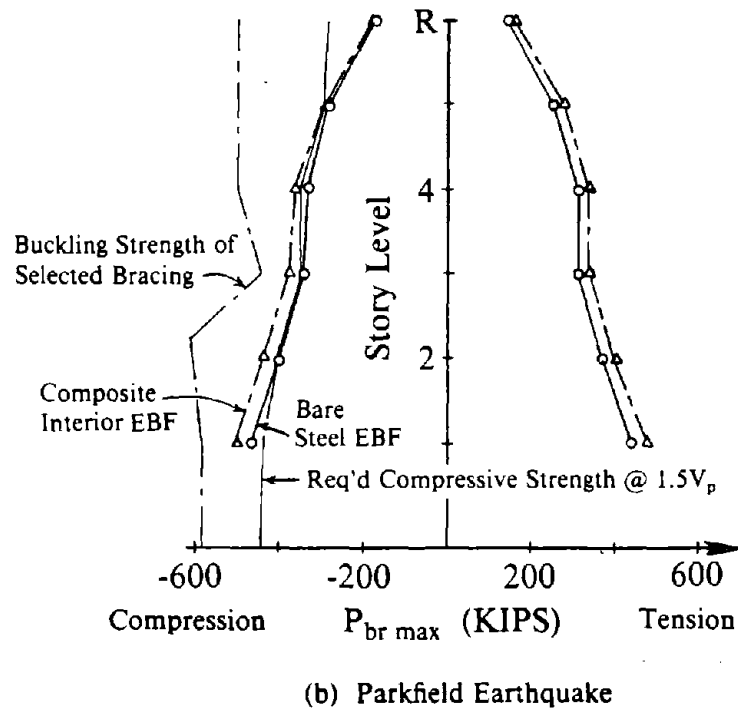
Fig. 8.46   Axial Column Force Envelopes for EBF Models of Design 1.
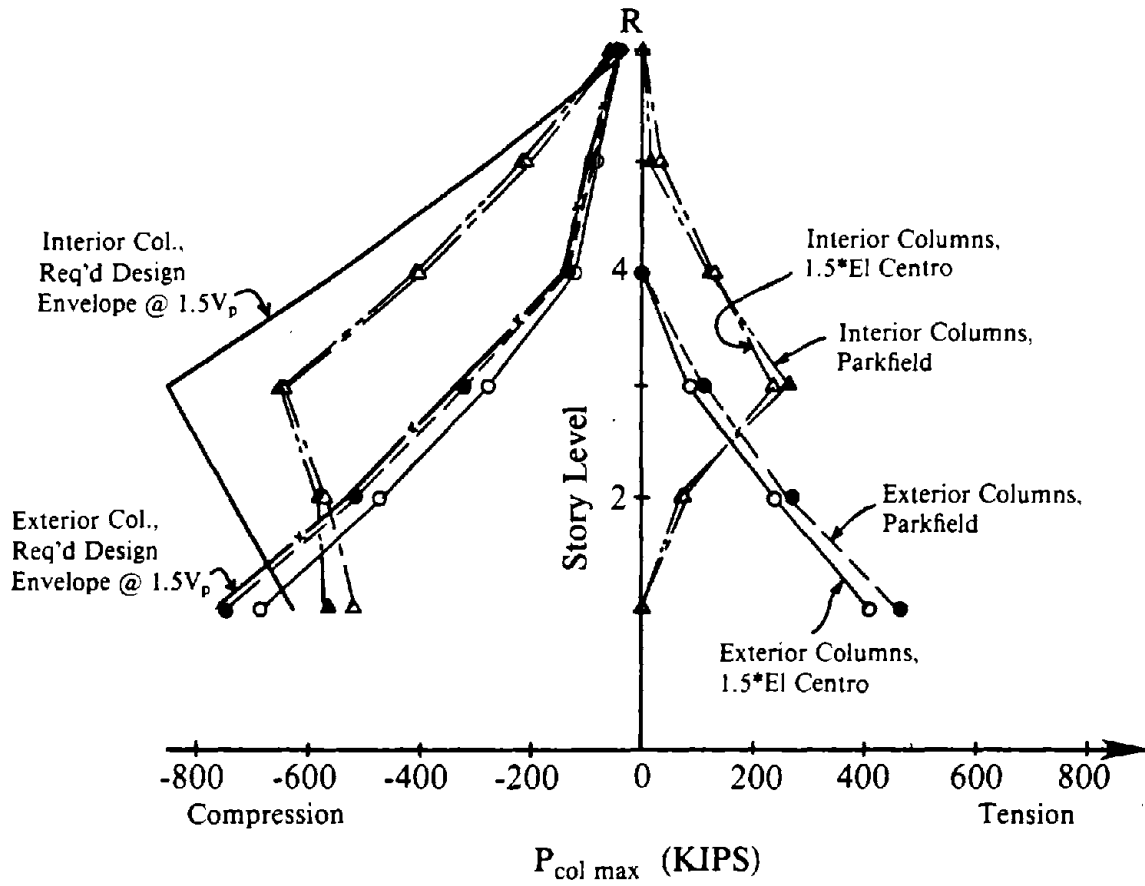
Fig. 8.47   Axial Column Force Envelopes for Response of Design 1 to 1.5 * El Centro Earthquake and Parkfield Earthquake, Nonproportional Damping.
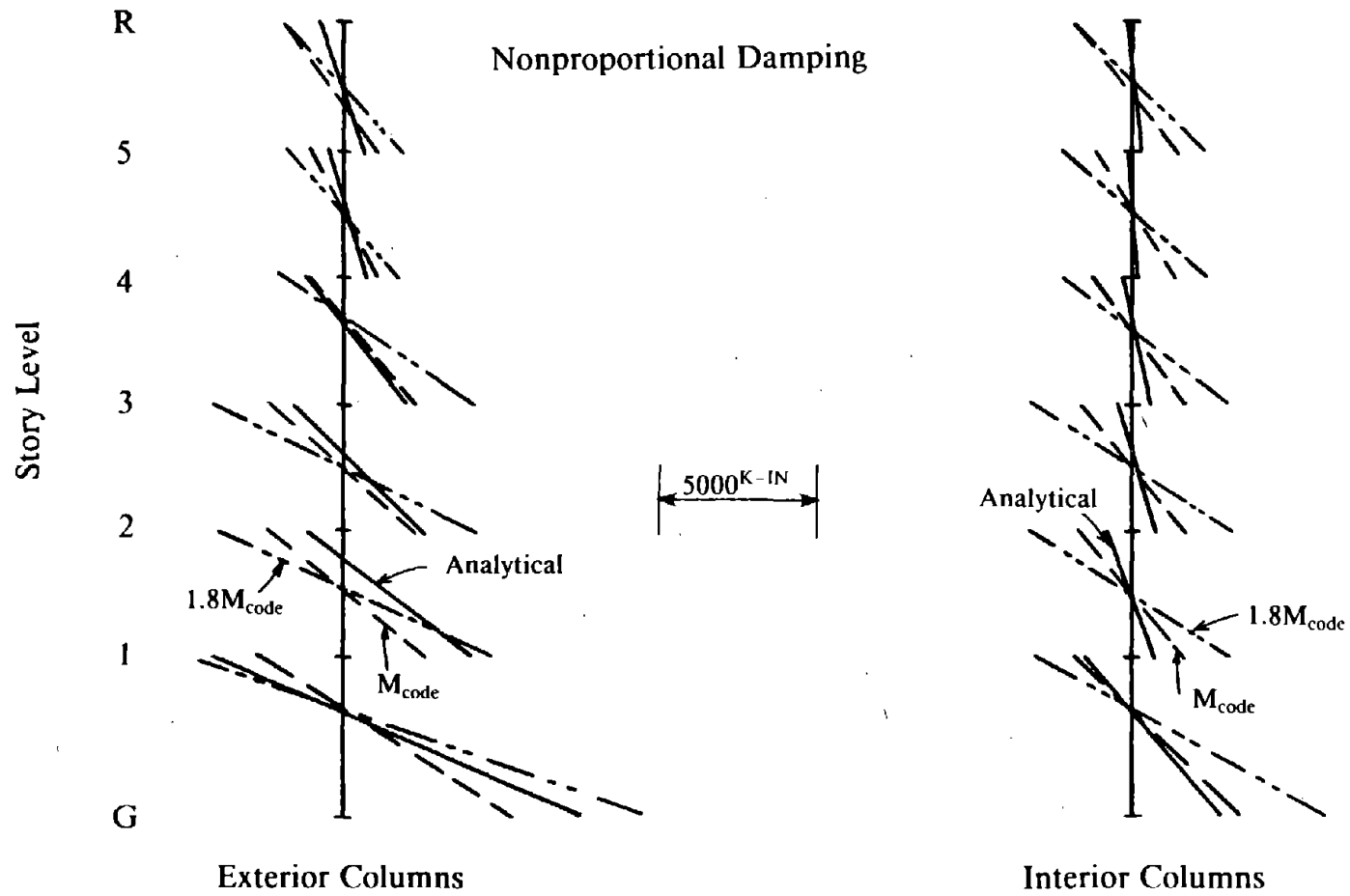
Fig. 8.48 Individual Column Moment Diagrams Corresponding to Maximum Column Moments of Design I with Strain Hardening, 1.5 * El Centro Earthquake.
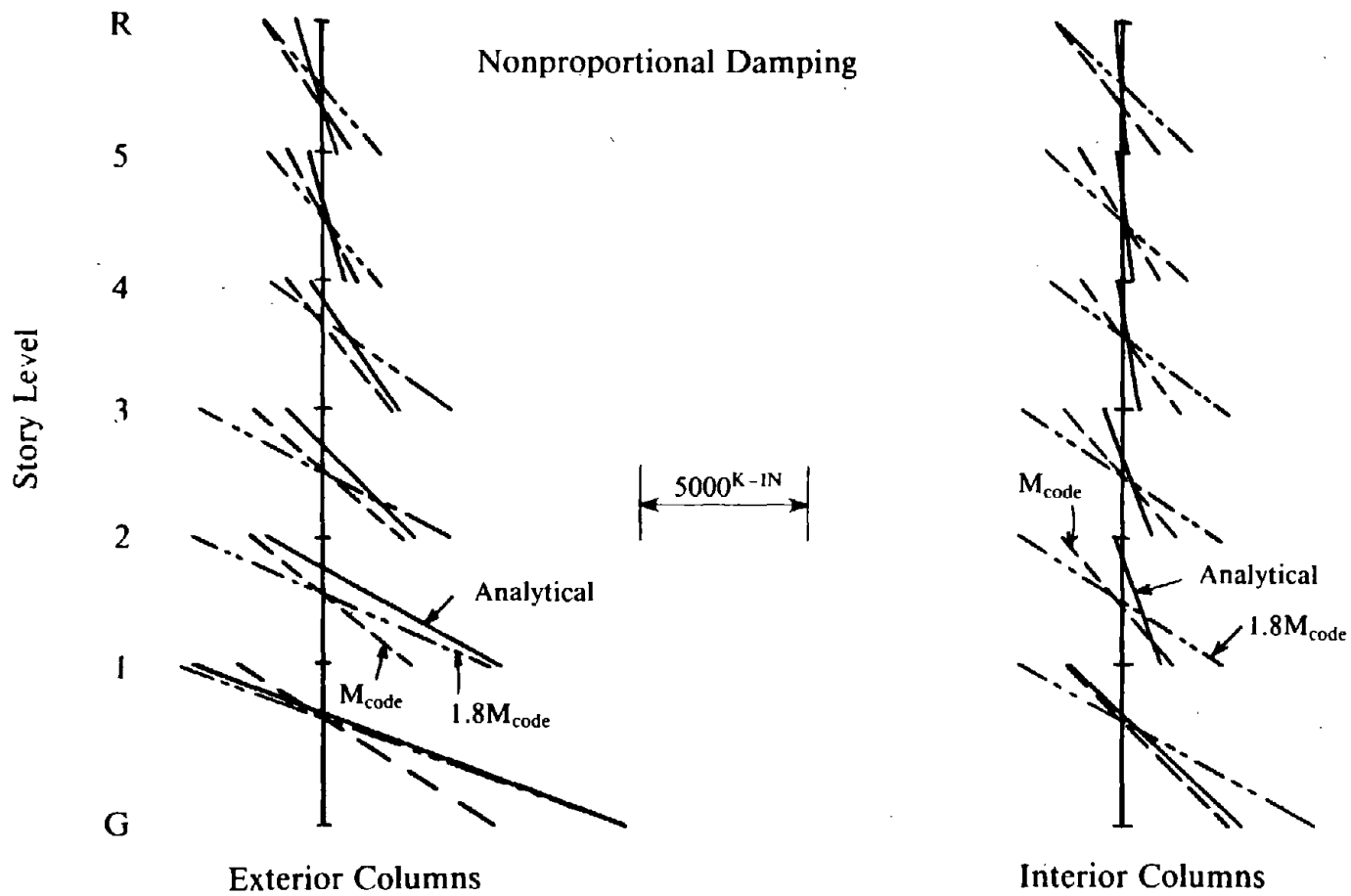
Fig. 8.49   Individual Column Moment Diagrams Corresponding to Maximum Column Moments of Design 1 with Strain Hardening, Parkfield Earthquake.
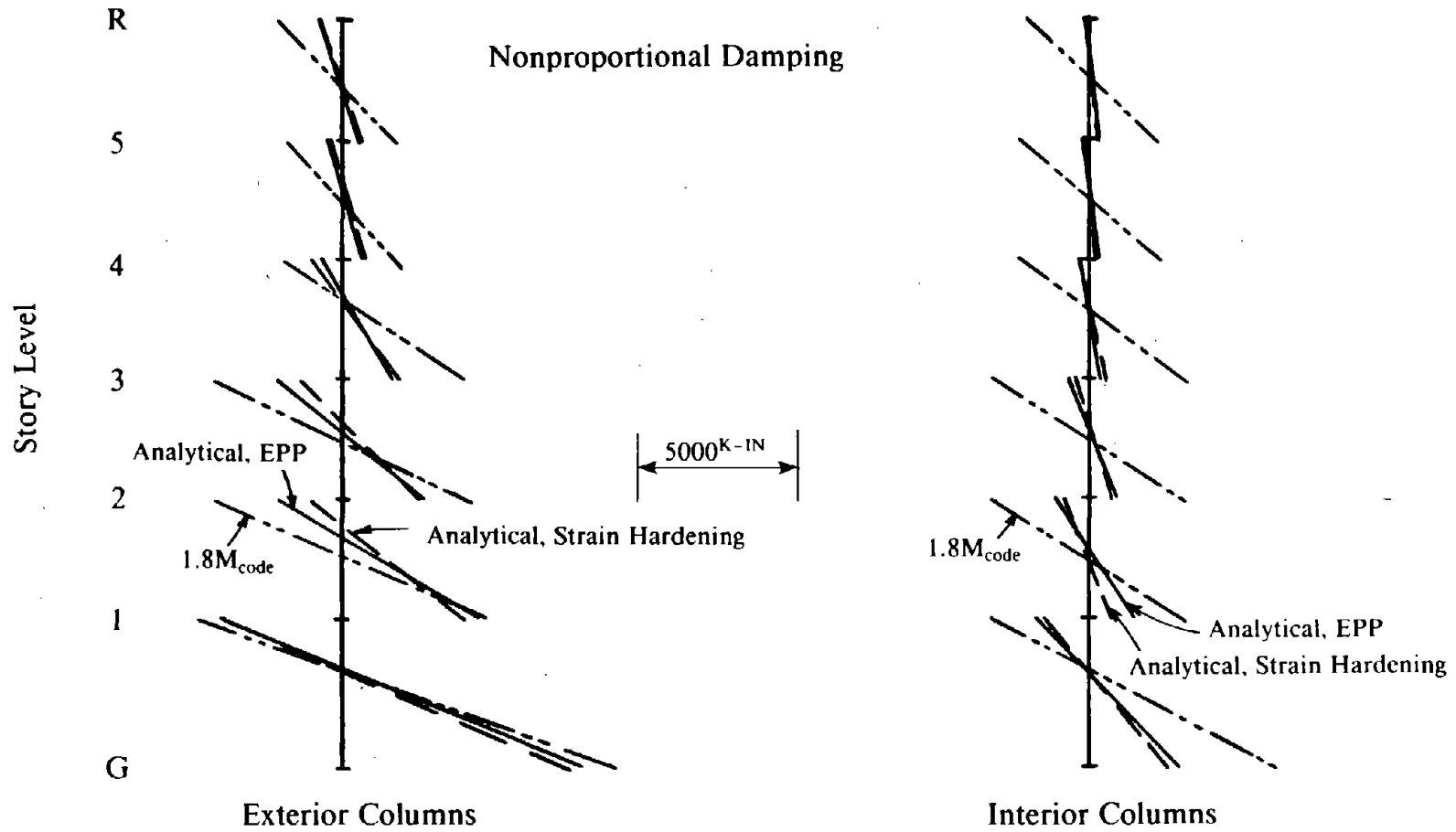
Fig. 8.50   Individual Column Moment Diagrams Corresponding to Maximum Column Moments of Design 1 with and without Strain Hardening, 1.5 * El Centro Earthquake.
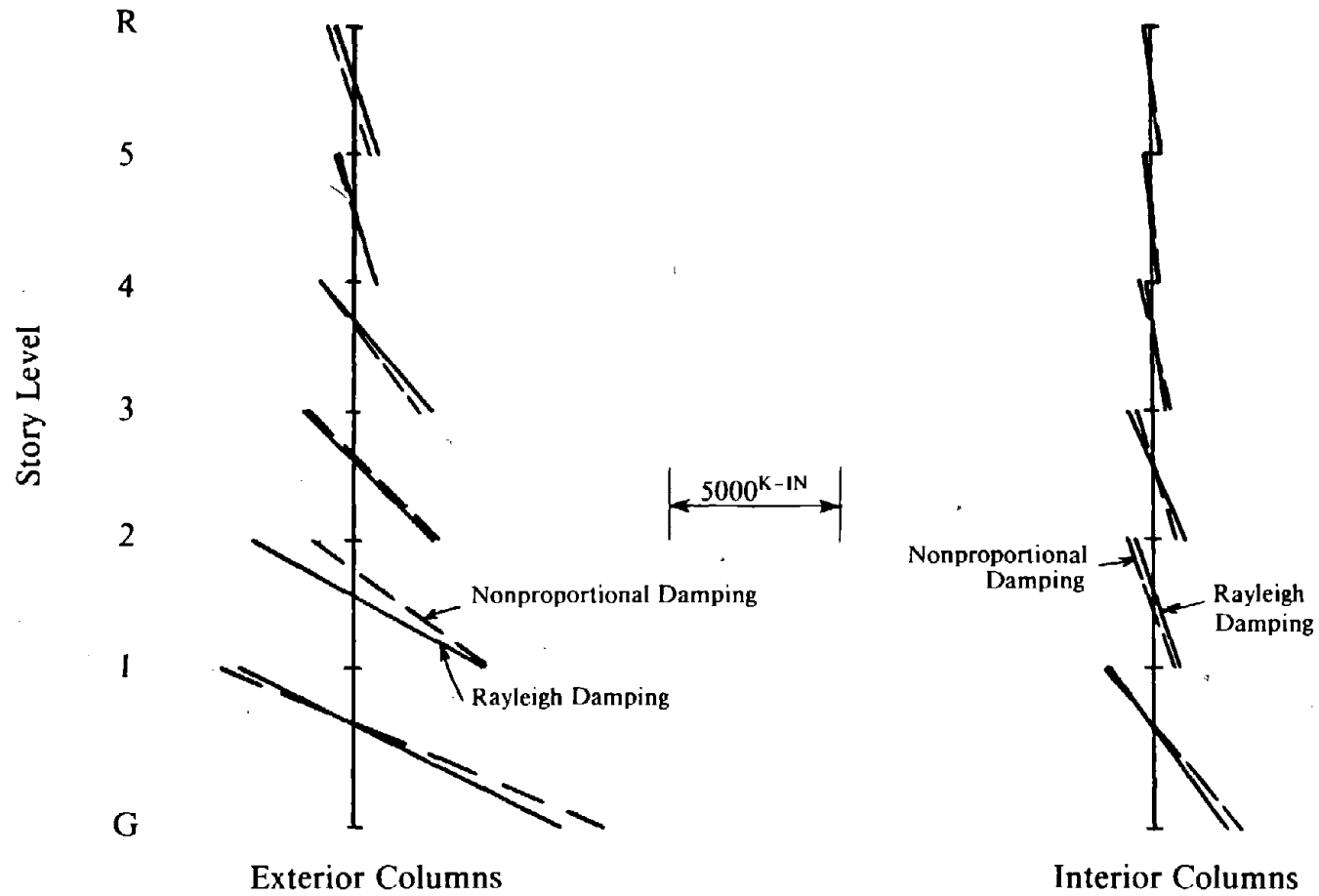
Fig. 8.51   Individual Column Moment Diagrams Corresponding to Maximum Column Moments of Design 1 with Rayleigh and Nonproportional Damping, 1.5 * El Centro Earthquake.

264
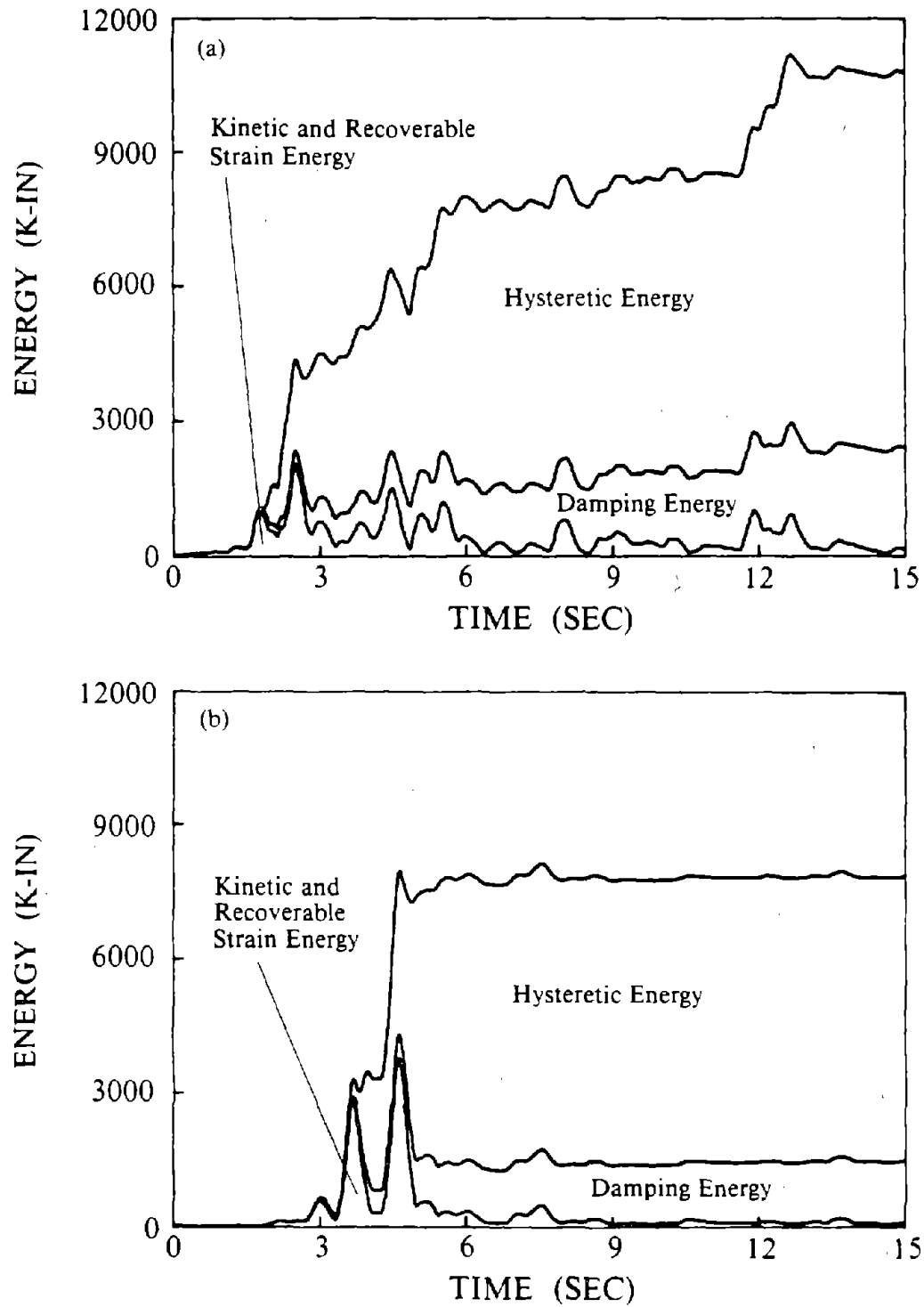
Fig. 8.52   Energy Time Histories for EBF Model of Design 1 with Strain Hardening and Nonproportional Damping Subjected to (a) 1.5 * El Centro and (b) Parkfield Earthquake Records.
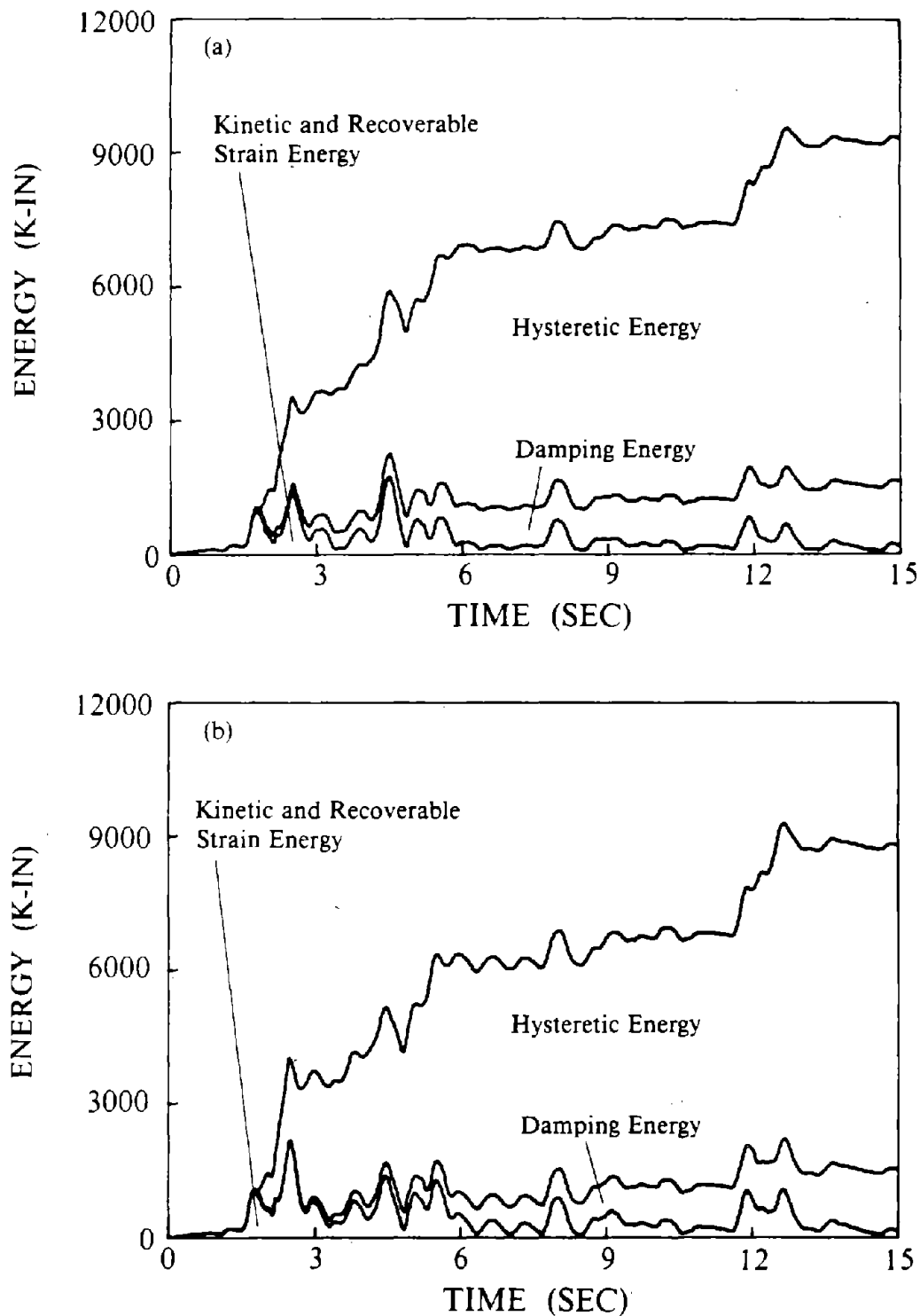
Fig. 8.53   Energy Time Histories for EBF Models of Design 1 with
(a) Nonproportional Damping Without Strain Hardening, and
(b) Rayleigh Damping With Strain Hardening Subjected to 1.5 * El Centro
Earthquake.

(a) 1.5 * El Centro Earthquake

(b) 1.5 * El Centro Earthquake and Parkfield Earth-
quake, Strain Hardening with Nonproportional
Damping
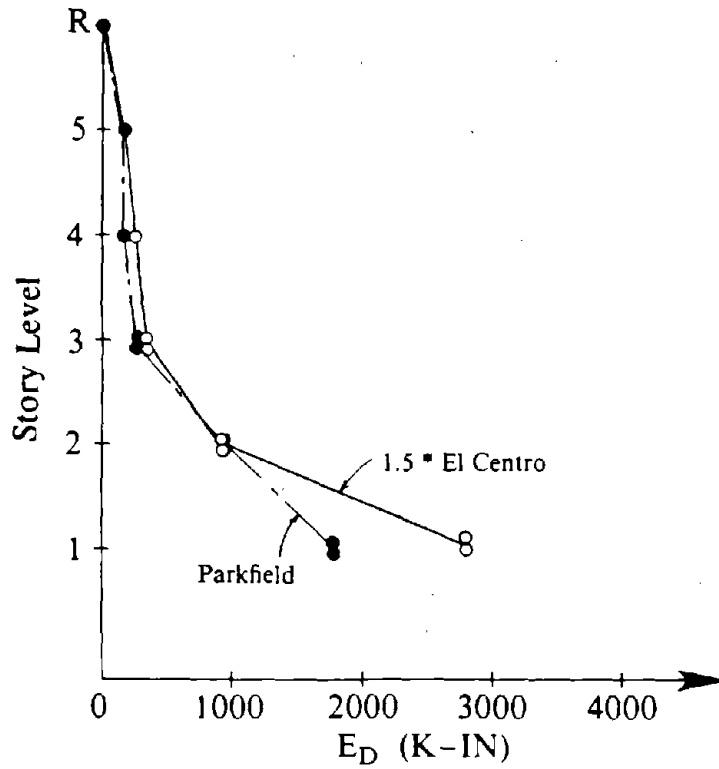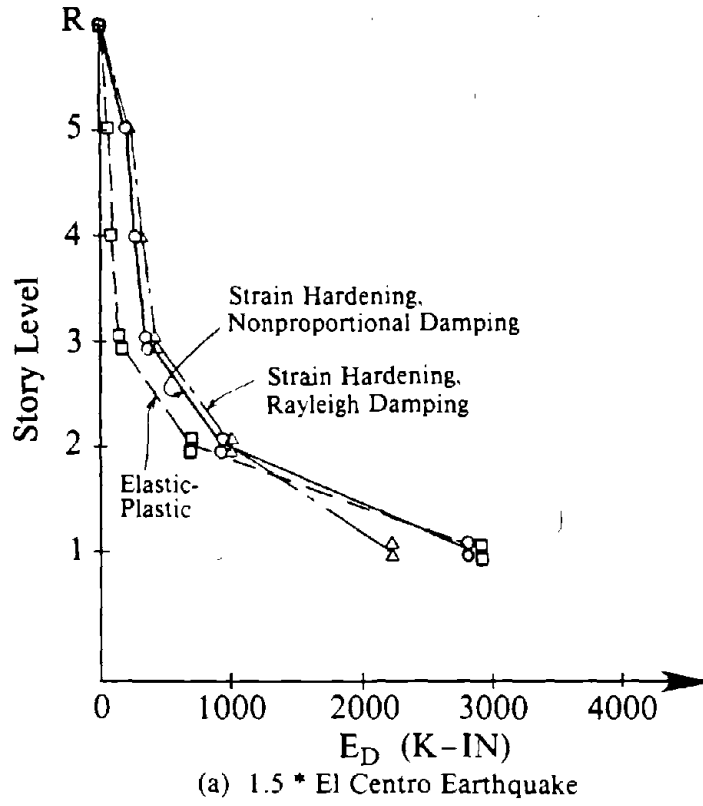
Fig. 8.54   Hysteretic Energy Dissipated By Links of Design 1.
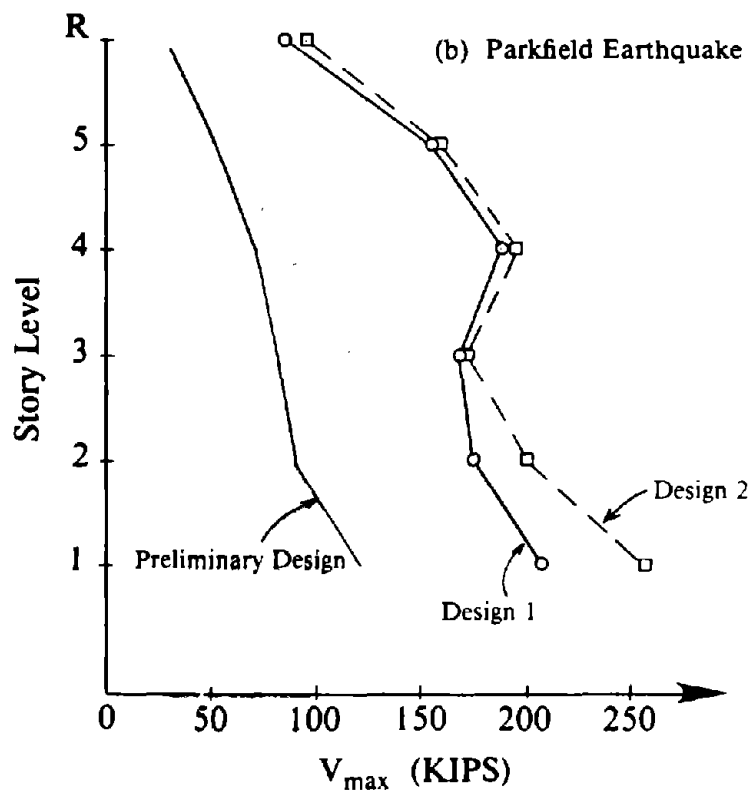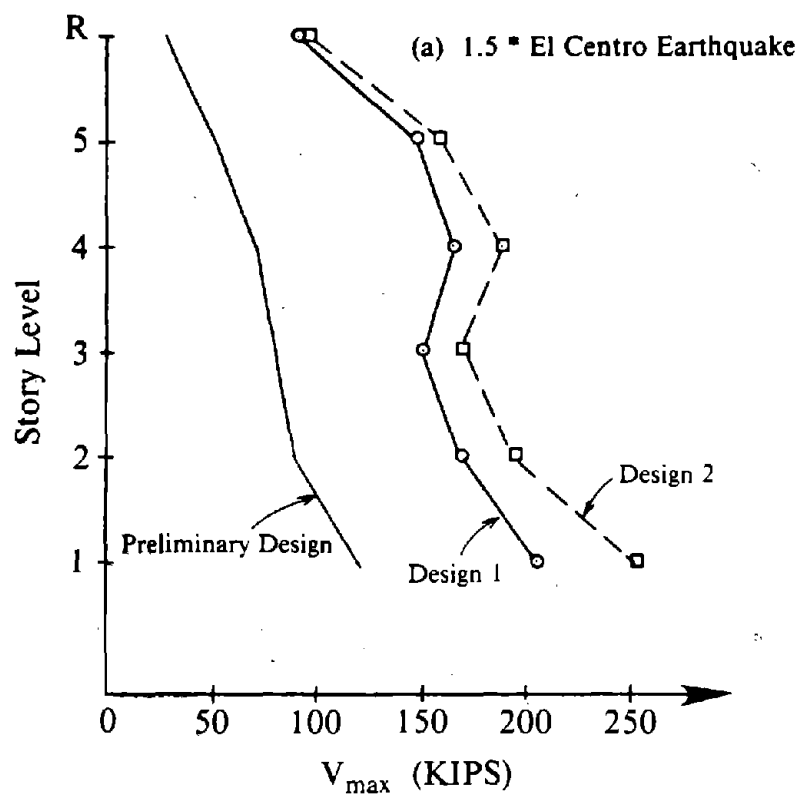
Fig. 8.55 Maximum Link Shear Forces of Designs 1 and 2, Nonproportional Damping with Strain Hardening.
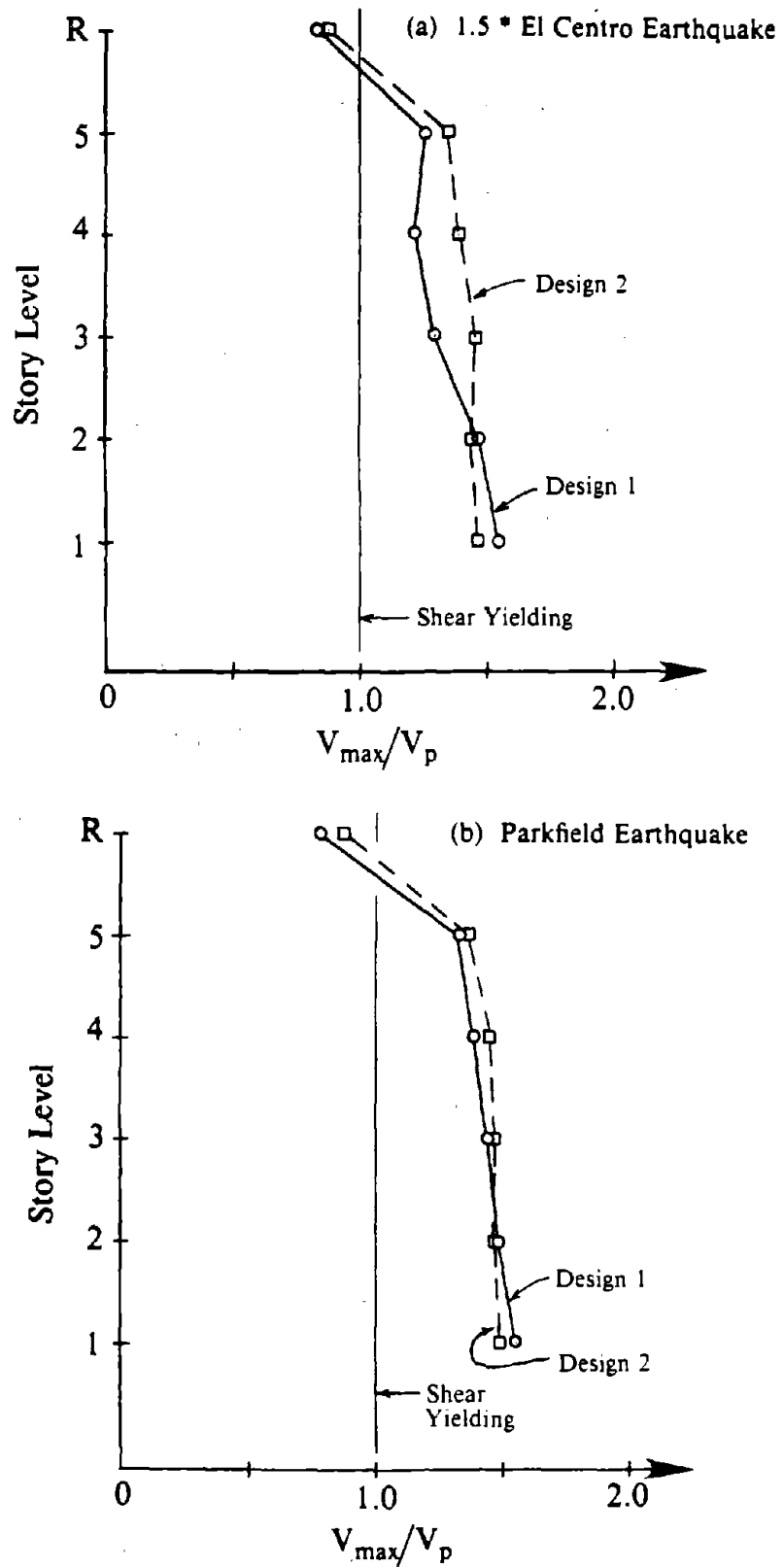
Fig. 8.56   Normalized Maximum Link Shear Forces for Designs 1 and 2, Nonproportional Damping with Strain Hardening.
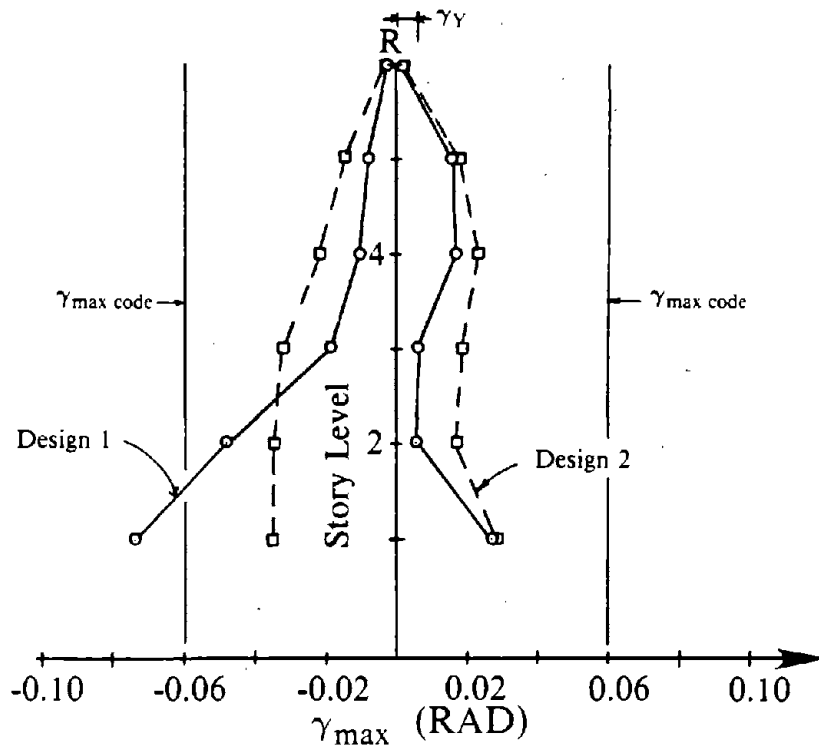
(a) 1.5*El Centro Earthquake
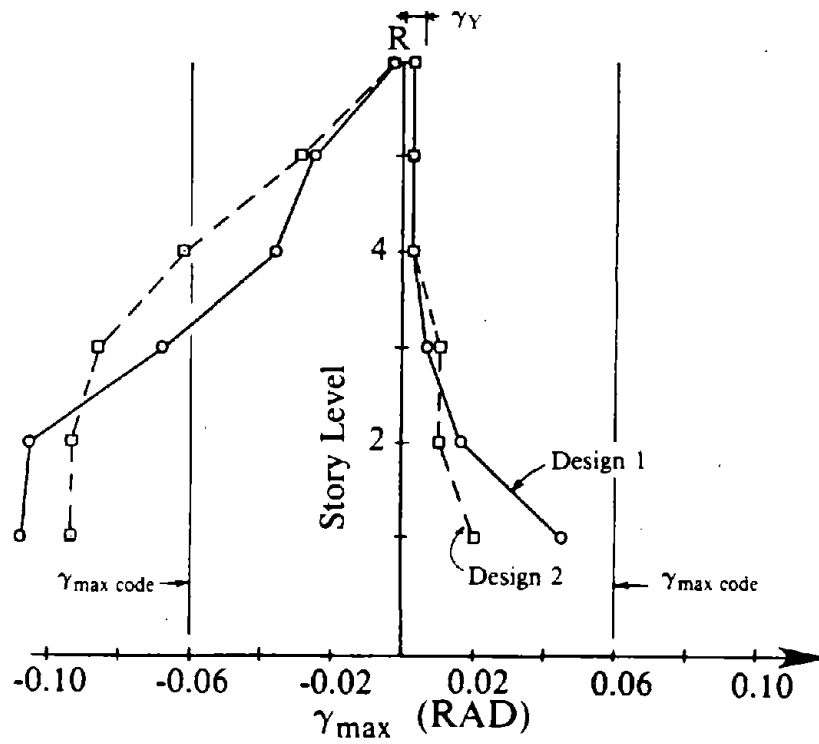
(b) Parkfield Earthquake

Fig. 8.57   Link Deformation Envelopes for Designs 1 and 2, Nonproportional Damping with Strain Hardening.
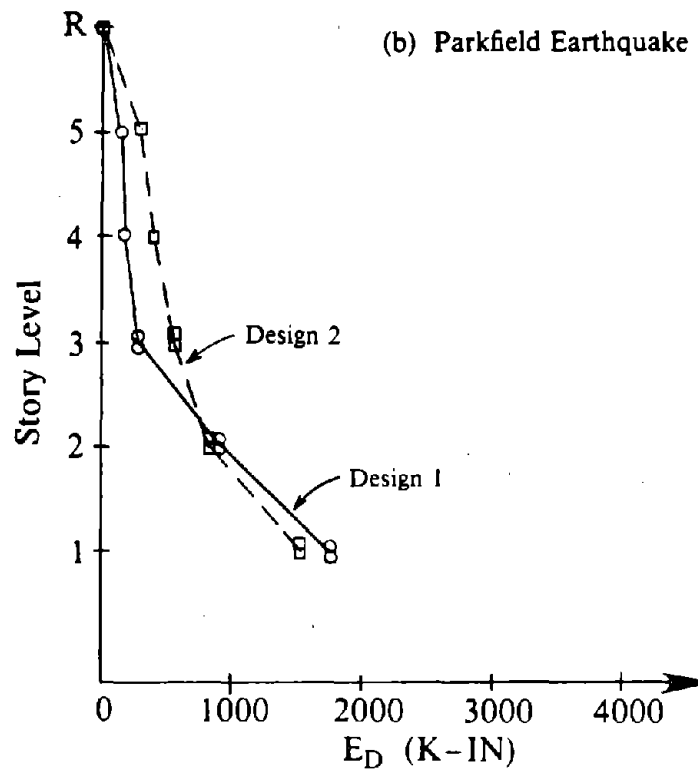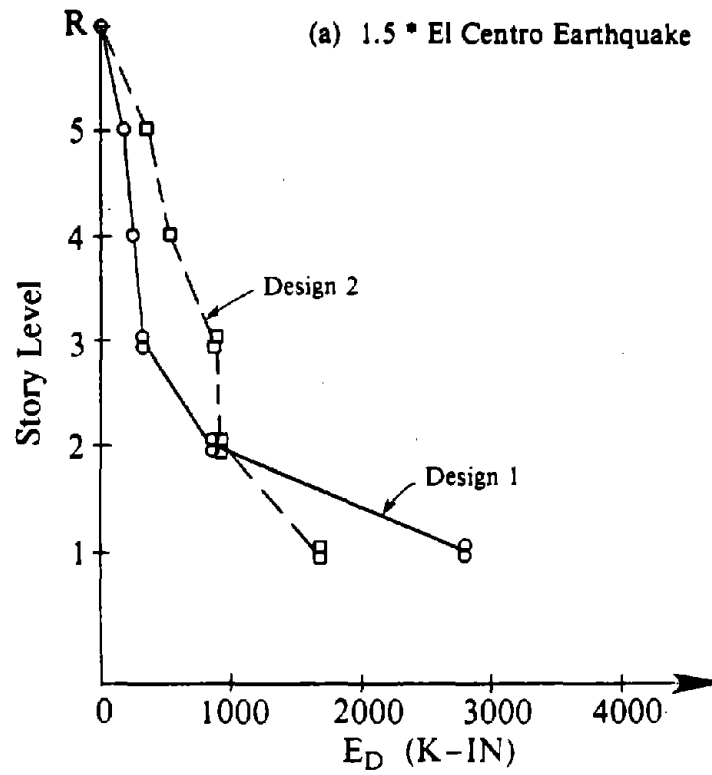
Fig. 8.58   Hysteretic Energy Dissipated by Links of Designs 1 and 2, Nonproportional
Damping with Strain Hardening.
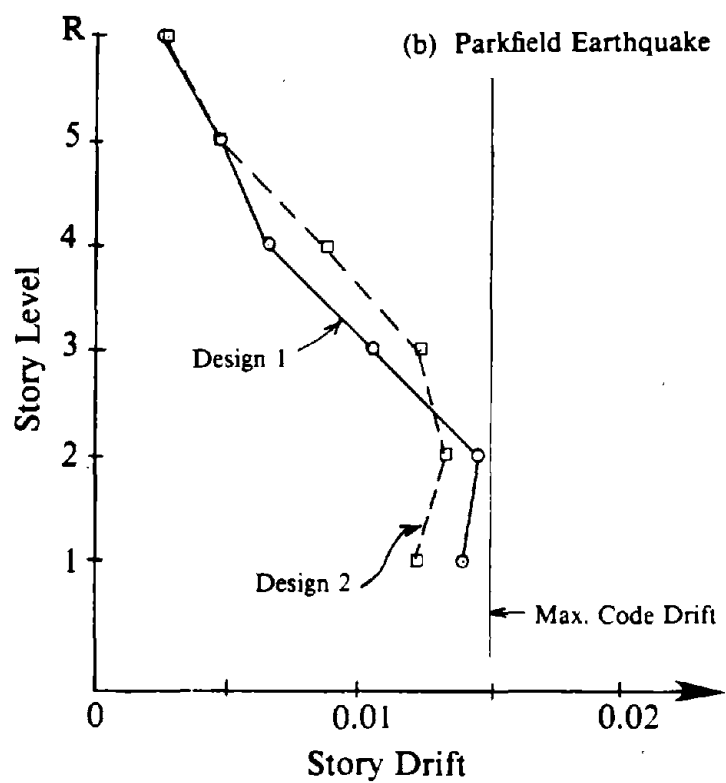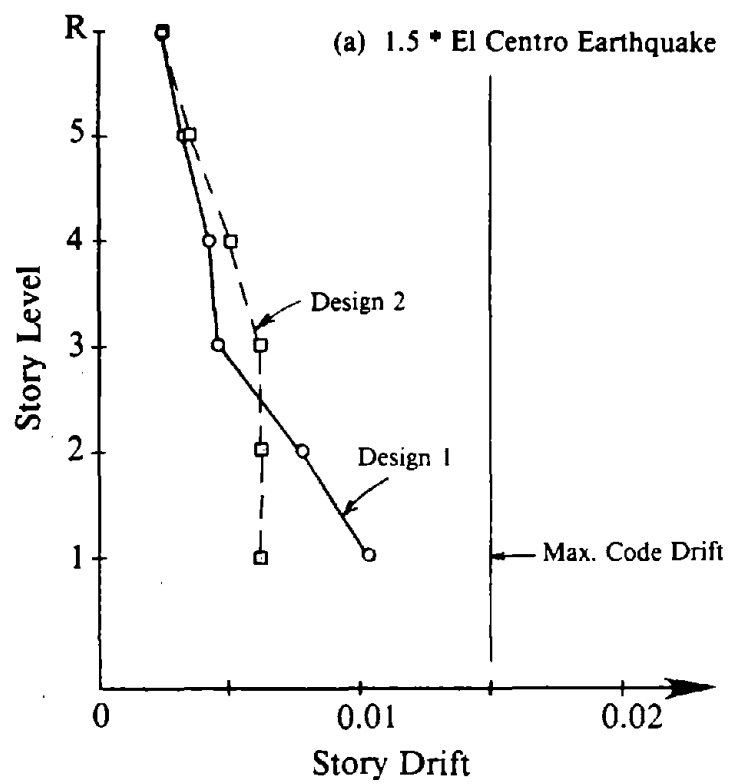
Fig. 8.59   Maximum Story Drift of Designs 1 and 2, Nonproportional Damping with Strain Hardening.
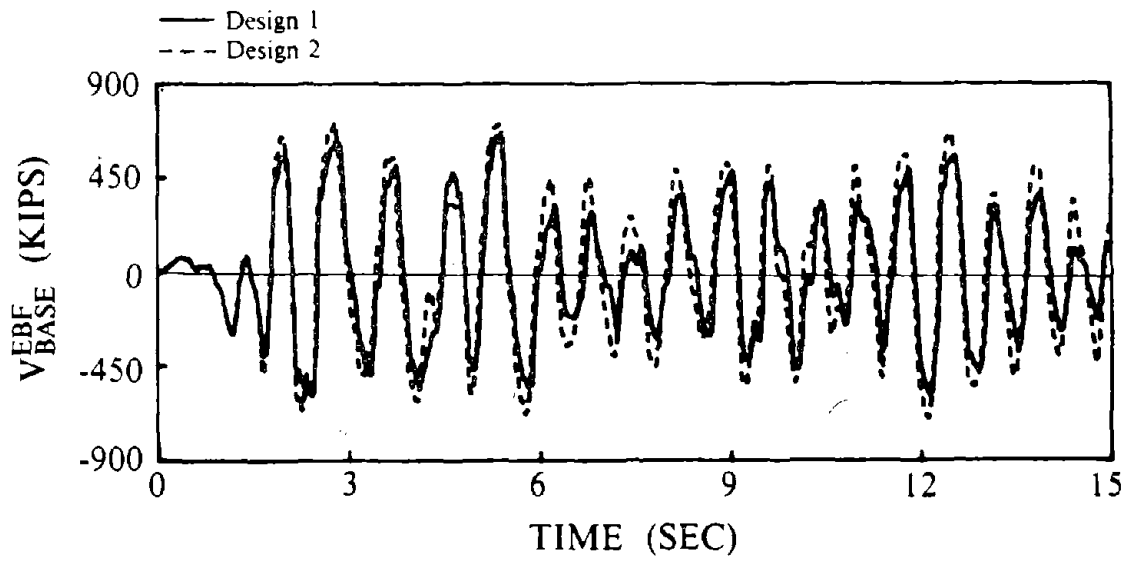
(a) 1.5 * El Centro Earthquake
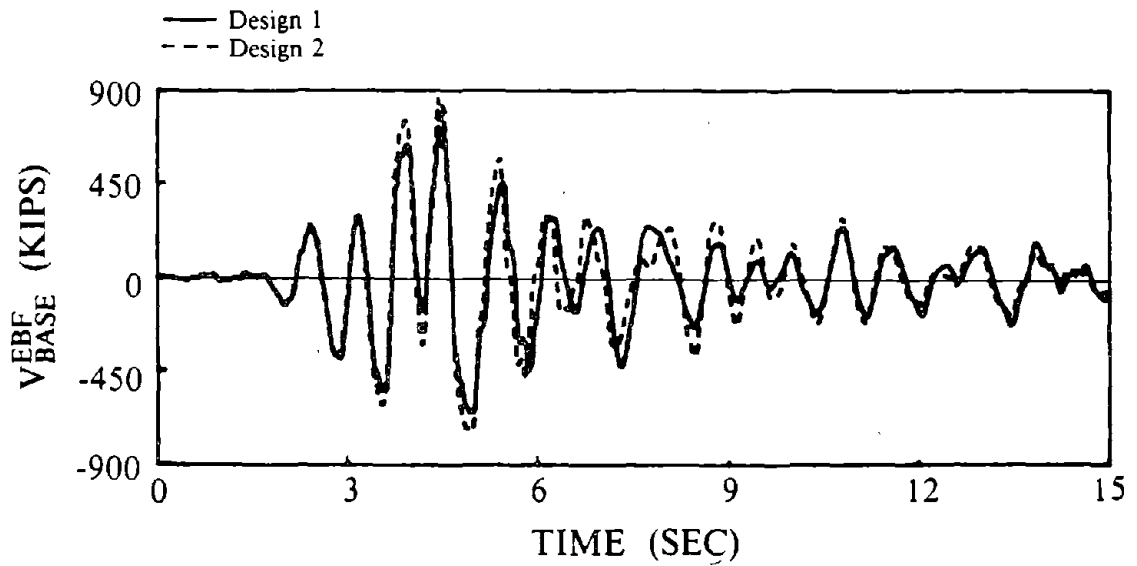
(b) Parkfield Earthquake

Fig. 8.60   Comparison of Base Shear Time Histories for Designs 1 and 2, Nonproportional Damping with Strain Hardening.

Fig. 8.61   Yielded Members of EBF Models for Design 2 Subjected to 1.5 * El Centro Earthquake.

(a) Bare Steel EBF, with and without
     Geometric Stiffness

(b) Composite Exterior EBF

(c) Composite Interior EBF
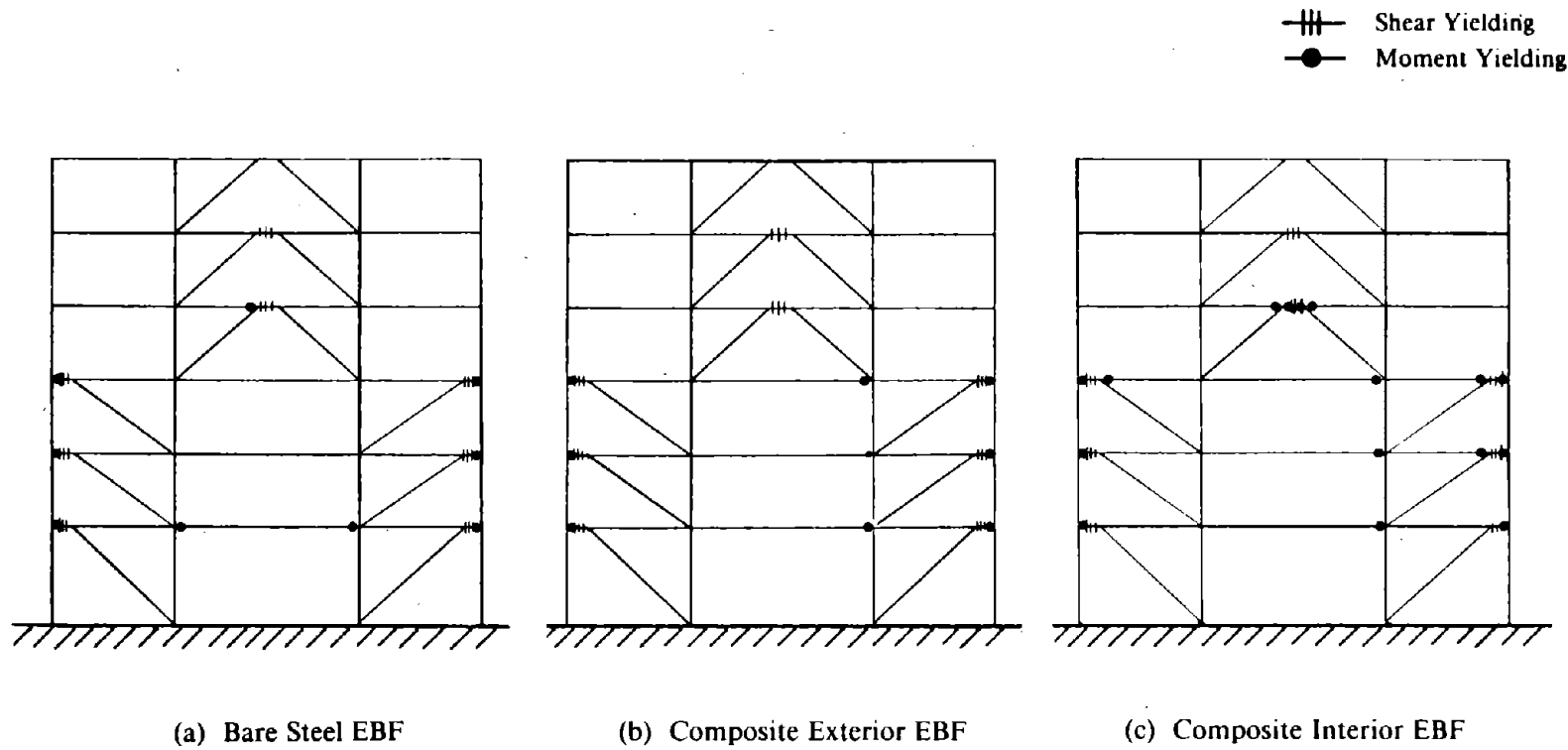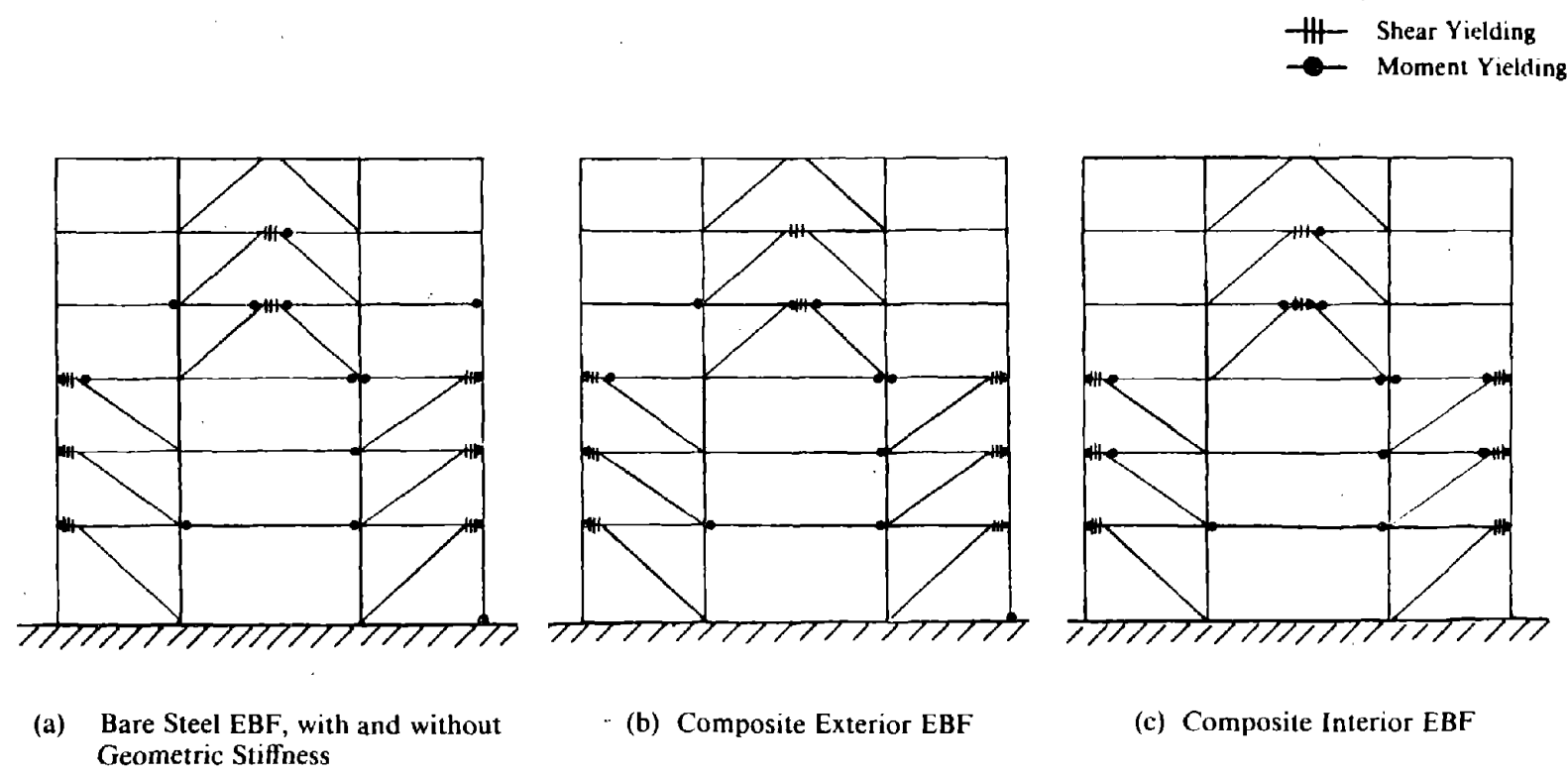
Fig. 8.62   Yielded Members of EBF Models for Design 2 Subjected to Parkfield Earthquake.
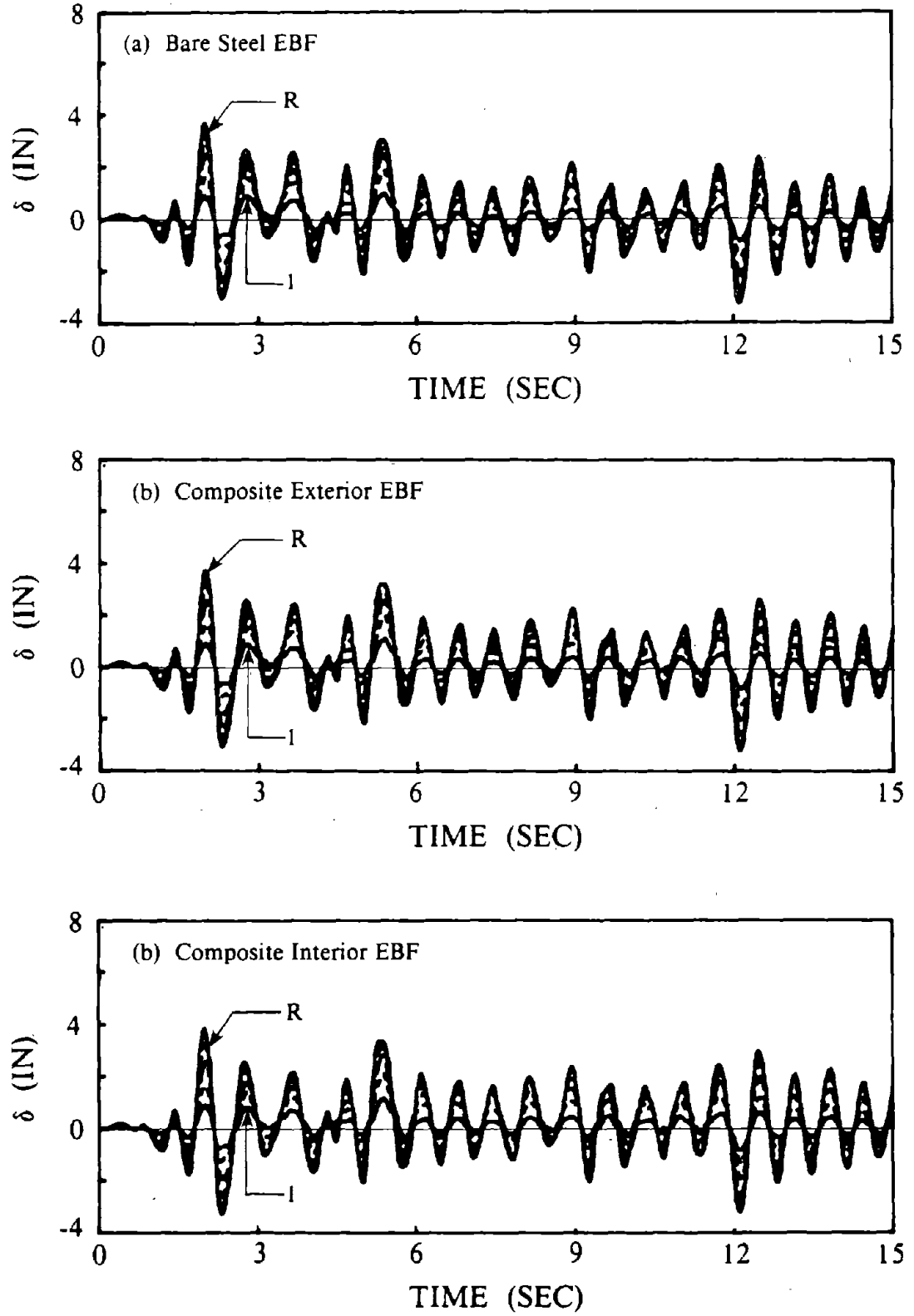
Fig. 8.63   Lateral Floor Displacements for EBF Models of Design 2 Subjected to 1.5 * El Centro Earthquake.
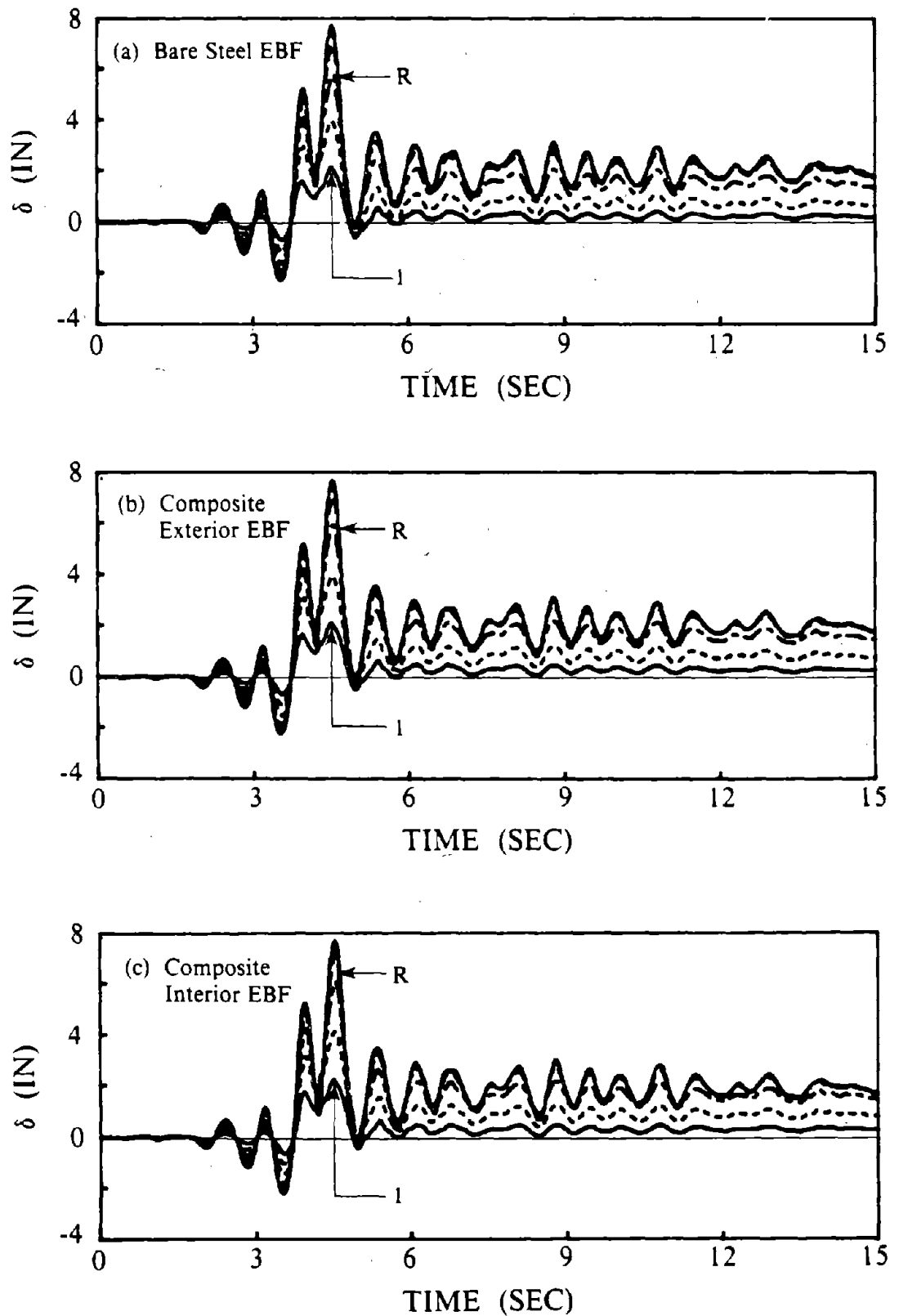
Fig. 8.64 Lateral Floor Displacements for EBF Models of Design 2 Subjected to Parkfield Earthquake.
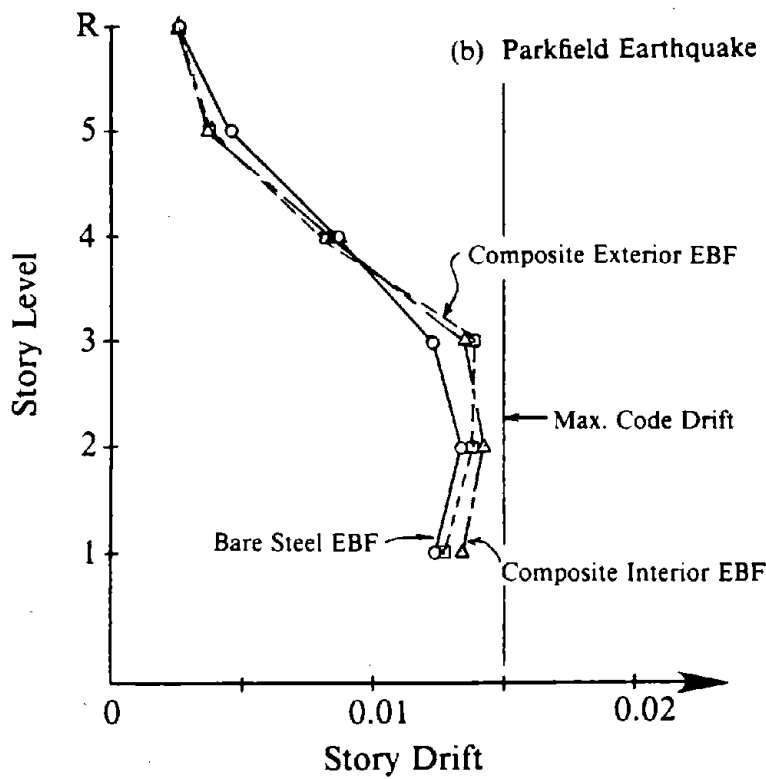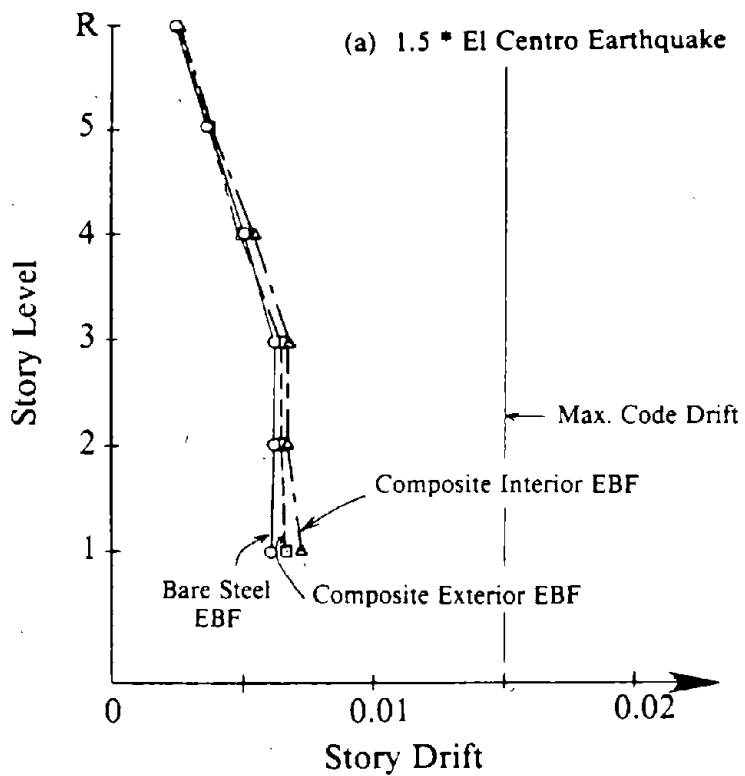
Fig. 8.65   Maximum Story Drift for EBF Models of Design 2.
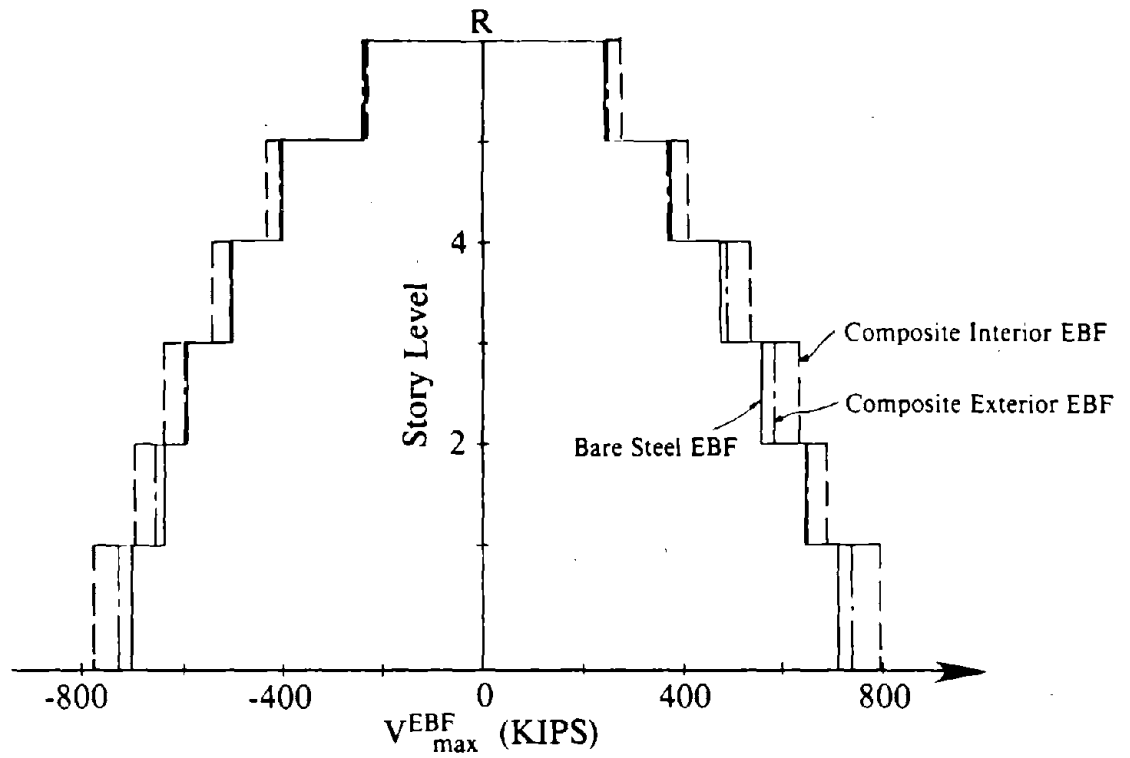
(a) 1.5 * El Centro Earthquake
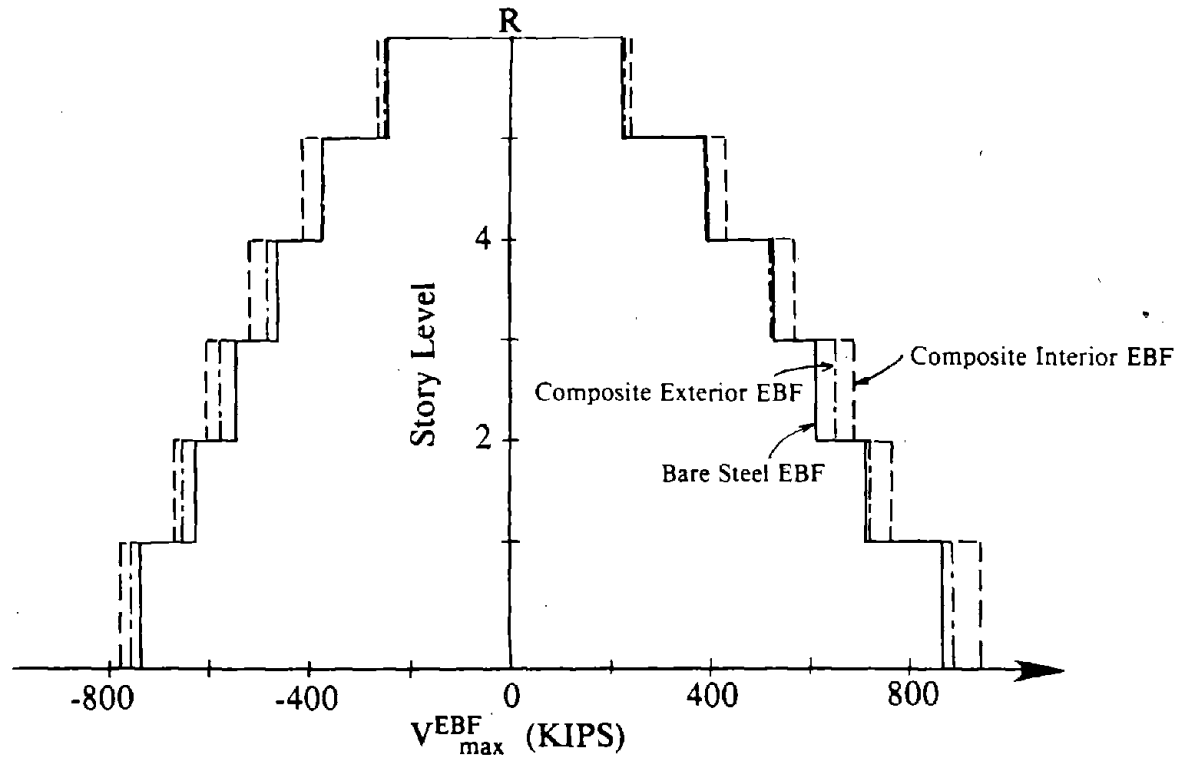
(b) Parkfield Earthquake

Fig. 8.66   Story Shear Envelopes for EBF Models of Design 2.
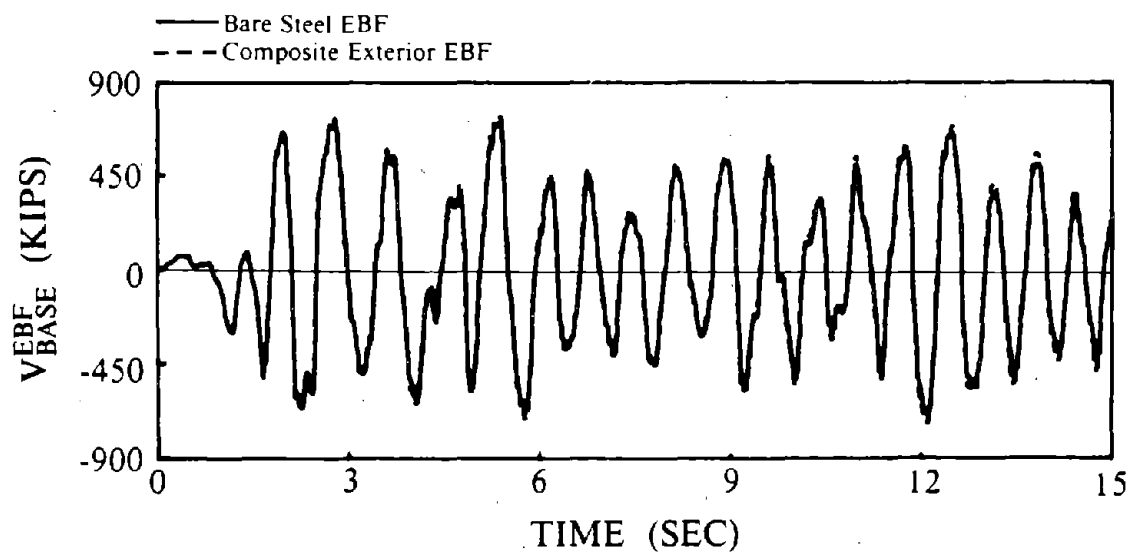
(a) Bare Steel and Composite Exterior EBFs.
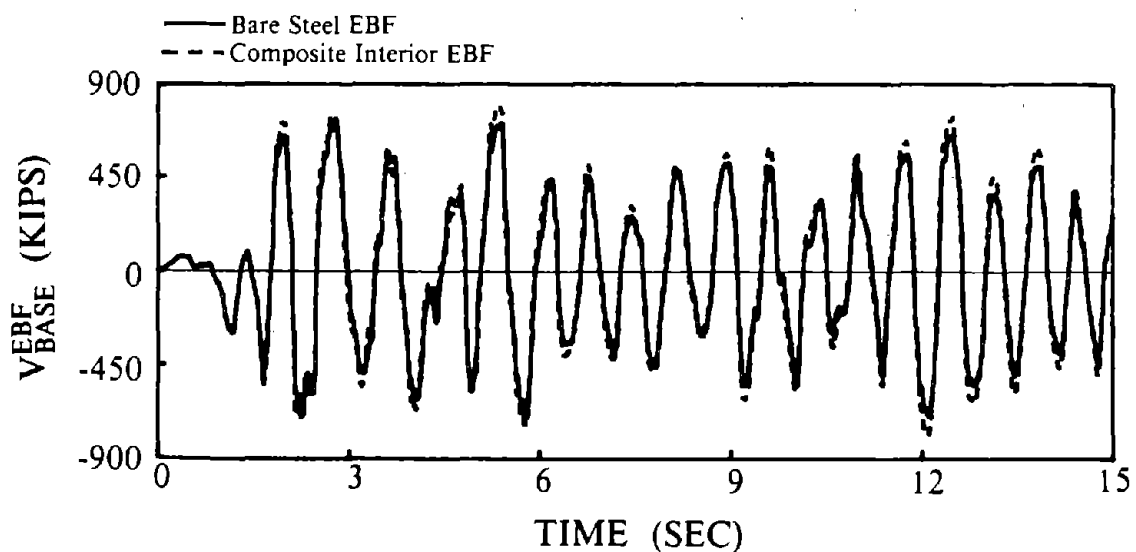
(b) Bare Steel and Composite Interior EBFs.

Fig. 8.67   Comparison of Base Shear Time Histories for EBF Models
of Design 2 Subjected to 1.5 * El Centro Earthquake.
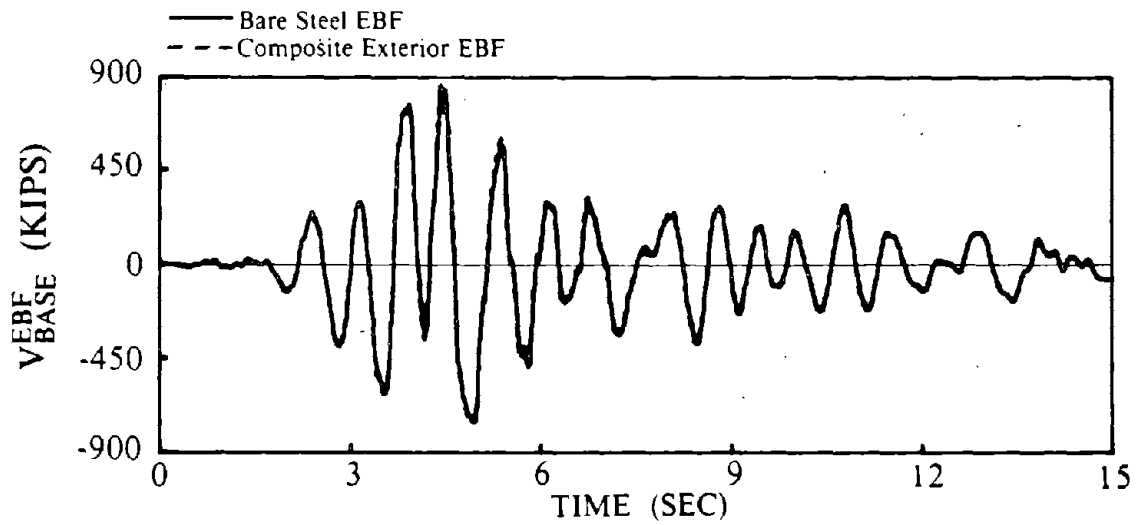
(a) Bare Steel and Composite Exterior EBFs.
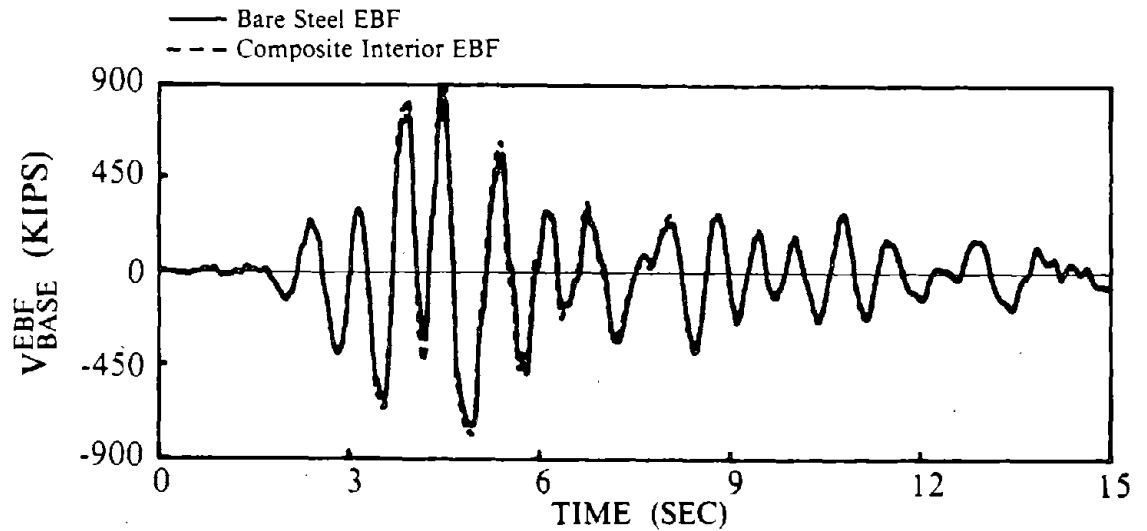
(b) Bare Steel and Composite Interior EBFs.

Fig. 8.68   Comparison of Base Shear Time Histories for EBF Models
of Design 2 Subjected to Parkfield Earthquake.
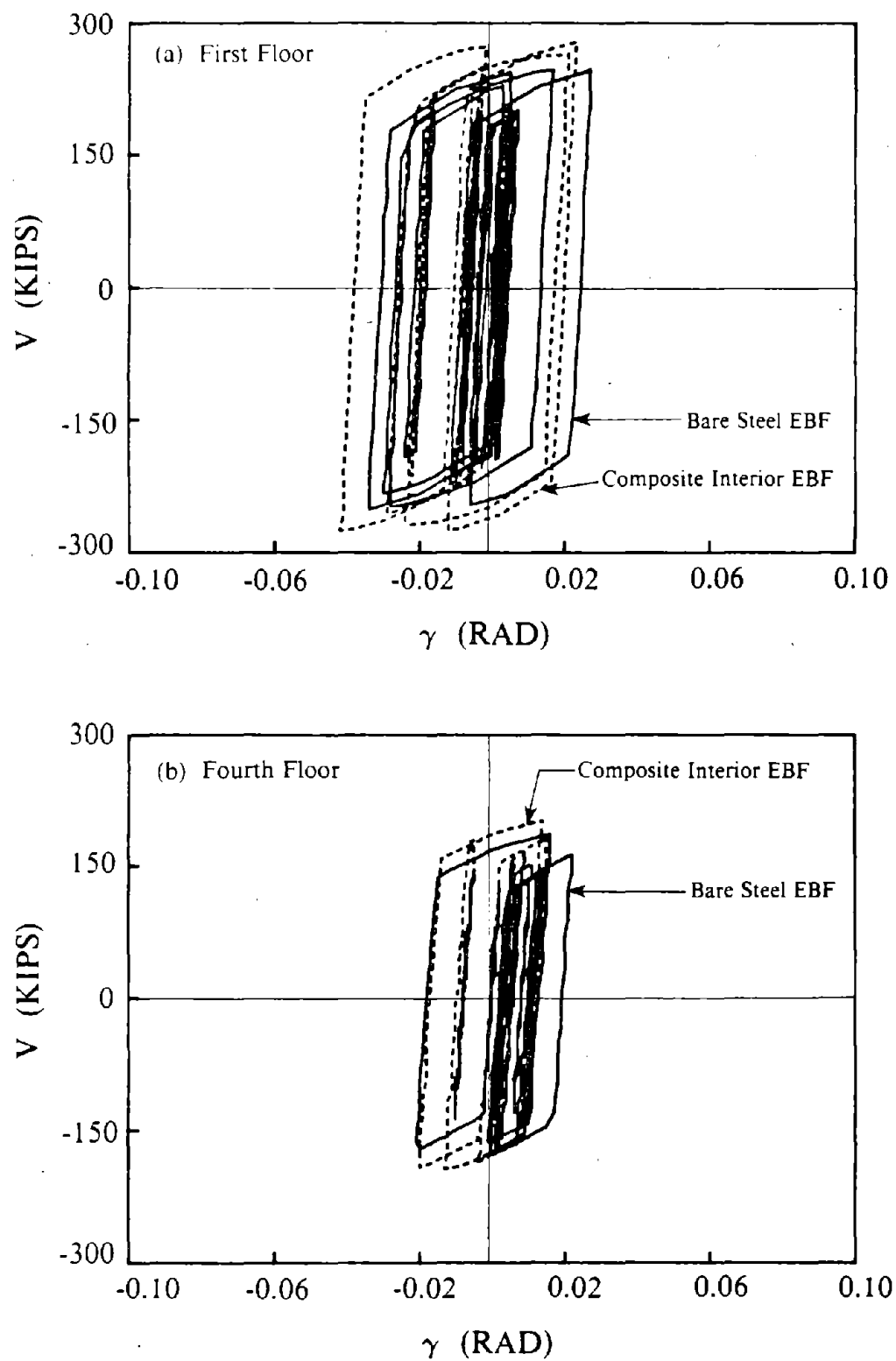
Fig. 8.69   Shear-Deformation Hysteretic Response of Links in Bare Steel and Composite
Interior EBF Models Subjected to 1.5 * El Centro Earthquake, Design 2.
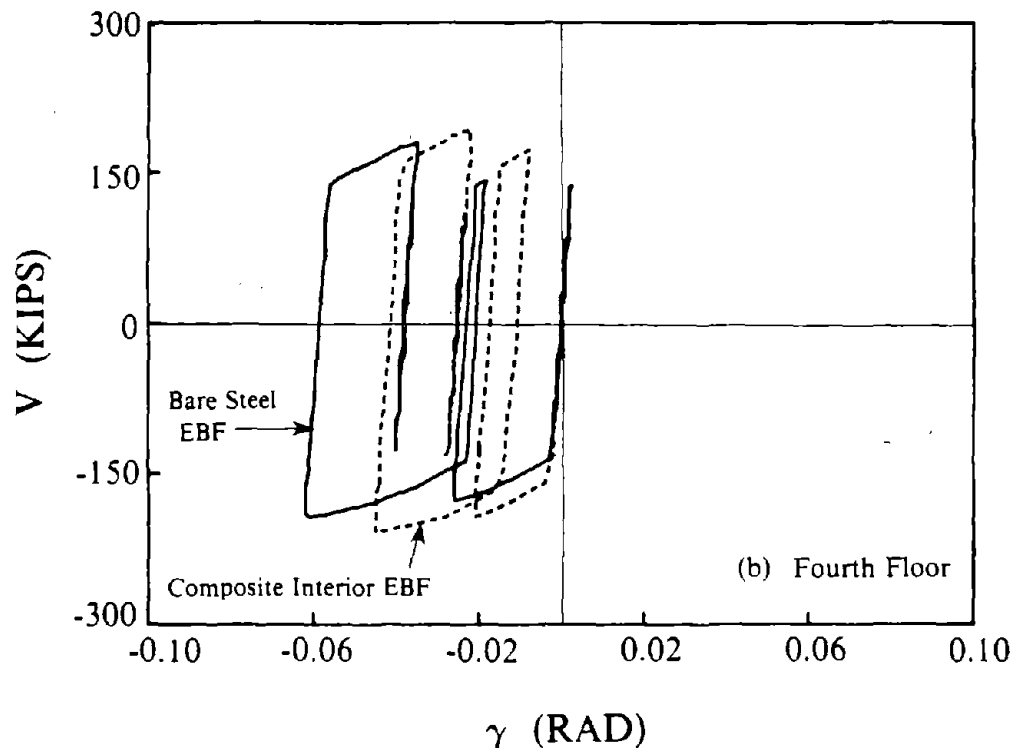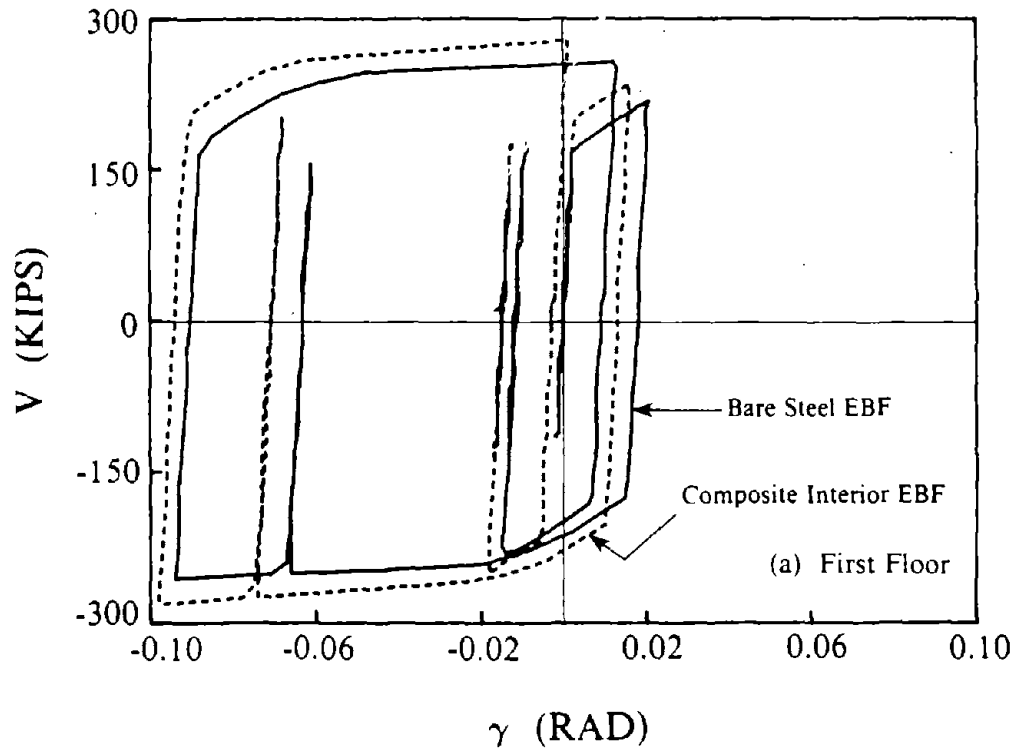
Fig. 8.70   Shear-Deformation Hysteretic Response of Links in Bare Steel and Composite Interior EBF Models Subjected to Parkfield Earthquake, Design 2.

(a) 1.5 * El Centro Earthquake

V_{max} (KIPS)

(b) Parkfield Earthquake

V_{max} (KIPS)
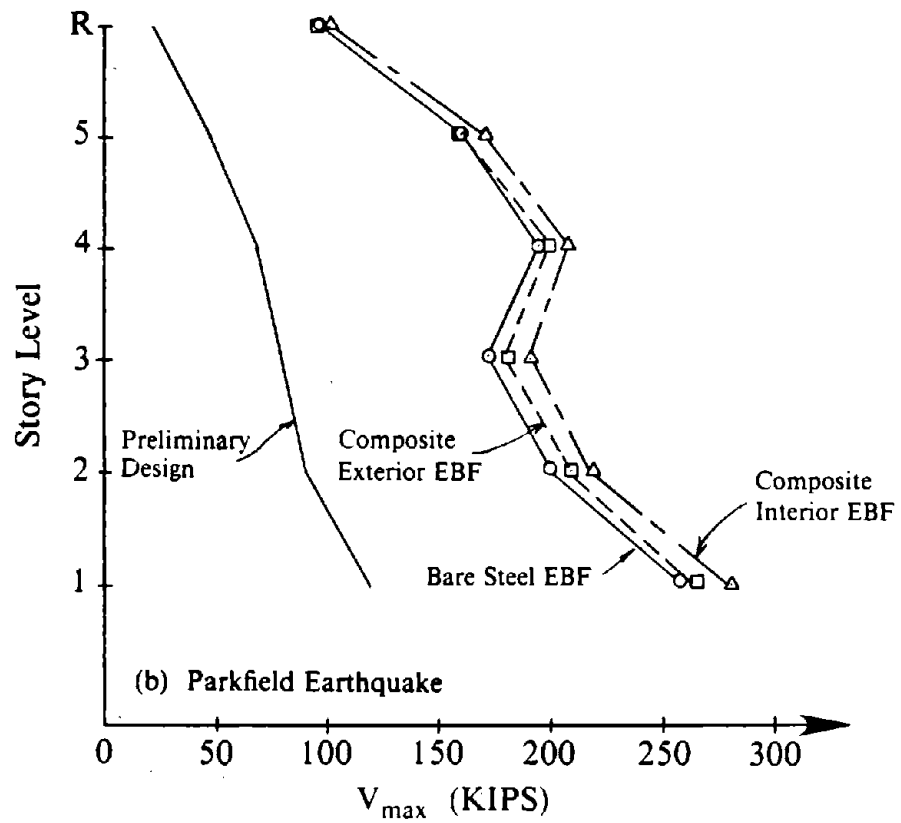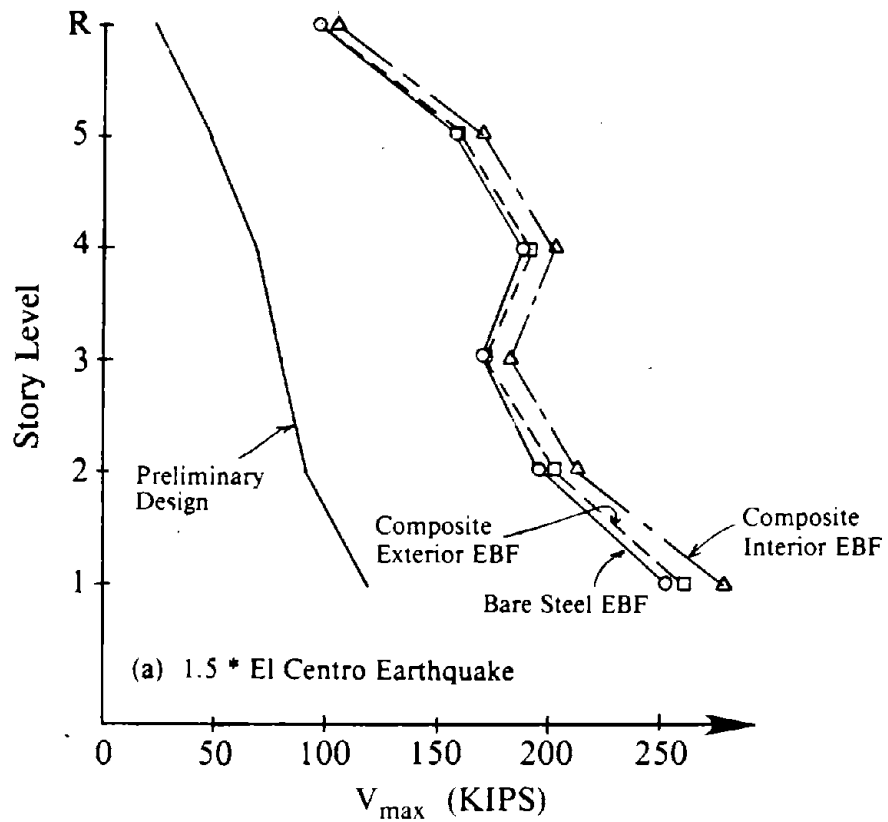
Fig. 8.71 Maximum Link Shear Forces for EBF Models of Design 2.

Fig. 8.72   Normalized Maximum Link Shear Forces for EBF Models of Design 2.

(a) 1.5 * El Centro Earthquake

(b) Parkfield Earthquake

Fig. 8.73   Link Deformation Envelopes for EBF Models of Design 2.

(a) 1.5 * El Centro Earthquake

(b) Parkfield Earthquake
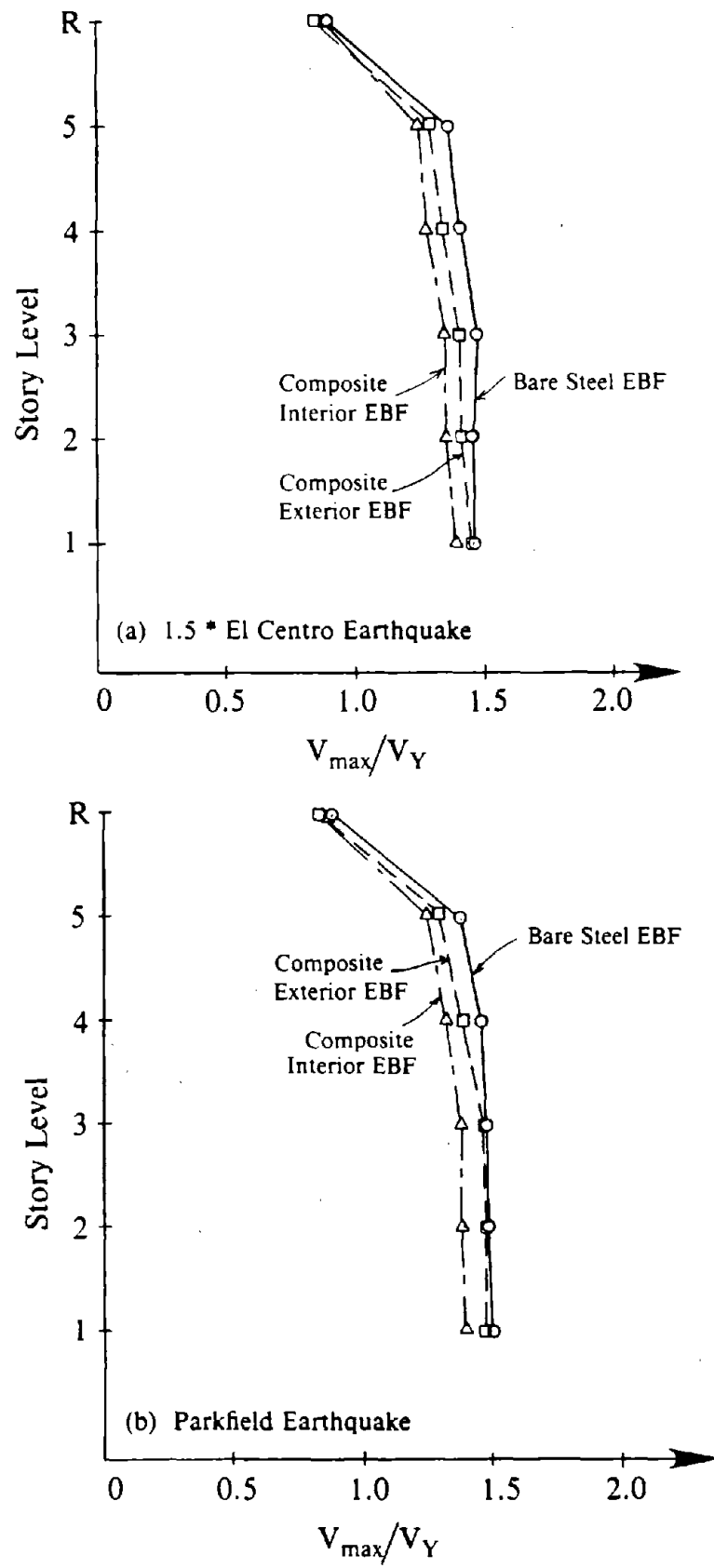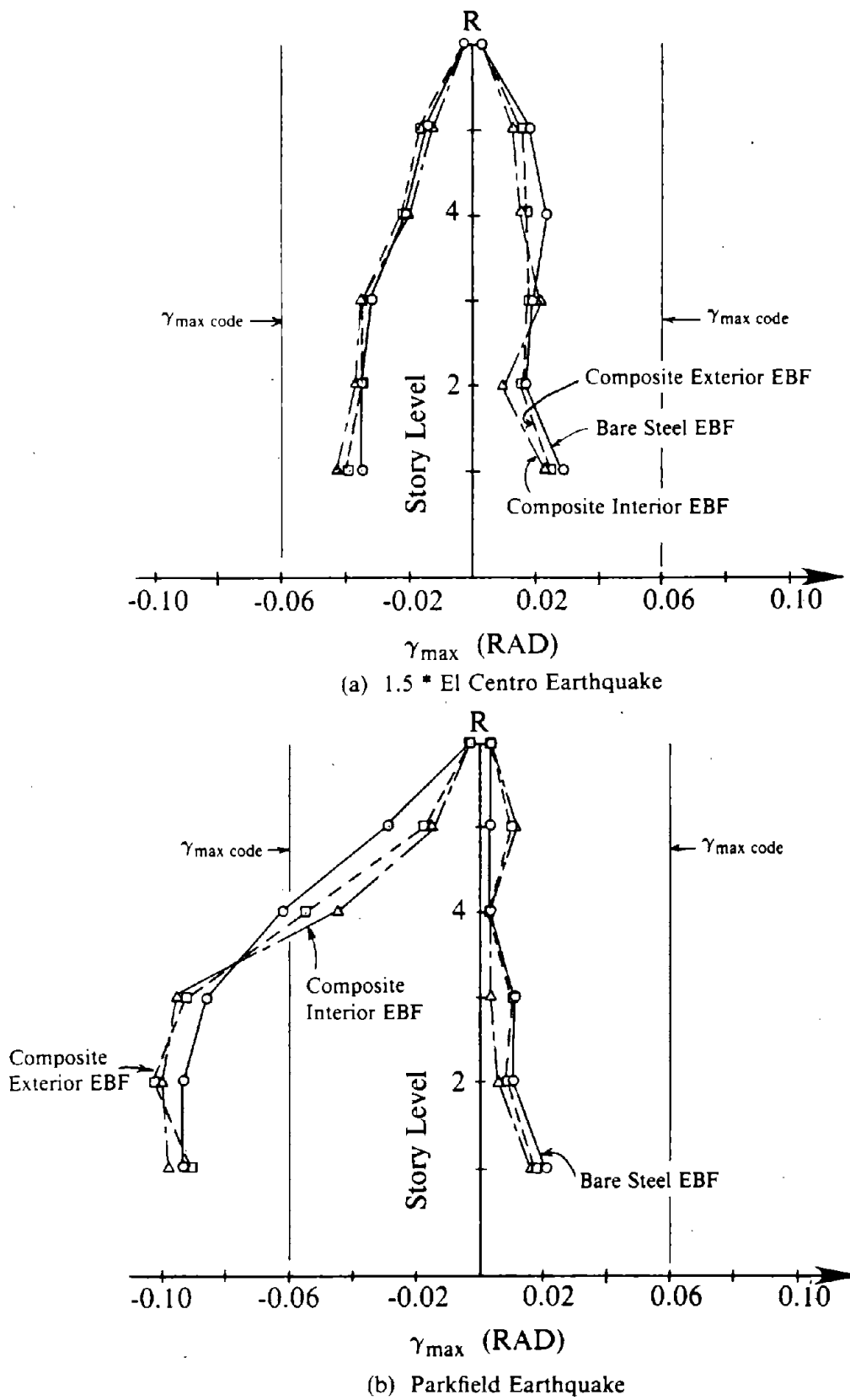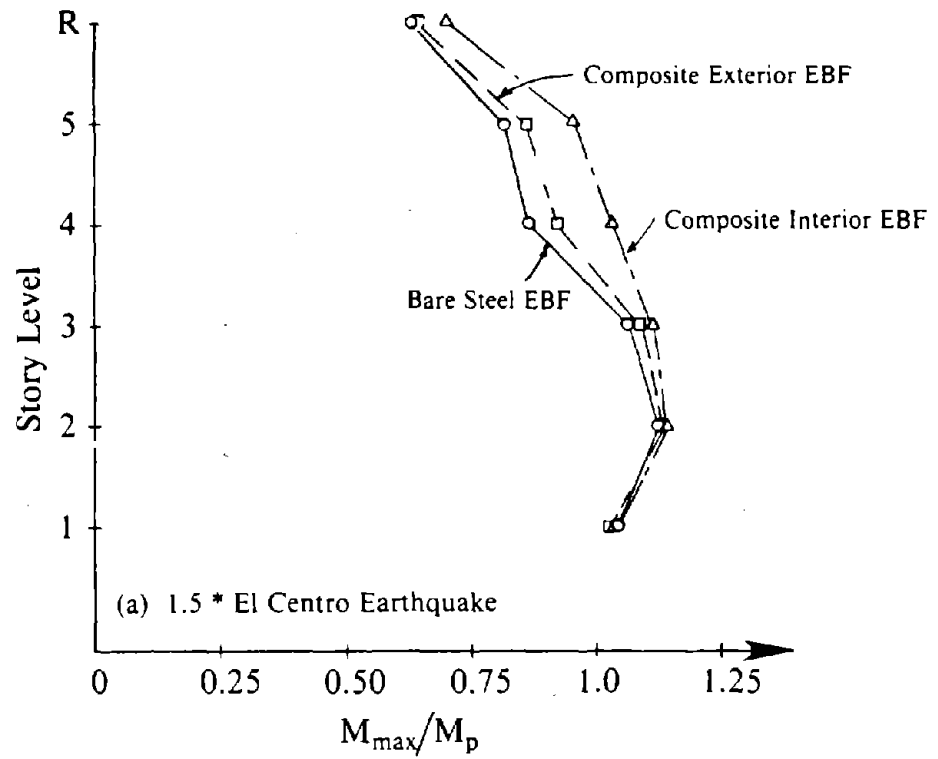
Fig. 8.74   Normalized Maximum Link End Moments for EBF Models of Design 2.
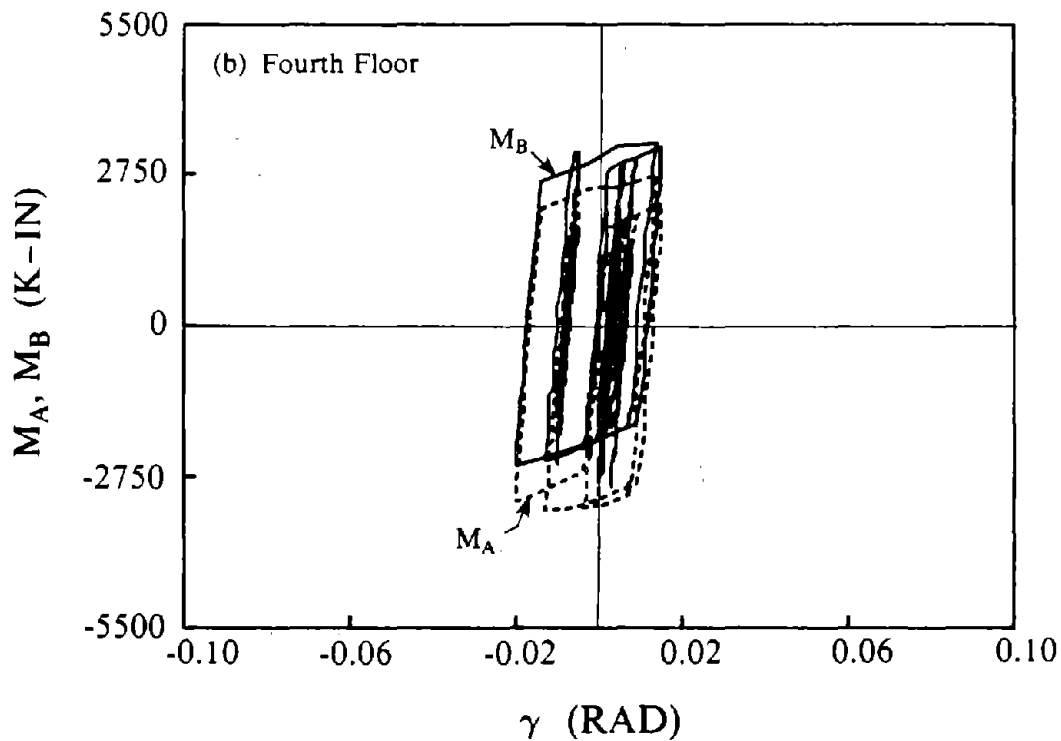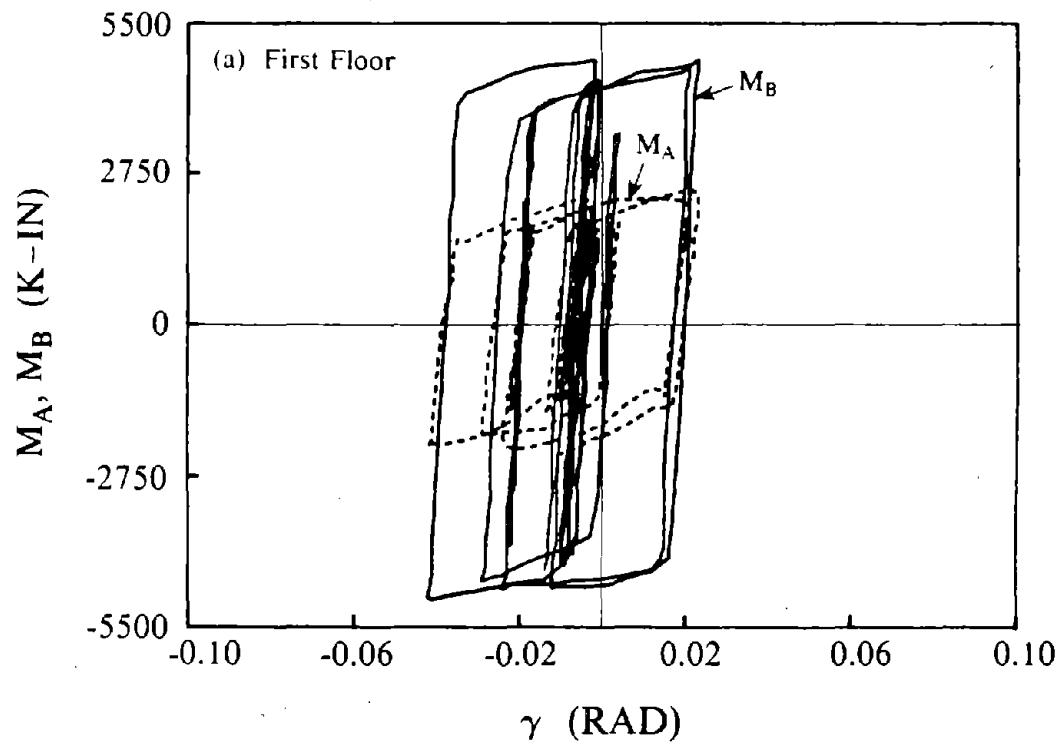
Fig. 8.75   Moment-Deformation Hysteretic Response of Links in Composite Interior EBF Model Subjected to 1.5 * El Centro Earthquake, Design 2.

288
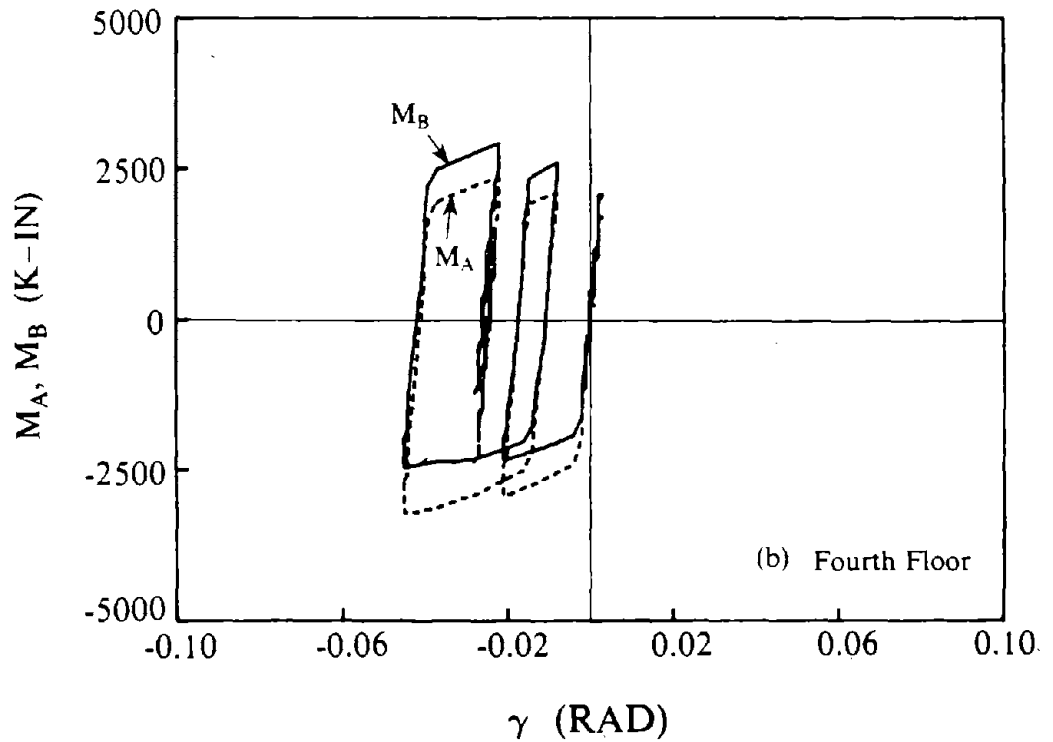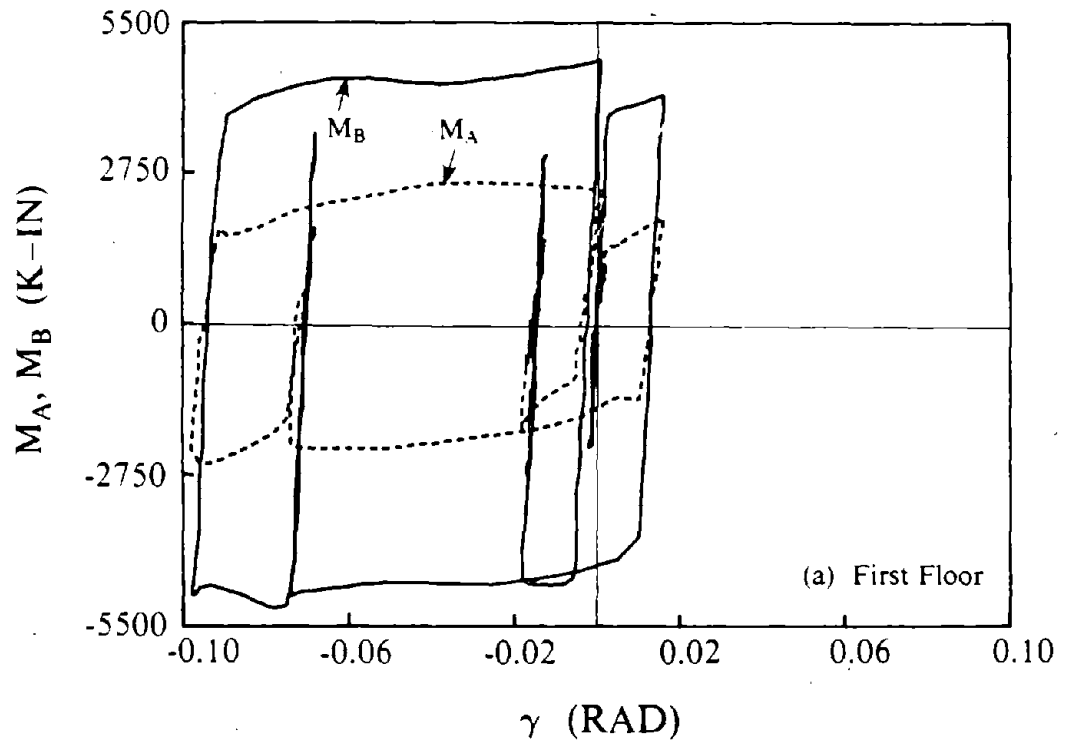
Fig. 8.76   Moment-Deformation Hysteretic Response of Links in Composite Interior EBF
Model Subjected to Parkfield Earthquake, Design 2.
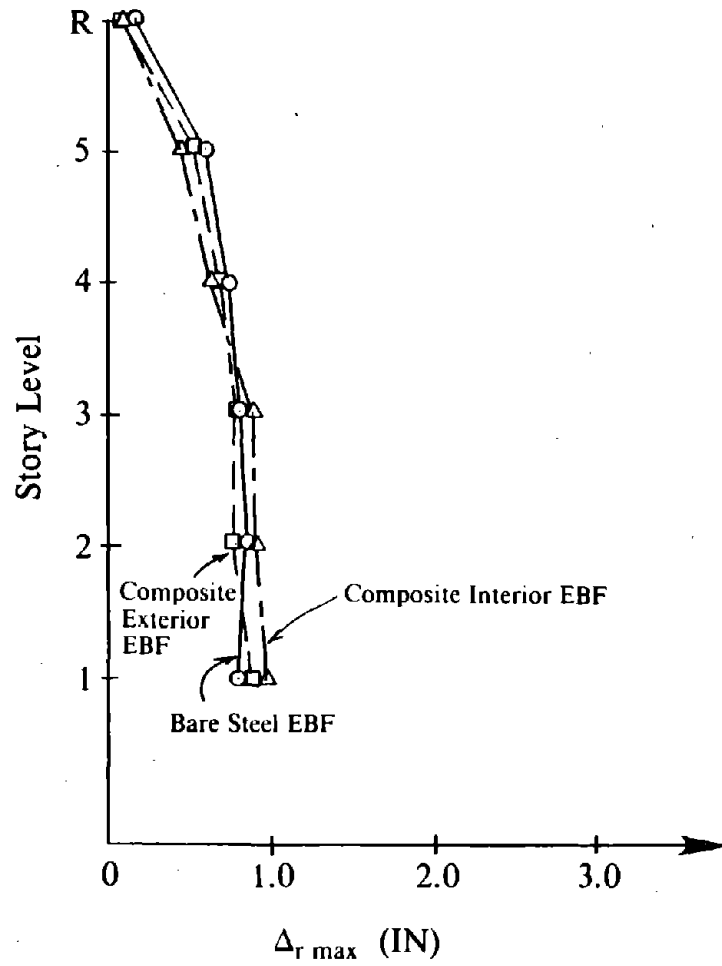
(a) 1.5 * El Centro Earthquake
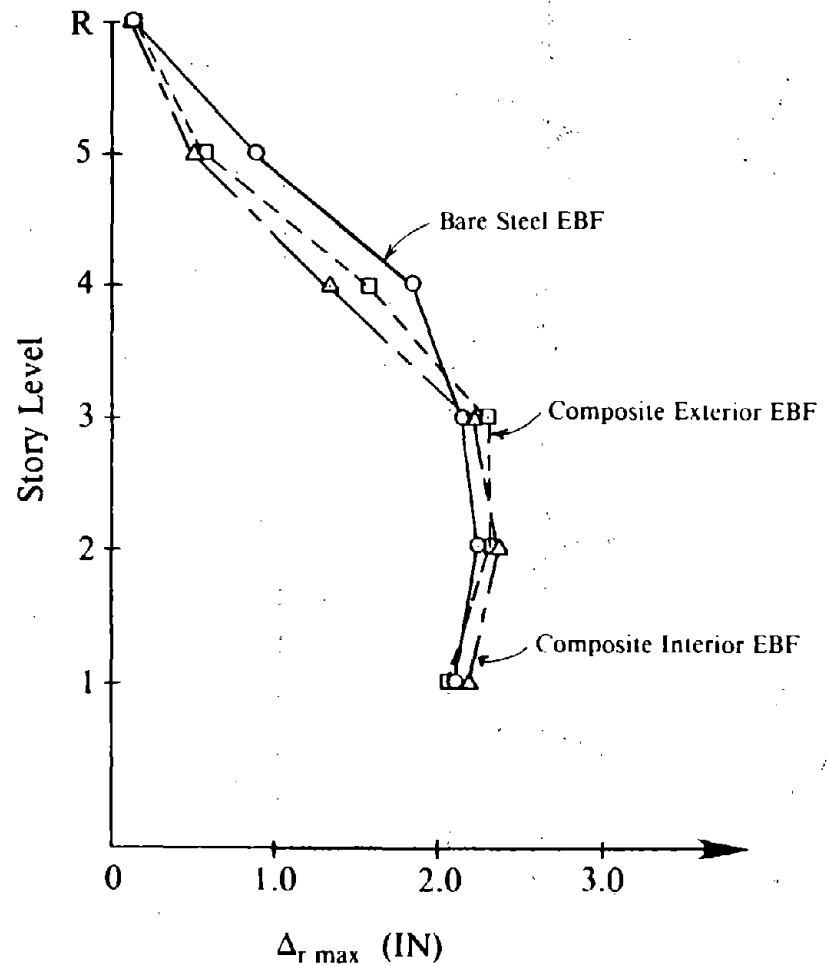
(b) Parkfield Earthquake

Fig. 8.77   Maximum Relative End Displacement of Links in EBF Models of Design 2.
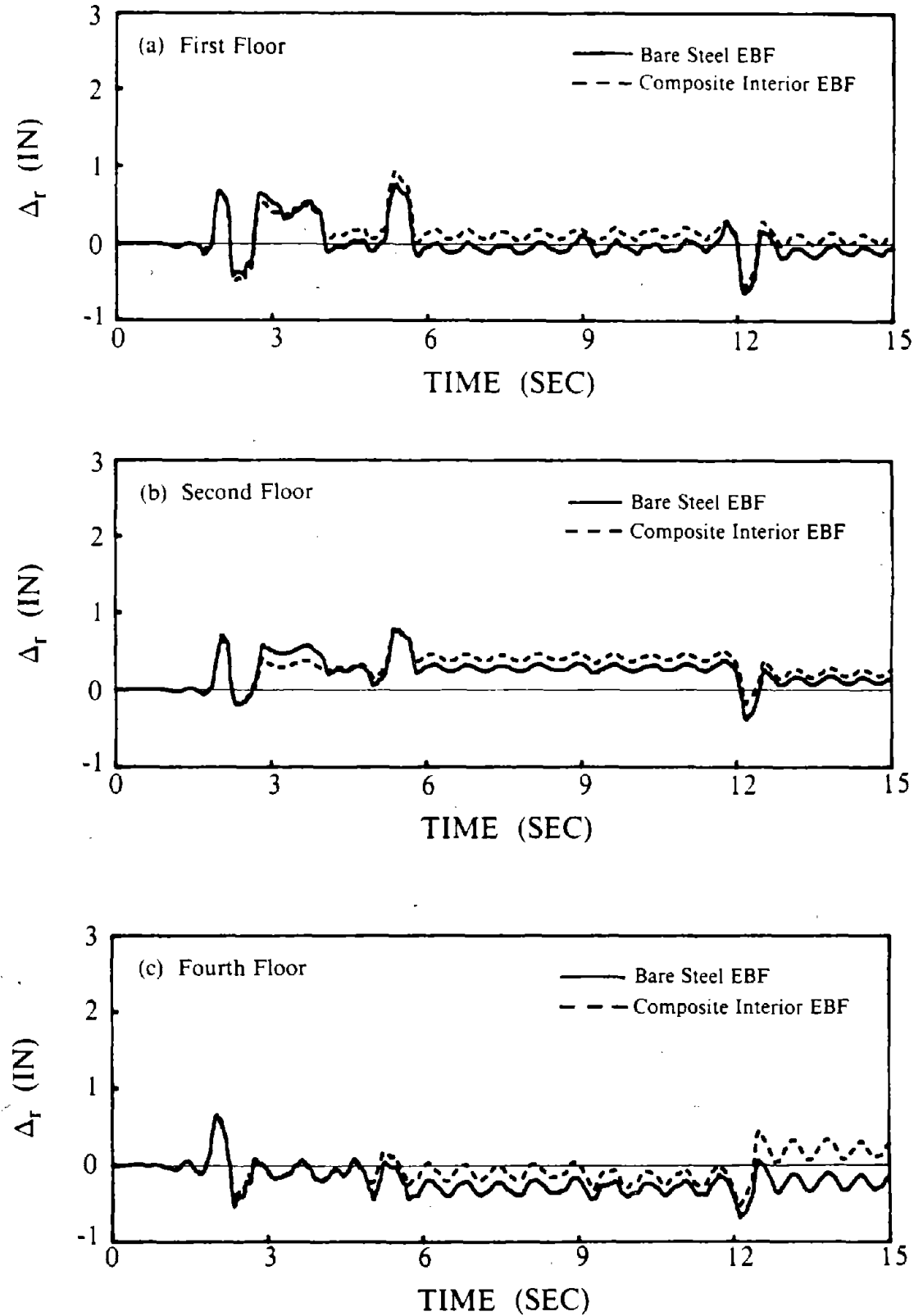
Fig. 8.78   Relative End Displacement Time Histories for Links of Design 2,
1.5 * El Centro Earthquake.
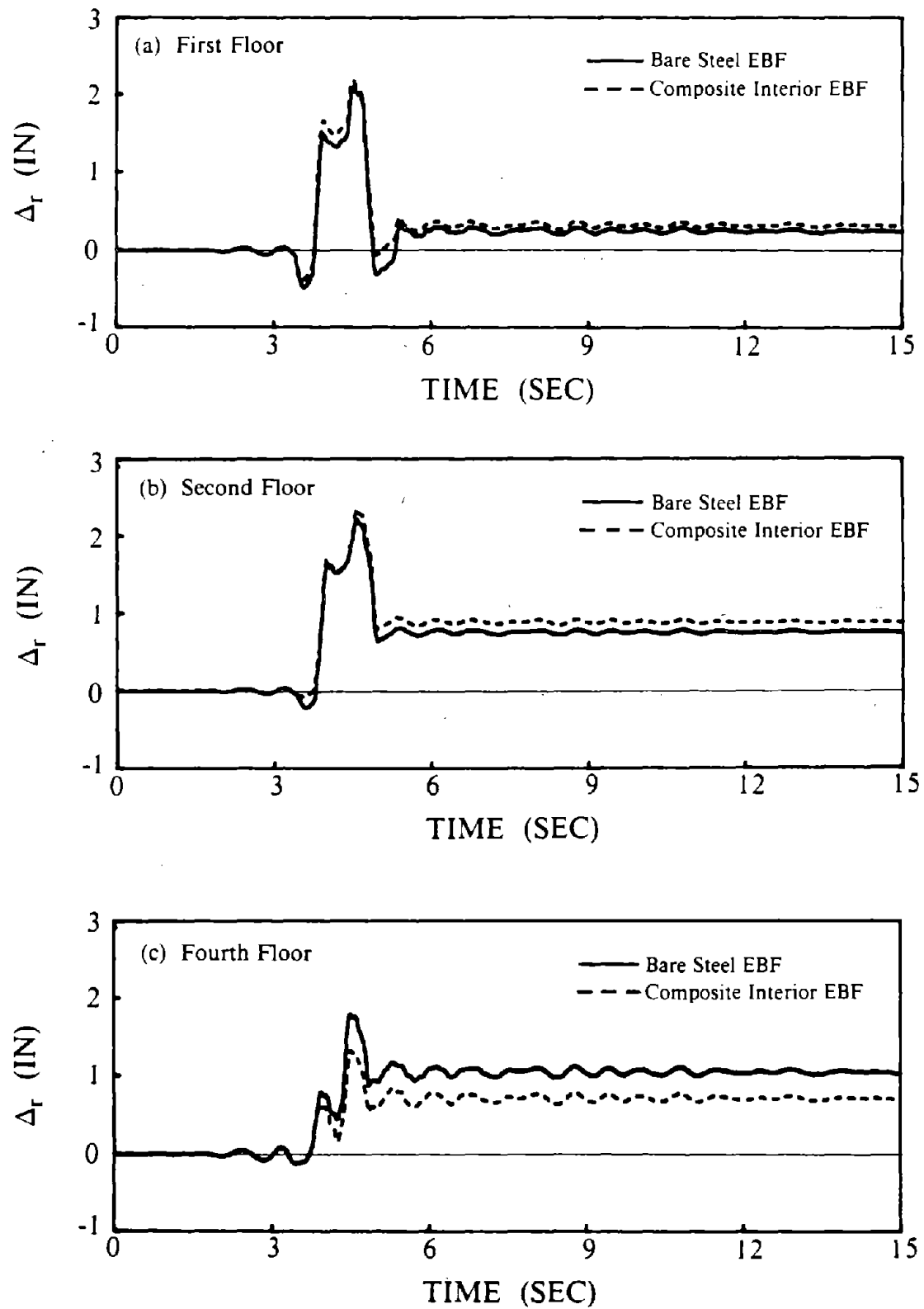
Fig. 8.79   Relative End Displacement Time Histories for Links of Design 2, Parkfield Earthquake.
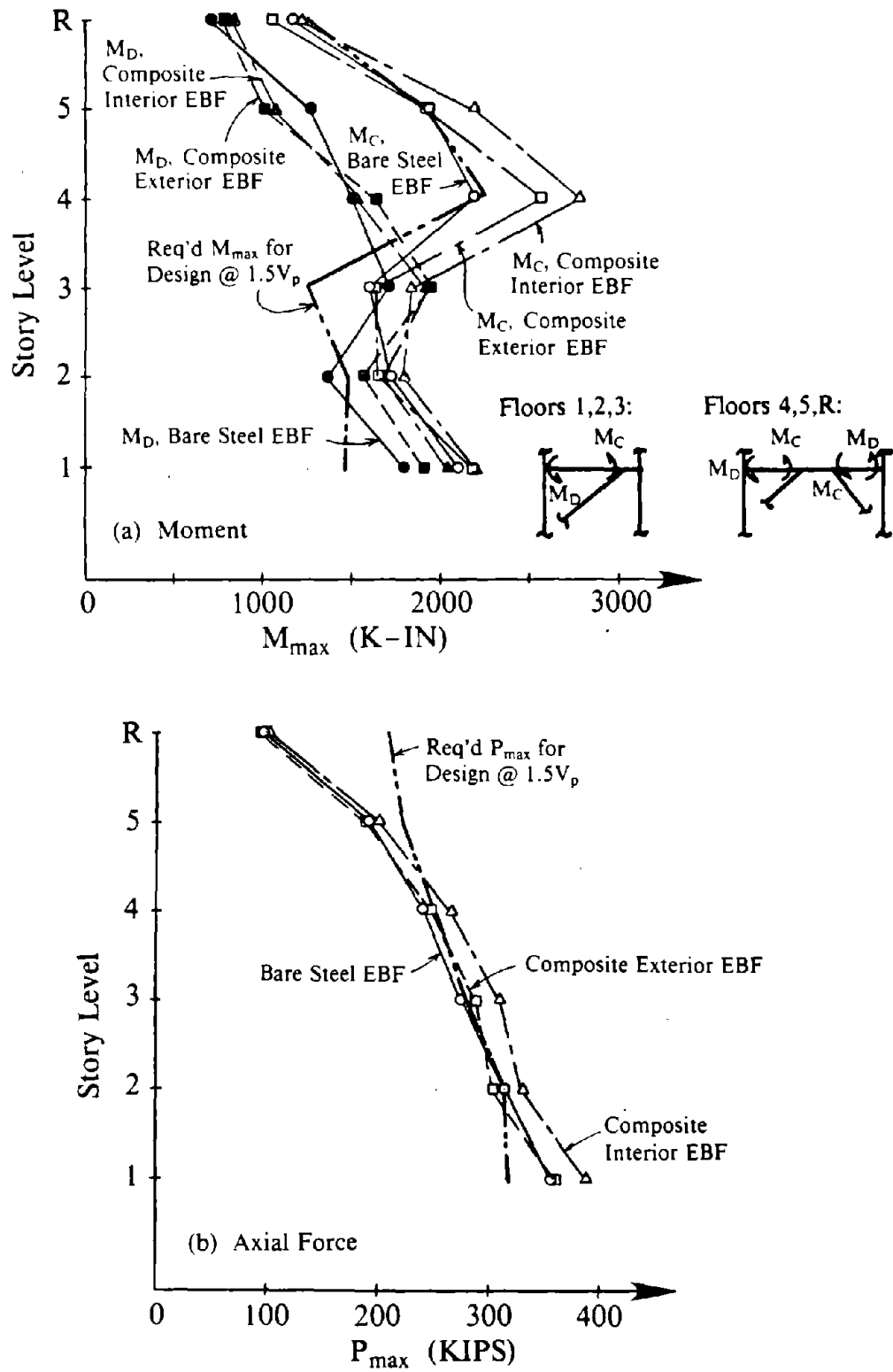
Fig. 8.80   Maximum Member Forces Developed in Floor Beams Outside the Links of Braced Panels in Design 2, Parkfield Earthquake.
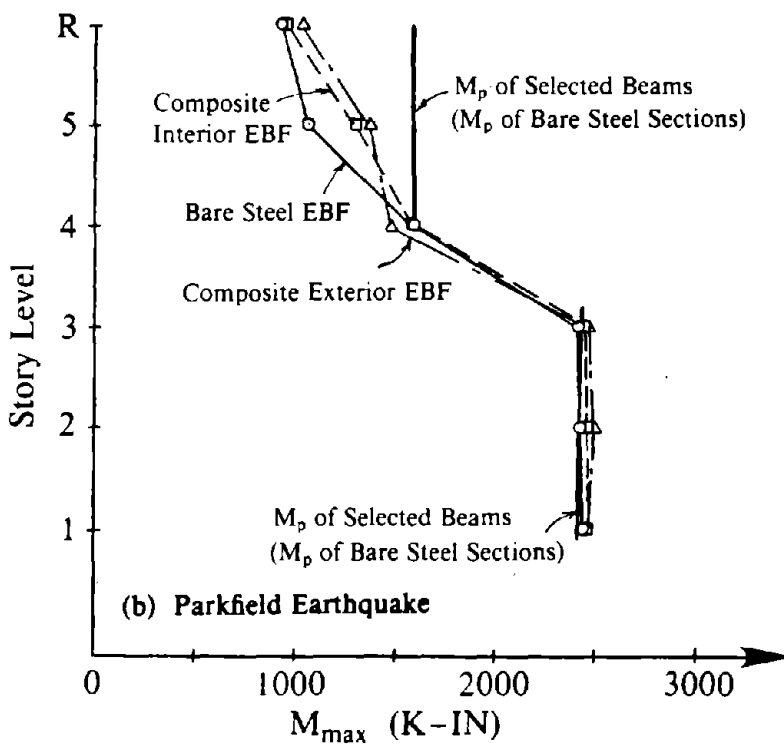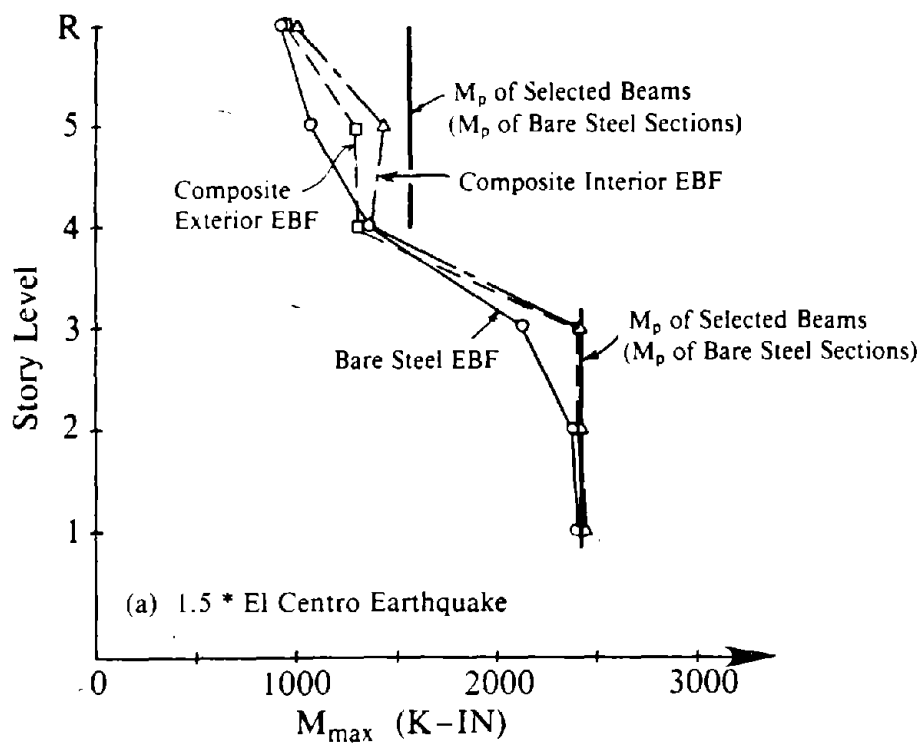
Fig. 8.81   Maximum Moments Developed in Floor Beams of Unbraced Panels
            for Design 2.

294

(a) 1.5 * El Centro Earthquake

(b) Parkfield Earthquake
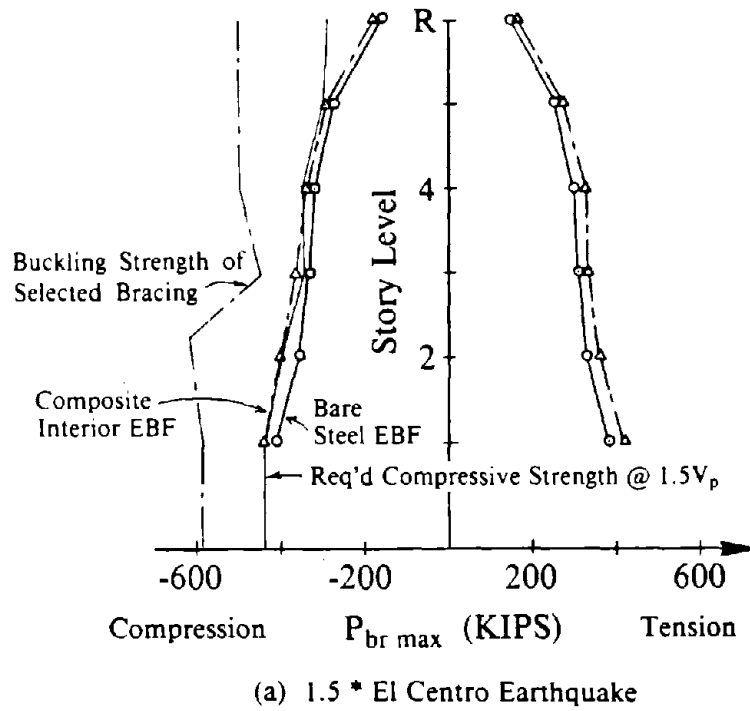
Fig. 8.82 Axial Brace Force Envelopes for EBF Models of Design 2.
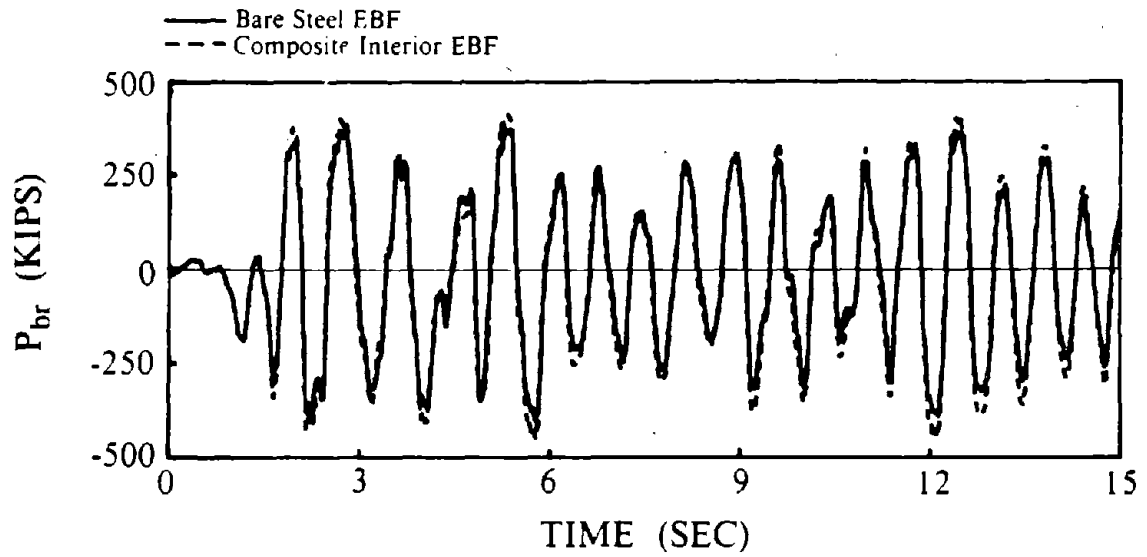
(a) 1.5 * El Centro Earthquake
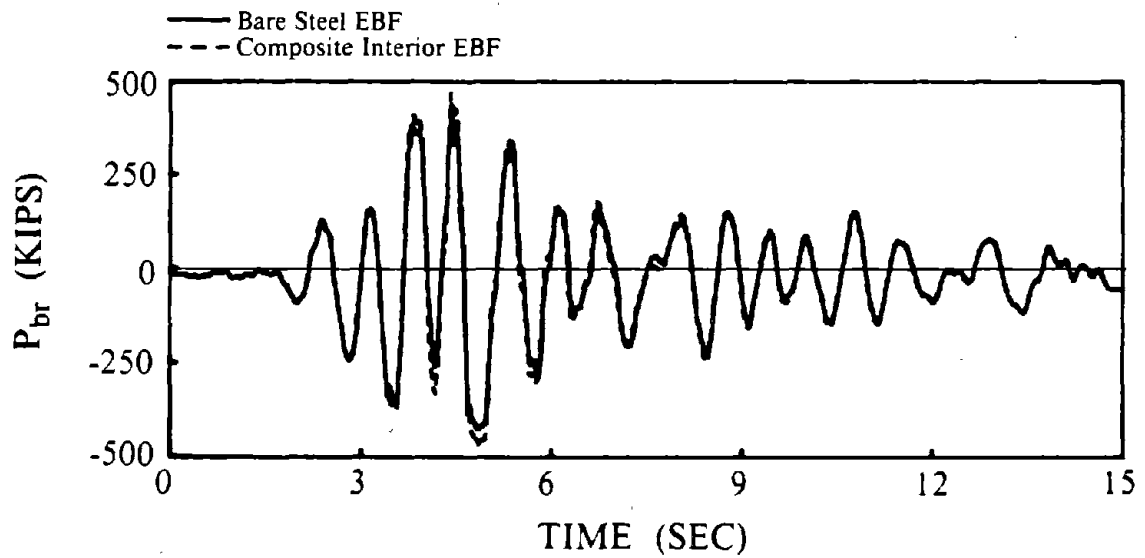
(b) Parkfield Earthquake

Fig. 8.83   Axial Force Time Histories for First Floor Brace of Bare Steel and Composite Interior EBF Models for Design 2.

(a) 1.5 * El Centro Earthquake

(b) Parkfield Earthquake
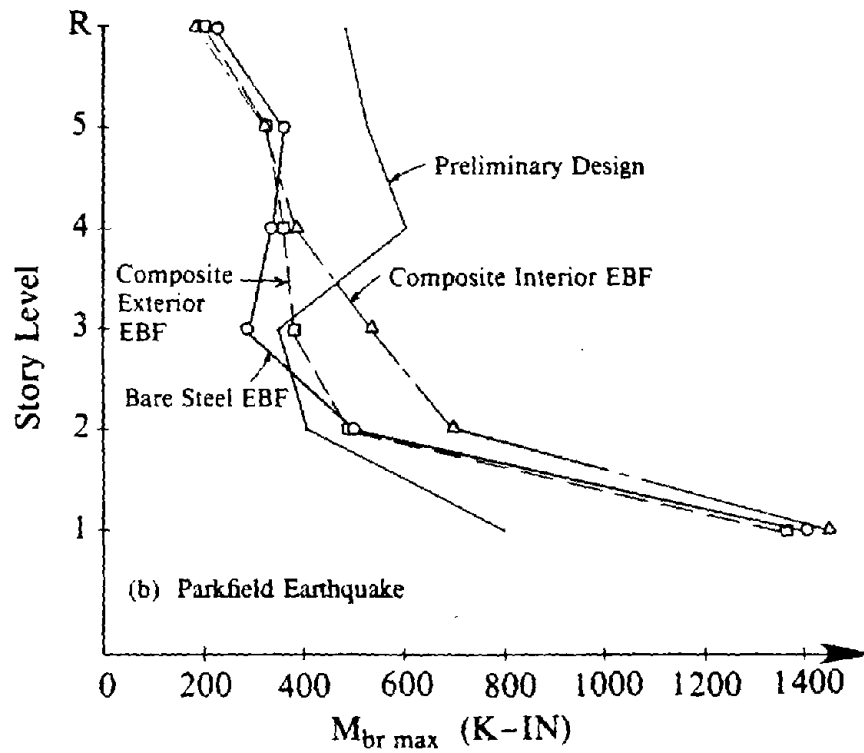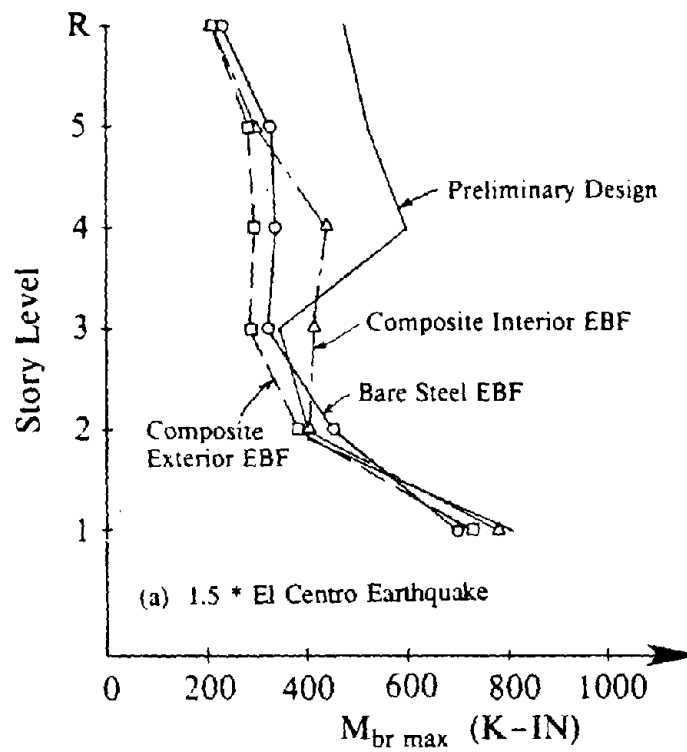
Fig. 8.84   Maximum Brace Moments for EBF Models of Design 2.

(a) 1.5 * El Centro Earthquake

Interior Col.,
Req'd Design
Envelope @ 1.5V$_p$

Exterior Col.,
Req'd Design
Envelope @ 1.5V$_p$

Interior Columns, Bare Steel EBF

Interior Columns,
Composite Interior EBF

Exterior Columns,
Composite Interior EBF

Exterior Columns, Bare Steel EBF

Story Level

-800 -600 -400 -200 0 200 400 600 800

Compression   Tension

$P_{col\ max}$ (KIPS)

(b) Parkfield Earthquake

Exterior Col.,
Req'd Design
Envelope @ 1.5V$_p$

Interior Col.,
Req'd Design
Envelope @ 1.5V$_p$

Interior Columns, Bare Steel EBF

Interior Columns,
Composite Interior EBF

Exterior Columns,
Composite Interior
EBF

Exterior Columns, Bare Steel EBF

Story Level

-800 -600 -400 -200 0 200 400 600 800

Compression   Tension

$P_{col\ max}$ (KIPS)

Fig. 8.85   Column Axial Force Envelopes for EBF Models of Design 2.
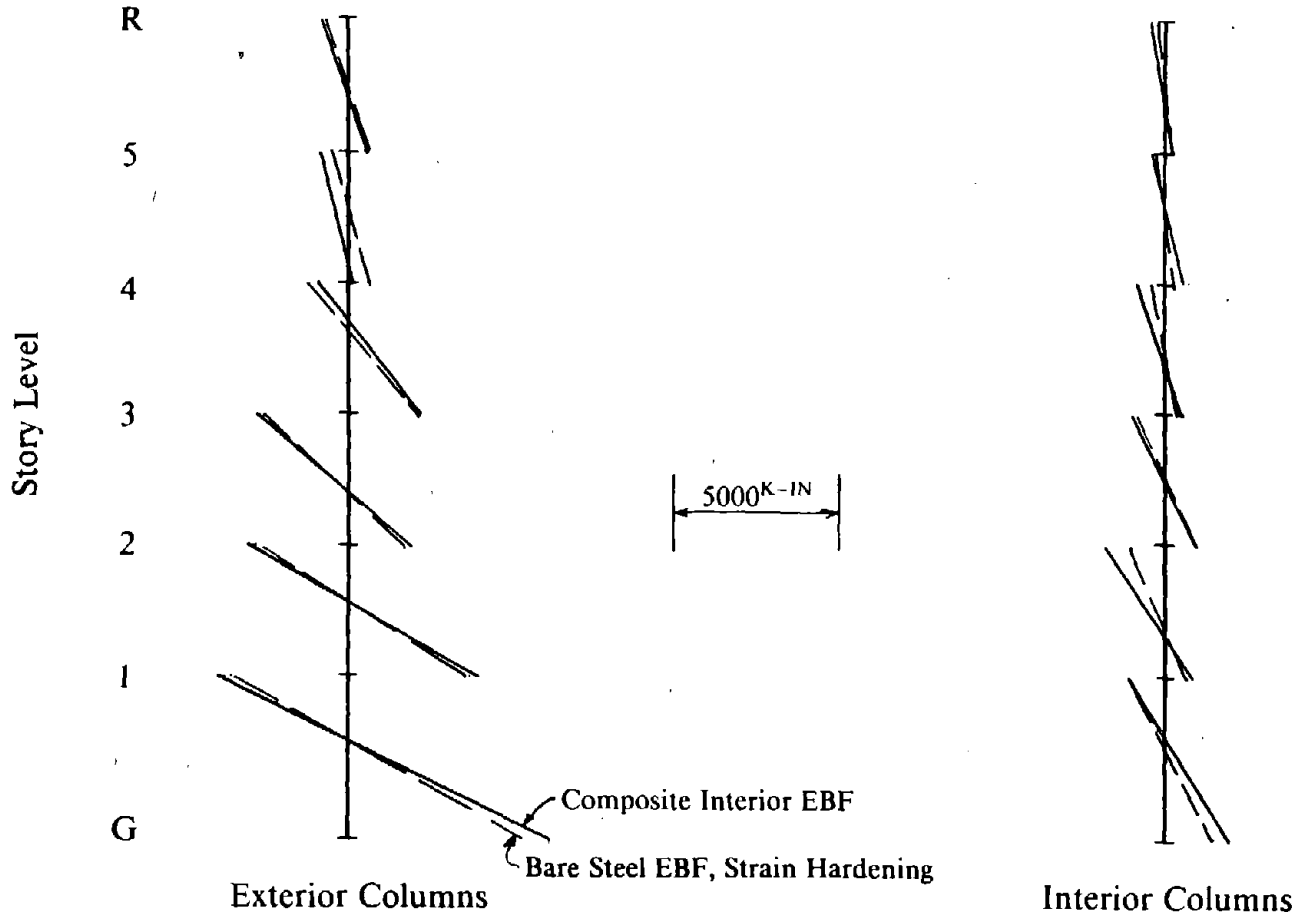
Fig. 8.86   Individual Column Moment Diagrams Corresponding to Maximum Column
Moments of Design 2 Bare Steel and Composite Interior EBF Models, 1.5 * El
Centro Earthquake.
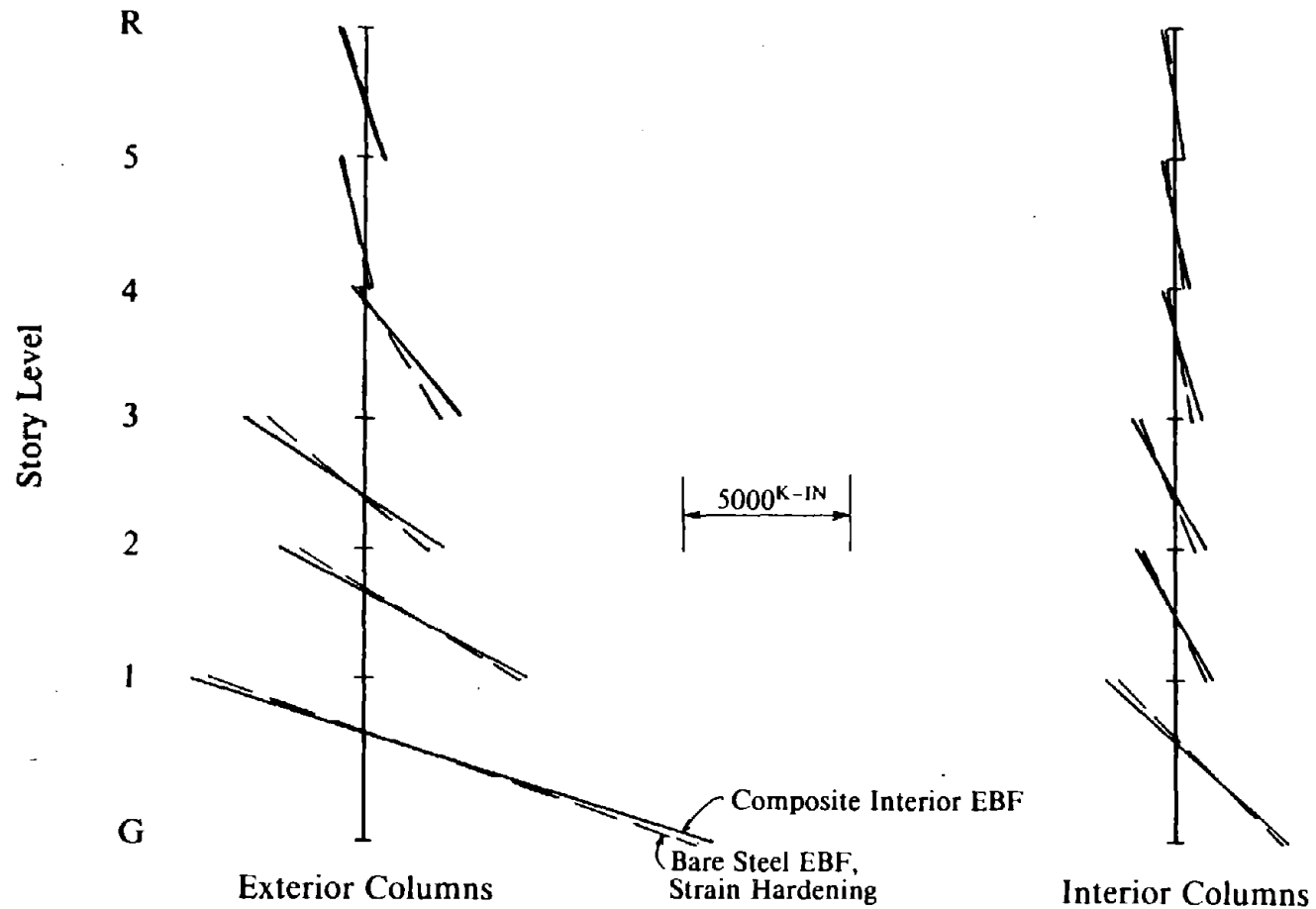
Fig. 8.87   Individual Column Moment Diagrams Corresponding to Maximum Column
Moments of Design 2 Bare Steel and Composite Interior EBF Models, Parkfield
Earthquake.
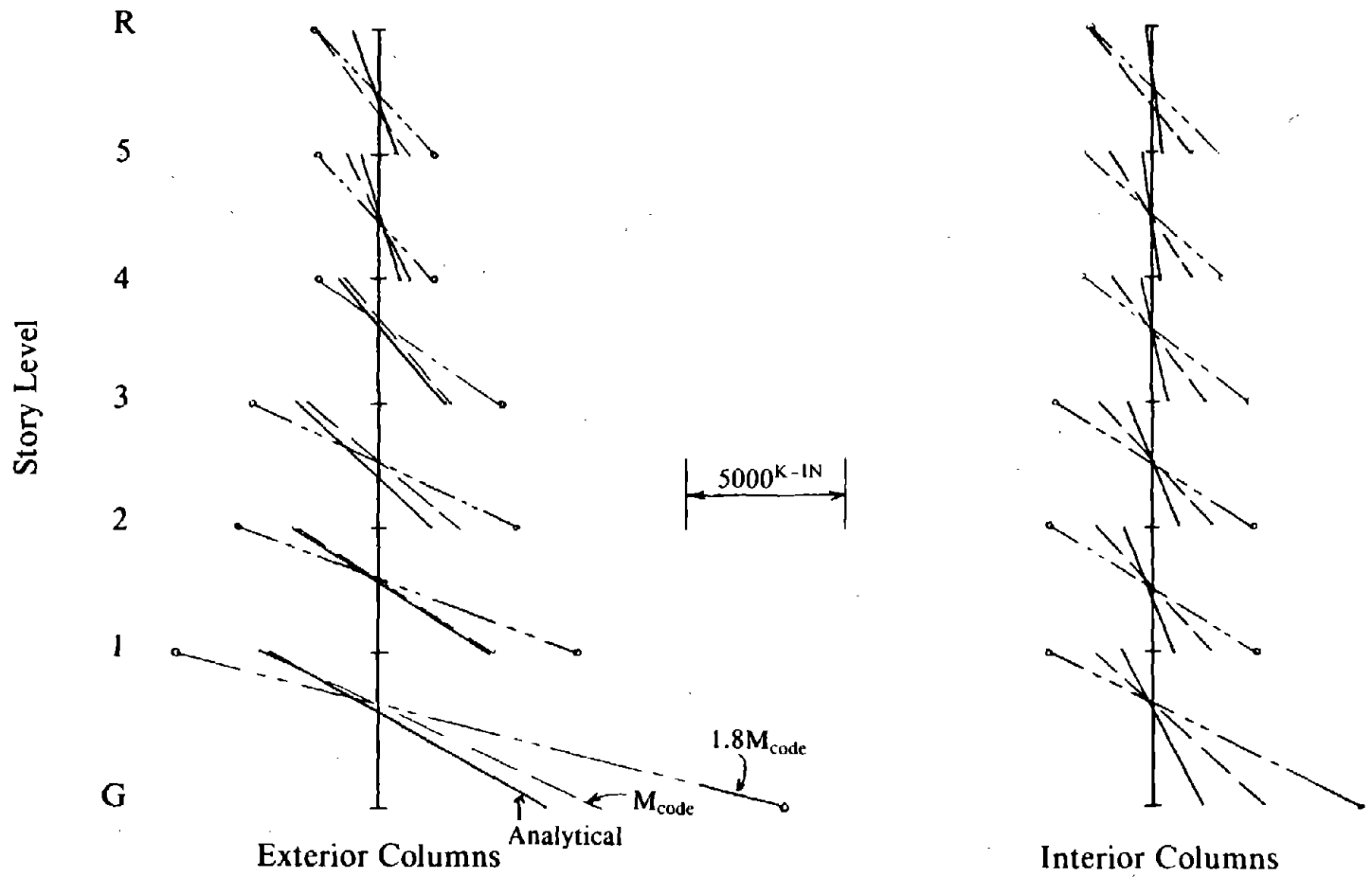
Fig. 8.88   Comparison of Maximum Column Moments with Design Moments for Bare
Steel EBF Model, Design 2 Subjected to 1.5 * El Centro Earthquake.
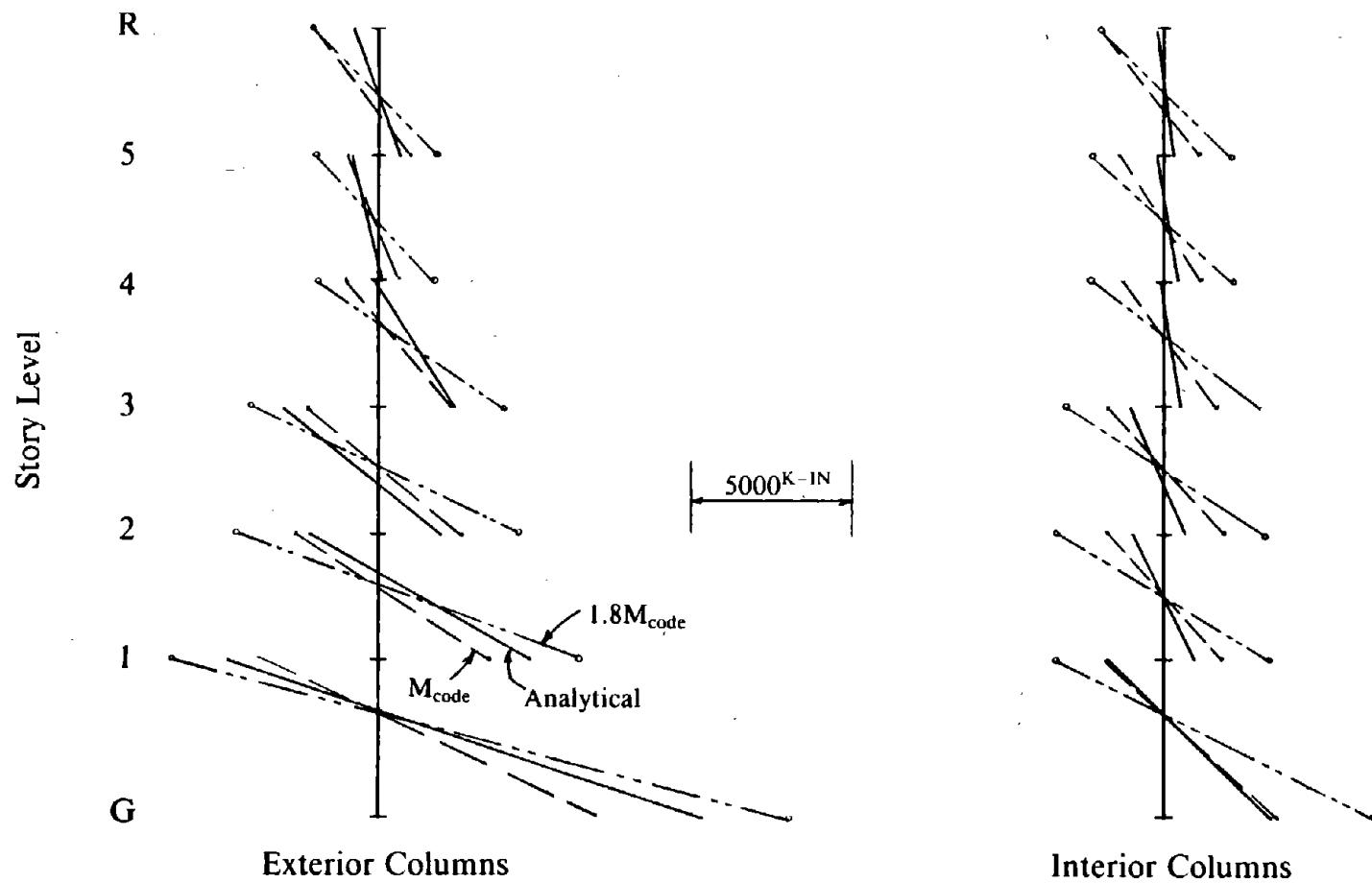
Fig. 8.89   Comparison of Maximum Column Moments with Design Moments for Bare
Steel EBF Model, Design 2 Subjected to Parkfield Earthquake.
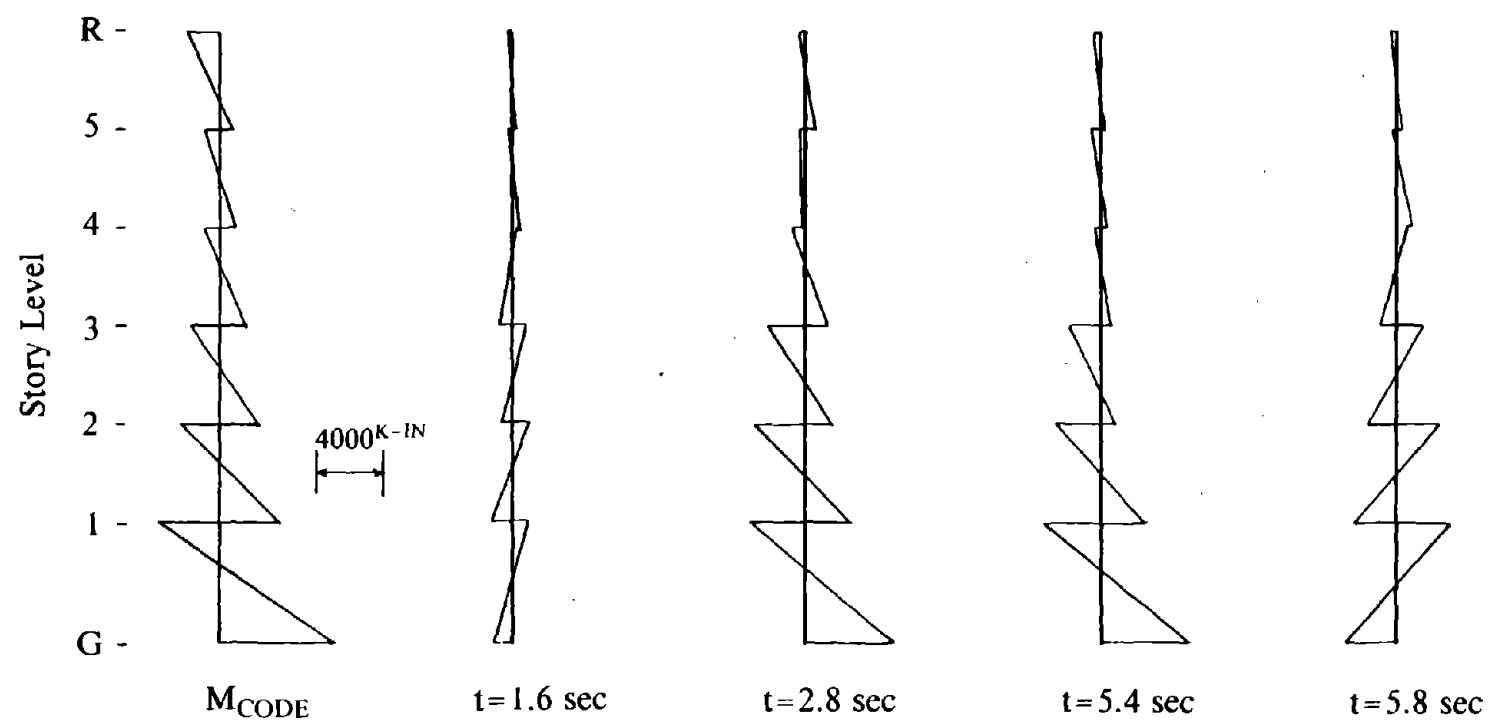
Fig. 8.90   Moments in Exterior Columns of Design 2 Bare Steel EBF Model at Selected
Times During Response to 1.5 * El Centro Earthquake.
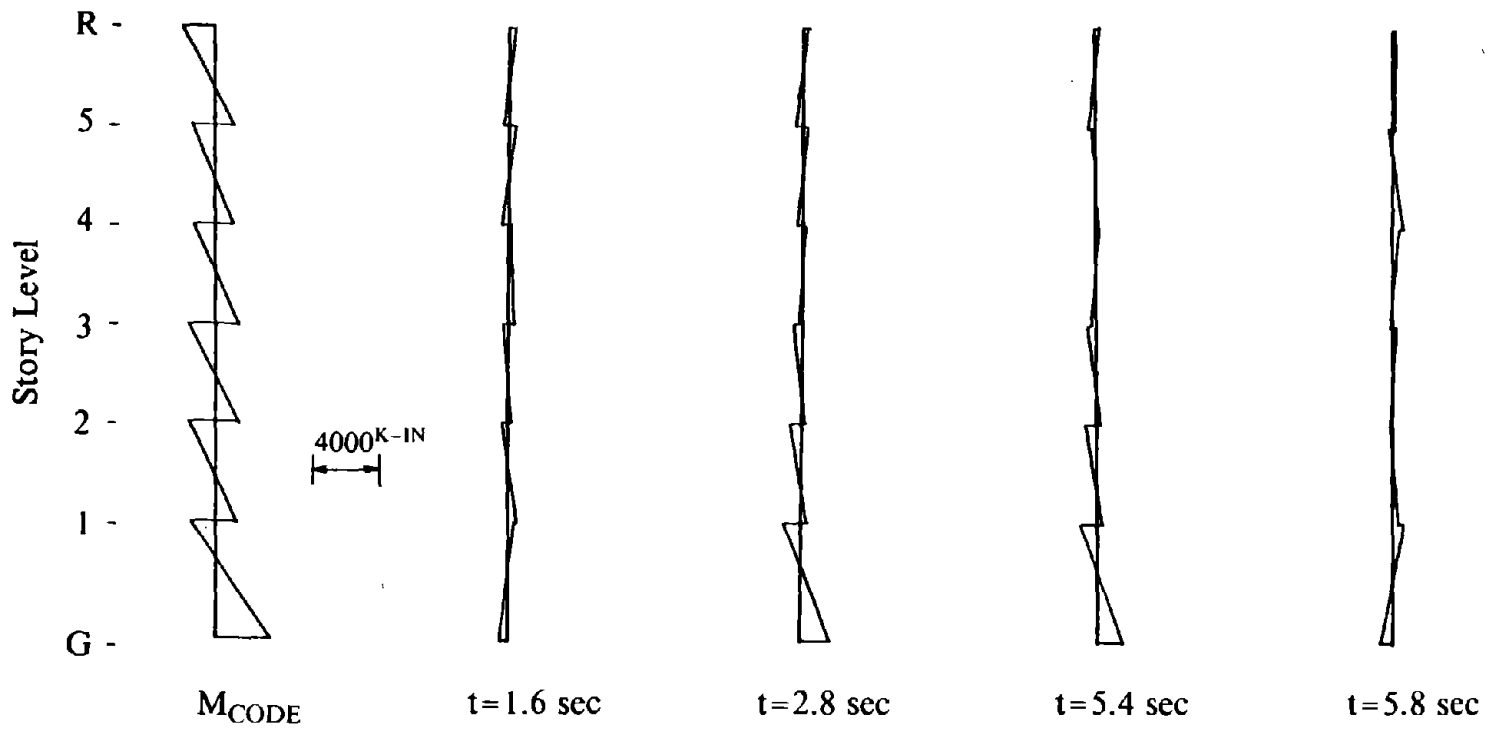
Fig. 8.91   Moments in Interior Columns of Design 2 Bare Steel EBF Model at Selected
Times During Response to 1.5 * El Centro Earthquake.
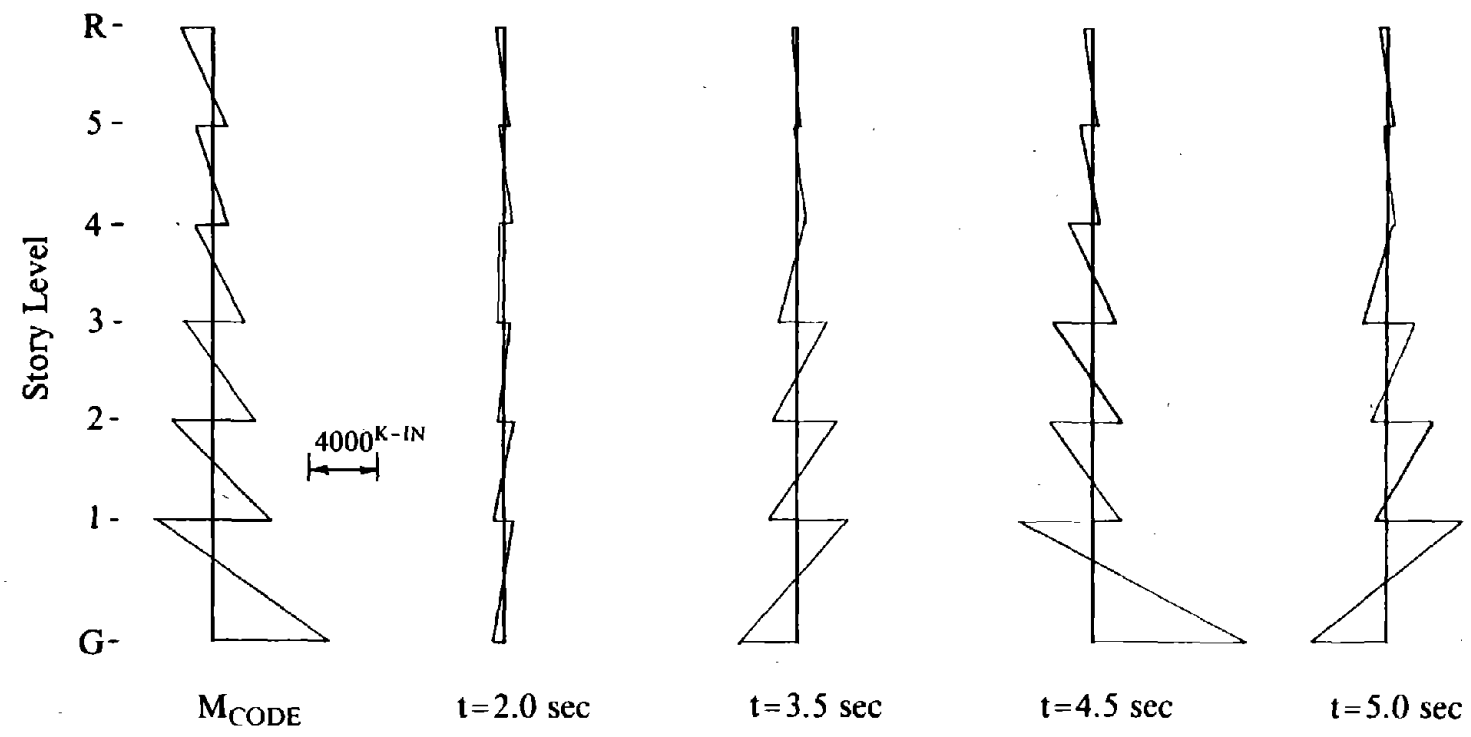
Fig. 8.92   Moments in Exterior Columns of Design 2 Bare Steel EBF Model at Selected
Times During Response to Parkfield Earthquake.
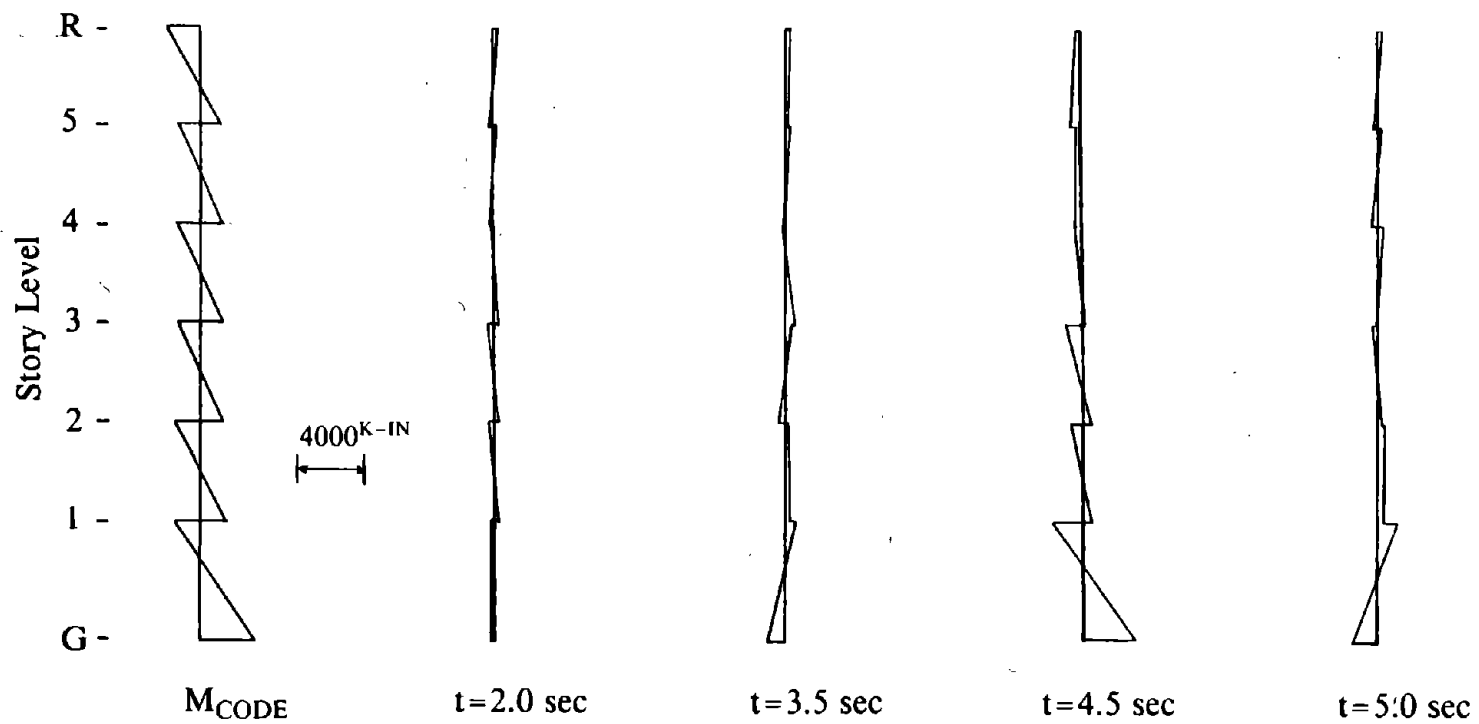
Fig. 8.93   Moments in Interior Columns of Design 2 Bare Steel EBF Model at Selected
Times During Response to Parkfield Earthquake.
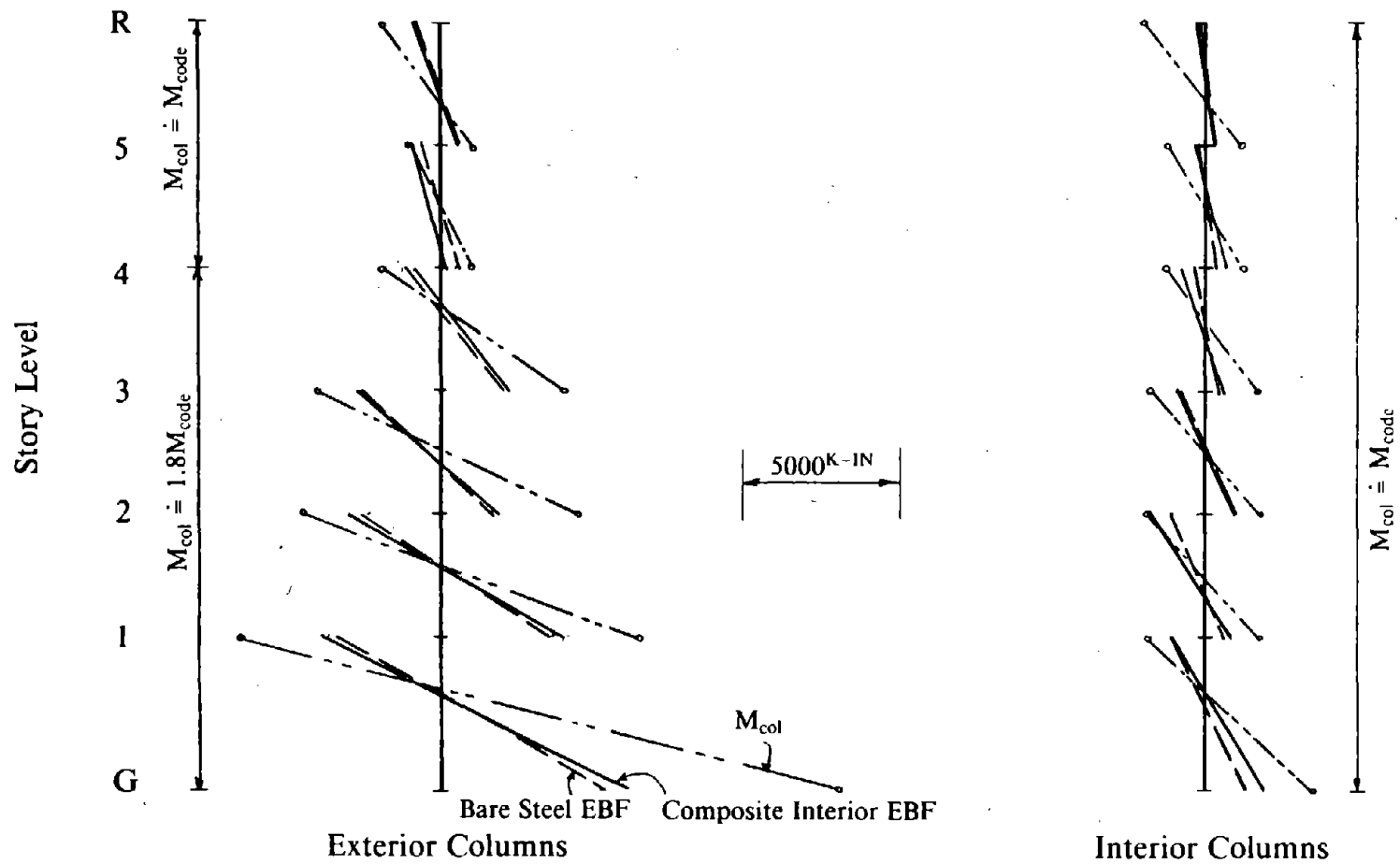
Fig. 8.94 Suggested Column Design Moments and Comparison with Maximum Column Moments of Design 2 for 1.5 * El Centro Earthquake.
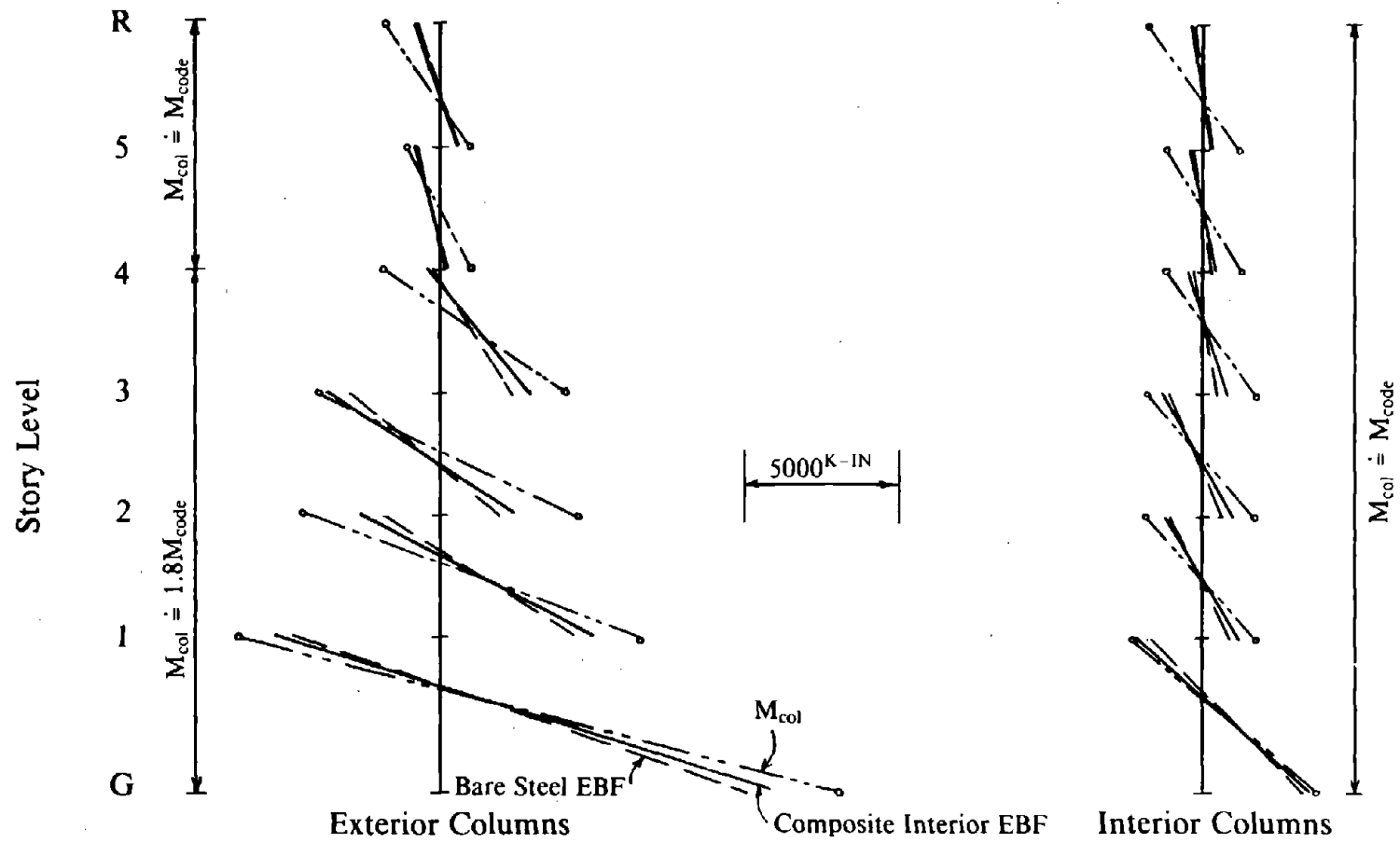
Fig. 8.95   Suggested Column Design Moments and Comparison with Maximum Column
Moments of Design 2 for Parkfield Earthquake.
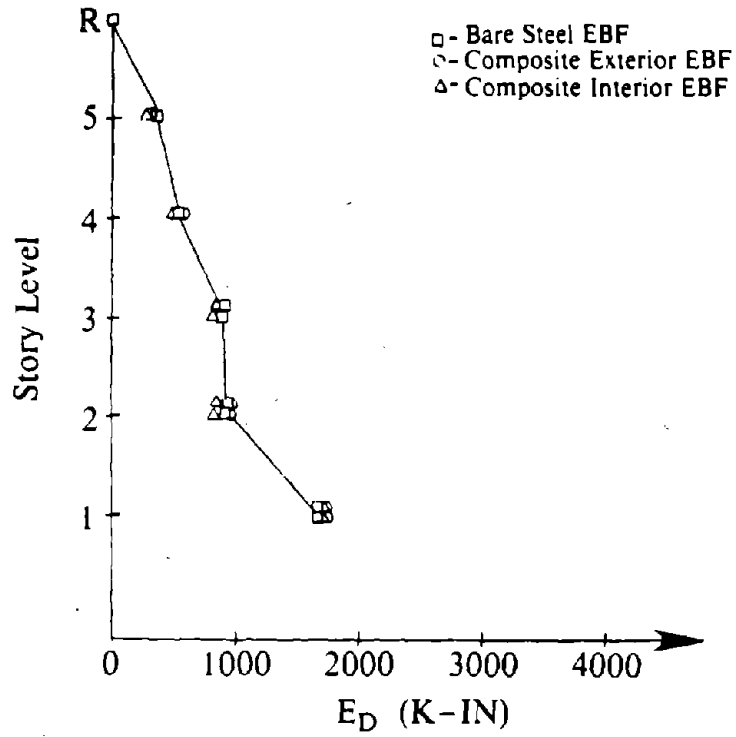
(a) 1.5 * El Centro Earthquake
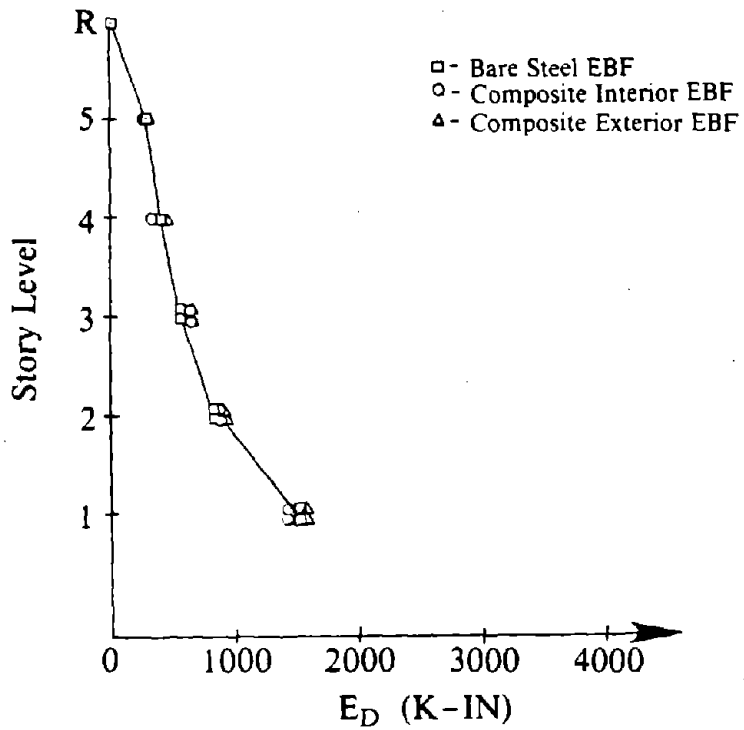
(b) Parkfield Earthquake

Fig. 8.96   Hysteretic Energy Dissipated by Links of Design 2.
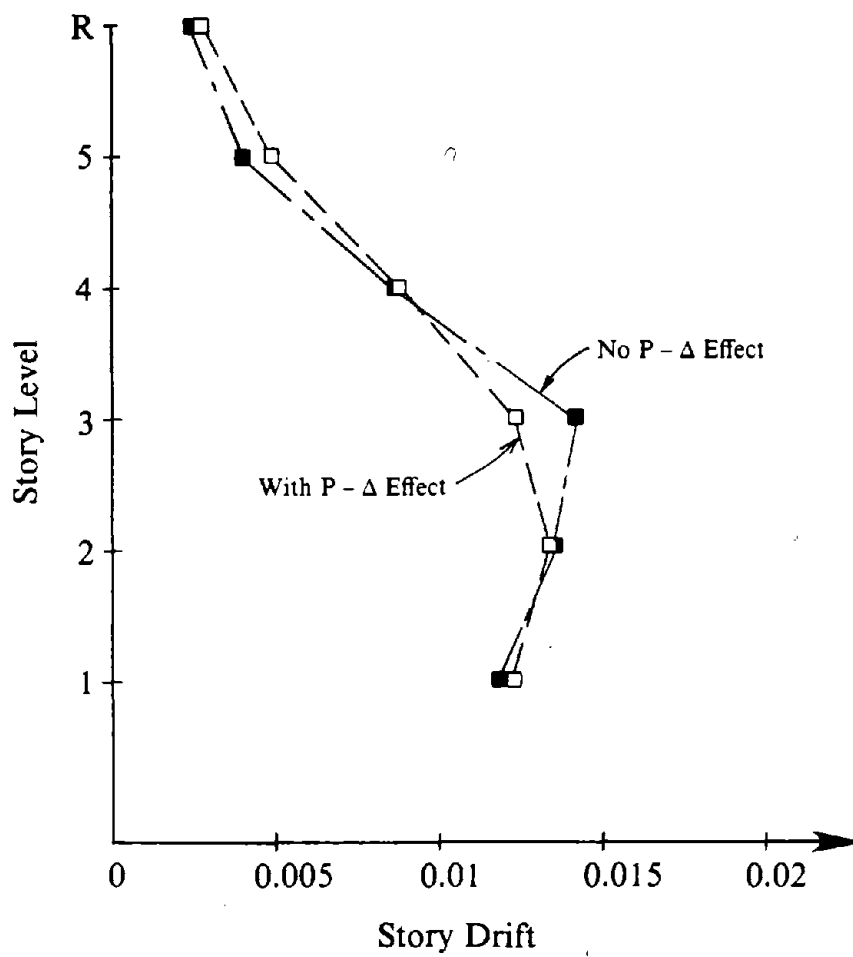
Fig. 8.97   Maximum Story Drift of Bare Steel EBF Models with and without Geometric Stiffness, Design 2 Subjected to Parkfield Earthquake.
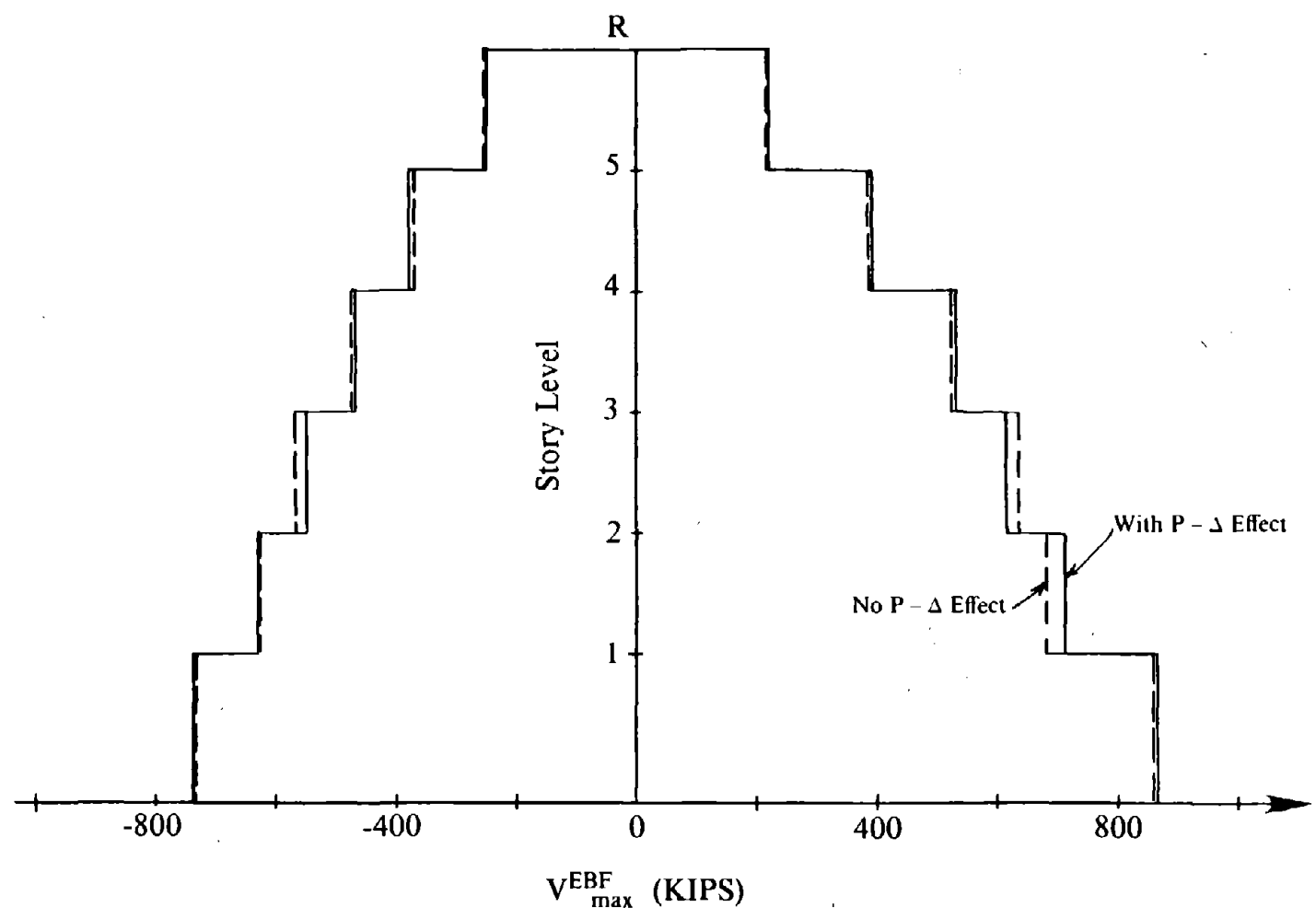
Fig. 8.98   Story Shear Force Envelopes for Bare Steel EBF Models with and without
Geometric Stiffness, Design 2 Subjected to Parkfield Earthquake.
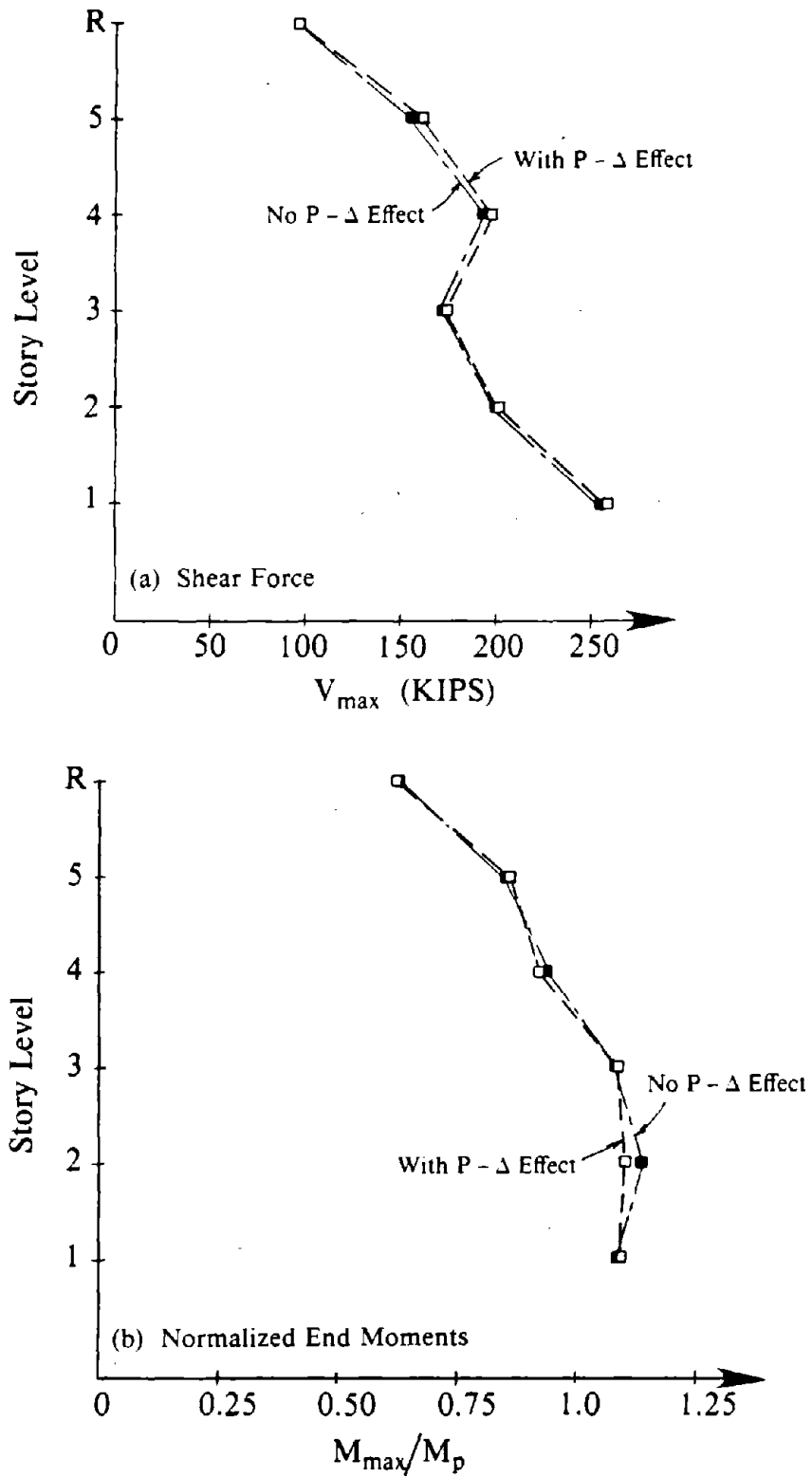
Fig. 8.99 Maximum Link Forces for Bare Steel EBF Models with and without Geometric Stiffness, Design 2 Subjected to Parkfield Earthquake.

312
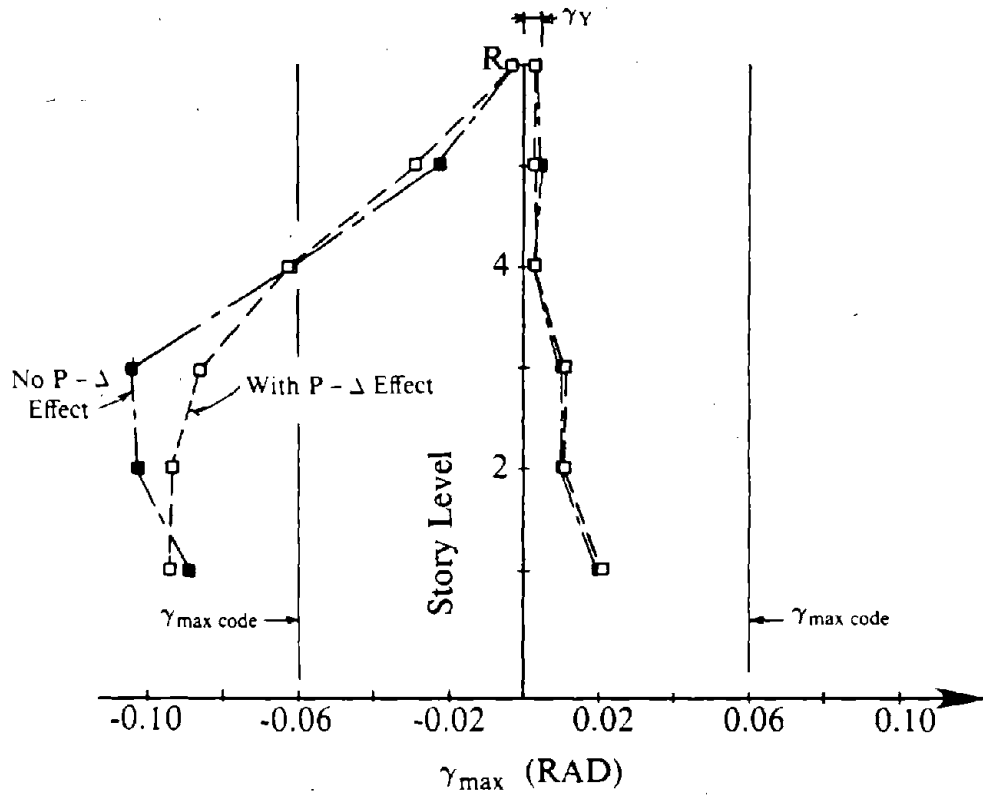
(a) Link Deformation Envelope
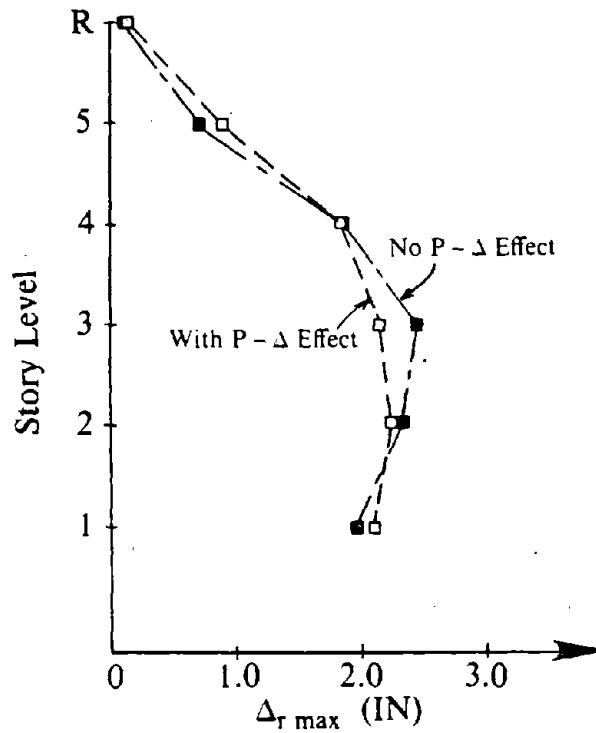
(b) Relative End Displacement

Fig. 8.100   Maximum Deformations Developed in Links of Bare Steel EBF Models with and without Geometric Stiffness, Design 2 Subjected to Parkfield Earthquake.

(a) Axial Force Envelopes

With P – Δ Effect

No P – Δ Effect

-600   -400   -200   0   200   -400   600

Compression $P_{br\,max}$ (KIPS)   Tension

(b) Maximum Moments

No P – Δ Effect

With P – Δ Effect

0   200   400   600   800   1000   1200   1400

$M_{br\,max}$ (K–IN)
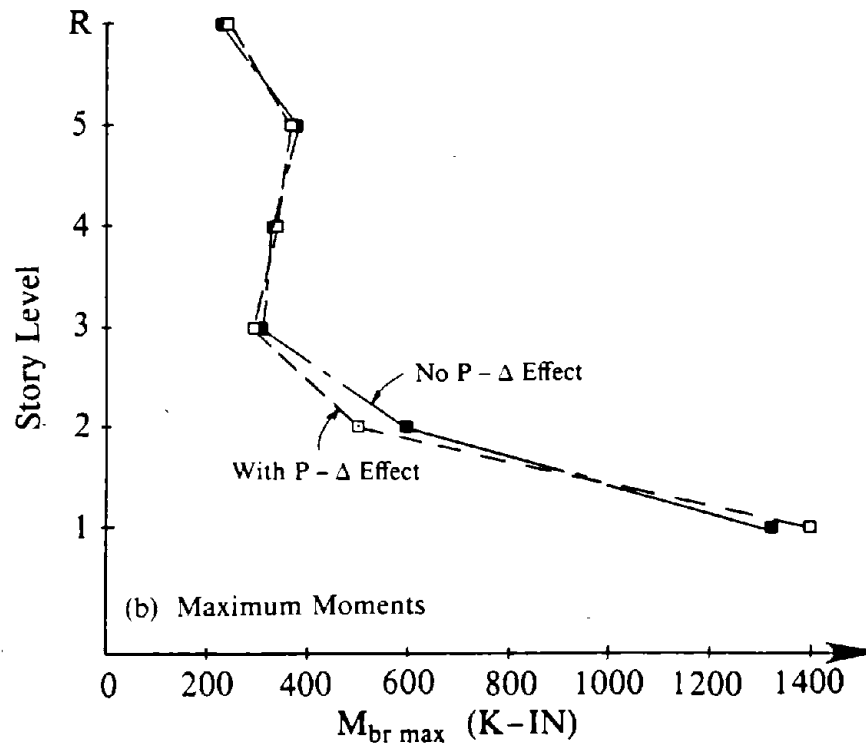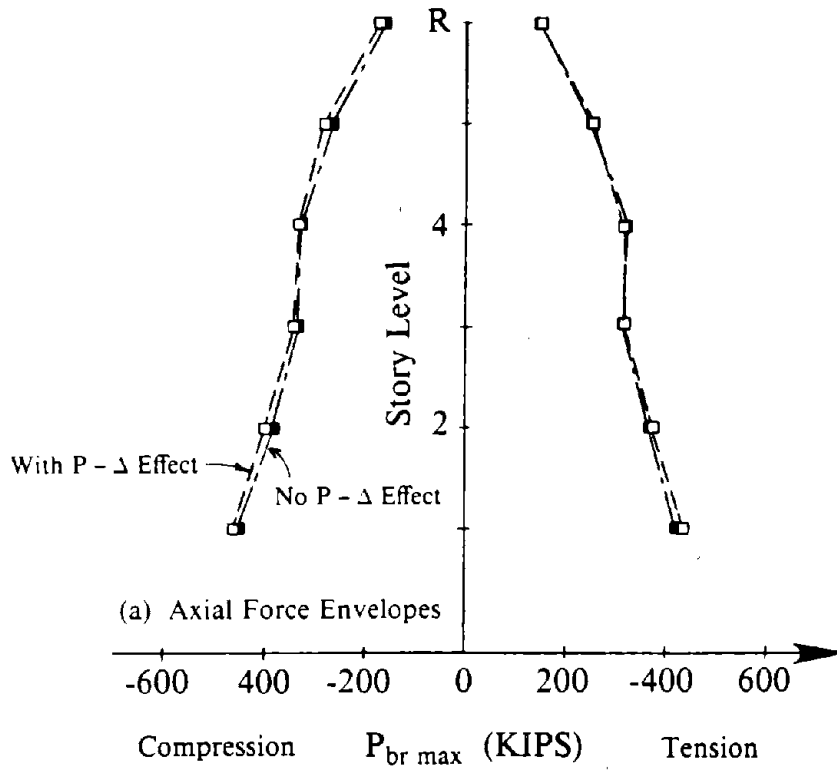
Fig. 8.101   Maximum Brace Forces for Bare Steel EBF Models with and without Geometric Stiffness, Design 2 Subjected to Parkfield Earthquake.
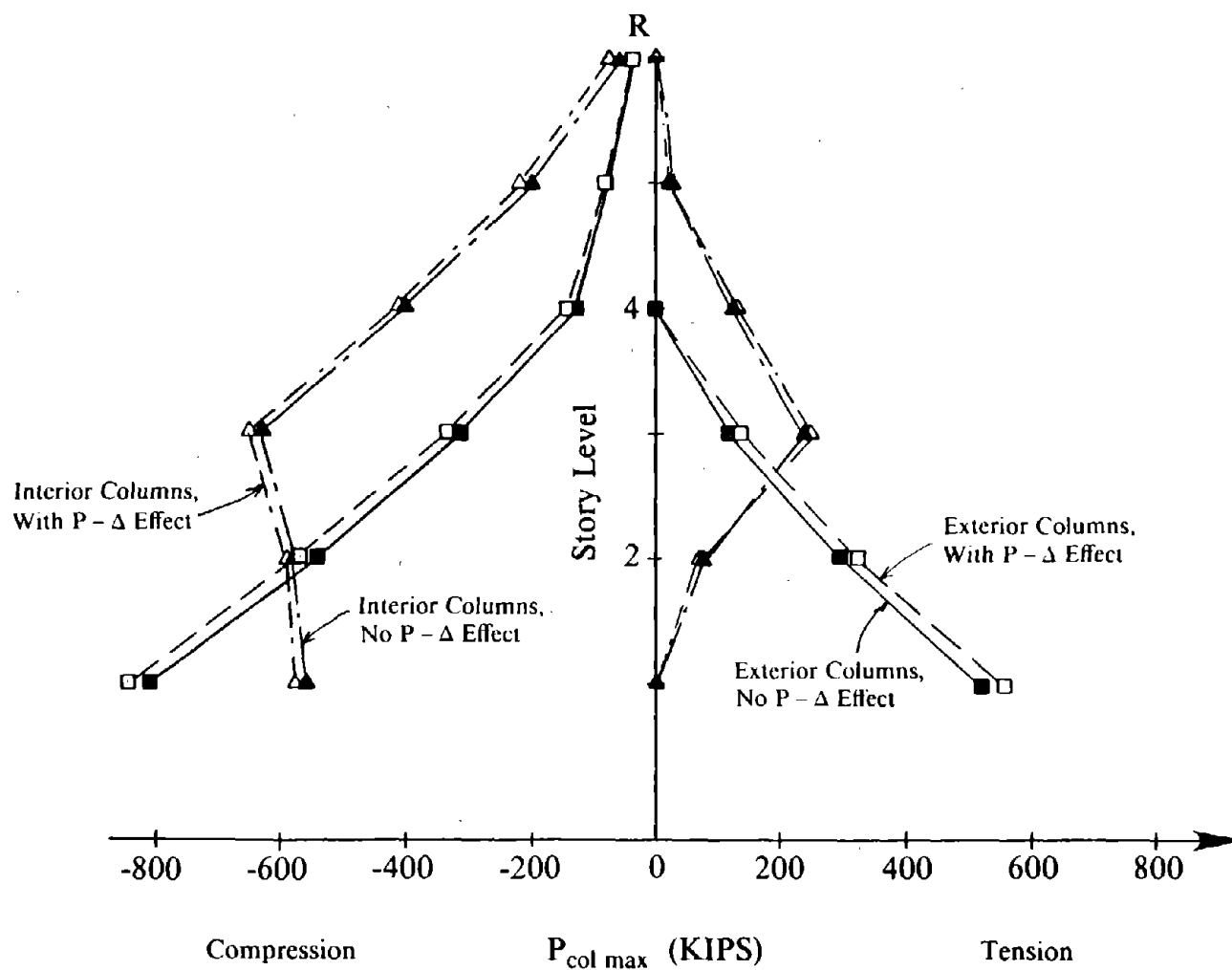
Fig. 8.102   Axial Column Force Envelopes for Bare Steel EBF Models with and without Geometric Stiffness, Design 2 Subjected to Parkfield Earthquake.
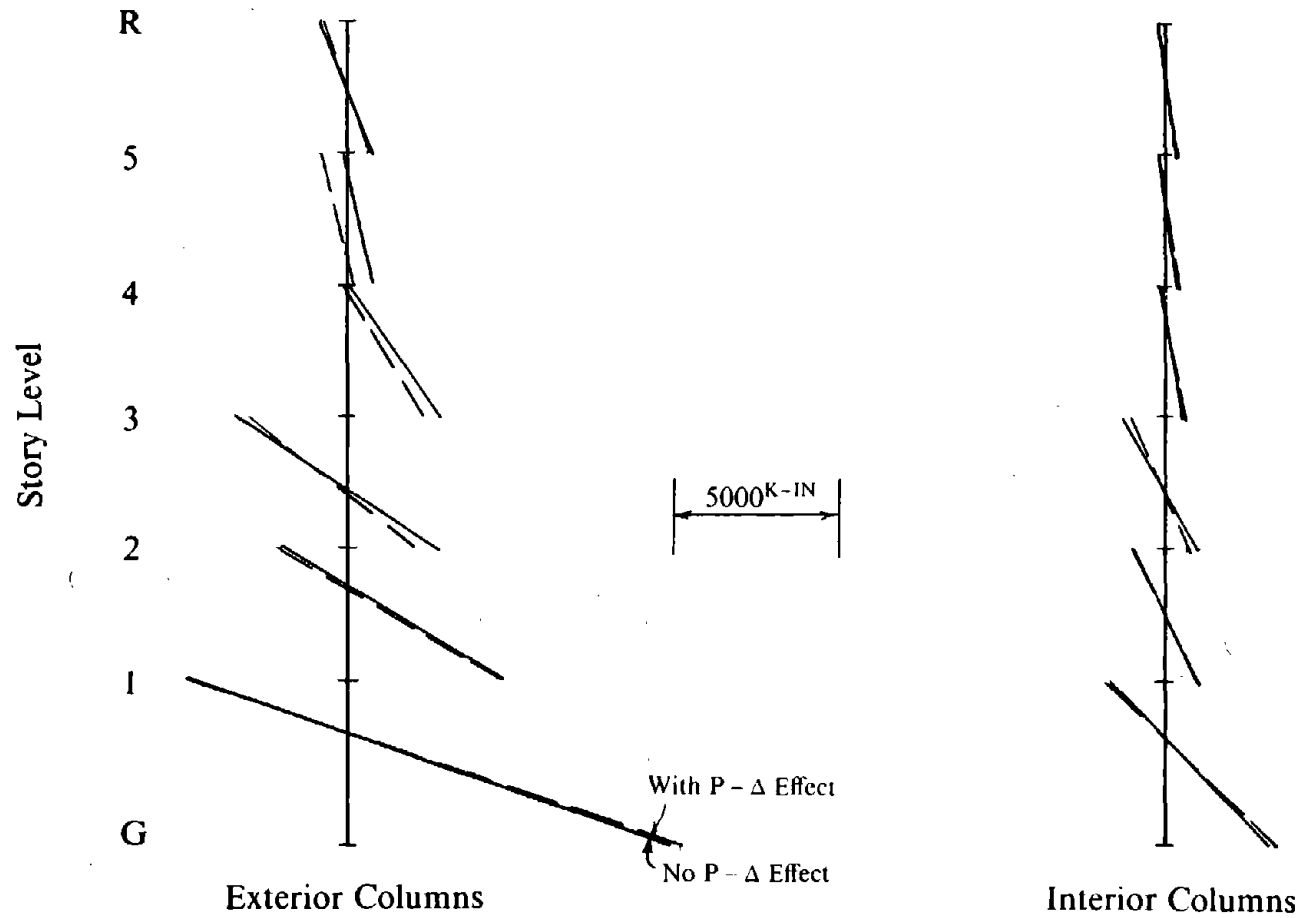
Fig. 8.103   Moment Diagrams Corresponding to Maximum Moments of Individual
Columns for EBF Models with and without Geometric Stiffness, Design 2 Sub-
jected to Parkfield Earthquake.

316

(a) EBF Model with Pin Connections   (b) EBF Model with All Moment Connections
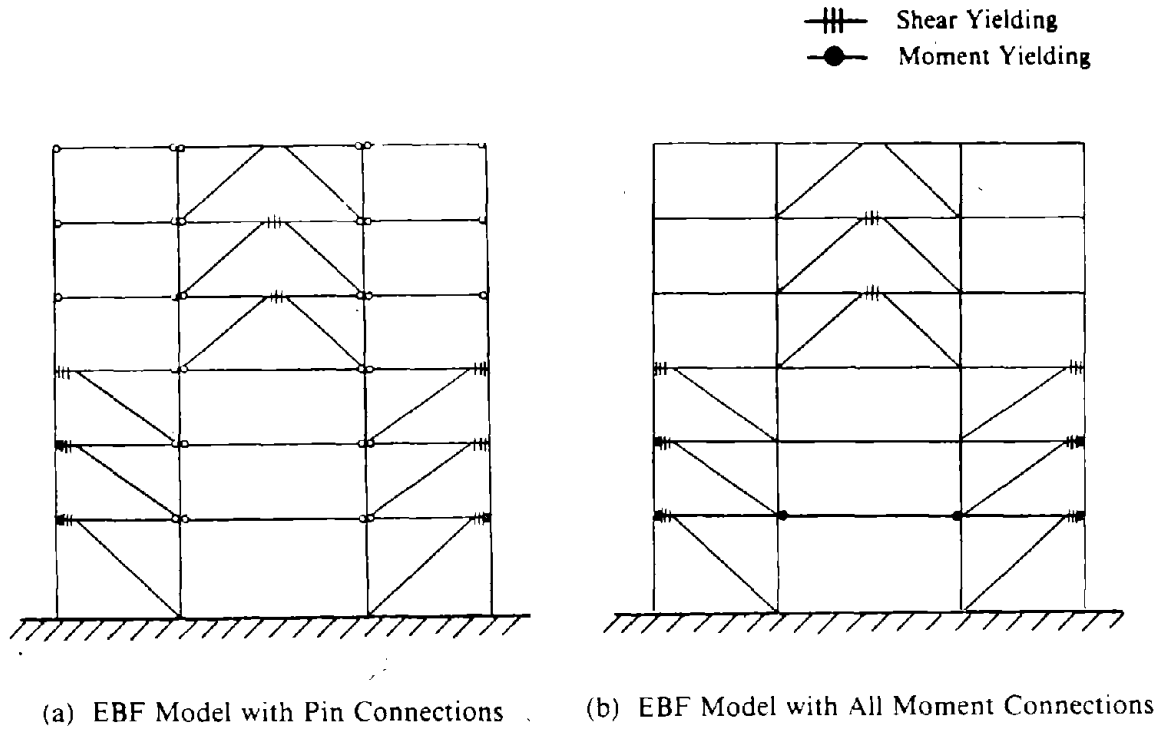
Fig. 8.104   Yielded Members of EBF Models for Design 3
Subjected to 1.5 * El Centro Earthquake.

(a) EBF Model with Pin Connections   (b) EBF Model with All Moment Connections
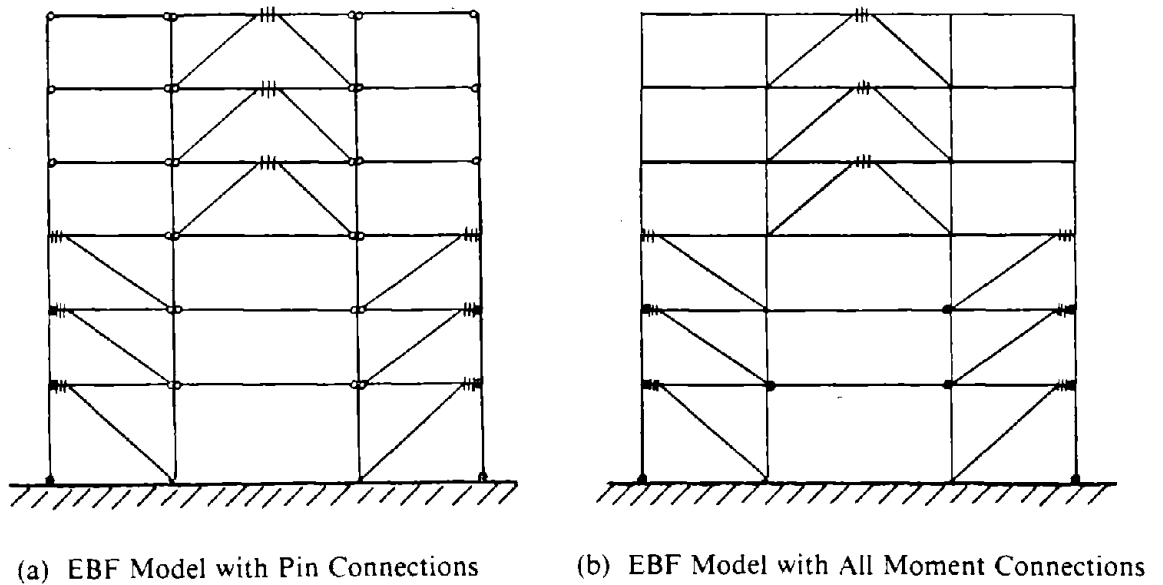
Fig. 8.105   Yielded Members of EBF Models for Design 3
Subjected to Parkfield Earthquake.
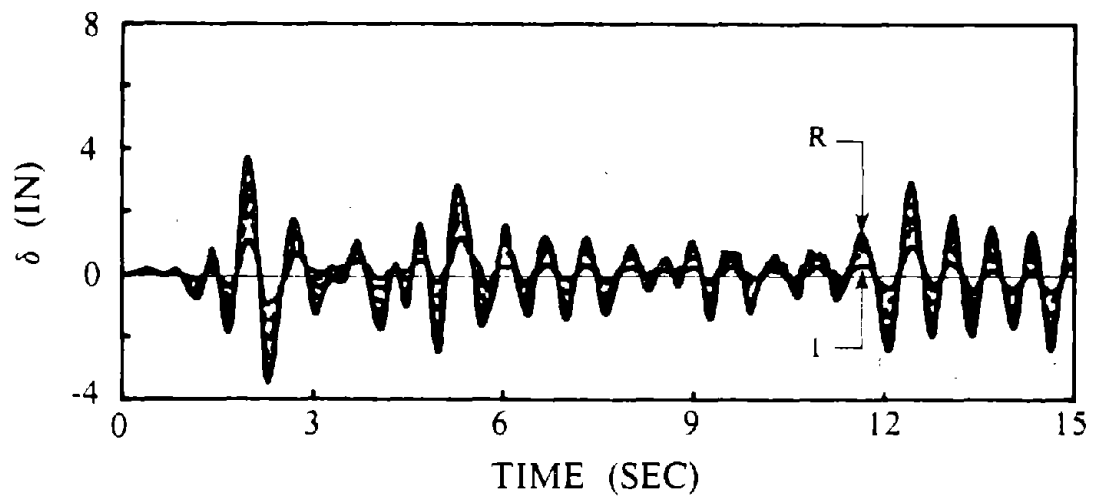
(a) EBF Model with Pin Connections
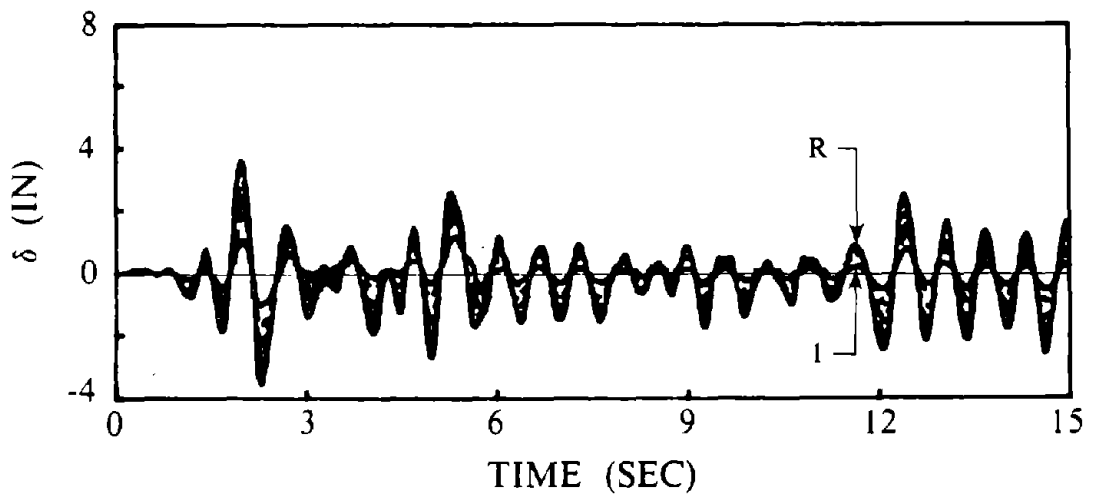
(b) EBF Model with All Moment Connections

Fig. 8.106   Lateral Floor Displacements for EBF Models of Design 3 Subjected to 1.5 * El Centro Earthquake.
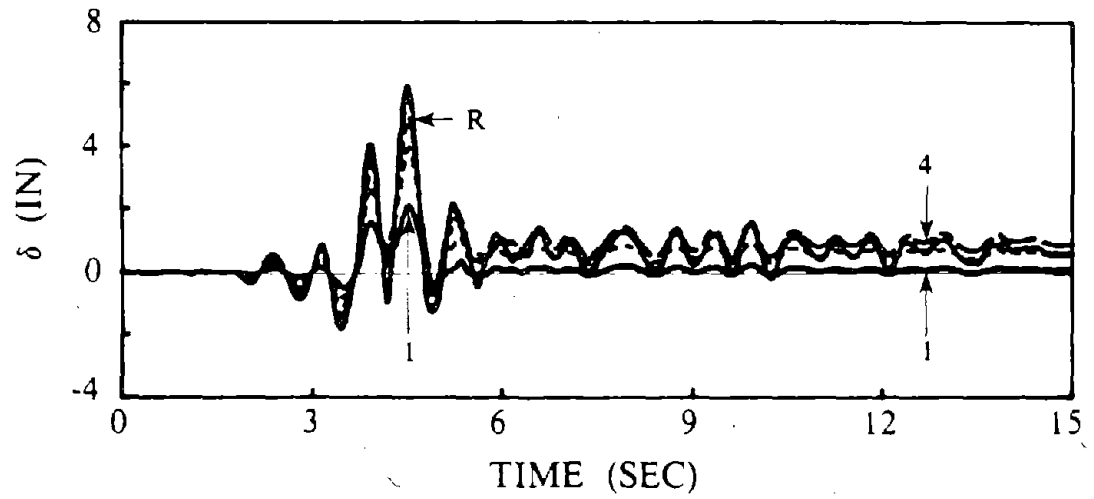
(a) EBF Model with Pin Connections
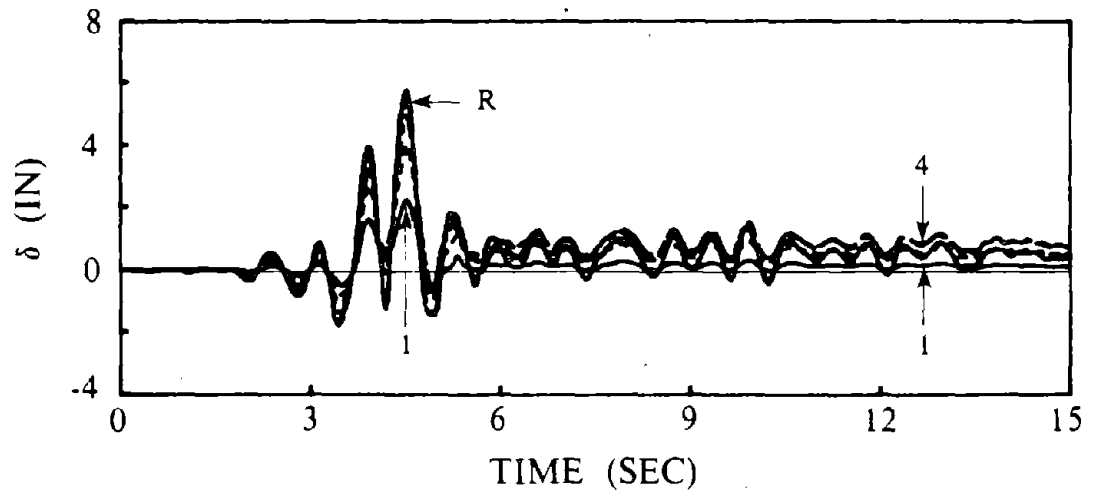
(b) EBF Model with All Moment Connections

Fig. 8.107   Lateral Floor Displacements for EBF Models of Design 3 Subjected to Parkfield Earthquake.
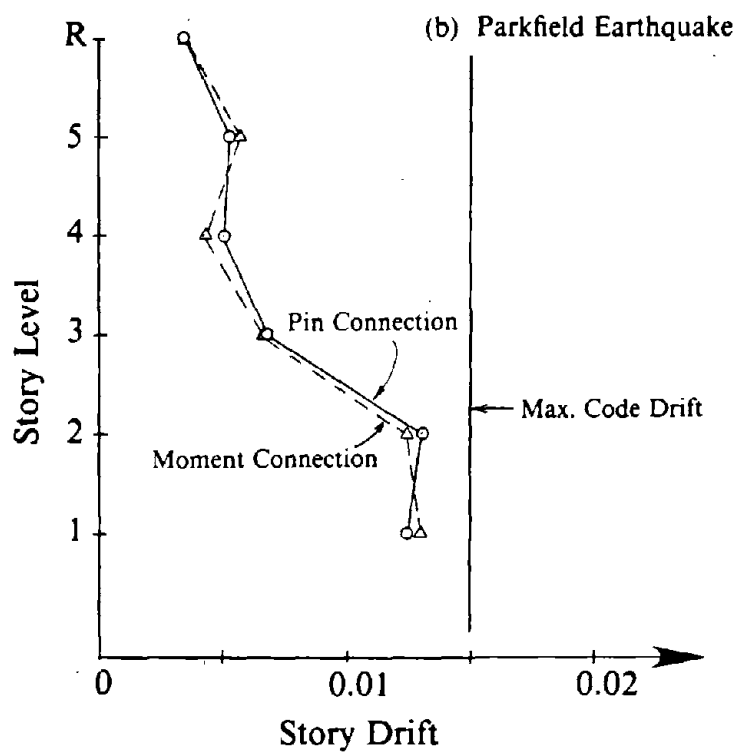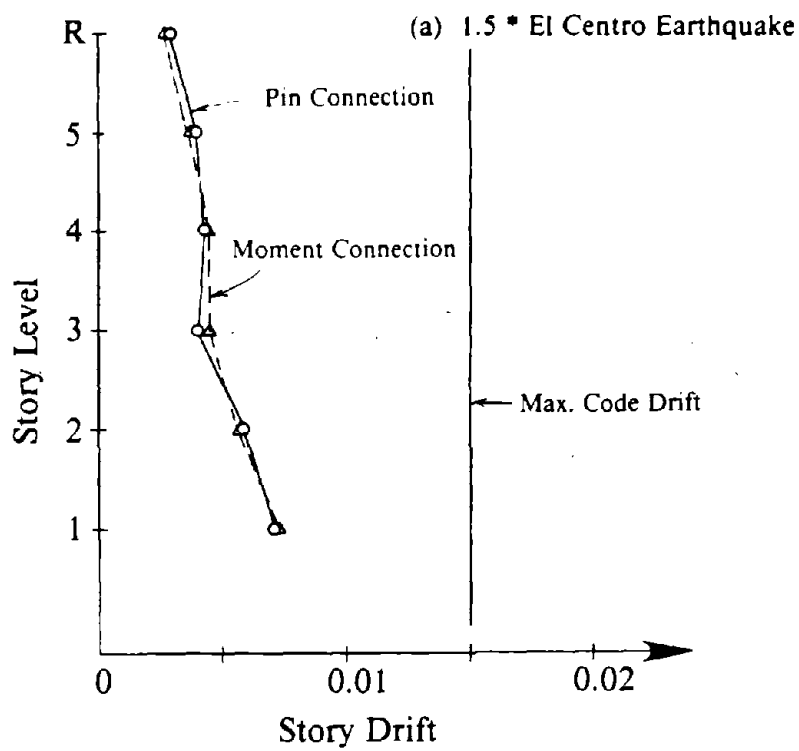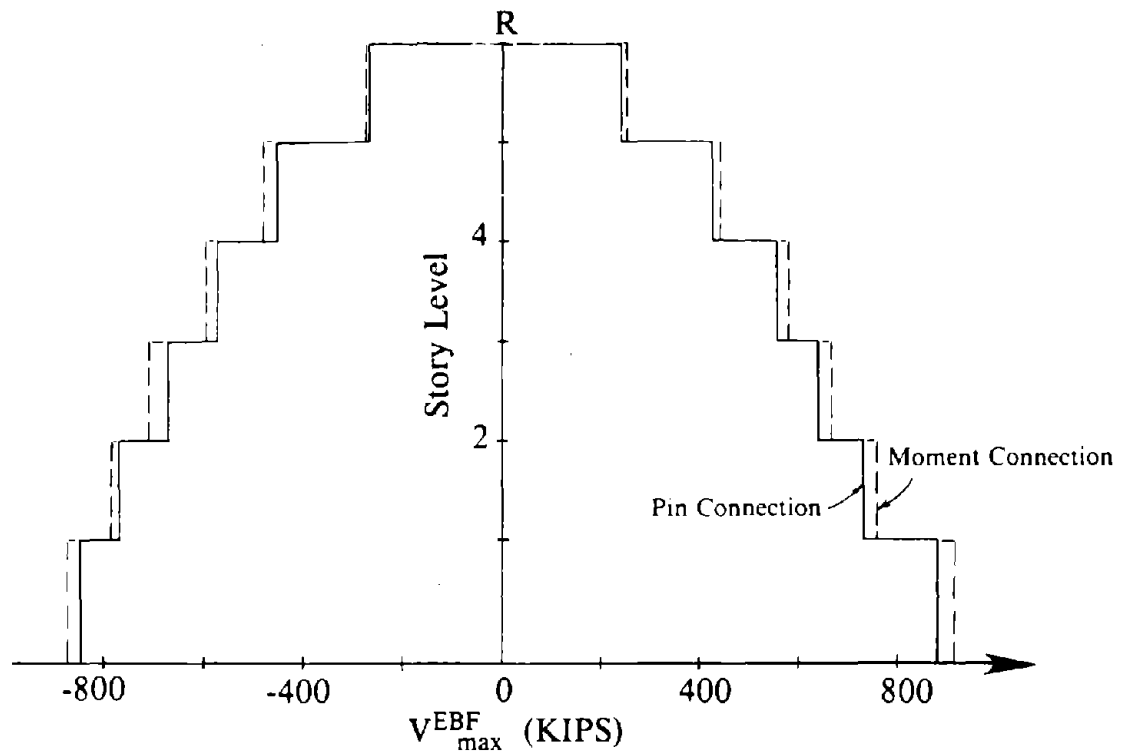
Fig. 8.108   Maximum Story Drift for EBF Models of Design 3.
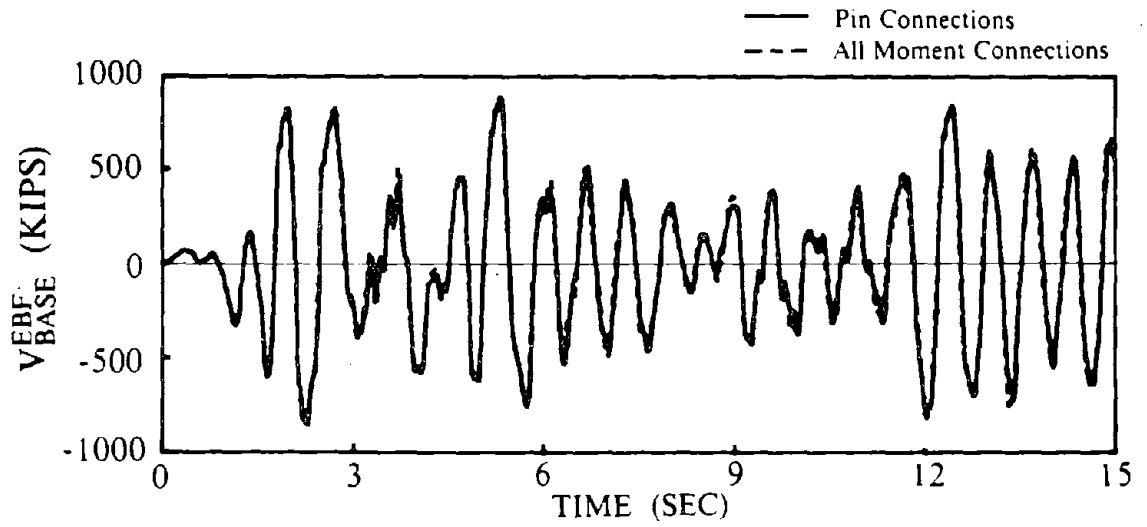
(a) 1.5 * El Centro Earthquake
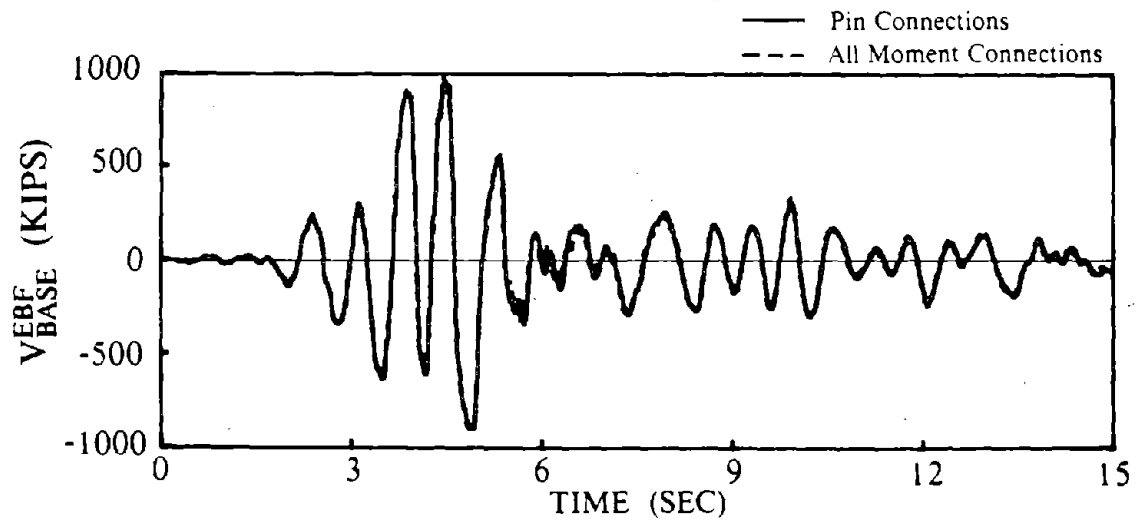
(b) Parkfield Earthquake

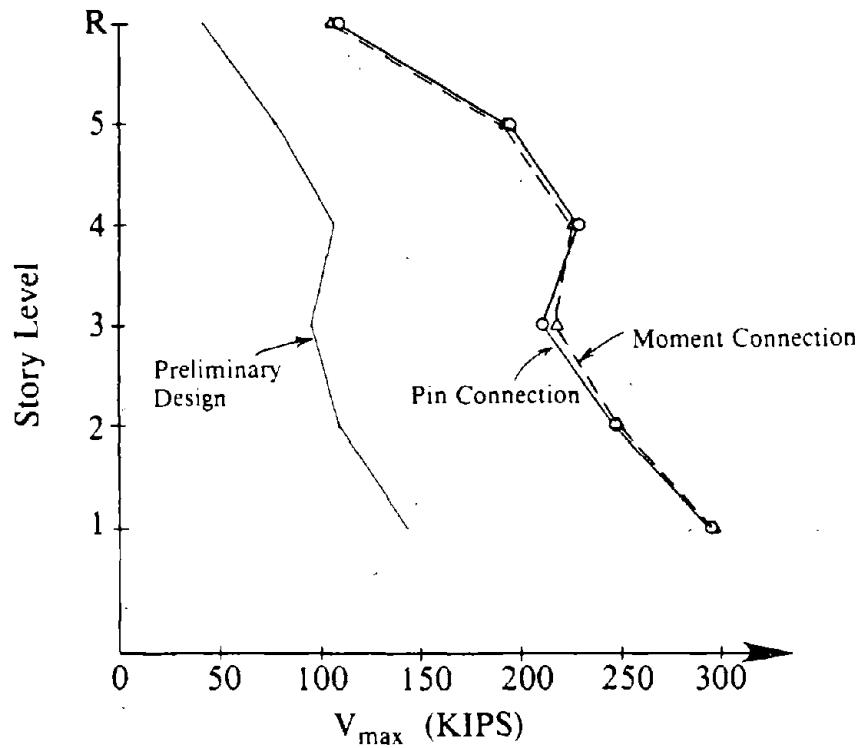Fig. 8.109   Comparison of Base Shear Time Histories for EBF Models of Design 3.
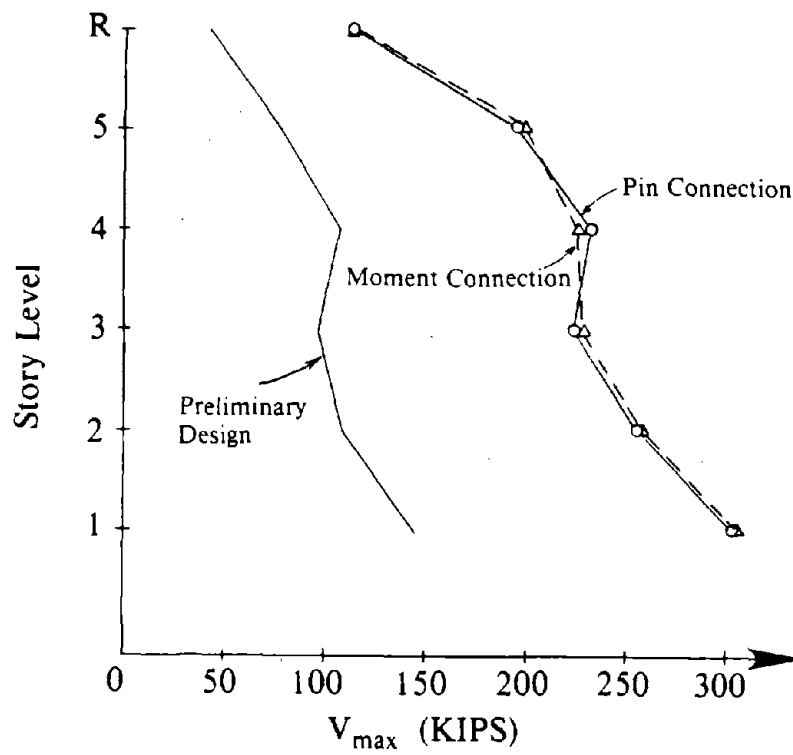
(a) 1.5 * El Centro Earthquake
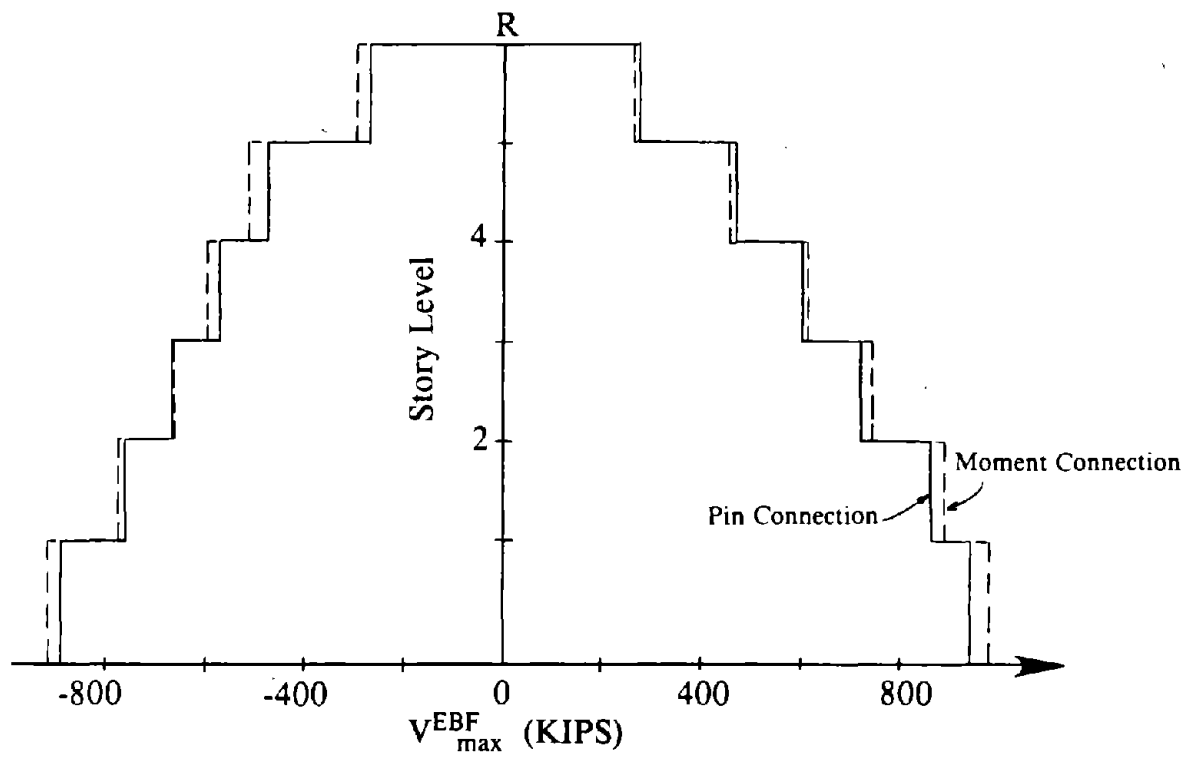
(b) Parkfield Earthquake

Fig. 8.110   Story Shear Envelopes for EBF Models of Design 3.

322

(a) 1.5 * El Centro Earthquake

(b) Parkfield Earthquake

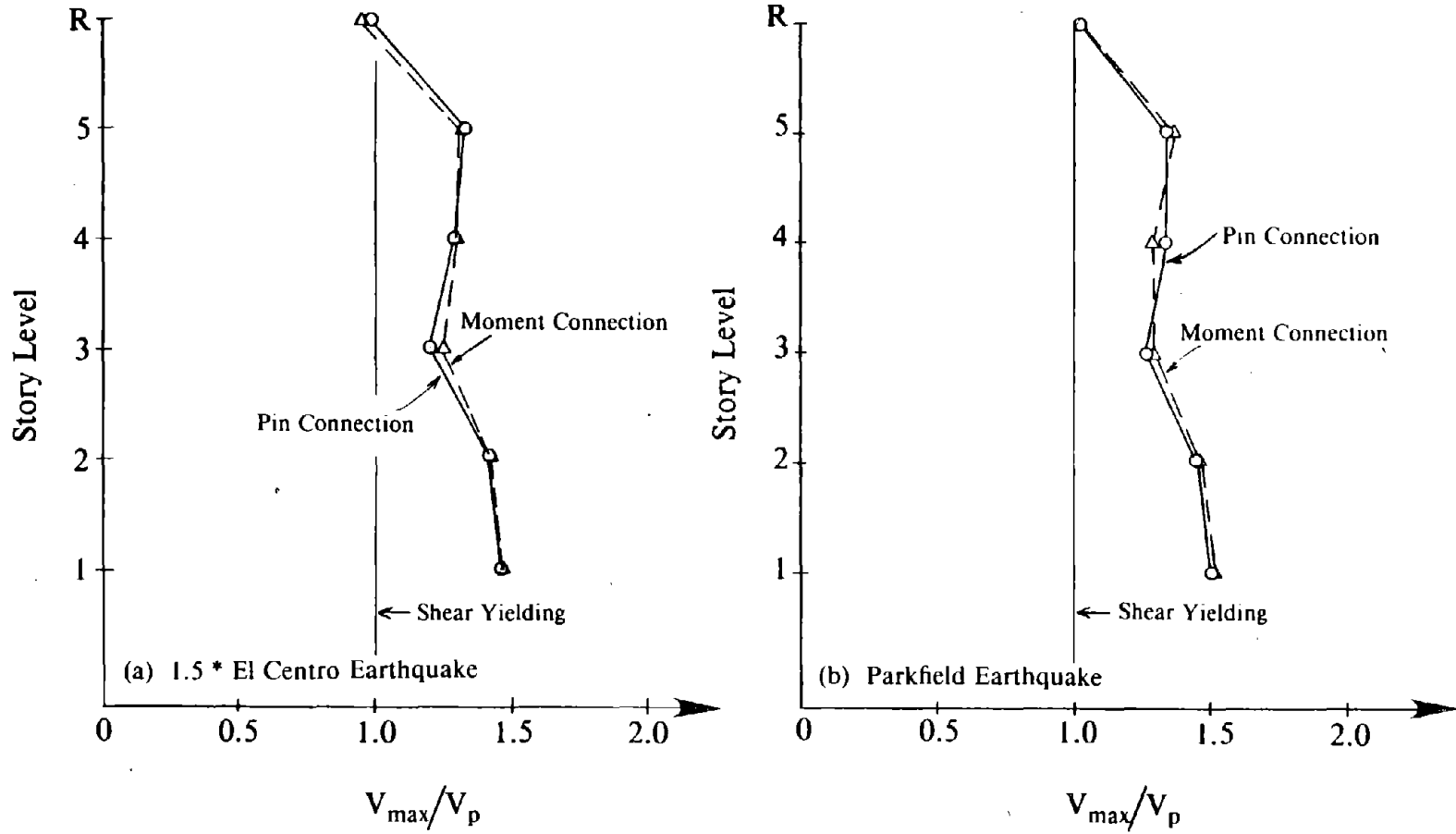Fig. 8.111   Maximum Link Shear Forces for EBF Models of Design 3.

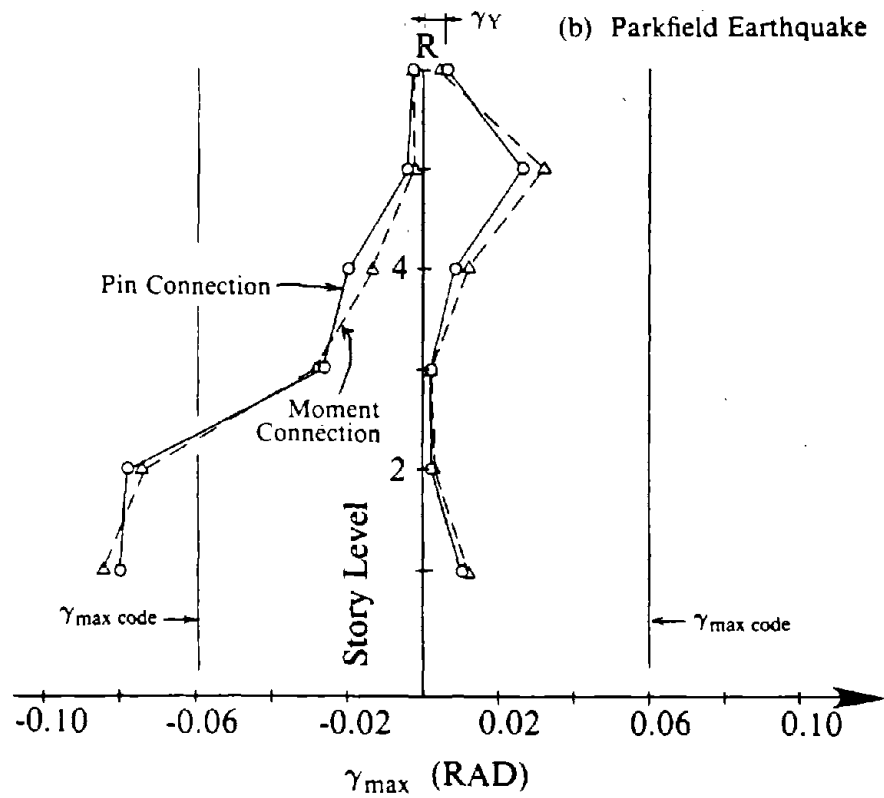Fig. 8.112   Normalized Maximum Link Shear Forces for EBF Models of Design 3.
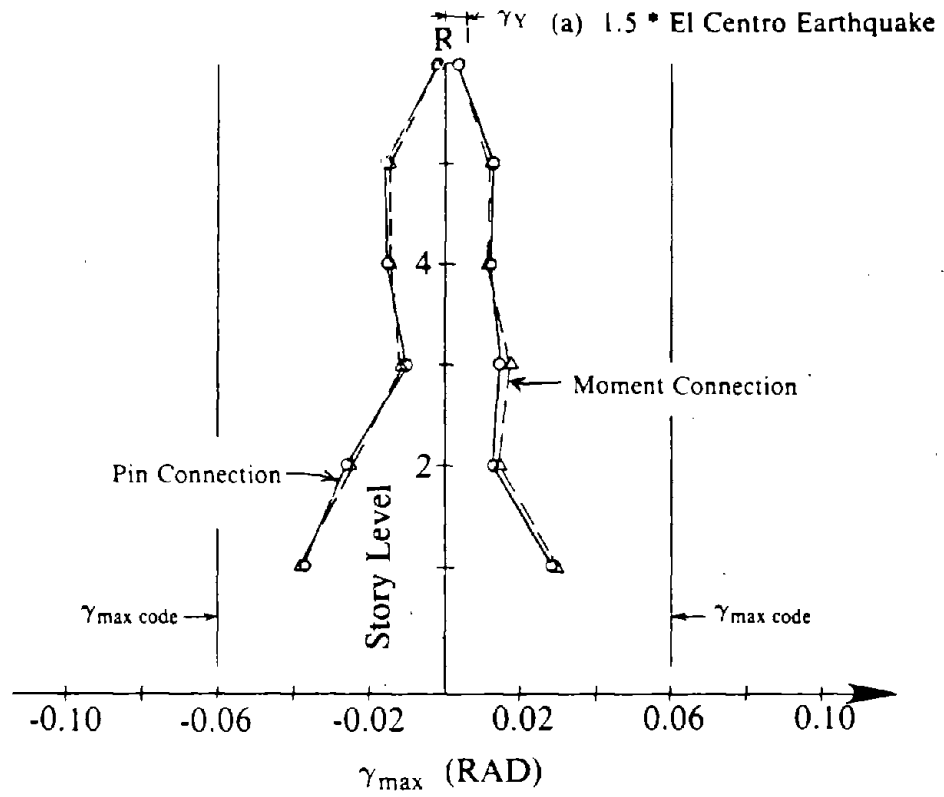
324

Fig. 8.113   Link Deformation Envelopes for EBF Models of Design 3.

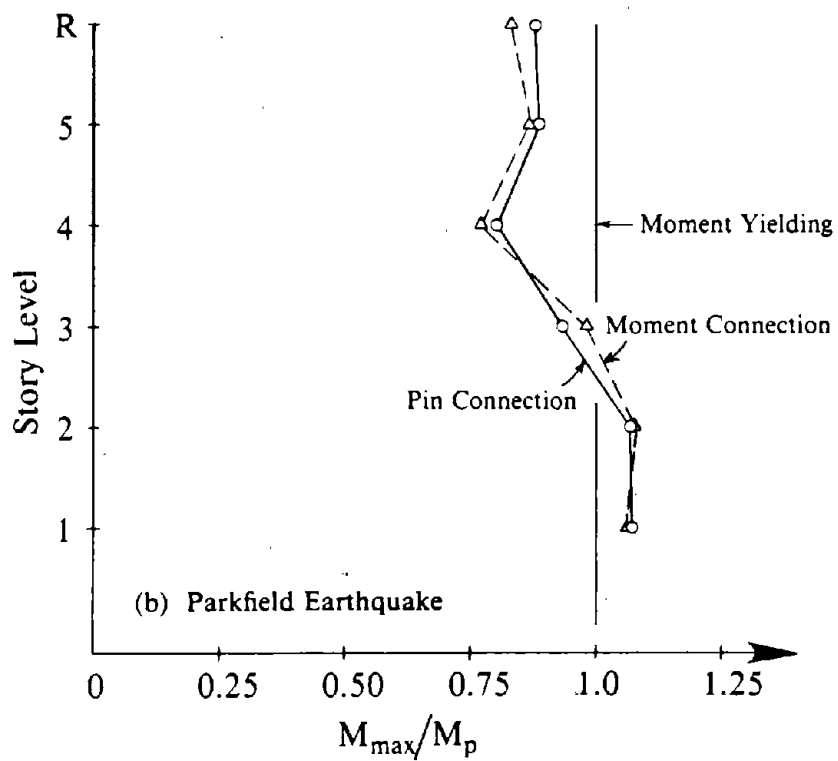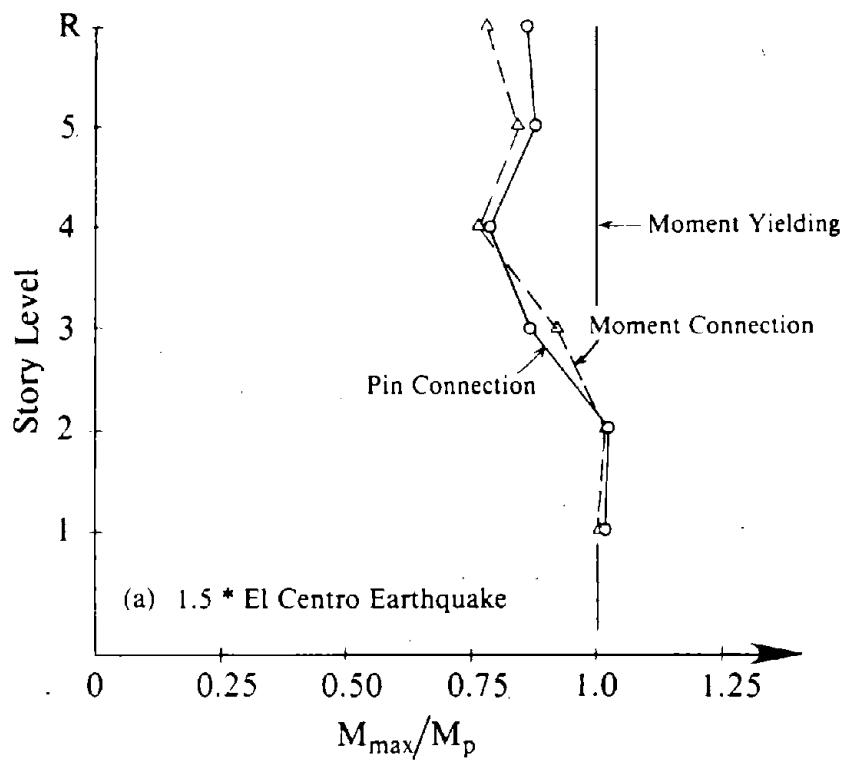Fig. 8.114   Normalized Maximum Link End Moments for EBF Models of Design 3.

(a) 1.5 * El Centro Earthquake

$\Delta_{r\,max}$ (IN)

(b) Parkfield Earthquake

$\Delta_{r\,max}$ (IN)
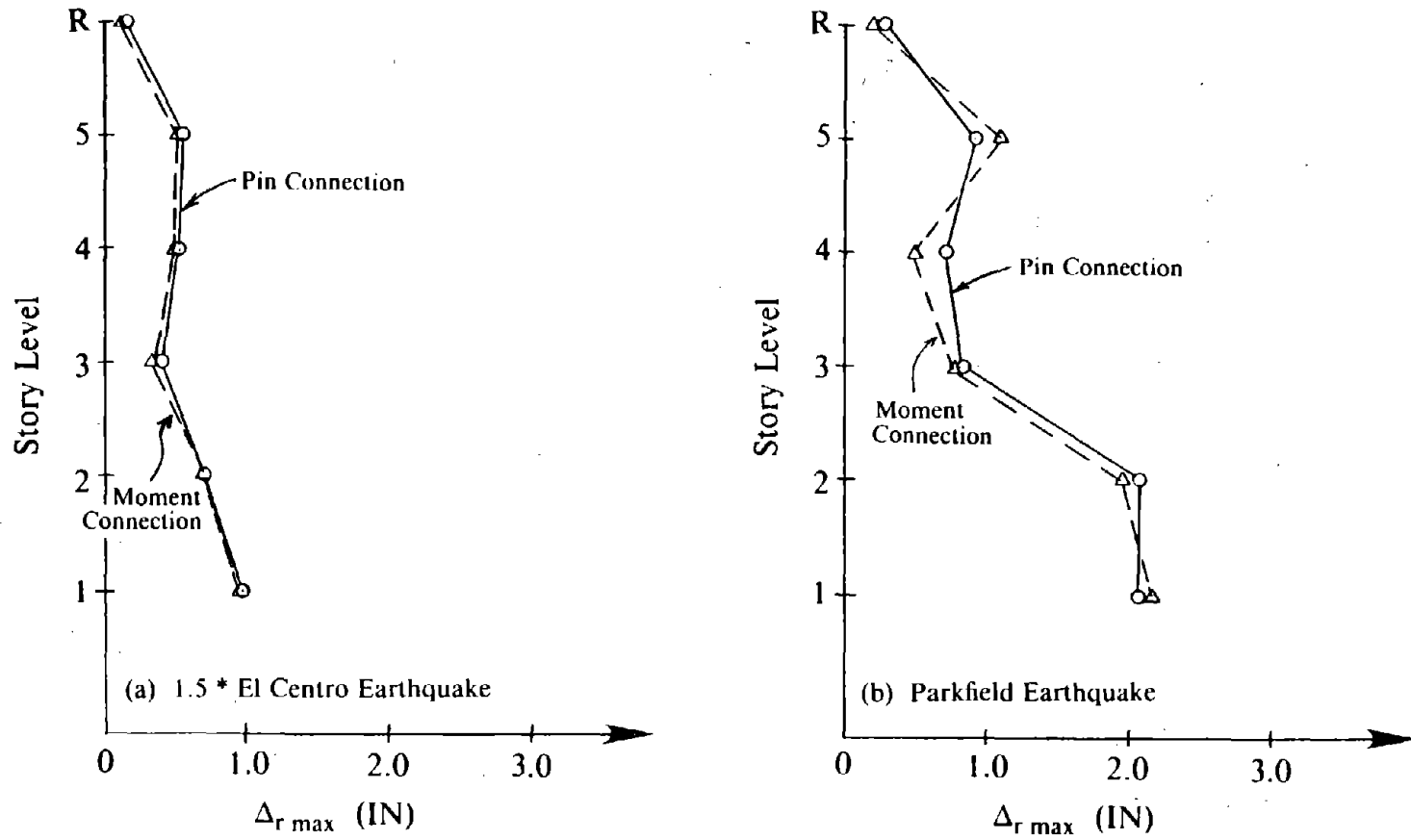
Fig. 8.115   Maximum Relative End Displacement of Links in EBF Models of Design 3.
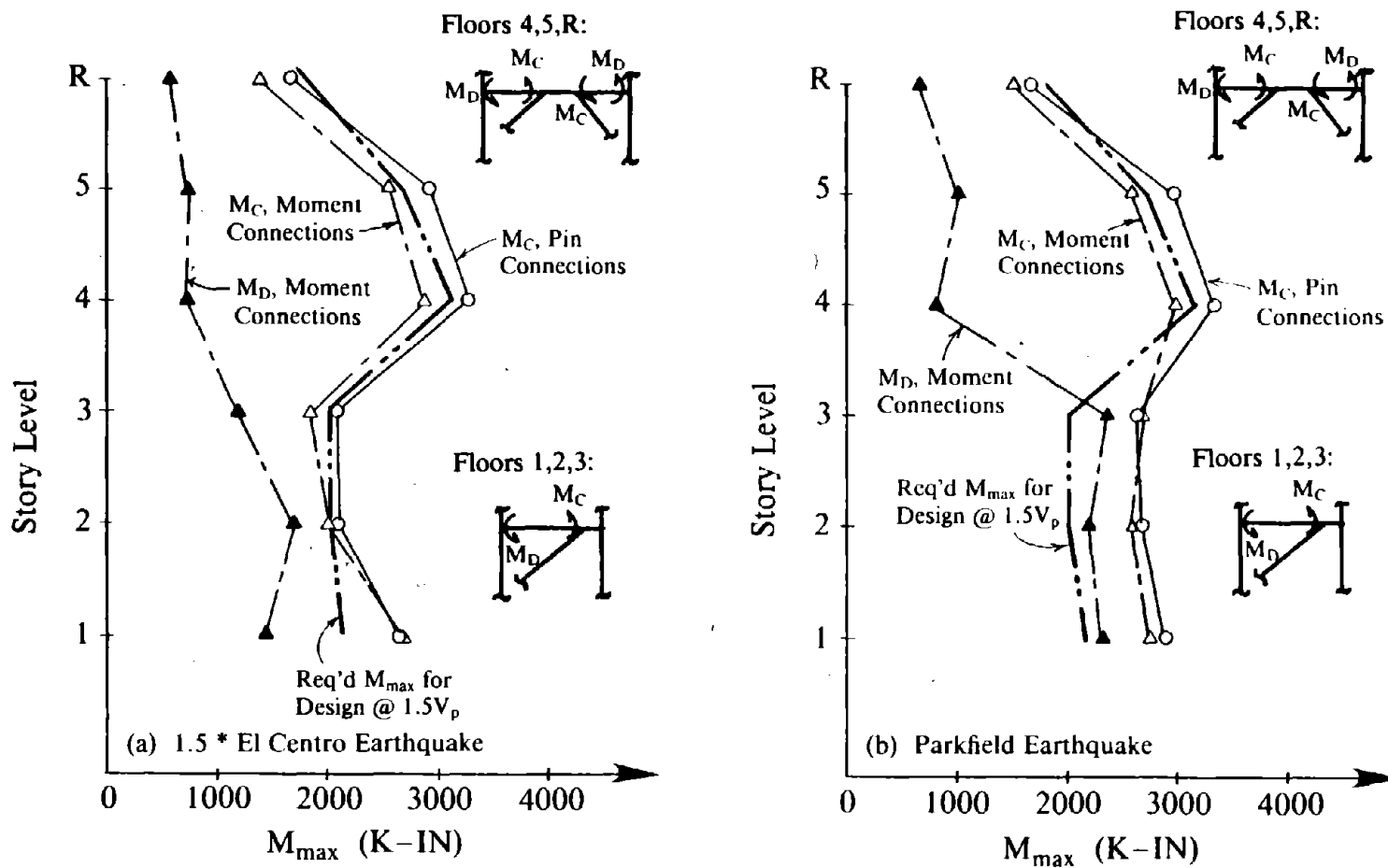
Fig. 8.116   Maximum Moments Developed in Floor Beams Outside the Links of Braced
            Panels for Design 3.

328
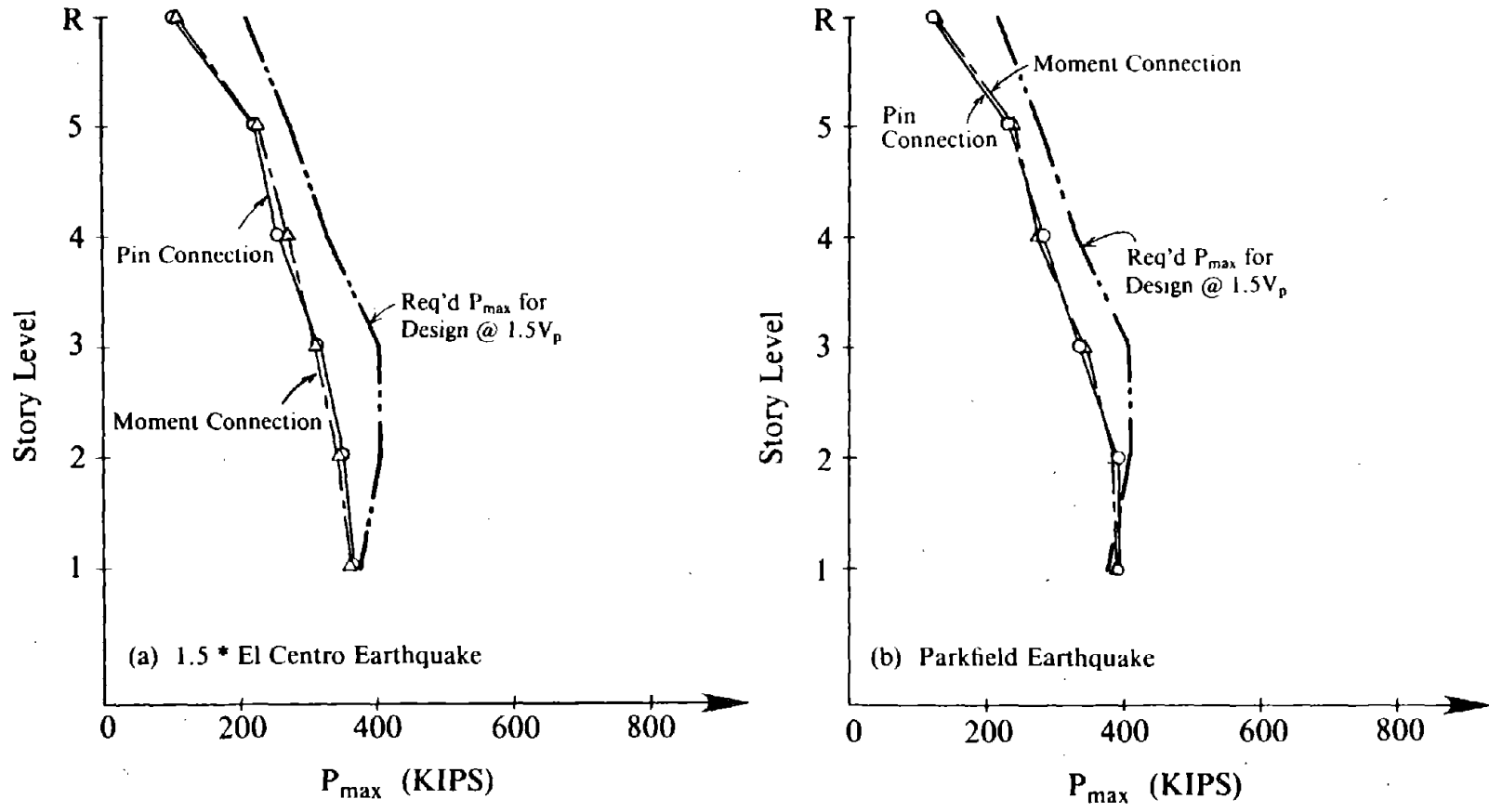
Fig. 8.117   Maximum Axial Forces Developed in the Floor Beams Outside the Links of Braced Panels for Design 3.
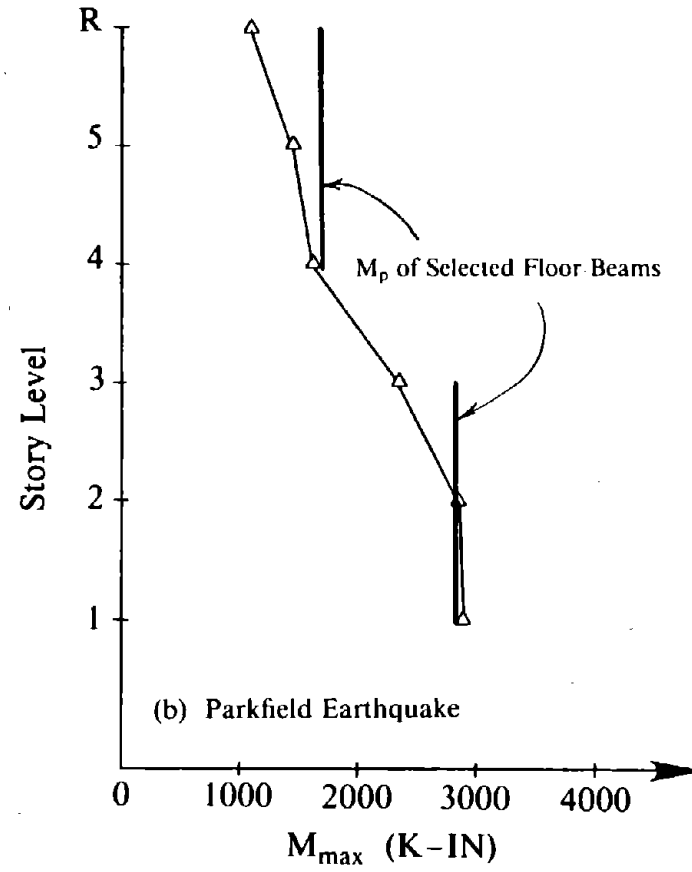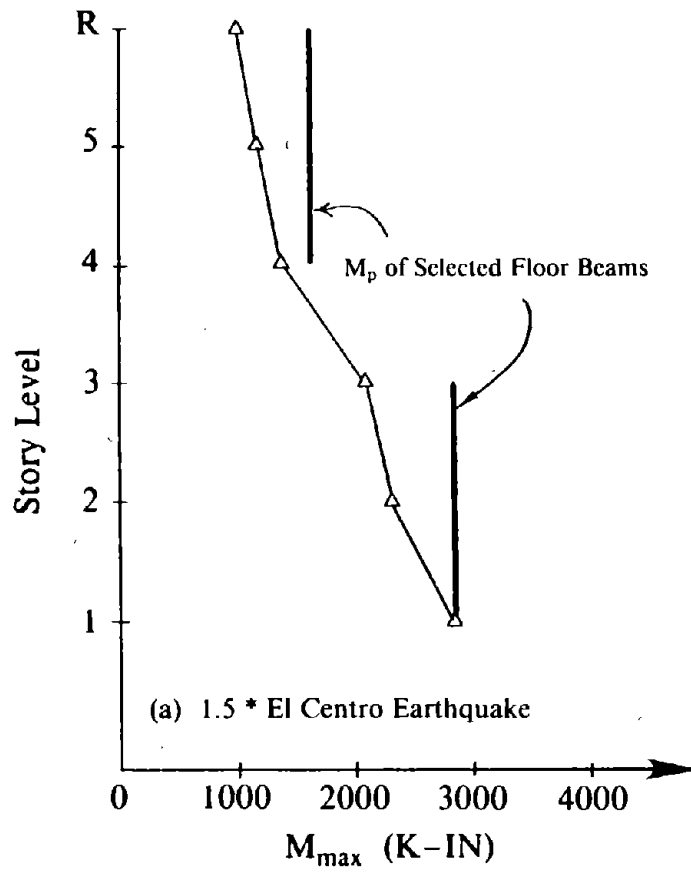
Fig. 8.118   Maximum Moments Developed in Floor Beams Outside the Links of Unbraced
Panels for Design 3 with All Moment Connections.

330

(a) 1.5 * El Centro Earthquake

(b) Parkfield Earthquake
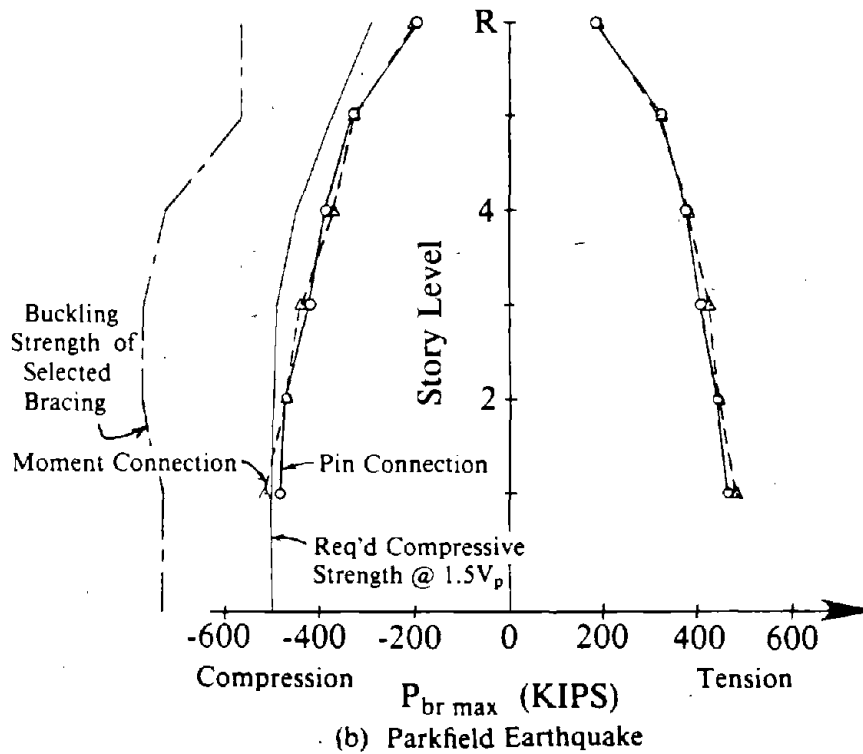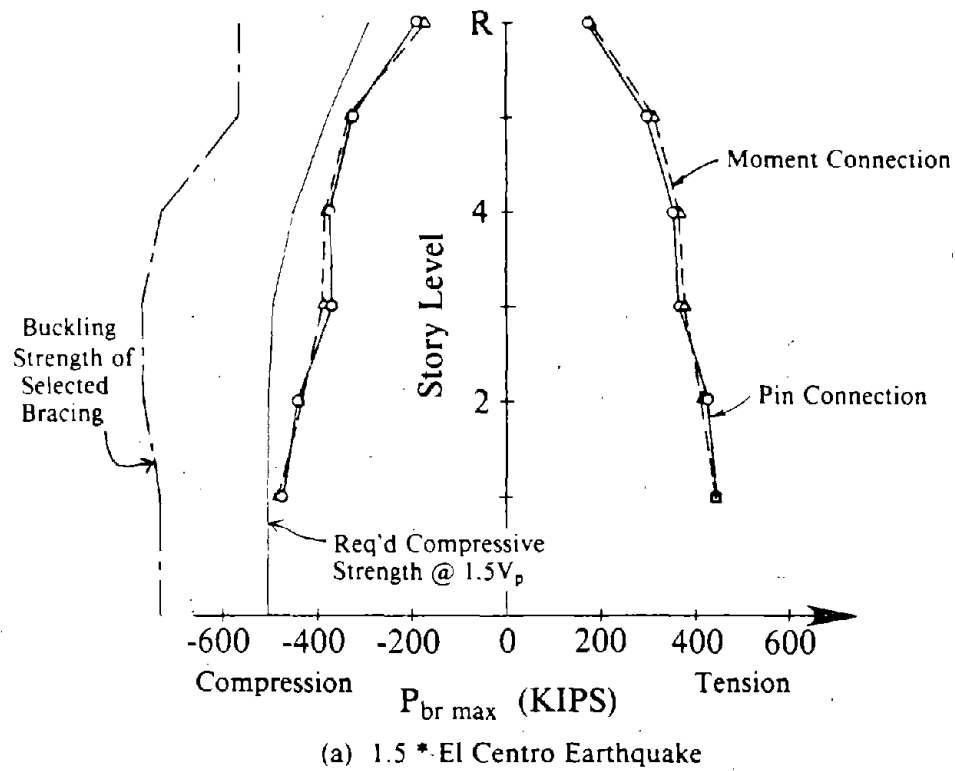
Fig. 8.119   Axial Brace Force Envelopes for Models of Design 3.
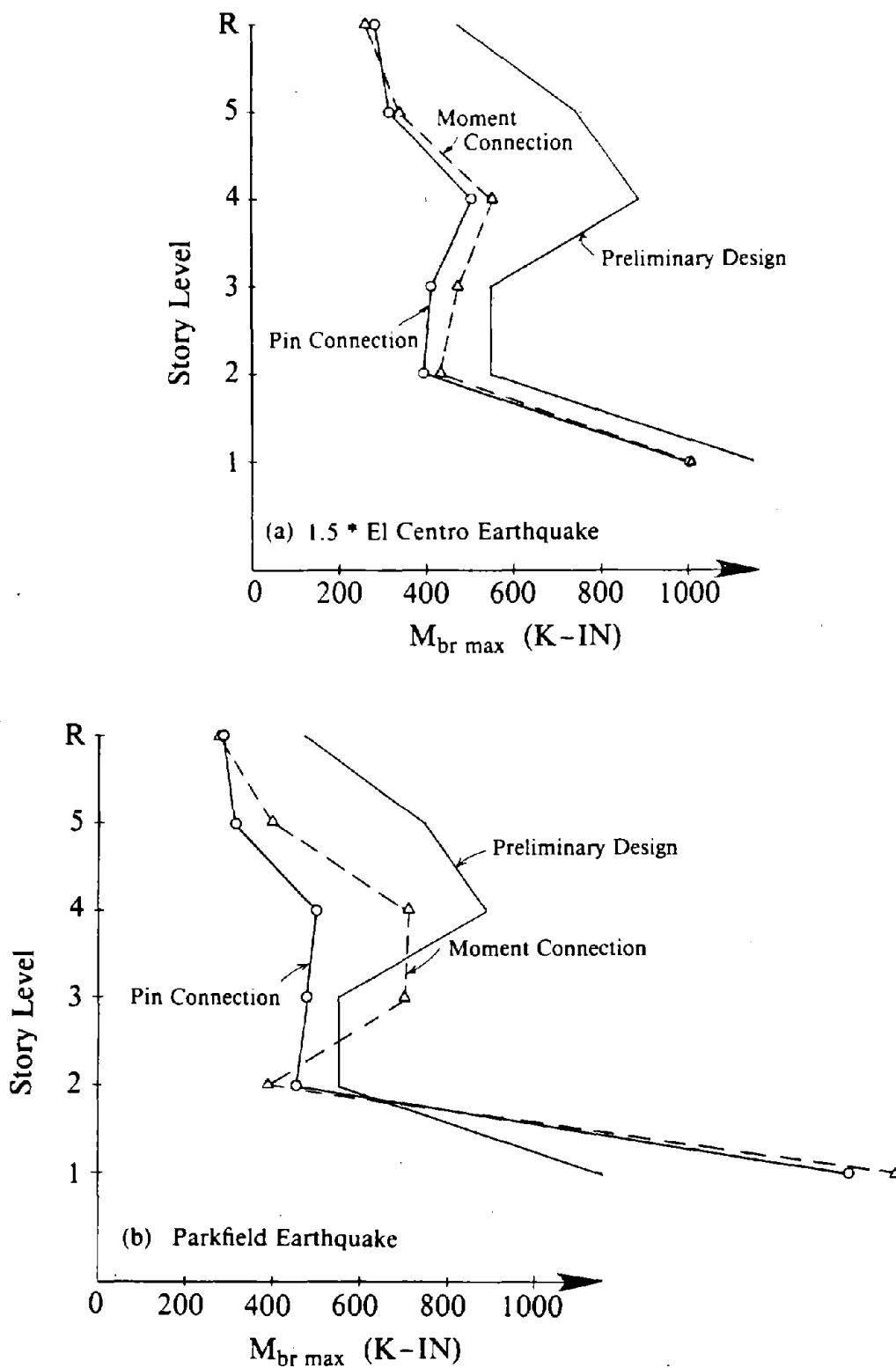
Fig. 8.120   Maximum Brace Moments for EBF Models of Design 3.

332
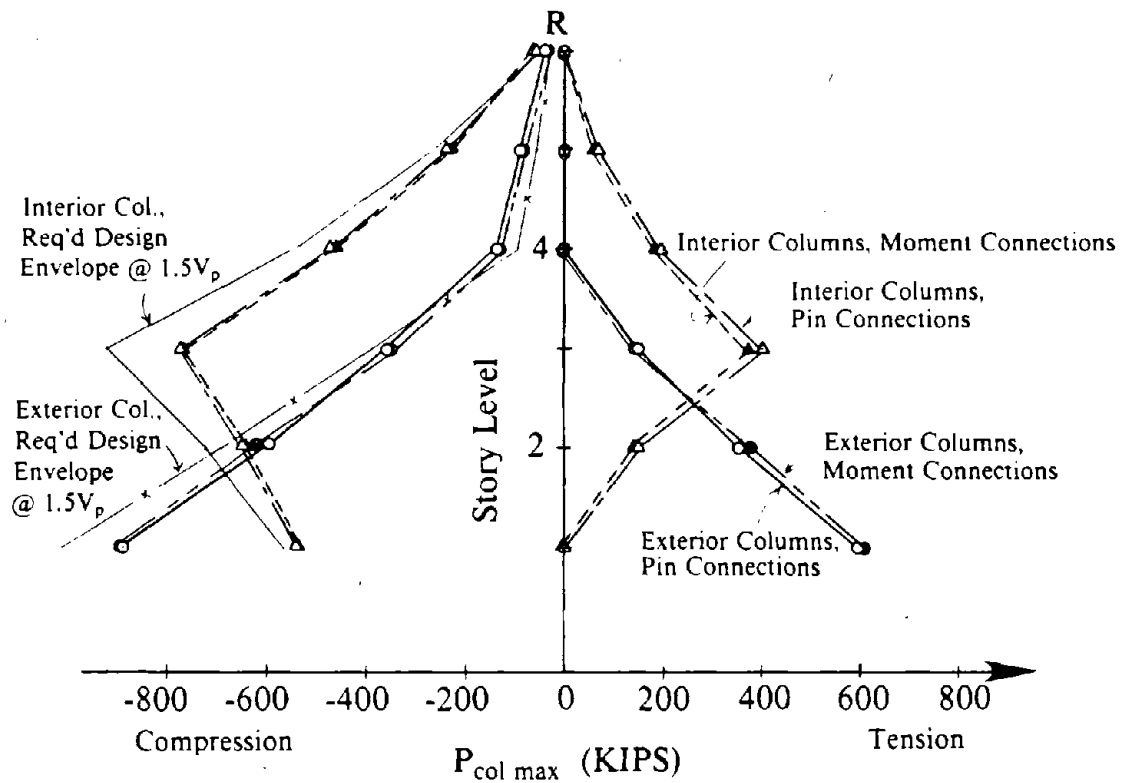
(a) 1.5 * El Centro Earthquake
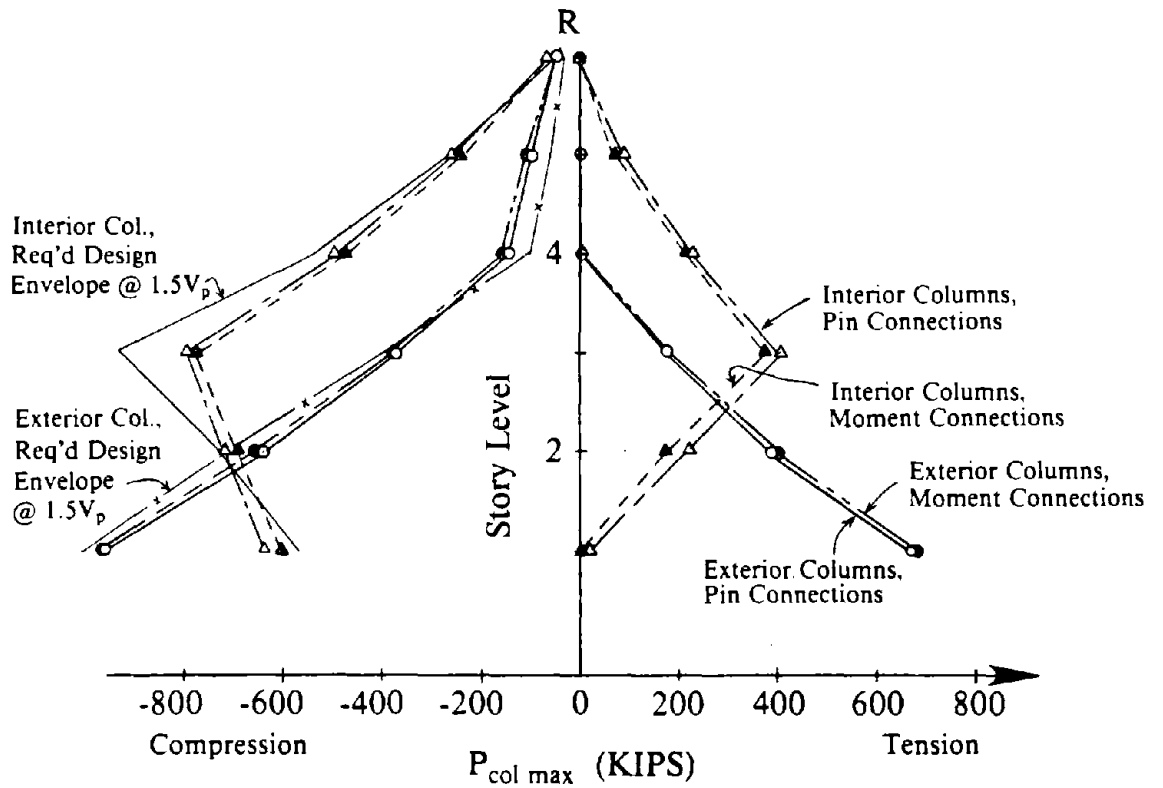
(b) Parkfield Earthquake

Fig. 8.121   Column Axial Force Envelopes for EBF Models of Design 3.

R

Θ_1

$P_{br\ R}$

5

Θ_1

$P_{br\ 5}$

4

Θ_1

$P_{br\ 4}$

3

Θ_2 $P_{br\ 3}$

2

Θ_2 $P_{br\ 2}$

1

Θ_2 $P_{br\ 1}$

G

$-P_{br\ R}\cos\Theta_1$

$(-P_{br\ R} - P_{br\ 5})\cos\Theta_1$

$(-P_{br\ R} - P_{br\ 5} - P_{br\ 4})\cos\Theta_1$

$(-P_{br\ R} - P_{br\ 5} - P_{br\ 4})\cos\Theta_1 + P_{br\ 3}\cos\Theta_2$

$(-P_{br\ R} - P_{br\ 5} - P_{br\ 4})\cos\Theta_1 + (P_{br\ 3} + P_{br\ 2})\cos\Theta_2$

Idealized EBF Seismic
Lateral Forces

Interior Column Subjected
to Ensuing Brace Forces

Axial Column
Force Diagram
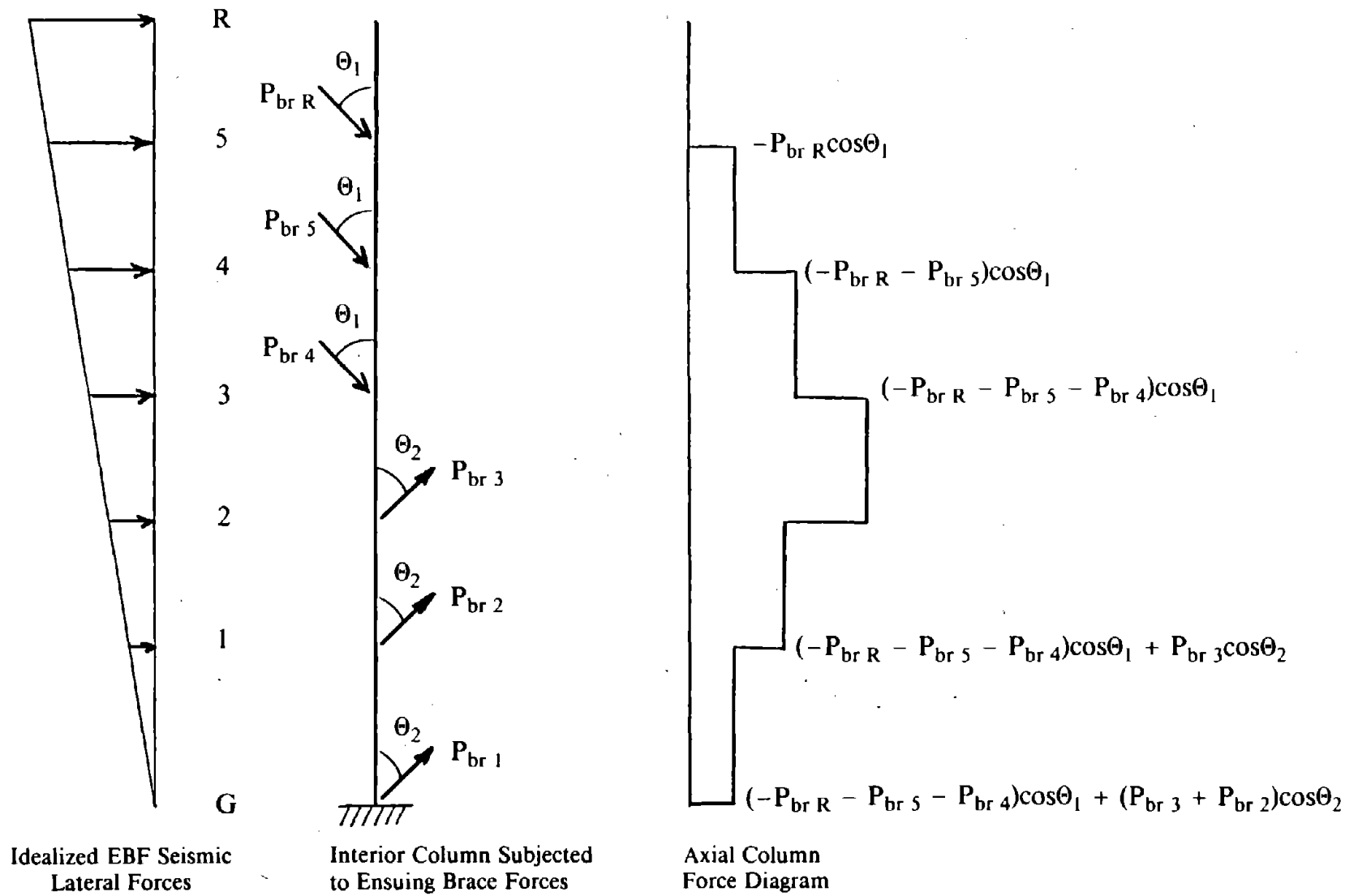
Fig. 8.122   Axial Forces Accumulated in Interior Column of EBF Due to Lateral Seismic
Forces.

Story Level

R
5
4
3
2
1
G

M_{col}

$1.8M_{code}$

M_{code}

5000^{K-IN}

Pin Connection

Moment Connection

M_{col}

Exterior Columns

Interior Columns
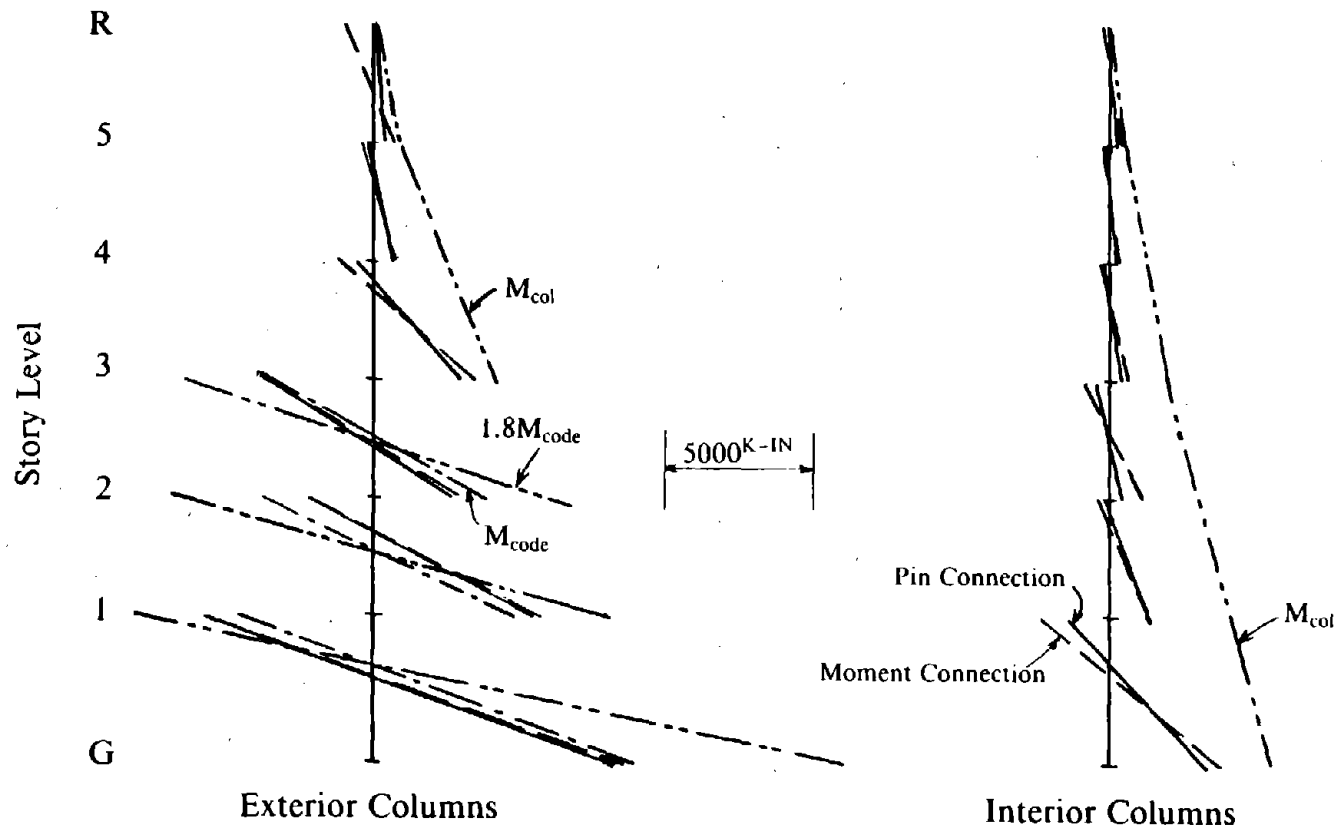
Fig. 8.123   Individual Column Moment Diagrams Corresponding to Maximum Column
Moments of Design 3, 1.5 * El Centro Earthquake.

R

5

4

M_{col}

3

5000^{K-IN}

Story Level

2

1

Pin Connection

M_{col}

Moment Connection

1.8M_{code}

G

M_{code}

Exterior Columns
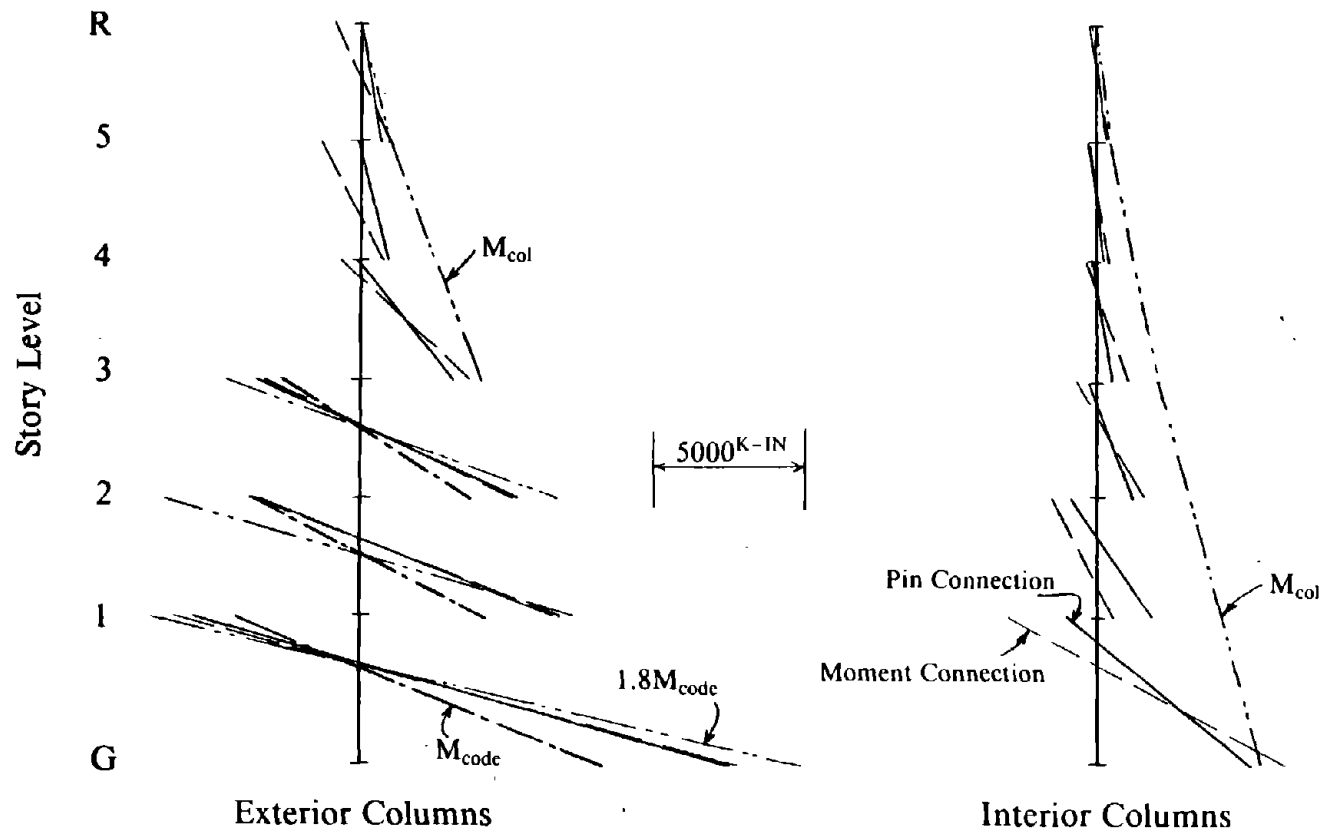
Interior Columns

Fig. 8.124   Individual Column Moment Diagrams Corresponding to Maximum Column Moments of Design 3, Parkfield Earthquake.
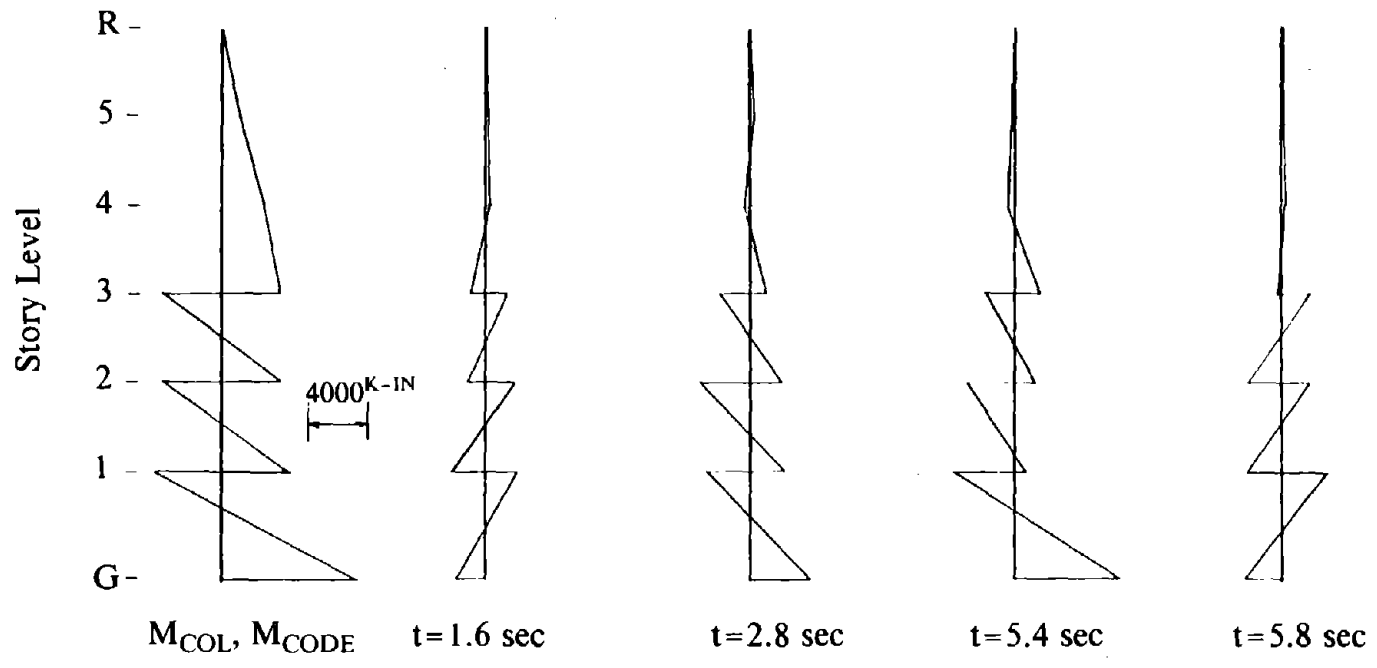
Fig. 8.125   Moments in Exterior Columns of Design 3 at Selected Times During Response
to 1.5 * El Centro Earthquake, EBF Model with Pin Connections.
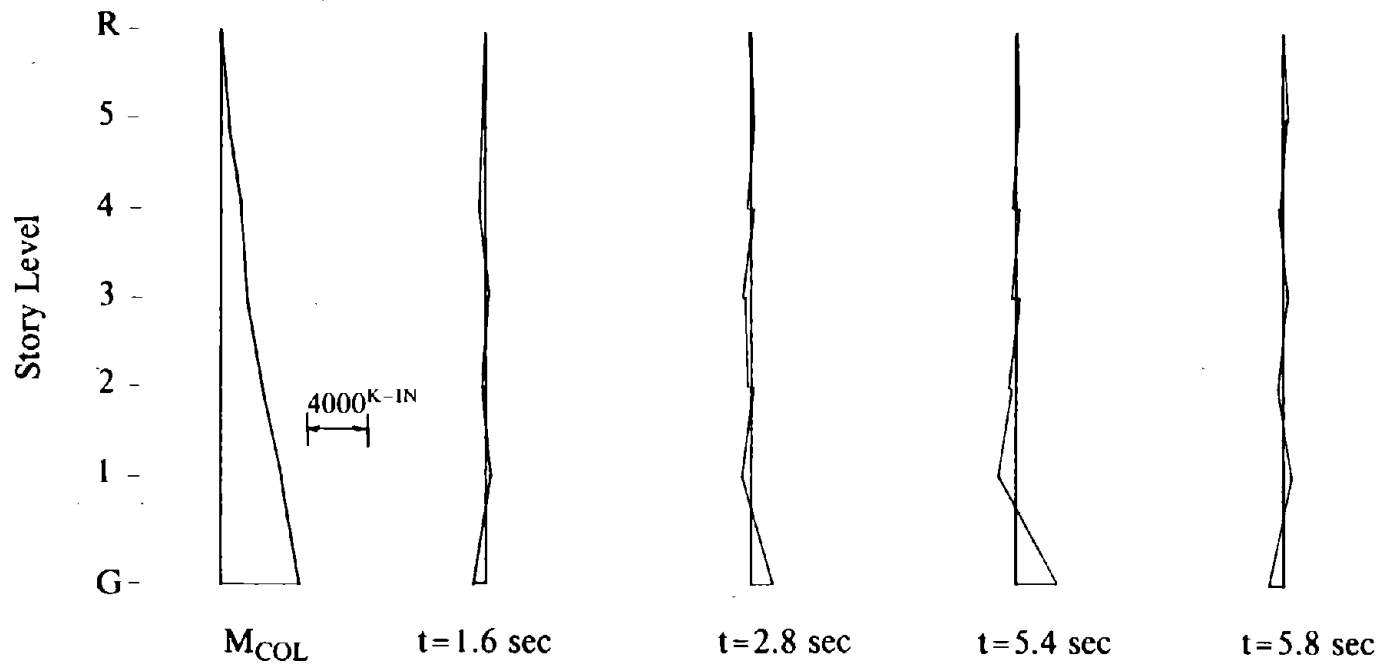
Fig. 8.126   Moments in Interior Columns of Design 3 at Selected Times During Response
to 1.5 * El Centro Earthquake, EBF Model with Pin Connections.
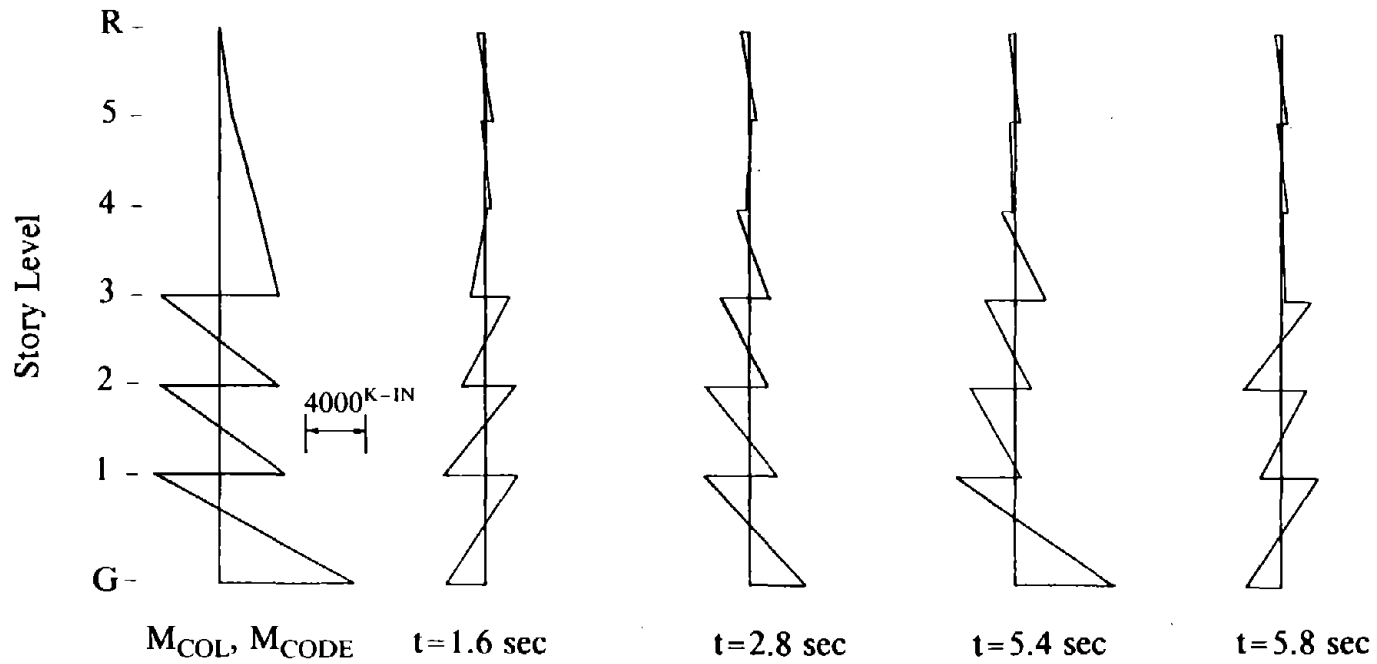
Fig. 8.127   Moments in Exterior Columns of Design 3 at Selected Times During Response to 1.5 * El Centro Earthquake, EBF Model with All Moment Connections.
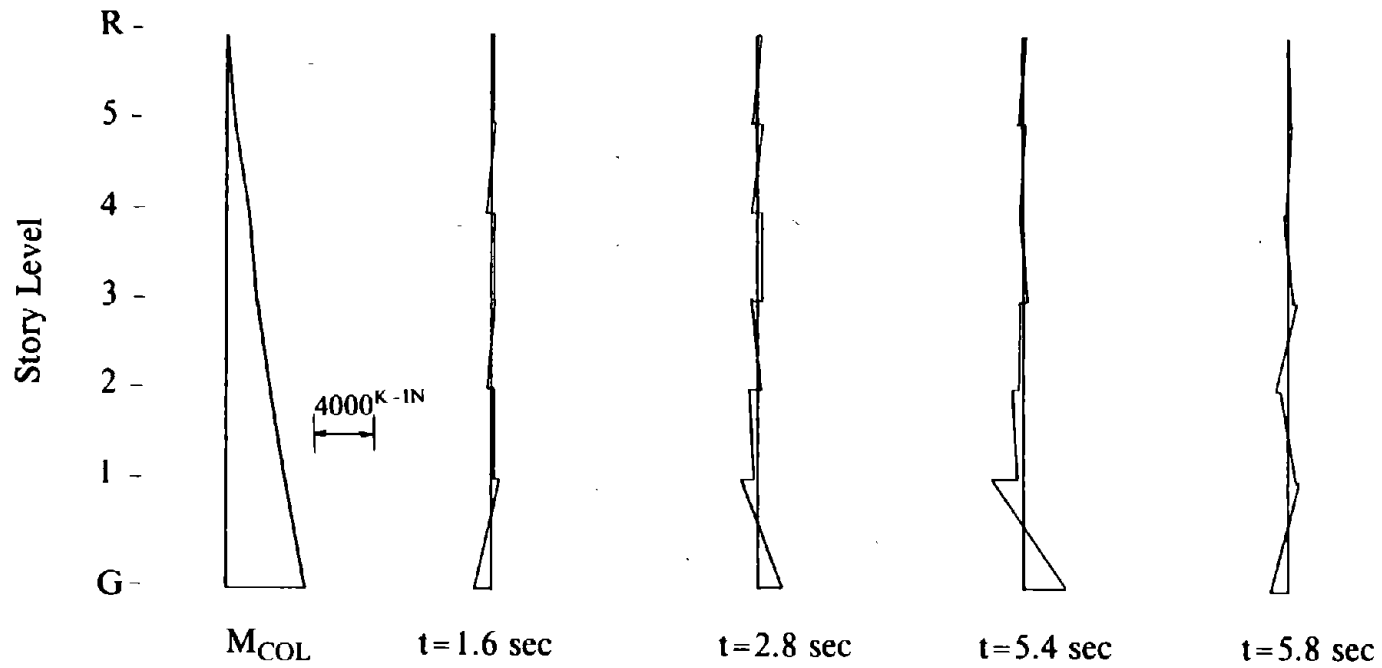
Fig. 8.128   Moments in Interior Columns of Design 3 at Selected Times During Response
to 1.5 * El Centro Earthquake, EBF Model with All Moment Connections.

Fig. 8.129   Moments in Exterior Columns of Design 3 at Selected Times During Response to Parkfield Earthquake, EBF Model with Pin Connections.

Fig. 8.130   Moments in Interior Columns of Design 3 at Selected Times During Response
to Parkfield Earthquake, EBF Model with Pin Connections.

Fig. 8.131   Moments in Exterior Columns of Design 3 at Selected Times During Response to Parkfield Earthquake, EBF Model with All Moment Connections.

Fig. 8.132   Moments in Interior Columns of Design 3 at Selected Times During Response
to Parkfield Earthquake, EBF Model with All Moment Connections.

(a) 1.5 * El Centro Earthquake

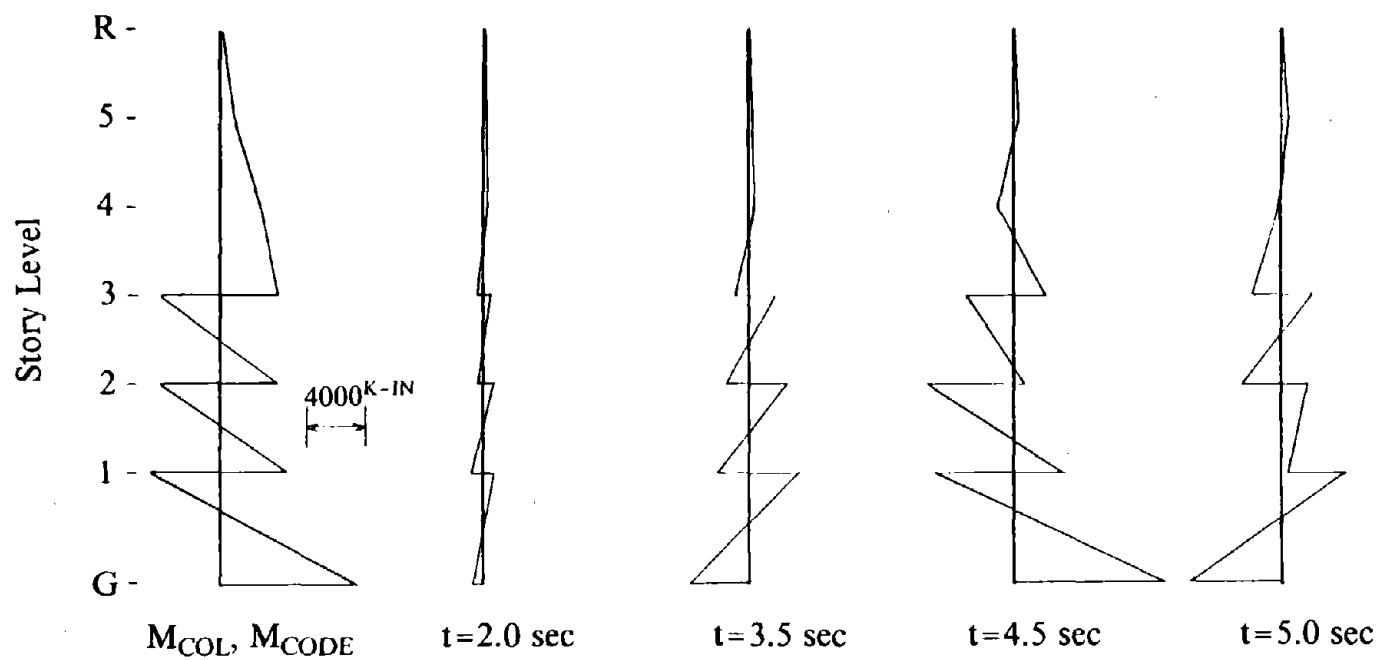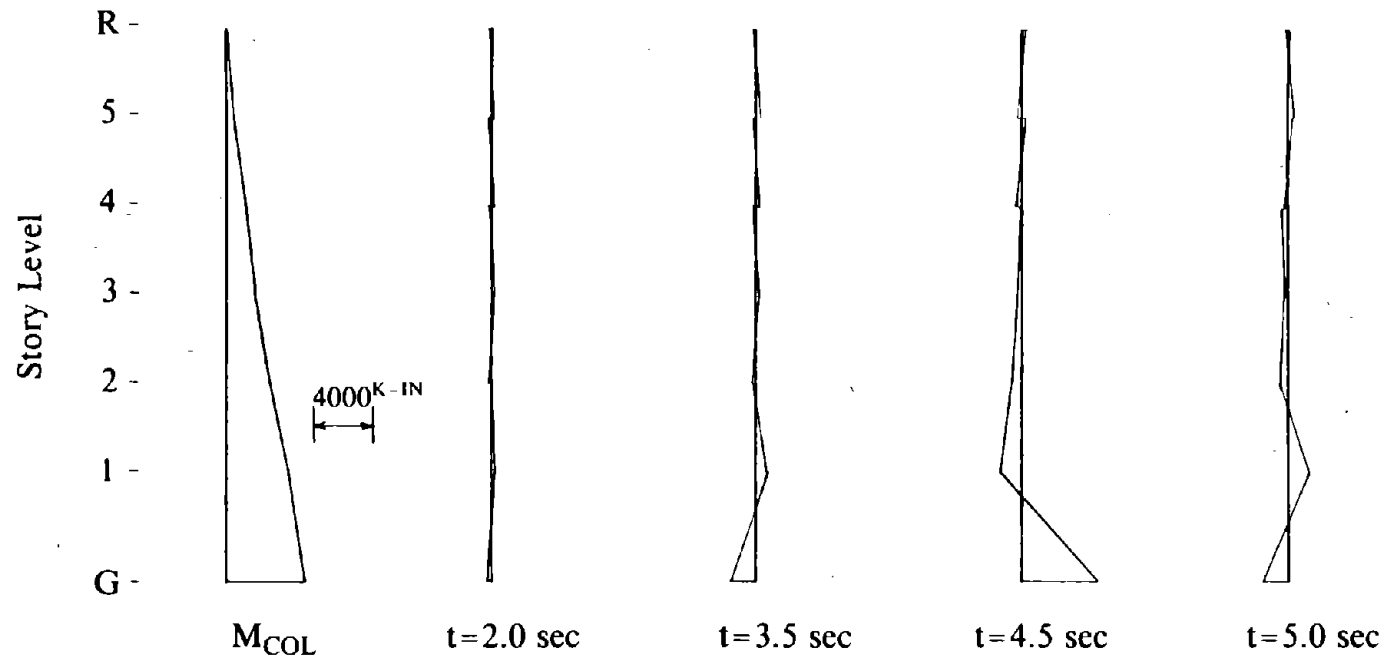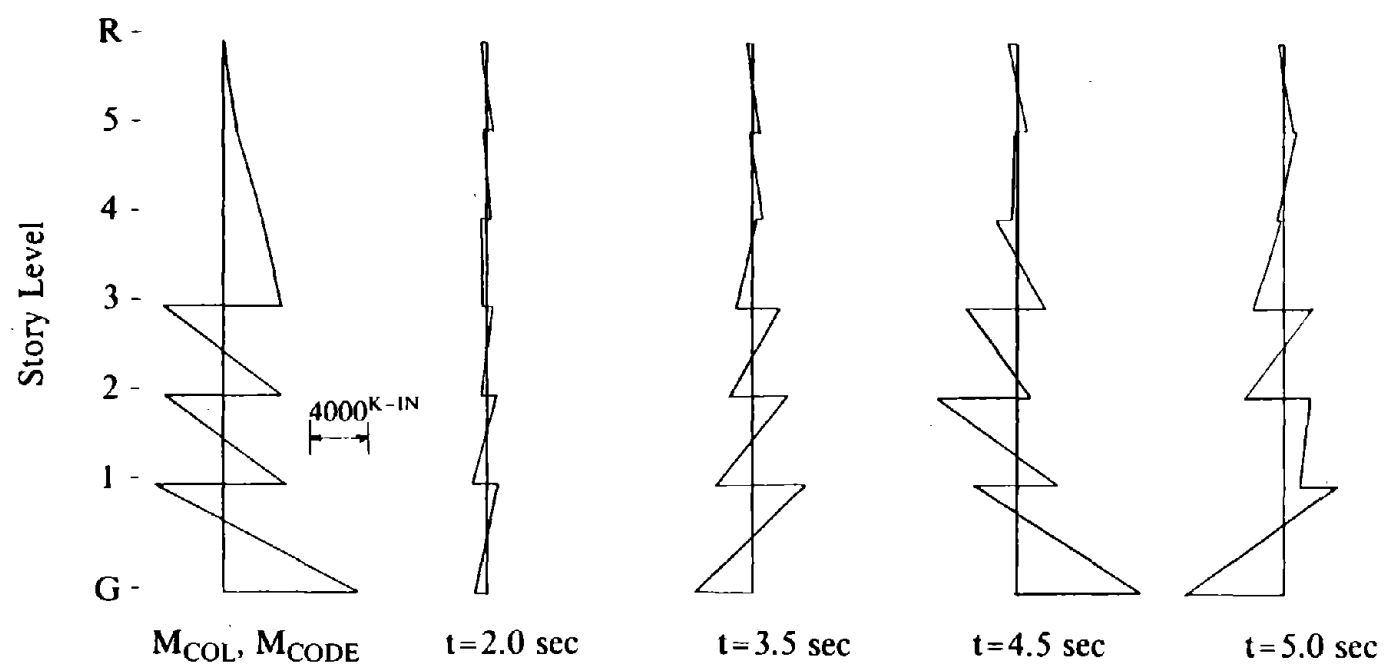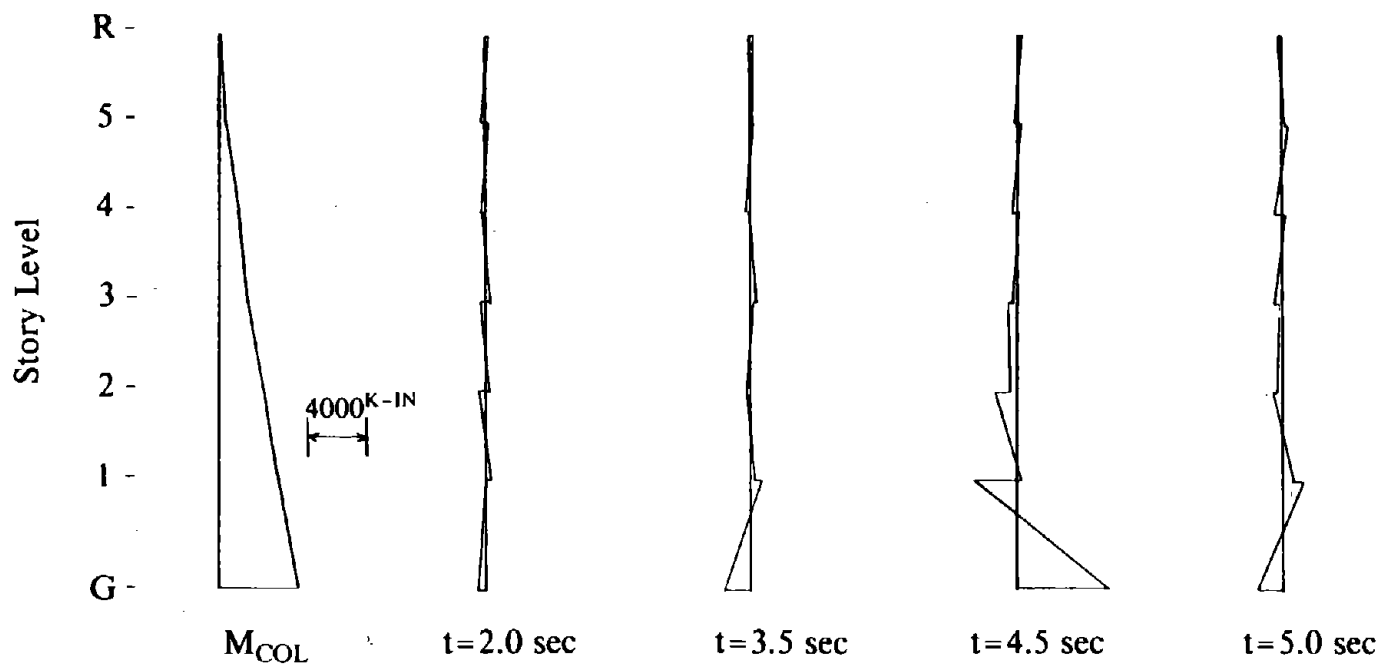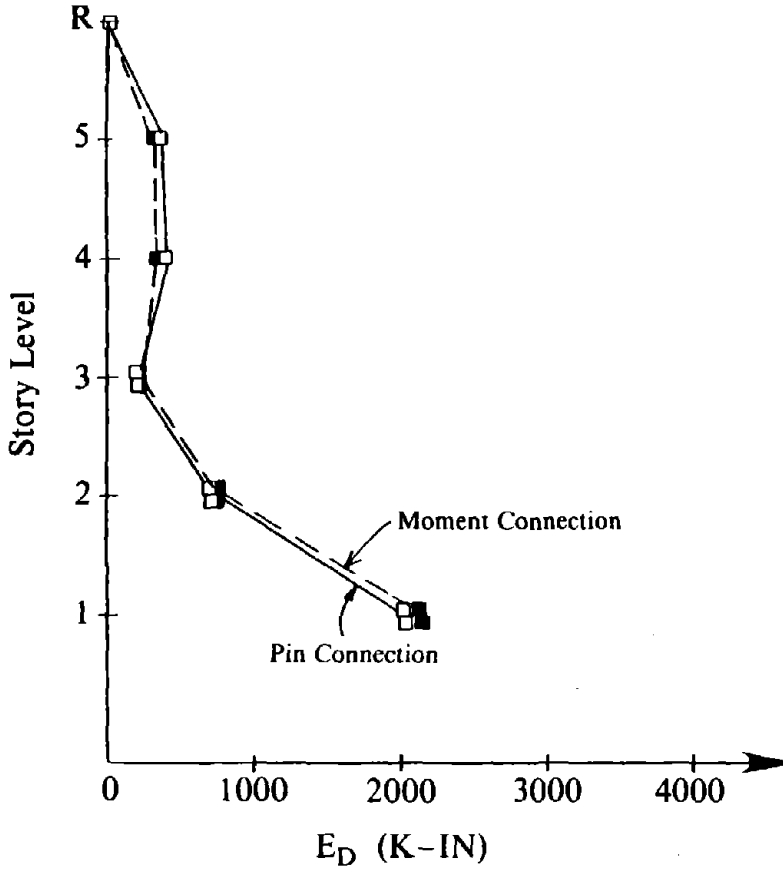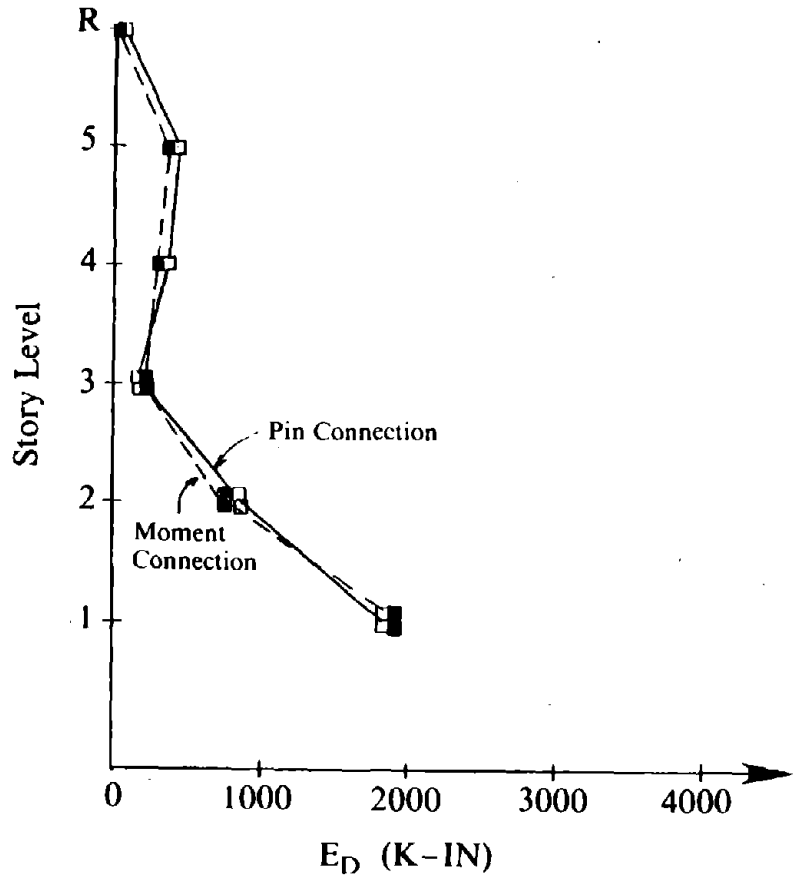(b) Parkfield Earthquake

Fig. 8.133   Hysteretic Energy Dissipated by Links of Design 3.

345

EARTHQUAKE ENGINEERING RESEARCH CENTER REPORT SERIES

EERC reports are available from the National Information Service for Earthquake Engineering(NISEE) and from the National Technical Information Service(NTIS). Numbers in parentheses are Accession Numbers assigned by the National Technical Information Service; these are followed by a price code. Contact NTIS, 5285 Port Royal Road, Springfield Virginia, 22161 for more information. Reports without Accession Numbers were not available from NTIS at the time of printing. For a current complete list of EERC reports (from EERC 67-1) and availablity information, please contact University of California, EERC, NISEE, 1301 South 46th Street, Richmond, California 94804.

UCB/EERC-80/01 "Earthquake Response of Concrete Gravity Dams Including Hydrodynamic and Foundation Interaction Effects," by Chopra, A.K., Chakrabarti, P. and Gupta, S., January 1980, (AD-A087297)A10.

UCB/EERC-80/02 "Rocking Response of Rigid Blocks to Earthquakes," by Yim, C.S., Chopra, A.K. and Penzien, J., January 1980, (PB80 166 002)A04.

UCB/EERC-80/03 "Optimum Inelastic Design of Seismic-Resistant Reinforced Concrete Frame Structures," by Zagajeski, S.W. and Bertero, V.V., January 1980, (PB80 164 635)A06.

UCB/EERC-80/04 "Effects of Amount and Arrangement of Wall-Panel Reinforcement on Hysteretic Behavior of Reinforced Concrete Walls," by Iliya, R. and Bertero, V.V., February 1980, (PB81 122 525)A09.

UCB/EERC-80/05 "Shaking Table Research on Concrete Dam Models," by Niwa, A. and Clough, R.W., September 1980, (PB81 122 368)A06.

UCB/EERC-80/06 "The Design of Steel Energy-Absorbing Restrainers and their Incorporation into Nuclear Power Plants for Enhanced Safety (Vol 1a): Piping with Energy Absorbing Restrainers: Parameter Study on Small Systems," by Powell, G.H., Oughourlian, C. and Simons, J., June 1980.

UCB/EERC-80/07 "Inelastic Torsional Response of Structures Subjected to Earthquake Ground Motions," by Yamazaki, Y., April 1980, (PB81 122 327)A08.

UCB/EERC-80/08 "Study of X-Braced Steel Frame Structures under Earthquake Simulation," by Ghanaat, Y., April 1980, (PB81 122 335)A11.

UCB/EERC-80/09 "Hybrid Modelling of Soil-Structure Interaction," by Gupta, S., Lin, T.W. and Penzien, J., May 1980, (PB81 122 319)A07.

UCB/EERC-80/10 "General Applicability of a Nonlinear Model of a One Story Steel Frame," by Sveinsson, B.I. and McNiven, H.D., May 1980, (PB81 124 877)A06.

UCB/EERC-80/11 "A Green-Function Method for Wave Interaction with a Submerged Body," by Kioka, W., April 1980, (PB81 122 269)A07.

UCB/EERC-80/12 "Hydrodynamic Pressure and Added Mass for Axisymmetric Bodies.," by Nilrat, F., May 1980, (PB81 122 343)A08.

UCB/EERC-80/13 "Treatment of Non-Linear Drag Forces Acting on Offshore Platforms," by Dao, B.V. and Penzien, J., May 1980, (PB81 153 413)A07.

UCB/EERC-80/14 "2D Plane/Axisymmetric Solid Element (Type 3-Elastic or Elastic-Perfectly Plastic) for the ANSR-II Program," by Mondkar, D.P. and Powell, G.H., July 1980, (PB81 122 350)A03.

UCB/EERC-80/15 "A Response Spectrum Method for Random Vibrations," by Der Kiureghian, A., June 1981, (PB81 122 301)A03.

UCB/EERC-80/16 "Cyclic Inelastic Buckling of Tubular Steel Braces," by Zayas, V.A., Popov, E.P. and Martin, S.A., June 1981, (PB81 124 885)A10.

UCB/EERC-80/17 "Dynamic Response of Simple Arch Dams Including Hydrodynamic Interaction," by Porter, C.S. and Chopra, A.K., July 1981, (PB81 124 000)A13.

UCB/EERC-80/18 "Experimental Testing of a Friction Damped Aseismic Base Isolation System with Fail-Safe Characteristics," by Kelly, J.M., Beucke, K.E. and Skinner, M.S., July 1980, (PB81 148 595)A04.

UCB/EERC-80/19 "The Design of Steel Emergy-Absorbing Restrainers and their Incorporation into Nuclear Power Plants for Enhanced Safety (Vol.1B): Stochastic Seismic Analyses of Nuclear Power Plant Structures and Piping Systems Subjected to Multiple Supported Excitations," by Lee, M.C. and Penzien, J., June 1980, (PB82 201 872)A08.

UCB/EERC-80/20 "The Design of Steel Energy-Absorbing Restrainers and their Incorporation into Nuclear Power Plants for Enhanced Safety (Vol 1C): Numerical Method for Dynamic Substructure Analysis," by Dickens, J.M. and Wilson, E.L., June 1980.

UCB/EERC-80/21 "The Design of Steel Energy-Absorbing Restrainers and their Incorporation into Nuclear Power Plants for Enhanced Safety (Vol 2): Development and Testing of Restraints for Nuclear Piping Systems," by Kelly, J.M. and Skinner, M.S., June 1980.

UCB/EERC-80/22 "3D Solid Element (Type 4-Elastic or Elastic-Perfectly-Plastic) for the ANSR-II Program," by Mondkar, D.P. and Powell, G.H., July 1980, (PB81 123 242)A03.

UCB/EERC-80/23 "Gap-Friction Element (Type 5) for the Ansr-II Program," by Mondkar, D.P. and Powell, G.H., July 1980, (PB81 122 285)A03.

UCB/EERC-80/24 "U-Bar Restraint Element (Type 11) for the ANSR-II Program," by Oughourlian, C. and Powell, G.H., July 1980, (PB81 122 293)A03.

UCB/EERC-80/25 "Testing of a Natural Rubber Base Isolation System by an Explosively Simulated Earthquake," by Kelly, J.M., August 1980, (PB81 201 360)A04.

UCB/EERC-80/26 "Input Identification from Structural Vibrational Response," by Hu, Y., August 1980, (PB81 152 308)A05.

UCB/EERC-80/27 "Cyclic Inelastic Behavior of Steel Offshore Structures," by Zayas, V.A., Mahin, S.A. and Popov, E.P., August 1980, (PB81 196 180)A15.

UCB/EERC-80/28 "Shaking Table Testing of a Reinforced Concrete Frame with Biaxial Response," by Oliva, M.G., October 1980, (PB81 154 304)A10.

UCB/EERC-80/29 "Dynamic Properties of a Twelve-Story Prefabricated Panel Building," by Bouwkamp, J.G., Kollegger, J.P. and Stephen, R.M., October 1980, (PB82 138 777)A07.

UCB/EERC-80/30 "Dynamic Properties of an Eight-Story Prefabricated Panel Building," by Bouwkamp, J.G., Kollegger, J.P. and Stephen, R.M., October 1980, (PB81 200 313)A05.

UCB/EERC-80/31 "Predictive Dynamic Response of Panel Type Structures under Earthquakes," by Kollegger, J.P. and Bouwkamp, J.G., October 1980, (PB81 152 316)A04.

UCB/EERC-80/32   "The Design of Steel Energy-Absorbing Restrainers and their Incorporation into Nuclear Power Plants for Enhanced Safety (Vol 3): Testing of Commercial Steels in Low-Cycle Torsional Fatigue," by Spanner, P., Parker, E.R., Jongewaard, E. and Dory, M., 1980.

UCB/EERC-80/33   "The Design of Steel Energy-Absorbing Restrainers and their Incorporation into Nuclear Power Plants for Enhanced Safety (Vol 4): Shaking Table Tests of Piping Systems with Energy-Absorbing Restrainers," by Stiemer, S.F. and Godden, W.G., September 1980, (PB82 201 880)A05.

UCB/EERC-80/34   "The Design of Steel Energy-Absorbing Restrainers and their Incorporation into Nuclear Power Plants for Enhanced Safety (Vol 5): Summary Report," by Spencer, P., 1980.

UCB/EERC-80/35   "Experimental Testing of an Energy-Absorbing Base Isolation System," by Kelly, J.M., Skinner, M.S. and Beucke, K.E., October 1980, (PB81 154 072)A04.

UCB/EERC-80/36   "Simulating and Analyzing Artificial Non-Stationary Earth Ground Motions," by Nau, R.F., Oliver, R.M. and Pister, K.S., October 1980, (PB81 153 397)A04.

UCB/EERC-80/37   "Earthquake Engineering at Berkeley - 1980," by , September 1980, (PB81 205 674)A09.

UCB/EERC-80/38   "Inelastic Seismic Analysis of Large Panel Buildings," by Schricker, V. and Powell, G.H., September 1980, (PB81 154 338)A13.

UCB/EERC-80/39   "Dynamic Response of Embankment, Concrete-Gavity and Arch Dams Including Hydrodynamic Interation," by Hall, J.F. and Chopra, A.K., October 1980, (PB81 152 324)A11.

UCB/EERC-80/40   "Inelastic Buckling of Steel Struts under Cyclic Load Reversal," by Black, R.G. , Wenger, W.A. and Popov, E.P., October 1980, (PB81 154 312)A08.

UCB/EERC-80/41   "Influence of Site Characteristics on Buildings Damage during the October 3,1974 Lima Earthquake," by Repetto, P., Arango, I. and Seed, H.B., September 1980, (PB81 161 739)A05.

UCB/EERC-80/42   "Evaluation of a Shaking Table Test Program on Response Behavior of a Two Story Reinforced Concrete Frame," by Blondet, J.M., Clough, R.W. and Mahin, S.A., December 1980, (PB82 196 544)A11.

UCB/EERC-80/43   "Modelling of Soil-Structure Interaction by Finite and Infinite Elements," by Medina, F., December 1980, (PB81 229 270)A04.

UCB/EERC-81/01   "Control of Seismic Response of Piping Systems and Other Structures by Base Isolation," by Kelly, J.M., January 1981, (PB81 200 735)A05.

UCB/EERC-81/02   "OPTNSR- An Interactive Software System for Optimal Design of Statically and Dynamically Loaded Structures with Nonlinear Response," by Bhatti, M.A., Ciampi, V. and Pister, K.S., January 1981, (PB81 218 851)A09.

UCB/EERC-81/03   "Analysis of Local Variations in Free Field Seismic Ground Motions," by Chen, J.-C., Lysmer, J. and Seed, H.B., January 1981, (AD-A099508)A13.

UCB/EERC-81/04   "Inelastic Structural Modeling of Braced Offshore Platforms for Seismic Loading. ," by Zayas, V.A., Shing, P.-S.B., Mahin, S.A. and Popov, E.P., January 1981, (PB82 138 777)A07.

UCB/EERC-81/05   "Dynamic Response of Light Equipment in Structures," by Der Kiureghian, A., Sackman, J.L. and Nour-Omid, B., April 1981, (PB81 218 497)A04.

UCB/EERC-81/06   "Preliminary Experimental Investigation of a Broad Base Liquid Storage Tank," by Bouwkamp, J.G., Kollegger, J.P. and Stephen, R.M., May 1981, (PB82 140 385)A03.

UCB/EERC-81/07   "The Seismic Resistant Design of Reinforced Concrete Coupled Structural Walls," by Aktan, A.E. and Bertero, V.V., June 1981, (PB82 113 358)A11.

UCB/EERC-81/08   "Unassigned," by Unassigned, 1981.

UCB/EERC-81/09   "Experimental Behavior of a Spatial Piping System with Steel Energy Absorbers Subjected to a Simulated Differential Seismic Input," by Stiemer, S.F., Godden, W.G. and Kelly, J.M., July 1981, (PB82 201 898)A04.

UCB/EERC-81/10   "Evaluation of Seismic Design Provisions for Masonry in the United States," by Sveinsson, B.I., Mayes, R.L. and McNiven, H.D., August 1981, (PB82 166 075)A08.

UCB/EERC-81/11   "Two-Dimensional Hybrid Modelling of Soil-Structure Interaction," by Tzong, T.-J., Gupta, S. and Penzien, J., August 1981, (PB82 142 118)A04.

UCB/EERC-81/12   "Studies on Effects of Infills in Seismic Resistant R/C Construction," by Brokken, S. and Bertero, V.V., October 1981, (PB82 166 190)A09.

UCB/EERC-81/13   "Linear Models to Predict the Nonlinear Seismic Behavior of a One-Story Steel Frame," by Valdimarsson, H., Shah, A.H. and McNiven, H.D., September 1981, (PB82 138 793)A07.

UCB/EERC-81/14   "TLUSH: A Computer Program for the Three-Dimensional Dynamic Analysis of Earth Dams," by Kagawa, T., Mejia, L.H., Seed, H.B. and Lysmer, J., September 1981, (PB82 139 940)A06.

UCB/EERC-81/15   "Three Dimensional Dynamic Response Analysis of Earth Dams," by Mejia, L.H. and Seed, H.B., September 1981, (PB82 137 274)A12.

UCB/EERC-81/16   "Experimental Study of Lead and Elastomeric Dampers for Base Isolation Systems," by Kelly, J.M. and Hodder, S.B., October 1981, (PB82 166 182)A05.

UCB/EERC-81/17   "The Influence of Base Isolation on the Seismic Response of Light Secondary Equipment," by Kelly, J.M., April 1981, (PB82 255 266)A04.

UCB/EERC-81/18   "Studies on Evaluation of Shaking Table Response Analysis Procedures," by Blondet, J. Marcial, November 1981, (PB82 197 278)A10.

UCB/EERC-81/19   "DELIGHT.STRUCT: A Computer-Aided Design Environment for Structural Engineering ," by Balling, R.J., Pister, K.S. and Polak, E., December 1981, (PB82 218 496)A07.

UCB/EERC-81/20   "Optimal Design of Seismic-Resistant Planar Steel Frames," by Balling, R.J., Ciampi, V. and Pister, K.S., December 1981, (PB82 220 179)A07.

UCB/EERC-82/01 "Dynamic Behavior of Ground for Seismic Analysis of Lifeline Systems," by Sato, T. and Der Kiureghian, A., January 1982, (PB82 218 926)A05.

UCB/EERC-82/02 "Shaking Table Tests of a Tubular Steel Frame Model," by Ghanaat, Y. and Clough, R.W., January 1982, (PB82 220 161)A07.

UCB/EERC-82/03 "Behavior of a Piping System under Seismic Excitation: Experimental Investigations of a Spatial Piping System supported by Mechanical Shock Arrestors," by Schneider, S., Lee, H.-M. and Godden, W. G., May 1982, (PB83 172 544)A09.

UCB/EERC-82/04 "New Approaches for the Dynamic Analysis of Large Structural Systems," by Wilson, E.L., June 1982, (PB83 148 080)A05.

UCB/EERC-82/05 "Model Study of Effects of Damage on the Vibration Properties of Steel Offshore Platforms," by Shahrivar, F. and Bouwkamp, J.G., June 1982, (PB83 148 742)A10.

UCB/EERC-82/06 "States of the Art and Pratice in the Optimum Seismic Design and Analytical Response Prediction of R/C Frame Wall Structures," by Aktan, A.E. and Bertero, V.V., July 1982, (PB83 147 736)A05.

UCB/EERC-82/07 "Further Study of the Earthquake Response of a Broad Cylindrical Liquid-Storage Tank Model," by Manos, G.C. and Clough, R.W., July 1982, (PB83 147 744)A11.

UCB/EERC-82/08 "An Evaluation of the Design and Analytical Seismic Response of a Seven Story Reinforced Concrete Frame," by Charney, F.A. and Bertero, V.V., July 1982, (PB83 157 628)A09.

UCB/EERC-82/09 "Fluid-Structure Interactions: Added Mass Computations for Incompressible Fluid," by Kuo, J.S.-H., August 1982, (PB83 156 281)A07.

UCB/EERC-82/10 "Joint-Opening Nonlinear Mechanism: Interface Smeared Crack Model," by Kuo, J.S.-H., August 1982, (PB83 149 195)A05.

UCB/EERC-82/11 "Dynamic Response Analysis of Techi Dam," by Clough, R.W., Stephen, R.M. and Kuo, J.S.-H., August 1982, (PB83 147 496)A06.

UCB/EERC-82/12 "Prediction of the Seismic Response of R/C Frame-Coupled Wall Structures," by Aktan, A.E., Bertero, V.V. and Piazzo, M., August 1982, (PB83 149 203)A09.

UCB/EERC-82/13 "Preliminary Report on the Smart 1 Strong Motion Array in Taiwan," by Bolt, B.A., Loh, C.H., Penzien, J. and Tsai, Y.B., August 1982, (PB83 159 400)A10.

UCB/EERC-82/14 "Shaking-Table Studies of an Eccentrically X-Braced Steel Structure," by Yang, M.S., September 1982, (PB83 260 778)A12.

UCB/EERC-82/15 "The Performance of Stairways in Earthquakes," by Roha, C., Axley, J.W. and Bertero, V.V., September 1982, (PB83 157 693)A07.

UCB/EERC-82/16 "The Behavior of Submerged Multiple Bodies in Earthquakes," by Liao, W.-G., September 1982, (PB83 158 709)A07.

UCB/EERC-82/17 "Effects of Concrete Types and Loading Conditions on Local Bond-Slip Relationships," by Cowell, A.D., Popov, E.P. and Bertero, V.V., September 1982, (PB83 153 577)A04.

UCB/EERC-82/18 "Mechanical Behavior of Shear Wall Vertical Boundary Members: An Experimental Investigation," by Wagner, M.T. and Bertero, V.V., October 1982, (PB83 159 764)A05.

UCB/EERC-82/19 "Experimental Studies of Multi-support Seismic Loading on Piping Systems," by Kelly, J.M. and Cowell, A.D., November 1982.

UCB/EERC-82/20 "Generalized Plastic Hinge Concepts for 3D Beam-Column Elements," by Chen, P. F.-S. and Powell, G.H., November 1982, (PB83 247 981)A13.

UCB/EERC-82/21 "ANSR-II: General Computer Program for Nonlinear Structural Analysis," by Oughourlian, C.V. and Powell, G.H., November 1982, (PB83 251 330)A12.

UCB/EERC-82/22 "Solution Strategies for Statically Loaded Nonlinear Structures," by Simons, J.W. and Powell, G.H., November 1982, (PB83 197 970)A06.

UCB/EERC-82/23 "Analytical Model of Deformed Bar Anchorages under Generalized Excitations," by Ciampi, V., Eligehausen, R., Bertero, V.V. and Popov, E.P., November 1982, (PB83 169 532)A06.

UCB/EERC-82/24 "A Mathematical Model for the Response of Masonry Walls to Dynamic Excitations," by Sucuoglu, H., Mengi, Y. and McNiven, H.D., November 1982, (PB83 169 011)A07.

UCB/EERC-82/25 "Earthquake Response Considerations of Broad Liquid Storage Tanks," by Cambra, F.J., November 1982, (PB83 251 215)A09.

UCB/EERC-82/26 "Computational Models for Cyclic Plasticity, Rate Dependence and Creep," by Mosaddad, B. and Powell, G.H., November 1982, (PB83 245 829)A08.

UCB/EERC-82/27 "Inelastic Analysis of Piping and Tubular Structures," by Mahasuverachai, M. and Powell, G.H., November 1982, (PB83 249 987)A07.

UCB/EERC-83/01 "The Economic Feasibility of Seismic Rehabilitation of Buildings by Base Isolation," by Kelly, J.M., January 1983, (PB83 197 988)A05.

UCB/EERC-83/02 "Seismic Moment Connections for Moment-Resisting Steel Frames.," by Popov, E.P., January 1983, (PB83 195 412)A04.

UCB/EERC-83/03 "Design of Links and Beam-to-Column Connections for Eccentrically Braced Steel Frames," by Popov, E.P. and Malley, J.O., January 1983, (PB83 194 811)A04.

UCB/EERC-83/04 "Numerical Techniques for the Evaluation of Soil-Structure Interaction Effects in the Time Domain," by Bayo, E. and Wilson, E.L., February 1983, (PB83 245 605)A09.

UCB/EERC-83/05 "A Transducer for Measuring the Internal Forces in the Columns of a Frame-Wall Reinforced Concrete Structure," by Sause, R. and Bertero, V.V., May 1983, (PB84 119 494)A06.

UCB/EERC-83/06 "Dynamic Interactions Between Floating Ice and Offshore Structures," by Croteau, P., May 1983, (PB84 119 486)A16.

UCB/EERC-83/07 "Dynamic Analysis of Multiply Tuned and Arbitrarily Supported Secondary Systems," by Igusa, T. and Der Kiureghian, A., July 1983, (PB84 118 272)A11.

UCB/EERC-83/08 "A Laboratory Study of Submerged Multi-body Systems in Earthquakes," by Ansari, G.R., June 1983, (PB83 261 842)A17.

UCB/EERC-83/09 "Effects of Transient Foundation Uplift on Earthquake Response of Structures," by Yim, C.-S. and Chopra, A.K., June 1983, (PB83 261 396)A07.

348

UCB/EERC-83/10   "Optimal Design of Friction-Braced Frames under Seismic Loading," by Austin, M.A. and Pister, K.S., June 1983, (PB84 119 288)A06.

UCB/EERC-83/11   "Shaking Table Study of Single-Story Masonry Houses: Dynamic Performance under Three Component Seismic Input and Recommendations," by Manos, G.C., Clough, R.W. and Mayes, R.L., July 1983, (UCB/EERC-83/11)A08.

UCB/EERC-83/12   "Experimental Error Propagation in Pseudodynamic Testing," by Shiing, P.B. and Mahin, S.A., June 1983, (PB84 119 270)A09.

UCB/EERC-83/13   "Experimental and Analytical Predictions of the Mechanical Characteristics of a 1/5-scale Model of a 7-story R/C Frame-Wall Building Structure," by Aktan, A.E., Bertero, V.V., Chowdhury, A.A. and Nagashima, T., June 1983, (PB84 119 213)A07.

UCB/EERC-83/14   "Shaking Table Tests of Large-Panel Precast Concrete Building System Assemblages," by Oliva, M.G. and Clough, R.W., June 1983, (PB86 110 210/AS)A11.

UCB/EERC-83/15   "Seismic Behavior of Active Beam Links in Eccentrically Braced Frames," by Hjelmstad, K.D. and Popov, E.P., July 1983, (PB84 119 676)A09.

UCB/EERC-83/16   "System Identification of Structures with Joint Rotation," by Dimsdale, J.S., July 1983, (PB84 192 210)A06.

UCB/EERC-83/17   "Construction of Inelastic Response Spectra for Single-Degree-of-Freedom Systems," by Mahin, S. and Lin, J., June 1983, (PB84 208 834)A05.

UCB/EERC-83/18   "Interactive Computer Analysis Methods for Predicting the Inelastic Cyclic Behaviour of Structural Sections," by Kaba, S. and Mahin, S., July 1983, (PB84 192 012)A06.

UCB/EERC-83/19   "Effects of Bond Deterioration on Hysteretic Behavior of Reinforced Concrete Joints," by Filippou, F.C., Popov, E.P. and Bertero, V.V., August 1983, (PB84 192 020)A10.

UCB/EERC-83/20   "Analytical and Experimental Correlation of Large-Panel Precast Building System Performance," by Oliva, M.G., Clough, R.W., Velkov, M. and Gavrilovic, P., November 1983.

UCB/EERC-83/21   "Mechanical Characteristics of Materials Used in a 1/5 Scale Model of a 7-Story Reinforced Concrete Test Structure," by Bertero, V.V., Aktan, A.E., Harris, H.G. and Chowdhury, A.A., October 1983, (PB84 193 697)A05.

UCB/EERC-83/22   "Hybrid Modelling of Soil-Structure Interaction in Layered Media," by Tzong, T.-J. and Penzien, J., October 1983, (PB84 192 178)A08.

UCB/EERC-83/23   "Local Bond Stress-Slip Relationships of Deformed Bars under Generalized Excitations," by Eligehausen, R., Popov, E.P. and Bertero, V.V., October 1983, (PB84 192 848)A09.

UCB/EERC-83/24   "Design Considerations for Shear Links in Eccentrically Braced Frames," by Malley, J.O. and Popov, E.P., November 1983, (PB84 192 186)A07.

UCB/EERC-84/01   "Pseudodynamic Test Method for Seismic Performance Evaluation: Theory and Implementation," by Shing, P.-S. B. and Mahin, S.A., January 1984, (PB84 190 644)A08.

UCB/EERC-84/02   "Dynamic Response Behavior of Kiang Hong Dian Dam," by Clough, R.W., Chang, K.-T., Chen, H.-Q. and Stephen, R.M., April 1984, (PB84 209 402)A08.

UCB/EERC-84/03   "Refined Modelling of Reinforced Concrete Columns for Seismic Analysis," by Kaba, S.A. and Mahin, S.A., April 1984, (PB84 234 384)A06.

UCB/EERC-84/04   "A New Floor Response Spectrum Method for Seismic Analysis of Multiply Supported Secondary Systems," by Asfura, A. and Der Kiureghian, A., June 1984, (PB84 239 417)A06.

UCB/EERC-84/05   "Earthquake Simulation Tests and Associated Studies of a 1/5th-scale Model of a 7-Story R/C Frame-Wall Test Structure," by Bertero, V.V., Aktan, A.E., Charney, F.A. and Sause, R., June 1984, (PB84 239 409)A09.

UCB/EERC-84/06   "R/C Structural Walls: Seismic Design for Shear," by Aktan, A.E. and Bertero, V.V., 1984.

UCB/EERC-84/07   "Behavior of Interior and Exterior Flat-Plate Connections subjected to Inelastic Load Reversals," by Zee, H.L. and Moehle, J.P., August 1984, (PB86 117 629/AS)A07.

UCB/EERC-84/08   "Experimental Study of the Seismic Behavior of a Two-Story Flat-Plate Structure," by Moehle, J.P. and Diebold, J.W., August 1984, (PB86 122 553/AS)A12.

UCB/EERC-84/09   "Phenomenological Modeling of Steel Braces under Cyclic Loading," by Ikeda, K., Mahin, S.A. and Dermitzakis, S.N., May 1984, (PB86 132 198/AS)A08.

UCB/EERC-84/10   "Earthquake Analysis and Response of Concrete Gravity Dams," by Fenves, G. and Chopra, A.K., August 1984, (PB85 193 902/AS)A11.

UCB/EERC-84/11   "EAGD-84: A Computer Program for Earthquake Analysis of Concrete Gravity Dams," by Fenves, G. and Chopra, A.K., August 1984, (PB85 193 613/AS)A05.

UCB/EERC-84/12   "A Refined Physical Theory Model for Predicting the Seismic Behavior of Braced Steel Frames," by Ikeda, K. and Mahin, S.A., July 1984, (PB85 191 450/AS)A09.

UCB/EERC-84/13   "Earthquake Engineering Research at Berkeley - 1984," by , August 1984, (PB85 197 341/AS)A10.

UCB/EERC-84/14   "Moduli and Damping Factors for Dynamic Analyses of Cohesionless Soils," by Seed, H.B., Wong, R.T., Idriss, I.M. and Tokimatsu, K., September 1984, (PB85 191 468/AS)A04.

UCB/EERC-84/15   "The Influence of SPT Procedures in Soil Liquefaction Resistance Evaluations," by Seed, H.B., Tokimatsu, K., Harder, L.F. and Chung, R.M., October 1984, (PB85 191 732/AS)A04.

UCB/EERC-84/16   "Simplified Procedures for the Evaluation of Settlements in Sands Due to Earthquake Shaking," by Tokimatsu, K. and Seed, H.B., October 1984, (PB85 197 887/AS)A03.

UCB/EERC-84/17   "Evaluation of Energy Absorption Characteristics of Bridges under Seismic Conditions," by Imbsen, R.A. and Penzien, J., November 1984.

UCB/EERC-84/18   "Structure-Foundation Interactions under Dynamic Loads," by Liu, W.D. and Penzien, J., November 1984, (PB87 124 889/AS)A11.

UCB/EERC-84/19 "Seismic Modelling of Deep Foundations," by Chen, C.-H. and Penzien, J., November 1984, (PB87 124 798/AS)A07.

UCB/EERC-84/20 "Dynamic Response Behavior of Quan Shui Dam," by Clough, R.W., Chang, K.-T., Chen, H.-Q., Stephen, R.M., Ghanaat, Y. and Qi, J.-H., November 1984, (PB86 115177/AS)A07.

UCB/EERC-85/01 "Simplified Methods of Analysis for Earthquake Resistant Design of Buildings," by Cruz, E.F. and Chopra, A.K., February 1985, (PB86 112299/AS)A12.

UCB/EERC-85/02 "Estimation of Seismic Wave Coherency and Rupture Velocity using the SMART 1 Strong-Motion Array Recordings," by Abrahamson, N.A., March 1985, (PB86 214 343)A07.

UCB/EERC-85/03 "Dynamic Properties of a Thirty Story Condominium Tower Building," by Stephen, R.M., Wilson, E.L. and Stander, N., April 1985, (PB86 118965/AS)A06.

UCB/EERC-85/04 "Development of Substructuring Techniques for On-Line Computer Controlled Seismic Performance Testing," by Dermitzakis, S. and Mahin, S., February 1985, (PB86 132941/AS)A08.

UCB/EERC-85/05 "A Simple Model for Reinforcing Bar Anchorages under Cyclic Excitations," by Filippou, F.C., March 1985, (PB86 112 919/AS)A05.

UCB/EERC-85/06 "Racking Behavior of Wood-framed Gypsum Panels under Dynamic Load," by Oliva, M.G., June 1985.

UCB/EERC-85/07 "Earthquake Analysis and Response of Concrete Arch Dams," by Fok, K.-L. and Chopra, A.K., June 1985, (PB86 139672/AS)A10.

UCB/EERC-85/08 "Effect of Inelastic Behavior on the Analysis and Design of Earthquake Resistant Structures," by Lin, J.P. and Mahin, S.A., June 1985, (PB86 135340/AS)A08.

UCB/EERC-85/09 "Earthquake Simulator Testing of a Base-Isolated Bridge Deck," by Kelly, J.M., Buckle, I.G. and Tsai, H.-C., January 1986, (PB87 124 152/AS)A06.

UCB/EERC-85/10 "Simplified Analysis for Earthquake Resistant Design of Concrete Gravity Dams," by Fenves, G. and Chopra, A.K., June 1986, (PB87 124 160/AS)A08.

UCB/EERC-85/11 "Dynamic Interaction Effects in Arch Dams," by Clough, R.W., Chang, K.-T., Chen, H.-Q. and Ghanaat, Y., October 1985, (PB86 135027/AS)A05.

UCB/EERC-85/12 "Dynamic Response of Long Valley Dam in the Mammoth Lake Earthquake Series of May 25-27, 1980," by Lai, S. and Seed, H.B., November 1985, (PB86 142304/AS)A05.

UCB/EERC-85/13 "A Methodology for Computer-Aided Design of Earthquake-Resistant Steel Structures," by Austin, M.A., Pister, K.S. and Mahin, S.A., December 1985, (PB86 159480/AS)A10 .

UCB/EERC-85/14 "Response of Tension-Leg Platforms to Vertical Seismic Excitations," by Liou, G.-S., Penzien, J. and Yeung, R.W., December 1985, (PB87 124 871/AS)A08.

UCB/EERC-85/15 "Cyclic Loading Tests of Masonry Single Piers: Volume 4 - Additional Tests with Height to Width Ratio of 1," by Sveinsson, B., McNiven, H.D. and Sucuoglu, H., December 1985.

UCB/EERC-85/16 "An Experimental Program for Studying the Dynamic Response of a Steel Frame with a Variety of Infill Partitions," by Yanev, B. and McNiven, H.D., December 1985.

UCB/EERC-86/01 "A Study of Seismically Resistant Eccentrically Braced Steel Frame Systems," by Kasai, K. and Popov, E.P., January 1986, (PB87 124 178/AS)A14.

UCB/EERC-86/02 "Design Problems in Soil Liquefaction," by Seed, H.B., February 1986, (PB87 124 186/AS)A03.

UCB/EERC-86/03 "Implications of Recent Earthquakes and Research on Earthquake-Resistant Design and Construction of Buildings," by Bertero, V.V., March 1986, (PB87 124 194/AS)A05.

UCB/EERC-86/04 "The Use of Load Dependent Vectors for Dynamic and Earthquake Analyses," by Leger, P., Wilson, E.L. and Clough, R.W., March 1986, (PB87 124 202/AS)A12.

UCB/EERC-86/05 "Two Beam-To-Column Web Connections," by Tsai, K.-C. and Popov, E.P., April 1986 , (PB87 124 301/AS)A04.

UCB/EERC-86/06 "Determination of Penetration Resistance for Coarse-Grained Soils using the Becker Hammer Drill," by Harder, L.F. and Seed, H.B., May 1986, (PB87 124 210/AS)A07.

UCB/EERC-86/07 "A Mathematical Model for Predicting the Nonlinear Response of Unreinforced Masonry Walls to In-Plane Earthquake Excitations," by Mengi, Y. and McNiven, H.D., May 1986, (PB87 124 780/AS)A06.

UCB/EERC-86/08 "The 19 September 1985 Mexico Earthquake: Building Behavior," by Bertero, V.V., July 1986.

UCB/EERC-86/09 "EACD-3D: A Computer Program for Three-Dimensional Earthquake Analysis of Concrete Dams," by Fok, K.-L., Hall, J.F. and Chopra, A.K., July 1986, (PB87 124 228/AS)A08.

UCB/EERC-86/10 "Earthquake Simulation Tests and Associated Studies of a 0.3-Scale Model of a Six-Story Concentrically Braced Steel Structure," by Uang, C.-M. and Bertero, V.V., December 1986.

UCB/EERC-86/11 "Mechanical Characteristics of Base Isolation Bearings for a Bridge Deck Model Test," by Kelly, J.M., Buckle, I.G. and Koh, C.-G., 1987.

UCB/EERC-86/12 "Modelling of Dynamic Response of Elastomeric Isolation Bearings," by Koh, C.-G. and Kelly, J.M., 1987.

UCB/EERC-87/01 "FPS Earthquake Resisting System: Experimental Report," by Zayas, V.A., Low, S.S. and Mahin, S.A., June 1987.

UCB/EERC-87/02 "Earthquake Simulator Tests and Associated Studies of a 0.3-Scale Model of a Six-Story Eccentrically Braced Steel Structure," by Whittaker, A., Uang, C.-M. and Bertero, V.V., July 1987.

UCB/EERC-87/03 "A Displacement Control and Uplift Restraint Device for Base-Isolated Structures," by Kelly, J.M., Griffith, M.C. and Aiken, I.G., April 1987.

350

UCB/EERC-87/04 "Earthquake Simulator Testing of a Combined Sliding Bearing and Rubber Bearing Isolation System," by Kelly, J.M. and Chalhoub, M.S., 1987.

UCB/EERC-87/05 "Three-Dimensional Inelastic Analysis of Reinforced Concrete Frame-Wall Structures," by Moazzami, S. and Bertero, V.V., May 1987.

UCB/EERC-87/06 "Experiments on Eccentrically Braced Frames With Composite Floors," by Ricles, J. and Popov, E., June 1987.

UCB/EERC-87/07 "Dynamic Analysis of Seismically Resistant Eccentrically Braced Frames," by Ricles, J. and Popov, E., June 1987.